School of Civil and Mechanical Engineering

A Novel Direct Drive Linear Ocean Energy Converter Based on Nonlinear Oscillator System

Raju Ahamed

0000-0001-6205-3229

This thesis is presented for the degree of

Doctor of Philosophy

of

Curtin University

November 2022

Abstract

The traditional wave energy converters (WEC) use hydraulic or turbine type power take-off (PTO) mechanisms which consist of many moving parts, creating complex mechanical components and increasing the installation and maintenance costs. Linear permanent magnet (PM) generator based direct drive WECs could be a solution to overcome this problem, but the efficiency of the single conventional linear PM generator is not high enough, and it cannot work satisfactorily in the low-frequency range. The bandwidth problem of the existing linear PM generator-based PTO system can be overcome by widening the frequency bandwidth of the WEC. Light damping nonlinear oscillators are expected to have larger operational frequency bandwidth than a conventional single-degree-of-freedom (SDOF) linear oscillator. The magnetic levitation (magnetic spring) system can be used in the translator design to make the oscillator nonlinear, which is more effective in the broadband frequency range, especially in the low-frequency ocean environment. However, the characteristics and dynamics of the linear PM generator based on the SDOF nonlinear oscillator system have not been studied yet. In addition, no study thus far has modelled two-degree-of-freedom (2DOF) and three-degree-of-freedom (3DOF) nonlinear oscillator system-based energy harvesters to harness ocean energy. This thesis presents novel analytical, numerical and experimental modelling of SDOF, 2DOF and 3DOF magnetic spring-based energy harvester systems. The design of the SDOF, 2DOF and 3DOF magnetic spring-based nonlinear oscillator systems have been analysed separately with or without winding coils.

At first, the characteristics and dynamics of the SDOF nonlinear oscillator system were studied. The proposed SDOF nonlinear oscillator system consists of a nonmagnetic shaft, a floating magnet and two fixed magnets where all magnets were placed in such a way that all magnets can repel the others. The magnetic properties of the proposed SDOF system were studied numerically and analytically to provide insight into its role in the nonlinear oscillatory behaviour of the system. The effect of the gravitational force, which changes the equilibrium position and the magnetic spring's nonlinear behaviour, were studied. The analytical analysis of the magnetic restoring force was validated using numerical and experimental analysis. Different orders of polynomial curve fittings such as cubic and quintic were used to model the magnetic restoring force between the moving magnet and the two fixed end magnets. The linear and nonlinear coefficients of the magnetic spring-based system for different positions of the floating magnet were investigated. Moreover, the effects of the gravitational

force and magnetic restoring forces were investigated analytically, numerically and experimentally for different heights of the oscillator. For various lengths of the oscillator, the coefficients, damping ratio, and frequency responses of the nonlinear oscillator system were determined. The measured linear and nonlinear stiffnesses of the SDOF nonlinear oscillator system were used to investigate the system's eigenvalues and frequency responses with and without winding coils (electromechanical coupling). The parametric studies were performed to investigate the maximum energy generation abilities of the proposed SDOF energy harvester. The test rig of the energy harvester based on the SDOF nonlinear oscillator system was developed and experimented with within the lab. Experimental results showed validation of the analytical model with the experimental model.

Secondly, the coefficients and dynamics of the 2DOF nonlinear oscillator system were analysed. The proposed 2DOF nonlinear oscillator system consists of a nonmagnetic shaft, two floating magnets and two fixed magnets. The magnetic restoring forces of both floating magnets were measured analytically and validated with the numerical study. The measured linear and nonlinear coefficients of the system were used to investigate the dynamics of the system with and without electromechanical coupling. Moreover, the energy harvester's experimental findings based on the 2DOF nonlinear oscillator system were compared with the analytical results to validate the analytical model. Following this, the 3DOF magnetic spring-based nonlinear oscillator system, which consists of three floating magnets, was studied analytically and experimentally. The magnetic restoring forces and coefficients of the system were determined using the analytical method and compared with the numerical findings. The magnetic properties and dynamics of the 3DOF system were investigated with and without adding winding coils to find the effects of the electromechanical coupling. The 3DOF nonlinear oscillator energy generator test rig was developed and experimented with to validate the analytical model.

Finally, the findings of the SDOF energy harvester were compared with the 2DOF and 3DOF energy harvesters. Comparison results showed that the 3DOF energy harvester could harness maximum energy in low-frequency ranges. In addition, the comparison results of the proposed magnetic spring-based PTO system with the existing magnetic spring-based PTOs system showed that the proposed techniques are more capable of working in broadband frequency ranges which result in harnessing maximum ocean energy. In brief, the outcomes of this research work provide the mathematical foundation for the modelling and upcoming advancement of multi-degree-of-freedom magnetic spring (nonlinear oscillator) based energy generators.

Declaration

To the best of my knowledge and belief, this thesis contains no material previously published by any other person except where due acknowledgment has been made.

This thesis contains no material which has been accepted for the award of any other academic degree or qualification in any university.

Raju Ahamed

07 November 2022

Acknowledgement

"**In the name of Almighty Allah, the most beneficent, most gracious, the most merciful**".

I would like to thank Dr Kristoffer McKee and Emeritus Professor Ian Howard for their guidance, encouragement, and support throughout my PhD studies. It would not have been possible for me to achieve what I have without their commitment, dedication, and persistence. My sincere thanks to Ian Howard for imparting his knowledge about vibrations and electromagnetic systems and his wisdom in research management. In spite of getting distracted by other research ideas, his patience and guidance helped me stay on track. Whenever I had questions about my work, he was always happy to answer them. In addition, I would like to express my sincere gratitude to Dr Kristoffer McKee, who had consistently provided inspirational guidance and support in MATLAB, as well as valuable input when I was writing my thesis.

It is my pleasure to thank the Australian Government for the Research Training Program (RTP) scholarship that I have been awarded to study PhD at Curtin University. I would also like to thank the Curtin Scholarships office for their assistance. My thanks go out to all the friendly staff at Curtin University for supporting my research.

I would also like to acknowledge the support received from Mr Graeme Watson and Mr David Collier to manufacture the test rig and provide the required tools. Additionally, I would like to thank Ms Cheryl Cheng for her enthusiastic support during my research-related activities, which included buying books and materials.

And lastly and most importantly, I want to thank all my family members for their support and sacrifice, especially my father, mother, brother, and sister.

To my parents, younger sister and brother & all the people who have supported me throughout my education!

Publications

1. **Raju Ahamed**, Kristoffer McKee, Ian Howard. (2020). Advancements of wave energy converters based on power take off (PTO) systems: A review. *Ocean Engineering*, Vol. 204, 107248.
2. **Raju Ahamed**, Ian Howard, Kristoffer McKee. (2022). Study of gravitational force effects, magnetic restoring forces and coefficients of the magnetic spring based nonlinear oscillator system. *IEEE Transactions on Magnetics*, (DOI: 10.1109/TMAG.2022.3180812).
3. **Raju Ahamed**, Kristoffer McKee, Ian Howard. (2022). A Review of the Linear Generator Type of Wave Energy Converters' Power Take-Off Systems. *Sustainability*, Vol. 14(16), 9936.

Table of Contents

List of Figures

List of Tables

List of Abbreviations and Symbols

The following is a list of abbreviations and symbols used within the text of this thesis. In addition, the symbols and abbreviation have also been described alongside their first usage. The list has been prepared in the logical ascending alphabetical order.

AlNiCo	Aluminium-nickel-cobalt
AWG	American wire gauge
AWS	Archimedes wave swing
EAP	Electro Active Polymers
EMG	Electromagnetic generator
FA	Force applied
FEA	Finite element analysis
FEM	Finite element method
FM	Floating magnet
ISWEC	Inertial sea wave energy converter
MEC	Magnetic equivalent circuit (MEC)
NdFeB	Neodymium magnet
OSU	Oregon State University
OWC	Oscillating-water column
PA	Point absorber
PM	Permanent magnet
PMLG	Permanent magnet linear generator
PTFE	Polytetrafluoroethylene
PTO	Power take off systems
TENG	Triboelectric nanogenerators
SDOF	Single-degree-of-freedom
2DOF	Two-degree-of-freedom
3DOF	Three-degree-of-freedom
UU	Uppsala university
WC	Winding coil
WEC	Wave energy converters
A	Surface area of the magnet
A_f	Amplitude of the wave
a	Coupling coefficient between the mechanical and electrical system
B_x, B_0	Magnetic flux density

B_r	Residual magnetic flux density or remanence
b	Radius of the buoy
c	Number of parallel current paths per phase
F	Magnetic force between two magnets
F_{buoy}	Buoy force
F_e	Electromagnetic forces
F_{gen}	Generator force
F_h	Hydrostatic force.
F_r	Wave radiation force
F_{res}	Magnetic restoring force
F_{we}	Wave excitation force
F_β	Damping forces
F_1	Wave force coefficient
g	Gravity acceleration
H, Q	Magnetic field intensity
H_c	Magnetic coercive force
I	Current inside the coil
k_w	Winding factor
k_1	Linear spring constant
k_2, k_3	Linear stiffnesses (Chapter 4 and 8)
k_3, k_5	Nonlinear stiffnesses (Chapter 5, 6, 9 and 10)
L	Inductance of the coil
L_{total}	Total length of the oscillator
l	Winding coil length
M, M_s	Magnetization
M	Mass of the magnet
m_a	Added mass
N	Number of turns
q	Number of slots per pole and phase
R, R_{in}	Internal resistance of the circuit
R_e	External load or resistance
R_y	Radiation damping
r	Distance between two magnetic poles
V	Voltage inside the coil or induced voltage
y	Position of the magnets
$\dot{y}$	Velocity of the magnets

$\ddot{y}$	Acceleration of the middle magnet
β_m, β	Mechanical damping coefficient
β_e	Electrical damping coefficient.
γ	Spring constant (Chapter 2)
ρ	Density of the seawater
ω_n	Natural frequency
ξ	Damping ratio
σ	Wave number
λ	Wavelength
n_s	Number of conductors per slot
Φ	Magnetic flux
μ_0	Magnetic permeability
μ_r	Relative permeability
J	Magnetic body polarisation
$\alpha_1, \alpha_3, \alpha_5$	Nonlinear stiffnesses
$\lambda_1, \lambda_3, \lambda_5$	Nonlinear stiffnesses

The contents of this chapter have been published in the Ocean Engineering, 2020, Vol. 204, P 107248. https://doi.org/10.1016/j.oceaneng.2020.107248

Chapter 1
Introduction

This chapter discusses the overview of the wave energy converters (WEC), problem statements, research objectives, research methodology, research scope, and the organisation of the thesis. The first part of this chapter discusses WEC classification, different power take off (PTO) systems and the working principle of the linear generator based direct electric drive PTO system. Moreover, different topologies of WEC with linear generator-based PTO systems are also discussed. The following part includes the problem statements, research objectives and the research methodology. The final part explains the organisation of the thesis.

1.1 Introduction

Energy plays a vital role in developing the economy and in social life. The demand rate for global energy increases with the increase in population and economic growth and the increasing development of wireless sensors and IT technologies. It is expected that this demand rate will be increased still further by almost one-third from 2013 to 2040 (International Energy Agency, 2015). Fossil fuels are currently still the primary source of energy, with about 80% of the required global energy sources coming from fossil fuels, one of the primary reasons for the greenhouse effect and environmental pollution (Ozkop & Altas, 2017). On the other hand, there are still around 1.1 billion (15% of the world population) people all over the world who are living without electricity (Sustainable Energy for All (SE4ALL), 2015). Increased fossil fuel prices, the problems with environmental pollution and the increasing uses of energy in the current IT and wireless sensor technology innovations push researchers to find new energy sources. Therefore, energy generation from the natural environment and waste sources such as vibration and industrial heat is an attractive research topic to solve energy crises and environmental problems. Among all renewable energy sources, solar photovoltaic and wind energy are well-known and increasingly being used to address energy needs, but these two sources depend on weather conditions. Another significant unused promising renewable energy source is the ocean in the forms of oceanic currents, tidal movements, waves, and salinity covering 70 % of the world's surface area. This energy source can be used to fulfil the world energy demand. Among all these forms, ocean wave energy has shown more significant opportunities and benefits for energy generation, as it is more constant reliable and has, on average,

a higher energy density (2-3 kW/m^2) than wind (0.4-0.6 kW/m^2) and solar power (0.1-0.2kW/m^2) (López et al., 2013).

Table 1.1: Wave Energy Resource (Theoretical Potential) in various areas of the world (IRENA, 2014)

Regions	Wave Energy Potential (TWh/y)
Mediterranean Sea and Atlantic Archipelagos (Azores, Cape Verde, Canaries)	1300
Central America	1500
Western and Northern Europe	2800
Africa	3500
North America and Greenland	4000
South America	4600
Australia, New Zealand and Pacific Islands	5600
Asia	6200
TOTAL	29,500

However, unfortunately, this energy is wasted daily because of the difficulty in capturing this energy. How much total ocean wave energy can be used? It is not easy to estimate, but researchers have calculated that the world's possible ocean wave energy sources are about 2 TW (Dean & Dalrymple, 1991; Thorpe, 1999). Other wave energy researchers have estimated that the ocean holds about 8,000-80,000 TWh/year or 1-10 TW worldwide, though about 3 TW wave energy could be harnessed as usable energy and among the wave energy sources, 574 GW could be generated in Australia and New Zealand, 768 GW in South and North America and 286 GW in Europe (Ayub et al., 2011; K. Dragoon, 2015; Muetze & Vining, 2006). The theoretical potential of the wave energy resource in various areas of the world is shown in Table 1.1. Since 2010, at least 25 countries worldwide have engaged in wave energy development, which continues to increase (Ahamed et al., 2020). The global wave energy resources and their variability have been discussed by many researchers (Antonio, 2010; López et al., 2013). Iraide Lopez et al. listed the benefits and challenges of wave energy power and have drawn some conclusions which are very helpful for developing the wave energy technology and selecting suitable sites. The Global wave power statistics are illustrated in Figure 1.1. Yoshio Masuda, a Japanese marine captain, began studying ocean energy informally in the 1940s. He developed a floating navigation buoy based on wave energy, called the floating oscillating-water column (OWC), primarily sold in Japan and the USA (Falcão & Henriques, 2016; Masuda, 1986). It

began academically in the 1970s when the price of fossil oil rose and the Middle East restricted oil supplies (Polinder & Scuotto, 2005).

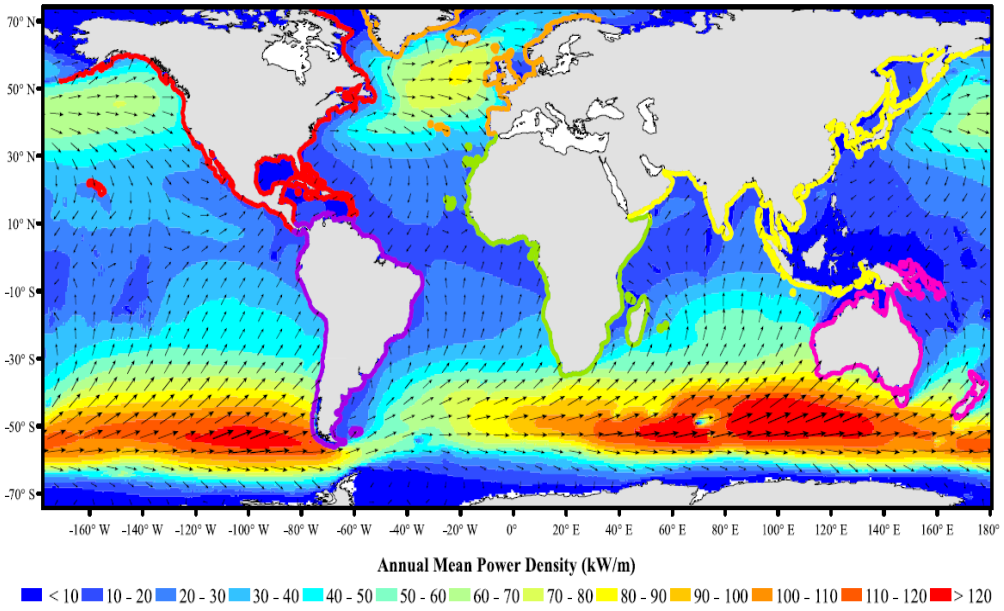

Figure 1.1: Yearly mean wave power density (shown by colour variation) and yearly mean best direction (indicated by → (arrows)) (Gunn & Stock-Williams, 2012)

In the 1980s, research on wave energy slowed because oil prices dropped again, and funds were lacking to continue this type of research. Researchers from Europe, especially those in the UK and Norway, conducted most early research. Researchers at this time focused primarily on hydrodynamics and developed point absorbing wave energy converters (WECs) and oscillating water column concepts with a basic understanding of ocean wave energy (Elwood et al., 2010; McArthur & Brekken, 2010). Energy demand, the price of conventional energy, and global warming prompted wave energy research to restart several decades later. Thus, the academic research into ocean wave energy has taken place in two phases, between the 1970s and today.

1.2 Classification of Wave Energy Converter (WEC)

It is known from all the recent reviews that there are several hundred WEC projects worldwide at various stages of development. New concepts and technologies constantly lead to an increase in this number. Day et al. summarised that more than one hundred projects and more than one thousand patents had been developed since 2015 in Europe, the USA, Japan, China, and Asia (Day et al., 2015).

Various researchers worldwide have conducted numerical and experimental studies to evaluate the WEC's performance. To harness energy from the ocean waves, WEC has been used various concepts, techniques, designs, and working principles. Thus, the classification of WEC depends on different factors. Several methods of classifying wave energy systems exist, including based on location, structure, working principle, size and orientation, and power take-off system (Antonio, 2010; Czech & Bauer, 2012; Falnes, 2007; Hong et al., 2014; Wang et al., 2018). The details of the advanced classification of the Wave energy converter (WEC) are shown Figure 1.2.

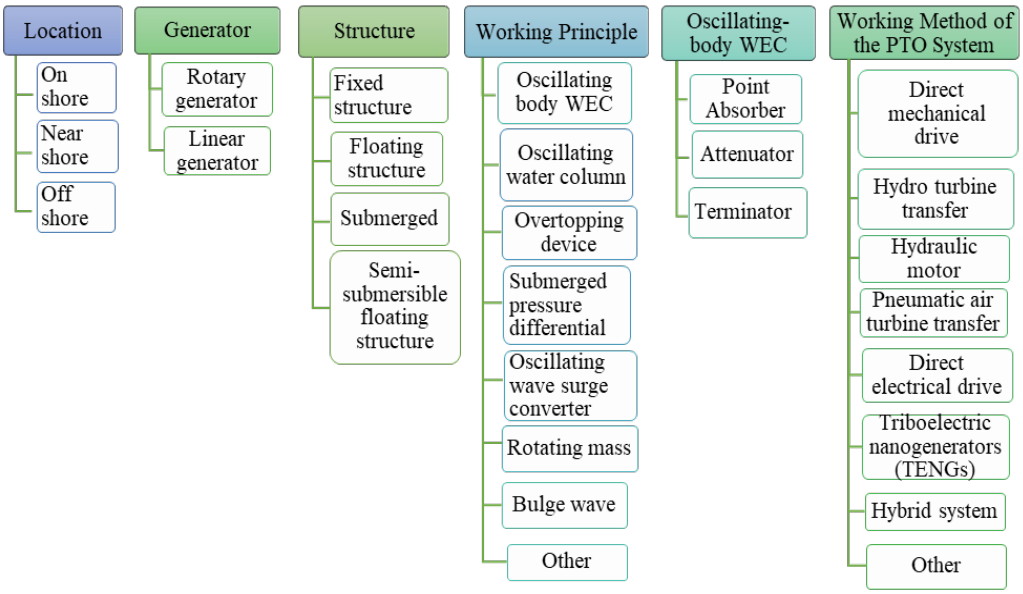

Figure 1.2: Classification of WEC

These devices can be classified as Onshore, Offshore, and Nearshore based on installation location: (1) Onshore devices, which are usually designed to be installed at or to the shoreline; (2) Offshore devices that are installed in deep water; (3) Nearshore devices which are deployed in shallow water regions. According to the size and direction of elongation, the WECs can be classified into three types: Attenuators, Point Absorbers and Terminators. The WECs can also be categorised into several types based on their working principle: Oscillating body; Oscillating Water Column; Overtopping; Submerged Pressure Differential; Oscillating Wave Surge; Rotating Mass; Bulge Wave; and others. Oscillating body, Oscillating water column and Overtopping are the most common working principles, and the majority of devices use one of these three (Day et al., 2015). Moreover, the WEC can be classified into four types based on their structure: (1) Fixed structure; (2) Floating structure; (3) Submerged; and (4) Semi-submersible floating structure. So far, numerous PTO systems have

been used; therefore, the WEC can be classified using these different types. The brief descriptions of each of these categories can be seen in Refs. (Ahamed et al., 2020). Falcão et al. presented the most well-known WEC classification diagram (Antonio, 2010). The WEC classification has been updated to reflect some new PTO technologies. The WEC classification has been updated to include some new PTO technologies.

1.3 Wave Energy Converters based on Power Take-off (PTO) Systems

Power take-off (PTO) systems are at the heart of wave energy research. Many research works have been done to develop the PTO system for wave energy technologies to generate maximum energy at a low cost. So far, many working methods have been used to develop the PTO systems, which can be seen in Figure 1.3.

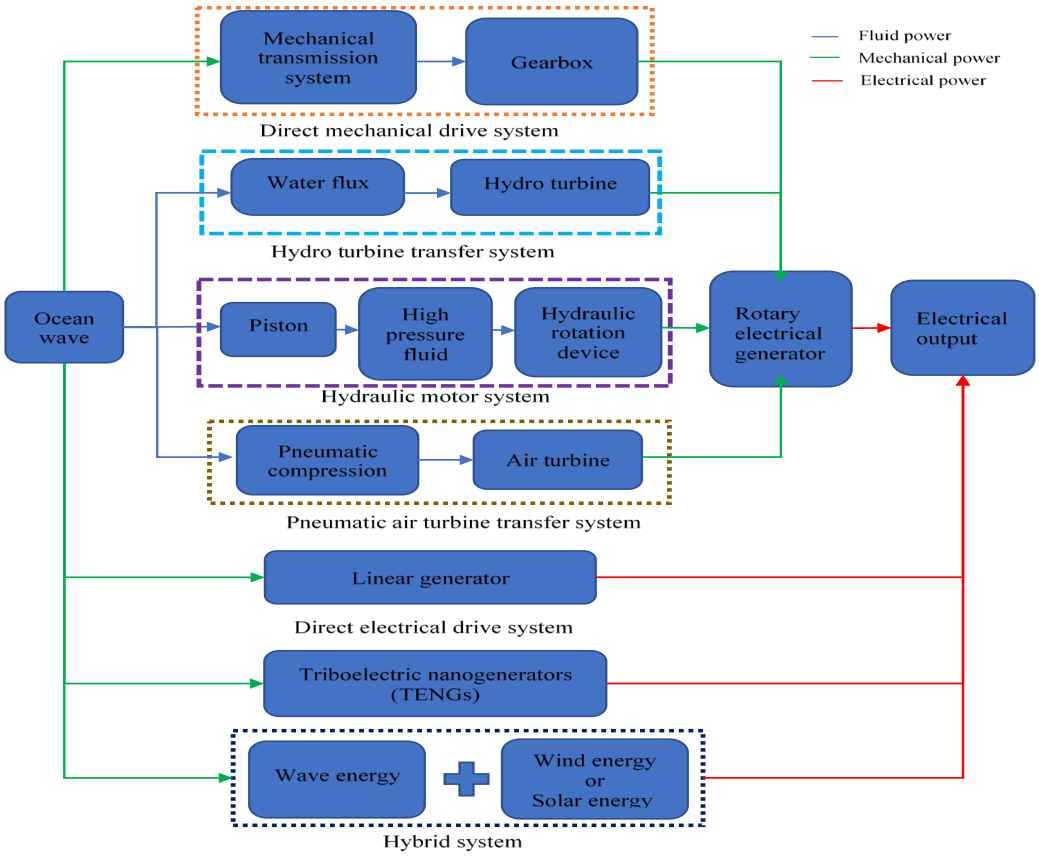

Figure 1.3: The working principles of the PTO system

Among all the working methods in PTO systems, the hydraulic motor, turbine transfer, direct mechanical and electrical drive system based working methods are very well known and the most

used methods. However, some new techniques such as the triboelectric nanogenerator, hybrid systems, and others have been developed only in the last couple of years. This section will review and discuss the PTO working techniques with their design methods and research work.

1.3.1 Hydraulic motor system

PTO systems based on hydraulic motors are well-known methods of converting low-speed oscillations into energy (Ahamed et al., 2020). Among the available wave energy conversion technologies, the hydraulic motor-based PTO system is the most suitable for converting wave energy into usable electricity. In particular, the wave-activated-bodies wave energy conversion system is the most appropriate device. Thus, both translation wave and rotation wave conversion systems can be utilised in hydraulic motors (Jusoh et al., 2019). Figure 1.4 shows a schematic diagram of a typical hydraulic motor type PTO system.

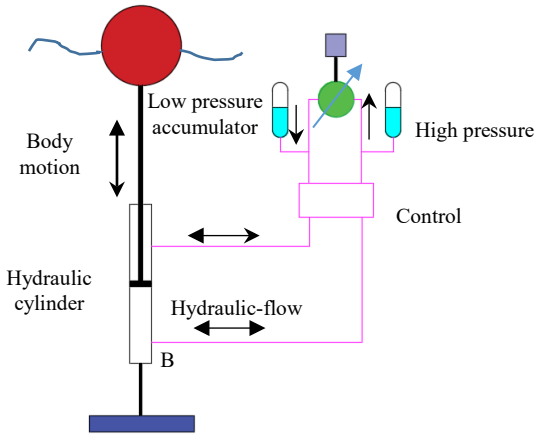

Figure 1.4: Typical hydraulic motor based PTO system (López et al., 2013).

It contains a hydraulic cylinder, a hydraulic motor, an accumulator, and a generator. A hydraulic ram converts the rotational or translational motion generated by ocean waves into hydraulic energy, which drives a hydraulic motor. The hydraulic ram works by increasing the pressure of a working medium (often hydraulic oil). The hydraulic motor then drives the generator to produce energy (Zhang et al., 2012).

Hydraulic motor-based PTO systems have significant advantages due to their large power density and low-frequency operation (Gaspar et al., 2016). Hydraulic motors can generate significant amounts of

power using low-frequency waves. It can be used to extract energy from wave energy converter movement, which is continuously changing. The hydro system is well suited and adequate for harvesting energy from waves because, generally, waves create large forces with slow speeds (Zhang et al., 2012). Incompressible fluid is usually used in hydraulic motor systems, making them more efficient. Although the system has been rated as effective as 69% to 80%, it would actually have a lower efficiency (Hansen et al., 2013). The hydraulic motor system can also be used to control the WEC device to maximise energy absorption and take into account the ocean wave condition (António, 2007). The hydraulic motor assembly can be assembled using locally-made components from hydraulic components suppliers (Lasa et al., 2012). Due to compression and decompression of the fluid inside the hydraulic actuator chamber, fluid flows inside the hydraulic system, potentially creating hydraulic oil leakage and causing harm to the marine environment (Zou & Abdelkhalik, 2018). Hydraulic motor-based PTO systems have many mechanical parts, so their structure is complicated and they require regular maintenance in ocean environments, which is expensive, risky, and time-consuming (Ahamed et al., 2020). Additionally, the end-stop issue is another challenge of the hydraulic motor-based PTO system. Due to unexpected extreme conditions, the hydraulic actuator can exceed its maximum displacement limit and damage the system (Jusoh et al., 2019).

1.3.2 Pneumatic air turbine transfer system

One of the most famous PTO systems for WEC is the pneumatic air turbine transfer system. In most systems, compressed air drives the air turbine, which drives the generator directly. Usually, the air turbine is used for breakwater integrated OWC and oscillating water column wave energy converters. Figure 1.5 illustrates the schematic of the air turbine transfer based PTO system.

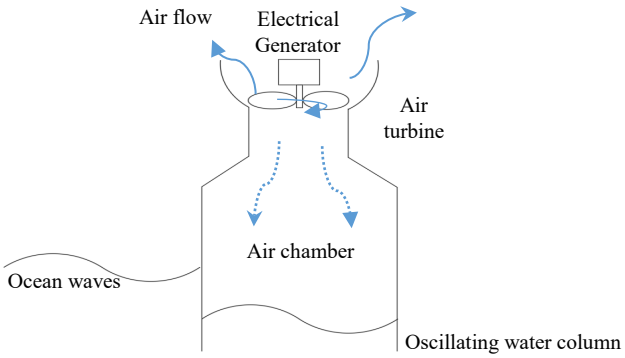

Figure 1.5: Schematic of the air turbine based PTO system (Têtu, 2017)

Seawater pressure creates air pressure in the wave energy converter system, which runs directly through the turbine, coupling with the generator, to generate energy. Wave energy converters with or without fixed or variable guide blades use wells or impulse turbines, which are common types of air turbine designs.

Using air as the working fluid of WEC increases the wave's slow velocities into high airflow rates. In contrast to hydraulic motor-based PTO systems, pneumatic air turbines have no environmental impact because they harness energy from the high airflow, and the technology has been mature for many decades. Air turbines are advantageous because they can be located away from the potentially corrosive saltwater and destructive high waves. In addition, they can be easily accessible for maintenance, as they are not located directly in contact with them (Soares et al., 2012). The bidirectional flow makes conventional turbines unsuitable. A non-return valve system coupled with a traditional turbine may be one solution to this problem. Still, the non-return valve airflow rectification system is complicated and challenging to maintain. This system, however, can't be implemented in a large-scale wave energy unit because the valve is too big (Maria-Arenas et al., 2019; Pecher & Kofoed, 2017). Pneumatic air turbine transfer systems designed with Wells turbines are the most popular because they rotate in the same direction, regardless of airflow direction. Its primary disadvantage is that it does not start itself: first, an external source must be used to drive the rotor (Pecher & Kofoed, 2017). This Wells turbine system is less efficient than the traditional system (around 60-65%) (Ahamed et al., 2020). Additionally, it has higher axial thrust and higher noise than conventional systems (Kim et al., 2001; Takao & Setoguchi, 2012). Further, the extra function reduces turbine stability and increases operation and maintenance costs by increasing the number of moving parts.

1.3.3 Hydro turbine transfer system

The hydro turbine transfer system utilises compressed water to power the turbine, which directly drives the generator to generate energy, as shown in Figure 1.6. Hydro turbines are used in overtopping wave energy converters. The Wave Dragon consists of two arms that collect water in a reservoir that is higher than the ocean's surface level and a submerged ramp that drives its turbines (Parmeggiani et al., 2011; Polinder & Scuotto, 2005). The stored water is moved back to the sea by channels located in the middle of the reservoir, which run the turbines to generate energy.

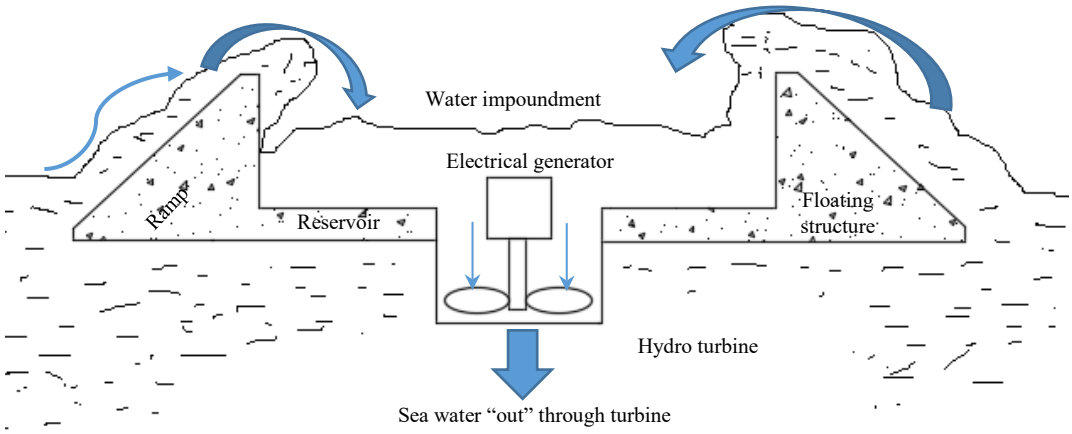

Figure 1.6: Schematic of the hydro turbine-based PTO system (Tutorials, 2019)

Hydraulic turbines are an established technology, such as the Kaplan turbine, which has been in use for decades. It can operate with 90 % efficiency and require little maintenance (Pecher & Kofoed, 2017). The bottleneck for wave energy conversion is getting enough head and flow from ocean waves to allow Kaplan's turbine generator units to be economically viable. Using a hydro turbine has the advantage of causing no environmental pollution due to fluid leaks (Ahamed et al., 2020). It has the disadvantage of being a dynamic fluid (ocean water) with unpredictable components that can damage the seals and the valves. Cavitation may also be an issue if the turbine isn't located deep enough to maintain positive pressure.

1.3.4 Direct mechanical drive systems

The direct mechanical drive system converts ocean waves directly into electricity using an electric generator. Mechanical transmission systems and gearboxes are typically used to drive electrical generators directly connected to the gearbox. Figure 1.7 illustrates the schematic for a direct mechanical drive-based PTO system. Several WEC prototypes utilising the direct mechanical drive have been developed and deployed. The Penguin is a WEC developed by Wello Ltd, which harnesses the power of waves through an electric generator (Amir et al., 2016).

Direct mechanical drive refers to the transmission of wave energy into electrical energy using linear-to-rotary converters without any pneumatic or hydraulic systems. Wave energy converters can be driven by various transmission systems, including rack-and-pinion, belt drive systems, ratchet

wheels, and screws. Due to reduced friction, the direct mechanical drive wave energy conversion system can convert more wave energy than the hydraulic system.

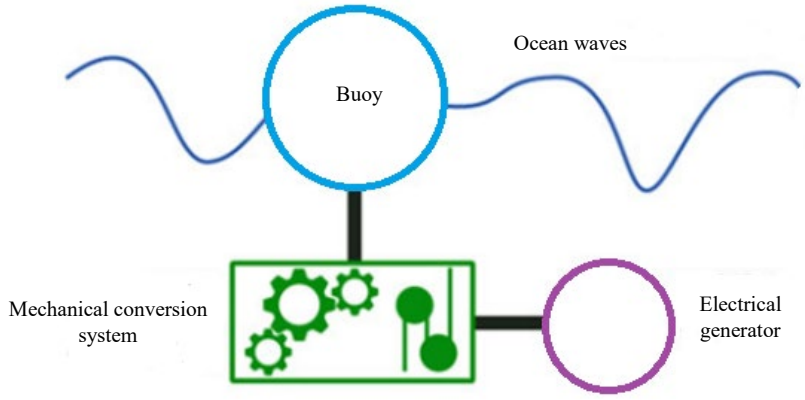

Figure 1.7: Schematic of the direct mechanical drive based PTO system (upgrade of Ref. (Têtu, 2017))

PTO systems that utilise this technology offer high performance since only three conversions are required. Rack and pinion mechanisms are highly efficient, as high as 97% was claimed (Penalba & Ringwood, 2016). Despite this, the direct mechanical drive system undergoes higher load cycles, and it is still uncertain whether this type of system is reliable. In terms of challenges, the rack and pinion mechanisms are mainly limited by their relatively short lifespans and higher maintenance costs. Additionally, the gearbox size for WEC devices depends on the shape and size of the system. The gearbox used in the smart power buoy had an outer dimension of 300mm x 400mm (diameter) and cost USD 1500. On the other hand, the gearing system at the PTO of Bolt Lifesaver costs about £40,000 (Ahamed et al., 2020).

1.3.5 Direct linear electrical drive systems

To overcome some of WEC's mechanical complexity, direct electrical drive systems and electromagnetic-based linear generators have been used in PTOs (Mueller & Baker, 2002; Henk Polinder et al., 2005). The linear generator concept works using a translator and a stator, with the translator is attached to a buoy and the stator fixed to the seafloor. The stator is equipped with coil windings, and the translator is equipped with permanent magnets. Due to the hydrodynamic action of the ocean waves on the buoy, the translator moves up and down while it generates the magnetic field

inside the coil windings and thus generates the electric power. The schematic of the direct electrical drive-based PTO system is shown in Figure 1.8.

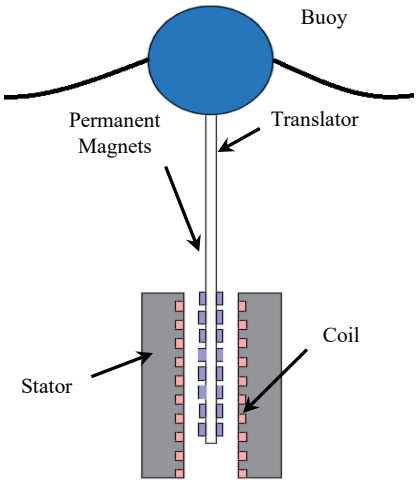

Figure 1.8: Schematic of the direct electrical drive based PTO system (Ahamed et al., 2020)

The term "Direct electrical drive" refers to converting the wave energy directly into electrical energy without using pneumatics or complicated linear-to-rotary conversion systems. Directly coupled to the moving part of the linear generator, this device extracts mechanical energy from the primary converter (Baker & Mueller, 2001; Mueller, 2002). The advantage of this system is that it does not require an intermediate mechanical interface (for example, a gearbox), which avoids the losses associated with turbines and hydraulic motors, thus reducing maintenance costs (Hong et al., 2014; Leijon et al., 2008; Muetze & Vining, 2006).

Direct electric drive systems (linear permanent magnet generators) have the main advantage of relatively high efficiency and the possibility of continuous force control (Danielsson, 2006). Additionally, the generated electricity must be converted to a form suitable for the electric grid by using power electronics (Hong et al., 2014). Due to the low frequencies of ocean waves, linear generators have the main disadvantage of having a much lower linear velocity than rotary generators, which is determined by the absorber velocity. Another disadvantage is the low power-to-weight ratio of the machines (huge machines are needed) as well as the need for a large structure due to the attraction between the stator and the translator (Penalba & Ringwood, 2016). Furthermore, the power transmission system is also very complex due to the irregular wave motion that produces an unequal voltage (Leijon et al., 2008).

1.3.6 Triboelectric nanogenerators

Triboelectric nanogenerators (TENG) were invented in January 2012 by combining triboelectrification with electrostatic induction, which offers high power density, high efficiency, low weight and low manufacturing costs (Fan et al., 2012). TENG could lead to new wave energy conversion methods and ocean-linked blue energy harvesting systems on a large scale (Wang, 2015). To increase efficiency and cut costs, researchers have been studying triboelectric nanogenerators (TENGs) for PTO systems (Chen et al., 2015; Khan & Kim, 2016). Modern TENGs are constructed using conventional materials such as aluminium polytetrafluoroethylene (PTFE) since they are lightweight, relatively inexpensive, easy to fabricate, and easily scaled up (Wang, 2013, 2015). A pair of materials creates electrostatic induction due to their two surfaces as electrostatic induction occurs when the contact electrification of their electrodes helps guide the charge between their electrodes and the polymer, and a metal pair is usually used as the friction layer (Fan et al., 2012; Hinchet et al., 2015; X.-S. Zhang et al., 2013). Figure 1.9(b) illustrates the working mechanism of TENG, while Figure 1.9(c) illustrates its performance in the low-frequency range. When two materials, A and B, interact, electrostatic surface charges are produced; the rolling of the ball changes the capacitance of the system, allowing electrons to flow between the two electrodes to balance the electrical potential drop (see Figure 1.9(b): (i), (ii) and (iii)).

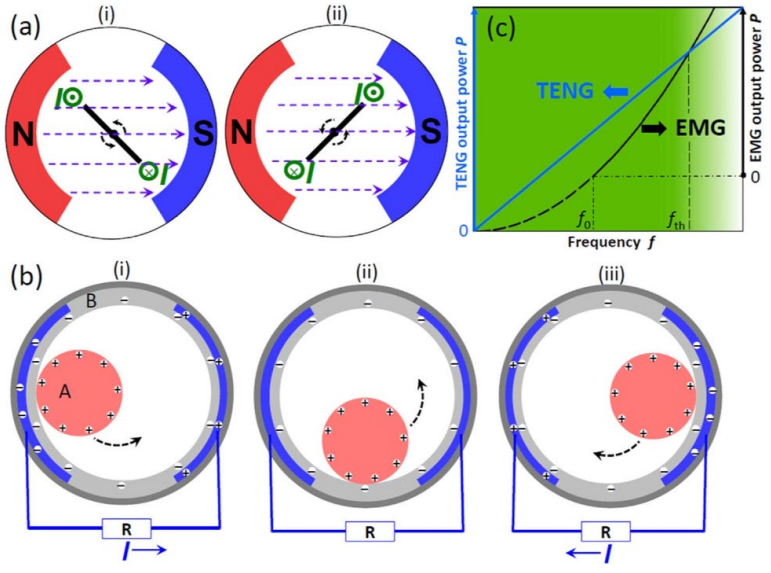

Figure 1.9: Working Principle (a) electromagnetic generator, (b) TENG coupling triboelectrification effect and electrostatic induction (c) Output comparison between EMG and TENG

Triboelectric nanogenerator-based PTO systems generally use polymer-metal pairs as friction layers, allowing charge transfer by electrostatic induction between electrodes and contact electrification between two materials (X.-S. Zhang et al., 2013). Thus, they are low cost, lightweight, easy to fabricate, well suited for scaling up, and provide a wide variety of materials to choose from (X. Wang et al., 2015). Additionally, these systems have the ability to convert up to 55% of the mechanical energy into electrical energy and can adapt to various kinds of mechanical energy in the form of different operational modes such as contact-separation mode, single-electrode mode, sliding mode, and freestanding mode (Wang, 2015, 2017). Triboelectric nanogenerators-based PTO systems have the advantage of being able to harvest energy in any frequency range (broad frequency range) (Wen et al., 2016). On the other hand, there are many significant challenges associated with using TENGs, such as power transfer to shore and device lifetime in an oceanic environment, as well as the cost and management of large networks of devices (Z. L. Wang et al., 2017).

1.3.7 Hybrid systems

Generally, hybrid-type PTO systems capture energy from ocean waves by combining two or more different techniques or PTO systems. Several WECs have also been proposed based on triboelectric nanogenerators and electromagnetic generators or piezoelectric materials.

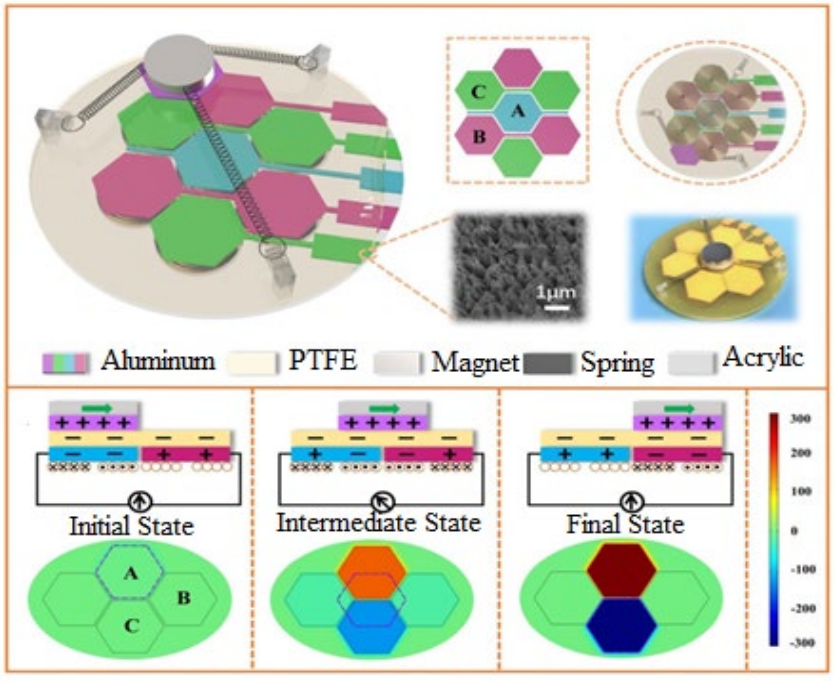

Figure 1.10: Design of the new system structure (Feng et al., 2018)

A new wave energy harvester was developed using a triboelectric nanogenerator (TENG) and an electromagnetic generator (EMG). The TENG contains three honeycombs like electrodes covered by hexagonal PTFE (seven hexagonal films in three groups) and magnets. Figure 1.10 shows that the EMG consists of seven copper coils attached beneath the electrodes on the back of the acrylic board (Feng et al., 2018).

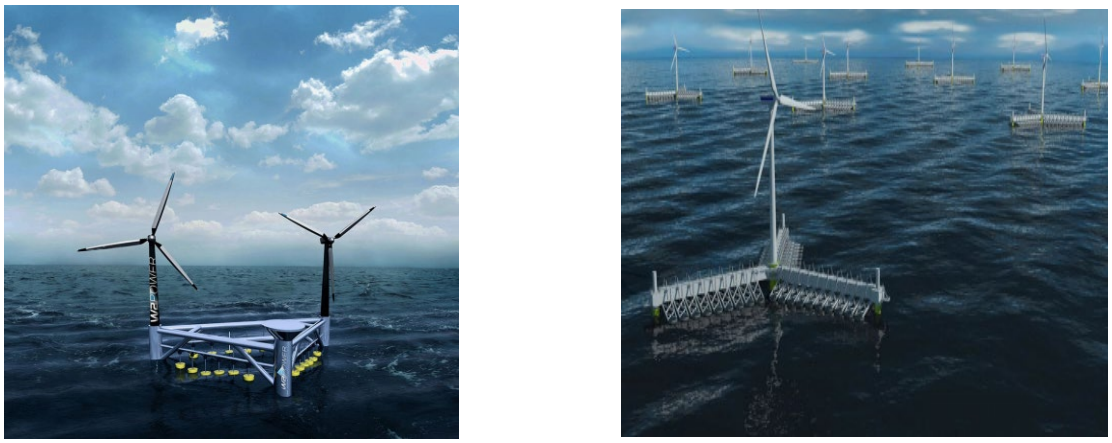

(a) (b)

Figure 1.11: Hybrid system concepts (a) courtesy of Pelagic Power AS (b) Courtesy of Wave Star AS (Pérez-Collazo et al., 2015)

As shown in Figure 1.11, offshore wind turbines and wave energy converters that work together are known as a hybrid concept. The wind turbine generates energy from the wind on the ocean surface, whereas the wave converter generates energy from the ocean waves (Kim et al., 2015; Pérez-Collazo et al., 2015; Rusu & Onea, 2018b). Some researchers have also proposed photovoltaic-wave energy and wind-photovoltaic-wave energy concepts to increase the system's efficiency (El-Sayed & Sharaf, 2011; Samrat et al., 2014; Xilin et al., 2004). The hybrid system is a new research topic in wave and wind energy research, and only a few articles have been published (Fusco et al., 2010; Veigas, Carballo, et al., 2014; Veigas & Iglesias, 2013, 2015; Veigas, Ramos, et al., 2014).

One of the main advantages of the hybrid system is that it combines two working methods to harvest energy into one structure, which reduces the installation and mooring costs. For instance, combining a floating or mooring wind turbine with wave energy converters to harvest energy from the offshore area reduces the initial investment requirements compared with the two independent systems. A hybrid system may be developed with the new or existing wind turbine infrastructure (Manasseh et al., 2017). Therefore, overall costs of installation, operation, and maintenance can be reduced.

Furthermore, the wave energy converters (WECs) should be integrated into the platform's overall motion response, providing a stabilising effect to the whole device (Ding et al., 2015). Due to its smoother integration into the grid network, the hybrid system delivers greater efficiency while being less influenced by the variability of a single resource (Rusu & Onea, 2018b). Additionally, offshore wind farms could reduce the cost of wave energy by sharing infrastructure, logistics, and grid connections. Due to mechanical and hydrodynamic couplings, the performances of the other operating system may change. When the wave energy converter is coupled with the floating wind turbine, the behaviour of the floating wind turbine is changed by mechanical and hydrodynamic interactions between the floating bodies (Ding et al., 2015). Therefore, the efficiency of the floating wind turbine could be reduced. Moreover, the two working systems will increase the loads on the structure. Coupling a wave energy converter with a floating wind turbine will also increase the loads of the substructure (Perez-Collazo et al., 2018).

1.3.8 Other systems

Various other techniques have also been used to harvest energy from waves, including piezoelectric materials (Hwang et al., 2017; Wu et al., 2015). An ocean wave harvesting device based on piezoelectric materials has been developed using a laminated structure made from elastic materials and piezoelectric paint (Mutsuda et al., 2019). In the presence of external forces such as wind, waves, and others, the laminated structure can easily deform. Another new WEC called S3 was developed and tested using Electro Active Polymers (EAP) in the PTO system (Babarit et al., 2013b; Jean et al., 2012). The new WEC can directly convert ocean waves into energy with distributed energy generation. Roll-to-roll and EAP processes are used in the PTO system.

Compared to electromagnetic energy harvesting, the piezoelectric energy harvesting system has a three times higher energy density and occupies a smaller space than turbine transduction systems (Nabavi et al., 2018; Priya, 2007). Due to its size and weight, ocean wave energy devices based on piezoelectric materials can generate power for a wide range of water motions at low frequencies (Hwang et al., 2017; Su et al., 2014). Since piezoelectric materials do not have moving parts, the materials can be easily integrated into the device and do not require frequent maintenance (Jbaily & Yeung, 2015). Piezoelectric energy harvesting systems are complex, expensive, and only work with shallow ocean waves (Viet et al., 2016). Due to the energy transduction principle, the energy efficiency is also very low compared to electromagnetic and triboelectric nanogenerators. Using these

methods, less than 10% of the available ocean energy can be converted into electricity (Wang, 2017). Compared to other conventional WECs, the EAP generator-based WEC is inexpensive to fabricate and install because the PTO system is also part of the structure, and it can be run until failure (Babarit et al., 2013a). Since the PTO system is distributed over the entire surface, this type of device avoids stress concentration and is flexible (Babarit et al., 2013a). This device can generate electricity directly from ocean waves (Wattez & van Kessel, 2016).

Basically, it acts as an antenna for amplifying the dynamic pressure of the ocean waves. There are a lot of degrees of freedom and consequently a lot of modes of resonance, which helps it generate energy in any condition period of wave activity. (Andritsch et al., 2012; Jean et al., 2012). The key challenges for this device still need to be addressed, and research and development are ongoing (Wattez & van Kessel, 2016). Because of the flexibility of the EAP generator based WEC, one of the key challenges is that it should be operated above 50 V/μm to achieve maximum energy yield (Andritsch et al., 2012). Due to segmented electrodes, the device has a shorter lifetime than conventional WECs (Jean et al., 2012). The fatigue life can also be reduced by operating under combined mechanical and electrical loads. Moreover, this device can be destroyed in survival conditions (Babarit et al., 2013a).

1.4 Problem Statement and its Significance

A great deal of the energy demand in the present energy crisis can be met by ocean waves - one of the world's largest untapped and predictable renewable energy sources. In different countries across the world, many devices have been proposed for harnessing wave energy through different power take-off (PTO) systems. The traditional wave energy converters (WEC) use hydraulic or turbine type power take-off (PTO) mechanisms which consist of many moving parts, creating complex mechanical components and increasing the installation and maintenance costs. Linear permanent magnet (PM) generator based direct drive WECs could be a solution to overcome this problem. Still, the efficiency of the conventional linear PM generator is not high enough, and it cannot work satisfactorily in the low-frequency range. The bandwidth problem of the existing linear PM generator-based PTO system can be overcome by widening the frequency bandwidth of the WEC. The frequency bandwidth of a light damping nonlinear oscillator is anticipated to be larger than that of a conventional single-degree-of-freedom (SDOF) linear oscillator. The magnetic levitation (magnetic spring) system can be used in the translator design to make the oscillator nonlinear, which is more effective in the broadband

frequency range, especially in the low-frequency ocean environment. However, the characteristics and dynamics of the linear PM generator based on the SDOF nonlinear oscillator system have not been studied yet. The generator system has not been analysed yet by applying external harmonic forces. In addition, no study thus far has modelled two-degree-of-freedom (2DOF) and three-degree-of-freedom (3DOF) nonlinear oscillator system-based energy harvesters to harness ocean energy.

With the aim of harnessing ocean energy, this research presents novel analytical, numerical and experimental modelling of SDOF, 2DOF and 3DOF magnetic spring-based energy harvester systems. The design of the SDOF, 2DOF and 3DOF magnetic spring-based nonlinear oscillator systems have been analysed separately with or without winding coils.

1.5 Research Objectives

The primary objective of this research proposal is to design a direct drive linear generator based on a nonlinear oscillator system for harvesting maximum energy from ocean waves in the broadband frequency range. It is predicted that understanding the key parameters will help generate maximum power. Moreover, the nonlinear behaviour of the magnetic spring, which will be used to build the multi-degree of freedom system, will help the generator generate maximum energy in the low-frequency range. Therefore, the overall aim of this research can be addressed by increasing the magnetic fields, magnet velocity and degrees of freedom to improve efficiency.

The main objectives of the thesis can be written as follows:

1. Research into a magnetic spring-based linear electromagnetic generator for harvesting maximum energy from ocean waves in the broadband frequency range.
2. Performance evaluation and optimisation of the linear electromagnetic generator with the magnetic spring-based nonlinear oscillator system
3. Investigating the electromagnetic field effects and the wave energy conversion performance of the generator using numerical simulation and experimental methods.
4. Optimising the energy conversion behaviour of multiple degrees of freedom nonlinear oscillator system.

1.6 Research Methodology

The literature review identified that the permanent magnet (PM) based linear generator was a viable option for research compared to other methods. Further literature research was conducted to identify possible research challenges regarding PM linear generator-based PTO systems for WEC. The study indicated that the two-degree-of-freedom (2DOF) and the three-degree-of-freedom (3DOF) systems had not been viable options for modularising the linear generator's design. Furthermore, the magnetic spring-based nonlinear oscillator system has not been seriously considered an option for broadband energy harvesting. Hence, the research topic chosen for this project was "A Novel Direct Drive Linear Ocean Energy Converter Based on Nonlinear Oscillator System". The term linear ocean energy converter in the research topic means the linear motion (i.e. motion in a straight line) of the magnets/translator. The nonlinear oscillator system means the oscillator can oscillate with different frequencies. The study of energy harvester with magnetic spring-based oscillator system was conducted step-by-step from the simple single-degree-of-freedom system aspect to the more complex multi-degree-of-freedom system.

The research methodologies adopted to accomplish the stated goals are as follows:

1. Study of various power take-off systems: Extensive literature review is carried out on well-known power take-off systems (PTO) and the latest research into the linear generator type of wave energy converters (WEC)' power take-off systems. The various topologies and mathematical analyses of the existing linear generator-based PTO system are also studied and identified as the shortcoming of the current model.

2. Study of magnet properties and electromagnetic system: Magnet properties are investigated for the feasibility study of the magnetic spring-based nonlinear oscillator model. Analytical, numerical and experimental methods are used to study the magnetic properties of the magnet and magnetic spring-based oscillator system. The experimentally measured magnetic restoring force for the nonlinear oscillator system is validated with the analytical and numerical simulations. Taylor series is used to determine the coefficient of the oscillator system from the analytical magnetic restoring force. Electromagnetic theories are studied to understand the linear generator and its working principle. MATLAB and ANSYS Maxwell

are selected for the analytical and numerical analysis, respectively. Autodesk Inventor is used for designing the test-rig setup.

3. Coefficients of the magnetic-spring based nonlinear oscillator system: The linear and nonlinear stiffnesses of the nonlinear oscillator system for various degrees of freedom are measured from magnetic restoring forces using polynomial curve fitting by considering gravitational force effects. For SDOF magnetic spring-based energy generator/PTO system, the coefficients are determined from the experimental measurements of the magnetic restoring force. For 2DOF and 3DOF PTO systems, the coefficients are determined from the analytical measurements of the magnetic restoring force.

4. Dynamics of the nonlinear oscillator system with and without electromechanical coupling: The log-decrement method is used to investigate the system's natural frequency from the oscillation graph of the system. State space model is used to analyse the dynamics of the nonlinear oscillator system with and without electromechanical coupling for different degrees of freedom systems. The frequency response of the analytical model is compared with the experimental model. Moreover, the Runge-Kutta method (ODE23t solver) is used to obtain the theoretical time responses (vibration and current).

5. Parametric study of the magnetic spring-based energy harvester: The parametric study uses numerical (ANSYS MAXWELL) and analytical (MATLAB) methods to evaluate system performance and achieve the best solution within different parameters sets.

6. Performance analysis of the magnetic spring-based linear generator system: A test rig is designed and fabricated using non-magnetic materials to study the proposed method. By increasing the number of floating magnets, the degree of freedom of the oscillator system is increased. The energy generation abilities of the generator are investigated analytically and experimentally under external harmonic forces. The servo motor is used to create a harmonic force (sine or cosine wave). IR distance sensors are used to measure the displacement of the floating magnet. A data acquisition system captures the data from the IR distance sensors and winding coils.

7. Validation of the analytical model: The test rig of the energy harvester based on the SDOF, 2DOF and 3DOF nonlinear oscillator systems are developed and experimented with within

the lab. The experimental results are compared with the analytical findings to validate the analytical models of the different degrees-of-freedom energy generators. Moreover, the findings of the SDOF energy harvester are compared with the 2DOF and 3DOF energy harvesters. In addition, the proposed magnetic spring-based PTO systems are compared with the existing magnetic spring-based PTOs system.

8. Report writing.

1.7 Research Scope

This research aims to design and develop a linear permanent magnet generator based on various degrees of freedom nonlinear oscillator systems to harness energy from ocean waves. Further main contributions can be outlined as follows;

1. Determine and validate the magnetic restoring force using numerical, analytical and experimental methods
2. Investigate the gravitational force effects on the magnetic restoring forces (effects on equilibrium position)
3. Dynamics analysis of the SDOF, 2DOF and 3DOF nonlinear oscillator systems with and without electromechanical coupling
4. Model analyses by applying external harmonic force on the floating magnet
5. Validation of SDOF, 2DOF and 3DOF generator's analyses with experimental analysis.

1.8 Organisation of the Thesis

This dissertation is organised into 12 chapters. The brief descriptions of each chapter are given below:

1. An overview of the WEC with different PTO systems, direct electric drive generators and motivation for the research with an emphasis on the magnetic spring-based nonlinear oscillator system are presented in **Chapter One**. The problem statement, objectives, research methodology, research scope and the outline of this dissertation are also discussed.

2. **Chapter Two** reviews the direct-drive generator type of wave energy converters' power take-off systems (PTOs). The direct drive PTO system based WEC literature focusing on the linear permanent magnet (PM) generator is presented. Furthermore, it gives the mathematical

analysis and development of the linear permanent magnet (PM) generator proposed and deployed to harness ocean energy.

3. **Chapter Three** studies the magnetic properties of the ring magnet and magnetic spring-based oscillator system and the electromagnetic theory. The magnetic restoring force of the magnetic spring-based oscillator system is analysed analytically without considering gravitational force effects.

4. **Chapter Four** describes the gravitational force effects on magnetic restoring force and dynamics of the single-degree-of-freedom (SDOF) magnetic spring-based oscillator system without considering the electromechanical coupling. It presents the experimental, analytical and numerical simulation of the magnetic restoring force for the proposed oscillator system. The coefficients analysis of the system from the magnetic restoring force is studied. Moreover, it investigates the gravitational force effects and the dynamics of the SDOF oscillator system by changing the length of the oscillator.

5. **Chapter Five** explains the magnetic properties, magnetic restoring forces, coefficients, mathematical modelling and the dynamics of the two-degree-of-freedom (2DOF) magnetic spring-based oscillator system. Moreover, it studies the dynamics of the 2DOF oscillator system by changing the length of the oscillator.

6. **Chapter Six** discusses the magnetic properties, magnetic restoring forces, coefficients, mathematical modelling and the dynamics of the three-degree-of-freedom (3DOF) magnetic spring-based oscillator system. Moreover, it presents the dynamics of the 3DOF oscillator system by changing the length of the oscillator.

7. **Chapter Seven** presents the experimental setup and analysis of the nonlinear oscillator system with and without electromechanical coupling. It clarifies the method of assembling all the test rig components. It also describes the calibration of the IR distance sensors and the subsequent instrumentation and the measurement signal paths from the sensors and winding coils to the Data Acquisition system.

8. **Chapter Eight** describes the numerical simulation analysis, mathematical modelling, dynamic analysis, and performance test of the SDOF nonlinear oscillator-based energy

generator. It also presents the parametric study of the energy generator and the system with the RLC circuit. Moreover, it discusses the energy generation ability of the generator for different lengths of the oscillator, experimental analysis and validation of the energy generator system.

9. **Chapters Nine and Ten** explain the numerical simulation analyses, mathematical modelling, dynamic analysis, validation, and performance tests of the 2DOF and 3DOF nonlinear oscillator-based energy generators.

10. **Chapter Eleven** summarises and discusses the crucial findings of the thesis. Moreover, conclusions are drawn in **this Chapter** and outline important recommendations for future work.

The contents of this chapter have been published in the Sustainability, 2022, Vol. 14(16), 9936, https://doi.org/10.3390/su14169936

Chapter 2
Literature Review

The aim of Chapter 2 is to specifically focus on and review the recent research developments of the WEC with the linear PM generator. In order to identify the most promising kinds of linear generators that can be used in WEC direct drive systems, this Chapter provides a timely and comprehensive critical comment on the distinctive linear permanent magnet (PM) based generator systems that have been studied and evaluated in recent years. It starts with a brief introduction and background of wave energy converters using linear generators. Following this, the working principle of the WECs with linear PM generators is briefly outlined. Subsequently, the analytical model of the linear PM generator based WEC is studied. The review provides an analysis of the major design parameters and improvement issues, performance analysis, and a discussion of the numerical and experimental analysis tools used by the researchers. Finally, conclusions about the significant beneficial characteristics and design choice of the WEC linear generator structure are provided and related to the application conditions.

2.1 Introduction

Increased energy demand, environmental pollution, and fossil fuel costs push researchers to find new energy sources. Therefore, energy generation from ocean waves has been seen as an attractive research topic to solve the energy demand and environmental problems. Ocean waves are among the world's largest untapped and predictable renewable energy resources that can be harnessed to meet future energy needs in an energy crisis situation. Numerous devices have been proposed and prototyped in different countries worldwide to harness wave energy using various power take-off (PTO) systems. All the latest reviews show several hundred WEC projects in different development stages worldwide (Ahamed et al., 2020). These numbers are continually rising as new technologies and concepts emerge. Although there are many devices and methods that have been proposed to harness wave energy, the designs are still in the early stages, as not a single commercial, mature technological model has been developed. Thus, it can still be seen as an immature and expensive technology. However, for the present time, the largest portion of wave energy projects that have been installed is based on the oscillating bodies' technology, especially the Point absorber (PA) type (López et al., 2013; Rusu & Onea, 2018a; Wang et al., 2018; Xu et al., 2019). The point absorber is an offshore type device that generally utilises heave motion for energy generation and was very

popular because of its advantages over other wave energy technologies (Clément et al., 2002; Hong et al., 2014), including that its size is smaller compared to other WEC technologies, it contains decidedly less mechanical complexity, and it can generate energy from any direction of waves at one point of the ocean (Budar & Falnes, 1975; Hong et al., 2014; Xie & Zuo, 2013). Two general electrical generators are used in Point absorber (PA) types WEC system, one being the rotary generator and the other being the linear generator. Generally, hydraulic motors or turbines or gearboxes are used in the traditional rotary generator based WEC to produce a high-speed rotating motion from slow-moving wave motions (Ahn et al., 2012; Frigaard et al., 2004; Gao et al., 2016; Henderson, 2006). This design consists of many moving parts, which creates a comparatively very complex mechanical system and can result in pollution of the ocean environment due to oil leakage of any moving part (Leijon et al., 2008; Zhang et al., 2018). To overcome this mechanical complexity, electromagnetic based linear generators can be used in WECs (Mueller & Baker, 2002; Henk Polinder et al., 2005). The advantages of this buoy type of linear generator set-up are that it has a simple mechanical design because it does not contain any gearbox or other mechanical or hydraulic conversion system, it has less environmental impacts, and it reduces the maintenance cost of the WEC due to reducing the need for maintenance (Leijon et al., 2008; Muetze & Vining, 2006). So far, many linear generator-based WECs have been proposed, tested, and deployed in the ocean. Among the well-known linear PM generator proposed WEC, the Archimedes Wave Swing (AWS) was the first device deployed in the ocean for performance testing (H Polinder et al., 2005). The second linear PM generator based WEC was developed and tested by Uppsala University (UU), and the third one was developed and tested by Oregon State University (OSU) in collaboration with industry partners (Hong et al., 2013; Von Jouanne & Brekken, 2011).

2.2 Wave Energy Converter with Linear Generator-based PTO System

The main components of the direct-drive linear generator based WECs are the linear PM generator type PTO system and the wave buoy. Usually, the linear PM generator consists of a translator which holds the permanent magnets (PMs) and the stator equipped with coil windings, or vice versa. According to the linear PM generator based WEC, the stator is fixed, and the translator is connected to a floating or submerged buoy or vice versa (Curto et al., 2020). With the hydrodynamic motion of the ocean waves, the translator goes up and down along with the buoy and produces the fluctuating magnetic field within the coil windings, generating electrical energy. Figure 2.1 displays the basic functional units of wave energy conversion.

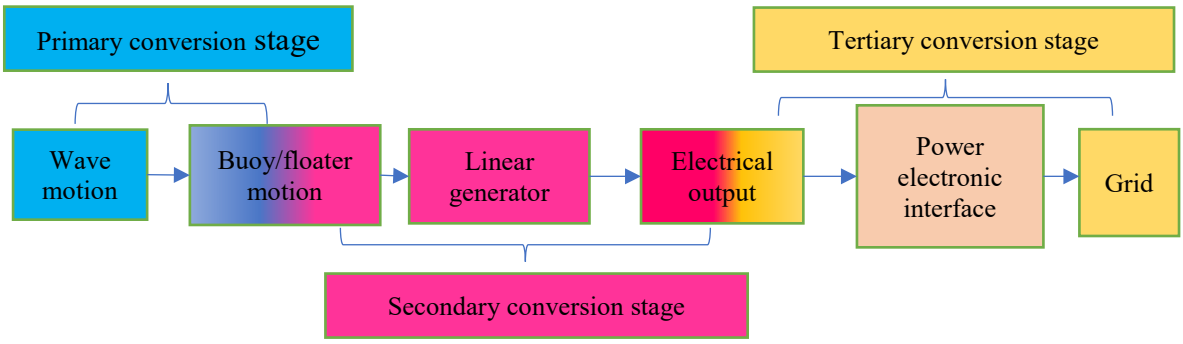

Figure 2.1: Basic functional units of a linear generator based WEC

Wave energy conversion systems are divided into primary, secondary, and tertiary stages (Rusu & Venugopal, 2019). During the first stage of wave energy conversion, the buoy is used to capture kinetic energy from the wave. By using a linear generator, the buoy motion energy is converted into electricity in the secondary conversion stage. At the tertiary conversion stage, the characteristics of the generated power are adapted to grid requirements using power electronic interfaces.

2.2.1 Different topologies of WEC with linear generator-based PTO system

This section is concerned with presenting an overall perspective of typical linear wave generator configurations, discussing their merits and shortcomings. The topologies of WEC with linear PM PTO can be classified based on the applications and the system principles. Some systems are based on a floating buoy on the sea surface, as displayed in Figure 2.2(a) (Elwood et al., 2010; Leijon et al., 2006), or a fully submerged heaving system as displayed in Figure 2.2(b) (Polinder et al., 2004; Henk Polinder et al., 2005) and others (Boscaino et al., 2017; Cappelli et al., 2013).

It is less susceptible to storm damage when the wave energy converter is entirely submerged in water. Most failures are related to cooling issues, hydraulics, and pneumatics and it requires more maintenance. In order to avoid these construction, operation and maintenance difficulties, it is not recommended to submerge the device in water (Rhinefrank et al., 2006).

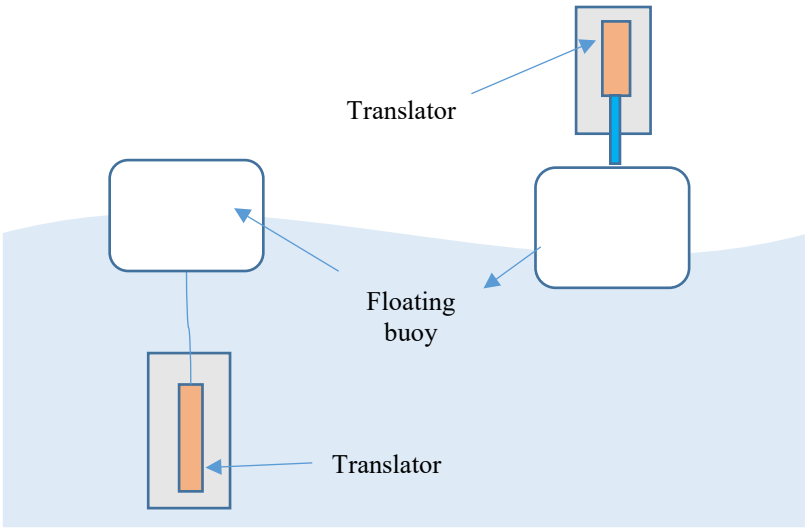

(a)

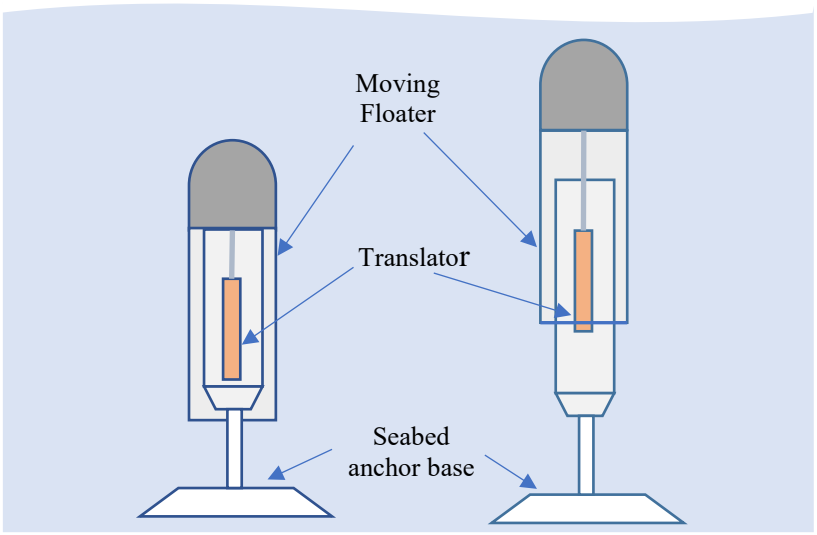

(b)

Figure 2.2: (a) Floating buoy on the sea surface (b) Fully submerged heaving system

2.2.2 Floating buoy on the sea surface

The most straightforward design using a floating buoy on the sea surface involves directly connecting the buoy to the generator moving part with a tether. In contrast, the linear generator is fixed onto the seabed, as shown in Figure 2.3(a) (Castellucci et al., 2016). Another possibility is placing the linear generator above the ocean surface, which is mounted with or without a fixed structure, and the translator of the generator is attached with the floating buoy (López et al., 2013; Zhang et al., 2018).

Figure 2.3(b) and Figure 2.3(c) present the WEC design schematic where the linear generator is placed above the sea surface.

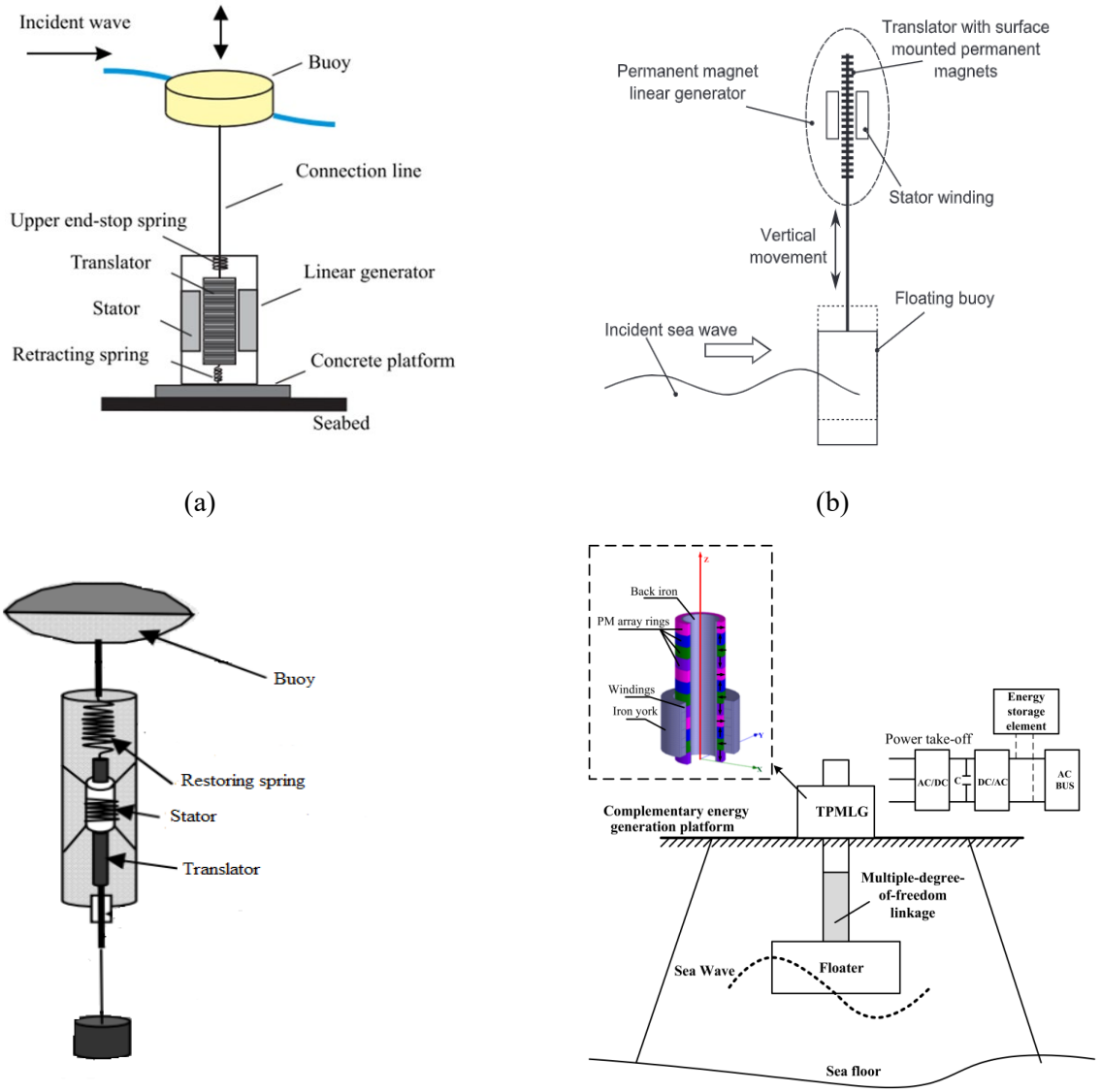

Figure 2.3: Floating buoy on the sea surface (a) Linear generator fixed in the seabed (Hai et al., 2015), (b) Linear generator above the sea surface (López et al., 2013), (c) Floating linear generator underneath the ocean surface (Bastien et al., 2009) and (d) Linear generator above the sea surface (Zhang et al., 2018)

The other common design concept is to leave the linear generator floating underneath the ocean surface and the translator directly connected with the floating buoy on the sea surface by tether

(Bastien et al., 2009), as presented in Figure 2.3(d). Figure 2.4 presents a new concept where the whole linear generator system floats on the sea surface. Based on these concepts, different types of direct drive linear generator WEC have been developed. The most appropriate technique might be to have the overall system partially above the sea surface because the submerged systems create difficulties such as moorings, seawater corrosion, and access for maintenance.

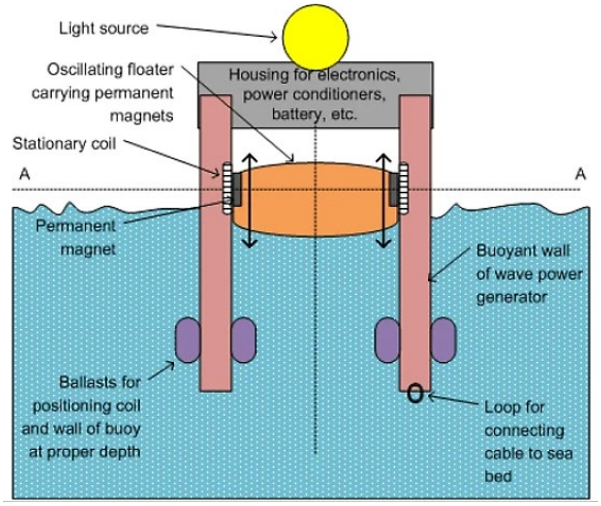

Figure 2.4: Floating linear generator on the sea surface (Panicker, 2012)

2.2.2.1 Single body heaving buoy system

The single body heaving system is the most common in the direct-drive linear wave energy converters research because of its simplicity. Figure 2.3 presents some single body heaving system type WEC with linear generators. The well-known direct drive linear generator based WEC developed at Uppsala University, and Oregon University was based on the single body heaving system (Brekken et al., 2009b; Castellucci et al., 2016). The WEC system, developed by the University of Uppsala, consisted of a buoy and a linear generator whose linear generator was fixed to the seabed and whose translator moved with the buoy. The rectangular-shaped translator had several permanent magnets, and the wound coils were connected with the stator (Waters, Stålberg, et al., 2007). Springs have been used to connect the translator with the linear generator foundation to retract the translator in the wave troughs (Leijon et al., 2008). A fixed component at the bottom of the sea spring counteracts the buoy's motion by driving the linear generator's moving part. End stops have been used at the top and bottom of the device to restrict the translator's stroke length during extreme oceanic conditions (Leijon et al., 2008). Oregon State University developed a linear generator consisting of a spar and a float in which

the spar was moored and the float moved with the waves. A cylindrical bobbin wound with a three-phase armature formed the spar, while a cylinder containing 960 magnets formed the float. When the float moved up and down with wave motion, the voltage was directly produced inside the armature since the inner surface of the float faces the outer surface of the spar (Prudell et al., 2009b; Prudell, 2007). It was roughly 3.3 meters high, 1.2 meters wide, and rated for 10 kW of power (Brekken et al., 2009a).

2.2.2.2 Two-body heaving buoy system

It is challenging to construct a device with a natural frequency that matches the low frequency of the incoming waves to achieve resonance with a single body heaving system. The distance between the floater and the seabed can be significant, and due to this significant distance, the single body heaving system has reduced efficiency. To solve these problems, some researchers proposed two-body heaving systems (Amiri et al., 2016; Engström et al., 2009; Liu, Yu, Hu, Liu, Zhou, et al., 2013). The two-body heaving system consists of either a floating section that deals directly with the wave and a fully submerged section or two floating sections (Gao et al., 2016). Submerged buoys or passive buoys provide inertia for damping, while floating buoys in combination with submerged buoys assist in following the wave frequencies closely (Rahman et al., 2020). The linear generator can be mounted between the two bodies to avoid the large linear generator connection distance between the seabed and the free surface. There are two common types of two body heaving systems, as shown in Figure 2.5. Both bodies move due to the wave motion and create relative motion between them, causing both translator and stator of the linear generator system to move, which helps increase efficiency. Elie Al Shami et al. reviewed the studies of single and two body heaving systems with their dynamics, hydrodynamics, advantages and disadvantages (Al Shami et al., 2019). The power capture ratio of the two-body heaving system's converter has been reported to be approximately 80% when the irregular waves. If a 14-ton translator was used, the coupling between the linear generator, submerged body (passive buoy), and floating buoy on the sea surface became rigid. In addition, if the submerged body (passive buoy) was placed at a depth of 40m, then the reported achieved power capture ratio was around 80%. The power capture ratio decreased to about 50% when the depth decreased by 30m. The resonance behaviour of the two-body heaving system has significantly affected the linear generators' efficiency.

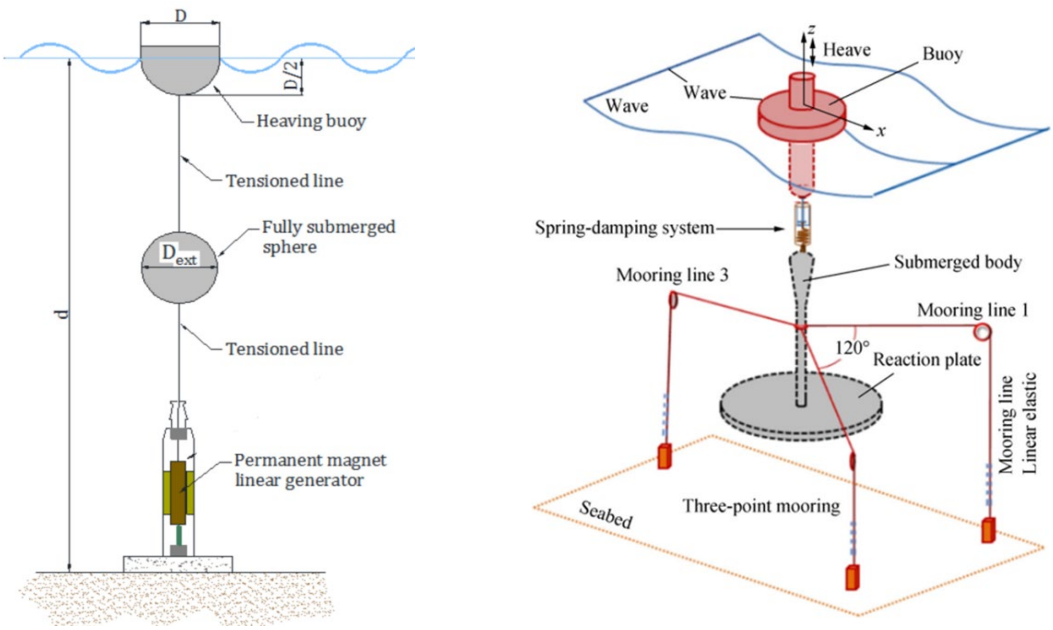

(a) (b)

Figure 2.5: Two-body heaving system (a) Linear generator fixed in the seabed (Piscopo et al., 2018) (b) Linear generator fixed between two bodies (Berenjkoob et al., 2019)

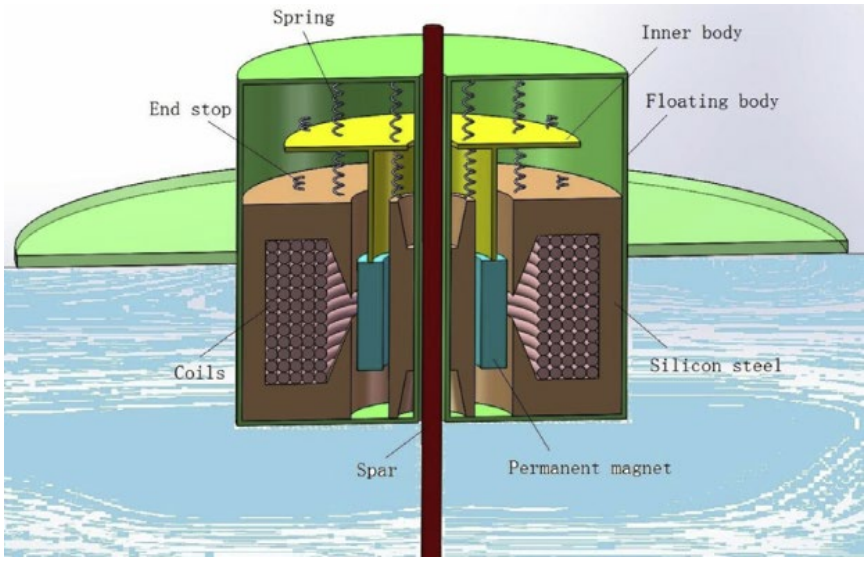

Figure 2.6: Fully floating two body heaving system (Gao et al., 2016)

Moreover, another novel topology has been developed, as shown in Figure 2.6, which may be categorised as a fully floating two body heaving direct drive linear generator WEC (Gao et al., 2016). The proposed system consists of a spar fixed on the seafloor and a floating system with two parts. The permanent magnets are mounted in the inner body, and the windings coils are mounted in the

outer body. Both outer and inner bodies freely move up and down along the spar, and during the movement, the outer body acts as a floating buoy to harness the wave energy. In contrast, the inner body experiences a forced oscillation.

2.2.3 Fully submerged heaving system

Archimedes Wave Swing (AWS) is a fully submerged direct-drive device and was the first WEC device to use a linear permanent magnet generator for PTO. (H Polinder et al., 2005). The linear generator of the device is attached to a compressed air chamber fixed on the seabed. The translator of the linear generator is connected with the floater that is fully submerged (underwater). The working principle of the AWS is based on the oscillating movement of the sea waves, which increases and decreases pressure levels successively under the sea surface because of the wave motion. The wave motion causes the floater to move vertically up and down relative to the fixed lower part, thereby increasing the wave pressure levels, which then causes the air inside the chamber to be compressed. When the air pressure inside the chamber is greater than the wave, the volume inside expands (Henk Polinder et al., 2005). Electrical energy was generated from the wave motion because of this reciprocating linear motion. However, the completely submerged system has the same advantages and disadvantages as the AWS. These fully submerged systems are not visibly gaining public acceptance, though they are less vulnerable in severe ocean conditions. On the other hand, ocean environmental conditions require higher maintenance costs. A fully submerged system also has the disadvantage of corroding metals and disturbing marine life.

2.2.4 Other topologies of WECs with linear generator-based PTO systems

Other than having the floating buoy on the sea surface and fully submerged heaving systems, there are different topologies of WECs with linear PM generators, such as the fully floating gyroscopic system and buoyant system, that have been proposed and tested experimentally (Boscaino et al., 2017; Cappelli et al., 2013). The fully floating gyroscopic system based WEC consists of gyroscope systems and linear permanent magnet generators located inside a fully sealed buoy (Boscaino et al., 2017). By using gyroscope inertial reactions, the device is slack-moored to the ocean floor (inertial sea wave energy converter (ISWEC)). During operation, the gyroscopic system, which drives linear generators, reciprocates motion between the hull and the cylinder. On the other hand, the buoyant electrical

generator based WEC is a point absorber type device that consists of a linear generator, boat shape buoy and a power electronic section, as shown in Figure 2.7(a) (Trapanese et al., 2018).

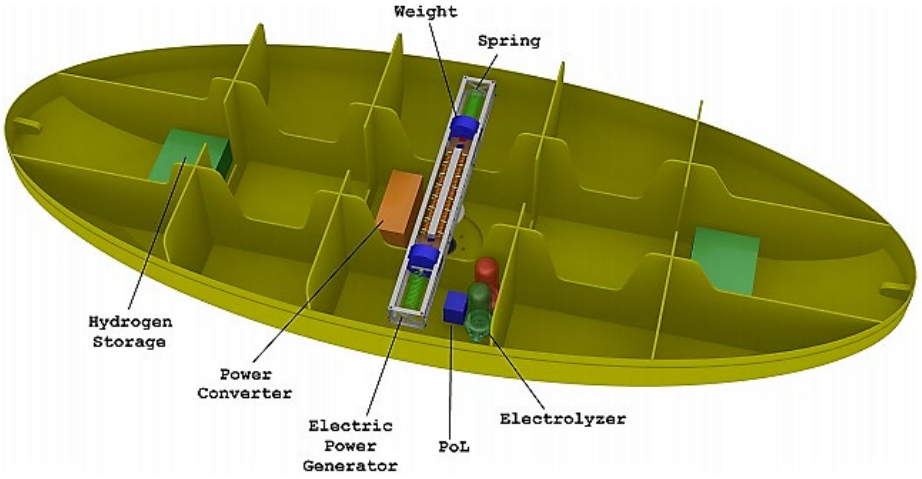

(a)

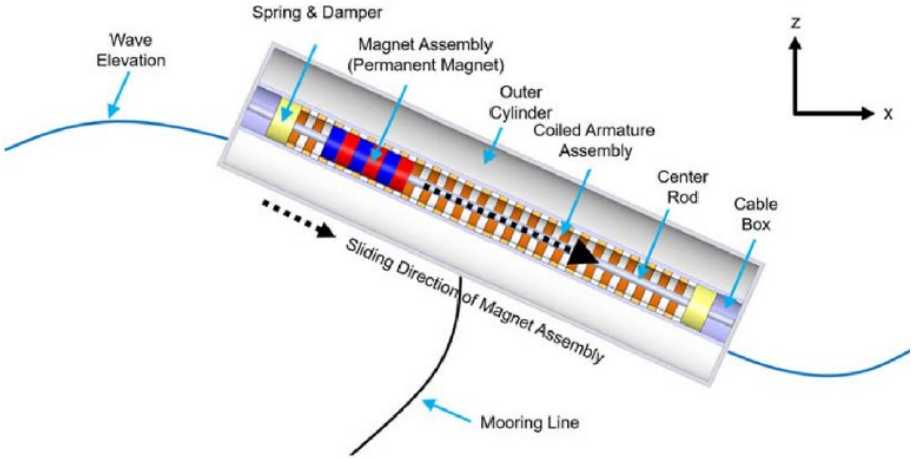

(b)

Figure 2.7: (a) Buoyant WEC (Trapanese et al., 2018) and (b) surface riding WEC (Jin et al., 2020)

The linear generator is placed inside the buoyant system. The proposed device provides a highly reliable wave energy conversion system that can also produce hydrogen to store energy. Another new topology of WEC with a linear PM generator has been proposed, known as a surface riding wave energy converter, where the magnet assembly slides inside the armature (Jin et al., 2020). The proposed surface riding WEC is presented in Figure 2.7(b).

2.3 PTO System based on Linear Permanent Magnet (PM) Generator

Thus far, different types of linear generators have been used for WEC, and these generators include linear permanent magnet synchronous generators (Antipov et al., 2017; Elwood et al., 2010; Niu, 2013; Polinder et al., 2004; Seo et al., 2020; Shibaike et al., 2007), flux-switching permanent magnet linear generators (Huang et al., 2013; Huang et al., 2011), switched reluctance linear generators (Di Dio et al., 2014), Vernier hybrid machines (Baker et al., 2018), and so on. PM based linear generators are suitable for energy harvesting across the broadband frequency ranges due to the availability of low-cost power electronic converters and the permanent magnet (PM) material's improvements in terms of remnant flux density, coercive force, magnetic flux leakage, and copper losses of field windings (Faiz & Nematsaberi, 2017b; Mueller et al., 2008).

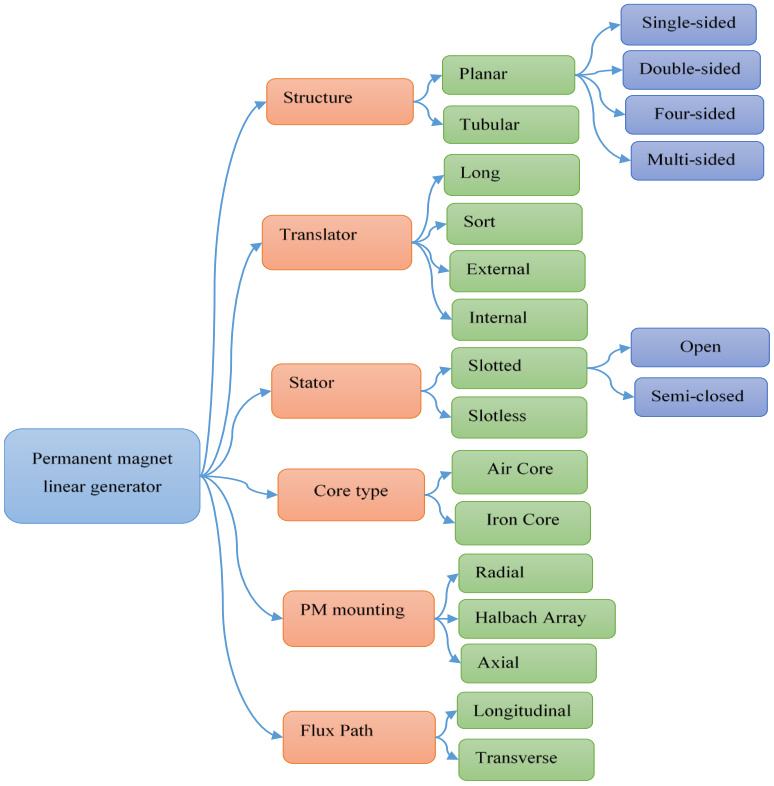

Figure 2.8: Linear PM generator topologies

Moreover, the exerted force and power density can be increased by using permanent magnet excitation. Syncernous permanent magnet generators are highly efficient at low speeds and are relatively cheap, so, up until now, linear generators for wave energy conversion have been developed using synchronous permanent magnet generators (Danielsson et al., 2005; Huang et al., 2013;

Polinder et al., 2004; Henk Polinder et al., 2005; Yu et al., 2012). The PM-based linear generator's geometry plays a significant role in design development, and its variation substantially affects overall performance and efficiency. In the literature, various PM linear generator topologies have been proposed for wave energy conversion systems, shown in Figure 2.8. The main components of the linear PM generator are permanent magnets and coils. The linear PM generator topologies can be classified according to various design methods based on the structure, translator size and location, stator shape, core type, location of the permanent magnet (PM), Flux path and the way of installing the PM. The structure of the linear PM generator may be tubular or planar/flat types (Baker et al., 2004; Hodgins et al., 2011; Oprea et al., 2010; Rao et al., 2017; Wahyudie, Jama, et al., 2017). It is easier to fabricate the planar type linear generator for WEC, and it can be constructed with different sides such as two-sided, four-sided planar, octagonal or multisided planar (I. A. Ivanova et al., 2005; Oprea et al., 2010; Wahyudie, Susilo, et al., 2017). Using the double-sided planar layout and tubular layout, a hybrid generator concept has been proposed, which creates higher force density due to more effective use of space (Joseph & Cronje, 2007). Different translator sizes and positions have been used in linear PM generators for direct drive WEC.

In order to maintain a system's generation operation for the larger fraction of the stroke, either the translator or the stator must be longer. In permanent magnet generators, the translator is usually longer than the stator to ensure the windings of the stator are active throughout the full stroke and reduce the amount of losses due to copper and conduction (Prudell et al., 2010). Moreover, the translator can be mounted internally or externally on the generator design for the direct drive WEC (Liu, Yu, Hu, Liu, Zhou, et al., 2013; Prudell et al., 2010). There are three possible ways to attach the permanent magnets: axially aligned-buried, radially aligned-buried and radially aligned-surface (Joseph & Cronje, 2007). To get maximum magnetic flux density, Halbach and quasi-Halbach arrays have been used in linear PM generators for WEC (Farrok, Islam, Sheikh, Guo, & Zhu, 2017; Liu, Yu, Hu, Liu, Zhou, et al., 2013). The linear generators can be classified as transverse flux and as longitudinal flux, according to the location of windings relative to translator motion (Curto et al., 2020). Using both transverse and longitudinal flux, a new hybrid transverse/longitudinal flux linear PM generator has been developed for WEC (Vining et al., 2009). Translators were sandwiched between stators that carried flux longitudinally, while they carried flux transversally. Both slotless and slotted stators have been used in the research to develop and find the best generator design (Liu et al., 2010; Tan et al., 2018). Based on using a core, the linear PM generator can be classified as an iron-core or air-core

generator. Both iron-core and air-core generators have been used in the direct electric drive PTO system based WEC (Brooking & Mueller, 2005; Hodgins et al., 2011; Mueller et al., 2006; Ran et al., 2011). All linear generator topologies with their advantages and drawbacks have been discussed briefly (Faiz & Nematsaberi, 2017a, 2017b; Khatri & Wang, 2019). There have also been some new design concepts proposed to capture the maximum amount of energy from ocean waves beyond these topologies (Beeby et al., 2013; Owens & Mann, 2012; Wang, 2016).

2.4 Mathematical Modelling

2.4.1 Dynamics of the WEC with linear permanent magnet (PM) based PTO system

The hydrodynamic modelling of the system analyses the forces acting on the submerged rigid bodies and the motion relative to them. Different theories, such as linear wave theory and Stokes theory, can be used to describe and solve the modelling related to wave-body interaction. The applicability of various wave theories can be found in (Le Méhauté, 2013). Figure 2.9 shows the schematic diagram of a typical WEC system consisting of a linear generator attached to a floating buoy by a tether.

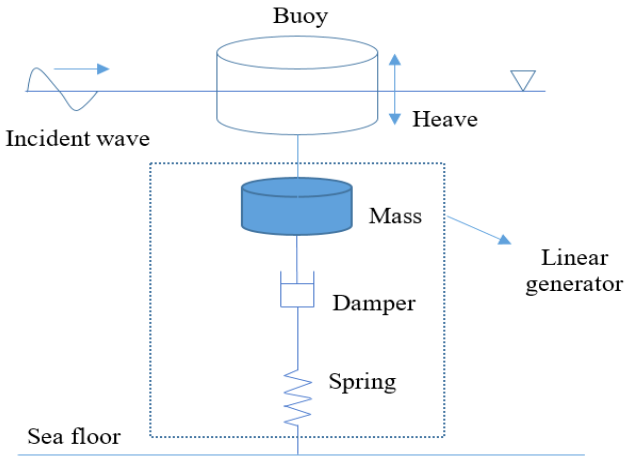

Figure 2.9: Schematic diagram of a heaving direct drive WEC with linear PM generator (Cheng et al., 2014)

For this situation, the linear wave theory has been verified experimentally to be good enough to explain the wave body interaction (Engström et al., 2011; Zurkinden et al., 2014). Thus, linear wave theory is accepted to find the hydrodynamic parameters and buoy force (wave forces) which help develop the dynamic model of the WEC with a linear PM generator. In addition, it is assumed that the linear generator based wave energy converter can be modelled using an equivalent spring-mass-

damper system, in which an opposing force is produced by the generator proportional to acceleration, velocity, and position (Brekken et al., 2009b; L. Wang et al., 2015). Even though the floating body has six degrees of freedom, only the heave motion has been taken into account for simplicity (Cheng et al., 2014; Gao et al., 2016). Based on Newton's second law, the system (heaving buoy) force equation can be expressed by equation 2.1 (Eriksson et al., 2005; Gao et al., 2016; Hong, 2016; Huang et al., 2016; I. Ivanova et al., 2005; Leijon et al., 2006).

$$m\ddot{y} = F_{buoy} + F_e + F_{gen} \qquad (2.1)$$

where m is equal to the sum of the translator and buoy mass, and only the translator mass if there is slack in the line/rope, F_{buoy} is the buoy force, F_{gen} is the generator force and F_e is the electromagnetic force. Moreover, $\ddot{y}$ is the buoy acceleration as well as translator acceleration under excitation from waves. The wave motion and acting spring drive the vertical motion of the translator. Electromagnetic forces (F_e) are generated between the stator and translator of a generator when the translator moves. The buoy force (F_{buoy}) is the lifting force that results from the Archimedes principle, which is proportional to the amount of water displaced by the buoy. Moreover, the buoy force (F_{buoy}) is known as hydrodynamic force that is acting on the buoy, which can be expressed by equation 2.2. In equation 2.2 F_{we} is the wave excitation force, F_r is the wave radiation force and F_h is the hydrostatic force.

$$F_{buoy} = F_{we} + F_r + F_h \qquad (2.2)$$

Moreover, y can be described as $y(i\omega) = y\,exp(i\omega t)$ in harmonic form; then $\dot{y}(i\omega) = i\omega y(i\omega)$, $\ddot{y}(i\omega) = -\omega^2 y(i\omega)$. The system force can be stated as follows after adding the buoy force (F_{buoy}) in the frequency domain and time domain by equation 2.3 and 2.4, respectively (Brekken, 2011; Cheng et al., 2014; Li et al., 2017; Rhinefrank et al., 2006).

$$-\omega^2 y(i\omega)m = F_{we}(i\omega) + F_r(i\omega) + F_h(i\omega) + F_e(i\omega) + F_{gen}(i\omega) \qquad (2.3)$$

$$m\ddot{y}(t) = F_e(t) + F_{we}(t) + F_r(t) + F_h(t) + F_{gen}(t) \qquad (2.4)$$

In equation 2.3, $-\omega^2 y(\omega)$ is the frequency domain second derivative of the buoy heave vertical position. During the second wave phase, the device's spring accelerates the translator. The spring force increases the velocity of the translator. The end stop force does not operate at normal operation conditions and acts only when the translator stroke exceeds its limits due to too high wave heights.

As expected, the movement of the translator of the linear generator is in accordance with the buoy, and the general generator force (F_{gen}) can be expressed in equation 2.5 (Cheng et al., 2014).

$$F_{gen} = -\beta_m \dot{y} - \gamma y \tag{2.5}$$

Here, β_m is the damping coefficient of the generator and γ is the spring constant of the generator system. From equation 2.5, it can be simplified that the inner magnet and coil work as a damper system. Many researchers in the WEC research field conducted their studies regarding the linear generator as a constant damper (Eriksson et al., 2005; Stålberg et al., 2008). Moreover, it can be said that the force provided by the linear generator (F_{gen}) opposes the movement of the buoy which means that the damping force of the generator is proportional to the translator speed with the damping coefficient. The wave radiation force (F_r) and hydrostatic force (F_h) can be expressed in frequency and time domains as,

$$F_r(i\omega) = -[R_y(\omega) + i\omega m_a(\omega)]\dot{y}(i\omega) \tag{2.6}$$

$$F_r(t) = -R_y \dot{y}(t) - m_a \ddot{y}(t) \tag{2.7}$$

$$F_h(i\omega) = -\rho g \pi b^2 y(i\omega) \tag{2.8}$$

$$F_h(t) = -\rho g \pi b^2 y(t) \tag{2.9}$$

where ρ is the density of the seawater, b is the radius of the buoy, and g is the gravity acceleration. R_y is the radiation damping and m_a is the added mass. The electromagnetic force F_e can be obtained from the FE-calculation of the field in the generator. According to Faraday's law, the electromagnetic force is created when the magnet oscillates through a coil. This moving magnet changes the magnetic flux and changes the current in the induction coil. The materials used in the stator, translator, and vibration frequency impact the generator's efficiency. It has a close relationship with the existence of eddy current losses and hysteresis of the generator. The generator's eddy current losses and hysteresis are normally ignored for general simplification because considering all uncontrollable variables becomes very complicated. For that reason, the generated current in the coil due to the magnet movement through the coil can be expressed by equation 2.10 by using Kirchoff's voltage law (Mann & Owens, 2010).

$$L\dot{I} + IR + a(y)\dot{y} = 0 \tag{2.10}$$

$$\frac{L}{R}\dot{V} + V + a(y)\dot{y} = 0 \tag{2.11}$$

where L is the inductance of the coil itself, R is the load resistance of the circuit, I is the current inside the coil, $a(y) = NB_x l$ is the coupling coefficient between the mechanical and electrical system, and $V = IR$ is the voltage inside the coil. y and $\dot{y}$ are the position and velocity of the magnets which attach with the translator. The item $L\dot{I}$ in equation 10 represents the counter electromotive force generated by the coil's current change and $a(y)\dot{y}$ denotes the electromotive force produced by coupling the coil and the moving magnet. The item of the coupling coefficient consists of the time-varying part of the inductance. The Laplace transform (ℓ) of the equation 2.12 under the initial conditions $\dot{y} = 0$ and $V = 0$ can be given as

$$V(s) = -\frac{\ell[Ra(y)\dot{y}]}{Ls + R} \tag{2.12}$$

In the research area of the wave energy converter, it is assumed that the electrical system behaves like a damper, which is a general simplification of the linear generator. It is also assumed that the resistance R is relatively large, so then the voltage is expressed as

$$V = -a(y)\dot{y} \tag{2.13}$$

Due to the movement of the magnet through the coil, the electromagnetic force works on the magnets, which can be expressed as

$$F_e = \frac{a(y)V}{R} \tag{2.14}$$

By replacing V (equation 2.13) in equation 2.14, the electromagnetic force can be written by equation 2.15, which can be used directly to calculate the electromagnetic force between a coil and the oscillating magnet (Williams & Yates, 1996).

$$F_e = -\frac{a(y)^2\dot{y}}{R} \tag{2.15}$$

If the electromagnetic damping of the linear generator is defined by equation 2.16, then the electromagnetic force can be calculated by equation 2.17.

$$\beta_e = \frac{a(y)^2}{R} \tag{2.16}$$

$$F_e = a(y)I = -\beta_e y \tag{2.17}$$

where, β_e is the generator electrical damping coefficient. After putting F_r, F_h, F_{gen} and F_{we} into equation 2.3, the system force can be stated in the frequency domain as,

$$\left[-\omega^2\big(m + m_a(\omega)\big) + i\omega\left(\beta_e + \beta_m + R_y(\omega)\right) + g\rho\pi b^2 + \gamma\right] y(i\omega) = F_{we}(i\omega) \tag{2.18}$$

$$\left[-\omega^2\big(m + m_a(\omega)\big) + i\omega\left(\beta + R_y(\omega)\right) + g\rho\pi b^2 + \gamma\right] y(i\omega) = F_{we}(i\omega) \tag{2.19}$$

In equation 2.19, the β ($\beta = \beta_m + \beta_e$) is the sum of the mechanical and electrical damping of the generator. Moreover, equation 2.19 can be written as the transfer function

$$H(i\omega) = \frac{F_{we}(i\omega)}{\left[-\omega^2\big(m + m_a(\omega)\big) + i\omega\left(\beta + R_y(\omega)\right) + g\rho\pi b^2 + \gamma\right]} \tag{2.20}$$

The system's natural frequency can be calculated by equation 2.21 (Engström et al., 2011; Li et al., 2017). The total damping ratio is denoted by ξ and it can be expressed by equation 2.22.

$$\omega_n = \sqrt{\frac{\rho g\pi b^2 + \gamma}{m + m_a}} \tag{2.21}$$

$$\xi = \frac{\beta + R_y}{2(m + m_a)\omega_n} \tag{2.22}$$

The mechanical damping constant can be measured by equation 2.23 where ξ_m is the mechanical damping ratio.

$$\beta_m = 2\xi_m\sqrt{(\rho g\pi b^2 + \gamma)(m + m_a)} \tag{2.23}$$

The dynamical response of the buoy and translator can be written as

$$y(t) = \left[\frac{F_{we}(i\omega)}{\left[-\omega^2\big(m + m_a(\omega)\big) + i\omega\left(\beta + R_y(\omega)\right) + g\rho\pi b^2 + \gamma\right]}\right] cos(\omega t + \sigma) \tag{2.24}$$

Moreover, after adding F_r, F_h, F_{gen} and F_e into equation 2.4, the system force can be stated in the time domain by equation 2.25.

$$(m + m_a)\ddot{y}(t) + (\beta + R_z)\dot{y}(t) + (g\rho\pi b^2 + \gamma)y(t) = F_{we}(t) \qquad (2.25)$$

Taking the inverse Fourier transformation of equation 2.25, the equation of motion in the time domain can be expressed by equation 2.26.

$$\big(m + m_a(\infty)\big)\ddot{y} + \int_0^t k(t-\tau)\dot{y}\,d\tau + \beta\dot{y} + \rho g\pi b^2 y + \gamma y = F_{we} \qquad (2.26)$$

The symbol $k(t)$ is the radiation function which is related to radiation damping R_y ($y(\omega) = \int_0^\infty k(t)\cos(\omega t)\,dt$). The state space representation of the WEC motion using the dependent radiation force can be shown to be given by equations (2.27) – (2.29), (So, 2017) using matrix representation. The WEC equation of motion given in (2.25) can be expressed in time-domain state space form as (Brekken, 2011),

$$\frac{d}{dt}\begin{bmatrix}\dot{y}\\ y\end{bmatrix} = \underbrace{\begin{bmatrix}\frac{-(\beta_e + R_y)}{m+m_a} & \frac{-g\rho\pi b^2}{m+m_a}\\ 1 & 0\end{bmatrix}}_{\boldsymbol{A}}\begin{bmatrix}\dot{y}\\ y\end{bmatrix} + \underbrace{\begin{bmatrix}\frac{1}{m+m_a}\\ 0\end{bmatrix}}_{\boldsymbol{B_u}}[F_{gen}] + \underbrace{\begin{bmatrix}\frac{1}{m+m_a}\\ 0\end{bmatrix}}_{\boldsymbol{B_v}}[F_{we}] \qquad (2.27)$$

$$\dot{y}(t) = \boldsymbol{A}y(t) + \boldsymbol{B}F_{gen}(t) + \boldsymbol{B}F_e(t) \qquad (2.28)$$

$$x(t) = Cy(t) + Du(t) \qquad (2.29)$$

where $\dot{y}$ is known as the state vector and y is called the output vector. $\boldsymbol{A}$ and $\boldsymbol{B}$ in equation 2.28 are known as the state or system matrix and input matrix, respectively. Moreover, *C* and *D* in equation 2.29 are called the output matrix and zero matrix, respectively. However, the excitation force (F_{we}) is often simplified as a harmonic term or series. The excitation force on the heaving buoy can be described by equation 2.30 (Zheng et al., 2015) or equation 2.31 (Rhinefrank et al., 2006).

$$F_{we}(t) = A_f F_1 sin(\omega t + \varphi) \qquad (2.30)$$

$$F_{we}(t) = F_0 cos(\omega t + \varphi) \qquad (2.31)$$

Where, A_f is the amplitude of the wave, F_1 is the wave force coefficient, ω is the frequency of the regular wave, and φ is the phase of the regular wave.

2.4.2 Electromagnetic model

Consider a linear translator with permanent magnets (PMs) attached with alternating polarity and that the translator is moving vertically sinusoidally. The relative motion between the translator and stator creates an induced voltage inside the winding coils. The governing equations for the electromagnetic mechanism of the linear permanent magnet generator based WEC can be expressed by equations 2.32 and 2.33, where equation 2.32 is the dynamics equation of the WEC and equation 2.33 is the dynamic equation of the current of the coils.

$$(m + m_a)\ddot{y} + \left(\beta_m + R_y\right)\dot{y} + (g\rho\pi b^2 + \gamma)y + F_e = F_{we} \tag{2.32}$$

$$RI + L\frac{dI}{dt} = a\frac{dy}{dt} \tag{2.33}$$

After adding $F_e = aI$ and $a = NB_x l$, the equations 2.32 and 2.33 can be expressed as

$$(m + m_a)\ddot{y} + \left(\beta_m + R_y\right)\dot{y} + (g\rho\pi b^2 + \gamma)y + aI = F_{we} \tag{2.34}$$

$$(m + m_a)\ddot{y} + \left(\beta_m + R_y\right)\dot{y} + (g\rho\pi b^2 + \gamma)y + NB_x lI = F_{we} \tag{2.35}$$

$$RI + L\frac{dI}{dt} = NB_x l\frac{dy}{dt} \tag{2.36}$$

The equations 2.35 and 2.36 can be solved by using the integration method, which can be written as

$$\ddot{y} = \frac{F_{we}}{(m + m_a)} - \frac{\left(\beta_m + R_y\right)}{(m + m_a)}\dot{y} - \frac{(g\rho\pi b^2 + \gamma)}{(m + m_a)}y - \frac{NB_x l}{(m + m_a)}I \tag{2.37}$$

$$\frac{dI}{dt} = \frac{1}{L}\left(NB_x l\frac{dy}{dt} - RI\right) \tag{2.38}$$

By considering the state variables z_1, z_2 and z_3 the system equations 2.37 and 2.38 can be written in state space form by the following

$$z_1 = y \tag{2.39a}$$

$$z_2 = \dot{y} = \frac{dz_1}{dt} \tag{2.39b}$$

$$\frac{dz_2}{dt} = \ddot{y} \tag{2.39c}$$

$$z_3 = I \tag{2.39d}$$

$$\frac{dz_3}{dt} = \dot{I} \tag{2.39e}$$

$$u = F_e = F_0 cos(\omega t + \varphi) \tag{2.39f}$$

The resulting state space matrix form of the differential equations 2.37 and 2.38 can be expressed as

$$\begin{bmatrix} \frac{dz_1}{dt} \\ \frac{dz_2}{dt} \\ \frac{dz_3}{dt} \end{bmatrix} = \underbrace{\begin{bmatrix} 0 & 1 & 0 \\ -\frac{(g\rho\pi b^2 + \gamma)}{(m + m_a)} & -\frac{(\beta_m + R_z)}{(m + m_a)} & -\frac{NB_x l}{(m + m_a)} \\ 0 & \frac{NB_x l}{L} & \frac{-R}{L} \end{bmatrix}}_{A} \begin{bmatrix} z_1 \\ z_2 \\ z_3 \end{bmatrix} + \underbrace{\begin{bmatrix} 0 \\ \frac{1}{(m + m_a)} \\ 0 \end{bmatrix}}_{B} [u] \tag{2.40a}$$

$$[x] = \underbrace{\begin{bmatrix} 1 & 0 & 0 \\ 0 & 1 & 0 \\ 0 & 0 & 1 \end{bmatrix}}_{C} \begin{bmatrix} z_1 \\ z_2 \\ z_3 \end{bmatrix} + [0][u] \tag{2.40b}$$

Calculating the translator's position and velocity and the generator's output voltage can be done by using Equations 2.40(a) and 2.40(b). The MATLAB ODE file or Simulink can be used to solve these equations. In addition, to calculate the induced voltage inside the stator coils of the WEC linear generator, the equation 2.41 (Faraday's law of induction) has been used by many researchers (Gao et al., 2016; Hong et al., 2016; Masoumi & Wang, 2016; Thorburn & Leijon, 2007).

$$e(t) = -N\frac{d\Phi}{dt} \tag{2.41}$$

Here Φ is the flux and N is the number of turns. Assuming that the magnetic flux has a sinusoidal form, it can be expressed by equation 2.42 (Hong et al., 2016).

$$\Phi = \Phi_0 . sin(\sigma y + \delta) \tag{2.42}$$

where, Φ_0 is the magnitude of the magnetic flux and δ is the phase angle. σ is the wave number that can be measured by the wavelength λ and can be expressed as $\sigma = 2\pi/\lambda$. If the magnetic flux is time dependent on the y-axis, then

$$\frac{d\Phi}{dt} = \sigma\Phi_0.cos(\sigma y + \delta).\frac{dy}{dt} \quad (2.43)$$

Adding equation 2.43 into equation 2.41 gives equation 2.44.

$$e(t) = -N\frac{d\Phi}{dt} = -N\sigma\Phi_0.cos(\sigma y + \delta).\frac{dy}{dt} \quad (2.44)$$

N is the number of effective turns per pole and phase, expressed by equation 2.45.

$$N = \frac{k_w q n_s}{2c} \quad (2.45)$$

where, k_w is the winding factor, q is the number of slots per pole and phase, n_s is the number of conductors per slot, and c is the number of parallel current paths per phase.

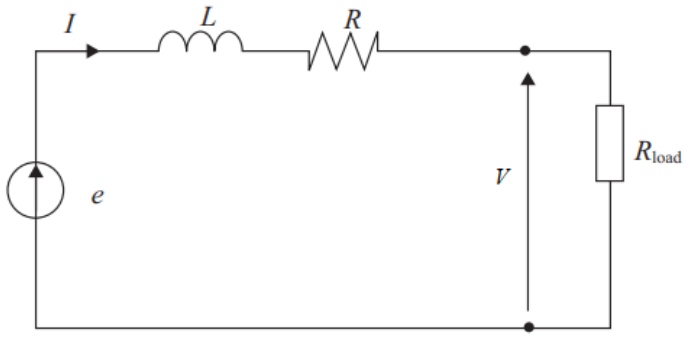

Figure 2.10: Equivalent circuit for linear generator (Zheng et al., 2015)

Through the equivalent electric circuit, as shown in Figure 2.10, the voltage V(t) at the terminals for a single phase can be expressed as well by equation 2.46 (Gao et al., 2016; Rhinefrank et al., 2006; Vermaak & Kamper, 2012) where R is the circuit resistance, L is the circuit inductance.

$$V(t) = e(t) - RI(t) - L\frac{dI(t)}{dt} \quad (2.46)$$

For the three-phase linear generator, the induced voltage measuring equation 2.44 can be written as follows (Hong, 2016)

$$e_a = -N\sigma\Phi_0.cos(\sigma y).\frac{dy}{dt} \quad (2.47a)$$

$$e_b = -N\sigma\Phi_0.cos\left(\sigma y + \frac{2\pi}{3}\right).\frac{dy}{dt} \quad (2.47b)$$

$$e_c = -N\sigma\Phi_0.cos\left(\sigma y - \frac{2\pi}{3}\right).\frac{dy}{dt} \quad (2.47c)$$

The three-phase resistive load can be added to the device's output ports to validate the linear generator model. As shown in Figure 2.11, the resistive load can be considered a delta link, and it can be connected to the sea cable on the output side of the generator.

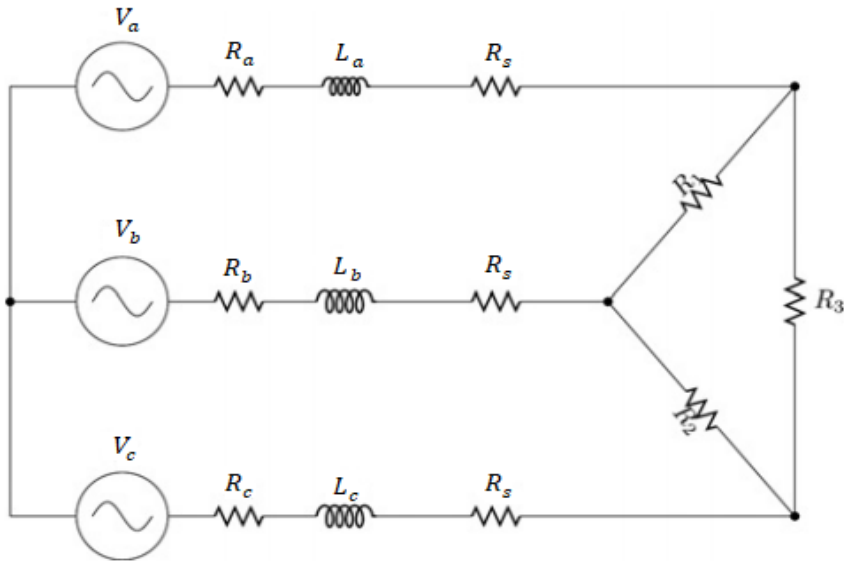

Figure 2.11: Circuit diagram of a generator connected with three-phase resistive load (Waters et al., 2011)

Table 2.1: The structural parameters of the linear generator and the buoy

Structure	Parameters and S.I. Units
Linear generator	Pole width (m), Pole pitch, Number of poles, Air gap magnetic flux density (T), Air gap (m), Number of turns, Number of slots, Width of a stator tooth (m), Teeth thickness (m), Width of the stator stack (m), Translator iron thickness (m), Length of the generator (m), Resistance of the coil (Ω), Circuit resistance (Ω), Load resistance (Ω), Number of phases, Mass of the magnets (kg), Load angle (rad)
Buoy	Wave period (s), Wave height (m), Mass of the buoy (kg), Diameter of the buoy (m), Height of the buoy (m), Density of the seawater (kg/m^3)

From the above discussion, there are many parameters that need to be considered to model the WEC, including the linear PM generator parameters and the buoy parameters. From theory, it can be stated that the generator's excitation force and damping force are the control variables of the linear PM generator based WEC. The typical structural parameters of the single buoy linear PM generator based WEC have been presented in Table 2.1.

2.5 Challenges of linear generator type PTO systems

Through linear motions between the fixed stator and moving translator, the linear PM generator harvests energy directly. Due to the translator motion, the resulting change of the magnetic field creates an induced voltage in the winding coils based on Faraday's law. In this type of WEC system, the waves act as driving forces, and the generator acts as dampers (Czech & Bauer, 2012). Therefore, damping is one of the most important factors of this type of device because the absorbed energy strongly depends on the damper. Moreover, another important factor is reaction force which needs to be big to get the same output power when the generator in the direct drive system moves slowly. Due to the attraction forces between the stator and translator, these systems have several disadvantages, including low power to weight ratios (large machines are required) and heavy structure requirements (Penalba & Ringwood, 2016). The incoming ocean waves continuously vary and their speeds are also different; therefore, the generator generates varying power. Because of that, extreme values are needed to consider. As a result, overload is considered another important factor of the device (Czech & Bauer, 2012). The stroke length of the generator is also an important factor of the device because it should be set according to the wave heights. Due to different wave inputs, the output induced voltage varies, and for that reason, to connect the device with a commercial grid, the voltage level needs to be set, the current needs to be rectified and the frequency changed. So, the grid connection is also an important factor of this type of device, and the power transmission system is very complicated.

Moreover, solving the complex electromechanical coupling issues as reviewed in the literature is also one of the important factors for the linear PM generator type PTO system design. Compared with other types of PTO systems such as hydro, pneumatic, hydraulic and direct mechanical drive, it can generate directly electrical energy from mechanical energy and has reasonable efficiency (95%) (Pecher & Peter Kofoed, 2017; Qiao et al., 2020). The device's structure is also simpler than other PTO systems, and it requires fewer maintenance costs but overall manufacturing costs are expensive.

It is known that the translator of the linear generator consists of magnets mounted on an iron or electrical steel plate between iron or aluminium spacers, and the stator is made of non-oriented laminated electrical steel or iron with a thin insulating coating to reduce eddy current losses. The magnet's fluctuating price increases the overall cost. The linear generator type PTO system based WEC is indeed the relatively low distribution of the technology, resulting in the need for a tailored generator that comes out with high investment cost and additional development risks (Bard & Kracht, 2013). Generally, it is difficult to estimate the total cost of the generator because it depends on many different variables (Eriksson, 2019). The translator height changes because of the stator height and wave height, and the translator cost varies. The magnet weight can be changed due to the number of poles and the number of conductors per slot. Using heavy magnets increases the mass of the whole system, which decreases the efficiency because of the low velocity of wave oscillations (Aderinto & Li, 2018). Solid steel can be used for the generator's translator body with low electrical frequency. Conductor (copper) costs per kg are higher than those for steel stator used in the original design, and translator costs are less than the cost of stator steel. Copper wire or standard cables are typically used in the stator winding, which is low priced material in the international market.

Moreover, the materials used in the concrete foundation are sea-water resistant materials that are twice as high as those of ordinary materials used in the civil building sector. According to the average total cost of a specialized assembly, manufacturing costs are also high. Based on a broad analysis of current international market prices, the calculated unit prices of the most significant item costs are shown in Table 2.2 (Piscopo et al., 2018).

Table 2.2: Materials costs (Piscopo et al., 2018)

Item	Material	Current Unit Cost	Unit Cost Range
Permanent magnets (PMs)	Neodymium-iron-Boron	96 USD/kg	72-120 USD/kg
Stator	Electrical steel	2.5 USD/kg	2-3 USD/kg
Translator	Electrical steel	2.5 USD/kg	2-3 USD/kg
Rim	Aluminium alloy	6 USD/kg	4.5-7.5 USD/kg
Winding coil	Copper coil	1 USD/m	0.5-1.5 USD/m

It can be seen from Table 2.2 that the permanent magnets are the most expensive materials among all materials which are being used to design the linear PM generator, and the total cost of a device is determined by the cost of the PM. Moreover, the decommissioning costs should be considered

because it is assumed that both the linear generator and the floating buoys are not reusable but rather recycled and sold for scrap. The annual operating costs are also a factor that will be added to the total costs. A couple of simplified approaches have been proposed to calculate the relative cost of the generator design (Eriksson, 2019; Polinder et al., 2003). Considering these all-important factors, challenges and materials costs, they are relatively expensive, which raises a question to the researchers whether this type of PTO system is economically viable or not? Few researchers addressed that linear PM generator based PTO system is not economically viable, and there are many research works going on worldwide to make these devices economically viable (Khatri & Wang, 2019; Liu et al., 2020). Linear PM generator type PTO system based WEC has been widely studied in different countries and universities worldwide that deployed many WEC devices in the ocean sea environment to optimize the entire system and reduce the unit costs of production.

In order to build an economical, robust system that can harness the energy from ocean waves, many challenges need to be overcome. To work effectively, the system needs to be tuned to the resource because of the variation in wave amplitude, phase and direction (Czech & Bauer, 2012). The main challenge is to achieve high energy conversion efficiency over a whole range of excitation parameters (Zhang et al., 2012). Compared with land-based structures, ocean-based devices present unique challenges during design, construction and installation (Aderinto & Li, 2018). In the case of the generator design, the design involves the generator actively coupling with the waves to extract power through a reciprocating motion at a low speed (Szabo et al., 2007). Another challenge is to couple the irregular and slow-motion (frequency 0.1 Hz) to drive the linear electromagnetic generator with an appropriate output quality for the utility network (Clément et al., 2002). There are many ways to solve this problem: incorporate a WEC operating principle-based energy storage system within the device or use a typical external energy storage (Ibrahim et al., 2008; Thorburn et al., 2004). To smooth the power, the device can connect to an array (Thorburn et al., 2004). However, due to the low speed, a large generator is required. How significant is an economical compromise between the size of the generator and the price and whether it's worth capturing the energy in larger, less common waves (Eriksson, 2019)? At a continuously different speed, a linear generator operates when the generator varies direction twice per wave period. Furthermore, with the wave variability, the speed will change for each wave. When comparing generator designs, a fixed speed is widely used, but variable speed operation needs to be considered.

The linear electromagnetic generator design must be of low cost and harness maximum energy for low velocities and, if possible, with an irregular motion to be commercially viable (Polinder, Mueller, Scuotto, & de Sousa Prado, 2007). The linear electromagnetic generator directly driven by sea waves would oscillate at a peak velocity of 0.5 to 2 m/s (Mueller, 2002). Moreover, linear generators are considered hard-to-mount underwater, and therefore they have to be maintenance free. They should also have as high force density and a low mass volume as possible (Szabo et al., 2007). For example, a direct drive WEC can generate a peak of 100 kW at a peak velocity of 1 m/s, where the required peak reaction force is 100 kN. In order to provide a shear stress of 20 kN/m2, the active surface area of the device should be at least 5 m^2 (Mueller, 2002). Using permanent magnets (Nd-Fe-B) and some innovative generator topologies can boost the power density and shear stress in the air gap of the WEC. This requires the design of such a device that has the potential for producing the required thrusts in the WEC. Though each wave differs in frequency, an average of approximately 0.1 Hz can be considered a nominal baseline around which the output voltage of the WEC fluctuates according to the velocity or frequency of the incoming waves of the sea. Obviously, power electronic converters are required to interface the WEC to the grid. The linear electromagnetic converter should be a variable speed or permanent frequency system. It is expected that other than using multi-MW WECs, several smaller devices (ratings might be 10-100 kW) can be used to make up a wave farm (Clifton et al., 2010; Elwood et al., 2009; Hodgins et al., 2011). For this application, the generator required special types of design. The costs are likely to be high for larger devices, but by operating with smaller units one may still be able to have the mass manufacturing benefit, holding costs down.

2.6 Development of the Linear PM Generator-based PTO System for WEC

The linear PM generator based WEC has attracted interest worldwide since the linear PM generator was first proposed for wave energy conversion. There are many different research techniques and prototype designs that have been reported using the linear PM generator based WEC concept, which can be seen in (Khatri & Wang, 2019). However, up to date, although there are many devices and methods that have been proposed to harness wave energy, it can still be said that the design is in its early stages, as not a single commercial, mature technological model has been developed. H. Polinder et al. reviewed linear PMs generator based WECs such as the AWS and the WEC developed at Uppsala University (UU) and their research issues (Polinder, Mueller, Scuotto, & Goden de Sousa Prado, 2007). Several research issues have been addressed with their potential solutions and sensible directions, such as improving the WEC linear motion speed for future testing and exploring other

generator forms with higher force densities and better efficiencies. The linear PM generator based WEC has some inherent disadvantages, such as high attractive force, because of the large number of magnetic materials, large dimensions, static and dynamic effects, high cogging force, high cost, and reduced performance due to its low speed (Faiz & Nematsaberi, 2017b). Erik Lejerskpg et al. experimentally tested a prototype developed by UU at the Lysekil wave research site. They found that the power generation of the WEC depends on parameters such as the translator, stator, buoy size, translator's speed, the weight of the translator, and damping of the generator, etc. (Lejerskog et al., 2015). Several technologies, methods and concepts have been proposed and modelled to solve these drawbacks. All these design parameters are important for developing and increasing the efficiency of the direct-drive linear WEC. From the literature, the previous work mainly focused on numerical modelling, design optimization, prototype design and test, and the control strategy (Wang et al., 2020). The aim of this section is to discuss the recent development of the linear PM generator for WEC.

2.6.1 Reduction of detent force (Cogging force and end effect force)

When the stator and the translator move relative to each other, they generate cogging forces (Yang et al., 2006; Youn et al., 2008; Zhu et al., 1997). The cogging force creates an exciting force ripple that produces vibrations and acoustic noise that can damage the magnets and the stator teeth (Kimoulakis et al., 2009). Cogging forces limit the translator's movement by keeping the path between the translator and stator teeth to a minimum. The generated cogging force can destabilize the system, shorten the device's lifetime, and increase the maintenance costs, so it is vital to decrease the cogging force for the linear PM generator (Faiz et al., 2009). The cogging force can be expressed by equation 2.48 based on the principle of the virtual work where W is the magnetic field energy, and y is the translator position (Liu, Yu, Hu, Liu, & Zhou, 2013).

$$F_{cog} = -\partial W/\partial y \tag{2.48}$$

$$W = \sum_{i=1}^{T} \int_{S_e} \left[\int_0^B (\bar{H}_i . d\bar{B}_i) \right] dS_i \tag{2.49}$$

Here T is the total number of local triangular elements on the translator surface, $\bar{B}_i$ and $\bar{H}_i$ are the magnetic flux density and magnetic field intensity at element i, respectively. On the other hand, the linear generator is open in both longitudinal ends, and this is one of the main fundamental differences

between the linear and rotating generators (Ekergård, 2013; Li et al., 2012). During the movement of the translator, the outmost magnets move in or out of the stator. Therefore, the magnets change their coupled partners and affect the translator's flux component, which does not exist in the rotor of the rotary generator. The end effect force is created because of the disconnection at the end of the two sides, and this end effect creates a non-linear magnetic circuit. Furthermore, the results of the longitudinal ends strongly influence the electrical frequency, saturation, and geometric parameters. Hence, it is not easy to make a common statement because those parameters differ from design to design and vary due to the mechanical frequency and electrical loading. As the longitudinal ends and its impact are unknown, the possible disadvantages leave the designer with an information gap to design the specific linear PM generator. Based on numerical calculations, longitudinal end effects have been investigated in the linear PM generator for WEC to assess the impacts of the disadvantages of the longitudinal ends (Ekergård & Leijon, 2020). The cogging force and end effect force are together known as the detent force. Increasing detent force could have an impact on the mechanical design (increases fatigue risk), generator efficiency, or energy generation. Therefore, it is essential to accurately predict the magnetic field distribution and decrease the cogging force because it affects both the linear and nonlinear reluctance models and the electromagnetic performance of the generator. In order to reduce the cogging force, a variety of techniques have been used so far. The notable ones are adjusting the PM length, magnetization orientation, skewed PM, pole-shifting, slotless generator, bulged stator and others (Faiz et al., 2009; Liu, Yu, Hu, Liu, & Zhou, 2013; Prudell et al., 2010; Trapanese et al., 2015).

On the other hand, several numerical and analytical methods have recently been proposed to solve the magnetic field problem of the linear generator. The finite element method (FEM), finite element analysis (FEA) and magnetic equivalent circuit (MEC) have been used to analyse the magnetic field and determine the related electromechanical parameters. The FEM method offers high accuracy and includes the impact of nonlinear factors, but this analysis method is comparatively slow and time-consuming. On the other hand, MEC analysis can find the nonlinearity, end effect, and armature reaction. However, this method analyses only the magnetic field at a number of separate points of the structure, and its accuracy is not good enough. Moreover, the analytical model based on the subdomain method can be used to get more accurate predictions of the magnetic field distribution. The analytical model based on the subdomain method has already been used in various PM-based devices (Guo et al., 2018). To predict the accurate air gap field distribution of the linear PM generator,

the improved conformal mapping (ICM) method and slotless analytical model could be used as well, which have been used in various PM-based generators.

2.6.2 Permanent magnet (PM) modifications

The permanent magnet's size and shape significantly impact the linear generator's performance efficiency; often, larger magnets mean better results. O. Danielsson et al. studied the effects of the magnet size and shape. According to the study, increasing the permanent magnet's size improves its performance and decreases its detent force (Danielsson et al., 2005). Rectangular shaped PMs were used for this study, and it was found that it increases the magnetic flux intensity and decreases the load angle but increases the normal force. Moreover, a study has been done by reducing the PM length, and the optimised results showed that it could reduce the cogging force (Kimoulakis et al., 2009).

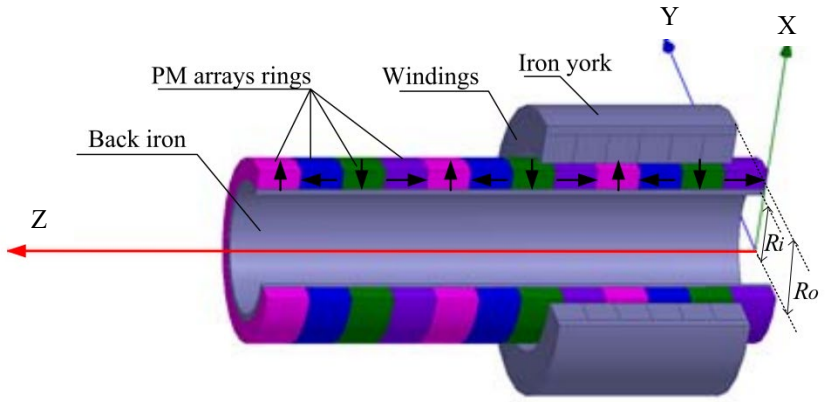

Figure 2.12: Using the Halbach array in the translator (Zhang et al., 2017)

However, reducing the PM length decreases the magnetic flux density and increases the load angle. There are different ways of installation that have been proposed to study the linear generator. Typically, PMs are attached to the outside diameter of the translator, but a study has been carried out by attaching PMs to the inside diameter of the translator (Prudell et al., 2009a). A linear PM generator has been proposed by applying PMs skewed in the translator to reduce the detent force (Viola et al., 2015). Although this was an effective method to reduce the detent force, it needs more complex PM shapes and increased manufacturing costs. Moreover, pole-shifting can reduce the harmonics of the detent force (Bianchi et al., 2005), though it can create an unbalanced voltage due to the PM asymmetric. Moreover, to increase the magnetic flux density in a particular direction, Halbach Arrays

have been used in PM arrangements (Liu, Yu, Hu, Liu, & Zhou, 2013; Zhang et al., 2017). Figure 2.12 shows a Halbach PM array-based WEC. The Halbach PM array-based linear generator was compared with other typical designs, and it has been found that Halbach PM arrays can reduce the overall detent force (J. Zhang et al., 2013). Chunyuan Liu et al. found that the detent force can be reduced by 82.56% using the Halbach array in the PM arrangement (Liu, Yu, Hu, Liu, & Zhou, 2013). The comparative result with the linear generator is shown in Figure 2.13.

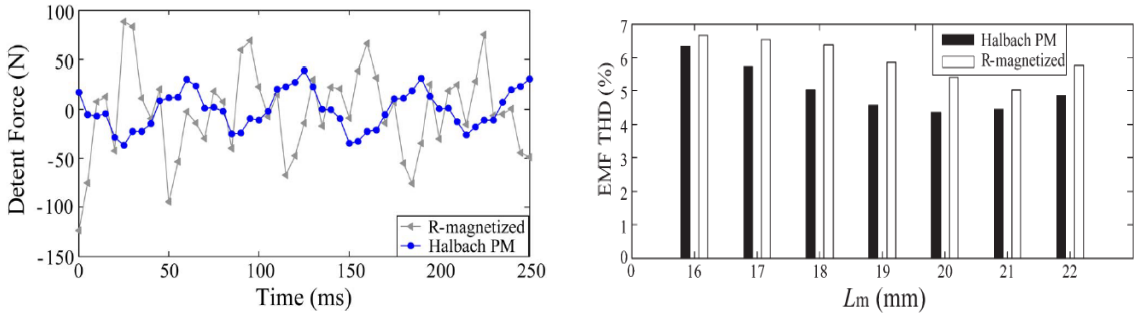

(a) (b)

Figure 2.13: (a) Detent force with or without Halbach PM (b) THD of EMF in the linear electromagnetic generator with and without Halbach PM arrays (J. Zhang et al., 2013)

To design the Halbach array-based linear generator, Yimin Tan et al. used the Fourier decomposition to describe the Halbach array's magnetisation components. They then extracted the magnetic field distribution based on the magnetic scalar potential method using specially treated boundary conditions (Tan et al., 2018). In the Halbach PM arrays, the magnetic flux can typically be cancelled on one side of the array while the magnetic flux is enhanced on the other side. The magnet's magnetizing angle in Halbach PM arrays can be calculated using equation 2.50 (J. Zhang et al., 2013).

$$\theta_M = \left(-\theta'_{m(i+1)}\right) - \left(-\theta'_{m(i)}\right) = 180°/M \qquad (2.50)$$

Here θ_M denotes the angle difference of two adjacent permanent magnets; M is the pole number of the permanent magnet, $\theta'_{m(i)}$ and $\theta'_{m(i+1)}$ represent the ith and $(i+1)$th magnetizing angles, respectively. The general formula for the magnetization vector of the Halbach magnet array is stated as (J. Zhang et al., 2013).

$$\widetilde{M} = \sum_{n=-\infty}^{\infty} \left[\widetilde{M}_{xn} e^{-jK_n Z} i_x + \widetilde{M}_{zn} e^{-jK_n Z} i_z\right] \qquad (2.51)$$

Here $\widetilde{M}_{xn}$ is the magnetization vector Fourier coefficients of the radial component and $\widetilde{M}_{zn}$ is the magnetization vector Fourier coefficients of the axial component. K_n is the angular frequency of the n-order harmonic component. It is comparatively challenging and costly to manufacture magnets having the ideal Halbach magnetization arrangement. Quasi-Halbach magnetisation concepts have been proposed to solve the problem and reduce the manufacturing cost (Liu, Yu, Hu, Liu, & Zhou, 2013; Xia et al., 2018). The quasi-Halbach and Halbach magnetisation can boost the sinusoidal distribution of the magnetic field and increase magnetic flux density, and the finite-element analysis solution is required to check them.

2.6.3 Changing the air gap

According to the critical design point of view, the distance, i.e. the air gap, between the translator and stator should be stable. Air gaps have a different magnetic field magnitude depending on their width. A small air-gap results in high power density and large detent force (Liu, Yu, Hu, Liu, & Zhou, 2013). Figure 2.14 presents the relationship of peak voltage and detent force with the air gap.

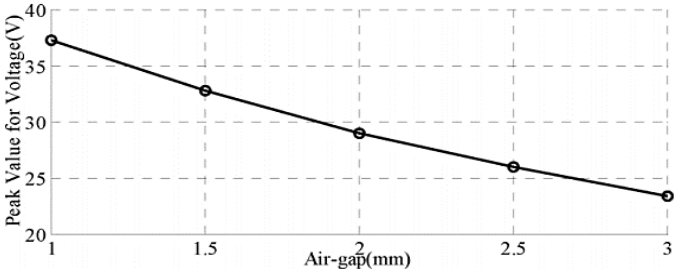

(a)

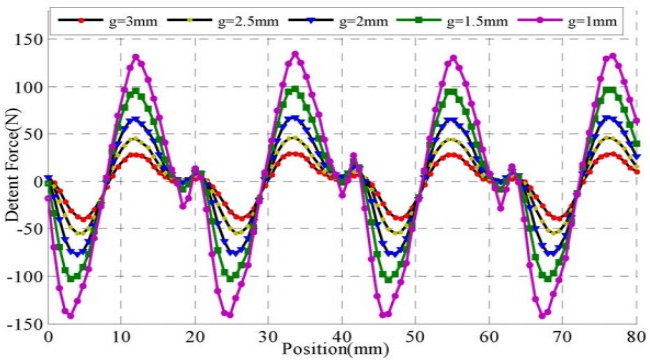

(b)

Figure 2.14: The relation between (a) peak voltage and air gap (b) Detent force and air gap (Liu, Yu, Hu, Liu, & Zhou, 2013)

In general, air gap magnetic flux density affects radial magnetization, and by changing the design, the air gap magnetic flux density can be increased. The optimal values for the radially magnetized magnet's ratio to the pitch of the pole and translator's outer radius to the stator's outer radius can be defined to achieve maximum efficiency and performance. Most of the linear generators have been studied with the fixed air gap, and it was found that a small gap can create demagnetization problems (Huang et al., 2011; Vermaak & Kamper, 2012). By changing the air gap, Omar Farrok et al. studied a permanent magnet linear generator (PMLG) and found it had an important role in increasing the generator efficiency (Farrok, Islam, Sheikh, Guo, Zhu, et al., 2017). However, reducing the attractive force or frictional force between them is also important for preventing damage to the generator (Nilsson et al., 2006). This attractive force or frictional force can also create the demagnetization problem with the generator. The length of the air gap d_{str} can be calculated by the following equations where z_{tr} is the translator vertical position.

$$d_{str}(t) = d_{min} + d_{var}\left[1 - \frac{cos\pi\{z_{tr}(t)\}}{H_{tr}}\right] \quad (2.52)$$

$$z_{tr}(t) = \frac{H_{tr}}{2} sin\left(\frac{2\pi}{T}t \pm \alpha_i\right) \quad (2.53)$$

Here, d_{min} and d_{var} are the minimum and variable air gap. R. Waters proposed a method for measuring the air gap width of linear generators using a search coil sensor (Waters, Danielsson, et al., 2007). From Figure 2.13, it can be seen that detent force and induced voltage decrease as air gap distance increases.

2.6.4 Modification of the stator design

Because of the low frequency and speed of the ocean wave, the detent force can be created in the linear PM wave energy generator. To raise the efficiency of the wave energy generator, it is important to decrease this detent force (Yu et al., 2012). With the aim of reducing this detent force, there have been many techniques or methods that have been used, such as stator with slots, without slots, U shaped stator and the M shaped stator (Dosiek & Pillay, 2007; Faiz & Nematsaberi, 2017b; Liu et al., 2010; Zhu et al., 2006). To reduce the detent force, a slotless generator has been proposed. The analysis of the proposed generator showed that the detent force could be reduced, while the power density is merely one-fifth to one-tenth lower than that of the slotted generator. Therefore, the slotless generator needs a larger volume than the slotted generator to generate the same wave energy. To

decrease the detent force, Chunyuan Liu et al. used bulged stators and auxiliary slots (Liu, Yu, Hu, Liu, & Zhou, 2013). Steel materials have been used in the stator, and modular windings have been used in the stator. Moreover, Haitao Yu et al. proposed a novel linear wave energy converter where an assistant tooth has been implemented with the 12 slotted stators to minimize the end and cogging effects (Yu et al., 2012). The structure and the effect of the assistant tooth are shown in Figure 2.15.

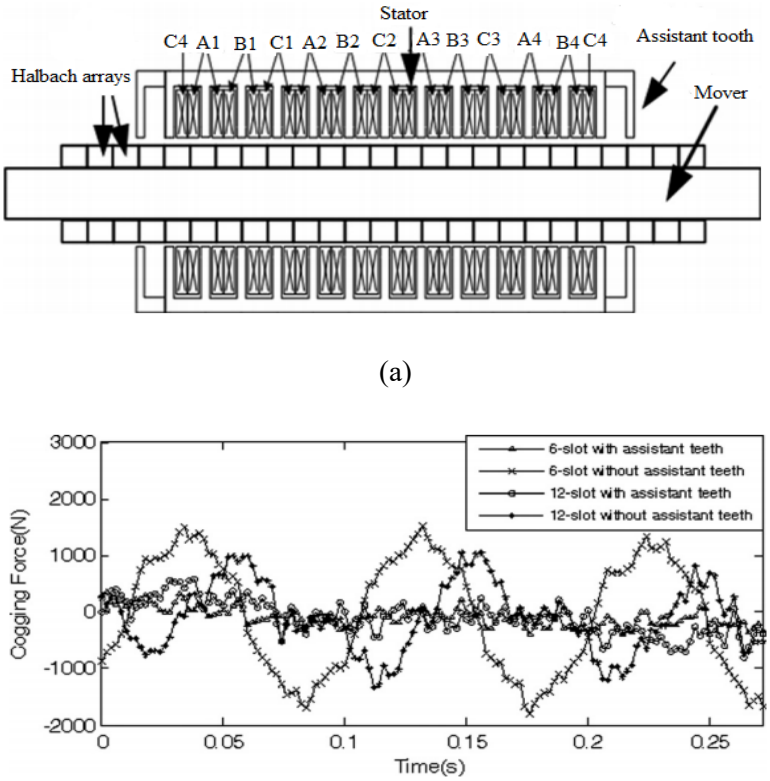

Figure 2.15: (a) Structure of the proposed model (b) Cogging force with and without assistant tooth (Yu et al., 2012)

It was found from the simulation results (Figure 2.15(b)) that by using the assistant tooth, more than 70% of the cogging force can be decreased compared with those without the assistant tooth. However, the core losses for the proposed linear generator were increased by 0.5% with the assistant tooth. To optimise the flux distribution, N.P.Gargov et al. used the shoe concept for the teeth arrangement of the semi-closed slot and found that it reduced power ripples and air gap reluctance (Gargov et al., 2014). Additionally, in linear machines, the cogging forces can also be reduced.

2.6.5 Magnetic cores

Since the heave motion of the waves is prolonged (1 – 2 m / s peak), the linear generators in direct drive WECs need to respond with very large forces to produce a substantial amount of energy (Ran et al., 2011). Hence the linear generators are becoming very large and costly. Many direct drive WECs based on iron-cored linear generators have been developed and tested because of their performance. Lorand Szabo et al. showed that the iron core-based stator could develop 3 times higher voltage (RMS voltages) than the ironless stator (air core) because due to the low reluctance, the Iron core has a higher magnetic flux (Szabo & Oprea, 2007). Figure 2.16 compares induced voltages for air-cored and iron-cored structures.

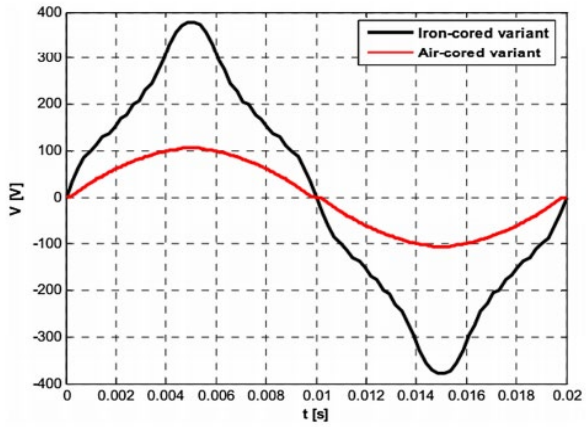

Figure 2.16: Comparison of air-cored and iron-cored induced voltages (Szabo & Oprea, 2007)

In addition to being large, linear generators also present significant challenges in the design and construction of bearings and machines due to the attractive forces between the PM translator and iron-core stators. In many cases, the structural material used to support these attractive forces represents a significant portion of the WEC cost. Cogging forces cause problems, mainly due to the pairwise flux coupling and the longitudinal ends of iron-cored generators (Danielsson & Leijon, 2007; Prudell et al., 2010). Moreover, iron-cored generators create copper losses and core losses, which decrease the generator's efficiency by minimizing the remanence magnetism of the PMs. To reduce the detent force and modular structure and increase the output efficiency, a permanent magnet linear generator based WEC was proposed by using hollow windings and a coreless iron structure (Mueller, 2002). The analysis results of the proposed design reduced the detent force and copper and core losses. Air-cored-based linear generators are attracting increased attention for direct drive WECs due to the iron-

cored device's problems previously discussed (Clifton et al., 2010; Hodgins et al., 2010; Mueller et al., 2008; Ran et al., 2011). An air-cored longitudinal tubular generator has been developed, consisting of axially magnetised PMs of opposing polarity separated by steel segments (Baker et al., 2004). The winding coils, called air-gap windings, are wound around the translator. Wave energy applications would be suitable since the air gap is infinite and the shear stress is around 10 kN /m^2 (McDonald et al., 2008). Another tubular type linear generator for WEC based on an air-cored design was developed using more permanent magnets than a comparable iron cored linear generator (Clifton et al., 2010). In order to make air-cored generators more suitable, the cogging forces between the stator and translator need to be reduced. Linear double-sided permanent magnets achieve higher air-gap flux densities than single-sided air-cored converters(Vermaak & Kamper, 2011).

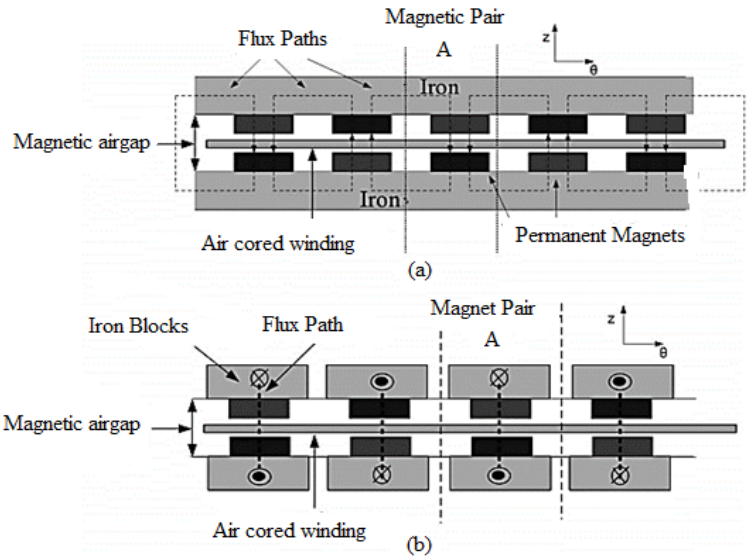

Figure 2.17: Air Cored winding (a) Double-sided planer device (b) Magnet pairs separated into modules (Hodgins et al., 2011).

The translator, however, is now subject to attractive forces between its two opposing sides, requiring increased structural mass. Neil Hodgins et al. proposed an air cored linear generator topology which was known as the core generator (C-Gen) for wave energy research (Hodgins et al., 2011). The C-Gen is a double-sided air-cored arrangement, as shown in Figure 2.17, consisting of air-cored windings and iron-cored permanent magnets. The proposed design topology analysis results showed no magnetic attraction forces between the stator and the PM translator, reducing structural mass and simplifying the assembly process. To reduce the magnetic forces between the stator and the translator, air cored permanent magnet linear generator (PMLGs) designs have been proposed. Since the

translator lacks stainless steel, the force of attraction between the stator and the translator has been reduced. Lorentz forces, however, still exist. The Lorentz forces are radial in the direction of motion in the recently proposed air-cored generator design. A new air cored tubular linear PM generator has been developed and simulated where it 'sandwiches' the windings between two sets of permanent magnets (PMs) inside the tubular structure (Gargov & Zobaa, 2012). The generator's key benefit is that the Lorentz forces acting on the bearing are minimised by approaching the force parallel to the direction of the motion axis and by removing the cogging forces. Furthermore, Rieghard Vermaak et al. have developed a novel air-cored linear electromagnetic generator system for WEC that almost eliminates the end effects of iron-cored devices and the forces of attraction between iron-cored stators and magnet translators (Vermaak & Kamper, 2011). The attraction forces between the translator's opposing sides of double-sided air-cored machines have been balanced. The analytical analysis of the model has shown the effectiveness of the proposed design.

On the other hand, to reduce the core loss and detent force problem, the high-grade steel core can be applied as well, which significantly increases the power-generating ability (Farrok, Kiran, et al., 2019). Moreover, using high-grade steel in the core can solve the rising temperature problem. A linear PM generator has been developed using steel materials in the stator to investigate the benefits and the drawbacks of using steel materials (Curto et al., 2020). The investigated results have shown that the cogging force can be removed entirely with increasing electrical energy production.

2.6.6 Application of high-grade PMs and solving demagnetization problem

Maximum linear PM generators for WEC have been developed using conventional NdFeB N30, N35, which have low remanence magnetism, coercive force and magnetic energy product (Rahman et al., 2020). Due to their high magnetic flux density, NdFeB PMs can retain their remanence magnetism even in elevated amounts of reverse magnetic fields. A comparative study has been carried out using NdFeB and ferrite magnets in the translator to find the magnetic property differences (Danielsson et al., 2003; Demenko et al., 2011). The study results showed that they have similar magnetic properties, but the significant parameter could be the economic difference because the price of a rare earth magnet (NdFeB) is expensive. Moreover, it is difficult to handle the rare earth magnet (NdFeB) but using ferrite magnets increases the weight of the translator. With the increasing grade number of the NdFeB, the magnetic flux density increases and therefore, the linear PM generator has been proposed for WEC by using high graded NdFeB PMs (Bashir & Farrok, 2019). The simulation results showed

that the output induced voltages could be increased by using high graded NdFeB PMs. Because of the high price of the NdFeB and the environmental aspects, the alternative has been proposed to replace the NdFeB magnets (Molla et al., 2020). High graded permanent magnets can be used to solve the demagnetization problem and keep the temperature low but it is very costly. To prevent the demagnetization problem temperature control could be one of the effective methods. A cooling system based linear generator has been proposed for WEC to reduce the rising temperature which consists of a control unit, chiller, dehumidifier-based air handling unit and water pipes for circulating the chilled water (Molla and Farrok, 2019b). Temperature rises during the operation of the linear generator, and this rising heat can create demagnetization of the magnets. Although the proposed structure is very complex, the simulation results showed that the proposed linear generator could minimize the temperature and increase efficiency.

2.6.7 Design concepts for low-frequency wave range

Many research works have been done for increasing the efficiency of the buoy type linear PM generator based WEC by changing many parameters. Still, very few studies have been done on changing the degree of freedom of the permanent magnet arrangement in the translator instead of the traditional method. All conventional arrangements used in the WEC were based on a single degree of freedom which cannot perform appropriately in the low-frequency range. Efficiency can be increased by arranging the translator based on a multi-degree of freedom system. Moreover, all existing linear WEC have used single translators to harvest energy, but the system cannot generate energy when the translator reaches either of the ends. To generate energy in that stage of motion, a novel linear generator has been proposed, as shown in Figure 2.18, which consists of two different bodies of translators (Farrok, Islam, et al., 2019). One is a driver translator, and the other is a driven translator among the two translators. The driver translator is directly connected to the buoy, but the driven translator is connected to it by means of a mechanical spring. The output results are shown in Figure 2.19.

Figure 2.19(a) and Figure 2.19(b) present the vertical positions and velocities of the driven translator (Translator-D) and the driver translator (Translator-U) for minimum and maximum values of the natural frequencies of the driver and driven translator, respectively. Figure 2.19(c) shows that the driven generator can generate an acceptable voltage at zero vertical oceanic wave velocity. Figure 2.19 demonstrates that power is being generated solely by the driver generator, whereas the driven

generator has zero vertical velocity. However, even when there is no velocity in the driver generator, the driven generator still generates power.

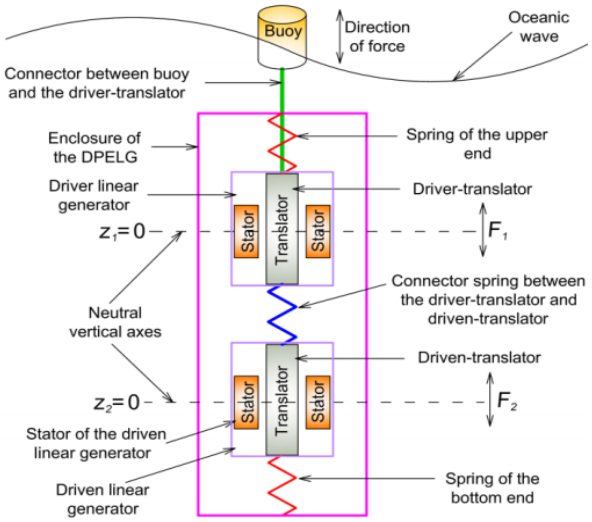

Figure 2.18: Proposed two body translator based WEC (Farrok, Islam, et al., 2019)

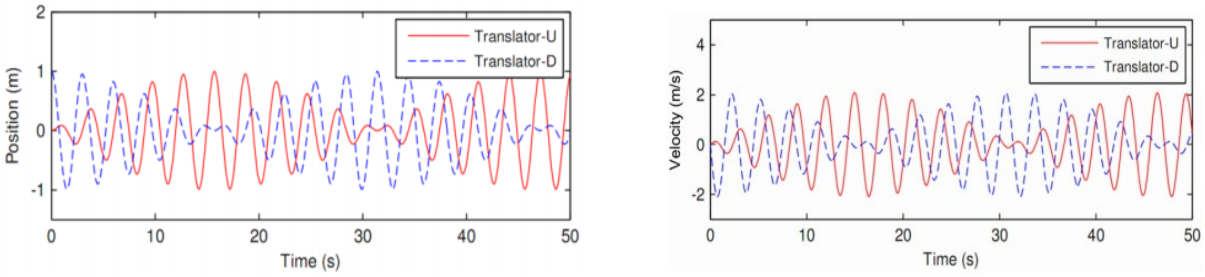

(a) (b)

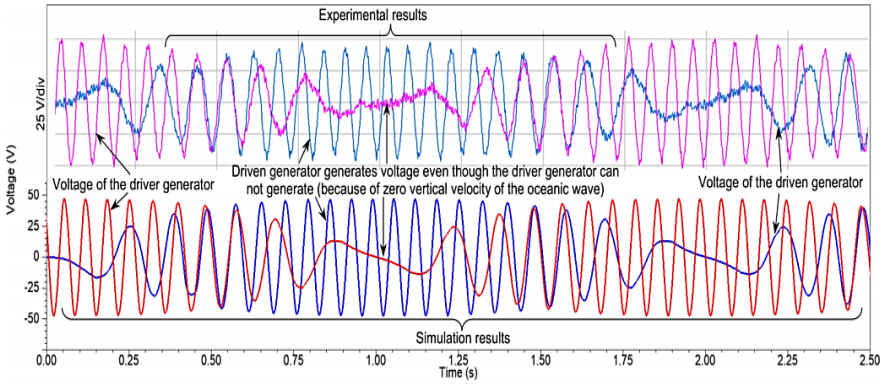

(c)

Figure 2.19: Two-body translator system (a) Vertical displacement, (b) Velocity, (c) Output voltage (Farrok, Islam, et al., 2019)

2.6.8 Using magnetic gearing to increase the speed of the Translator

The translator speed is also an essential parameter to increase the efficiency of the WEC. Due to the low frequency of the ocean waves, the existing linear generator cannot generate enough energy. Furthermore, the use of a linear magnetic gear has also been proposed by researchers, whose analytical and experimental results proved that the concept could increase the speed of the translator (Faiz & Nematsaberi, 2017b; Feng et al., 2016; Li et al., 2011; Li et al., 2017). The linear magnetic gear consists of two movers and a field modulation core, as shown in Figure 2.20. The mover can consist of magnetizing windings and permanent magnets (like aluminium-nickel-cobalt (AlNiCo)) (Li et al., 2011; Li et al., 2017). One mover (mover 2 or low-speed mover) can be connected with the buoy, which moves due to the wave, and another mover (mover 1) is connected with the translator (high-speed mover). A linear magnetic gear based WEC is also illustrated in Figure 2.21. The motion of mover 2 increased the opposite motion of mover 1, increasing the translator's speed. This means that the gear ratio variation only changes the motion speed of mover 1.

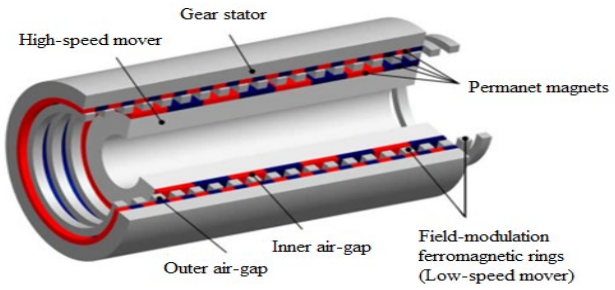

Figure 2.20: Linear magnetic gear concept (Li et al., 2011)

This new translator speed and spring displacement are the original ones multiplied by the gear ratio (G_r). The corresponding relationships can be expressed by equation 2.54 (Chau et al., 2008; Chau et al., 2007).

$$G_r = \frac{v_1}{v_2} = \frac{N_2}{N_1} \qquad (2.54)$$

where, v_1 and v_2 represent the speed of the mover 1 and 2, respectively. N_1 is the number of active PM pole-pairs in the mover 1 and N_2 is the number of active PM pole-pairs in the mover 2. The Force transmission capability for the different gear ratios is displayed in Figure 2.22.

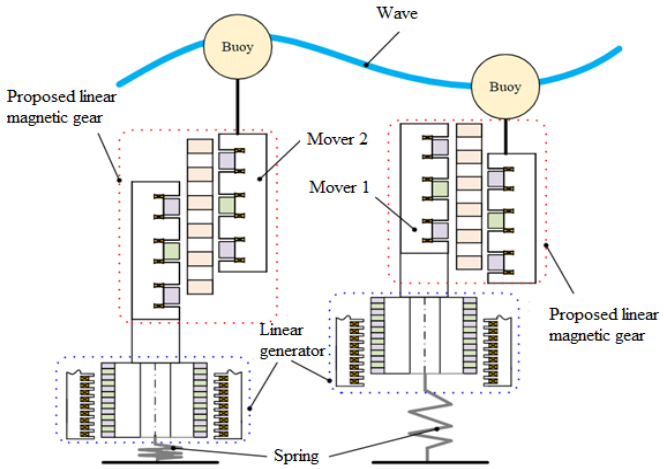

Figure 2.21: Linear magnetic gear based wave energy converter (Li et al., 2017)

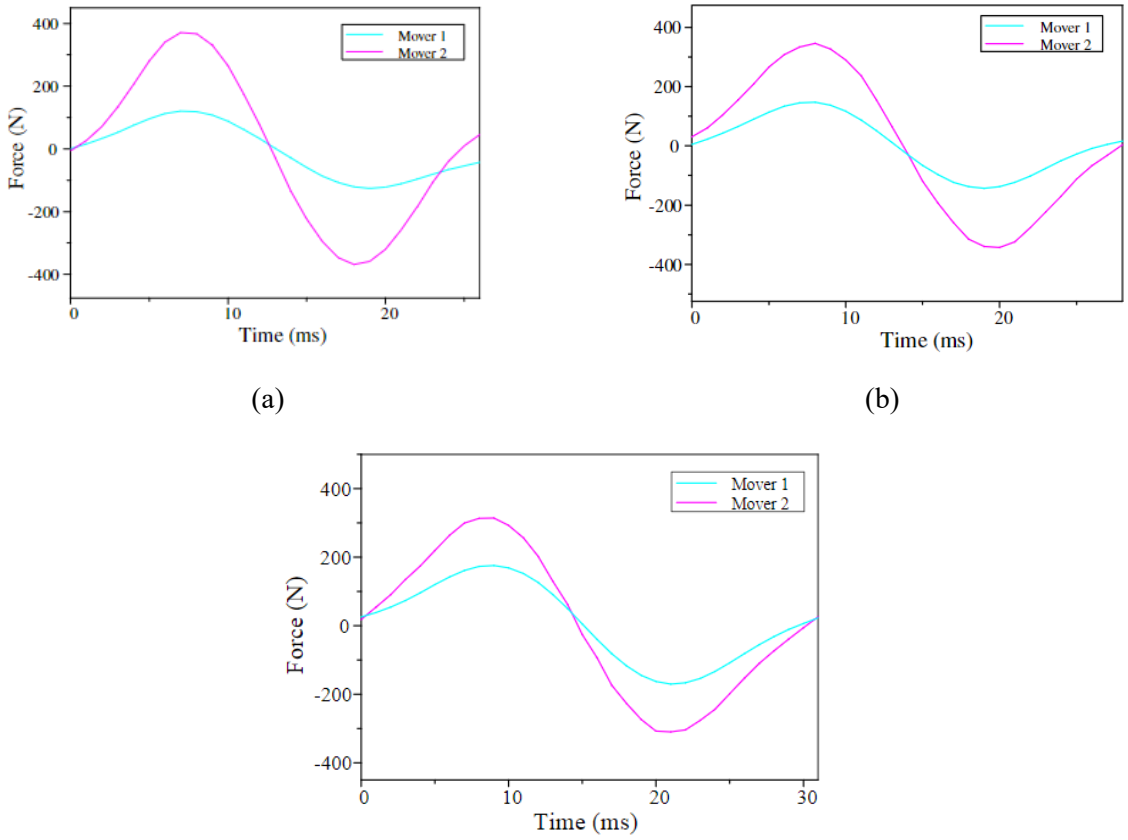

Figure 2.22: Force transmission capability(a) gear ratio 13:4 (a) gear ratio 12:5, (b) gear ratio 11:6 (Li et al., 2017)

Since the gear ratio variation only changes the linear generator's movement speed, the linear generator's new translator velocity and spring's new displacement are the original ones multiplied by G_r. Also, the motion directions of the two movers of the proposed linear magnetic gear are opposite each other. As a result, the spring force F_s and the generator force F_g are changed as

$$F_s' = -\gamma(-G_r z(t) = \gamma G_r z(t) \quad (2.55)$$

$$F_g' = -\beta(-G_r \dot{z}(t) = \beta G_r \dot{z}(t) \quad (2.56)$$

where γ and β are the spring constant and damping coefficient of the generator. The natural frequency of the linear magnetic gear based WEC can be measured by equation 2.57 (Li et al., 2017).

$$\omega = \sqrt{\frac{\rho g \pi a^2 - \gamma G_r}{m + m_a}} \quad (2.57)$$

In Figure 2.22(a), the pole-pair numbers of mover 1 and mover 2 are 4 and 13, respectively. The pole-pair numbers of mover 1 and mover 2 are 5 and 12 for Figure 2.22(b) and 6 and 11 for Figure 2.22(c), respectively. It can be seen from Figure 2.22 that the mover 1 and mover 2 pull-out forces under the ratios are 371.5 N and 114.2N for 13:4, 343.8 N and 142.7 N for 12:5 and 314.2 N and 170.6 N for 11:6, respectively which means the force of the mover 1 can be increased or decreased by changing the gear ratio. From Figure 2.22, it also can be said that with the increase of the pole-pair numbers of mover 1, the pull-out forces of mover 1 increase and with the decrease of the pole-pair numbers of mover 2, the pull-out forces of mover 2 decrease. That means the pull-out forces of the mover are directly proportional to the pole-pair numbers. Therefore, it can be stated that with the increase of the pull-out forces of mover 1, the velocity of mover 1 decreases or vice versa. By using this relation, equation 2.54 can be expressed as

$$G_r = \frac{v_1}{v_2} = \frac{F_2}{F_1} \quad (2.58)$$

Where, F_1 and F_2 are the pull-out forces of the mover 1 and 2, respectively. Moreover, such findings show that the pole-pair numbers of permanent magnets on the two movers are adjusted correctly, and it is possible to achieve the adjustable gear ratios. By selecting the proper gear ratio, it is possible to control the force and the velocity of the mover 1, which is connected with the linear generator.

2.6.9 Other design concepts to increase the efficiency of the generator

There are many factors related to the stator design that play an essential role in increasing the efficiency of the linear generator. Among them, proper lamination selection is an essential factor in increasing the efficiency of the linear generator (Gargov et al., 2014). The high magnetic flux density of the PMs can saturate the stator lamination materials in the teeth and back iron. N.P. Gargov et al. investigated the impact of the number of slots per pole, phase and the number of windings in the stator (Gargov et al., 2014). De Sousa Prado et al. showed that increasing the number of slots can lead to large pole pitches. As a result, demagnetization can be created, and due to the additional space harmonics, the decreasing number of slots will cause eddy current losses (de Sousa Prado et al., 2006). Therefore, the slot number selection is also an essential factor. To design the stator of the AWS, one slot per pole per phase was selected (de Sousa Prado et al., 2006). To find the optimized design of the stator, slot geometry, such as slot design and teeth design, is essential. It has been found that the stator tooth shape also affects power generation (Farrok, Islam, et al., 2019).

Omar Farrok et al. divided the stator into a primary and supporting stator for increasing the output voltage of the WEC (Farrok, Islam, Guo, et al., 2018; Farrok, Islam, Sheikh, et al., 2018). Lei Huang et al. used two stators known as inner and outer primary and a mover, which can move with the buoy between the inner and outer primary (Huang et al., 2013). Jing Zhang added an asymmetric slot iron york structure and pie windings to increase the efficiency of the previous WEC design. Experimental results proved that the asymmetric slot structure increased the efficiency (Zhang et al., 2018). A new concept known as the snapper generator has been proposed where the stator consists of permanent magnets, winding coils and a physical spring (Crozier et al., 2013). The physical spring connects the stator with the fixed seabed. When the stator moves because of magnetic attraction, then the physical spring extends and applies a reverse force to the stator. Since both translator and stator consist of magnets and face each other, due to the applied force on the translator, the magnetic attraction pulls the stator along with the translator. Finally, the spring forces are enough to resolve the magnetic attraction, where the stator accelerates quickly in the translator's opposite direction. This high speed increases the power output efficiency and can decrease the magnets' size and associated costs. The flux linkage measuring equation 2.59(a) can be used for the electromechanical model of the proposed generator.

$$\Phi = \frac{Nl_s}{S}\left(\int_S A_+ dS - \int_S A_- dS\right) \tag{2.59a}$$

where S is the cross-section area of the coil, and A is the vector potential in the positive and negative parts of the coil. l_s is the stack length. The relative position (z_R) and velocities ($\dot{z}_R$) of the stator and translator are required to measure the flux linkage and induced voltage during the operation of the generator.

$$e(t) = -\frac{d\Phi}{dt} = -\frac{d\Phi}{dz_R}\frac{dz_R}{dt} = -\frac{d\Phi}{dz_R}\dot{z}_R \tag{2.59b}$$

2.6.10 Innovative oscillator design concept

Up to date, most of the proposed linear PM generators type direct electric drive PTO systems for wave energy conversion have been developed based on linear oscillator systems (single degree of freedom oscillator system) and traditional design concepts (all permanent magnets are mounted in the translator, having opposite poles facing each other with an iron core used between them, and with coil windings attached in the stator). Typically, the translator moves inside the stator and this movement creates magnetic flux changes inside the winding coils, generating electrical energy. The linear energy harvesting technology has been compared with nonlinear systems based on actual data. It was found that the linear energy harvester has the highest power output in most cases. Still, the nonlinear system has a broader harvesting frequency bandwidth, and the bistable system can harness more energy from random vibration (Beeby et al., 2013). Moreover, Owens et al. also found that the nonlinear oscillating system is better than the linear oscillation for broadening the frequency response bandwidth (Owens & Mann, 2012). To create maximum magnetic flux density inside the coil, some permanent magnets could be added outside the stator coil, as shown in Figure 2.23(a). This system is known as the bistable system (Xiao et al., 2017). It has been found that the proposed bistable system can increase the magnetic flux density inside the winding coils (Gao et al., 2018). The linear generator converter's resonant power and efficiency with light damping and multi-degree of freedom oscillators are expected to be larger than those with a conventional single degree of freedom oscillator (Gatti, 2013; Wang, 2016). Figure 2.23(b) displays the two-degree of freedom system where the set of magnets are connected by physical springs (Xiao et al., 2017). The device will be more efficient in the low-frequency range if the bistable system is coupled with the increased degree of freedom oscillator system, as displayed in Figure 2.23(C).

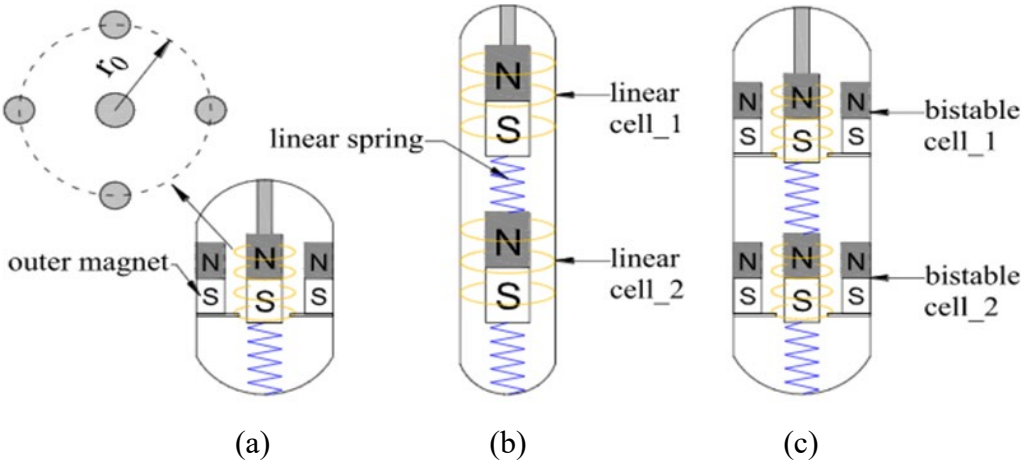

Figure 2.23: Physical models of the PM linear generator (a) bistable impulse linear generator, (b) two-degree of freedom system, and (c) coupled bistable two-degree of freedom system (Xiao et al., 2017)

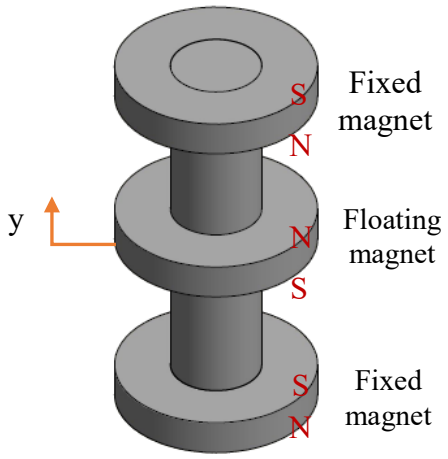

Figure 2.24: Schematic diagram of a single-degree of freedom nonlinear oscillator

The bandwidth problem of the existing PM linear generator can be overcome by widening the frequency bandwidth of the WEC. Light damping nonlinear oscillators are expected to have larger operational frequency bandwidth than a conventional single degree of freedom linear oscillator. The magnetic levitation system can be used in the translator design to make the oscillator nonlinear, which is more effective in the broadband frequency range, especially in the low-frequency ocean environment (Masoumi & Wang, 2016). In the magnetic levitation system, the magnetic spring works like a physical spring and is created when two magnets are facing each other at the same poles (N-N or S-S), as presented in Figure 2.24. In addition, the use of the light damping multi-degree of freedom

nonlinear oscillators is expected to develop larger operational frequency bandwidth than that of a single degree of freedom nonlinear oscillator.

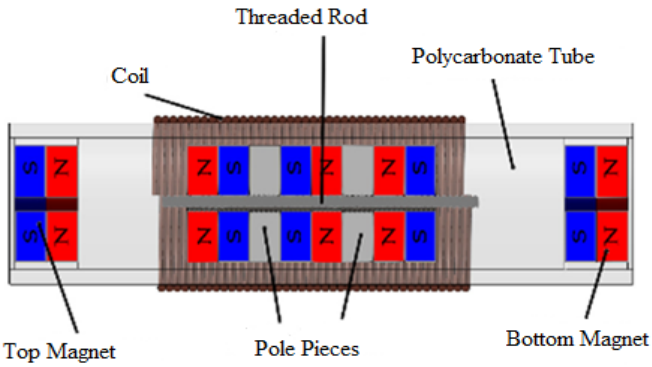

Figure 2.25: Structure of the repulsive magnetic levitation-based WEC (Masoumi & Wang, 2016)

Magnetic springs can be used in the magnet arrangement for harvesting energy over a broadband frequency range (Chiu et al., 2012; Gatti, 2013; W. Wang et al., 2017). Moreover, to increase the generator efficiency in the broadband frequency range, Masoud Masoumi and Ya Wang proposed a vibration-based generator for WEC known as the repulsive magnetic scavenger (Masoumi & Wang, 2016). The levitating magnets are lined around a threaded rod together so that the same poles face one another. The generator consists of two fixed magnets, as shown in Figure 2.25, placed at each end. It delivers a collocated harvesting and braking mechanism in the face of high amplitude vibrations. Usually, the concept has been used to generate energy from vibration in the low-frequency range (Foisal et al., 2012; Salauddin et al., 2016; W. Wang et al., 2017; Zhang et al., 2014).

2.7 Motivation for Choosing Magnetic Spring-based Nonlinear Oscillator System to Harness Ocean Wave Energy

The energy from ocean waves is a largely untapped renewable energy source globally, but harnessing this energy reliably and cost-effectively presents significant challenges. Ongoing improvements and progress of wave energy technologies continue to develop very fast. Different techniques have been used to harness this energy, and among them, the linear PM generator based direct drive WEC is very well known because of its mechanically simple structure. The working principles of the linear PM generator based WEC have been discussed in this paper with the support of mathematical modelling. Different WEC topologies with a linear generator-based PTO system have been outlined to provide

a brief understanding of their design and working principles. It is challenging to choose the best WEC linear generator design concept because of the continuously increasing development of the WEC. Depending on the application conditions, the linear generator structure for WEC is either designed for high-power applications or low-power applications. The outcome of the comparative studies can be concluded as follows:

- Linear generators are suitable for use in wave energy conversion if the devices are buoyant moored with linear motion and operate with speeds of 1 m/s or more.
- Compared with other linear generator types, the linear PM synchronous generator is the most suitable for wave energy conversion because it has higher reliability and efficiency due to the larger driving force.
    - The planar/flat type linear PM synchronous generators are preferred for high-power applications.
    - The tubular type linear PM synchronous generators are suitable for low-power applications because they offer high power or force density.
    - Tubular type linear PM generator with a long translator inside the generator gives better performance with less cogging force.
    - Three-phase generators are more efficient than single-phase generators due to their higher energy generation.
    - Iron cored generators are more suitable than air-cored generators because their power generation ability is higher.
    - The largest power is produced when the PMs are attached to the translator.
    - QuasiHalbach arrangements are preferred for improving the power generation efficiency with minimum losses.
- The generator size is mainly determined by the force it has to create. In wave energy conversion, the speeds are typically relatively low. The force should be high if the aim is to generate a large amount of power at a low speed. Therefore, the cost of the generator increases. The switched reluctance generators, variable reluctance generators, transverse flux PM machines, and Vernier hybrid machines are suitable designs with high force density. The performances of these types of generators are not influenced by this limited force density, and they are suitable for low power applications. However, they have some disadvantages, such as complex construction structure, low power factor, complex iron losses and eddy current

losses. Although they have some disadvantages, they can be viewed as an alternative to the typical linear PM generator in the future.

- Clever designs such as double-sided and cylindrical arrangements could decrease the cost.
- Superconducting linear generators are suitable for the WEC based on the linear generator in low power applications. It has a high current carrying ability, producing much higher flux density with low-speed motion and lighter weight. However, it has a high manufacturing and material cost difficulty.

This chapter has reviewed the developments of the WEC with linear PM generators such as translator design, translator speed, stator design and others. To increase the performance efficiency and reduce the cost of the WEC with linear PM generators, many design concepts have been proposed. Overall, various WEC designs, working principles, design optimization and advancements have been appraised in this chapter.

Moreover, from the literature, it has been shown that all developed linear generator based WECs still have some drawbacks, and very few have been deployed in the ocean. The bandwidth problem of the existing linear PM generator-based PTO system can be overcome by widening the frequency bandwidth of the WEC. Light damping nonlinear oscillators are expected to have larger operational frequency bandwidth than a conventional single-degree-of-freedom (SDOF) linear oscillator. The magnetic levitation (magnetic spring) system has been used in the translator design to make the oscillator nonlinear, which is more effective in the broadband frequency range, especially in the low-frequency ocean environment. However, the characteristics and dynamics of the linear PM generator based on the SDOF nonlinear oscillator system have not been studied yet. The SDOF magnetic spring-based system had only one degree of freedom and was limited to only one resonant natural frequency. Preferably, the energy generator should pick up and resonate at every frequency present in the source vibration. One can use double and triple resonant frequencies and achieve maximum power by employing a two-degree-of-freedom (2DOF) and three-degree-of-freedom (3DOF) oscillator systems. Moreover, the 2DOF and 3DOF nonlinear oscillators are estimated to advance higher operational frequency bandwidth than the SDOF nonlinear oscillator. But, no study thus far has modelled 2DOF and 3DOF nonlinear oscillator system-based energy harvesters to harness ocean energy.

The contents of this chapter have been published in the IEEE Transactions on Magnetics, 2022. DOI: 10.1109/TMAG.2022.3180812

Chapter 3
Magnet Characterisation and Electromagnetic Theory

Permanent magnets can be used to generate electrical forces from mechanical forces or convert mechanical forces into electrical forces. The magnet and coil arrangement known as the electromagnetic system usually generates electricity from a mechanical force. The maximum power generation in electromagnetic systems depends on either the properties of the permanent magnet or the magnet and coil combination. Therefore, the study of permanent magnets and electromagnetic systems are very important. This chapter will discuss the properties of the permanent magnets and the relevant theory of the electromagnetic system.

3.1 Magnet and Magnetic field

Magnets produce an invisible magnetic field, and it is this field of electromagnetic energy that transfers the forces of a magnet. The significant and effective properties of magnets, such as attracting other magnetic materials (such as iron) or magnets and repelling other magnets, are dependent on their magnetic fields. Magnets have a north pole and a south pole, similar to the north and south magnetic poles of the earth. The like or same poles repel from one another but unlike poles attract each other. The internal structure of the permanent magnets manufactured from rare earth materials create the magnetic field. The atoms contain both electrons and the nucleus of the atom, which consists of protons and neutrons, and both the electrons and nucleus themselves act like miniature magnets, like small spinning components of electric charge. Moreover, they have magnetic field characteristics in the particles themselves. The orbits of the electrons generate the magnetic field as they move about the nucleus. A strong permanent magnet should have a strong magnetic field. Figure 3.1 represents the typical nature of the magnetic field around a magnet, showing how the magnetic field always goes from the north pole to the south pole, regardless of the design and shape of the magnet. Permanent magnets have a variety of uses in daily life as field sources. There are various types of machines such as motors, generators, acoustic transducers, magnetic field and imaging systems and magneto-mechanical devices and magnetic-levitation or maglev trains that usually use permanent magnets as a magnetic field source (Chan & Lai, 2007; Zhu & Howe, 2001). The permanent magnets have also been used in magnetostrictive and magnetoresistive sensors to detect position and displacement. Compared to other magnets, the rare earth magnets are much stronger. The term “grade” is used to express the magnet specifications and is a measurement of how strong

the magnetic material used in the magnet is or how concentrated the magnet is. Two magnets with the same size and shape can have different grades, for example, one may have grade N45 and the other N52. In this comparison, the grade N52 magnet will be the stronger since it is more concentrated. The symbol N stands for Neo which is short for neodymium, a rare earth material. Among all rare earth magnets, neodymium magnets are the strongest and most affordable permanent magnets. Moreover, the neodymium magnet is magnetically more stable than other magnets due to its highest magnetic field strength and higher coercivity.

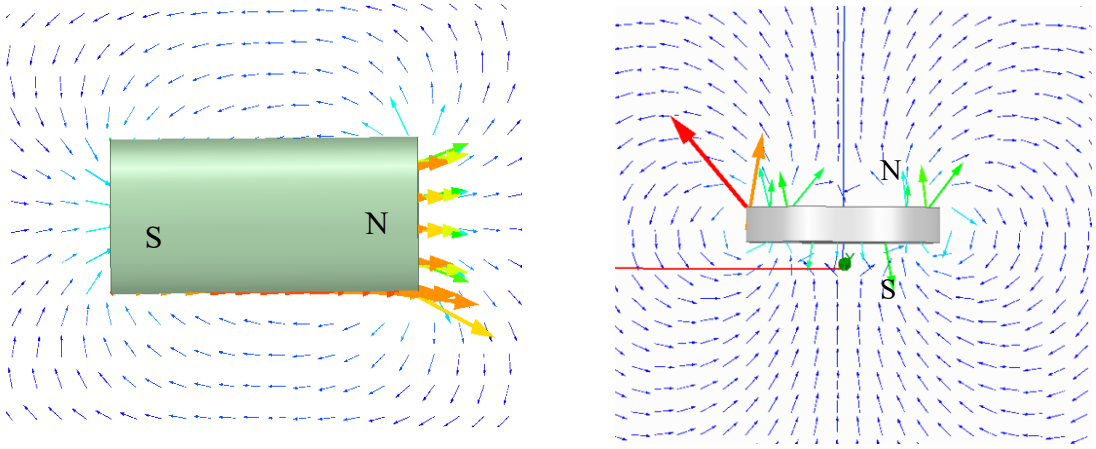

(a) (b)

Figure 3.1: Magnetic field around a typical magnet; (a) Bar magnet, (b) Ring magnet (axially magnetized)

3.2 Magnetization and Demagnetization

Magnetisation refers to the local value of the magnet's magnetic moment per unit volume, typically represented by M, with the units of A/m. Magnetisation is a vector field, instead of just a vector (similar to the magnetic moment), and thus for that reason, the magnet's different areas can be magnetised with various directions and strengths (for instance, because of domains). The magnetisation can be measured as,

$$M = \frac{dm}{dV} \tag{3.1}$$

where the elementary magnetic moment is denoted by dm and the volume element is represented by dV. There are different types of magnetisation of permanent magnets that exists such as axial, radial,

parallel, Quasi-Halbach and Halbach array. Under some circumstances, a permanent magnet may lose some or all its magnetic field which is known as demagnetisation of the magnet. Excessive exposure to high temperatures is often the cause of demagnetisation. The happens at the Curie temperature, which is one of the known parameters of all magnetic materials, at which the domains of the magnet randomise due to thermal agitations applying an extra force strong enough to overcome the magnetic domain's resistance to move.

3.3 Magnetic Field Strength and Magnetic Flux density

Mathematically the magnetic field can be signified by vector quantities having direction and magnitude. A magnetic field is often represented by two different vectors: the magnetic field strength and magnetic flux density. The magnetic field intensity and magnetic flux density are used to characterise the strength of the permanent magnets. The magnetic field strength, which is also known as magnetic field intensity and is typically represented by *H*, is the vector quantity which defines the capability at a given point of a magnetic body to induce a magnetic field and has the units of A/m or Oersted (Oe). The magnetic flux density, which is also known as magnetic induction and is symbolised by B, is the amount of magnetic flux (Φ) per unit surface area and has the units of Weber per square metre (Wb/m^2) or Tesla (T). The magnetic flux density can be mathematically represented as,

$$B = \frac{\Phi}{A} \tag{3.2}$$

where the magnetic flux is Φ and is denoted by Webers (Wb), the surface area is A in square meters (m^2). Every permanent magnet generates a magnetic field (B) in its core and its peripheral surroundings. Every point within and outside of the magnet can be attributed with a directional B field strength. There is a relationship between magnetic flux density (B) and magnetic field strength (H) and the relationship in a vacuum can be expressed as,

$$B = \mu_0 \cdot H \tag{3.3}$$

where the vacuum's magnetic permeability is μ_0 ($4\pi \times 10\text{^}(-7)$). If material is present in the field then the relationship between them can be expressed as,

$$B = \mu_0 \cdot \mu_r \cdot H \tag{3.4}$$

where the relative permeability of the material is denoted by μ_r. Moreover, within the magnetic body, the magnetic flux density (B) is the sum of the total magnetic field strength (H) and the magnetic body polarisation (J) and it can be expressed as,

$$B = \mu_0 H + J \tag{3.5}$$

$$J = M \cdot \mu_0 \tag{3.6}$$

$$B = \mu_0 (H + M) \tag{3.7}$$

In many cases, the permanent magnet's properties can be defined by magnetic coercive force (H_c), with units of Oe (Oersted), and residual magnetic flux density or remanence (B_r), with units of Tesla (T). Magnetic coercive force is the strength of the magnetic field that is required to either reverse the direction of the magnetic pole, or to force the magnetic flux within the material to zero.

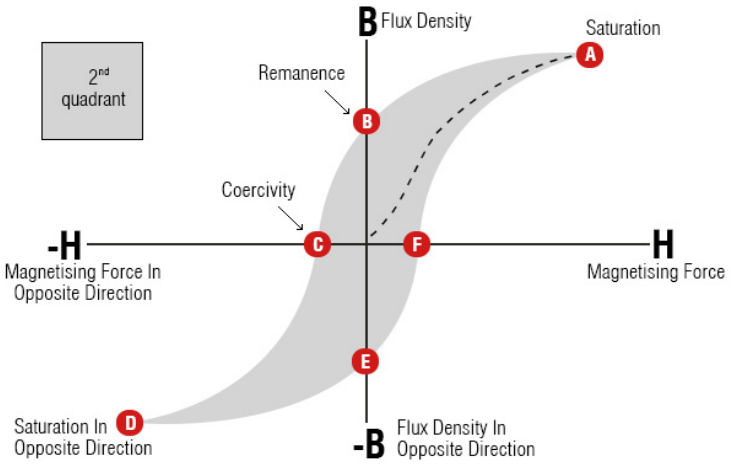

Figure 3.2: B-H curves (First4Magnets, 2020)

This value does not certainly mean, however, that the material's magnetisation goes down to zero. In that situation normally, a high-grade magnet does not lose magnetisation. Because of the external magnetic field, the materials become saturated and when the external magnetic field is removed from it, then the remaining magnetic flux density is known as remanence. In general, permanent magnets are strong magnets because they have high coercivity (Hc) and high remanence (Br). The coercivity and remanence are indicated in the B-H curve as presented in Figure 3.2. Generally, the B-H curve is used to find how the magnetic flux density changes in the presence of an externally applied magnetic field. Figure 3.3 presents the demagnetisation curve that is sometimes known as the intrinsic B-H curve since the same plot can be done by plotting B vs. H.

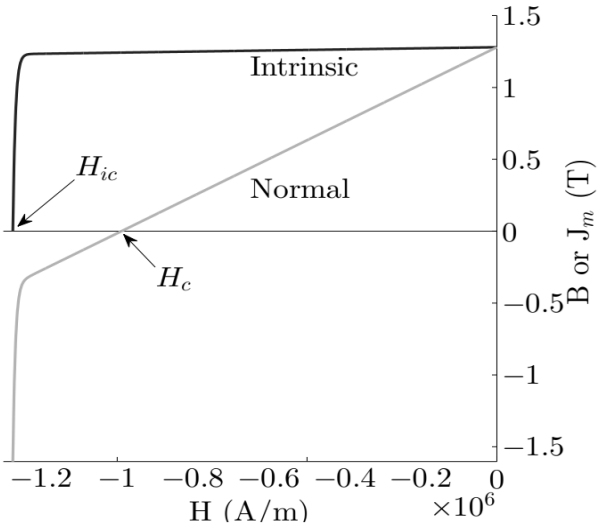

Figure 3.3: Demagnetisation curve (intrinsic and normal B-H curves) for a typical permanent magnet material (Sjökvist, 2014)

The field strength required to decrease the magnetisation to zero is called intrinsic coercivity and is denoted by H_{ic}. Moreover, Figure 3.3 displays how the magnetic polarisation ($J_m = \mu_0 M$) and the magnetic flux density is associated with an external field. The magnetic properties of the permanent magnet change with temperature. Usually, for all materials, the remanence's temperature coefficient is negative, which means the remanence declines along with the rising temperature. The coercivity's temperature coefficient can be positive, which depends on the types of material. For example, the Ferrites and Alnico have a positive coefficient, which means the coercivity rises as the temperature increases, however, it is negative for other types of magnetic materials. To study the magnet demagnetisation behaviour based on temperature dependence, the demagnetisation curve can be defined by temperatures, which can be found in the datasheets of the supplier company. A typical demagnetisation curve is temperature dependent, as shown in Figure 3.4. For a good illustration of how any type of magnet can be described using a function, it is useful to work with an intrinsic flux density B_i versus H curve, as a replacement for a flux density B vs H curve. The relationship between B_i and B can be expressed as,

$$B = B_i + \mu_0 H \qquad (3.8)$$

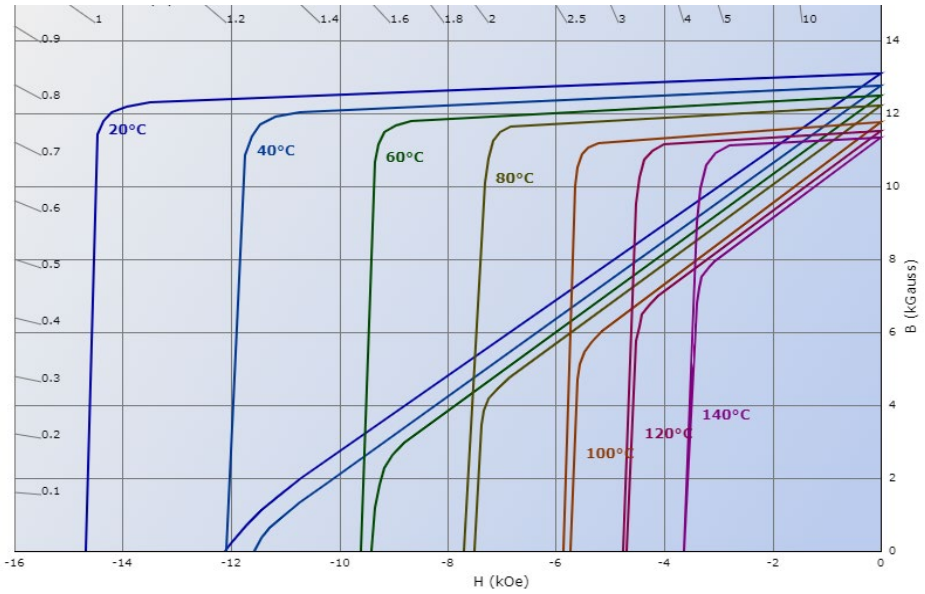

Figure 3.4: Typical demagnetisation curve (K&J Magnetics, 2020)

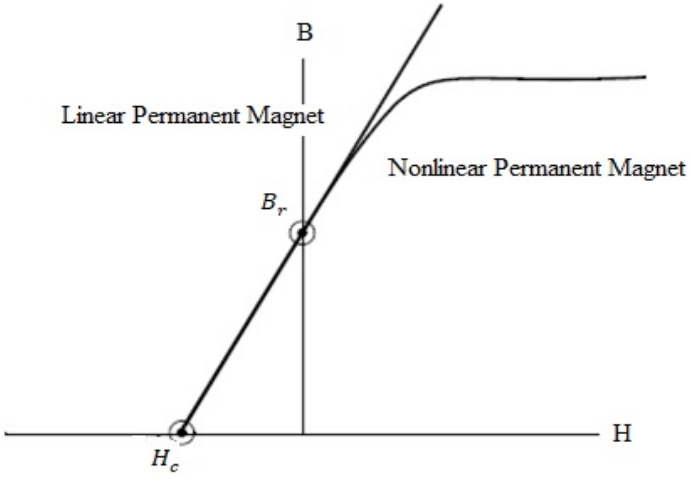

Figure 3.5: Linear Vs Nonlinear permanent magnet

Moreover, both the linear and nonlinear type's of permanent magnets can be defined by the B-H curve. A general B-H curve for linear and nonlinear permanent magnets is shown in Figure 3.5 where the magnetic coercivity, H_c, is well-defined as the B-H curve's H-axis intercept, and the magnetic remanence, B_r, as its B-axis intercept.

3.4 Analysis of Magnetic Properties

The magnetic flux density has the axial, radial, normal, and tangential components. Since there are no simple formulas for estimating the magnetic flux density (B) of the different magnetic components

as well as different shapes, to model the flux density B, various computer algorithms were developed. However, for less complex symmetrical geometries, simple formulas can be used to estimate the B field on a symmetry axis in the direction of the north-south pole. The magnetic properties have been presented in Table 3.1.

Table 3.1: Properties of the design magnet

Property	Value
Permanent magnet (PM) outer diameter	72 mm
Permanent magnet inner diameter	32.5 mm
Thickness of each magnet	13 mm
Weight of each magnet	110 gm
Weight of the middle magnet with plastic bush	367.45 gm
Magnetisation	$1.03 \times 10^6\ A/m$, axially magnetised thru the 13 mm
Maximum pull force	60 kg
Permanent magnet composition	NdFeB grade 42
Remanence Magnetic flux density (B_r)	1.3 to1.35 (T)
Coercivity (bH_c)	>= 836 (kA/m)
Intrinsic Coercivity (iH_c)	>= 955 (kA/m)
Maximum Energy Product $(BH)_{max}$	334 (kJ/m^3)
Relative Recoil permeability (μ_r)	1.05
Maximum operating temperature (ºC)	80-240
Density (g/cm^3)	7.4

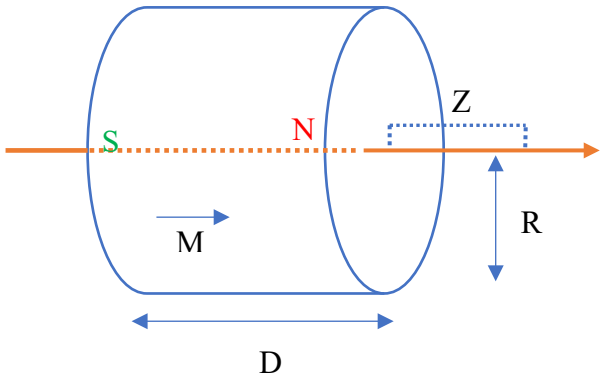

(a)

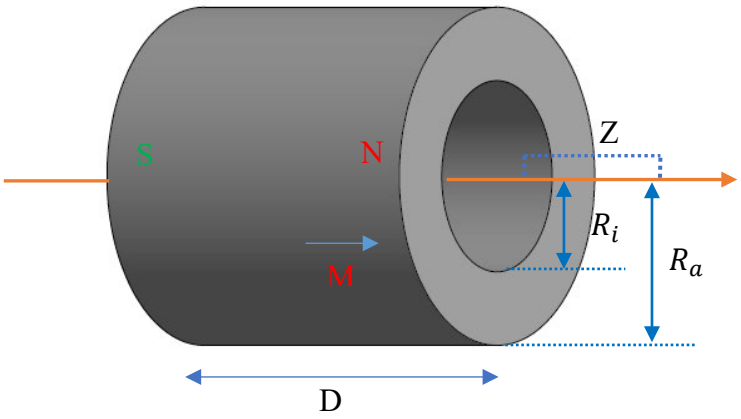

(b)

Figure 3.6: Magnet shape (a) Cylinder and (b) Ring

The magnetic flux density (B) in the axial direction on the symmetry axis of an axially magnetised cylindrical magnet, as shown in Figure 3.6(a) can be determined as (Selvaggi et al., 2010),

$$B_z = \frac{B_r}{2}\left[\left(\frac{D+Z}{\sqrt{R^2+(D+Z)^2}}\right)-\left(\frac{Z}{\sqrt{R^2+Z^2}}\right)\right] \tag{3.9}$$

$$B_z = \frac{B_r}{2}\left[\left(\frac{Z+D}{\sqrt{{R_a}^2+(Z+D)^2}}\right)-\left(\frac{Z+D}{\sqrt{{R_i}^2+(Z+D)^2}}\right) + \left(\left(\frac{Z-D}{\sqrt{{R_i}^2+(Z-D)^2}}\right)-\left(\frac{Z-D}{\sqrt{{R_a}^2+(Z-D)^2}}\right)\right)\right] \tag{3.10}$$

If the magnet is an axially magnetised ring type as displayed in Figure 3.6(b) then the magnetic flux density (B) in the axial direction on the symmetry axis can be measured by equation 3.10 (Camacho & Sosa, 2013). Here, the remanence field, denoted by B_r, is independent of the geometry of the magnet; Z is the distance from the spherical edge on the symmetry axis; and D is the thickness of the magnet. R is the radius of the cylindrical magnet but R_a and R_i are the outside and inside radius of the ring magnet, respectively. Figure 3.7 presents the calculated magnetic flux density in the axial direction.

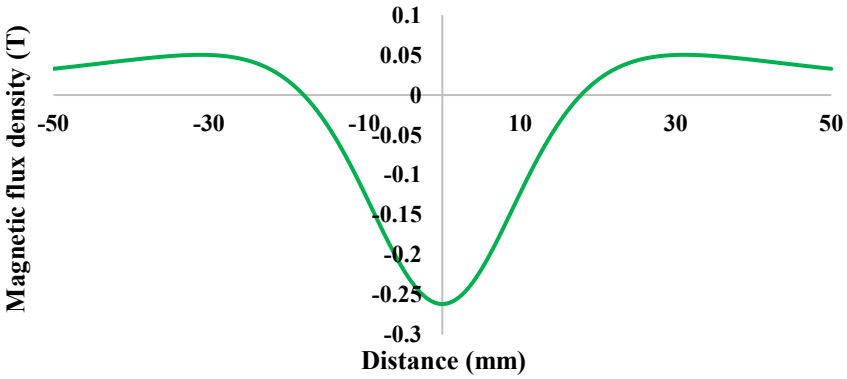

Figure 3.7: Magnetic flux density in the axial direction (analytical measurement based on equation 3.12).

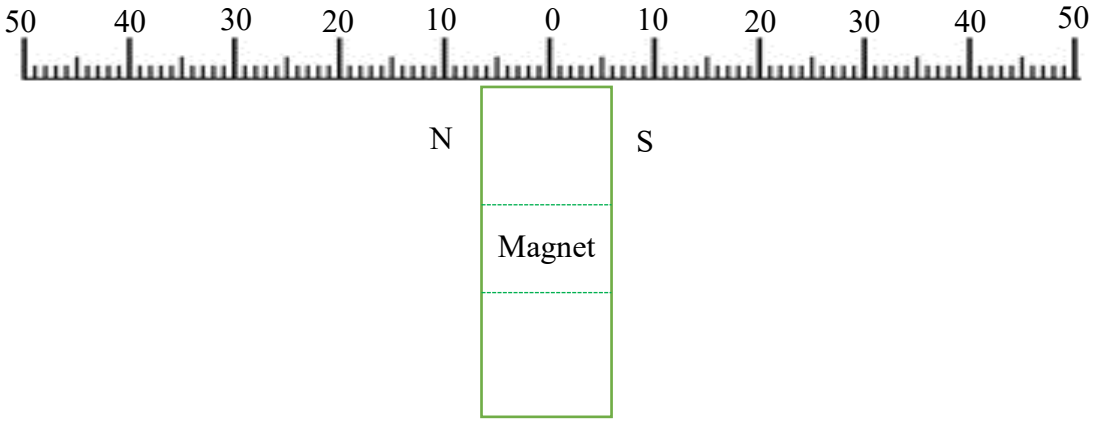

Figure 3.8: Ring Magnet

It is seen from Figure 3.7 that the highest magnetic flux density has been found in the centre of the ring magnet. A line outside the surface (in the radial direction; parallel to the axis of symmetry) of the ring magnet, as shown in Figure 3.8, is utilised to calculate the magnetic flux density in the radial direction. Figure 3.9 displays the calculated (by using Gauss meter) magnetic flux density in the radial direction. It is known that measuring the magnetic flux density is a very challenging task. There are very complex and sometimes very expensive computer programmes that can be used for analysing the magnetic flux density (B) along each symmetry axis or fields of different magnetic types. Moreover, the computer programmes not only calculate and estimate the B fields but also much more. ANSYS MAXWELL, COMSOL, EMS, FEMM software's are normally used to analyse or compute the magnetic flux density around the magnet using the finite element method. ANSYS MAXWELL is an interactive high-performance software package that solves electric, magnetic, or electromagnetic problems.

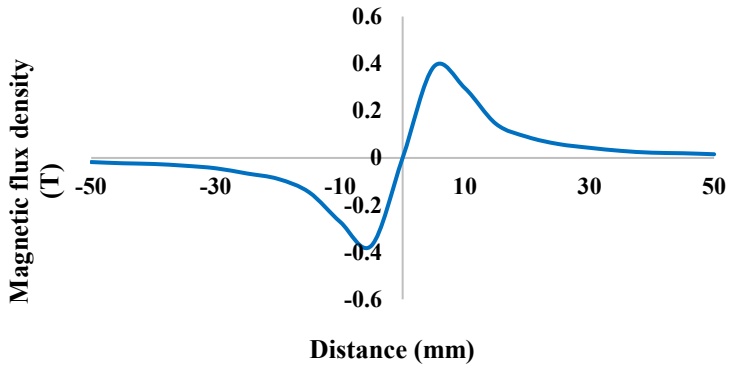

Figure 3.9: Magnetic flux density in Radial direction (experimental measurement)

Finite element analysis (FEA) is used as the theoretical principle of ANSYS MAXWELL, and it has been recognised as being a very strong numerical modelling tool for general electromagnetic and magnetic analysis. It works by solving Maxwell's equations in a finite region of space with proper boundary conditions and user-specified initial conditions to attain a solution with a certain uniqueness. The relevant Maxwell's equations are shown as,

$$\begin{cases} \nabla \times \vec{H} = \vec{J} \\ \nabla \cdot \vec{B} = 0 \\ \vec{B} = \mu_0(\vec{H} + \vec{M}) = \mu_0 \cdot \mu_r \cdot \vec{H} + \mu_0 \cdot \vec{M}_p \end{cases} \tag{3.11}$$

Here $\vec{B}(x,y,z)$, $\vec{H}(x,y,z)$, $\vec{j}(x,y,z)$ and $\vec{M}_p(x,y,z)$ are the magnetic flux density, magnetic field strength, conduction current density and permanent magnetisation of the permanent magnet, respectively. Moreover, μ_0 and μ_r are the permeability of the vacuum, and relative permeability, respectively. A N42 ring magnet has been designed (using the Grade N42 ring magnet's properties) in ANSYS MAXWELL 3D to analyse the magnetic flux density around the magnet. The corresponding magnetic properties of the magnet are shown in Table 3.1. The simulation has been done for both magnetostatic modes for different magnet arrangements to understand the properties of the permanent magnet during stationary and moving situations. The designed magnet is shown in Figure 3.10, where the axial magnetisation direction is indicated. Figure 3.11 displays the BH curve of the designed magnet. The maximum energy product, or BHmax, of any magnet is the power density of the magnet and it is equal to the largest rectangle's area that can be inscribed under the normal curve, as displayed in Figure 3.11. To design nonlinear permanent magnet in ANSYS Maxwell BHmax is an important parameter. Moreover, the value of the BHmax depend on B and H.

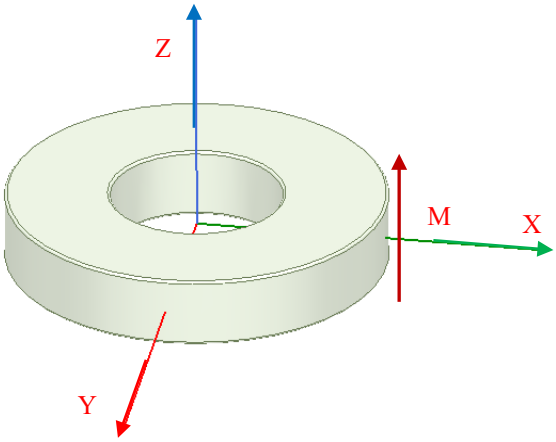

Figure 3.10: Designed Ring Magnet in ANSYS Maxwell

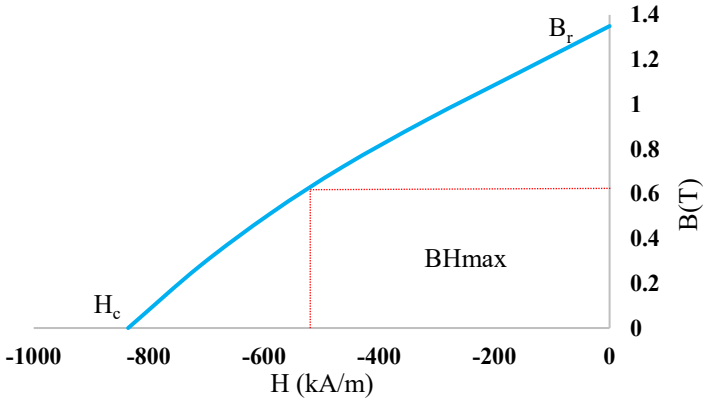

Figure 3.11: BH curve with indicating BHmax

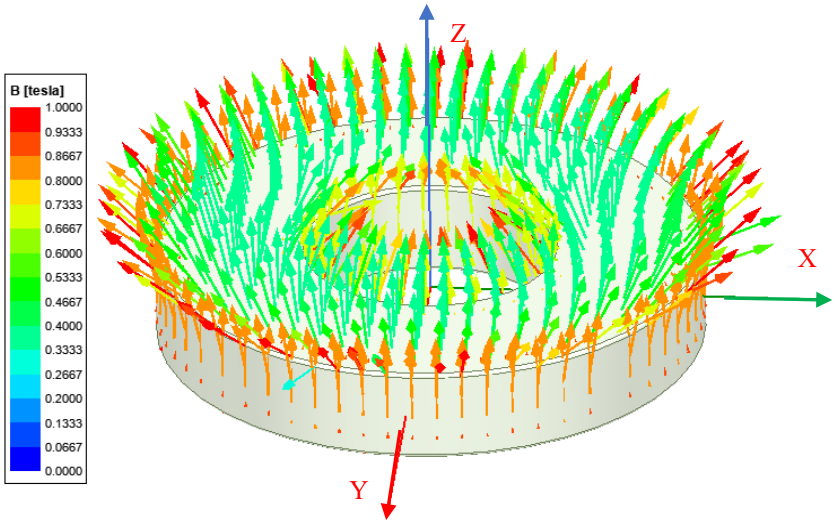

(a)

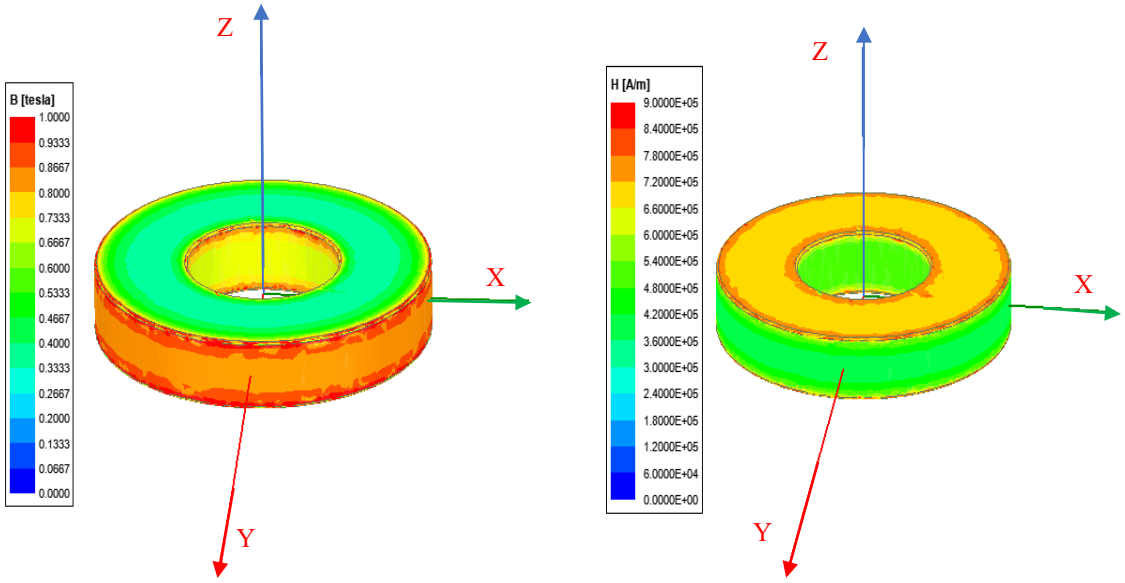

(b) (c)

Figure 3.12: (a) Magnetisation direction (Axaily magnetised) (b) Magnetic flux density on the surface of the magnet (c) Magnetic field strength of the surface of the magnet

Figure 3.12(a) presents the magnetisation direction of the designed magnet. The designed magnet is axially magnetised which can be seen from Figure 3.12(a). Moreover, Figure 3.12(b) and Figure 3.12(c) display the magnitude of the magnetic flux density and magnetic field strength of the surface of the magnet. Figure 3.13 and Figure 3.14 present the magnitude (Mag_B) and vector (B_vector) of the magnetic flux density in the XZ plane, respectively.

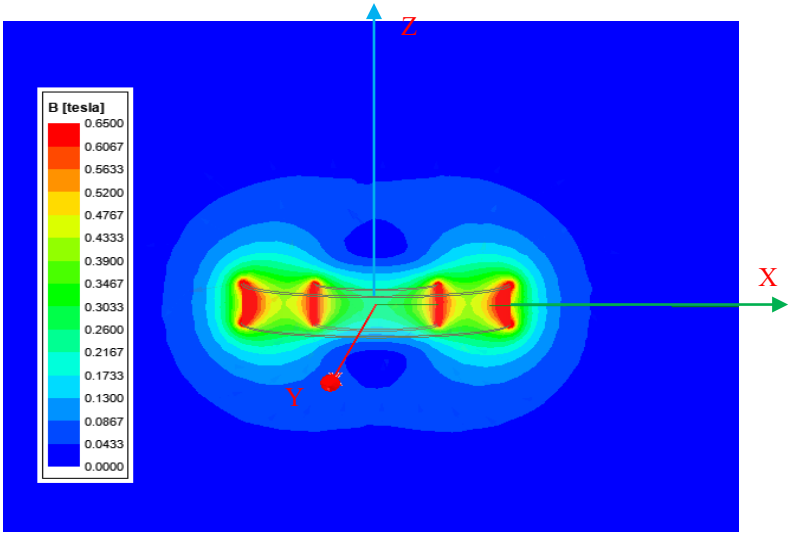

Figure 3.13: Mag_B in XZ plane

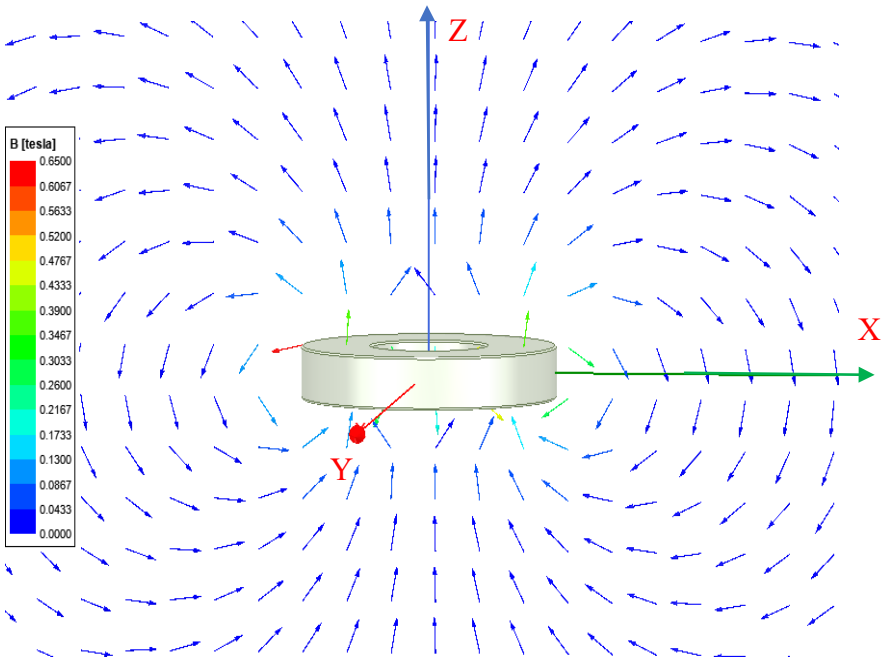

Figure 3.14: B_Vector in XZ plane

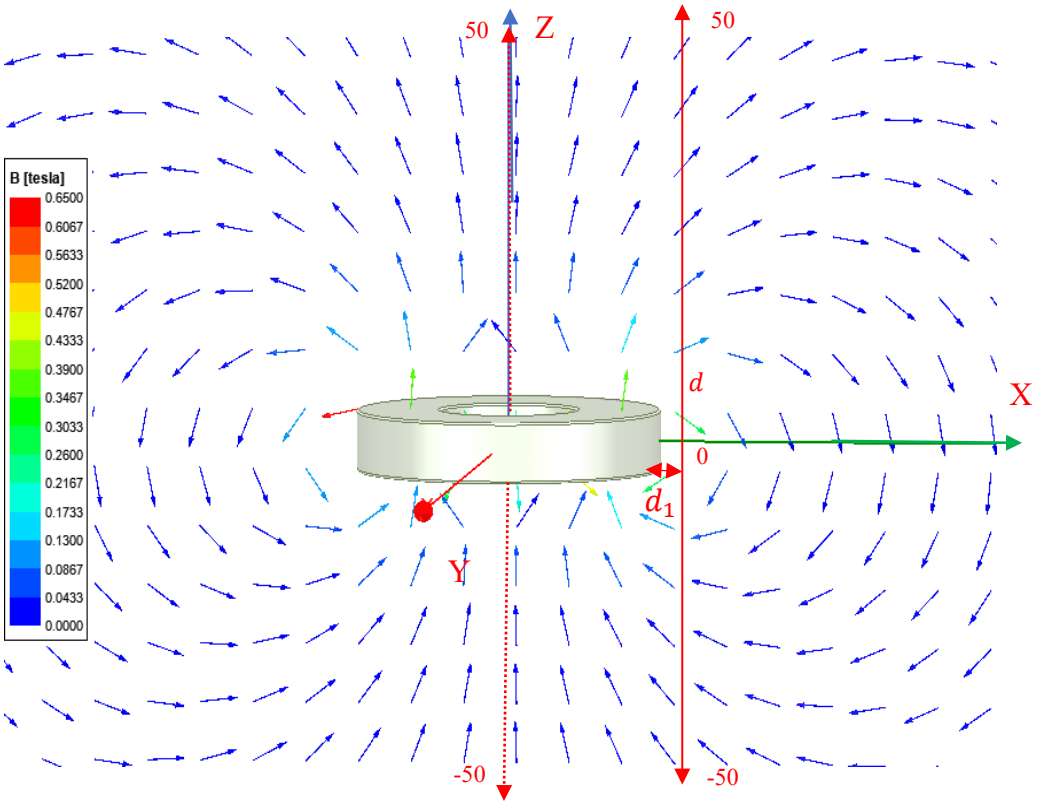

(a)

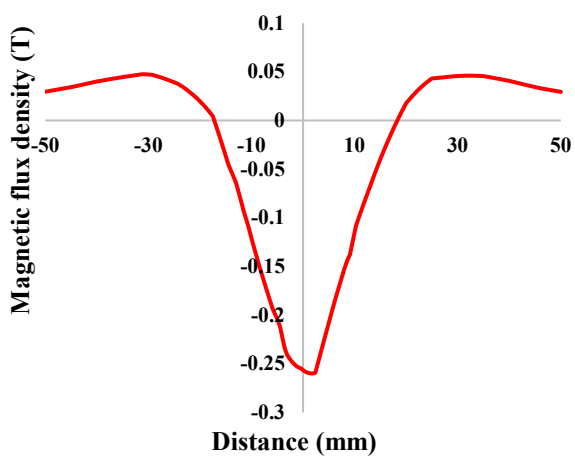

(b)

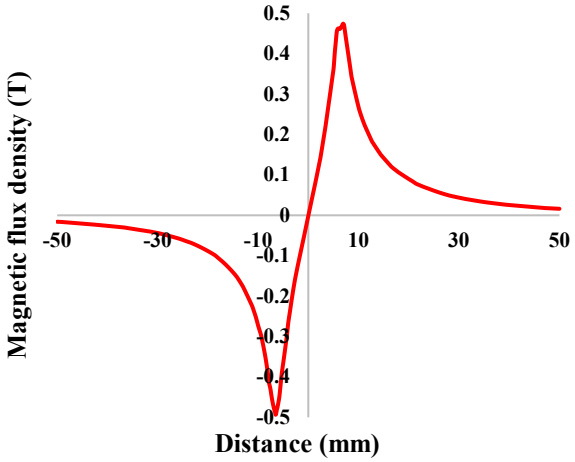

(c)

Figure 3.15: (a) B_Vector in XZ plane with d_1 and d (b) Magnetic flux density in the axial direction along in the centre line (ANSYS Maxwell Simulation result) and (c) Magnetic flux density in the radial direction in d_1 distance (ANSYS Maxwell Simulation result)

Figure 3.15(a) shows the magnetic field line, which is the closed curve in space traced out by following the direction in which the magnetic field vector points. Moreover, the intensity of the arrow in Figure 3.15(a) represents the magnetic field strength. The Z axis is a line considered axially through the centre of the magnet and the magnetic flux density, shown in Figure 3.15(b) is measured along this axis. Figure 3.15(c) shows the magnetic flux density measured at different points along a line, perpendicular to the X axis at 37mm from the Z axis. The way of measuring the magnetic flux density using ANSYS MAXWELL is: Field Overlays→ Calculator→ Select B_Vector from Named Expressions→ Copy to stack→ Scalar in Vector→ Scalar X/Y/Z for 3D model or Scalar R/Phi/Z for 2D model→ Add→ Name→ OK→ Results→ Create Field Reports→ Any Plot (Rectangular Plot) → Polyline 1 from Geometry→$B_x/B_z/B_z/B_{phi}$ from Calculator Expressions→ New Report.

The magnetic flux density in axial direction has been measured analytically and is presented in Figure 3.16, which also compared it with the measured magnetic flux density by ANSYS MAXWELL. Moreover, Figure 3.17 shows the comparison of the results from simulation to those done experimentally for the radial magnetic flux density. From Figure 3.17, it can be said that the experimentally measured peak magnetic flux density in the radial direction is almost the same as the numerically measured peak magnetic flux density in the radial direction. The radial magnetic flux density shows maximum values near the centre of the ring magnet. Figure 3.18 shows the radial magnetic flux density for different air gap distances.

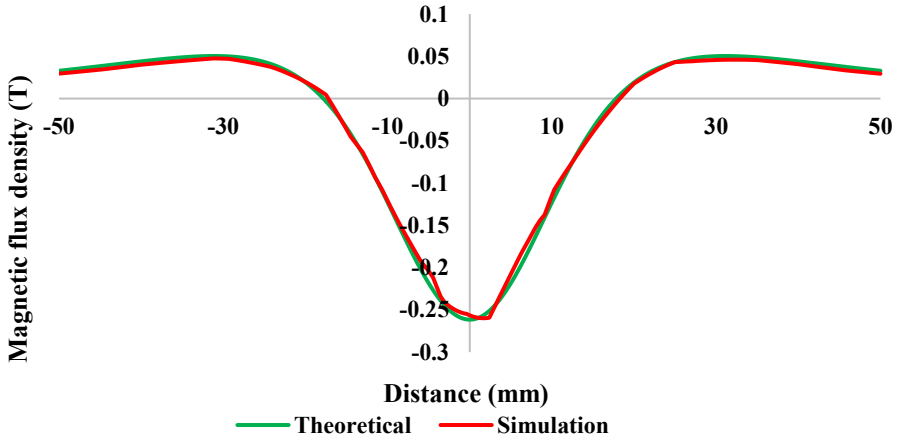

Figure 3.16: Comparison of magnetic flux density (Theoretical and simulation result)

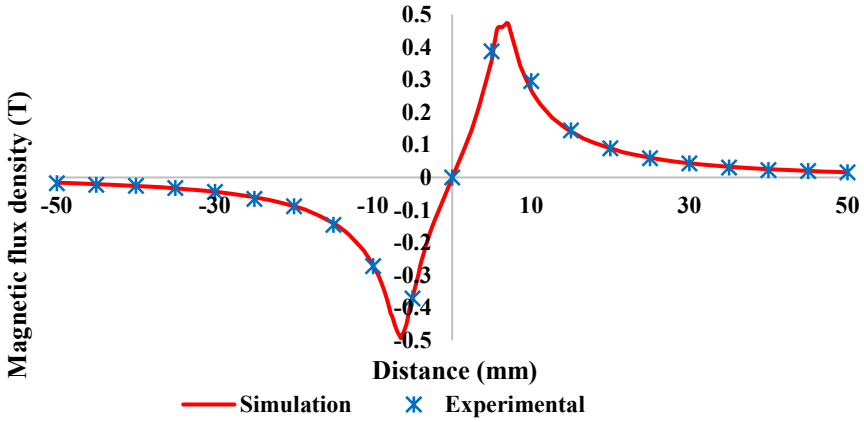

Figure 3.17: Comparison of Radial magnetic flux density (measured by ANSYS MAXWELL and experimentally)

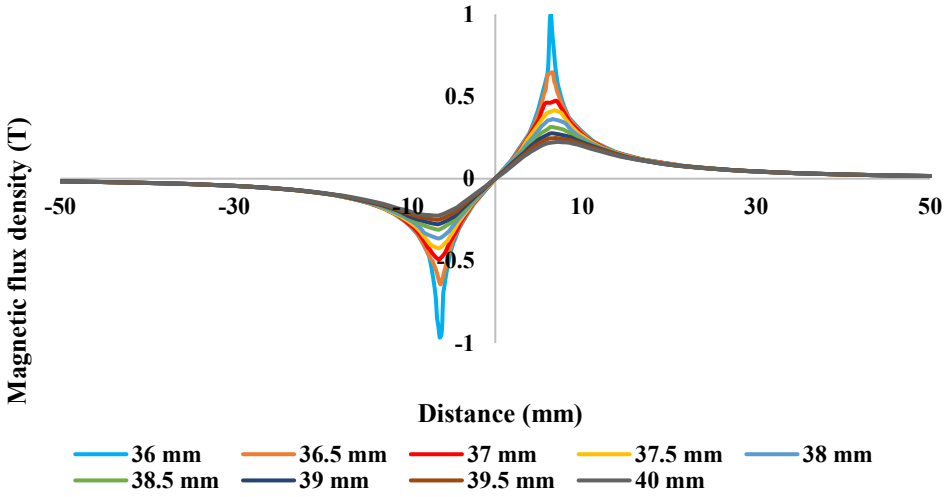

Figure 3.18: Radial magnetic flux density for different d_1

It can be said from Figure 3.18 that the magnetic flux density decreases with the increase of the air gap distance (d_1). The height magnetic flux density around 1 T has been seen on the outside surface in the radial direction of the magnet (outer radius 36 mm) and this value decreases to about 0.22 T with the increase of d_1. The magnetic field **B** is usually high at the poles and low in the middle portions of the ring magnets. The magnetic flux density also decreases going away from the centre of the magnet. However, the change of magnetic flux density with respect to the location of the magnet can be measured as (Zhu & Evans, 2018),

$$\frac{\Delta\Phi}{\Delta D} = \frac{\Delta B \cdot A}{\Delta D} \qquad (3.12)$$

where ΔB is the change of the magnetic flux density for the change of magnet position (ΔD). The permeability and relative permeability of the magnet can be measured by Field Overlays Calculator in ANSYS Maxwell by using equations 3.3 and 3.4. With the aim to better describe and understand the magnetic field distribution, the magnetic flux density of two unalike configurations (opposite poles facing (NS-NS) and same pole facing (NS-SN)) are studied.

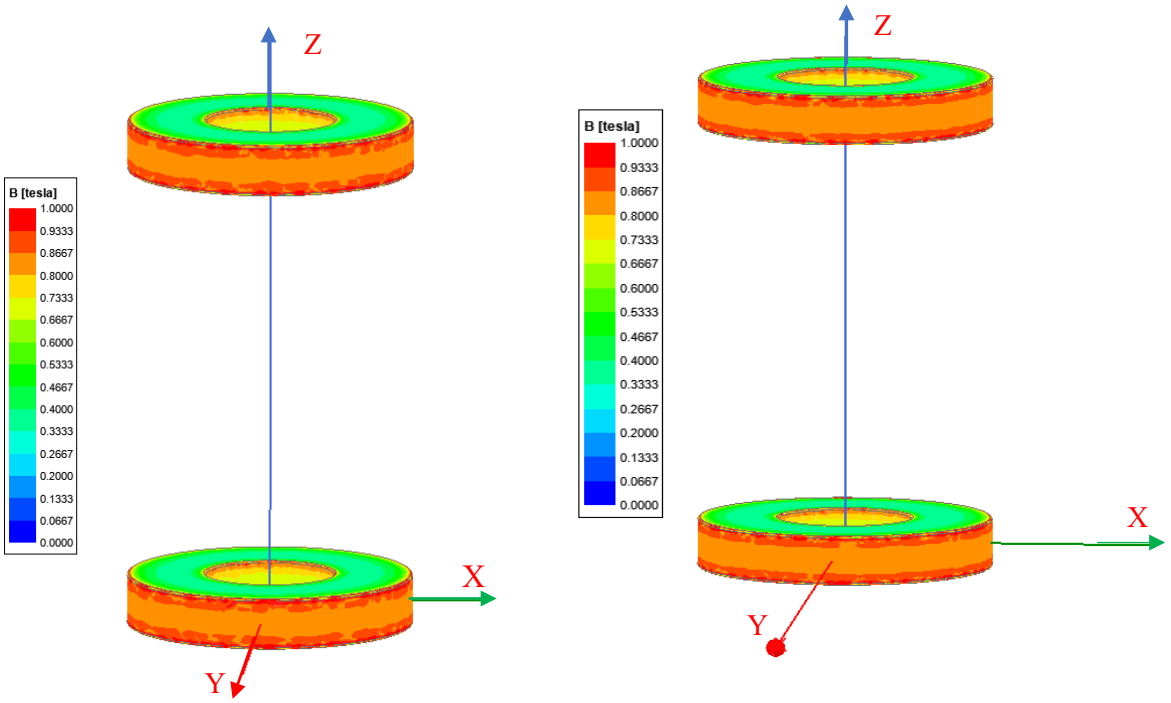

(a) (b)

Figure 3.19: Magnetic flux density in the surface of the magnet (a) opposite poles facing (NS-NS) (b) same pole facing (NS-SN)

Both ring magnets are the same size and shape, and their properties can be seen in Table 3.1. At first, the distance between the two magnets (same poles facing (SN-NS)) was set to a position (104 mm) where both magnets are at equilibrium under gravitational effects. The magnetic flux density at the surface of the magnet and the magnetisation direction of the magnets for both two configurations are shown in Figure 3.19 and Figure 3.20, respectively.

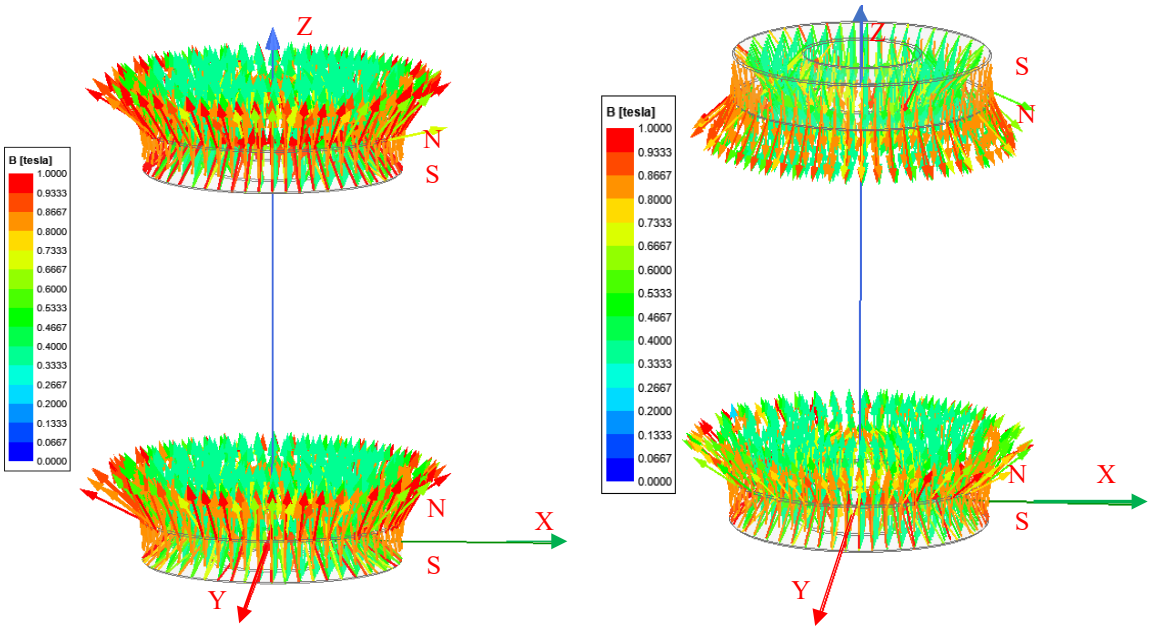

(a) (b)

Figure 3.20: Magnetisation (a) opposite poles facing (SN-SN) (b) same pole facing (SN-NS)

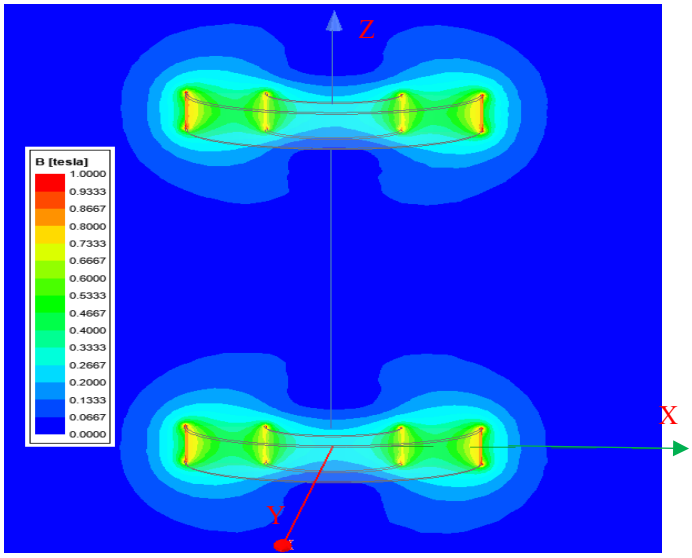

Figure 3.21: Magnetic flux density (Mag_B) when facing opposite poles (SN-SN)

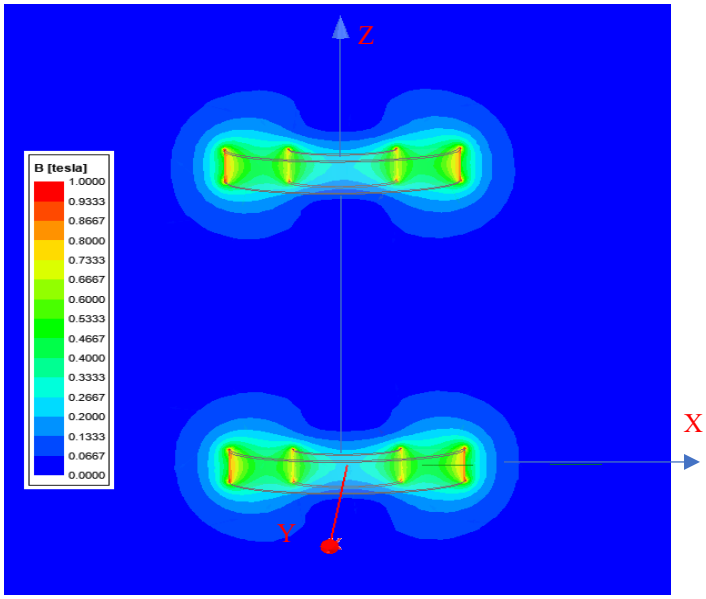

Figure 3.22: Magnetic flux density (Mag_B) when facing same poles (SN-NS)

The magnitudes of the magnetic flux density (Mag_B) for both configurations are presented in Figure 3.21 and Figure 3.22, respectively. A line (d) is considered parallel to the Z axis at a distance d_1 (37 mm) from the outside surface of the magnets' arrangement, as shown in Figure 3.23. In Figure 3.23, the length of d is the same for both configurations. Going from $d = 0$ to $d = 200$ mm the movement of the vertical arrows on one side is equivalent to the other side in Figure 3.23. The radial magnetic flux densities can be measured simultaneously. The measured axial magnetic flux density is shown in Figure 3.24 and the measured magnetic flux density in radial direction is shown in Figure 3.25 to illustrate how the magnetic flux density behaviour changes according to magnets pole's positions. If both magnets are facing with the same poles (NS-SN), then the magnetic flux density behaviour will not be the same as when both magnets are facing the opposite poles (NS-NS) which can be seen from Figure 3.24 and Figure 3.25, respectively. As presented in Figure 3.25(c), the same poles facing arrangement produces an axial flux density that ranges from the maximum value to the minimum value along an arctan shaped curve, while the opposite poles facing arrangement produces an axial flux density that resembles a parabolic shape between the two ring magnets.

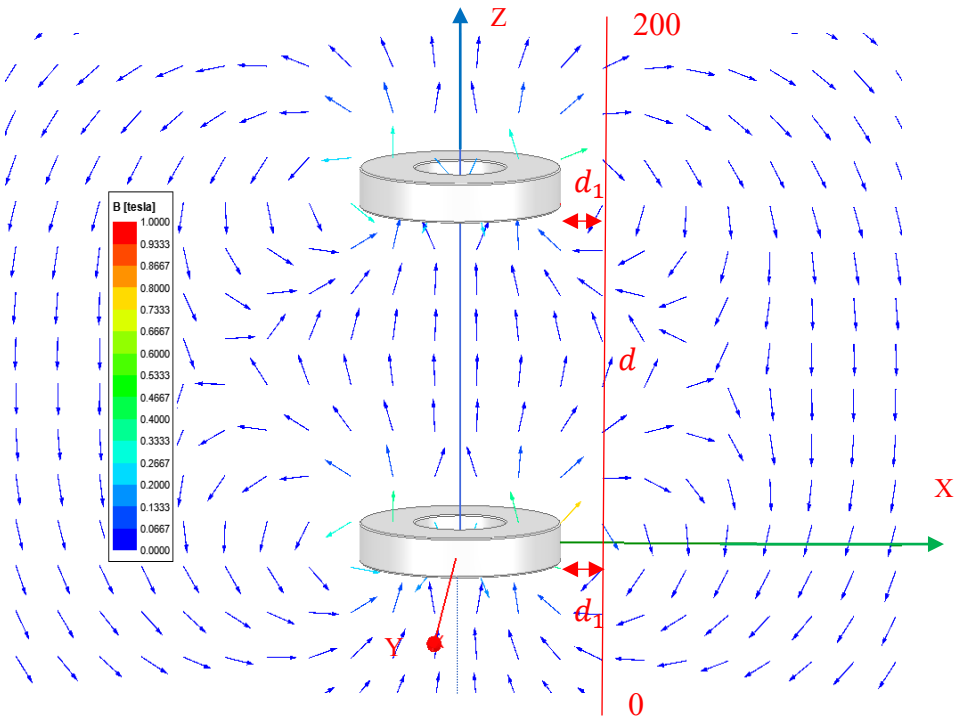

(a)

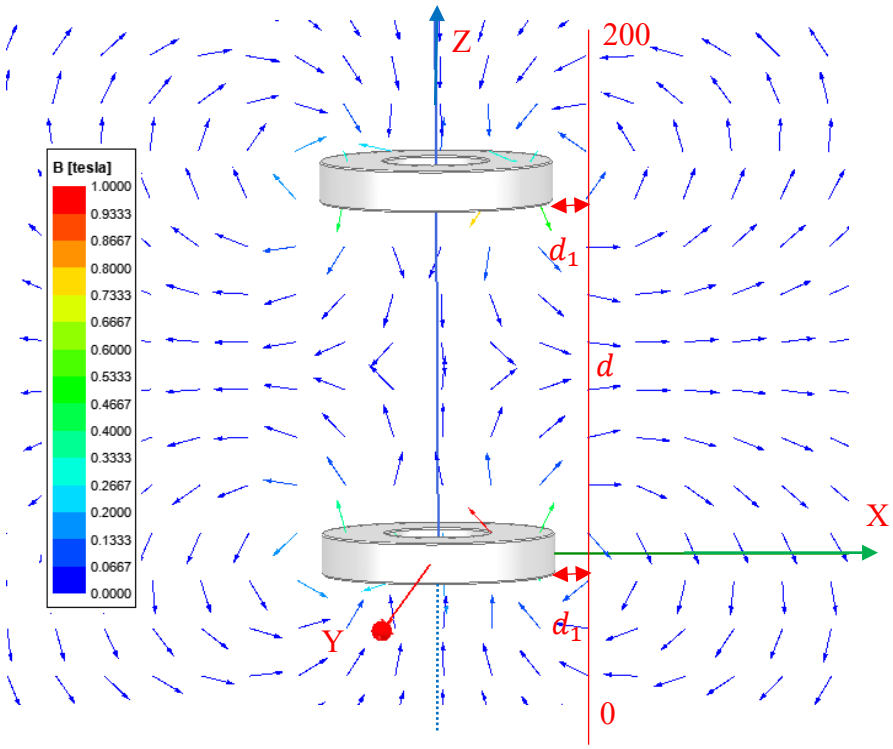

(b)

Figure 3.23: Magnetic flux density (B_Vector) (a) opposite poles facing (SN-SN) (b) same poles facing (SN-NS)

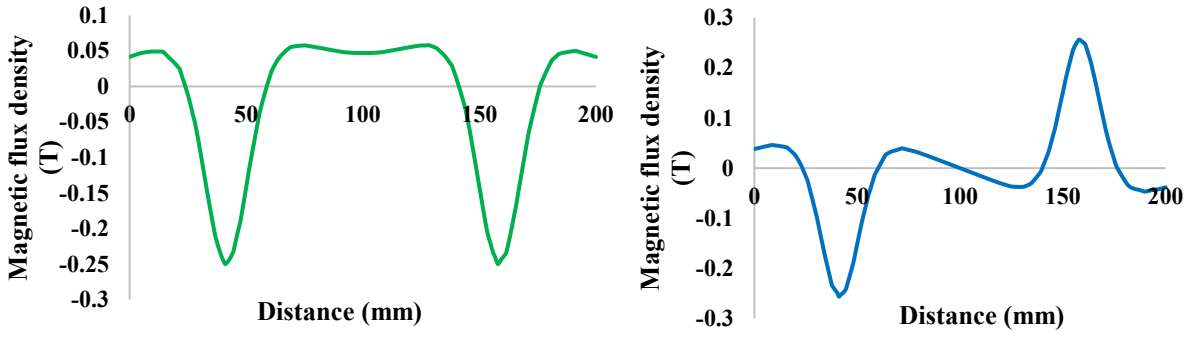

(a) (b)

Figure 3.24: Axial flux density (measured by ANSYS Maxwell) (a) facing opposite poles (b) facing same poles

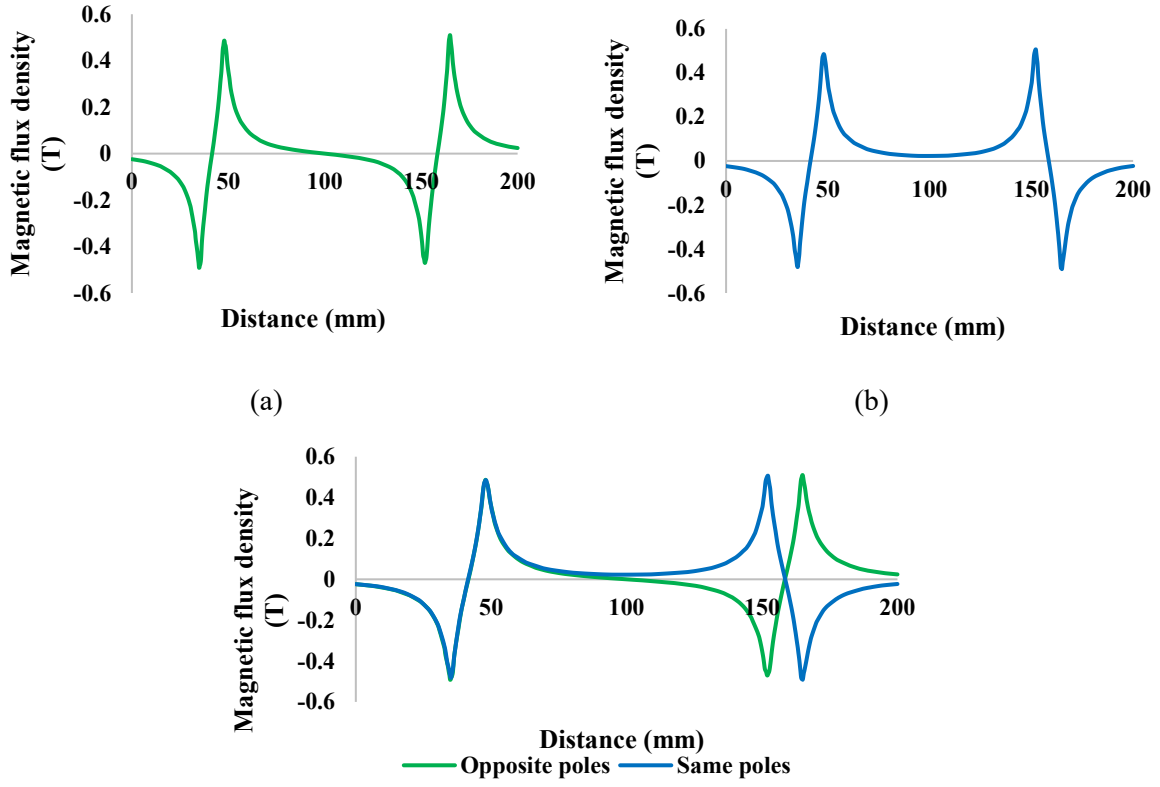

(a) (b)

(c)

Figure 3.25: Radial flux density (measured ANSYS Maxwell) (a) facing opposite poles, (b) facing same poles, and (c) comparison between (a) and (b)

If the magnets are brought closer to each other, the average magnetic flux density becomes much stronger when the same poles face each other compared to when opposite poles face each other, as seen in Figure 3.26 and Figure 3.27.

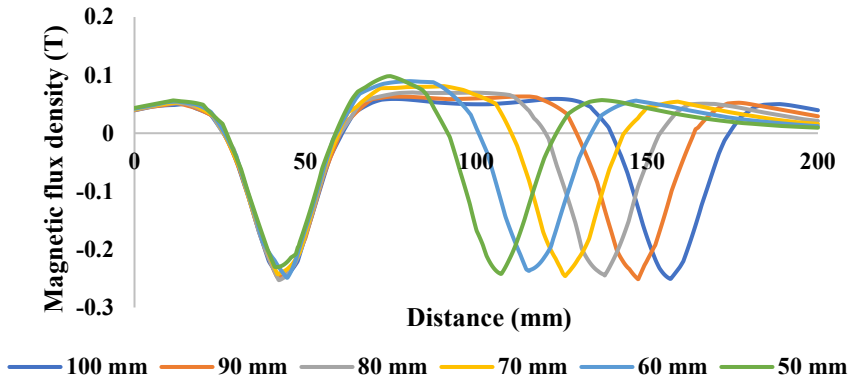

(a)

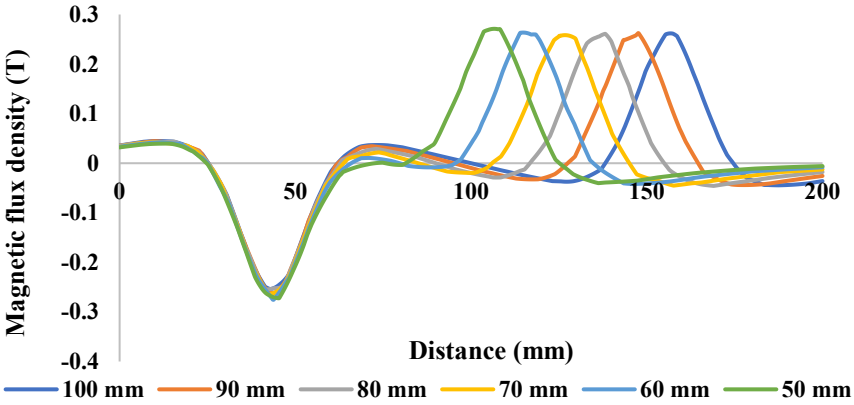

(b)

Figure 3.26: Axial flux density (a) Opposite poles facing each other (Top magnet in different positions) (b) Same poles facing each other (Top magnet in different positions)

The values of magnetic flux density in Figure 3.26 were taken along the axial direction at various positions in the centre line and the values of magnetic flux density in Figure 3.27 were taken along the radial direction at various positions in the line d which is d_1 far from the magnet outer surface. From Figure 3.26 and Figure 3.27 it can be noted that the change of magnetic flux densities is not the same when the same poles face each other compared to when the opposite poles are facing each other. Moreover, it should also be noticed that the magnetic field between the two impinging magnets creates an attractive force, as shown in Figure 3.26(a) and Figure 3.27(a), and creates the repelling force, as displayed in Figure 3.26(b) and Figure 3.27(b).

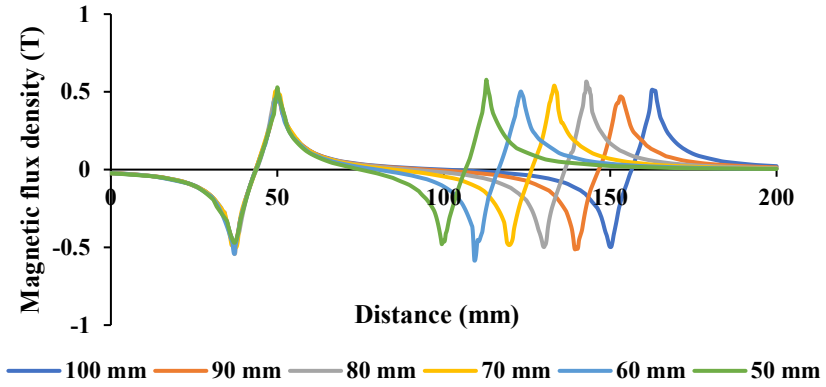

(a)

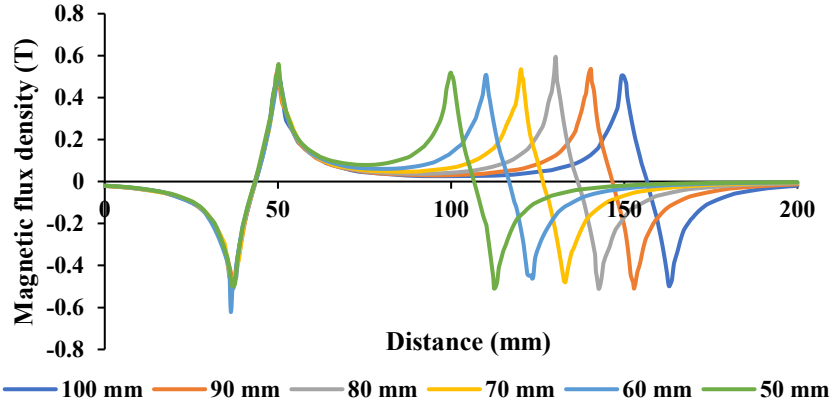

(b)

Figure 3.27: Radial flux density (a) Opposite poles facing each other (Top magnet in different position) (b) Same poles facing each other (Top magnet in different position)

The next configuration consists of three magnets, where the middle magnet is floating and found to settle in equilibrium between the two fixed magnets at a distance of 104 mm from the bottom magnet and a distance of 104 mm from the top magnet. The magnetic poles are oriented (SN-NS-SN) to repel each other. The magnetic flux density on the magnet surface and the magnetisation direction are displayed in Figure 3.28. The magnitude of the magnetic flux density is shown in Figure 3.29. In addition, the distributed magnetic field passing through the air gap is simulated as shown in Figure 3.30. The magnetic flux density is calculated for the system in the radial direction through the line d which is 37mm (d_1) from the magnet stack. This location (d_1) is very important in linear permanent magnet-based generator design because it could be the coil location. The measurement of the magnetic flux density in the air gap is important for calculating the system power output. There is a symmetry in the magnitude and direction of the magnetic flux as the distance, d, increases from $d =$

0 to either $d = 250mm\ or\ -250mm$, as shown in Figure 3.30. The measured magnetic flux density in the axial direction and radial direction are displayed in Figure 3.31.

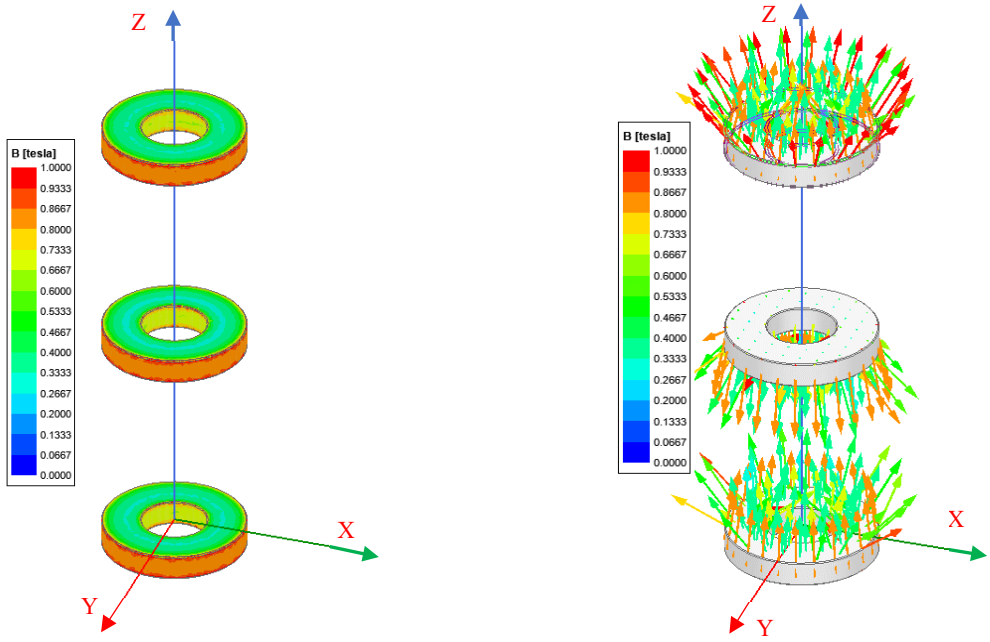

(a) (b)

Figure 3.28: (a) Magnetic flux density on the magnet surface and (b) Magnetisation direction

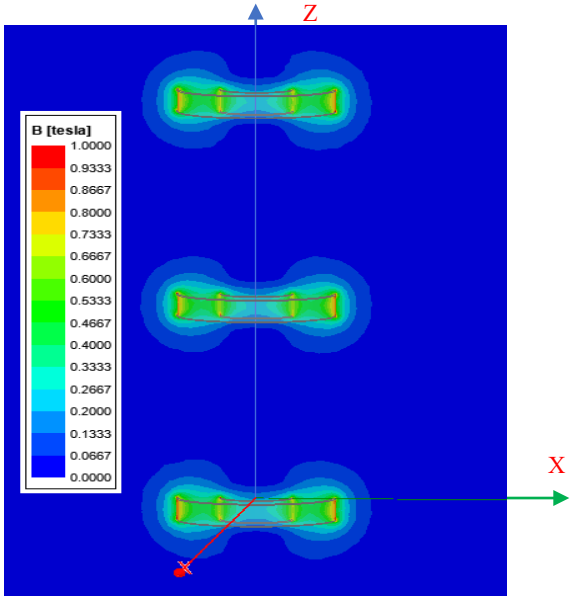

Figure 3.29: Magnetic flux density (Mag_B) when 3 magnets are facing same poles (SN-NS-SN)

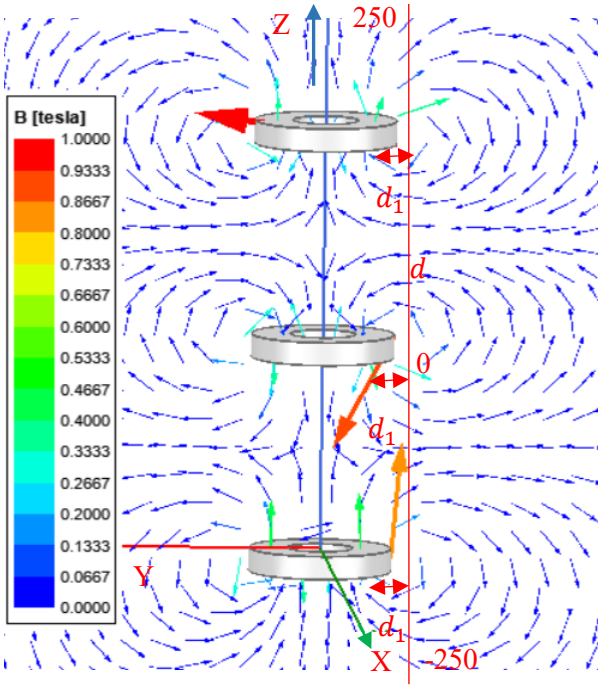

Figure 3.30: Magnetic flux density (B_Vector) in XZ plane

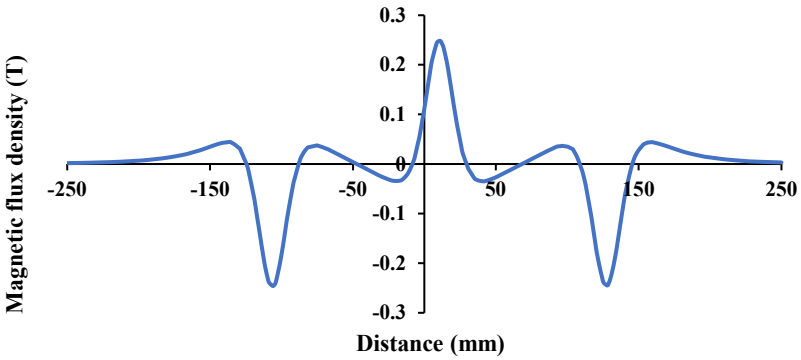

(a)

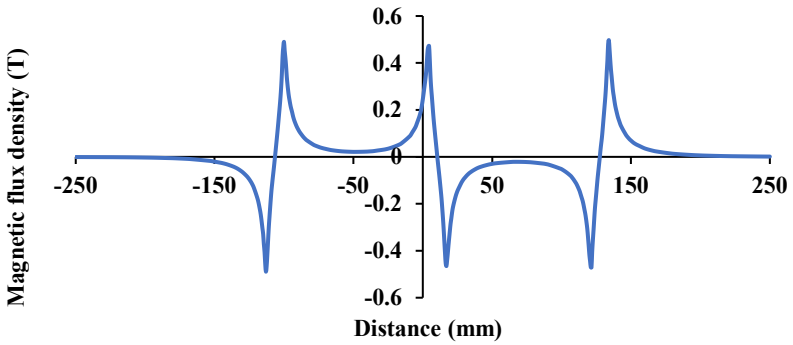

(b)

Figure 3.31: Magnetic flux density (a) axial direction, (b) radial direction

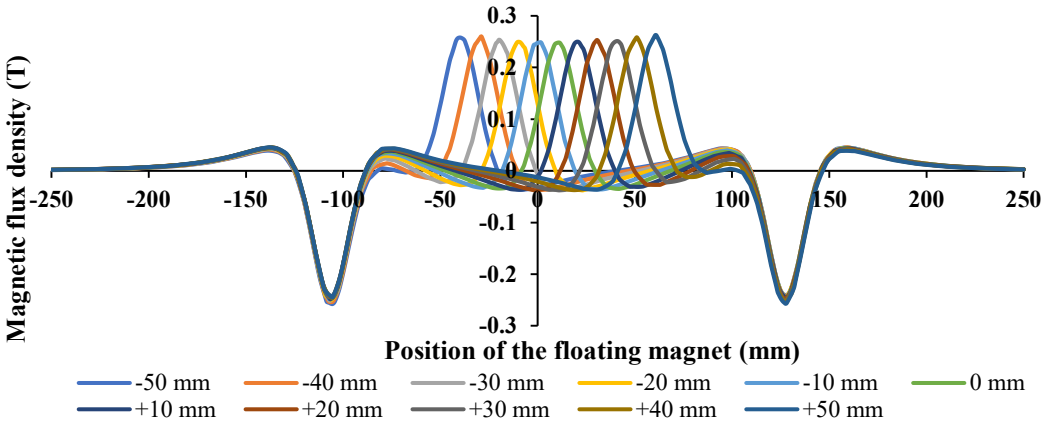

(a)

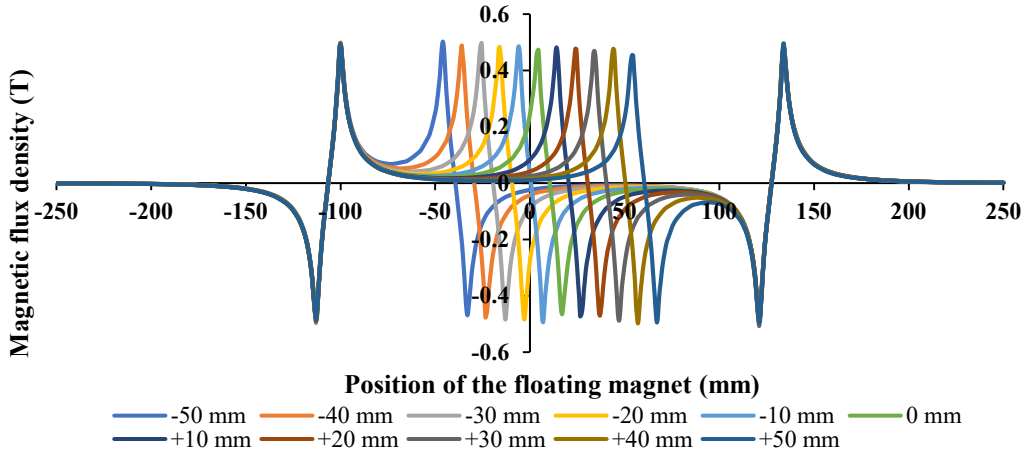

(b)

Figure 3.32: Magnetic flux density B_Vector (a) axial direction and (b) radial direction

Moreover, if an external force is applied or the middle magnet is moved up and down vertically then the change of average magnetic flux density is much higher than if they were kept stationary, as seen in Figure 3.32(a) and Figure 3.32(b). The repelling force between the impinging magnets can be considered as equivalent to the restoring force of the effective magnetic spring and it can create a bounce on the floating magnet. The vibration of the magnet creates the change of magnetic flux density which can be important for maximising the harvested power.

3.5 Magnet Force

If a magnet moves closer to another magnet, then either they will attract or repel each other, and it depends on their pole's orientation. Attraction occurs due to opposite poles being oriented together (NS-NS or SN-SN) and repulsion occurs when the same poles are aligned (SN-NS or NS-SN).

Because of the magnetic field between the two impinging magnets, the repelling force can be equivalent to the restoring force of the resulting magnetic spring. In the general case, calculating these attractive and repulsive forces between two magnets is a very complex task. The forces will be dependent on the shape, orientation, magnetisation direction and separation of the magnets. These attractive and repulsive forces can be calculated both numerically and theoretically and can be measured experimentally. The force (F) between two magnetic poles can be calculated as (Mukhopadhyay et al., 2003),

$$F = \frac{\mu Q_t Q_b}{4\pi r^2} \tag{3.13}$$

where the distance between two magnetic poles is r. The magnetic field intensity is $Q = M_s A$ where M_s is the magnetisation of the magnet (Furlani, 2001), and Q_t and Q_b are the magnetic field intensity of the top and bottom magnet, respectively. The unit of Q is *ampere-meter.* If two magnets are placed end to end at a great distance $x \gg R$ then the force between two identical cylindrical bar magnets can be calculated as (Apo & Priya, 2014),

$$F \simeq \left[\frac{{B_0}^2 A^2 (L^2 + R^2)}{\pi \mu_0 L^2}\right]\left[\frac{1}{x^2} + \frac{1}{(x+2L)^2} - \frac{2}{(x+L)^2}\right] \tag{3.14}$$

Here, B_0 and A are the magnetic flux density between two magnets, respectively. L and R are the length and radius of each magnet, respectively. The separation between the two magnets is expressed by x. If $x \gg R$ the force between two cylindrical magnets can be calculated as (Vokoun et al., 2009),

$$F(x) \simeq \frac{\pi \mu_0 M^2 R^4}{4}\left[\frac{1}{x^2} + \frac{1}{(x+2L)^2} - \frac{2}{(x+L)^2}\right] \tag{3.15}$$

When $L \ll x$ then the magnetic force can be calculated as,

$$F(x) = \frac{3\pi \mu_0 M^2 R^4 L^2}{2}\frac{1}{x^4} = \frac{3\mu_0 M^2 V^2}{2\pi}\frac{1}{x^4} = \frac{3\mu_0 m_1 m_2}{2\pi}\frac{1}{x^4} \tag{3.16}$$

When $L \ll x$, the force between two ring magnets can be calculated as,

$$F(x) = \frac{3\pi \mu_0 M^2 \left({R_{out}}^4 - {R_{in}}^4\right) L^2}{2}\frac{1}{x^4} = \frac{3\mu_0 M^2 V^2}{2\pi}\frac{1}{x^4} = \frac{3\mu_0 m_1 m_2}{2\pi}\frac{1}{x^4} \tag{3.17}$$

where M $\left(M = {}^{2B_0}/_{\mu_0}\right)$ is the magnetisation of the magnets and V $\left(V = {}^{m}/_{M}\right)$ is the volume of the magnet. The effective magnetic dipole is represented by m. R_{out} and R_{in} are the outside and inside diameters of the ring magnets. These formulations are useful for simple configurations but do not work outside the ideal conditions. Therefore, numerical and experimental methods provide a more effective means to determine the magnetic forces between magnets.

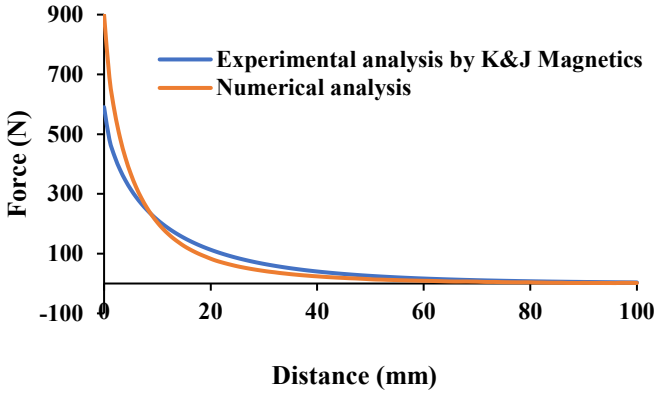

(a)

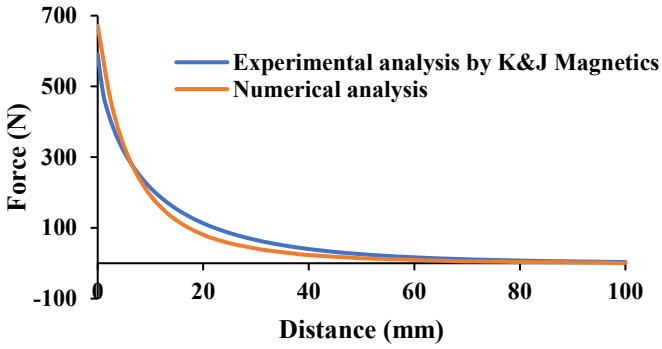

(b)

Figure 3.33: Magnetic force (a) Attractive force (b) Repulsive force

The magnetic forces can be estimated by ANSYS Maxwell and compared with experimental analysis such as those cases measured by K&J Magnetics (https://www.kjmagnetics.com/), as shown in Figure 3.33. The magnetic attractive force is shown to be higher than the magnetic repulsive force. To compute the virtual force in ANSYS Maxwell the system uses the principle of virtual work. The equation of the force for the displacement, s, can be expressed as,

$$F = \frac{dW(s,i)}{ds}\Big|_{i=Constant} = \frac{\partial}{\partial s}\left[\int_V \left(\int_0^H B.dH\right) dV\right] \tag{3.18}$$

where W (s,i) is the magnetic co-energy of the system which is dependent on B and H of the magnets and the current (i) is held constant.

3.6 Magnetic Restoring Forces

Figure 3.34 presents a schematic diagram of a magnetic system where the central floating magnet is moving due to the externally applied force where the top and bottom magnets are fixed. All three magnets are of the ring design and their size and shape (diameter and height) are the same. In this magnetic system, the magnetic poles of each magnet are oriented to repel the middle magnet so that the middle magnet is suspended with the nonlinear restoring force.

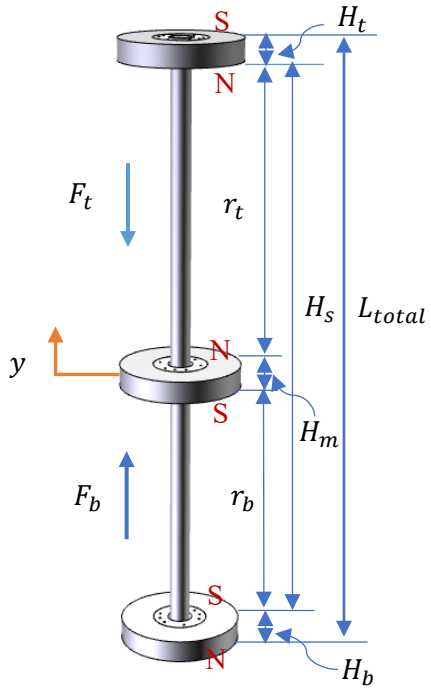

Figure 3.34: Magnetic system where the middle magnet is floating

The nonlinear behaviour of the system allows the linear response to be modified by simply varying the position between the top and bottom magnets. The magnetic force between the top fixed magnet and middle floating magnet can be written as (Liu et al., 2014),

$$F_t = \frac{\mu_0 Q_t Q_m}{4\pi {r_t}^2} \tag{3.19}$$

where r_t is the distance between the top and middle magnet poles. Q_t, Q_b and Q_m are the magnetic field intensity ($Q = MA$) of the top, bottom, and middle magnet, respectively. The magnetisation of the magnet is denoted by M and the surface area of the magnetic poles is represented by A. Similarly, the equation 3.19 can be rewritten for the floating middle magnet and bottom fixed magnet as,

$$F_b = \frac{\mu_0 Q_b Q_m}{4\pi {r_b}^2} \tag{3.20}$$

where r_b is the distance between the bottom and middle magnet poles. For the case of in-plane movement, the expression for r_t and r_b can be written as,

$$r_b = r_t = \frac{L_{total} - (H_t + H_m + H_b)}{2} \tag{3.21a}$$

$$r_t = H_s - (r_b + H_m) \tag{3.21b}$$

where L_{total} is the total length of the system, H_t, H_m and H_b are the height of the top, middle and bottom magnets, respectively. The distance between top and bottom magnet is represent by H_s. As the moving middle magnet is represented by the distance y as presented in Figure 3.34, the resultant magnetic force or magnetic spring restoring force (F_{res}) applied to the middle moving magnet can be calculated as,

$$F_{res} = F_t - F_b = \frac{\mu_0 Q_m}{4\pi}\left(\frac{Q_t}{(r_t - y(t))^2} - \frac{Q_b}{(r_b + y(t))^2}\right) \tag{3.22}$$

Magnetic spring's restoring forces can be calibrated from the calculation of the restoring force and the separation distance of the middle magnet (r_t, r_b) from the top and bottom magnet. Equation 3.22 can be expressed by the Taylor series at equilibrium points as,

$$F_{res} = \frac{\mu_0 Q_m Q_{t=b}}{4\pi}\left(\frac{2}{(r_t - y(t))^3}y + \frac{4}{(r_t - y(t))^5}y^3 + \frac{2}{(r_b + y(t))^3}y + \frac{4}{(r_b + y(t))^5}y^3\right) \tag{3.23}$$

Considering the separation distance of the middle magnet from the bottom magnet and top magnet are the same ($r_t = r_b = r$) then the equation 3.23 can be written as,

$$F_{res} = \frac{\mu_0 Q_m Q_{t=b}}{4\pi}\left(\frac{2}{(r-y(t))^3}y + \frac{4}{(r-y(t))^5}y^3 + \frac{2}{(r+y(t))^3}y + \frac{4}{(r+y(t))^5}y^3\right) \quad (3.24)$$

Considering $y(t) = 0$ at the equilibrium position then equation 3.24 can be stated as,

$$F_{res} = \frac{\mu_0 Q_m Q_{t=b}}{4\pi}\left(\left(\frac{2}{r^3}y + \frac{4}{r^5}y^3\right) + \frac{2}{r^3}y + \frac{4}{r^5}y^3\right) \quad (3.25a)$$

$$F_{res} = \frac{\mu_0 Q_m Q_{t=b}}{\pi r^3}y + \frac{2\mu_0 Q_m Q_{t=b}}{\pi r^5}y^3 \quad (3.25b)$$

For simplification, the constants can be stated as,

$$k_1 = \frac{\mu_0 Q_m Q_{t=b}}{\pi r^3} \quad (3.26a)$$

$$k_3 = \frac{2\mu_0 Q_m Q_{t=b}}{\pi r^5} \quad (3.26b)$$

If the separation distances of the middle magnet ($r_t = r_b$) from the top and bottom magnet are the same then equation 3.25b can be expressed by a Taylor series as,

$$F_{res} = k_1 y + k_3 y^3 \quad (3.27)$$

where k_1 is the linear constant and k_3 is the non-linear constant. Moreover, the equation 3.27 can be expressed by 5th order Taylor series as,

$$F_{res} = k_1 y + k_3 y^3 + k_5 y^5 \quad (3.28)$$

where k_1 is the linear constant k_3 and k_5 are the non-linear constant, respectively. The theoretical and simulated (ANSYS MAXWELL) magnetic force for different positions of the floating magnet has been presented in Figure 3.35 and Figure 3.36, respectively.

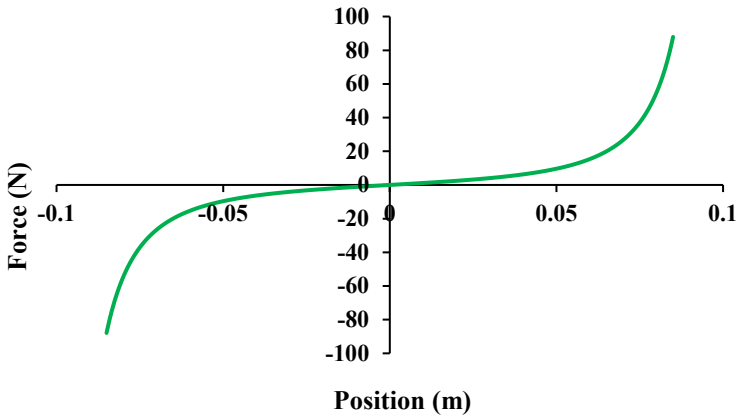

Figure 3.35: Theoretical force displacement curve

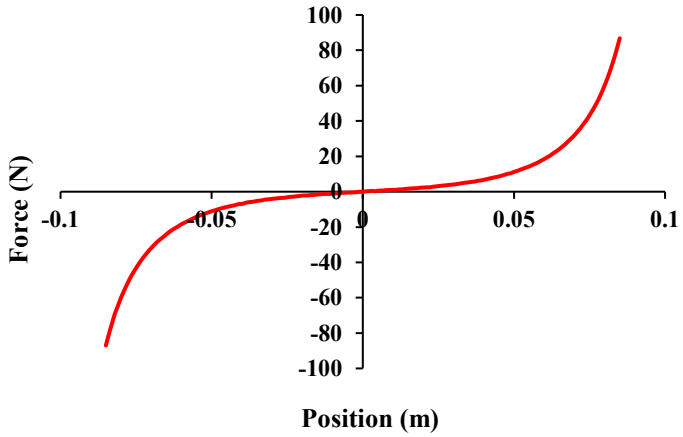

Figure 3.36: Simulation force displacement curve

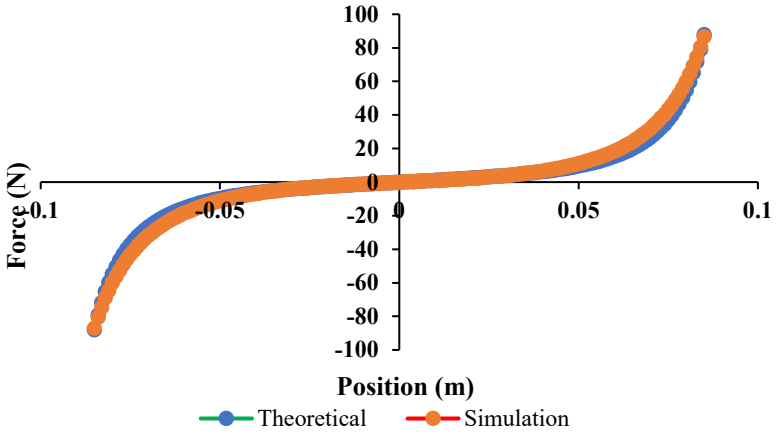

Figure 3.37: Comparison of magnetic restoring force (measured by ANSYS MAXWELL and theoretically)

From Figure 3.35 and Figure 3.36, when the middle/floating magnet moves from the equilibrium position towards either the top or bottom magnets, the magnetic force increases. Since different positions of the floating magnet create different magnitudes of the magnetic forces, it can be concluded that changes in the floating magnet position will change the stiffness and resonance of the system. The simulated magnetic force analysis of the system has been validated with the theoretical analysis as shown in Figure 3.37.

3.7 Electromagnetic Theory

As stated by Faraday's law, the change of the magnetic environment of the coils creates an induced voltage or emf (electromotive force) in the coil. By exciting the magnets or coils the change of magnetic field can be created. The magnet and coil arrangement are as shown in Figure 3.38.

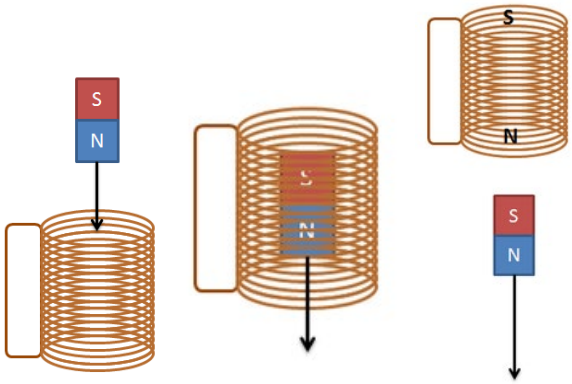

Figure 3.38: Magnet and coil

The induced voltage inside the coil can be written as,

$$V = -\frac{Nd\Phi}{dt} \qquad (3.29)$$

Here, the symbols V and Φ represent the induced voltage (V) and the magnetic flux, respectively. The coil turn number is denoted by N and the time is represented by t. If the wire length is l to complete the circuit through the magnetic flux density, then the force of the conductor can be stated as,

$$F = BIl \qquad (3.30)$$

Work done because of the force if the magnet moves a distance ΔS can then be written as,

$$W = F\Delta S \tag{3.31}$$

The charge transferred along the coil in this time can be expressed as,

$$W = BIl\Delta S \tag{3.32}$$

$$Q = I\Delta t \tag{3.33}$$

Therefore, the induced voltage or emf in the coil caused by the moving magnet can be written as,

$$V = \frac{W}{Q} = \frac{BIl\Delta S}{I\Delta t} = \frac{Bl\Delta S}{\Delta t} \tag{3.34}$$

$$V = Blv \tag{3.35}$$

where v is the velocity of the magnet. Equation 3.35 shows that the maximum power can be generated from an electromagnetic system by increasing the magnetic flux density, velocity of the magnet and total length of the coil. Proper coil selection is also an important factor for the electromagnetic system design because the diameter of the tube and the number of coil turns are used to calculate the total length of the coil. The coil terminals can be connected to load resistance, R_{Load}, to allow the current to flow in the coil and in this way, the power can be extracted from the linear generator. The interaction between the magnetic field generated by the induced current and field increase results in a force that opposes the motion. The electrical energy was generated from mechanical energy by acting against the electromagnetic force, F_{em}. The electromagnetic force, F_{em}, is related by the current and velocity as well as the electromagnetic damping, β_e, and the velocity. The relationship between electromagnetic force and electromagnetic damping can be stated as,

$$F_{em} = \beta_e \frac{dy}{dt} \tag{3.36}$$

Electromagnetic damping is the mechanical energy that transfers into electrical energy, and it is acting against the electromagnetic force. To obtain the maximum electrical power, the maximization of the electrical damping is an essential objective during a linear PM generator design. To maximise the electromagnetic damping, the study of design parameters is very important. The instantaneous power is related to the electromagnetic force and velocity which can be expressed as,

$$P_e = F_{em}(t)\frac{dy(t)}{dt} \tag{3.37}$$

This instantaneous power is decreased in the coil and load impedance. Equating the power decrease in the coil and load to that found from the electromagnetic force can be expressed as,

$$F_{em}\frac{dy}{dt} = \frac{V^2}{R_{Load} + R_i + j\omega L} \tag{3.38}$$

Here the load and coil resistances are represented by R_{Load} and R_i, respectively, and the coil inductance is denoted by L. Moreover, equation 3.38 can be expressed in terms of electromagnetic damping, flux linkage gradient and velocity as,

$$\beta_e = \frac{1}{R_{Load} + R_i + j\omega L}\left(\frac{d\Phi}{dy}\right)^2 \tag{3.39}$$

According to this equation, the maximum electromagnetic damping can be achieved by maximising the flux linkage gradient and minimising the coil impedance. The actual magnet, arrangement of the magnets, number of turns for the coil and area are very important to determine the flux linkage gradient. The coil impedance is dependent on the coil resistance. Moreover, the coil resistance's magnitude is dependant on the number of turns and technology of the coil such as wire winding. Moreover, the inductance, L, of the coil can be calculated as,

$$L = \pi\mu_0\mu_r\left(\frac{N^2{D_0}^2}{4h}\right) \tag{3.40}$$

Here the permeability of the coil is μ_r. The unit of the inductance is Henry's (H). Therefore, the characteristics of the coil design are very important in the electromagnetic theory as discussed in the following section. Consider a mass-spring system as shown in Figure 3.39 where an external force is applied to the magnet. The mass of the magnet (oscillator) is M which is suspended by spring k and the relative displacement of the magnet is y and the relative velocity and acceleration of the magnet are $\dot{y}$ and $\ddot{y}$, respectively. The magnetic flux density of the magnet in the radial direction is B_x and the total length of the coil is l. $\alpha(\alpha = NBl)$ is the electromagnetic coupling coefficient and I is the current. The dynamic equation of the motion of the system will be written as,

$$M\frac{d^2y}{dt^2} + \beta\frac{dy}{dt} + ky + \alpha I = F_b Sin(\omega t) \quad (3.41)$$

$$R_i I + L\frac{dI}{dt} = \alpha\frac{dy}{dt} \quad (3.42)$$

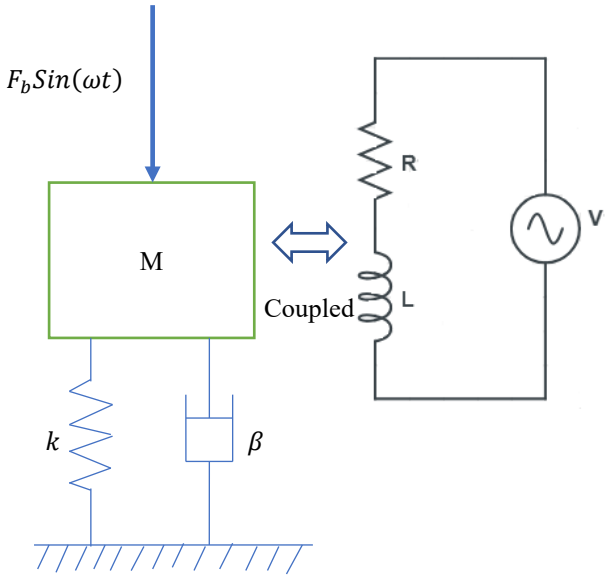

Figure 3.39: Simple energy harvester model based on linear oscillator system

Consider a nonlinear system where the middle magnet can move, and the top and bottom magnets are fixed as displayed in Figure 3.40. When the external force is applied to the middle magnet, the movement up and down of the middle magnet creates an elastic restoring force of the magnetic spring. The mass of the magnet is M, k_1 is the linear spring constant and k_3 is the nonlinear spring constant of the system. The relative displacement of the middle magnet is y. The relative velocity and acceleration of the middle magnet are $\dot{y}$ and $\ddot{y}$, respectively. The dynamic equation of the motion of the system can be stated as,

$$M\frac{d^2y}{dt^2} + \beta\frac{dy}{dt} + k_1 y + k_3 y^3 + \alpha I = F_b Sin(\omega t) \quad (3.43)$$

$$R_i I + L\frac{dI}{dt} = \alpha\frac{dy}{dt} \quad (3.44)$$

In equations 3.42 and 3.44 the symbols L and R_i represent the inductance (H) and internal resistance (Ω) of the coil, respectively. In equation 3.41 and 3.43, β is the total damping coefficient of the system which is the sum ($\beta = \beta_m + \beta_e$) of the mechanical ($\beta_m$) and electrical ($\beta_e$) coefficient.

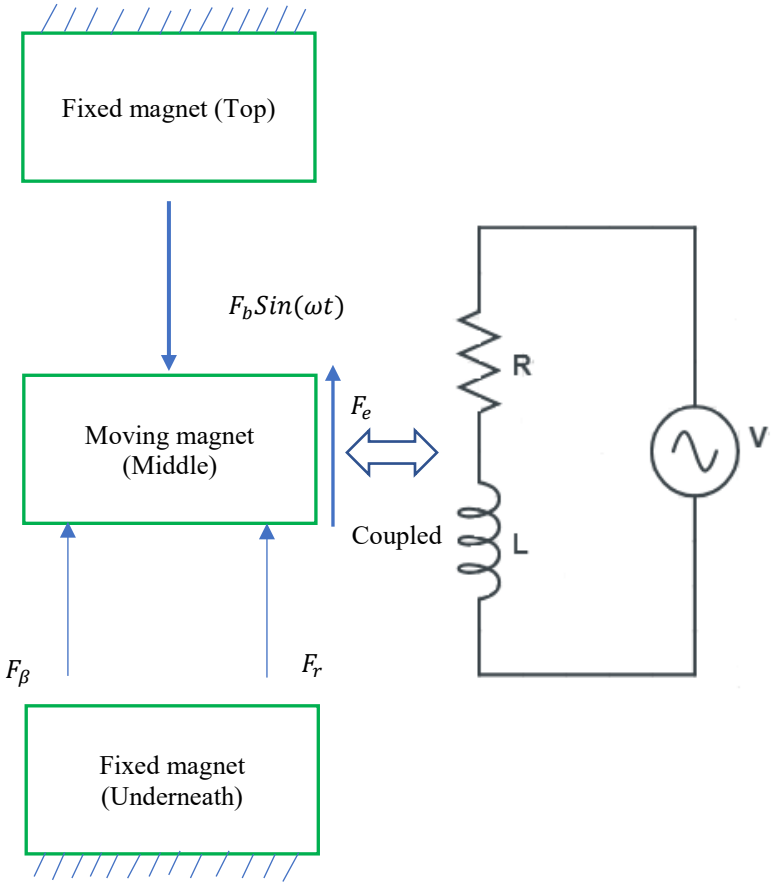

Figure 3.40: Simple energy harvester model based on nonlinear oscillator system

The electrical damping coefficient can be written as,

$$\beta_e = \frac{\alpha^2}{R_{in}} \tag{3.45}$$

If an external circuit with the then the resistance of the circuit R_{load} is added with the internal resistance, the equation can be written as,

$$\beta_e = \frac{\alpha^2}{R_{load} + R_{in}} \tag{3.46}$$

The generated electric power and loss from the system can be expressed as,

$$P = R_{load} I^2 \tag{3.47}$$

$$P_{loss} = R_{in} I^2 \tag{3.48}$$

The power factor of the electric circuit can be written as,

$$P_f = \frac{1 + R_r}{\sqrt{L_r^2 + (1 + R_r)^2}} \tag{3.49}$$

where $R_r = R_{load}/R_i$ is the resistance ratio and $L_r = \omega L/R_i$ is the impedance ratio.

3.8 Conclusion

In this chapter, the characteristics of the permanent magnet along with the governing analytical equations have been discussed and analysed by ANSYS Maxwell. The changes of radial magnetic flux density (B_x) outside the magnet have been analysed analytically and theoretically. The magnetic force and magnetic spring have been analysed as well. Moreover, the relevant electromagnetic theory has been discussed along with the governing equations. The most important conclusions, specifically related to this study, were that the theoretical and numerical studies of the magnet characterisation and its application in an electromagnetic system can be used to model the resulting energy harvesting system.

The contents of this chapter have been published in the IEEE Transactions on Magnetics, 2022. DOI: 10.1109/TMAG.2022.3180812

Chapter 4
Dynamic Behaviours of Magnetic Spring-based Nonlinear Oscillator Systems

The correct modelling of the magnetic flux density is a crucial part of predicting the magnetic restoring force as well as nonlinear responses of the magnetic spring. Analytical modelling of magnetic flux is superior to numerical modelling in terms of accuracy and processing cost, according to certain studies (Dos Santos et al., 2016). Analytical methods, on the other hand, can only deal with very simple geometries. In addition, the gravitational force affects the equilibrium position of the magnetic spring-based system due to its vertical arrangement. The magnetic restoring force as a function of the floating magnet's position has been estimated by determining the polynomial coefficients of a power series by curve fitting. Correct measurement of the magnetic restoring force is very important to identify the linear and nonlinear coefficients of the system. The numerical model, analytical model and experimental model have been used to measure the magnetic restoring force. Therefore, this chapter aims to investigate the magnetic properties and coefficients of the magnetic spring-based system with validation, including how the gravitational effect changes the equilibrium position and analysis of the dynamics of the magnetic spring.

4.1 Design Configuration of the Nonlinear Oscillator System

The basic architecture of the nonlinear oscillator comprises of three permanent ring magnets (axially magnetised through the height (13mm)) and a circular aluminium shaft. A plastic bush is used inside each magnet ring, between the magnet and the shaft, to keep the magnet straight and prevent flipping. The fixed magnets are attached to the end of the shaft, and their polarity is set in such a way that the repulsive force is created between the levitating magnet and the fixed magnets. The magnetic poles are oriented (SN-NS-SN) to repel each other. The height and width of the test rig (single degree of freedom system (SDFS)) are 300 mm and the height and diameter of the shaft are 550 mm and 12 mm, respectively. For the test rig design as presented in Figure 4.1, initially when the middle magnet is added to the setup prior to the addition of the top magnet, the distance between middle and bottom magnets is 104 mm. When the top magnet is added, the distance between the middle and bottom magnet is reduced to 79 mm due to the gravitational force, while the top magnet and the floating middle magnet are separated by 104 mm.

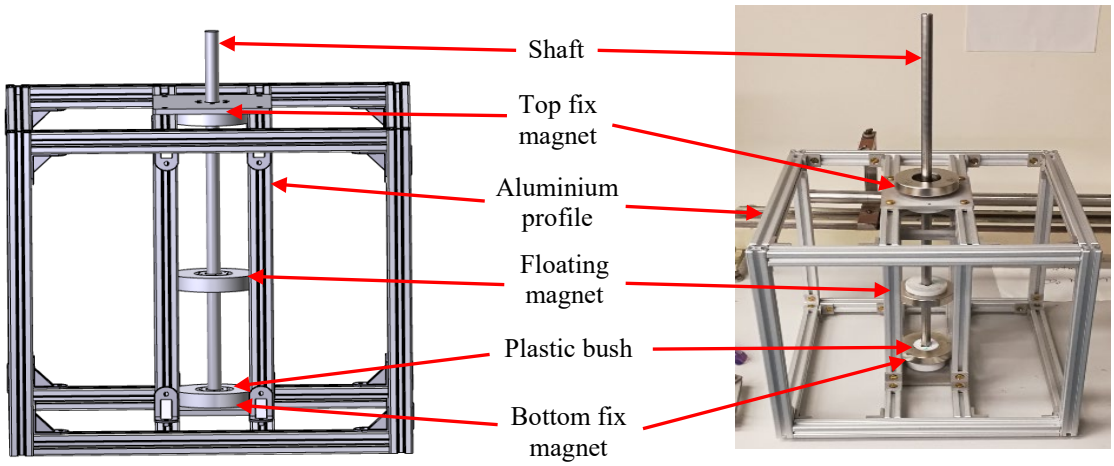

Figure 4.1: Test rig without winding coil

The floating magnet is connected to the servo motor pulley by a fishing line to create a sine wave. The displacement of the middle floating magnet is measured by the displacement sensor. At first, the magnetic properties and dynamics of the oscillator are investigated without a winding coil.

4.2 Investigation of the Magnetic Properties

Since the gravitational force affects the middle magnet by shifting it down from the centre of the top and bottom magnet, the distances between the 3 magnets in the test rig design change to 79 mm between the middle and bottom magnets and 104 mm between the middle and top magnets. The magnetic flux density on the magnet surface and the magnetisation direction are displayed in Figure 4.2. Figure 4.3 depicts the magnitude of the magnetic flux density. The distributed magnetic field passing through the air gap is simulated, as presented in Figure 4.4. The magnetic flux density is calculated for the system in the radial direction through the line *d*, which is 37mm from the magnet stack and chosen because it could be the coil location. To select the proper position of the winding coil the measurement of the magnetic flux density in the air gap must be considered. Due to symmetry, moving from $d = 0$ to either $d = 175mm\ or\ -175mm$ results in the equivalent movement of the vertical arrows, as seen in Figure 4.4. The measured magnetic flux density in the axial and radial directions are displayed in Figure 4.5.

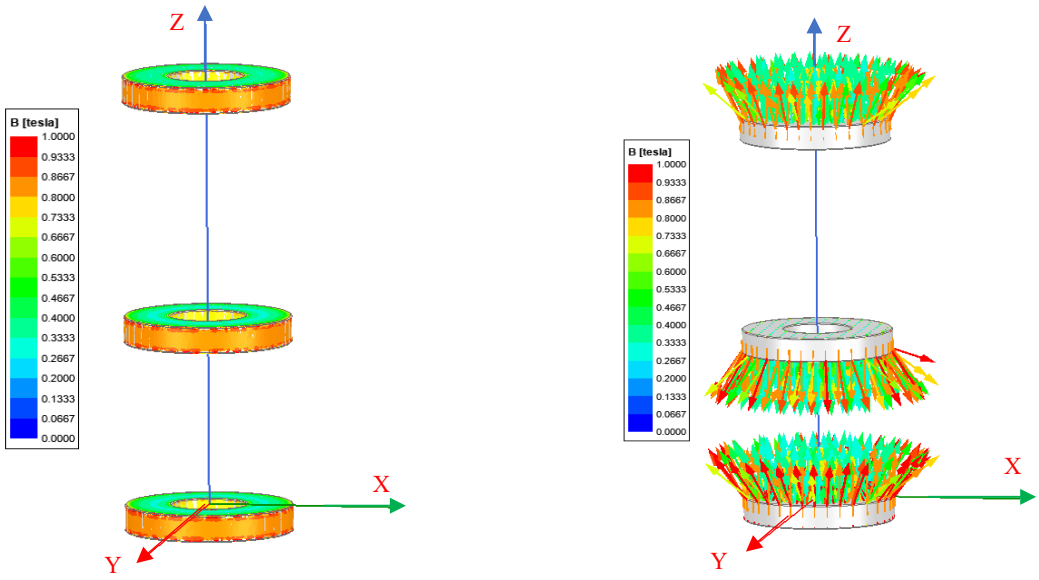

(a) (b)

Figure 4.2: (a) Magnetic flux density on the magnet surface and (b) Magnetisation direction

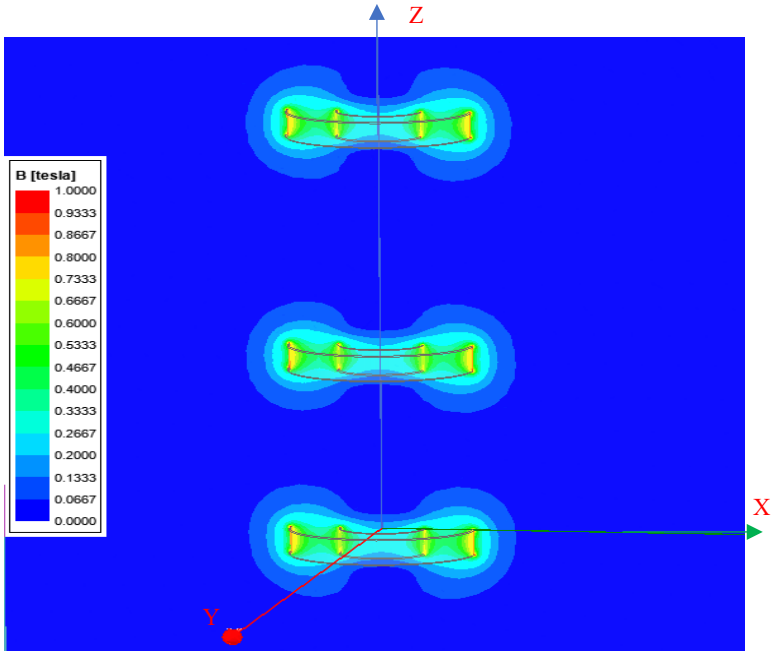

Figure 4.3: Magnetic flux density (Mag_B) when 3 magnets are facing same poles (SN-NS-SN)

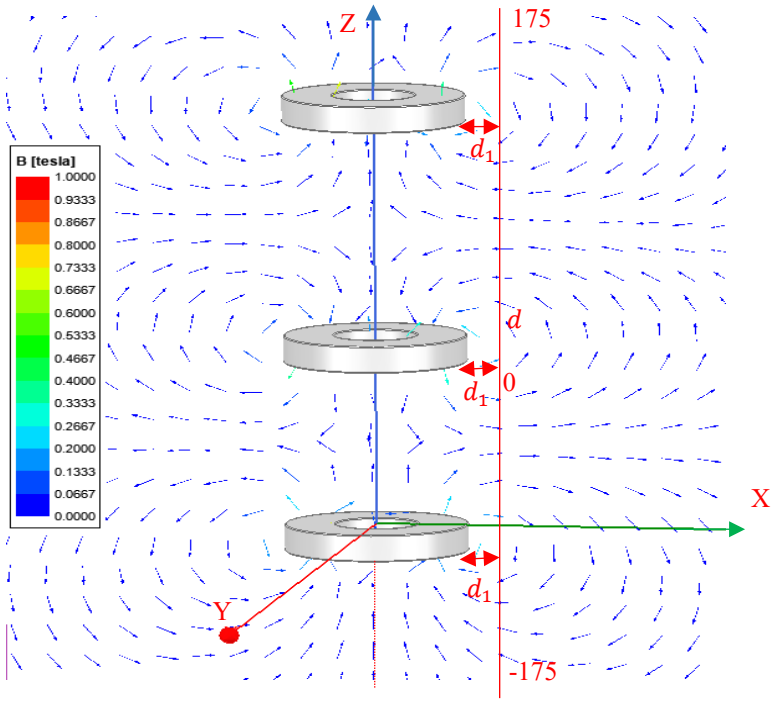

Figure 4.4: Magnetic flux density (B_Vector) in XZ plane

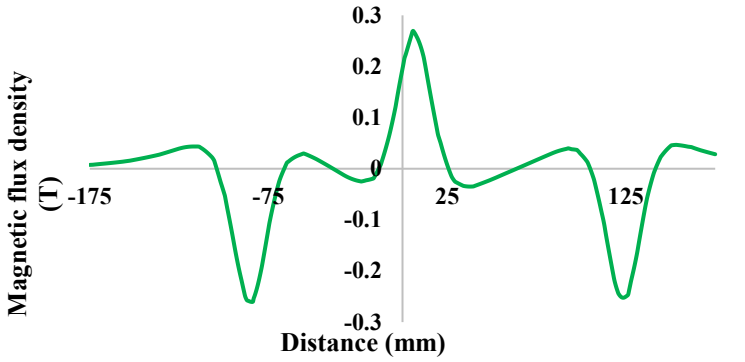

(a)

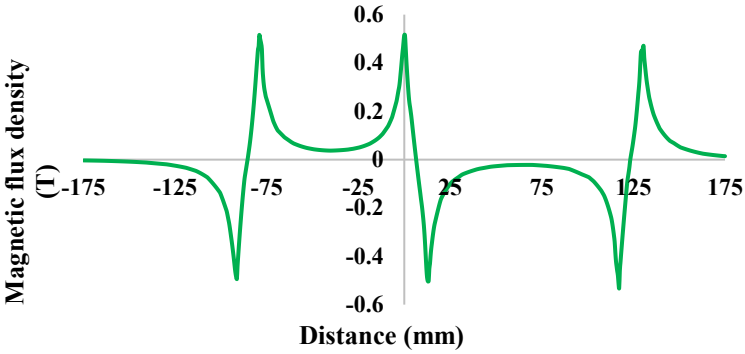

(b)

Figure 4.5: Magnetic flux density (a) axial direction, (b) radial direction

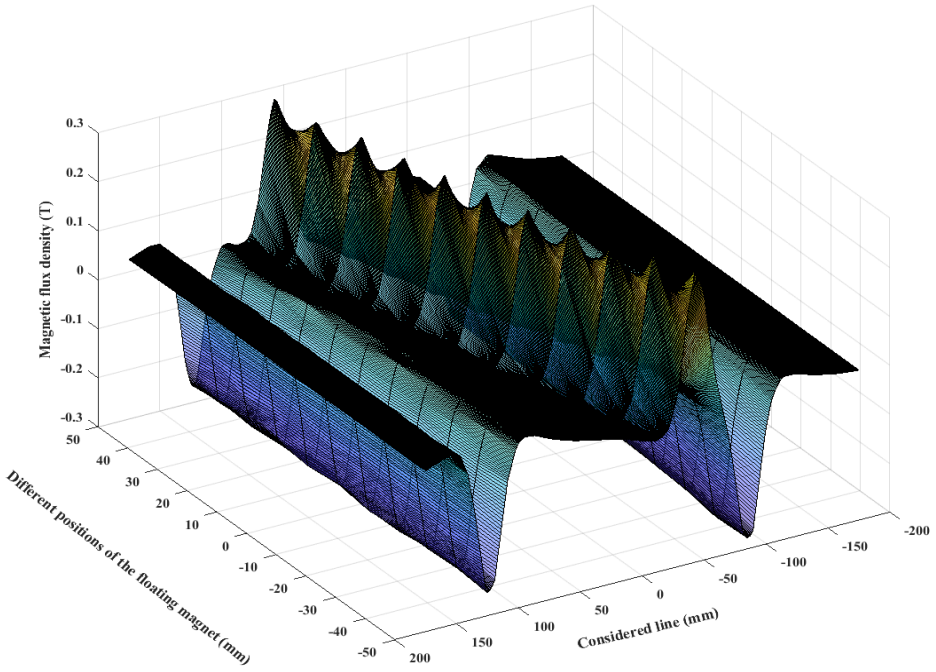

(a)

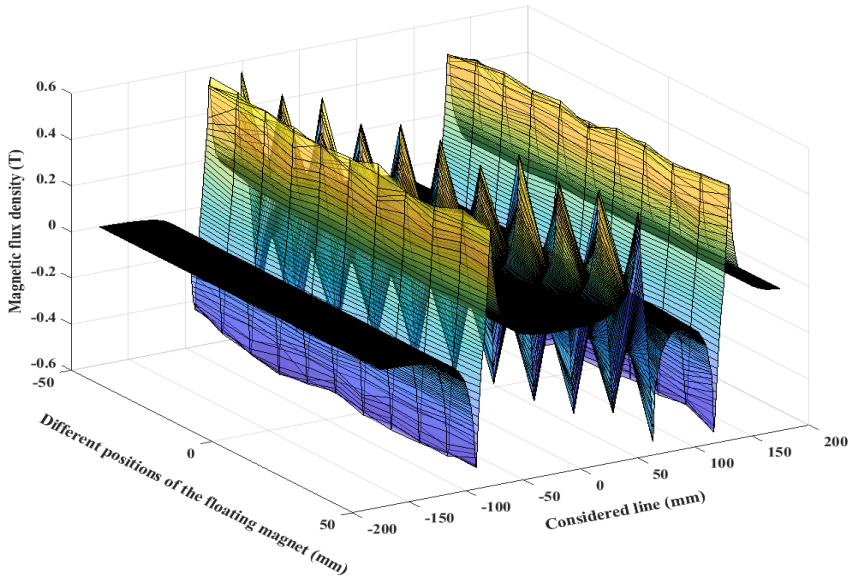

(b)

Figure 4.6: Magnetic flux density B_Vector (a) axial direction and (b) radial direction

If an external force is applied or the middle magnet is moved up and down vertically then the change of the average magnetic flux density is much higher than if they were kept stationary, as seen in Figure 4.6(a) and Figure 4.6(b). The repelling force between the impinging magnets is equivalent to

the effective magnetic spring's restoring force, and can cause the floating magnet to bounce. The vibration of the magnet creates the change of magnetic flux density which can be important for maximising the harvested power.

4.3 Magnetic Restoring Force Analysis of the Magnetic Spring-based Oscillator System

The magnetic force increases when the middle/floating magnet moves from the equilibrium position towards the top or bottom magnets. Different positions of the floating magnet create different magnitudes of the magnetic force and therefore it can be concluded that changes in the floating magnet position will change the stiffness and resonance of the system. The simulated magnetic force analysis of the system has been validated with the theoretical analysis. While analysing the linear and nonlinear stiffness of the system, it has been seen that their values change with the changing of the excitation/displacement of the floating magnet. When the shaft of the nonlinear oscillator is oriented vertically, gravity must be included in the force balance calculation, but it can be omitted in a horizontal system (Dallago et al., 2010). From the literature, it has been seen that many researchers did not consider the gravitational effect although their proposed systems were vertical (Mann & Sims, 2009). All these researchers assumed that the floating magnet's distances from the top and bottom magnets are the same. In reality, it is difficult and almost impossible to keep the floating magnet at the same distance from the two fixed end magnets (same size and shape as the floating magnet) with the vertical system. For the proposed nonlinear oscillator system, all magnets are placed with the vertical shaft which can be seen in Figure 4.1. The gravitational force shifted the equilibrium position from the expected equilibrium point and the distance between the middle and bottom magnets is 79 mm and the middle and top magnets is 104 mm, changing the behaviour of the magnetic restoring force curve. For the test rig setup equation 3.22 can be expressed by the Taylor series as,

$$F_{res} = \frac{\mu_0 Q_m Q_{t=b}}{2\pi}\left(\frac{1}{(r_t - y(t))^3} + \frac{1}{\left(r_b + y(t)\right)^3}\right)y + \frac{3\mu_0 Q_m Q_{t=b}}{4\pi}\left(\frac{1}{(r_t - y(t))^4} - \frac{1}{\left(r_b + y(t)\right)^4}\right)y^2 + \frac{\mu_0 Q_m Q_{t=b}}{\pi}\left(\frac{1}{(r_t - y(t))^5} + \frac{1}{(r_b + y(t))^5}\right)y^3 \quad (4.1)$$

If consider $y(t) = 0$ at the equilibrium position, the equation can be written as,

$$F_{res} = \frac{\mu_0 Q_m Q_{t=b}}{2\pi}\left(\frac{1}{(r_t)^3}+\frac{1}{(r_b)^3}\right)y + \frac{3\mu_0 Q_m Q_{t=b}}{4\pi}\left(\frac{1}{(r_t)^4}-\frac{1}{(r_b)^4}\right)y^2 + \frac{\mu_0 Q_m Q_{t=b}}{\pi}\left(\frac{1}{(r_t)^5}+\frac{1}{(r_b)^5}\right)y^3 \quad (4.2)$$

$$k_1 = \frac{\mu_0 Q_m Q_{t=b}}{2\pi}\left(\frac{1}{(r_t)^3}+\frac{1}{(r_b)^3}\right) \quad (4.3a)$$

$$k_2 = \frac{3\mu_0 Q_m Q_{t=b}}{4\pi}\left(\frac{1}{(r_t)^4}-\frac{1}{(r_b)^4}\right) \quad (4.3b)$$

$$k_3 = \frac{\mu_0 Q_m Q_{t=b}}{\pi}\left(\frac{1}{(r_t)^5}+\frac{1}{(r_b)^5}\right) \quad (4.3c)$$

For the test rig setup, equation 4.2 can be expressed by the Taylor series as,

$$F_{res} = k_1 y + k_2 y^2 + k_3 y^3 \quad (4.4)$$

where k_1 is the linear spring constant, and k_2 and k_3 are the nonlinear coefficients of the system. The magnetic restoring forces are calculated theoretically, numerically using ANSYS MAXWELL, and experimentally as presented in Figures 4.7, 4.8 and 4.9, respectively.

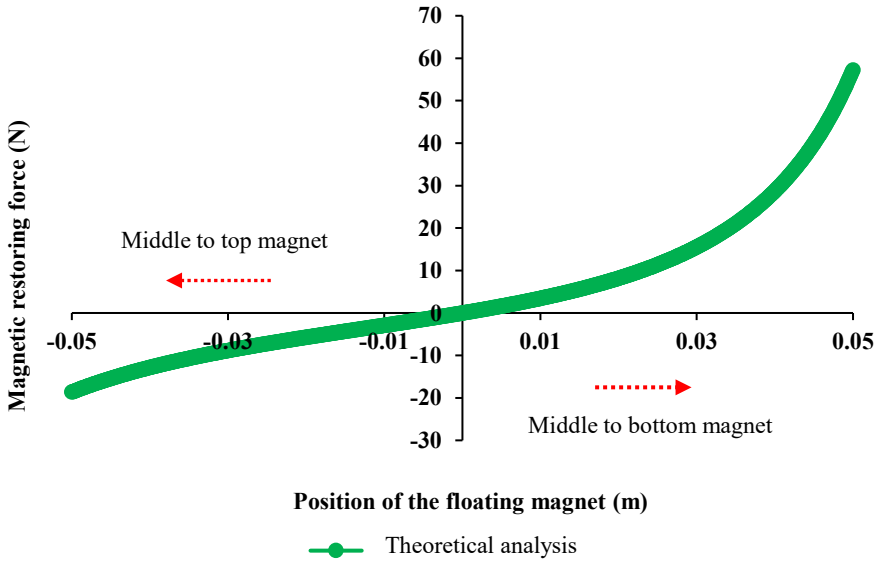

Figure 4.7: Magnetic restoring force (Theoretical analysis)

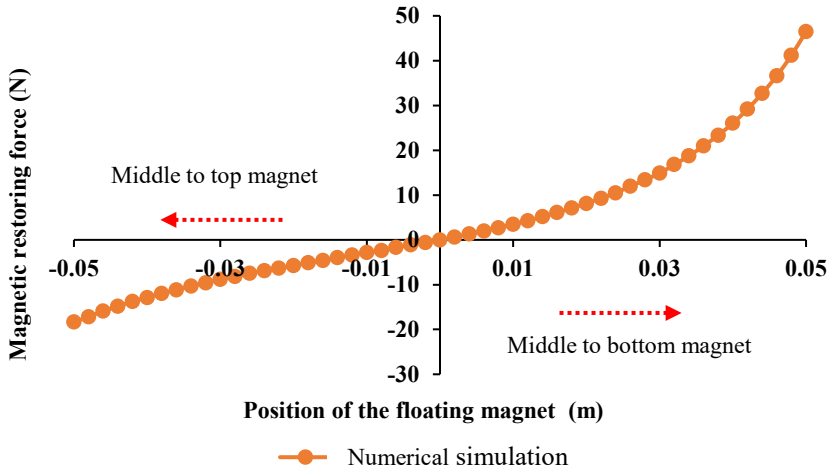

Figure 4.8: Magnetic restoring force (Numerical simulation)

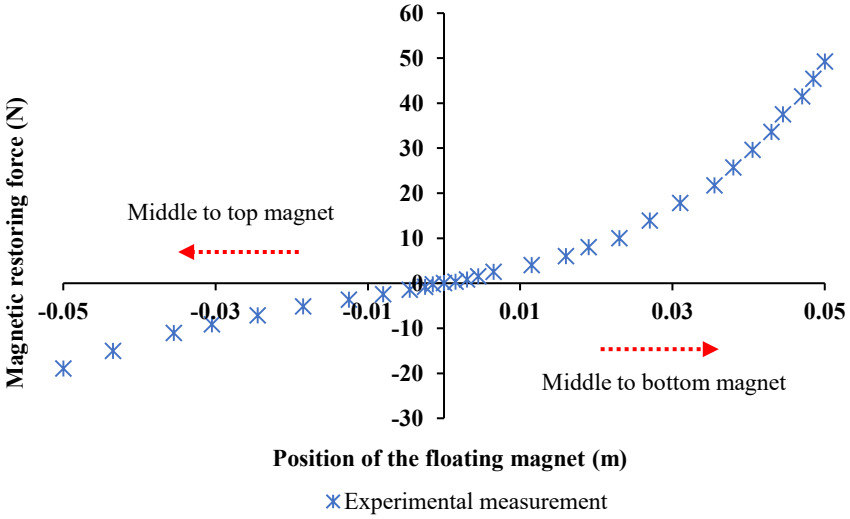

Figure 4.9: Magnetic restoring force (Experimental measurement)

Figure 4.10 shows the validation of the experimental, theoretical and numerical model. To calculate the magnetic restoring force experimentally, a fishing line was added with the middle magnet holder (plastic bush) to tie a hanger. Known masses were added with the hanger and the displacement of the middle magnet from the equilibrium point was measured. This step was repeated many times until a 50mm displacement of the middle magnet was achieved and the known masses on the hanger were incrementally increased with each repetition of these steps. From Figure 4.10 it can be seen that the magnetic restoring force is higher between the bottom and middle magnets than the restoring force between the top to middle magnets due to the gravitation effect. The experimentally measured magnetic restoring forces are almost similar to the numerical and theoretical measured values.

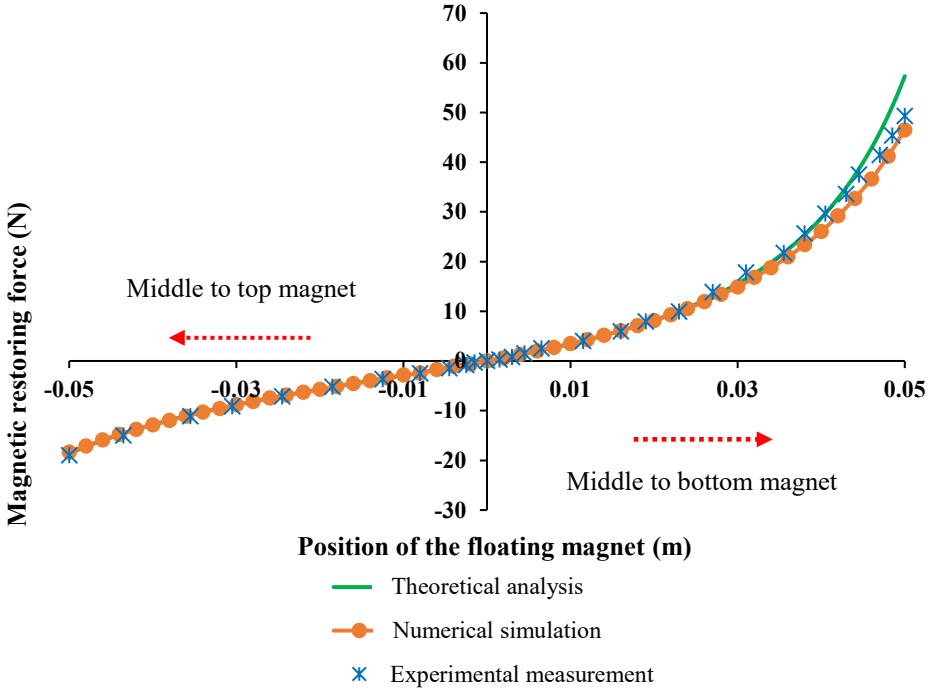

Figure 4.10: Comparison of magnetic restoring force

The literature shows that not a single researcher has validated the theoretical and numerical model with the experimental model. Instead, researchers used either the numerical model (Saha et al., 2008) (Dallago et al., 2010), analytical model (Foisal et al., 2012; Liu et al., 2014) or experimental model (Kecik et al., 2017; Mann & Sims, 2009; Masoumi & Wang, 2016; W. Wang et al., 2017). Based on the literature study, this novel validation graph (Figure 4.10) will bring more understanding of the magnetic spring-based oscillator system.

4.4 Coefficient Analysis of the Magnetic Restoring Force

Although some research articles have been published in the literature to understand the dynamics of the magnetic levitation based nonlinear oscillator system, the dynamics of the system are still not clear. Some researchers considered the system to be linear for small excitations of the floating magnet and used the linear equation. Other researchers considered the system to be nonlinear and used both the cubic (3^{rd} order) and quintic (5^{th} order) polynomial curve fit to measure the magnetic restoring force between the floating magnet and the two fixed end magnets. The aim of this section is to determine the coefficient of the magnetic restoring force of the proposed nonlinear oscillator. Magnetic spring restoring forces can be calibrated for the test rig setup from the calculation of the

restoring force when the separation distance of the middle magnet (r_t, r_b) from the top and bottom magnet are not the same. Equation 4.4 can be expressed by higher terms in the Taylor series as,

$$F_{res} = k_1 y + k_2 y^2 + k_3 y^3 + k_4 y^4 + k_5 y^5 \qquad (4.5)$$

where k_1 is the linear spring constant and k_2, k_3, k_4 and k_5 are the nonlinear coefficients of the system. If r_t and r_b are the same, then all nonlinear coefficients with even powers in equation 4.2 and 4.3 will be zero. The linear and nonlinear stiffness can be calculated from the magnetic restoring force curves are shown in Figure 4.7, Figure 4.8 and Figure 4.9. The theoretical, numerical and experimental measurements for the proposed test rig's restoring forces are used to measure and compare the linear and nonlinear stiffness of the oscillator system. The values of k_1, k_2, k_3, k_4 and k_5 can be measured from the least-squares curve fitting of the graph. According to the literature in most publications, a cubic polynomial was utilised to describe the magnetic restoring force (Saravia et al., 2017). In certain cases when the displacements of the floating magnet are small (near the equilibrium point) the cubic (3rd order) polynomial may not be a good choice since it could lead to instabilities. This problem can be improved if the 3rd order polynomial fit is completed without data collection when the magnet is near to the equilibrium position. However, this prediction for large displacements of the floating magnet is then significantly worsened. Moreover, the polynomial of fifth or higher order can be chosen to represent the magnetic restoring force. The polynomial of cubic and fifth-order are selected to represent the magnetic restoring force as presented in Figure 4.11 (magnetic restoring force vs displacement of the middle magnet).

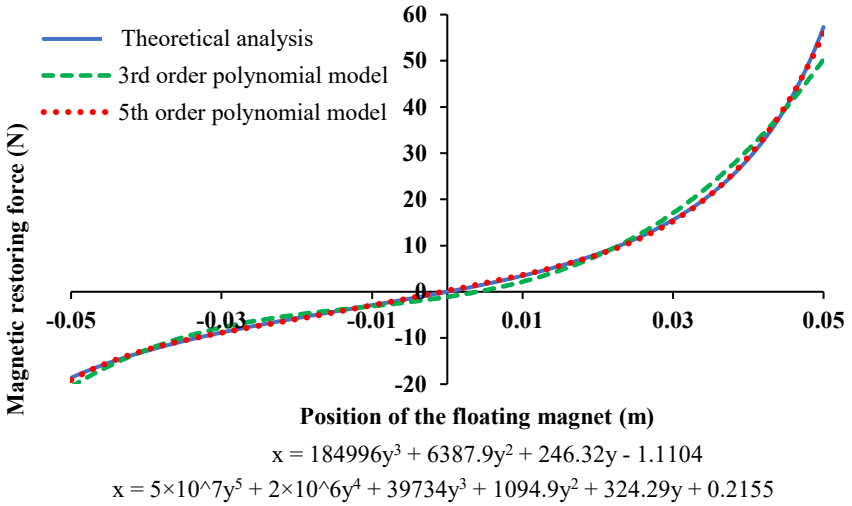

(a)

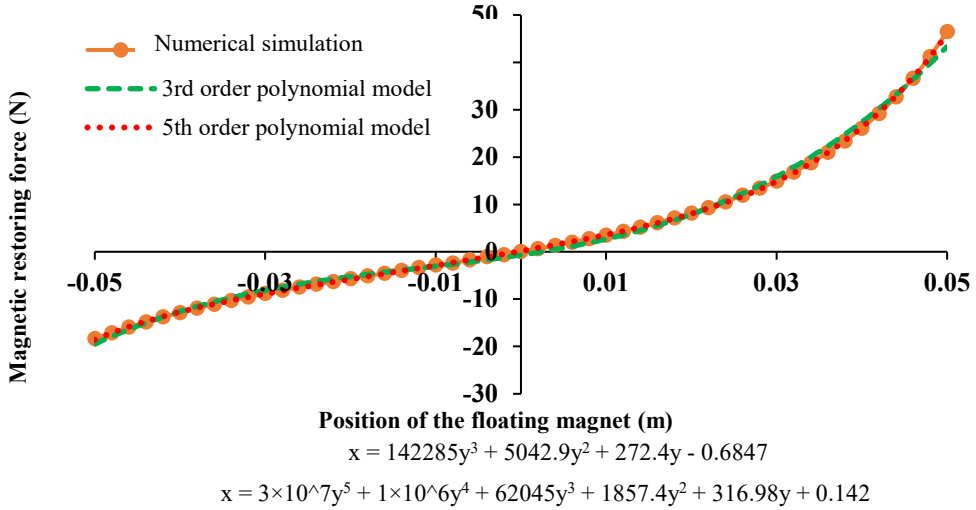

$x = 142285y^3 + 5042.9y^2 + 272.4y - 0.6847$

$x = 3\times10^{7}y^5 + 1\times10^{6}y^4 + 62045y^3 + 1857.4y^2 + 316.98y + 0.142$

(b)

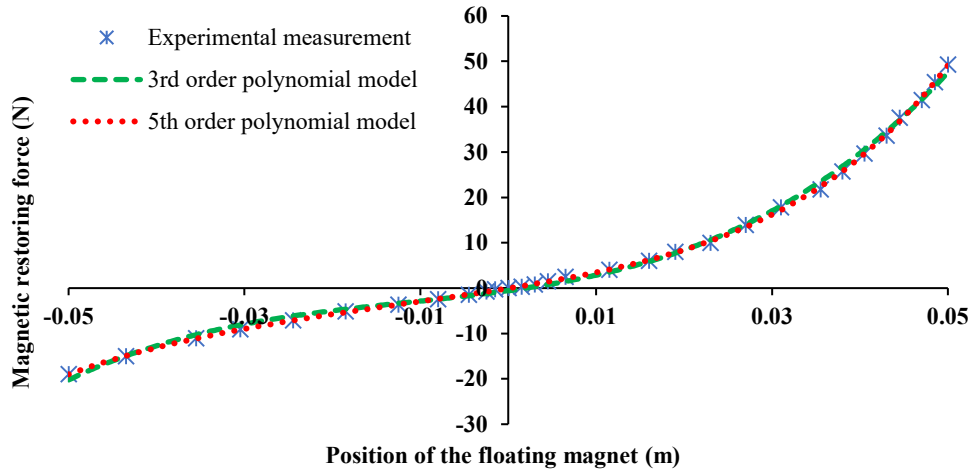

$x = 163159y^3 + 5680.4y^2 + 269.31y - 0.5672$

$x = 2\times10^{7}y^5 + 1\times10^{6}y^4 + 107874y^3 + 2925.5y^2 + 309.43y - 0.0351$

(c)

Figure 4.11: Magnetic restoring force for 50mm excitation (3rd order and 5th order polynomial model) (a) Theoretical analysis, (b) Numerical simulation and (c) Experimental measurement

Figure 4.11 shows that the 5th order (quintic) polynomial fits the data better than the 3rd order (cubic) polynomial. The magnetic restoring force graph for different excitation ranges have been presented in Appendix A. It is worth noting that the proposed system's coefficients are greatly dependent on the distance between permanent magnets (Kecik et al., 2017). As a result, a change in this distance results in a significant change in this characteristic. B.P. Mann and N.D. Sims concluded two important statements: (1) changes of the position of the floating magnet, will change the linear stiffness and (2) the nonlinear term is independent of the position of the floating magnet (Mann & Sims, 2009). By

changing the position of the floating magnet, the statements concluded by Mann and Sims are investigated as presented in the following Table 4.1.

Table 4.1: Coefficients of the magnetic spring-based oscillator system

Excitation (mm)	Polynomial model		Coefficients				
			k_1 (N/m)	k_2 (N/m^2)	k_3 (N/m^3)	k_4 (N/m^4)	k_5 (N/m^5)
-5 to 5	3rd order	Theoretical	309.79	2745.5	87022	---	---
		Numerical	306.09	5784	-87522		
		Experimental	307.35	819.63	1×10^6	---	---
	5th order	Theoretical	309.8	2719.6	86479	1×10^6	2×10^7
		Numerical	317.16	8557.1	-2×10^6	-1×10^8	7×10^{10}
		Experimental	309.69	-2590.6	874377	1×10^8	1×10^{10}
-10 to 10	3rd order	Theoretical	309.75	2805.8	88656	---	---
		Numerical	305.1	2816.2	133906	---	---
		Experimental	304.28	6447.5	814030	---	---
	5th order	Theoretical	309.8	2725.9	86451	922478	2×10^7
		Numerical	295.11	2330.8	603144	5×10^6	-4×10^9
		Experimental	308.93	2512	592100	4×10^7	2×10^9
-15 to 15	3rd order	Theoretical	309.55	2907.6	91483	---	---
		Numerical	306.22	2907.2	104197	---	---
		Experimental	308.68	2676.3	91634	---	---
	5th order	Theoretical	309.8	2722.2	86325	954584	2×10^7
		Numerical	307.1	2998.2	87525	-414164	6×10^7
		Experimental	311.02	510.13	64803	9×10^6	3×10^7
-20 to 20	3rd order	Theoretical	308.98	3059.2	95681	---	---
		Numerical	306.53	2964.2	103000	---	---
		Experimental	305.95	3484.6	118276	---	---
	5th order	Theoretical	309.82	2709.7	85962	1×10^6	2×10^7
		Numerical	305.5	2868.1	114074	256725	-2×10^7
		Experimental	311.29	186.47	74024	9×10^6	9×10^7
-25 to 25	3rd order	Theoretical	307.68	3271.8	101542	---	---
		Numerical	308.05	3118.6	96128	---	---
		Experimental	307.13	3629	119073	---	---
	5th order	Theoretical	309.89	2680.1	85118	1×10^6	2×10^7

		Numerical	305.93	2655.6	110903	816684	-2×10^7
		Experimental	311.99	2601.6	69187	2×10^6	7×10^7
-30 to 30	3rd order	Theoretical	305.06	3562.8	109513	---	---
		Numerical	307.33	3302.2	97937		
		Experimental	292.08	4254.8	150648	---	---
	5th order	Theoretical	310.12	2618.9	83374	1×10^6	3×10^7
		Numerical	307.92	2718.9	95062	711304	3×10^6
		Experimental	312.11	2264.3	66356	2×10^6	7×10^7
-35 to 35	3rd order	Theoretical	300.12	3959.4	120294	---	---
		Numerical	303.11	3599.8	106771	---	---
		Experimental	302.95	4204.3	128199	---	---
	5th order	Theoretical	310.73	2500.4	79999	1×10^6	3×10^7
		Numerical	310.56	2587.4	80116	890525	2×10^7
		Experimental	311.04	2965.8	106608	1×10^6	1×10^7
-40 to 40	3rd order	Theoretical	291.16	4504.8	134997	---	---
		Numerical	298.04	3909.8	114646	---	---
		Experimental	293.98	4671.7	142945	---	---
	5th order	Theoretical	312.23	2278.8	73676	2×10^6	3×10^7
		Numerical	310.87	2489.4	78857	988332	2×10^7
		Experimental	310.04	3102.3	106234	1×10^6	2×10^7
-45 to 45	3rd order	Theoretical	275.14	5271.7	155475	---	---
		Numerical	287.52	4455	127539	---	---
		Experimental	283.72	5205.1	152028	---	---
	5th order	Theoretical	315.83	1867.7	61921	2×10^6	4×10^7
		Numerical	313.27	2211.8	71328	1×10^6	2×10^7
		Experimental	314.25	2916.7	94869	1×10^6	2×10^7
-50 to 50	3rd order	Theoretical	246.32	6387.9	184996	---	---
		Numerical	272.4	5042.9	142285	---	---
		Experimental	269.31	5680.4	163159	---	---
	5th order	Theoretical	324.29	1094.9	39734	2×10^6	5×10^7
		Numerical	316.98	1857.4	62045	1×10^6	3×10^7
		Experimental	309.43	2925.5	107874	1×10^6	2×10^7

From Table 4.1 it can be seen that a 3rd order polynomial model is suitable for small excitation ranges. For small excitation ranges such as 5 mm, 10 mm and 15 mm the linear stiffnesses for both 3rd and 5th order polynomial models are almost similar. The 5th order polynomial model is more suitable for high excitation ranges as seen in Table 4.1. Moreover, the linear stiffness changes with changing the

excitation ranges. Moreover, the measured coefficients of the proposed nonlinear oscillator for 3rd and 5th order polynomials curve fitting are presented in Table 4.1. Table 4.1 shows that the coefficients of the nonlinear oscillator change as the spacing of the floating magnet changes. The better polynomial fit is obtained by choosing the polynomial with the least Root Mean Squared Error (RMSE) values, as presented in Table 4.2. The linear stiffnesses and natural frequencies of the theoretical, numerical and experimental measurements have been presented in Figure 4.12 and Figure 4.13, respectively for 3rd order polynomial model curve fitting and 5th order polynomial model curve fitting.

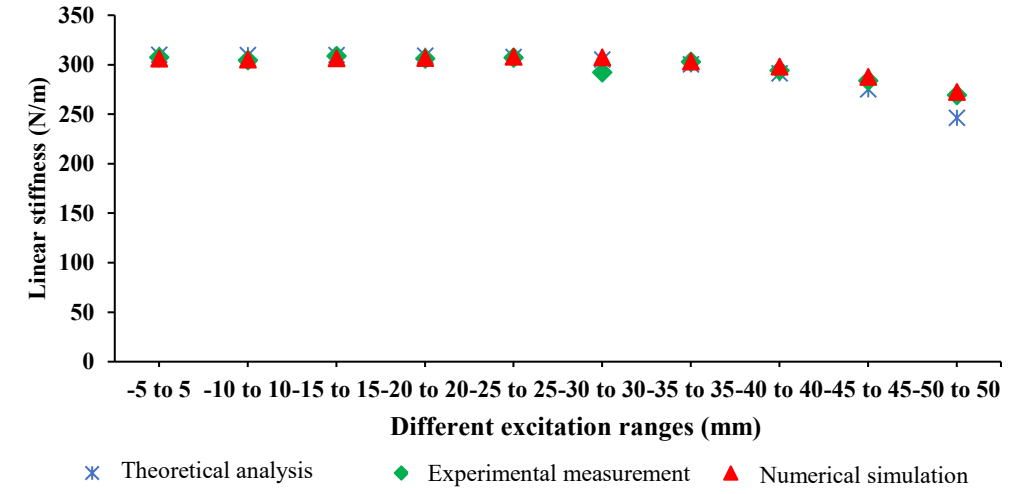

(a)

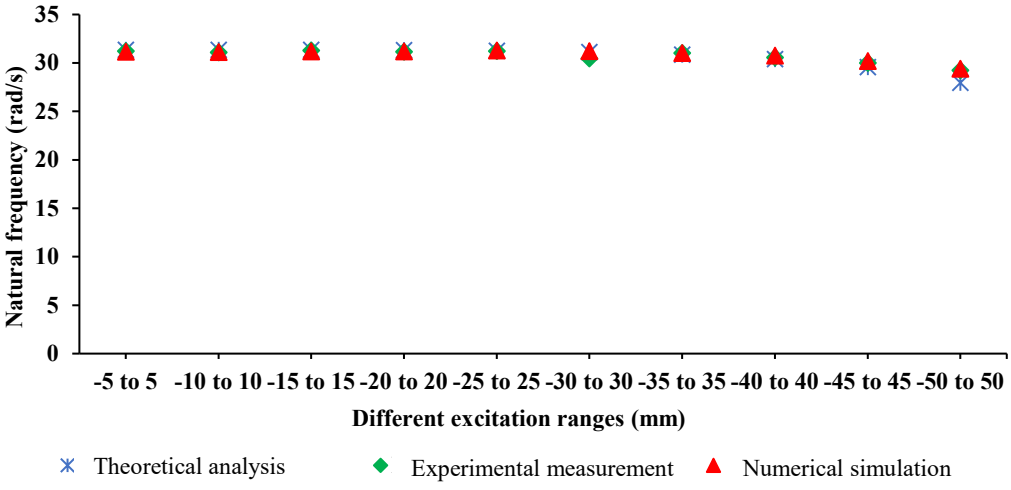

(b)

Figure 4.12: 3rd order polynomial curve fitting (a) linear stiffness and (b) natural frequency

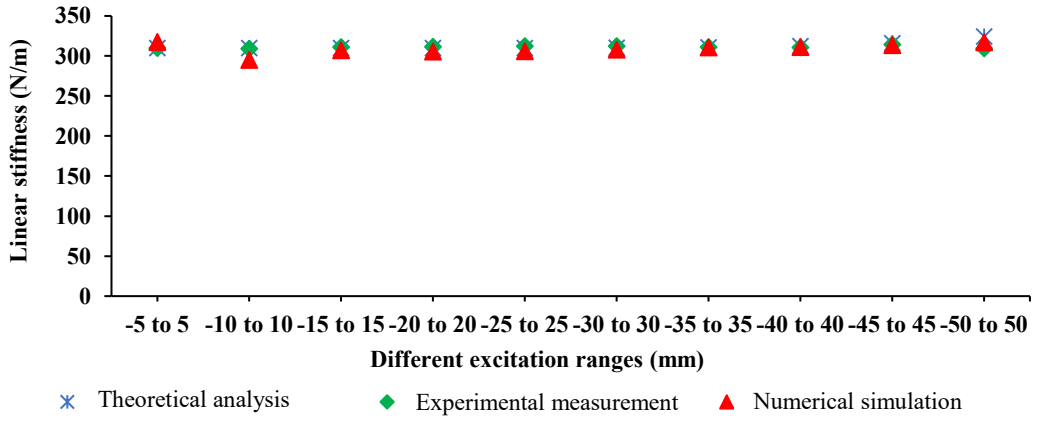

(a)

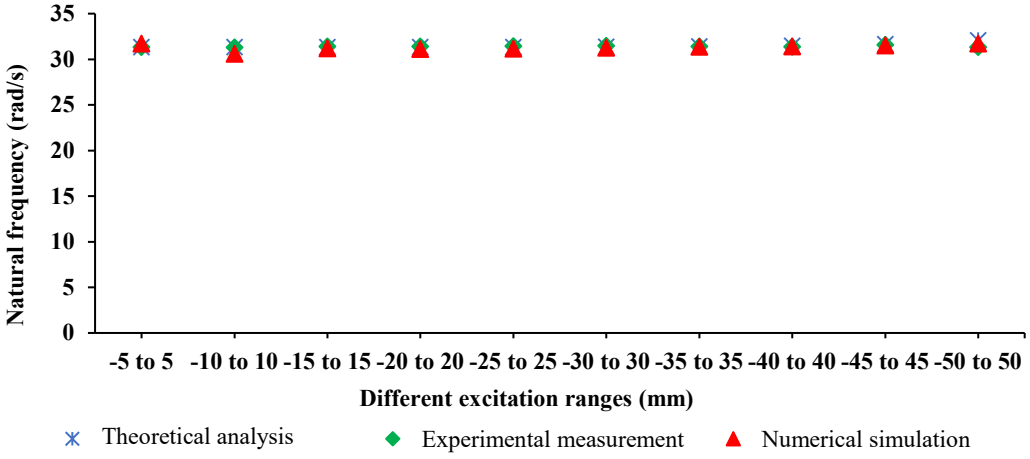

(b)

Figure 4.13: 5th order polynomial curve fitting (a) linear stiffness and (b) natural frequency

The theoretical linear stiffnesses and natural frequencies for different excitation ranges of the floating magnet are almost identical compared with numerical and experimental measurements which can be seen in Figure 4.12 and Figure 4.13, respectively. Moreover, for small excitation ranges as shown in Figure 4.12 and Figure 4.13, the measured natural frequencies for 3rd order polynomial curve fitting are almost similar with 5th order polynomial curve fitting for all theoretical, numerical and experimental measurements. The average measured natural frequencies for 3rd order and 5th order polynomial curve fittings are around 30.5 rad/s and 31.5 rad/s, respectively. The R-square values in Table 4.2 show that higher-order polynomial models have better results than the lower order polynomial modes, namely 5th order has a better fit than the 3rd order. Table 4.2 shows that the higher-order polynomial model can provide a better match for high excitation and small excitation ranges based on the Root Mean Squared Error (RMSE) values.

Table 4.2: Goodness of fit

Excitation (mm)	Polynomial model		R-square	Adjusted R-square	SSE	RMSE
-5 to 5	3rd order	Theoretical	1	1	2.001e-06	0.0001436
		Numerical	0.9997	0.9995	0.001818	0.02462
		Experimental	0.9999	0.9998	0.001131	0.01504
	5th order	Theoretical	1	1	1.654e-06	0.0001319
		Numerical	0.9998	0.9988	0.001394	0.03734
		Experimental	0.9999	0.9998	0.0006922	0.01519
-10 to 10	3rd order	Theoretical	1	1	0.0001061	0.000734
		Numerical	0.9994	0.9992	0.02947	0.05429
		Experimental	0.9997	0.9994	0.01491	0.06106
	5th order	Theoretical	1	1	1.674e-06	9.266e-05
		Numerical	0.9995	0.9992	0.02446	0.05529
		Experimental	0.9999	0.9997	0.003573	0.04227
-15 to 15	3rd order	Theoretical	1	1	0.004302	0.003806
		Numerical	0.9998	0.9998	0.03132	0.04908
		Experimental	0.9989	0.9986	0.1468	0.1106
	5th order	Theoretical	1	1	2.41e-06	9.038e-05
		Numerical	0.9998	0.9997	0.03118	0.05324
		Experimental	0.9991	0.9986	0.1204	0.1097
-20 to 20	3rd order	Theoretical	1	1	0.06549	0.01284
		Numerical	0.9999	0.9999	0.03433	0.04494
		Experimental	0.9984	0.998	0.2826	0.1681
	5th order	Theoretical	1	1	4.348e-05	0.0003318
		Numerical	0.9999	0.9999	0.03381	0.04747
		Experimental	0.9995	0.9992	0.09092	0.1066
-25 to 25	3rd order	Theoretical	1	1	0.5862	0.03434
		Numerical	0.9999	0.9999	0.05966	0.0533
		Experimental	0.9992	0.9991	0.3384	0.1613
	5th order	Theoretical	1	1	0.0009536	0.001388
		Numerical	0.9999	0.9999	0.03797	0.0447
		Experimental	0.9994	0.9992	0.2521	0.1514
-30 to 30	3rd order	Theoretical	0.9995	0.9995	3.822	0.08001
		Numerical	0.9999	0.9999	0.1294	0.06923
		Experimental	0.9986	0.9983	1.131	0.2746
	5th order	Theoretical	1	1	0.01333	0.004733
		Numerical	1	1	0.05391	0.04644

		Experimental	0.9995	0.9993	0.4149	0.1787
-35 to 35	3rd order	Theoretical	0.9988	0.9986	20.43	0.1712
		Numerical	0.9998	0.9997	0.6345	0.1387
		Experimental	0.9986	0.9983	1.422	0.3079
	5th order	Theoretical	1	1	0.1376	0.01407
		Numerical	1	1	0.07357	0.04871
		Experimental	0.9991	0.9987	0.9593	0.2717
-40 to 40	3rd order	Theoretical	0.9988	0.9988	96.61	0.3482
		Numerical	0.9995	0.9994	2.197	0.2437
		Experimental	0.9989	0.9987	3.176	0.3985
	5th order	Theoretical	1	1	1.169	0.03835
		Numerical	1	1	0.08481	0.04923
		Experimental	0.9994	0.9993	1.614	0.2994
-45 to 45	3rd order	Theoretical	0.9971	0.9971	426.9	0.6898
		Numerical	0.9987	0.9986	10.29	0.4893
		Experimental	0.9985	0.9983	8.292	0.6004
	5th order	Theoretical	0.9999	0.9999	8.834	0.09935
		Numerical	1	1	0.2596	0.07958
		Experimental	0.9997	0.9996	1.814	0.2939
-50 to 50	3rd order	Theoretical	0.9931	0.9931	1848	1.361
		Numerical	0.9971	0.9969	35.14	0.8646
		Experimental	0.9981	0.9979	18.52	0.844
	5th order	Theoretical	0.9998	0.9998	63.22	0.2521
		Numerical	0.9999	0.9999	0.9464	0.145
		Experimental	0.9997	0.9997	2.479	0.3214

Comparing the measured RMSE values for all curve fitting analyses for different ranges of position of the floating magnet, the 5th order polynomial model gave the lowest RMSE values. However, for the smaller excitation ranges such as 5 mm and 10 mm, the 3rd order polynomial model produced the lowest RMSE values. Therefore, it can be said that in general for small excitation ranges, the lower order polynomial model is more suitable but for the long excitation range the higher-order polynomial model would be more suitable.

4.5 Design Analysis for Various Positions of the Top Fixed Magnet

To select the best model of the oscillator which can harvest maximum energy in low-frequency ranges, the design of the magnetic spring based nonlinear oscillator system has been analysed by changing the position of the top fixed magnet. The model has been discussed in the earlier section

where the centre magnet is located between the two fixed magnets and the distance between middle and bottom magnets is 79 mm and middle and top magnets is 104 mm (equilibrium position under gravitational effects for these particular magnets as presented in Table 3.1). In the previously discussed model, the bottom magnet is attached and locked at first in the bottom end of the vertical shaft and later the second magnet is put (same poles facing each other) above the bottom magnet along the vertical shaft. The 2nd magnet settled at 104 mm away from the bottom magnet. After that, the 3rd magnet (top magnet) is placed above the 2nd magnet (middle magnet) with the same poles facing each other in the vertical shaft as shown in Figure 4.1. The top magnet is settled 104 mm away from the middle magnet but the distance between middle and bottom magnets is reduced to 79 mm due to the gravitational effects. The top magnet is locked in position along the shaft, and is considered as the equilibrium position of the magnet arrangement.

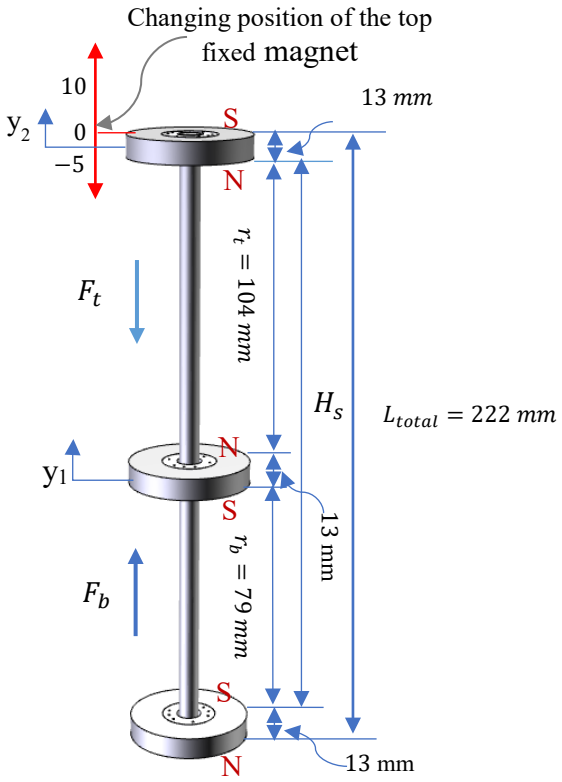

Figure 4.14: Magnetic spring based nonlinear oscillator system

The total length of the system for this equilibrium position is 222 mm. Figure 4.14 presents the equilibrium position of the top fixed magnet. Figure 4.14 shows the magnetic spring based nonlinear oscillator system. In Figure 4.14, the distance between the middle magnet and bottom magnet is

denoted by r_b and the distance between the middle magnet and top magnet is symbolised by r_t. The total length of the oscillator is L_{total}. The equilibrium position of the top magnet is considered as the 0 position. When the top magnet moves toward the middle magnet from the equilibrium position, the travelling distance is considered as negative (-) distance. If the top magnet moved by 5 mm toward the middle magnet, the travelling distance is considered -5 mm, as shown in Figure 4.14.

Table 4.3: Different position of the top fixed magnet

Changing position of the top fixed magnet, mm	r_b (mm)	r_t (mm)	L_{total} (mm)	Floating magnet moved toward bottom magnet due to the gravitational effects (mm)		Damping ratio	Natural frequency (rad/s)
				Experimental	Analytical		
-10	76	97	212	10.5	10.5	0.0463	34.42
-5	77.5	100.5	217	11.5	11.5	0.04	33.10
0	79	104	222	13	12.5	0.031	32.35
10	82	111	232	14.5	15	0.0251	29.73
20	85.5	117.5	242	16	16	0.022	27.76
30	87.5	125.5	252	19	19	0.0183	26.09
40	89.5	133.5	262	22	22	0.0161	24.07
50	91	142	272	25.5	25.5	0.0153	23.67

On the other hand, when the top magnet moved away from the equilibrium position, the travelling distance is considered as positive (+) distance. The distance is 10 mm when the top magnet moved 10 mm away from the equilibrium position. Table 4.3 presents different resultant distances between middle and bottom magnets and middle and top magnets due to the different positions of the top fixed magnet. The position of the floating magnet changed as expected due to gravitational force effects when the top magnet moved or varies the total length of the oscillator as seen in Figure 4.15. Figure 4.15 presents the analytical study of the gravitational force effects for different positions of the top fixed magnet. During the equilibrium position of the oscillator, the floating magnet moved by 13 mm toward the bottom magnet from the expected position (equilibrium position for floating magnet) due to gravitational force effects. This length, due to the gravitational force effects, decreased when the top magnet shifted toward the middle magnet, but it increased when the top magnet moved away from its equilibrium position, as seen in Table 4.3.

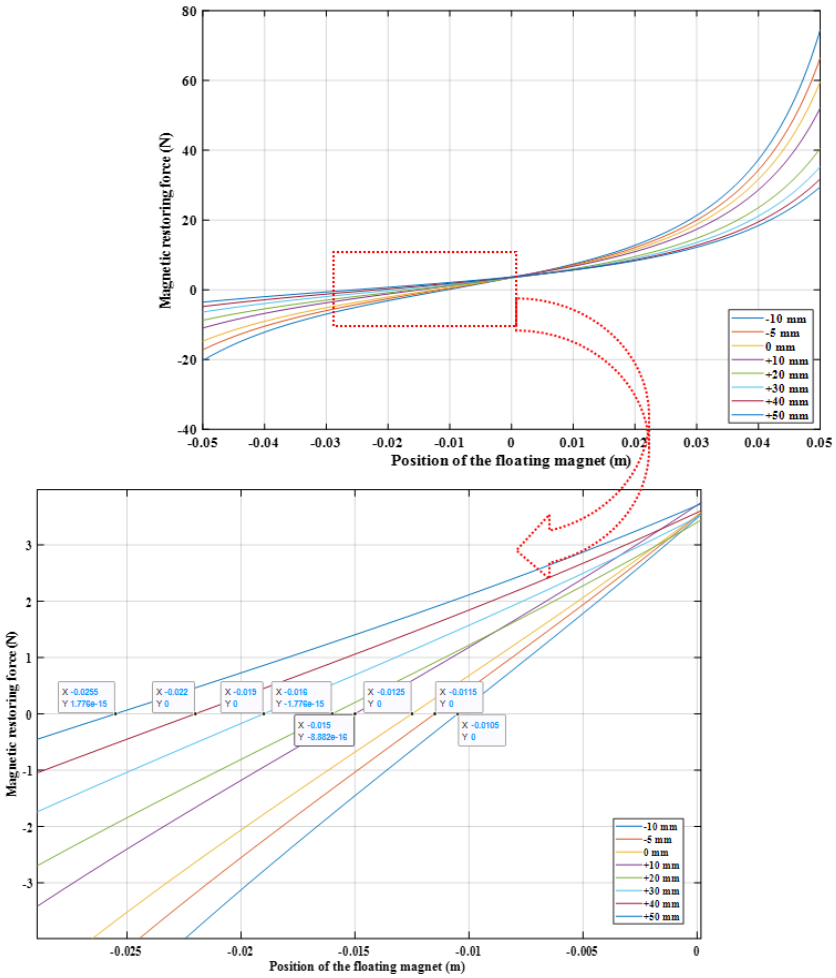

Figure 4.15: Gravitational force effects on equilibrium position

Moreover, with changing the position of the top fixed magnet the distance between the middle and bottom magnet changes as well. From Table 4.3, the distance between middle and bottom magnets and the distance between middle and top magnets changed with the changing position of the top fixed magnet. The distance between the middle and bottom magnets changes very slightly compared to the changing distance between the top and middle magnets. Moreover, the damping ratio and natural frequency of the oscillator changed with changing the fixed position of the top magnet. The damping ratio and natural frequency have been measured experimentally for different positions of the top fixed magnet. Figure 4.16 presents the change of damping ratio and natural frequency of the oscillator for different top fixed magnet positions.

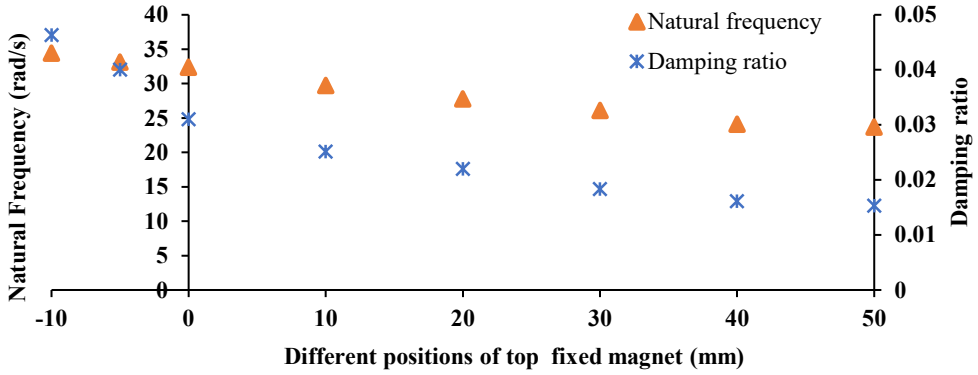

Figure 4.16: Change of damping ratio and natural frequency for different positions of the top magnet.

It is clear from Figure 4.16 that when the top fixed magnet moved toward the middle magnet from the equilibrium position, the damping ratio and natural frequency increased. On the other hand, the damping ratio and the natural frequency decreased when the top fixed magnet moved away from the equilibrium position. For example, when the top magnet was moved by 5 mm toward the middle magnet from its equilibrium position, the oscillator's total length was reduced to 217 mm. The new distance between the middle magnet and bottom magnet is 77.5 mm and the distance between the middle magnet and top magnet is 100.5 mm. It is expected that the damping ratio and natural frequency will be increased if the total length of the oscillator is reduced. The measured damping ratio and natural frequency are 0.040 and 33.10 rad/s, respectively, which are higher than the equilibrium position's damping ratio and natural frequency (0.031 and 32.35 rad/s, respectively). If the top fixed magnet is shifted more towards the middle magnet by 10 mm, then the middle magnet also moved towards the bottom magnet. The total length of the oscillator is then reduced to 212 mm and the damping ratio and frequency increased to 0.0463 and 34.42 rad/s, respectively, as shown in Figure 4.16.

On the other hand, if the top magnet moved 10 mm away from its equilibrium position, the oscillator total length increased to 232 mm. The new distance between the middle magnet and bottom magnet is 82 mm and the distance between the middle magnet and top magnet is 111 mm. The damping ratio and natural frequency are reduced by increasing the total length of the oscillator. The measured natural frequency and damping ratio are 29.73 rad/s and 0.0251 respectively, which are lower than the equilibrium position's natural frequency and damping ratio (32.35 rad/s and 0.031, respectively).

The damping ratios and natural frequencies continuously decreased with the increase in the total length of the oscillator, which can be seen from Table 4.3.

4.5.1 Magnetic restoring forces for different positions of the top magnet

When the top magnet moved by 5 mm toward the middle magnet from its equilibrium position, the oscillator's total length reduced to 217 mm. This resulted in the distance between the middle magnet and bottom magnet to be 77.5 mm and the distance between the middle magnet and top magnet to be 100.5 mm. The magnetic restoring force for this new oscillator setup is measured experimentally, numerically and theoretically, respectively, as shown in Figure 4.17, Figure 4.18 and Figure 4.19, respectively.

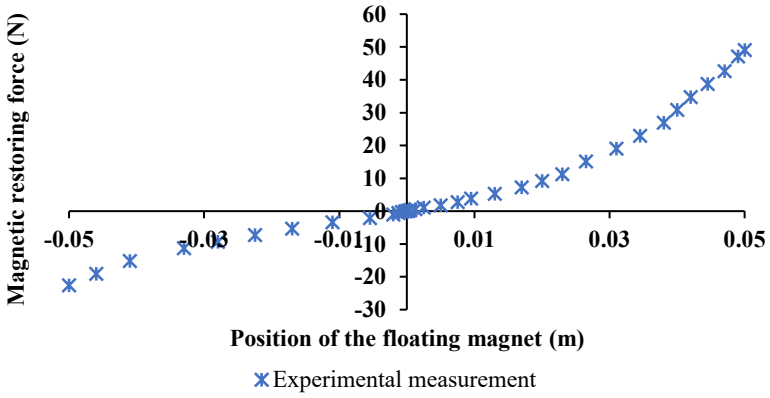

Figure 4.17: Magnetic restoring force when top magnet moved by 5 mm and fixed toward middle magnet from equilibrium position (Experimental measurement)

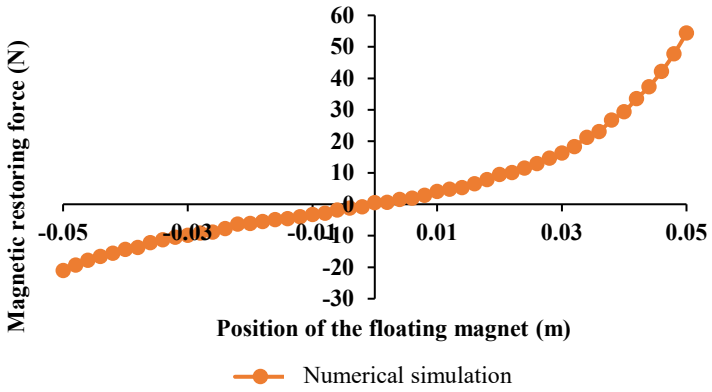

Figure 4.18: Magnetic restoring force when top magnet moved by 5 mm and fixed toward middle magnet from equilibrium position (Numerical simulation)

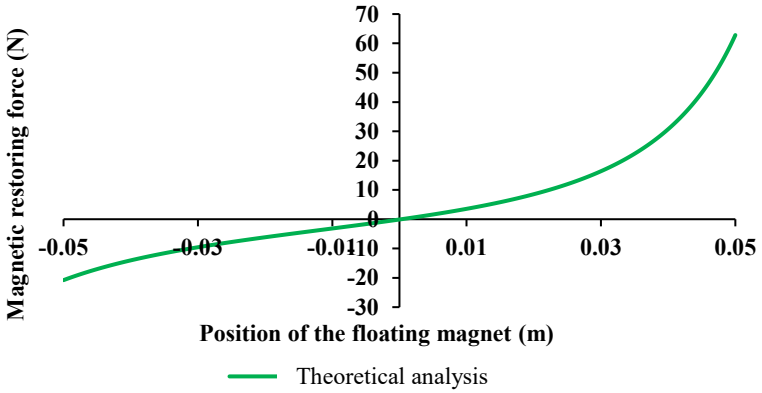

Figure 4.19: Magnetic restoring force when top magnet moved by 5 mm and fixed toward middle magnet from equilibrium position (Theoretical analysis)

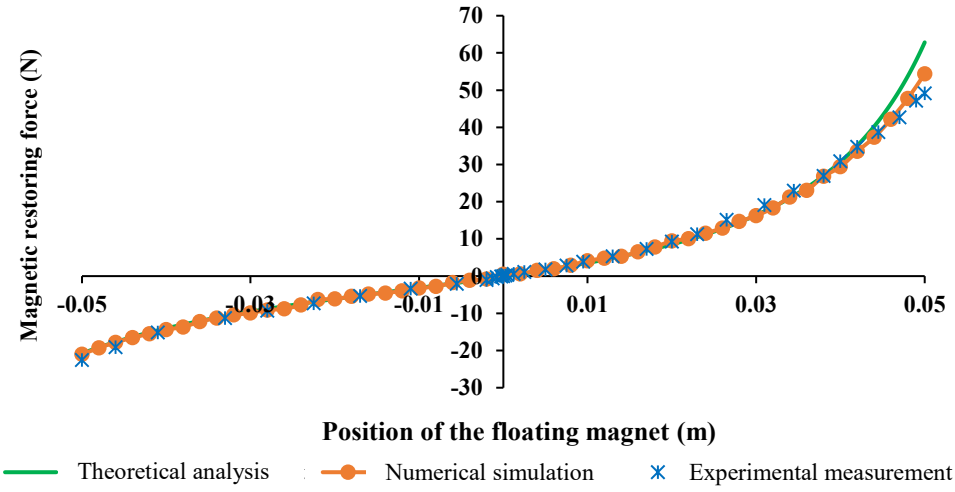

Figure 4.20: Comparison of magnetic restoring (-5 mm)

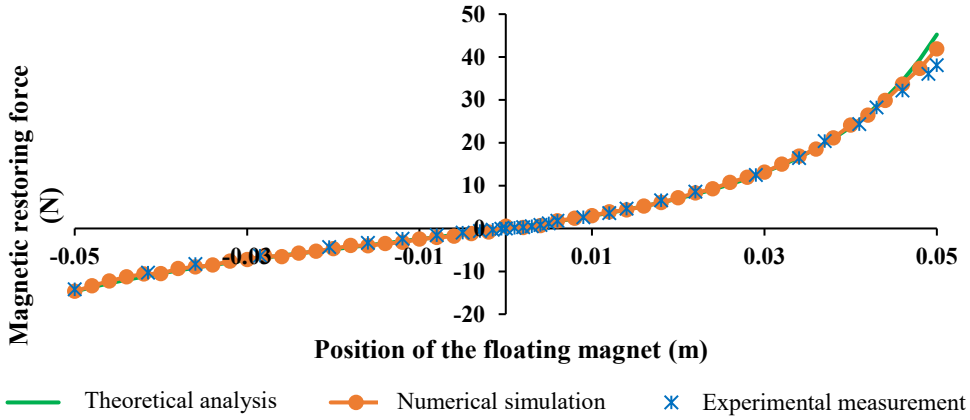

Figure 4.21: Comparison of magnetic restoring (10 mm)

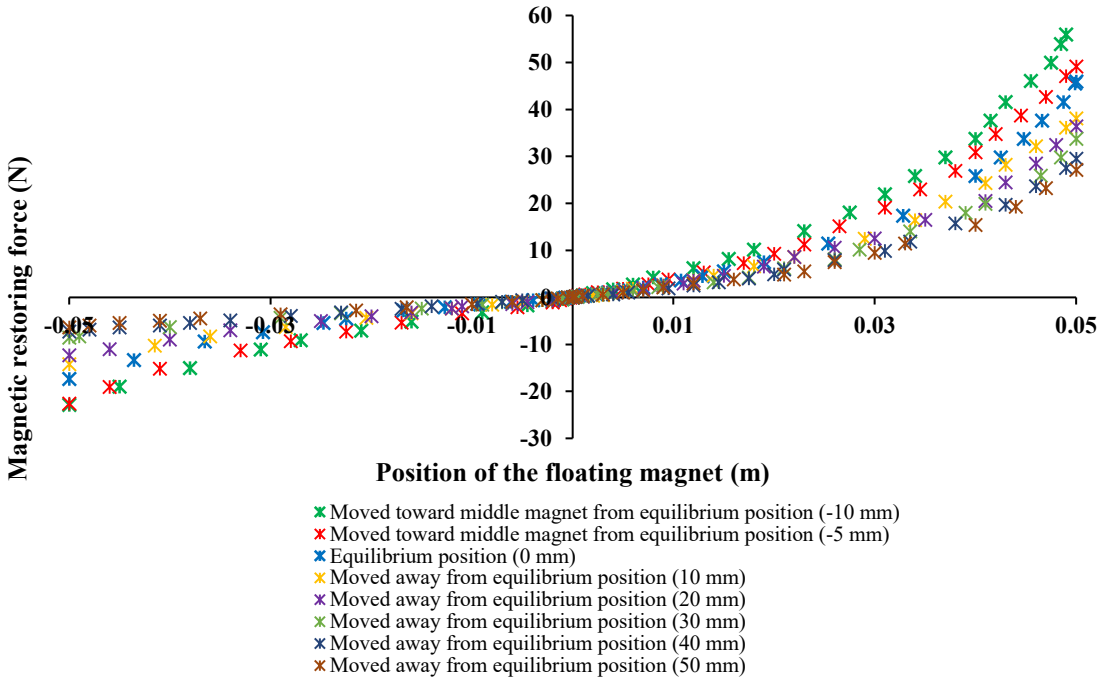

Figure 4.22: Magnetic restoring force for different positions of the top fixed magnet (experimental measurement)

Figure 4.20 shows the comparison of magnetic restoring forces which are calculated theoretically, numerically (ANSYS MAXWELL) and experimentally. Figure 4.20 shows the validation of the theoretical and numerical model with the experimental model. The experimentally measured magnetic restoring forces are similar to the numerical and theoretical measured values. From Figure 4.20, it can be seen that the magnetic restoring force is greater than the equilibrium positions' magnetic restoring force due to the top magnet move toward the middle magnet (reduced the oscillator's total length) from the equilibrium position. The magnetic restoring force increases with reducing the total length of the oscillator which can be seen in Figure 4.22. If the top magnet is then fixed at a distance of 10 mm away from its equilibrium position, the oscillator's total length is increased to 232 mm. The new distance between the middle magnet and bottom magnet is 82 mm and the distance between the middle magnet and top magnet is 111 mm. The experimentally measured magnetic restoring has been validated with the theoretical and numerical model, as shown in Figure 4.21. It can be said from Figure 4.22 that the magnetic restoring force increases when the top fixed magnet moves toward the middle magnet from the equilibrium position and decreases when the top magnet moves away from the equilibrium position (top magnet's equilibrium position). The further away the top magnet goes from the equilibrium position, the less the magnetic restoring force

becomes. Hence, increasing the total length of the oscillator decreases the magnetic restoring force, as shown in Figure 4.22.

4.5.2 Coefficients of the magnetic restoring force for various positions of the top magnet

Both the cubic (3rd order) and quintic (5th order) polynomials curve fits have been used to measure the magnetic restoring force between the floating magnet and the two fixed end magnets for various positions of the top fixed magnet. The magnetic restoring force curve is shown in Figure 4.23 and from this curve, the linear and nonlinear stiffness have been calculated.

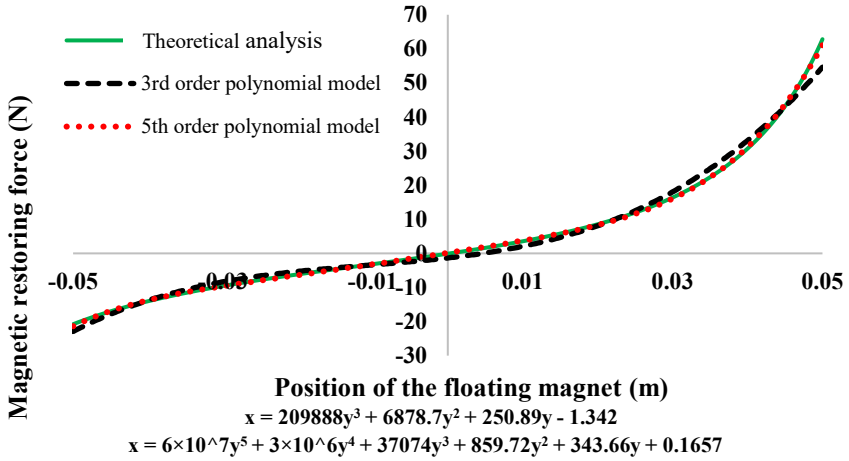

Figure 4.23: Magnetic restoring force with polynomial models (-5 mm)

The analytical measurement for the restoring force has been used to measure the linear and nonlinear stiffness of the system by changing the fixed position of the top magnet. The values of k_1, $k_2, k_3, k_4, and\ k_5$ have been measured from the least-squares curve fitting of the above graph. Figure 4.23 displays that the 5th order (quintic) polynomial fits the data better than the 3rd order (cubic) polynomial. For the 3rd order polynomial curve fit the linear stiffness is 250.89 N/m but for the 5th order polynomial curve, the linear stiffness is 343.66 N/m. For each change in the position of the top magnet, the floating magnet was moved 50 mm toward bottom magnet and 50 mm toward top magnet, and the linear and nonlinear coefficients for these excitation ranges are investigated. Moreover, Table 4.4 presents the coefficients of the magnetic spring-based oscillator system for the different positions of the top fixed magnet. It can be seen from Table 4.4 that when the top fixed magnet shifted towards the middle magnet, the total length of the oscillator was reduced, and the coefficients of the magnetic restoring forces changed. The coefficients of the magnetic restoring forces also changed as well when the top fixed magnet moved away from the equilibrium position.

Table 4.4: Coefficients of the magnetic spring-based oscillator system for different position of the top fixed magnet (Theoretical analysis)

Excitation (mm)	Polynomial model	Coefficients				
		k_1 (N/m)	k_2 (N/m^2)	k_3 (N/m^3)	k_4 (N/m^4)	k_5 (N/m^5)
-10 mm	3rd order	259.87	7580.7	244955	---	---
	5th order	373.58	560.68	33122	3×10^6	8×10^7
-5 mm	3rd order	250.89	6878.7	209888	---	---
	5th order	343.66	859.72	37074	3×10^6	6×10^7
Equilibrium position (0 mm)	3rd order	246.32	6387.9	184996	---	---
	5th order	324.29	1094.9	39734	2×10^6	5×10^7
10 mm	3rd order	221.7	5167	1.377×10^5	---	---
	5th order	274.7	1298	3.903×10^4	1.802×10^6	3.546×10^7
20 mm	3rd order	202.53	4313.3	106770	---	---
	5th order	240.2	1375.9	36592	1×10^6	3×10^7
30 mm	3rd order	183.56	3832.6	86119	---	---
	5th order	212.08	1436	32993	1×10^6	2×10^7
40 mm	3rd order	169	3504.6	72985	---	---
	5th order	192.03	1455.6	30051	954285	2×10^7
50 mm	3rd order	157.32	3308	64428	---	---
	5th order	177.02	1474.3	27720	854025	1×10^7

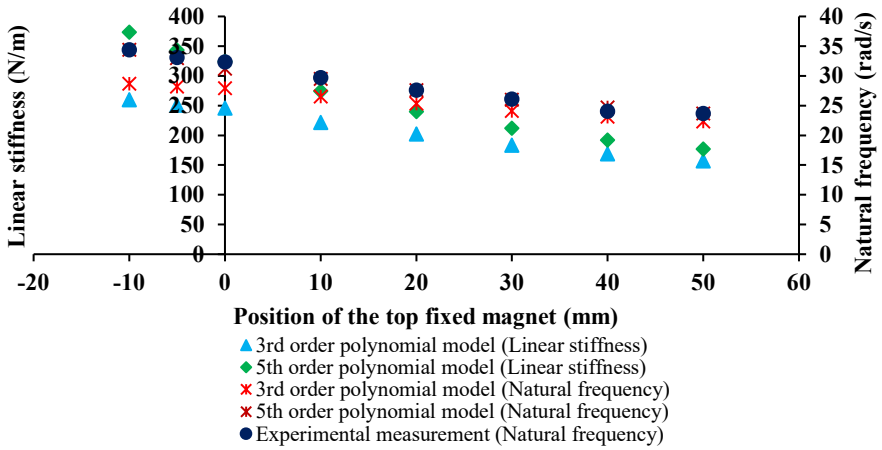

Figure 4.24: Linear stiffness and frequency for different positions of the top fixed magnet

The linear stiffness of the oscillator system increased when the top fixed magnet moved towards the middle magnet, and it decreased when the top fixed magnet moved away from the equilibrium

position, which can be seen from Table 4.4. The natural frequencies of the oscillator for different positions of the top fixed magnet have been determined theoretically and experimentally. Figure 4.24 shows the graphical presentation of the linear stiffnesses and natural frequencies for different positions of the top magnet.

Table 4.5: Natural frequencies for different positions of the top fixed magnet

Position of the top fixed magnet from the equilibrium position	Natural frequency (rad/s)		
	Theoretical analysis		Experimental measurement (log decrement)
	3rd order Polynomial model	5th order Polynomial model	
-10 mm	28.72	34.43	34.42
-5 mm	28.22	33.03	33.10
Equilibrium position (0 mm)	27.96	31.21	32.35
10 mm	26.53	29.53	29.73
20 mm	25.35	27.61	27.76
30 mm	24.14	26	26.09
40 mm	23.16	24.7	24.07
50 mm	22.34	23.7	23.67

The measured frequencies for the 3rd and 5th order polynomial curve fittings have been compared with the experimental measurement, as presented in Figure 4.24 and Table 4.5. The theoretical calculated natural frequencies for 5th order curve fitting are almost identical with experimental measurement (log decrement). The measured natural frequencies for different positions of the top fixed magnet have been shown in Table 4.5. The natural frequency increased when the total length of the oscillator reduced, and it decreased when the total length of the oscillator increased, as can be seen in Table 4.5.

4.6 Model Analysis of the Magnetic Spring-based Nonlinear Oscillator System

Figure 4.25 presents the free body diagram of the proposed nonlinear oscillator system. The mass of the floating magnet is M. F_β is the damping force of the system written as $F_\beta = \beta\dot{y}$. The relative displacement of the magnet is y, and the relative velocity and acceleration of the magnet are $\dot{y}$ and $\ddot{y}$, respectively. The equation of the motion of the system can be written as,

$$M\frac{d^2y}{dt^2} + F_\beta + F_r = F_b Sin(\omega t) \tag{4.6}$$

$$M\frac{d^2y}{dt^2} + \beta\frac{dy}{dt} + k_1 y + k_2 y^2 + k_3 y^3 = F_b Sin(\omega t) \tag{4.7}$$

$$M\frac{d^2y}{dt^2} + \beta\frac{dy}{dt} + k_1 y + k_2 y^2 + k_3 y^3 + k_4 y^4 + k_5 y^5 = F_b Sin(\omega t) \tag{4.8}$$

where k_1 is the linear spring constant and k_2, k_3, k_4 and k_5 are the nonlinear coefficients of the system.

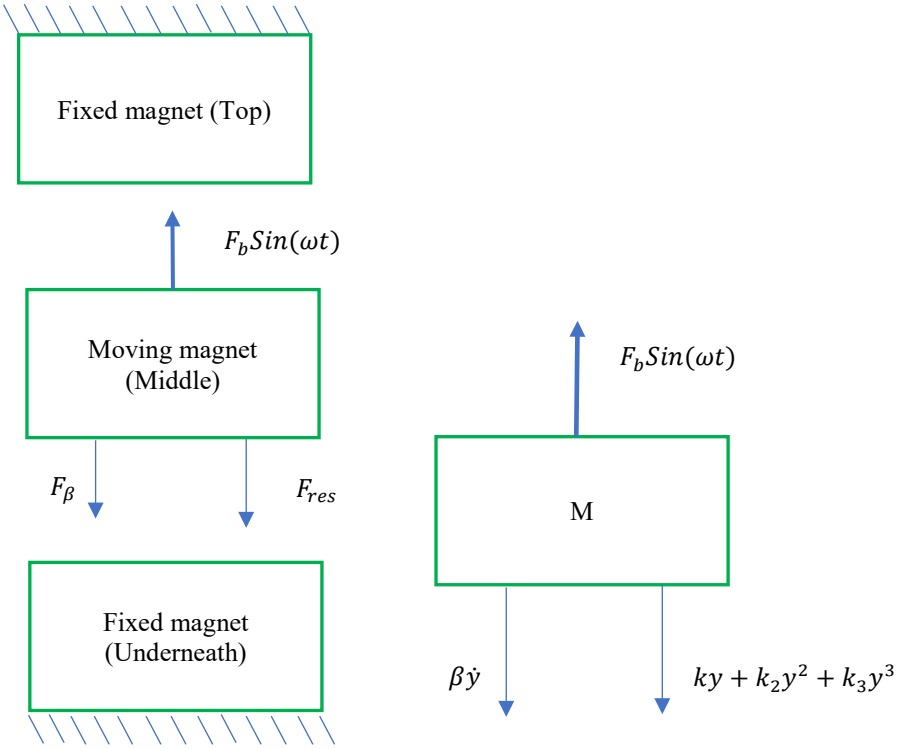

Figure 4.25: Free body diagram of magnetic spring based nonlinear oscillator system

A state space model is a linear representation in discrete or continuous time of a dynamic system. The continuous time form of a model in state space form can be written by

$$\dot{Z} = AZ + Bu \tag{4.9}$$

$$X = CZ + Du \tag{4.10}$$

Where ***A*** is the system matrix, ***B*** is the input matrix and ***C*** is the output matrix. The remaining matrix is ***D***, which is typically zero because the direct input does not typically affect the output.

$$M\frac{d^2y}{dt^2} + \beta\frac{dy}{dt} + k_1y + k_2y^2 + k_3y^3 = F_bSin(\omega t) \tag{4.11}$$

$$\ddot{y} = \frac{1}{M}(F_bSin(\omega t) - \beta\dot{y} - k_1y - k_2y^2 - k_3y^3) \tag{4.12}$$

$$\ddot{y} = \frac{1}{M}(F_bSin(\omega t) - \beta\dot{y} - k_1y - k_2y^2 - k_3y^3 - k_4y^4 - k_5y^5) \tag{4.13}$$

By considering the state variables Z_1 and Z_2 the system Equation 4.13 can be written in state space form by following:

$$Z_1 = y \tag{4.14}$$

$$Z_2 = \dot{y} = \dot{Z}_1 \tag{4.15}$$

$$\frac{dZ_2}{dt} = \ddot{y} \tag{4.16}$$

$$u = F_bSin(\omega t) \tag{4.17}$$

The resulting state space matrix form of the differential equation gives:

$$\dot{Z}_2 = \frac{1}{M}\left(U_1 - \beta Z_2 - k_1Z_1 - k_2{Z_1}^2 - k_3{Z_1}^3\right) \tag{4.18}$$

$$\dot{Z}_2 = \frac{1}{M}\left(U_1 - \beta Z_2 - k_1Z_1 - k_2{Z_1}^2 - k_3{Z_1}^3 - k_4{Z_1}^4 - k_5{Z_1}^5\right) \tag{4.19}$$

The resulting state space matrix for 3rd order polynomial model form of the differential equation gives:

$$\begin{bmatrix}\frac{dZ_1}{dt}\\ \frac{dZ_2}{dt}\end{bmatrix} = \underbrace{\begin{bmatrix}0 & 1\\ \frac{-k_1 - k_2Z_1 - k_3{Z_1}^2}{M} & \frac{-\beta}{M}\end{bmatrix}}_{A}\begin{bmatrix}Z_1\\ Z_2\end{bmatrix} + \underbrace{\begin{bmatrix}0\\ \frac{1}{M}\end{bmatrix}}_{B}[U_1] \tag{4.20}$$

$$[X] = \underbrace{\begin{bmatrix}1 & 0\\ 0 & 1\end{bmatrix}}_{C}\begin{bmatrix}Z_1\\ Z_2\end{bmatrix} + \underbrace{[0]}_{D}[u] \tag{4.21}$$

The resulting state space matrix for 5th order polynomial model form of the differential equation gives:

$$\begin{bmatrix} \frac{dZ_1}{dt} \\ \frac{dZ_2}{dt} \end{bmatrix} = \begin{bmatrix} \frac{dZ_1}{dt} \\ \frac{dZ_2}{dt} \end{bmatrix} = \underbrace{\begin{bmatrix} 0 & 1 \\ \frac{-k_1 - k_2 Z_1 - k_3 {Z_1}^2 - k_4 {Z_1}^3 - k_5 {Z_1}^4}{M} & \frac{-\beta}{M} \end{bmatrix}}_{A} \begin{bmatrix} Z_1 \\ Z_2 \end{bmatrix} + \underbrace{\begin{bmatrix} 0 \\ \frac{1}{M} \end{bmatrix}}_{B} [U_1] \tag{4.22}$$

$$[X] = \underbrace{\begin{bmatrix} 1 & 0 \\ 0 & 1 \end{bmatrix}}_{C} \begin{bmatrix} Z_1 \\ Z_2 \end{bmatrix} + \underbrace{[0]}_{D} [u] \tag{4.23}$$

Moreover, the resulting state space matrix for 7th order polynomial model form of the differential equation gives:

$$\begin{bmatrix} \frac{dZ_1}{dt} \\ \frac{dZ_2}{dt} \end{bmatrix} = \begin{bmatrix} \frac{dZ_1}{dt} \\ \frac{dZ_2}{dt} \end{bmatrix} = \underbrace{\begin{bmatrix} 0 & 1 \\ \frac{-k_1 - k_2 Z_1 - k_3 {Z_1}^2 - k_4 {Z_1}^3 - k_5 {Z_1}^4 - k_6 {Z_1}^5 - k_7 {Z_1}^6}{M} & \frac{-\beta}{M} \end{bmatrix}}_{A} \begin{bmatrix} Z_1 \\ Z_2 \end{bmatrix} + \underbrace{\begin{bmatrix} 0 \\ \frac{1}{M} \end{bmatrix}}_{B} [U_1] \tag{4.24}$$

$$[X] = \underbrace{\begin{bmatrix} 1 & 0 \\ 0 & 1 \end{bmatrix}}_{C} \begin{bmatrix} Z_1 \\ Z_2 \end{bmatrix} + \underbrace{[0]}_{D} [u] \tag{4.25}$$

Where $\dot{Z}$ is known as the state vector and X is called the output vector. A and B in equations 4.20, 4.22 and 4.24 are known as the state or system matrix and input matrix, respectively. Moreover, C and D in equations 4.21, 4.23 and 4.25 are called the output matrix and zero matrix, respectively.

4.6.1.1 Investigation of 3rd order polynomial model

In the beginning, the dynamics of the 3rd order polynomial model have been analysed. The linear and nonlinear coefficients of the magnetic spring-based oscillator system for different excitation have been presented in Table 4.6. The log decrement method has been used to measure the damping ratio, damping constant and natural frequency of the oscillator (total length 222 mm). The measured damping ratio, damping constant and natural frequency are 0.031, 0.74 Ns/m and 32.35 rad/s, respectively. The theoretical simulation of the system has been run by MATLAB code using the values of M (mass including plastic bush), β, k_1, k_2 and k_3 are 0.37 Kg, 0.74 Ns/m, 269.31 N/m, 5680.4 N/m^2 and 163159 N/m^3 respectively. The simulation results of the system are displayed in Table 4.7. When the magnet is in the expected equilibrium position (0mm), the resulting eigenvalues are $\lambda_{i=1\ to\ 4}$ = -1.0000+26.9604i, 0, 0 and -1.0000 +26.9604i, and the corresponding frequency is 26.9790 rad/s or 4.296 Hz. It has been seen from the analysis using the 3rd order polynomial model

that the real parts of the eigenvalues remained constant for all different positions of the floating magnet when it moved toward the top and bottom magnets.

Table 4.6: Linear and nonlinear coefficients of the magnetic spring-based oscillator system (3rd order polynomial model)

Excitation (mm)	Coefficients		
	k_1 (N/m)	k_2 (N/m2)	k_3 (N/m3)
-5 to 5	307.35	819.63	1×10^6
-10 to 10	304.28	6447.5	814030
-15 to 15	308.21	2588.2	94713
-20 to 20	306.58	3494.3	116588
-25 to 25	302.01	3732	128941
-30 to 30	292.33	4255.2	150269
-35 to 35	302.95	4204.3	128199
-40 to 40	293.98	4671.7	142945
-45 to 45	283.72	5205.1	152028
-50 to 50	269.31	5680.4	163159

However, the imaginary parts of the eigenvalues, and thus the frequencies, changed with the changing position of the floating magnet. There is a considerable decrease in the imaginary part of the eigenvalues, and thus frequencies, until 17 mm is reached before increasing when the floating magnet moved toward the top magnet from the equilibrium position. The minimum resulting eigenvalues and frequency were -1.0000 +24.3580i, 0, 0 and -1.0000 -24.3580i and 24.3786 rad/s, respectively, which were found at 17 mm up towards the top magnet. After 17 mm towards the top magnets, the imaginary parts of the eigenvalues and natural frequencies rose steadily. On the other hand, the imaginary parts of the eigenvalues and frequencies increased steadily with the increasing distance of the floating magnet from the equilibrium position towards the bottom magnet. The minimum values for the imaginary part of the eigenvalues and natural frequency should be found in the equilibrium position. However, it did not take place due to the effect of the gravitational force on equilibrium position. Because of the gravitational effects, the equilibrium position moved 17 mm away toward the bottom magnet where it should be. When the position of the floating magnet is 50 mm towards the top magnet (-50 mm), the resulting eigenvalues are $\lambda_{i=1\ to\ 4}$ =-1.0000 +32.5833i, 0, 0 and -1.0000+32.5833i. Moreover, when the position of the floating magnet is 50 mm towards the bottom magnet (+50 mm),

the resulting eigenvalues found are $\lambda_{i=1\ to\ 4}$ = -1.0000+50.9599i, 0, 0 and -1.0000-50.9599i as displayed in Table 4.7.

Table 4.7: Eigenvalue when floating magnet moved 50 mm toward top magnet and 50 mm toward bottom magnet from the equilibrium position (3rd order polynomial model)

Position of the floating magnet	Eigenvalue	Natural frequency (rad/s)
-50 mm	-1.0000 +32.5833i	32.5986
-45 mm	-1.0000 +30.4790i	30.4954
-40 mm	-1.0000 +28.6063i	28.6238
-35 mm	-1.0000 +27.0133i	27.0318
-30 mm	-1.0000 +25.7520i	25.7714
-25 mm	-1.0000 +24.8729i	24.8930
-20 mm	-1.0000 +24.4173i	24.4378
-15 mm	-1.0000 +24.4089i	24.4294
-10 mm	-1.0000 +24.8483i	24.8684
-05 mm	-1.0000 +25.7124i	25.7318
0 mm	-1.0000 +26.9604i	26.9790
05 mm	-1.0000 +28.5421i	28.5596
10 mm	-1.0000 +30.4054i	30.4218
15 mm	-1.0000 +32.5018i	32.5172
20 mm	-1.0000 +34.7894i	34.8038
25 mm	-1.0000 +37.2328i	37.2462
30 mm	-1.0000 +39.8034i	39.8160
35 mm	-1.0000 +42.4781i	42.4899
40 mm	-1.0000 +45.2384i	45.2495
45 mm	-1.0000 +48.0696i	48.0800
50 mm	-1.0000 +50.9599i	50.9697

The eigenvalues can be calculated by using the following equations.

$$\lambda_i = -\frac{\beta}{2M}, -\frac{1}{2M}\sqrt{4Mk - \beta^2}i \qquad (4.26)$$

$$\lambda_i = -\frac{\beta}{2M}, \frac{1}{2M}\sqrt{4Mk - \beta^2}i \qquad (4.27)$$

The calculated eigenvalues were -1.000+26.9604i and -1.000 -26.9604i when the position of the floating magnet is 0 mm (expected equilibrium position). These equations work when the system is

linear, as when in the proposed system, the displacement of the floating magnet is very small (near equilibrium position). For the other displacement (high displacement) this system works as a nonlinear system and these equations will not work. Moreover, with the changing of the position of the floating magnet, the frequency of the oscillator changes, as shown in Table 4.7. The corresponding natural frequencies could be measured by using the following formula:

$$\omega_i = \sqrt{Re(\lambda_i)^2 + Im(\lambda_i)^2} \qquad (4.28)$$

The calculated natural frequencies for -50 mm, 0 mm and +50 mm positions of the floating magnet are $32.5986\, rad/s$, $26.9790\, rad/s$ and $50.9697\, rad/s$, respectively which are close to the measured frequency given by the MATLAB Bode plot comments, as shown in Figure 4.26.

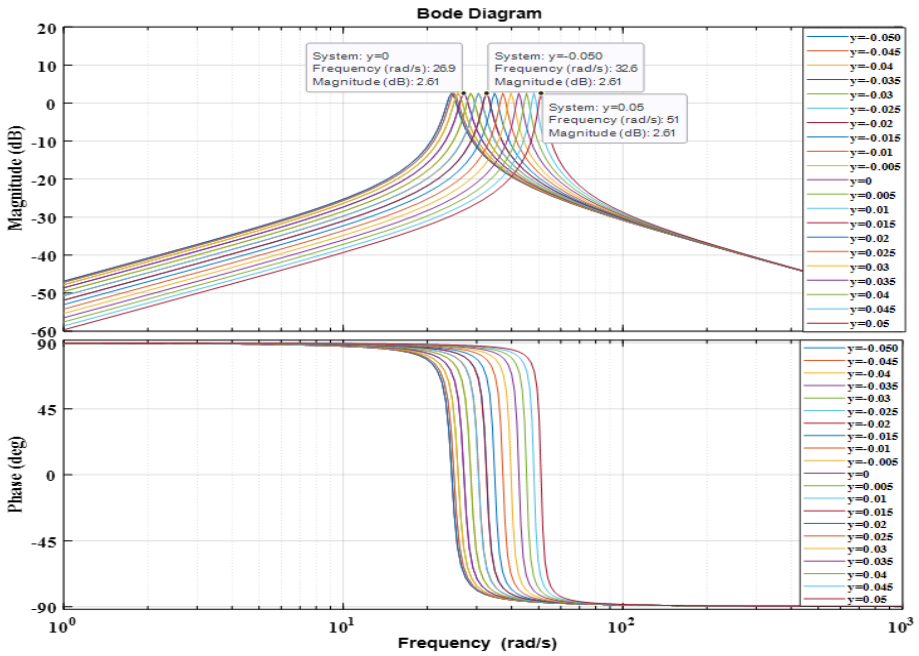

Figure 4.26: Frequency response of the system when floating magnet moved 50 mm toward top magnet and 50 mm toward bottom magnet from the equilibrium position (3rd order polynomial model)

The legend y in Figure 4.26 is the position of the floating magnet from the equilibrium position. In the legend y=0 means the floating magnet is in equilibrium position. In legend y=-0.05 means the position of the floating magnet is 50 mm away from the equilibrium position toward top magnet. The position of the floating magnet 50 mm away from the equilibrium position toward bottom magnet is

presented in legend as y=0.05. The analytically calculated average natural frequency for this test rig setup (total length of the oscillator is 222 mm) is 32.66 rad/s which is almost similar to the experimentally measured (log-decrement) natural frequency of 32.35 rad/s. Moreover, both eigenvalues' real numbers are negative and therefore the model is stable. The damping ratio can be found using the formula

$$\zeta_i = Re(\lambda_i)/\sqrt{Re(\lambda_i)^2 + Im(\lambda_i)^2} \qquad (4.29)$$

The calculated average damping ratio is 0.032 when the total length of the oscillator is 222 mm which is almost similar to the experimentally measured damping ratio of 0.031. The linear and nonlinear coefficients of the magnetic spring system change with the changing of the excitation position of the floating magnet. When the floating magnet moved 5 mm towards the top magnet and 5 mm towards the bottom magnet from the equilibrium position, the k_1, k_2 and k_3 values changed to 307.35 N/m, 819.63 N/m^2 and 1×10^6 N/m^3, respectively. The eigenvalues and frequency response are presented in Figure 4.27 and Figure 4.28, respectively.

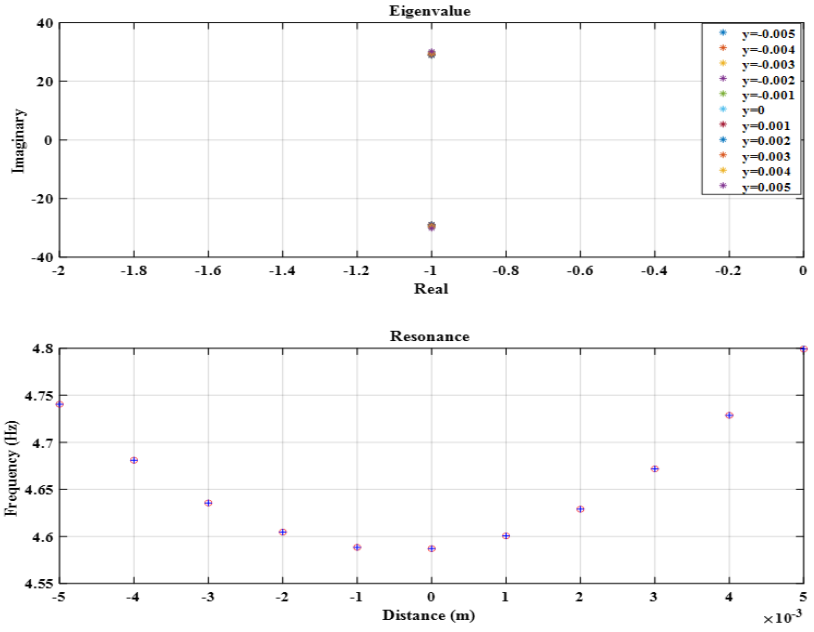

Figure 4.27: Eigenvalue when floating magnet moved 5 mm toward top magnet and 5 mm toward bottom magnet from the equilibrium position (3rd order polynomial model)

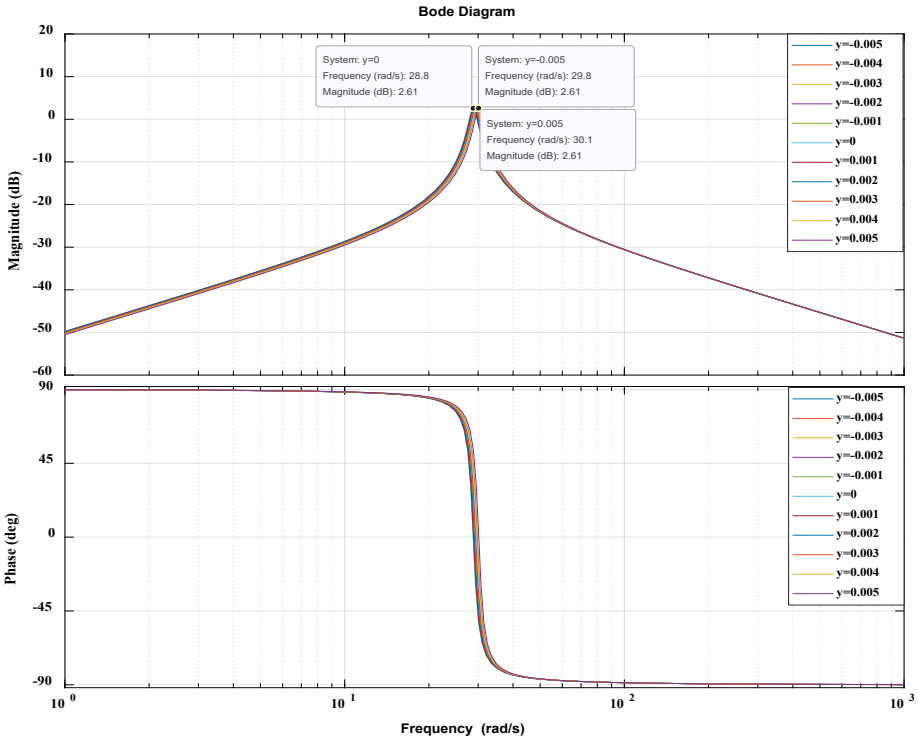

Figure 4.28: Frequency response of the system when floating magnet moved 5 mm toward top magnet and 5 mm toward bottom magnet from the equilibrium position (3rd order polynomial model)

The imaginary parts of the eigenvalues and natural frequencies decrease steadily until 5 mm when the floating magnet moved towards the top magnet, and it rose steadily until the end (5 mm) when the floating magnet moved toward the bottom magnet. Figure 4.29 presents the resulting eigenvalues and frequencies for different ranges of excitation of the floating magnet. The measured eigenvalues are $\lambda_{i=1\ to\ 4}$ = -1.0000 +28.8041i, 0, 0, -1.0000-28.8041i when the floating magnet is in the expected equilibrium position (0mm) and the natural frequency is 28.8214 rad/s or 4.5893 Hz. The resulting eigenvalues and frequency are $\lambda_{i=1\ to\ 4}$ =-1.0000 +29.7686i, 0, 0 and -1.0000+29.7686i and 29.7854 rad/s, respectively, when the position of the floating magnet is 5 mm towards the top magnet. Furthermore, the measured eigenvalues and frequencies are $\lambda_{i=1\ to\ 4}$ = -1.0000 +30.1383i, 0, 0, -1.0000 -30.1383i and 30.1549 rad/s when the position of the floating magnet is 5 mm towards bottom magnet.

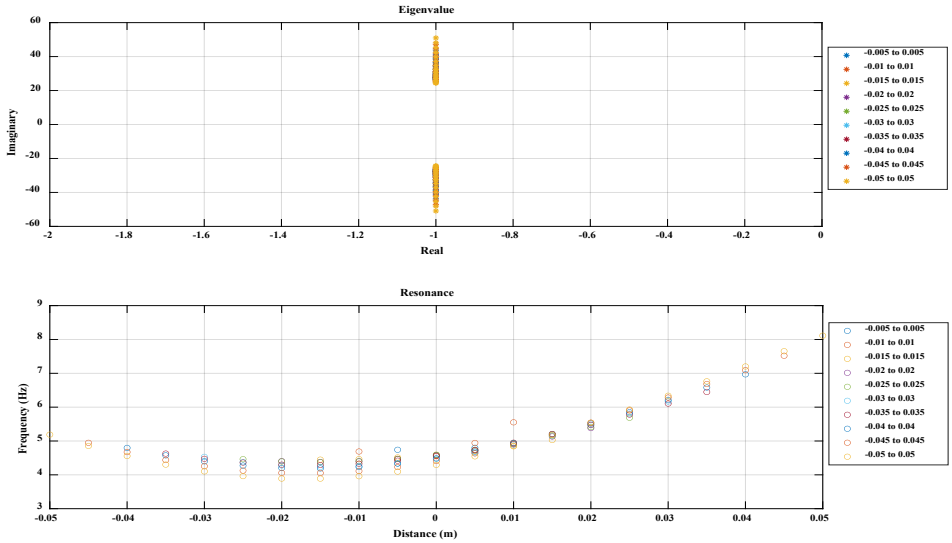

Figure 4.29: Eigenvalues and frequency response for different positions of the floating magnet (3rd order polynomial model)

The legends in Figure 4.29 present the excitation ranges of the floating magnet. The variable -0.005 to 0.005 in the legend is indicated that the floating magnet moved 5mm toward the top magnet and 5mm toward the bottom magnet from the equilibrium position. From Figure 4.29 it can be seen that the real parts of the eigenvalues stayed constant for all excitation ranges of the floating magnet, but the imaginary parts of the eigenvalues changed with the changing of the excitation ranges of the floating magnet.

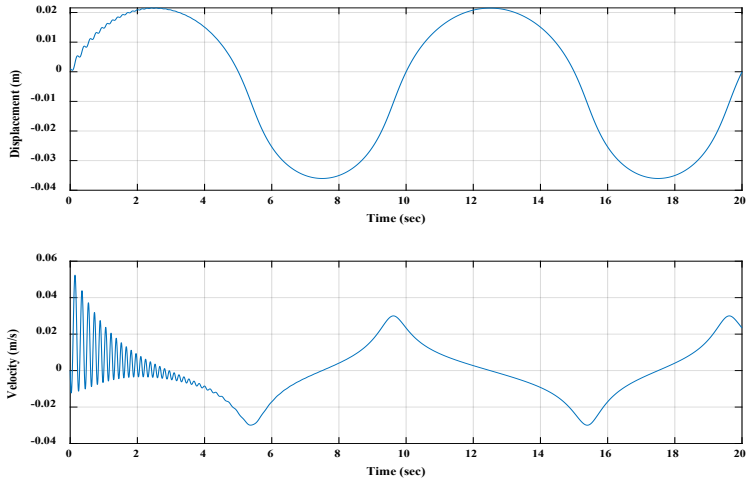

Figure 4.30: Displacement and velocity of the floating magnet under harmonic force

Moreover, the resulting frequency responses for all excitation ranges are closer to each other. If an external force is applied to the floating magnet, then the displacement and velocity of the magnet are shown in Figure 4.30. The amplitude of the applied external harmonic force (F_b) is 10N and the frequency (f) is 0.1 Hz. Moreover, the values of M, β, k_1, k_2 and k_3 are 0.37 Kg, 0.74 Ns/m, 269.31 N/m, 5680.4 N/m^2 and 163159 N/m^3 respectively. The ode23t solver has been used in MATLAB to find the displacement and velocity of the floating magnet. The excitation of the floating magnet was assumed to have the initial displacement $y = 0$ and its corresponding velocity $\dot{y} = 0$. The frequency of the harmonic force was 0.1 Hz. As expected, the displacement and the velocity were sinusoidal and were 90° out of phase with one another. The amplitude of displacement was around 20 mm toward the bottom magnet and about 30 mm toward the top magnet. This confirms the amplitude of the displacement signal, as shown in Figure 4.30. Moreover, the velocity vs displacement graph of the floating magnet under this harmonic force has been presented in Figure 4.31 as well.

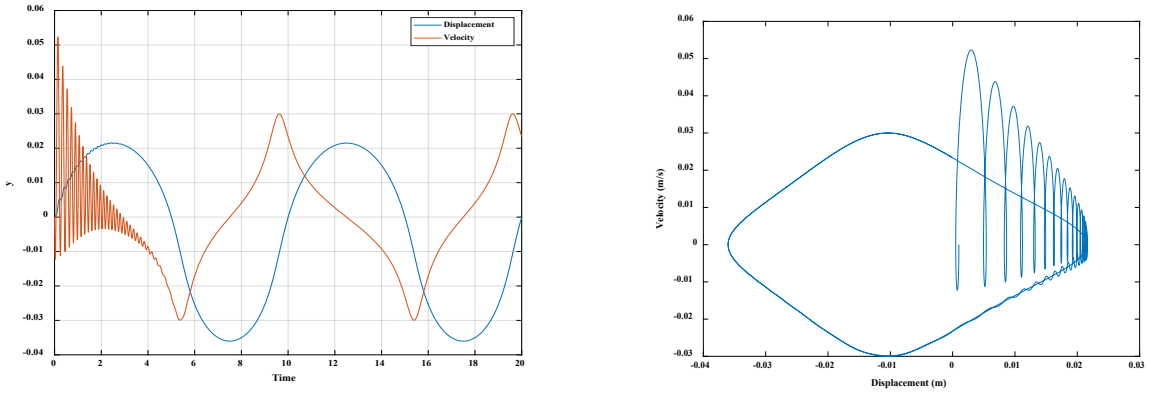

(a) (b)

Figure 4.31: (a) Displacement and velocity of the floating magnet under harmonic force (b) Displacement vs velocity

From Figure 4.31 it can be seen that at the beginning of the middle magnet's movement under the harmonic force, it creates some noises and became smooth after that.

4.6.1.2 Investigation of 5th order polynomial model

To analyse the proposed model, the 5th order polynomial model also has been used. The change of linear and nonlinear magnetic spring coefficients with the changes of the excitation position of the

floating magnet have presented in Table 4.8. When the floating magnet moved 50 mm away from equilibrium position towards the top and bottom magnets, then the measured linear and nonlinear magnetic spring coefficients k_1, k_2, k_3, k_4 and k_5, are 309.43 (N/m), 2925.5(N/m^2), 107874 (N/m^3), $1 \times 10\text{^}6$ (N/m^4) and $2 \times 10\text{^}7$ (N/m^5), respectively. From Table 4.8 it can be seen that all coefficients change with the changing of the position of the floating magnet. To determine the eigenvalues and frequency responses, the theoretical simulation of the system was run by MATLAB code using the values of M, β, k_1, k_2, k_3, k_4 and k_5 are 0.37 Kg (including plastic bush), 0.74 Ns/m, 309.43 (N/m), 2925.5 (N/m^2), 107874 (N/m^3), $1 \times 10\text{^}6$ (N/m^4) and $2 \times 10\text{^}7$ (N/m^5), respectively. The simulation results of the system are displayed in Table 4.9. When the floating magnet moved 50 mm away from the equilibrium position towards the top magnet (-50 mm), the resulting eigenvalues are $\lambda_{i=1\ to\ 4}$ = -1.0000 +34.1883i, 0, 0 and -1.0000-34.1883i.

Table 4.8: Magnetic spring coefficients for different excitation ranges (5th order polynomial model)

Excitation (mm)	Coefficients				
	k_1 (N/m)	k_2 (N/m^2)	k_3 (N/m^3)	k_4 (N/m^4)	k_5 (N/m^5)
-5 to 5	309.69	-2590.6	874377	1×10^8	1×10^{10}
-10 to 10	308.93	2512	592100	4×10^7	2×10^9
-15 to 15	307.58	563.72	124094	9×10^6	-2×10^8
-20 to 20	311.63	351.21	72167	8×10^6	9×10^7
-25 to 25	309.88	2675.1	80123	2×10^6	6×10^7
-30 to 30	312.56	2286	64796	2×10^6	7×10^7
-35 to 35	311.04	2965.8	106608	1×10^6	1×10^7
-40 to 40	310.04	3102.3	106234	1×10^6	2×10^7
-45 to 45	314.25	2916.7	94869	1×10^6	2×10^7
-50 to 50	309.43	2925.5	107874	1×10^6	2×10^7

When the middle magnet started moving from the equilibrium position towards the top magnet due to the gravitational effects, the eigenvalues (imaginary parts) and frequencies initially decreased with the changing of the position until 16 mm and then started increasing until the last position of the magnet. The measured minimum eigenvalues and frequencies at 16 mm away from the equilibrium position towards the top magnet are -1.0000 +27.8550i, 0, 0, -1.0000 -27.8550i and 27.8729 rad/s. When the position of the floating magnet was 50 mm away from the equilibrium position (0 mm) towards the bottom magnet (+50 mm), the resulting eigenvalues are $\lambda_{i=1\ to\ 4}$ = -1.0000+51.3341i, 0,

0 and -1.0000-51.3341i, as presented in Table 4.9. The eigenvalues (imaginary parts) and frequencies steadily increased until the end of the excitation ranges when the middle magnet moved toward the bottom magnet. The resulting eigenvalues found are $\lambda_{i=1\ to\ 4}$ = -1.0000 +28.9015i, 0, 0 and -1.0000 -28.9015i when the magnet is in its equilibrium position (0mm). The calculated (theoretical) eigenvalues and frequency are -1.00 +28.9015i, 0, 0 and -1.00 -28.9015i and 28.9188 rad/s when the position of the floating magnet is 0 mm (equilibrium position). Moreover, with the changing of the position of the floating magnet, the frequency of the oscillator changes, as shown in Table 4.9.

Table 4.9: Eigenvalue when floating magnet moved 50 mm toward top magnet and 50 mm toward bottom magnet from the equilibrium position (5th order polynomial model)

Position of the floating magnet	Eigenvalues	Natural Frequency (rad/s)
-50 mm	-1.0000 +34.1883i	34.20
-45 mm	-1.0000 +32.3304i	32.34
-40 mm	-1.0000 +30.8369i	30.85
-35 mm	-1.0000 +29.6808i	29.69
-30 mm	-1.0000 +28.8323i	28.84
-25 mm	-1.0000 +28.2619i	28.27
-20 mm	-1.0000 +27.9430i	27.96
-15 mm	-1.0000 +27.8552i	27.87
-10 mm	-1.0000 +27.9861i	28.00
-05 mm	-1.0000 +28.3328i	28.35
0 mm	-1.0000 +28.9015i	28.91
05 mm	-1.0000 +29.7068i	29.72
10 mm	-1.0000 +30.7695i	30.78
15 mm	-1.0000 +32.1147i	32.13
20 mm	-1.0000 +33.7687i	33.78
25 mm	-1.0000 +35.7565i	35.77
30 mm	-1.0000 +38.1006i	38.11
35 mm	-1.0000 +40.8188i	40.83
40 mm	-1.0000 +43.9249i	43.93
45 mm	-1.0000 +47.4282i	47.43
50 mm	-1.0000 +51.3341i	51.34

The calculated natural frequencies for -50 mm, 0 mm and +50 mm position of the floating magnet are $34.2029\,rad/s$, $28.9188\,rad/s$ and $51.3438\ rad/s$, respectively which are close to the

measured frequency obtained by the MATLAB Bode comments, as shown in Figure 4.32. The eigenvalues and frequency responses are analysed for different excitation ranges which can be seen in Figure 4.33.

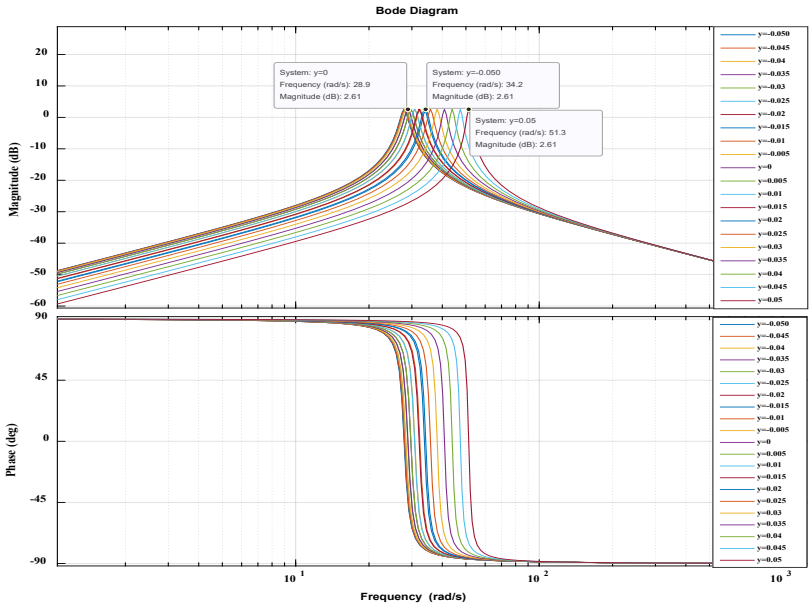

Figure 4.32: Frequency response of the system when floating magnet moved 50 mm toward top magnet and 50 mm toward bottom magnet from the equilibrium position (5th order polynomial model)

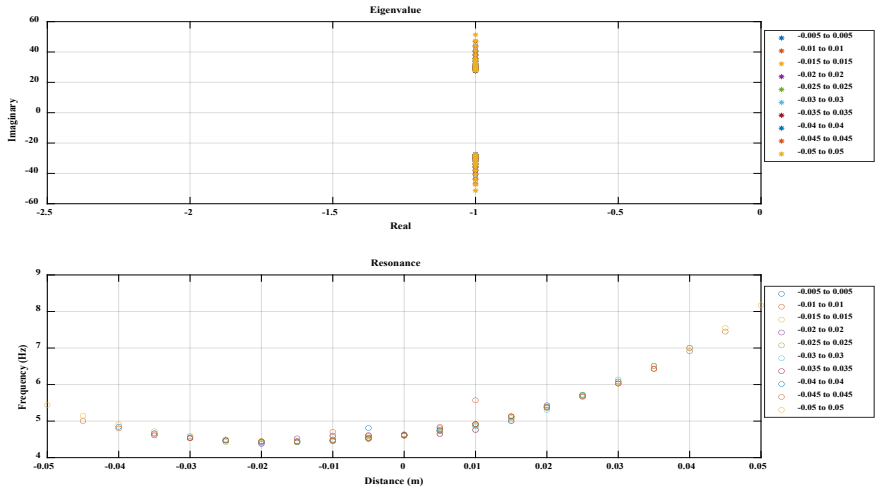

Figure 4.33: Eigenvalues and frequency response for different excitation ranges (5th order polynomial model).

The analytical average natural frequency and damping ratio for this test rig setup (total length of the oscillator 222 mm) are 33.77 rad/s and 0.0306, respectively. Moreover, both eigenvalues' real numbers are negative and therefore the model is stable. The legends in Figure 4.33 present the excitation ranges of the floating magnet. The variable -0.05 to 0.05 in the legend is indicated that the floating magnet moved 50mm toward the top magnet and 50mm toward the bottom magnet from the equilibrium position. It can be seen from Figure 4.33 that the frequency responses fluctuated for all excitation ranges (small excitation ranges) nearby equilibrium position but the frequencies are similar when the moving magnet goes away far from the equilibrium position toward the top and bottom magnets. Figure 4.34 presents the displacement and velocity of the floating magnet after the applied harmonic force, where the amplitude of the force and frequency are 10N and 0.1 Hz, respectively.

Moreover, the used values of M, β, k_1, k_2, k_3, k_4 and k_5 were 0.37 Kg, 0.74 Ns/m, 309.43 (N/m), 2925.5 (N/m^2), 107874 (N/m^3), $1 \times 10\text{^}6$ (N/m^4) and $2 \times 10\text{^}7$ (N/m^5), respectively. To find the displacement and velocity of the moving magnet the ode23t solver has been used in MATLAB. The excitation of the moving magnet is assumed to have the initial displacement ($y = 0$) and its corresponding velocity ($\dot{y} = 0$). Compared to the 3rd order polynomial model, the 5th order polynomial model gives better results. Furthermore, the velocity vs displacement graph of the floating magnet under the same harmonic force has been displayed in Figure 4.35(b) as well.

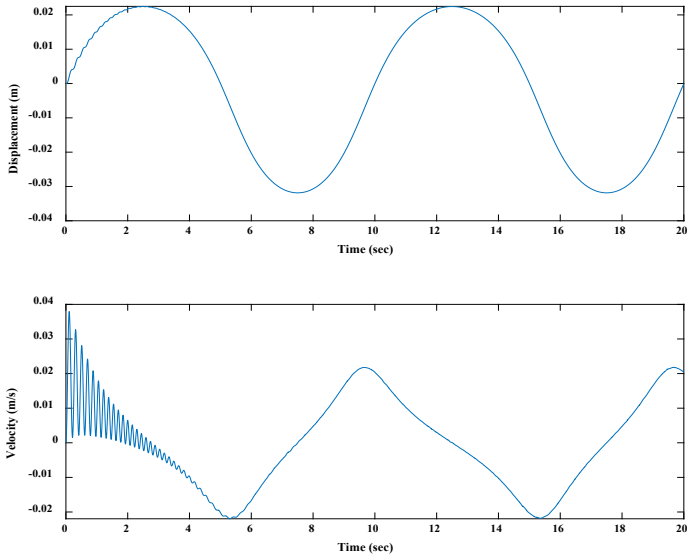

Figure 4.34: Displacement and velocity of the floating magnet under harmonic force (5th order polynomial model)

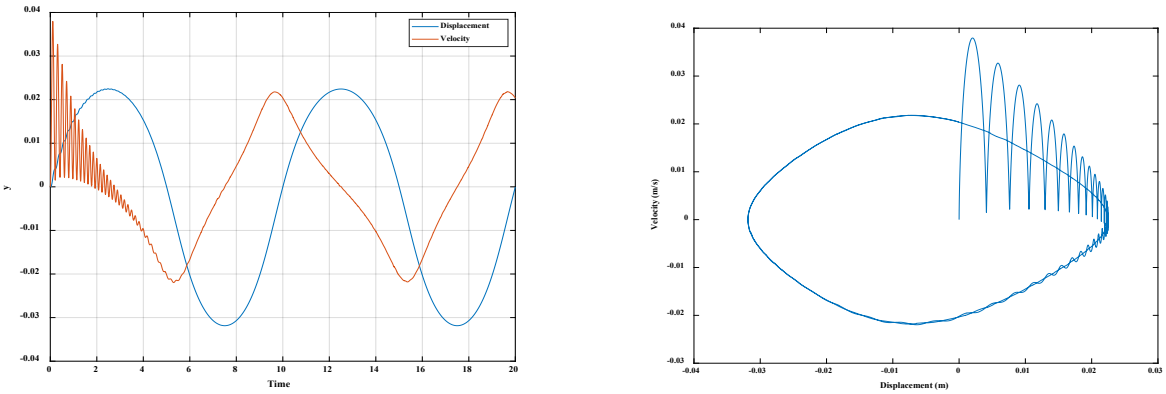

(a) (b)

Figure 4.35: (a) Displacement and velocity of the floating magnet under harmonic force (b) Displacement vs velocity

At the beginning of the middle magnet's movement under the same harmonic force, it creates some noise as well, like the 3rd order polynomial model which can be seen in Figure 4.35.

4.7 Model Analysis of the Nonlinear Oscillator System for Different Positions of the Top Fixed Magnet

The eigenvalues and frequencies have been analysed for different positions of the top fixed magnet. The values of damping constant, linear and nonlinear constant have been taken from Table 4.5 to determine the eigenvalues and natural frequencies. All linear and nonlinear values have been used here for -50 mm to 50 mm excitation ranges. The eigenvalues and frequency responses have been measured by using the theoretical 3rd order polynomial curve fitting's data. As seen from Table 4.5, the increases in the damping ratio mean the damping constant increases when the total length of the oscillator decreases and the damping constant declines when the total length of the oscillator rises. Therefore, it can be said that the system becomes more unstable when the total length of the oscillator increases. To check these findings the eigenvalues of the system have been measured as shown in Figure 4.36. The real parts of the eigenvalues are always -1 for different positions of the floating magnet when the total length of the oscillator is 222 mm (considered equilibrium position means 0 mm position of the top mixed magnet). The real parts of the eigenvalues increase on the negative side when the top fixed magnet moves toward the middle magnet (decreases the total length of the oscillator) from 0 mm position (222 mm, equilibrium position for this particular magnet setup), as seen in the Figure 4.36.

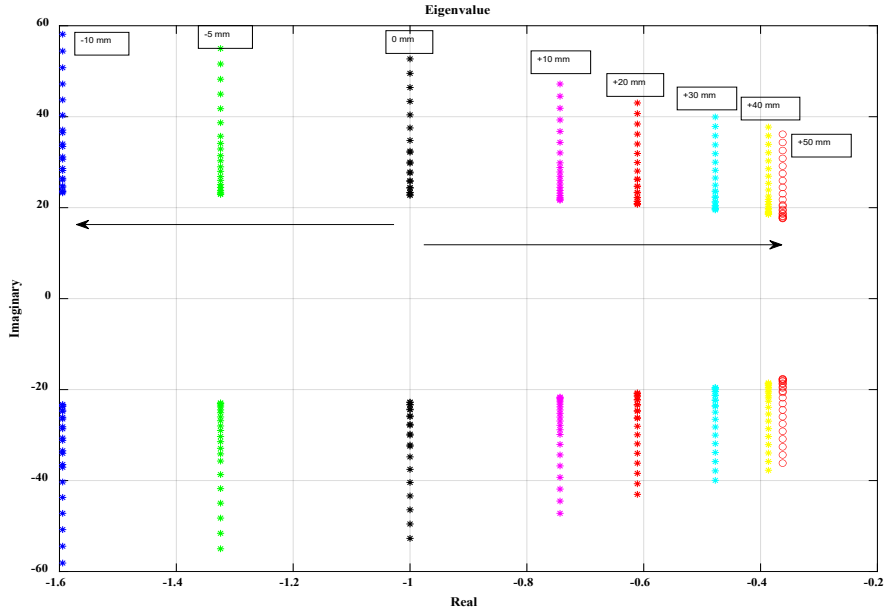

Figure 4.36: Eigenvalues for different positions of the top fixed magnet

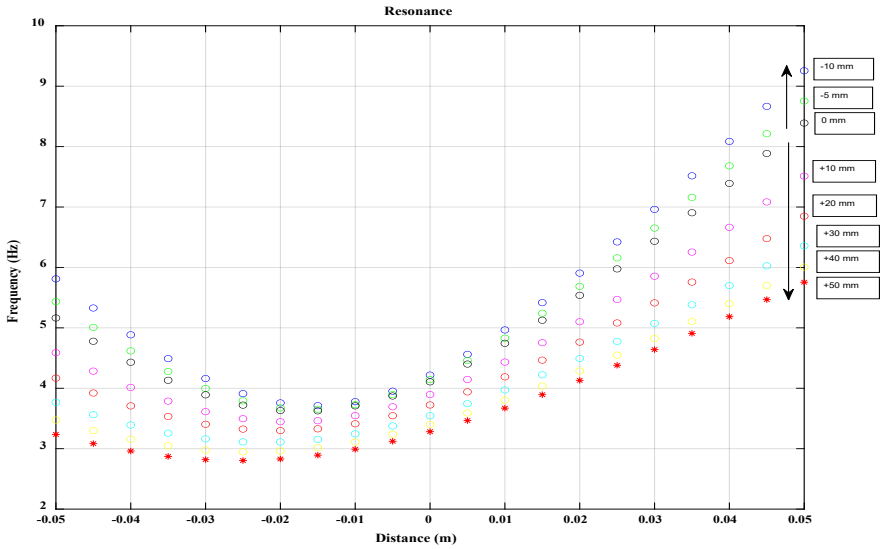

Figure 4.37: Frequency response for different positions of the top fixed magnet

On the other hand, when the top fixed magnet moves away from the 0 mm position, then the real parts of the eigenvalues decrease on the negative side and come close to zero in the scale. The system becomes more stable when the top fixed magnet moves toward the middle magnet (decreases the total length of the oscillator) and it becomes more unstable when the top fixed magnet moves away continuously from the equilibrium position. Figure 4.37 displays the frequency responses of the

system for the different total lengths of the oscillator (different positions of the top fixed magnet). Moreover, Figure 4.37 shows that the natural frequency increases when the top fixed magnet moves toward the middle magnet and decreases when it moves away from the middle magnet. The model has been analysed by using the same harmonic force with changing the position of the top fixed magnet. The amplitude of the harmonic force is 10 N and the frequency is 0.1 Hz. The values of the linear, nonlinear constants and damping ratios have been taken from Table 4.4 and Table 4.5. The excitation of the moving magnet is assumed to have the initial displacement ($y = 0$) and its corresponding velocity ($\dot{y} = 0$).

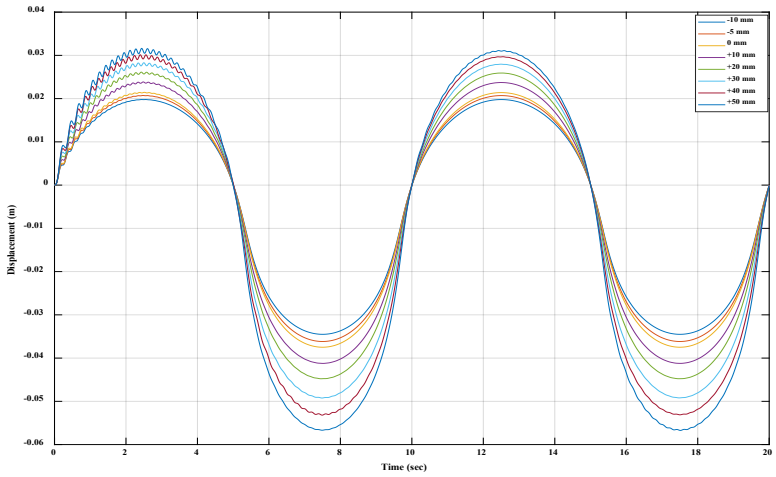

Figure 4.38: Displacement of the floating magnet under the different positions of the top fixed magnet

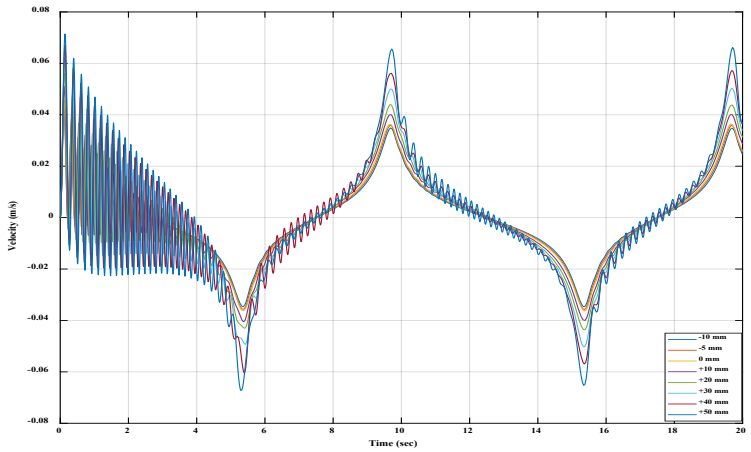

Figure 4.39: Velocity of the floating magnet under the different positions of the top fixed magnet

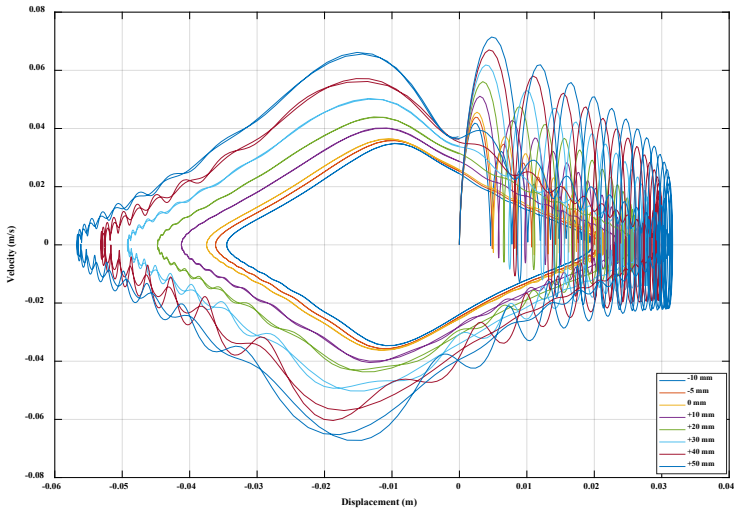

Figure 4.40: Velocity and displacement of the floating magnet under the different positions of the top fixed magnet

Moreover, the displacement vs time and velocity vs time graphs of the floating magnet under the different positions of the top fixed magnet have been presented in Figure 4.38 and Figure 4.39, respectively. The displacement and velocity of the floating magnet increase under the same harmonic force when the total length of the oscillator increases and decreases with decreasing the total length of the oscillator, as seen in Figure 4.38 and Figure 4.39. Figure 4.40 presents the velocity vs displacement graph. It can be seen from Figure 4.40 that the displacement, as well as the velocity of the floating magnet, increases with the increasing of the total length of the oscillator under the same externally applied harmonic force. Therefore, it can be said that the displacement and velocity of the floating magnet can be changed with the changing of the position of the floating magnet.

4.8 Linearization of the Magnetic Spring-based Nonlinear System

For a better understanding of magnetic spring based nonlinear system, the nonlinear system can be linearised. It has been considered that in the equilibrium position, the velocity and the applied harmonic force are zero. The nonlinear oscillator's state space model has been linearized by using the following method.

$$U_{1e} = 0 \qquad (4.30)$$

$$Z_{2e} = 0 \qquad (4.31)$$

$$0 = \frac{1}{M}\left(u_e - \beta Z_{2e} - kZ_{1e} - k_2 {Z_{1e}}^2 - k_3 {Z_{1e}}^3\right) \quad (4.32)$$

$$0 = \frac{1}{M}\left(-kZ_{1e} - k_2 {Z_{1e}}^2 - k_3 {Z_{1e}}^3\right) \quad (4.33)$$

$$0 = \frac{1}{M}\left(-k - k_2 Z_{1e} - k_3 {Z_{1e}}^2\right) Z_{1e} \quad (4.34)$$

$$0 = -k - k_2 Z_{1e} - k_3 {Z_{1e}}^2 \ , \ Z_{1e} = 0 \quad (4.35)$$

$$k_3 {Z_{1e}}^2 + k_2 Z_{1e} + k = 0 \quad (4.36)$$

$$Z_{1e} = \frac{-k_2 \pm \sqrt{{k_2}^2 - 4k_3 k}}{2k_3} \quad (4.37)$$

The value of the Z_{1e} at equilibrium position are $Z_{1e} = 0$ and $Z_{1e} = \frac{-k_2 \pm \sqrt{{k_2}^2 - 4k_3 k}}{2k_3}$. The linearized model can be stated as,

$$Z_1 = Z_{1e} + \delta Z_1 \quad (4.38)$$

$$Z_2 = Z_{2e} + \delta Z_2 \quad (4.39)$$

$$U_1 = U_{1e} + \delta U_1 \quad (4.40)$$

$$\delta \dot{Z}_1 = \delta Z_2 \quad (4.41)$$

$$\dot{Z}_2 = \frac{1}{M}\left(U_1 - \beta Z_2 - kZ_1 - k_2 {Z_1}^2 - k_3 {Z_1}^3\right) \quad (4.42)$$

$$\delta \dot{Z}_2 = f(Z_{1e}, Z_{2e}, U_{1e}) + \frac{1}{M}\left(-k - 2k_2 Z_{1e} - 3k_3 {Z_{1e}}^2\right)\delta Z_1 + \frac{1}{M}(-\beta)\delta Z_2 \quad (4.43)$$

$$f(Z_{1e}, Z_{2e}, U_{1e}) = 0 \quad (4.44)$$

When $Z_{1e} = 0$ then the state space model can be expressed as

$$\begin{bmatrix} \delta \dot{Z}_1 \\ \delta \dot{Z}_2 \end{bmatrix} = \begin{bmatrix} 0 & 1 \\ \frac{-k}{M} & \frac{-\beta}{M} \end{bmatrix} \begin{bmatrix} \delta Z_1 \\ \delta Z_2 \end{bmatrix} + \begin{bmatrix} 0 \\ 1 \end{bmatrix} [\delta U_1] \quad (4.45)$$

$$X = \begin{bmatrix} 1 & 0 \\ 0 & 1 \end{bmatrix} \begin{bmatrix} \delta Z_1 \\ \delta Z_2 \end{bmatrix} + [0][\delta U_1] \quad (4.46)$$

The theoretical simulation (3rd order polynomial model) of the system was run by MATLAB code using the values of M, β, and k are 0.37 Kg, 0.74 Ns/m and 269.31 N/m, respectively. The eigenvalues of the system are shown in Figure 4.41.

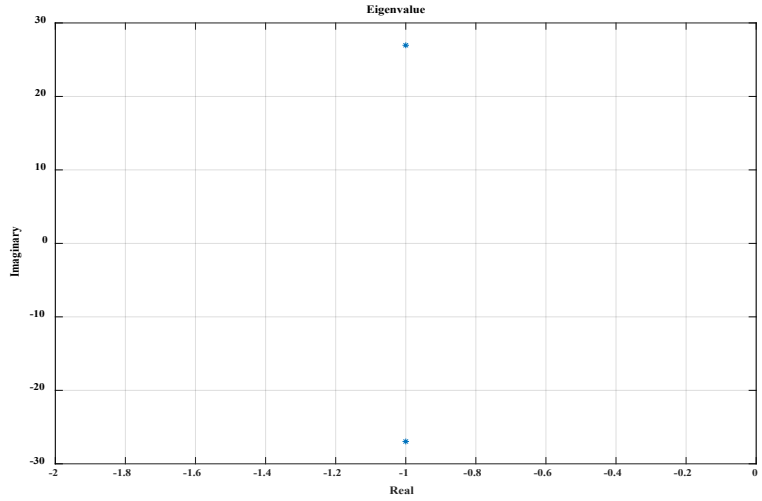

Figure 4.41: Eigenvalues of the linearized system (3rd order polynomial model)

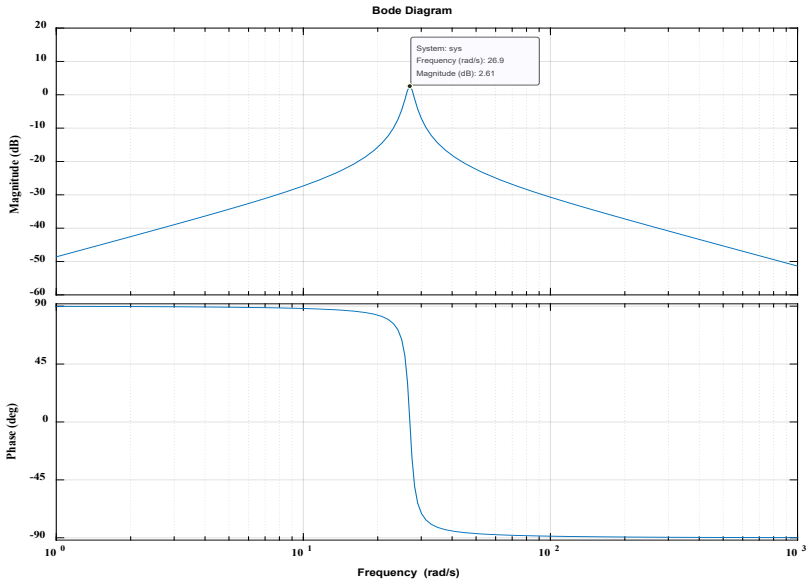

Figure 4.42: Frequency response of the linearized system (3rd order polynomial model)

The measured eigenvalues were -1.0000 +26.9604i,0,0 and -1.0000 -26.9604i. The measured frequency response was 26.9789 rad/s, which is similar to the nonlinear model's measured frequency (26.9790 rad/s) when the floating magnet was in equilibrium position. Moreover, the measured damping ratio is 0.037 which is closer to the experimentally calculated damping ratio (0.031). The calculated (theoretical) eigenvalues were -1.0000 +26.9604i and -1.0000-26.9604i which are similar to measured eigenvalues when the position of the floating magnet was 0 mm (equilibrium position).

Figure 4.42 presents the frequency response of the linearized system. On the other hand, if $Z_{1e} = \frac{-k_2+\sqrt{{k_2}^2-4k_3k}}{2k_3}$ then the state space model can be stated as,

$$\begin{bmatrix}\delta\dot{Z}_1\\ \delta\dot{Z}_2\end{bmatrix} = \begin{bmatrix} 0 & 1 \\ \frac{1}{M}\left(2k - \frac{{k_2}^2}{2k_3} - \left(1-\frac{3k_2}{2}\right)\frac{\sqrt{{k_2}^2-4k_3k}}{k_3}\right) & \frac{-\beta}{M}\end{bmatrix}\begin{bmatrix}\delta Z_1\\ \delta Z_2\end{bmatrix} + \begin{bmatrix}0\\1\end{bmatrix}[\delta U_1] \quad (4.47)$$

$$X = \begin{bmatrix}1 & 0\\ 0 & 1\end{bmatrix}\begin{bmatrix}\delta Z_1\\ \delta Z_2\end{bmatrix} + [0][\delta U_1] \quad (4.48)$$

Moreover, when $Z_{1e} = \frac{-k_2-\sqrt{{k_2}^2-4k_2k}}{2k_3}$ then the state space model can be written as

$$\begin{bmatrix}\delta\dot{Z}_1\\ \delta\dot{Z}_2\end{bmatrix} = \begin{bmatrix} 0 & 1 \\ \frac{1}{M}\left(2k - \frac{{k_2}^2}{2k_3} + \left(1-\frac{3k_2}{2}\right)\frac{\sqrt{{k_2}^2-4k_3k}}{k_3}\right) & \frac{-\beta}{M}\end{bmatrix}\begin{bmatrix}\delta Z_1\\ \delta Z_2\end{bmatrix} + \begin{bmatrix}0\\1\end{bmatrix}[\delta U_1] \quad (4.49)$$

$$X = \begin{bmatrix}1 & 0\\ 0 & 1\end{bmatrix}\begin{bmatrix}\delta Z_1\\ \delta Z_2\end{bmatrix} + [0][\delta U_1] \quad (4.50)$$

Figure 4.43 and Figure 4.44 present the eigenvalues and frequency response when $Z_{1e} = \frac{-k_2\pm\sqrt{{k_2}^2-4k_3k}}{2k_3}$. The imaginary part of the measured eigenvalues and frequency responses are too high.

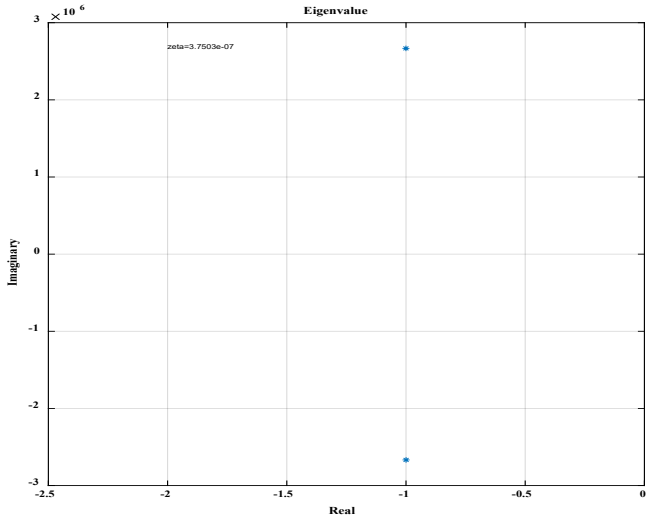

Figure 4.43: Eigenvalues of the linearized system (3rd order polynomial model)

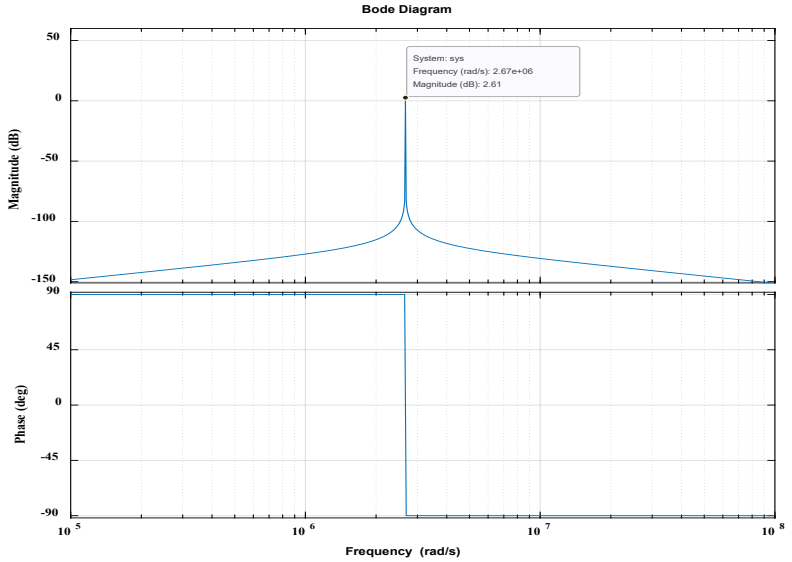

Figure 4.44: Frequency response of the linearized system (3rd order polynomial model)

Furthermore, the nonlinear and linear models of the oscillator (total length 222 mm) system have been compared with each other as shown in Figures 4.45, 4.46 and 4.47, respectively. The amplitude of the applied external harmonic force (Fb) is 10 N and the frequency (f) is 0.1 Hz. Moreover, the values of M, β, k_1, k_2 and k_3 are 0.37 Kg, 0.74 Ns/m, 269.31 N/m, 5680.4 N/m^2 and 163159 N/m^3 respectively.

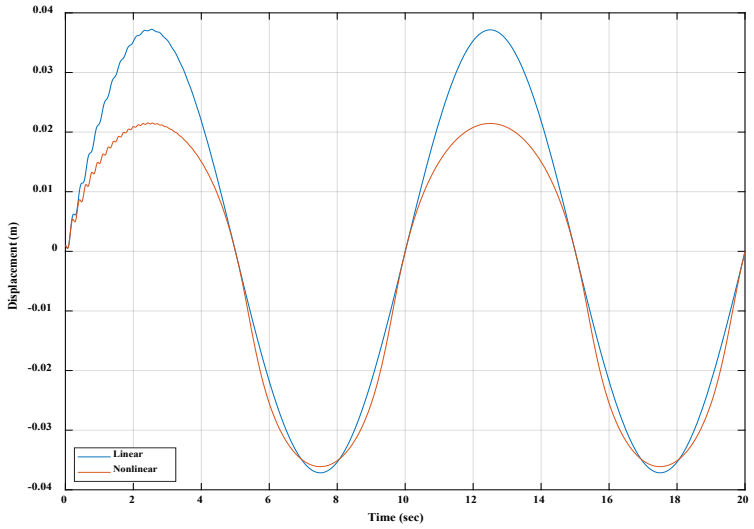

Figure 4.45: Displacement of the floating magnet for linear and nonlinear model analysis

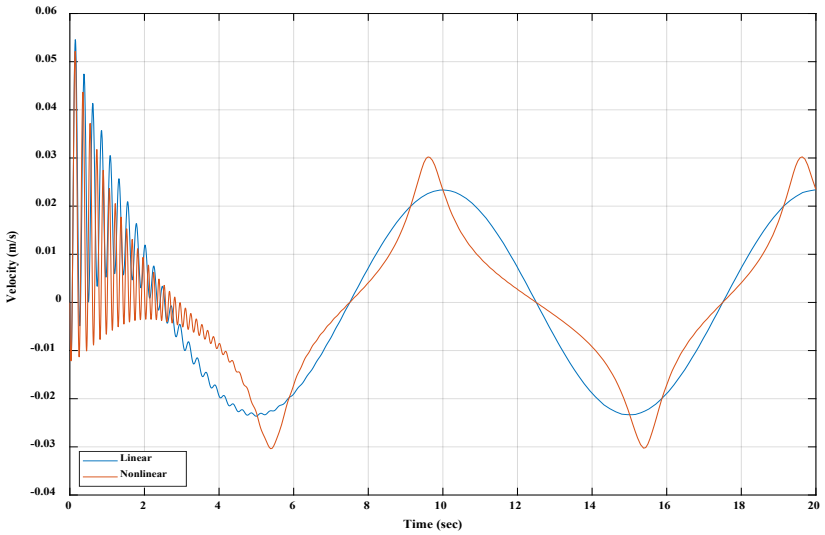

Figure 4.46: Velocity of the floating magnet for linear and nonlinear model analysis

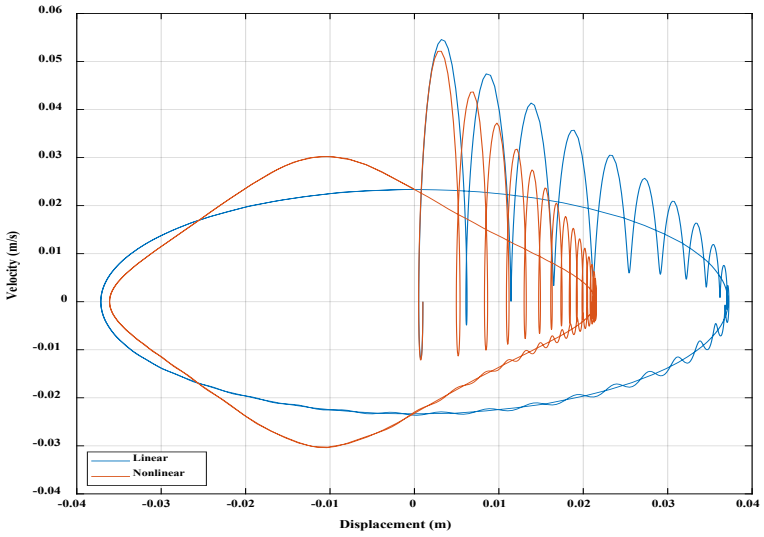

Figure 4.47: Velocity vs displacement

It can be seen from the above figures that the floating magnet creates higher displacement in the linearised model than the nonlinear model, but it achieves higher velocity in the nonlinear model than the linear model under the same external applied harmonic forces after the transient behaviour dies out. Therefore, the nonlinear model is more effective to generate a higher velocity of the floating magnet.

4.9 Conclusion

In this chapter, the characteristics of the magnetic spring based nonlinear system and dynamics of the system have been discussed and analysed using analytical, experimental and simulation methods. The proposed system's magnetic force and spring rates have been investigated numerically, theoretically, and experimentally. The experimentally measured magnetic restoring force has been validated by simulation and theoretical values. To analyse the nonlinear behaviour of the magnetic spring-based system and determine the coefficients from the modelled magnetic restoring force the cubic, quintic and 7^{th} order polynomial curve fitting models have been used. Moreover, how the gravitational force effect changes the equilibrium position of the magnetic spring-based system (vertical) have been studied. With the change of the position of the floating magnet, the linear and nonlinear coefficients of the system have been investigated. Based on this investigation the dynamics of the nonlinear system have been analysed. The gravitational effects on the equilibrium position are determined for the proposed system. It has been concluded that the separation distance between magnets has a significant influence on the vibration and output power. This parameter is capable of changing the system's nonlinear behaviour from hardening to softening. The position of the top fixed magnet has a great impact on the oscillator system which have been analysed as well by changing the position of the top fixed magnet. Finally, the linearised model of the nonlinear system has been investigated in this chapter. These investigations will help researchers to understand the magnetic properties of the magnetic spring, magnetic restoring forces and coefficients of the single-degree-of-freedom magnetic spring based nonlinear oscillator system.

Chapter 5

Dynamic Behaviours of Two-degree-of-freedom Magnetic Spring-based Nonlinear Oscillator System

In chapter 4, the single degree of freedom (SDOF) magnetic spring-based system and its dynamics were investigated. However, the SDOF magnetic spring-based system had only one degree of freedom and was limited to only one resonant frequency. Preferably, the energy generator should pick up and resonate at every frequency present in the vibration source. One can use two resonant frequencies and achieve maximum power by employing a two-degree-of-freedom (2DOF) oscillator system. The simplest form of a two-degree-of-freedom system has two magnet masses. This chapter deals with the 2DOF magnetic spring-based oscillator system and its behaviour concerning various design criteria. The study of the simple 2DOF system is a prerequisite to designing complex 2DOF magnetic spring-based wave energy convertor systems that will be discussed in Chapter 7 and Chapter 8. Therefore, this chapter aims to investigate the magnetic restoring forces and coefficients of the 2DOF magnetic spring-based system and analyse the dynamics of the system.

5.1 Design Configuration of the Two-degree-of-freedom Nonlinear Oscillator System

The two-degree-of-freedom nonlinear oscillator system consists of four permanent ring magnets (axially magnetised through the height of 13mm) and a circular aluminium shaft. To create a two-degree-of-freedom model, another magnet could be added to the top of the previous model discussed in chapter 3, or the top magnet (3rd magnet of the previous model) could be kept as a floating magnet aligned with the shaft. For the first concept, the 4th magnet is put on top of the 3rd magnet and fixed with the shaft and the 3rd magnet is kept as a floating magnet along with the 2nd magnet; hence, the 1st and 4th magnets are fixed with the shaft. The fixed magnets are attached to the end of the shaft, and their polarity is set in such a way that the repulsive force is created between the levitating magnet and the fixed magnets. The magnetic poles are oriented (NS-SN-NS-SN) to repel each other. The height and width of the test rig are 550 mm and 300 mm, respectively. Moreover, the height and diameter of the shaft are 550 mm and 12 mm, respectively. As presented in Figure 5.1, the test rig design initially shows that when the 2nd magnet is added from the bottom end to the setup before the 3rd magnet, the distance between the middle and bottom magnets is 104 mm. When the 3rd magnet is added, the distance between the 2nd and bottom magnet decreases to 79 mm due to the gravitational force, while the 3rd magnet and the floating 2nd magnet are separated by 104 mm. When the 4th

magnet is added, the distance between the 2nd magnet and bottom magnet is reduced to 68 mm, and the distance between the 3rd magnet and the floating 2nd magnet is decreased as well to 79 mm due to the gravitational force. In contrast, the 3rd floating magnet and the top fixed magnet are separated by 104 mm. The notable thing is that when the 4th magnet is added above the 3rd magnet, only the distance between the bottom magnet and the 2nd magnet is reduced to 68 mm, but other magnets remain the exact distances as in the SDOF system (total length 222 mm).

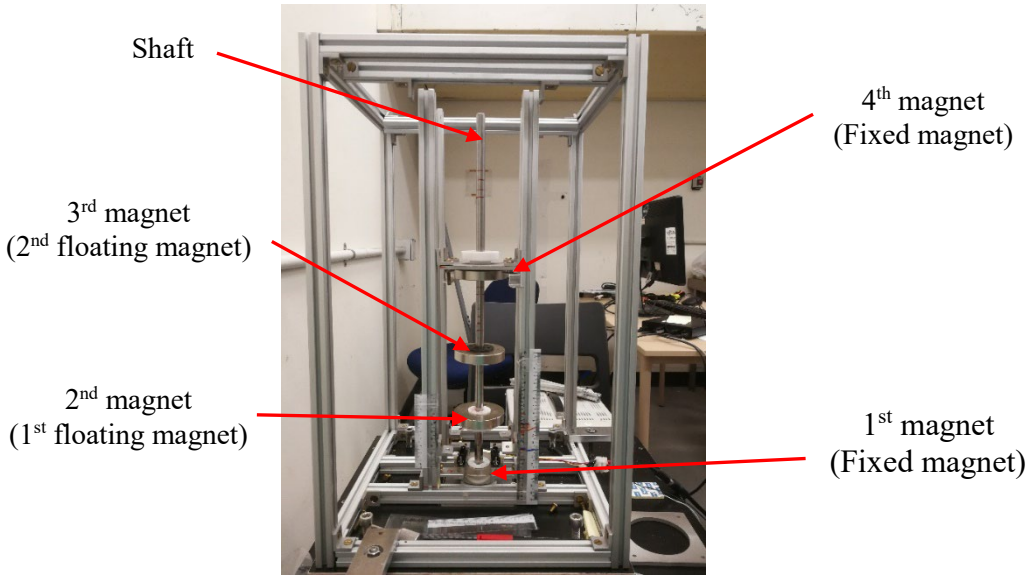

Figure 5.1: Test rig without winding coil

5.2 Magnetic Properties Analysis of the 2DOF System

Four (same size and shape) ring-type permanent magnets have been used to design the two-degree-of-freedom magnetic spring-based nonlinear oscillator system. The properties of the magnet have been presented in Table 3.1. Since the gravitational force affects the floating magnets by shifting them down from the centre position between the top (4th magnet) and bottom (1st magnet) magnet, the distances between the four magnets in the test rig design change to 68 mm between the 2nd magnet (1st floating magnet) and bottom magnets, 79 mm between 2nd magnet (1st floating magnet) and 3rd magnet (2nd floating magnet), and 104 mm between the 3rd magnet (2nd floating magnet) and top fixed magnets (4th magnet). The magnetic poles are oriented (NS-SN-NS-SN) to repel each other. The magnetic flux density on the magnets' surface and the magnetisation direction are displayed in Figure 5.2.

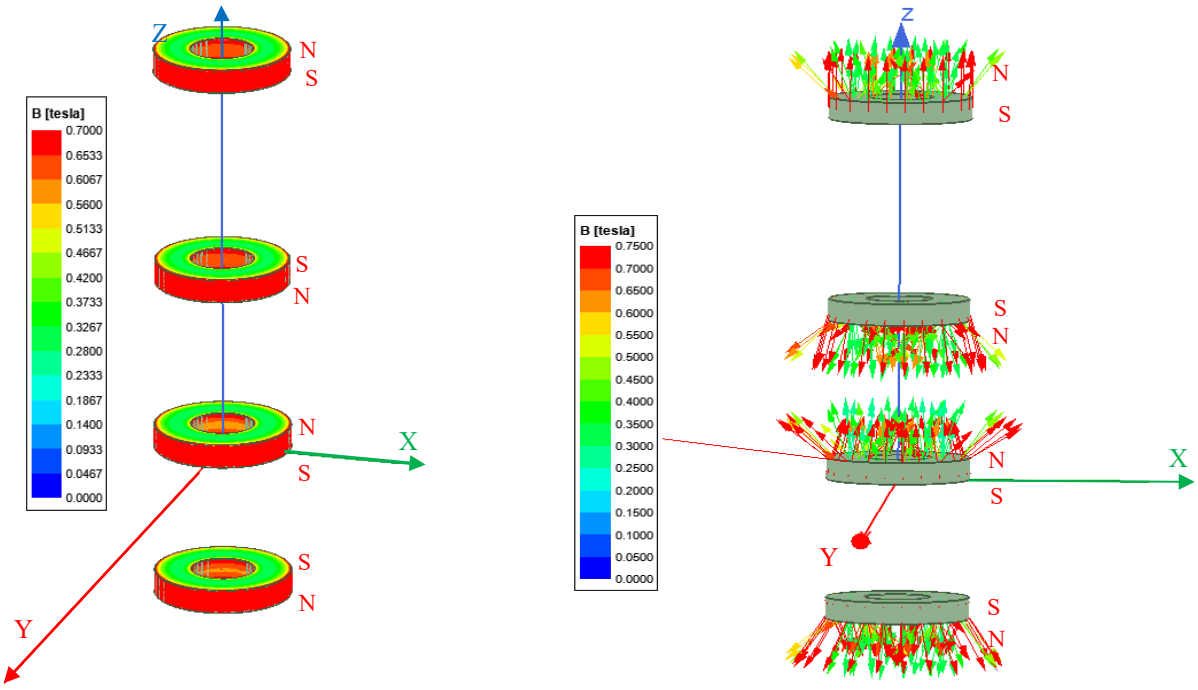

(a) (b)

Figure 5.2: (a) Magnetic flux density and (b) Magnetization direction

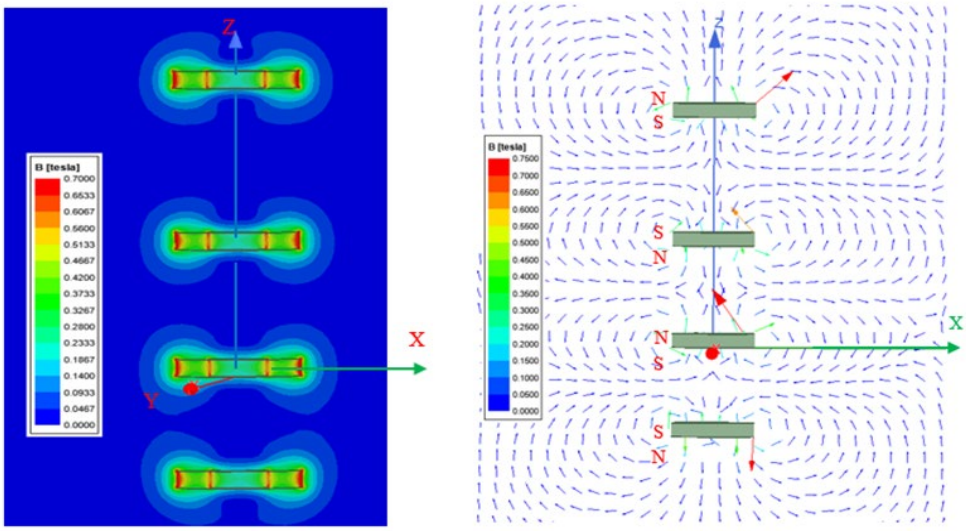

(a) (b)

Figure 5.3: (a) Mag_B in XZ plane and (b) B_Vector in XZ plane

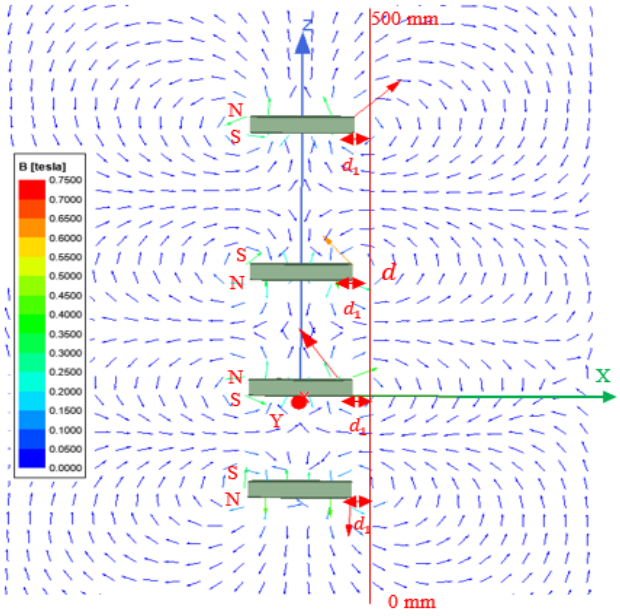

(a)

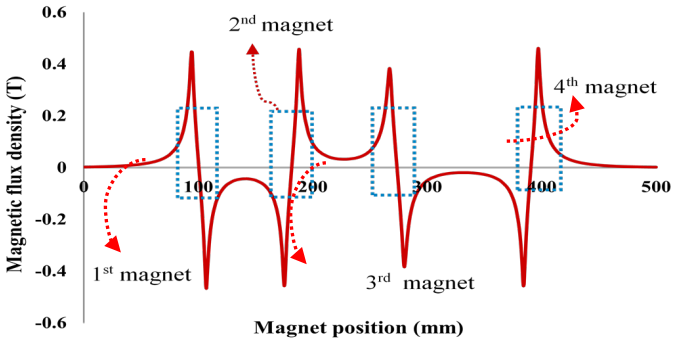

(b)

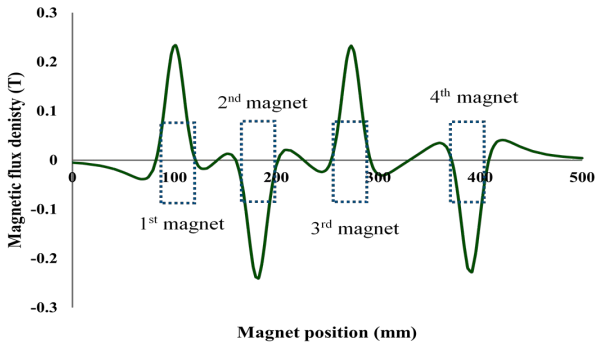

(c)

Figure 5.4: (a) Magnetic flux density (B_Vector) in XZ plane (b) Radial magnetic flux density and (c) Axial magnetic flux density

All magnets are axially magnetised (towards the North Pole), as shown in Figure 5.2(b). Figure 5.3 depicts the magnitude of the magnetic flux density. The magnetic field line is the closed loop curve in space traced out by following the direction in which the magnetic field vector points, as seen in Figure 5.3(b). The Z axis is considered to be the line through the centre of all the magnets. A line is considered perpendicular to the X-axis, which was 37mm from the centre line in the radial direction and parallel to the Z-axis, as shown in Figure 5.4, to measure the magnetic flux density in the axial and radial direction. The magnetic flux density is calculated for the system in the radial direction through the line d, which is 37mm (d_1) from the magnet stack. Due to the symmetry of the magnetic stack, going from $d = 0$ (sudden position below the 1st magnet) to $d = 500\ mm$ (sudden position in the upper part of the 4th magnet) shows the movement of the vertical arrows on one side is equivalent to the other side in Figure 5.3.

To help explain magnetic flux density behaviour change according to magnet pole's positions, the measured magnetic flux density in the axial and radial directions are displayed in Figure 5.4. The values of magnetic flux density in Figure 5.4(c) were taken along the axial direction at various positions in the centre line, and the values of magnetic flux density in Figure 5.4(b) were taken along the radial direction at different places in the line d which is d_1 distance away from the magnet's outer surface. The correct measurements of the magnetic flux density in both radial and axial directions are essential because they are responsible for the magnetic attractive or repulsive force and induced voltage inside the winding coils, if they were added to the system. The magnetic flux density of the vertical system is presented in a horizontal view. The magnetic flux density between the 1st and 2nd magnets is higher than the magnetic flux density between 2nd and 3rd magnets and between 3rd and 4th magnets as the distance between 1st and 2nd magnets are smaller than the other magnets' separation distances. The radial magnetic flux densities in the north pole are positive (+), and when the pole changes to the south poles, the radial magnetic flux densities become negative (-), which can be seen in Figure 5.4(b).

5.3 Magnetic Restoring Force of 2DOF

The magnetic poles of each magnet are oriented to repel the adjacent magnet, causing the floating magnets to be suspended with the nonlinear restoring force. The system's nonlinear behaviour allows the linear response to be modified by simply varying the position of the floating magnet between the top (4th magnet) and bottom (1st magnet) magnets. Figure 5.5 presents the schematic of the 2DOF

system. The magnetic force between the 1st magnet (fixed magnet) and 2nd magnet (floating magnet) can be written as,

$$F_b = \frac{\mu_0 Q_{1st} Q_{2nd}}{4\pi {r_b}^2} \quad (5.1)$$

where r_b is the distance between the 1st and 2nd magnet poles. Q_{1st} and Q_{2nd} are the magnetic field intensity of the 1st and 2nd magnet, respectively. The permeability of the air is μ_0. Similarly, equation 5.1 can be rewritten for the 2nd magnet (1st floating magnet from the bottom magnet) and 3rd magnet (2nd floating magnet) as,

$$F_m = \frac{\mu_0 Q_{2nd} Q_{3rd}}{4\pi {r_m}^2} \quad (5.2)$$

where r_m is the distance between the 2nd magnet and 3rd magnet poles. The equation 5.1 can be rewritten as well for the 3rd magnet (2nd floating magnet) and 4th magnet (top fixed magnet) as,

$$F_b = \frac{\mu_0 Q_{3rd} Q_{4th}}{4\pi {r_t}^2} \quad (5.3)$$

where r_t is the distance between the 3rd magnet and 4th magnet poles. For the case of in-plane movement, the expression for r_m and r_b can be written as

$$r_m = H_{s1} - (r_b + H_2) \quad (5.4)$$

Moreover, for the case of in-plane movement, the expression for r_m and r_t can be written as

$$r_t = H_{s2} - (r_m + H_3) \quad (5.5)$$

where H_{s1} is the distance between the upper surface of the bottom magnet and the lower surface of the 3rd magnet. On the other hand, H_{s2} is the between the upper surface of the 2nd magnet and the lower surface of the 4th magnet. H_1, H_2, $H_3$and H_4 are the heights of the 1st, 2nd, 3rd and 4th magnets, respectively. To determine the magnetic restoring force for the first moving magnet, the 2nd moving magnet is considered a fixed magnet. To measure the magnetic restoring force for the 2nd moving magnet, the 1st moving magnet is considered a fixed magnet. The distance y_2 represents the 1st moving magnet (2nd magnet), and the 2nd moving magnet (3rd magnet) is represented by the distance y_3, the

resultant magnetic forces or magnetic spring restoring forces (F_{res1} and F_{res2}) applied to the moving magnets can be calculated as,

$$F_{res1} = F_m - F_b = \frac{\mu_0 Q_{2nd}}{4\pi}\left(\frac{Q_{3rd}}{(r_m - y_2(t))^2} - \frac{Q_{1st}}{(r_b + y_2(t))^2}\right) \quad (5.6)$$

$$F_{res2} = F_t - F_m = \frac{\mu_0 Q_{3rd}}{4\pi}\left(\frac{Q_{4th}}{(r_t - y_3(t))^2} - \frac{Q_{2nd}}{(r_m + y_3(t))^2}\right) \quad (5.7)$$

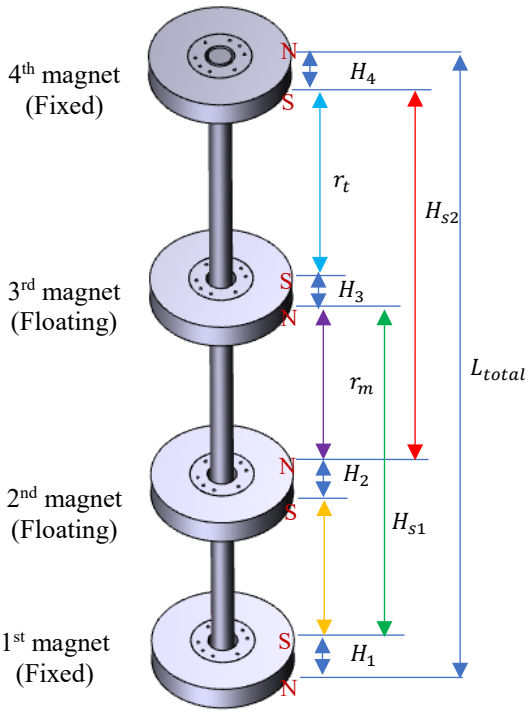

Figure 5.5: Magnetic system where the two magnets are floating

Magnetic spring's restoring forces can be calibrated from the calculation of the restoring force. A Taylor series can express the equations 5.6 and 5.7 as,

$$F_{res1} = k_1 y_2 + \alpha_1 {y_2}^2 + \lambda_1 {y_2}^3 \quad (5.8)$$

$$F_{res2} = k_3 y_3 + \alpha_3 {y_3}^2 + \lambda_3 {y_3}^3 \quad (5.9)$$

where k_1 and k_3 are the linear constants. The nonlinear constants are denoted by α_1, λ_1, α_3 and λ_3. The analytical and numerical magnetic restoring forces for different positions of the 1st and 2nd floating magnets have been presented in Figure 5.6.

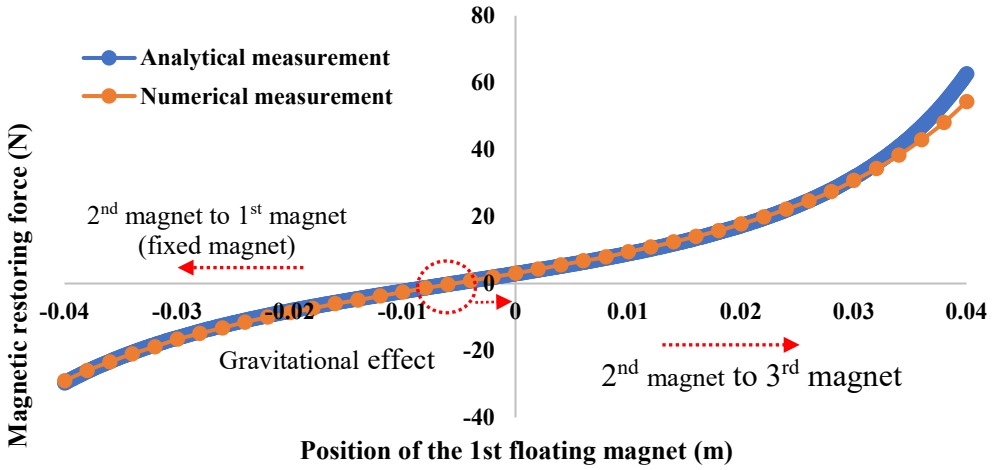

(a)

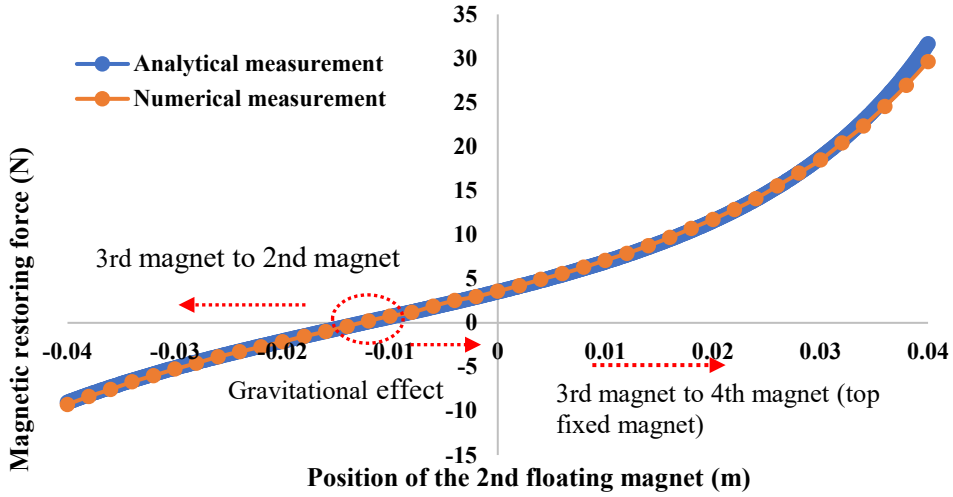

(b)

Figure 5.6: Magnetic restoring force (a) 1st floating magnet and (b) 2nd floating magnet

The distance between the 2nd magnet (1st floating magnet) and 1st magnet (fixed magnet) is smaller than the distance between the 2nd (1st floating magnet) and 3rd magnet (2nd floating magnet). Therefore, the magnetic restoring force is higher between the 1st and 2nd magnets (2nd floating magnet) than the restoring force between 2nd and 3rd magnets, as presented in Figure 5.6(a). Similarly, the distance between the 3rd magnet (2nd floating magnets) and 2nd magnet (1st floating magnet) is smaller than the distance between the 3rd magnet and 4th magnet (fixed magnet). As a result, the magnetic restoring force between the 3rd and 2nd magnets is higher than the magnetic restoring force between the 3rd and 4th magnet, as seen in Figure 5.6(b).

5.4 Coefficients Analysis of the 2DOF System

The proposed 2DOF system consists of two floating and two fixed ring magnets (All axially magnetised). Magnetic spring restoring forces has been calibrated for the 2DOF system from the calculation of the restoring forces. To determine the magnetic restoring force for the 1st moving magnet, the 2nd moving magnet is considered a fixed magnet. In the same way for the 2nd moving magnet, the 1st moving magnet is assumed as a fixed magnet. The linear and nonlinear coefficients of the magnetic restoring forces have been measured in the graphs in Figure 5.7(a) and Figure 5.8(a) (Magnetic Restoring Force vs Position of the Floating Magnet) by using the curve fitting tools.

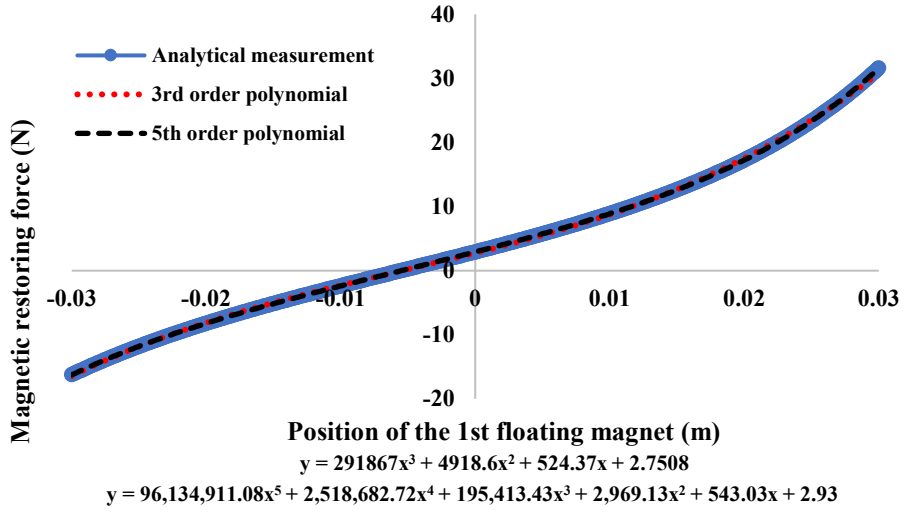

(a)

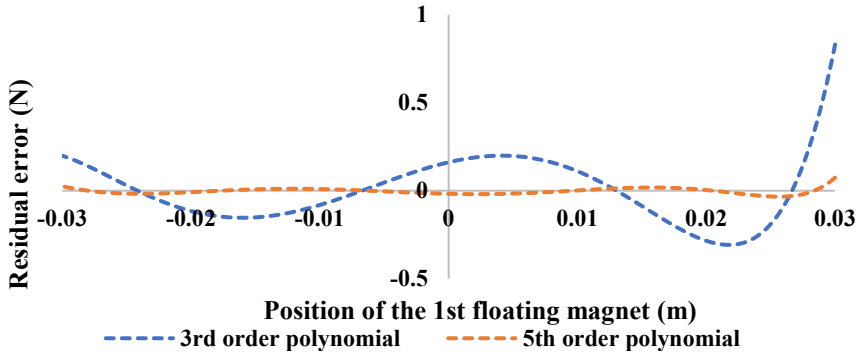

(b)

Figure 5.7: (a) Magnetic restoring force of the 1st floating magnet (b) Residual errors of the fitting curves versus the analytical force

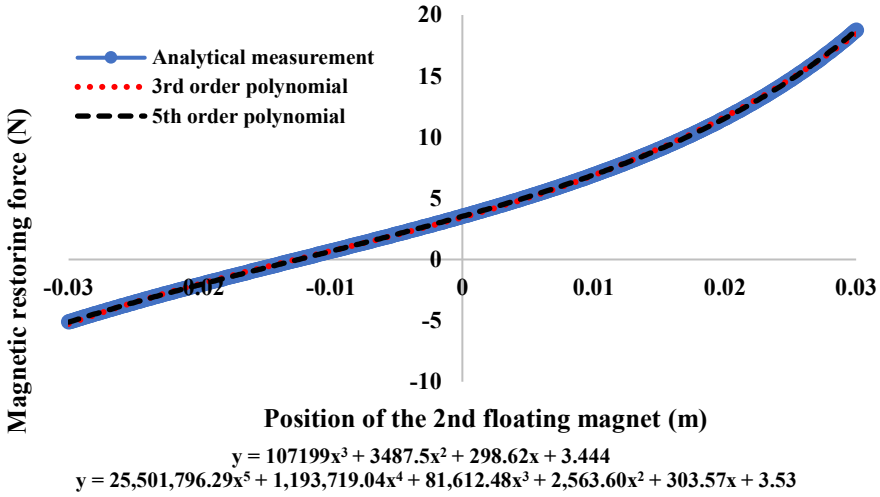

(a)

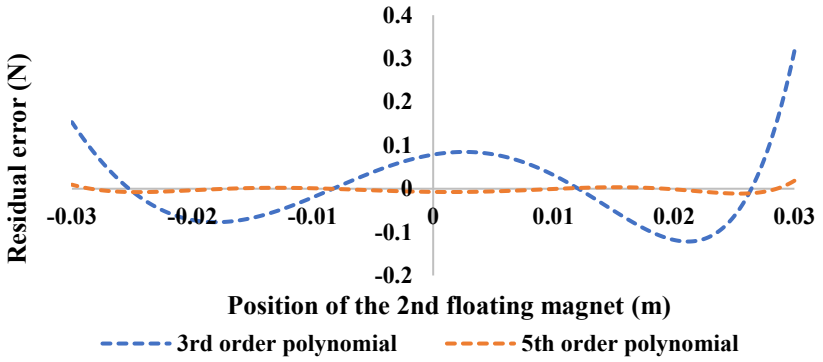

(b)

Figure 5.8: (a) Magnetic restoring force of the 1st floating magnet (b) Residual errors of the fitting curves versus the analytical force

Subsequently, from these curves, the linear and nonlinear stiffness have been determined. For the 2DOF oscillator system, the analytical measurements for the restoring forces are used to measure the linear and nonlinear stiffness of the system. The values of k_1, k_3, α_1, λ_1, α_3 and λ_3 for Equations 5.8 and 5.9 can be measured from the least-squares curve fitting of the graphs. Both 3rd and 5th order polynomials have been used to determine the linear and nonlinear stiffness from both floating magnet's restoring forces. Figure 5.7(a) and Figure 5.8(a) show the analytical measurement of the magnetic restoring forces versus deflections of the floating magnets within the maximum deflection of 30 mm. Meanwhile, the fitting curves' 3rd order polynomial and 5th order polynomial are plotted for both floating magnets, with linear and nonlinear coefficients listed in Table 5.1. Moreover, the

residual errors of the analytical measurement for both floating magnets minus the fitting data are displayed in Figure 5.7(b) and Figure 5.8(b), respectively, which indicates the 5th order fit is the best.

Table 5.1: Fitting polynomials (30 mm excitation ranges)

Coefficients	Fitting polynomials			
	1st moving magnet		2nd moving magnet	
	3rd order	5th order	3rd order	5th order
k_1 (N/m)	524.37	543.03	---	---
k_3 (N/m)	---	---	298.62	303.57
α_1 (N/m^2)	4918.6	2969.13	---	---
α_3 (N/m^2)	---	---	3487.5	2563.60
λ_1 (N/m^3)	291867	195413.43	---	---
λ_3 (N/m^3)	---	---	107199	81612.48
σ_1 (N/m^4)	0	2518682.72	---	---
σ_3 (N/m^4)	---	---	0	1193719.04
φ_1(N/m^5)	0	96134911.08	---	---
φ_3(N/m^5)	--	---	0	25501796.29

Table 5.2: Coefficients of the 2DOF system for different excitation ranges (3rd order polynomial)

Excitation ranges (mm)	Magnetic restoring forces	k_1 (N/m)	k_3 (N/m)	α_1 (N/m^2)	α_3 (N/m^2)	λ_1 (N/m^3)	λ_3 (N/m^3)
-15 mm to 15 mm	1st MM	540.61	---	3613.8	---	227286	---
	2nd MM	---	303.01	---	2846.2	---	89550
-20 mm to 20 mm	1st MM	538.66	---	3898.4	---	241719	---
	2nd MM	---	302.45	---	2994.5	---	93660
-25 mm to 25 mm	1st MM	534.06	---	4314.9	---	262472	---
	2nd MM	---	301.18	---	3202.7	---	99396
-30 mm to 30 mm	1st MM	524.37	---	4918.6	---	291867	---
	2nd MM	---	298.62	---	3487.5	---	107199

Note: MM=Moving magnet

The coefficients of the system for both floating magnets for different excitation ranges have been measured as well. The resulting 3rd order polynomial is plotted for both floating magnets for different excitation ranges, with linear and nonlinear coefficients listed in Table 5.2. The values of linear

stiffness k_1 and k_3 for -30 mm to 30 mm excitation range are 524.37 N/m and 298.62 N/m, respectively. The linear stiffness of the floating magnets for different excitation ranges have been presented in Figure 5.9. The values of nonlinear stiffness α_1 and α_3 are 4918.6 N/m^2 and 3487.5 N/m^2, respectively. On the other hand, the other nonlinear stiffness ($\lambda_1 \; and \; \lambda_3$)'s values are 291867 N/m3 and 107199 N/m3, respectively. The natural frequencies have been determined, as well as shown in Figure 5.9. Moreover, it can be seen from Table 5.2 that, for small excitation ranges, the linear stiffness for both floating magnets are slightly higher than the large excitation ranges. On the other hand, the nonlinear stiffness is higher in the large excitation ranges compared to the small excitation ranges.

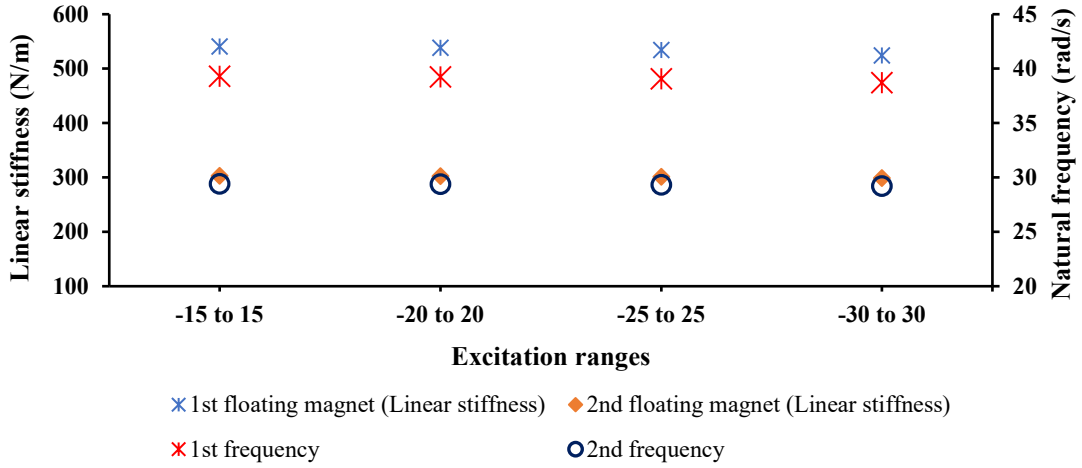

Figure 5.9: Natural frequencies of both floating magnets in the different excitation ranges

From Figure 5.9, it can be said that for all excitation ranges, the 1st frequency are almost identical when the 2nd floating magnet is fixed. Similarly, the 2nd frequency floating magnet are nearly the same in the different excitation ranges of the magnet when it is assumed the 1st floating magnet is fixed.

5.5 Modelling of the Two-degree-of-freedom Magnetic Spring-based Nonlinear Oscillator

The schematic of the proposed 2DOF nonlinear oscillator system is presented in Figure 5.10. The masses of the 2nd (1st floating magnet) and 3rd (2nd floating magnet) magnets are M_2 and M_3, respectively. The damping forces of the 1st floating magnet is $F_{\beta 1} = \beta_1 \dot{y}_2$ and 2nd floating magnet is $F_{\beta 3} = \beta_3 \dot{y}_3$. The relative displacement of the 1st floating magnet is y_2 and the relative velocity and acceleration of the 1st floating magnet are $\dot{y}_2$ and $\ddot{y}_2$, respectively. Moreover, the relative

displacement, velocity and acceleration of the 2nd floating magnet are y_3, $\dot{y}_3$ and $\ddot{y}_3$, respectively. The linear stiffness of the 1st floating magnet is k_1 and the 2nd floating magnet is k_3. The nonlinear stiffness of the 1st floating magnet is α_1 and λ_1 and for 2nd floating magnet, are α_3 and λ_3. Figure 5.11 displays the free body diagram of the proposed 2DOF nonlinear oscillator system.

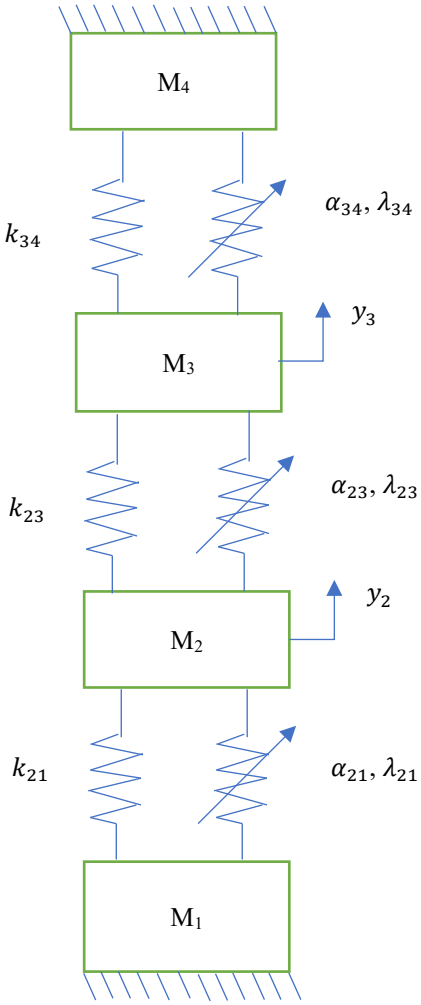

Figure 5.10: Two-degree-of-freedom magnetic spring-based oscillator system

In Figure 5.11, the linear stiffness $k_{21} = k_1$, $k_{23} = k_{32} = k_2$ and $k_{34} = k_3$. The damping constants $\beta_{21} = \beta_1$, $\beta_{23} = \beta_{32} = \beta_2$ and $\beta_{34} = \beta_3$. The nonlinear coefficient, α_{21}, is equal to α_1. Moreover, α_{23} and α_{32} are equal to α_2, and α_{34} is equal to α_3. In addition, the other nonlinear stiffness $\lambda_{21} = \lambda_1$ and $\lambda_{23} = \lambda_{32} = \lambda_2$ and $\lambda_{34} = \lambda_3$. Figure 5.11 can be represented by Figure 5.12 after replacing the linear and nonlinear coefficients' values. The dynamic equation of the motion of the system can be written as,

$$M_2\ddot{y}_2 + \beta_1\dot{y}_2 - \beta_2(\dot{y}_3 - \dot{y}_2) + k_1y_2 - k_2(y_3 - y_2) + \alpha_1{y_2}^2 - \alpha_2(y_3 - y_2)^2 + \lambda_1{y_2}^3 - \lambda_2(y_3 - y_2)^3 = F_1Sin(\omega t) \quad (5.10)$$

$$M_3\ddot{y}_3 + \beta_3\dot{y}_3 + \beta_2(\dot{y}_3 - \dot{y}_2) + k_3y_3 + k_2(y_3 - y_2) + \alpha_3{y_3}^2 + \alpha_2(y_3 - y_2)^2 + \lambda_3{y_3}^3 + \lambda_2(y_3 - y_2)^3 = F_2Sin(\omega t) \quad (5.11)$$

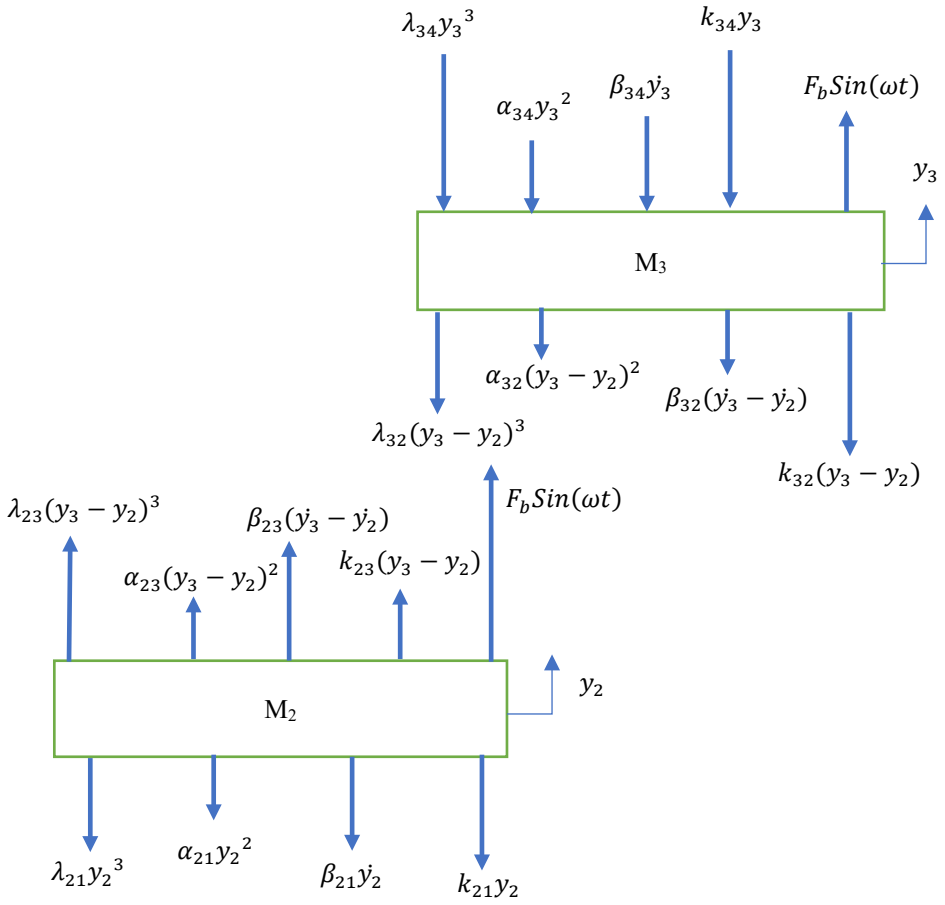

Figure 5.11: Free-body diagram of the Two-degree-of-freedom system

Equation 5.10 can be expressed as,

$$M_2\ddot{y}_2 + \beta_1\dot{y}_2 + \beta_2\dot{y}_2 - \beta_2\dot{y}_3 + k_1y_2 + k_2y_2 - k_2y_3 + \alpha_1{y_2}^2 - \alpha_2({y_3}^2 - 2y_2y_3 + {y_2}^2) + \lambda_1{y_2}^3 - \lambda_2({y_3}^3 - {y_2}^3 + 3{y_2}^2y_3 - 3y_2{y_3}^2) = F_1Sin(\omega t) \quad (5.12)$$

$$M_2\ddot{y}_2 + \beta_1\dot{y}_2 + \beta_2\dot{y}_2 - \beta_2\dot{y}_3 + k_1y_2 + k_2y_2 - k_2y_3 + \alpha_1{y_2}^2 - \alpha_2{y_3}^2 + 2\alpha_2y_2y_3 - \alpha_2{y_2}^2 + \lambda_1{y_2}^3 - \lambda_2{y_3}^3 + \lambda_2{y_2}^3 - 3\lambda_2{y_2}^2y_3 + 3\lambda_2y_2{y_3}^2 = F_1Sin(\omega t) \quad (5.13)$$

$$M_2\ddot{y}_2 + (\beta_1 + \beta_2)\dot{y}_2 - \beta_2\dot{y}_3 + (k_1 + k_2 + \alpha_1y_2 - \alpha_2y_2 + \lambda_1{y_2}^2 + \lambda_2{y_2}^2 + 2\alpha_2y_3 + 3\lambda_2{y_3}^2)y_2 - (k_2 + 3\lambda_2{y_2}^2 + \alpha_2y_3 + \lambda_2{y_3}^2)y_3 = F_1Sin(\omega t) \quad (5.14)$$

To make things easier of Equation 5.14, the following parameters are considered

$$P = k_1 + k_2 + \alpha_1 y_2 - \alpha_2 y_2 + \lambda_1 {y_2}^2 + \lambda_2 {y_2}^2 + 2\alpha_2 y_3 + 3\lambda_2 {y_3}^2 \quad (5.15)$$

$$Q = k_2 + 3\lambda_2 {y_2}^2 + \alpha_2 y_3 + \lambda_2 {y_3}^2 \quad (5.16)$$

$$F_1 = F_1 Sin(\omega t) \quad (5.17)$$

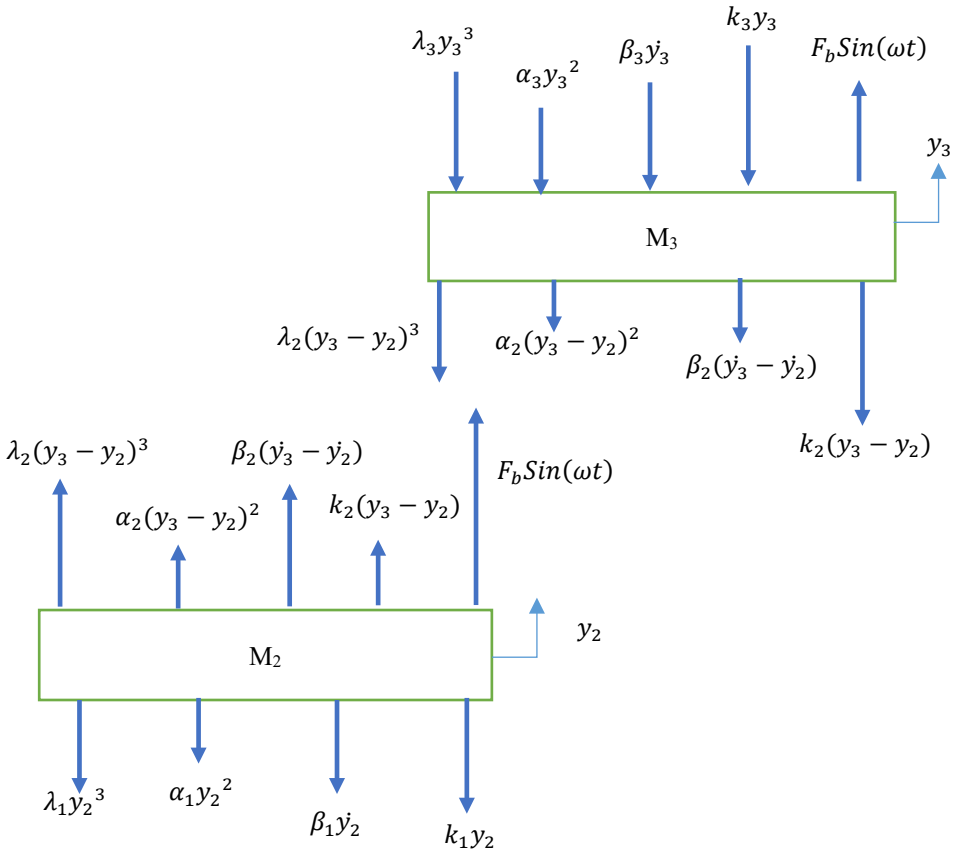

Figure 5.12: Free-body diagram of the Two-degree-of-freedom system

After adding P, Q and F_1, equation 5.14 can be stated as,

$$M_2 \ddot{y}_2 + (\beta_1 + \beta_2)\dot{y}_2 - \beta_2 \dot{y}_3 + P y_2 - Q y_3 = F_1 \quad (5.18)$$

Equation 5.11 can be expressed by equation 5.19,

$$M_3 \ddot{y}_3 + \beta_3 \dot{y}_3 + \beta_2 \dot{y}_3 - \beta_2 \dot{y}_2 + k_3 y_3 + k_2 y_3 - k_2 y_2 + \alpha_3 {y_3}^2 + \alpha_2 {y_3}^2 - 2\alpha_2 y_3 y_2 + \alpha_2 {y_2}^2 + \lambda_3 {y_3}^3 + \lambda_2 ({y_3}^3 - {y_2}^3 - 3{y_3}^2 y_2 + 3 y_3 {y_2}^2) = F_2 Sin(\omega t) \quad (5.19)$$

$$M_3 \ddot{y}_3 + (\beta_3 + \beta_2)\dot{y}_3 - \beta_2 \dot{y}_2 - (k_2 + 2\alpha_2 y_3 - \alpha_2 y_2 + \lambda_2 {y_2}^2 + 3\lambda_2 {y_3}^2) y_2 + (k_3 + k_2 + \alpha_3 y_3 + \alpha_2 y_3 + \lambda_3 {y_3}^2 + \lambda_2 {y_3}^2 + 3\lambda_2 {y_2}^2) y_3 = F_2 Sin(\omega t) \quad (5.20)$$

To simplify Equation 5.20, the following parameters are considered

$$T = k_2 + 2\alpha_2 y_3 - \alpha_2 y_2 + \lambda_2 {y_2}^2 + 3\lambda_2 {y_3}^2 \quad (5.21)$$

$$S = k_3 + k_2 + \alpha_3 y_3 + \alpha_2 y_3 + \lambda_3 {y_3}^2 + \lambda_2 {y_3}^2 + 3\lambda_2 {y_2}^2 \quad (5.22)$$

$$F_2 = F_b Sin(\omega t) \quad (5.23)$$

After adding T, S and F_2, Equation 5.23 can be detailed as

$$M_3 \ddot{y}_3 + (\beta_3 + \beta_2)\dot{y}_3 - \beta_2 \dot{y}_2 - T y_2 + S y_3 = F_2 \quad (5.24)$$

The system can be presented as matrix form as well

$$\begin{bmatrix} M_2 & 0 \\ 0 & M_3 \end{bmatrix} \begin{Bmatrix} \ddot{y}_2 \\ \ddot{y}_3 \end{Bmatrix} + \begin{bmatrix} (\beta_1 + \beta_2) & -\beta_2 \\ -\beta_2 & (\beta_3 + \beta_2) \end{bmatrix} \begin{Bmatrix} \dot{y}_2 \\ \dot{y}_3 \end{Bmatrix} + \begin{bmatrix} P & -Q \\ -T & S \end{bmatrix} \begin{Bmatrix} y_2 \\ y_3 \end{Bmatrix} = \begin{Bmatrix} F_1 \\ F_2 \end{Bmatrix} \quad (5.25)$$

State space variables can be used to solve equations 5.14 and 5.20. State space variables can be defined as:

$$x_1 = y_2 \quad (5.26)$$

$$x_2 = \dot{y}_2 = \frac{dx_1}{dt} \quad (5.27)$$

$$\frac{dx_2}{dt} = \ddot{y}_2 \quad (5.28)$$

$$x_3 = y_3 \quad (5.29)$$

$$x_4 = \frac{dx_3}{dt} = \dot{y}_3 \quad (5.30)$$

$$\frac{dx_4}{dt} = \ddot{y}_3 \quad (5.31)$$

$$u = F_b sin(\omega t) \quad (5.32)$$

Using the above state variables, Equation 5.14 can be written as

$$\frac{dx_2}{dt} = \ddot{y}_2 = \frac{1}{M_2}[u - (\beta_1 + \beta_2)x_2 + \beta_2 x_4 - (k_1 + k_2 + \alpha_1 x_1 - \alpha_2 x_1 + \lambda_1 {x_1}^2 + \lambda_2 {x_1}^2 + 2\alpha_2 x_3 + 3\lambda_2 {x_3}^2)x_1 + (k_2 + 3\lambda_2 {y_2}^2 + \alpha_2 y_3 + \lambda_2 {y_3}^2)x_3 \quad (5.33)$$

The following parameters are considered to help simplify Equation 5.33

$$P1 = (k_1 + k_2 + \alpha_1 x_1 - \alpha_2 x_1 + \lambda_1 {x_1}^2 + \lambda_2 {x_1}^2 + 2\alpha_2 x_3 + 3\lambda_2 {x_3}^2) \quad (5.34)$$

$$Q1 = (k_2 + 3\lambda_2 {x_1}^2 + \alpha_2 x_3 + \lambda_2 {x_3}^2) \quad (5.35)$$

Equation 5.33 can then be rewritten as

$$\frac{dx_2}{dt} = \ddot{y}_2 = \frac{1}{M_2}[u - P1x_1 - (\beta_1 + \beta_2)x_2 + Q1x_3 + \beta_2 x_4] \quad (5.36)$$

Equation 5.20 can be written as

$$\frac{dx_4}{dt} = \ddot{y}_3 = \frac{1}{M_3}[u - (\beta_3 + \beta_2)x_4 + \beta_2 x_2 + (k_2 + 2\alpha_2 x_3 - \alpha_2 x_1 + \lambda_2 {x_1}^2 + 3\lambda_2 {x_3}^2)x_1 - (k_3 + k_2 + \alpha_3 x_3 + \alpha_2 x_3 + \lambda_3 {x_3}^2 + \lambda_2 {x_3}^2 + 3\lambda_2 {x_1}^2)x_3] \quad (5.37)$$

To shorten Equation 5.37, q the following parameters are considered

$$T1 = (k_2 + 2\alpha_2 x_3 - \alpha_2 x_1 + \lambda_2 {x_1}^2 + 3\lambda_2 {x_3}^2) \quad (5.38)$$

$$S1 = (k_3 + k_2 + \alpha_3 x_3 + \alpha_2 x_3 + \lambda_3 {x_3}^2 + \lambda_2 {x_3}^2 + 3\lambda_2 {x_1}^2) \quad (5.39)$$

After adding T1 and S1, equation 5.37 can be stated as

$$\frac{dx_4}{dt} = \ddot{y}_3 = \frac{1}{M_3}[u + T1x_1 + \beta_2 x_2 - S1x_3 - (\beta_3 + \beta_2)x_4] \quad (5.40)$$

The state space model of the 2DOF system can be written as

$$\begin{bmatrix} \frac{dx_1}{dt} \\ \frac{dx_2}{dt} \\ \frac{dx_3}{dt} \\ \frac{dx_4}{dt} \end{bmatrix} = \underbrace{\begin{bmatrix} 0 & 1 & 0 & 0 \\ \frac{-P1}{M_2} & \frac{-(\beta_1+\beta_2)}{M_2} & \frac{Q1}{M_2} & \frac{\beta_2}{M_2} \\ 0 & 0 & 0 & 1 \\ \frac{T1}{M_3} & \frac{\beta_2}{M_3} & \frac{-S1}{M_3} & \frac{-(\beta_3+\beta_2)}{M_3} \end{bmatrix}}_{A} \begin{bmatrix} x_1 \\ x_2 \\ x_3 \\ x_4 \end{bmatrix} + \underbrace{\begin{bmatrix} 0 \\ \frac{1}{M_2} \\ 0 \\ \frac{1}{M_3} \end{bmatrix}}_{B} [u] \quad (5.41)$$

$$[z] = \underbrace{\begin{bmatrix} 1 & 0 & 0 & 0 \\ 0 & 1 & 0 & 0 \\ 0 & 0 & 1 & 0 \\ 0 & 0 & 0 & 1 \end{bmatrix}}_{C} \begin{bmatrix} x_1 \\ x_2 \\ x_3 \\ x_4 \end{bmatrix} + \underbrace{\begin{bmatrix} 0 \\ 0 \end{bmatrix}}_{D} [u] \tag{5.42}$$

Where ***A*** is the system matrix, ***B*** is the input matrix, and ***C*** is the output matrix. The remaining matrix is ***D*** which is typically zero because the input directly does not usually affect the output.

5.6 Dynamics Analysis of the 2DOF System

The mass of the 2nd magnet (1st floating magnet) is 0.37 kg (mass including plastic bush), and the 3rd magnet (2nd floating magnet) is 0.32728 kg (mass including plastic bush). Table 5.3 displays the values of the required parameters.

Table 5.3: Required parameters

Parameters	Values	Units
β_1	0.98	Ns/m
β_2	0.235	Ns/m
β_3	0.51	Ns/m
k_1	524.37	N/m
k_2	112.875	N/m
k_3	298.62	N/m
α_1	4918.6	N/m^2
α_2	715.55	N/m^2
α_3	3487.5	N/m^2
λ_1	291867	N/m^3
λ_2	92334	N/m^3
λ_3	107199	N/m^3

The distance between 1st (fixed magnet) and 2nd magnets (1st floating magnet) is 0.068 m, and between 2nd (1st floating magnet) and 3rd (2nd floating magnet) magnets is 0.079 m. Moreover, the distance between 3rd (2nd floating magnet) and 4th (fixed magnet) magnets is 0.104 m. The total length of the oscillator is 0.303 m. The measured damping ratio for the 1st floating magnet was 0.029 and for the 2nd floating magnets was 0.021. The measured resonance frequencies were 44.89 rad/s and 32.87 rad/s, respectively. The simulation results of the system are shown in Table 5.4.

Table 5.4: Eigenvalues and resonance frequencies of the system for different positions of both floating magnet

PFM		Eigenvalue		Resonance frequency (rad/s)	
1st	2nd				
-20	-20	-1.7959 +51.1241i	-0.9841 +33.1288i	51.1557	33.1434
-15	-15	-1.8030 +47.2198i	-0.9771 +32.4700i	47.2542	32.4847
-10	-10	-1.8084 +44.5184i	-0.9716 +32.2040i	44.5551	32.2187
-05	-05	-1.8108 +43.2233i	-0.9692 +32.3706i	43.2612	32.3851
0	0	-1.8112 +43.4235i	-0.9689 +33.0119i	43.4612	33.0261
05	05	-1.8108 +45.0812i	-0.9693 +34.1246i	45.1176	34.1384
10	10	-1.8084 +48.0638i	-0.9716 +35.6407i	48.0978	35.6539
15	15	-1.8037 +52.1713i	-0.9764 +37.4735i	52.2025	37.4862
20	20	-1.7978 +57.1763i	-0.9822 +39.5583i	57.2046	39.5704

Note: PFM= Position of the floating magnets, FM= Floating magnet

From Table 5.4, it can be seen that different positions of both floating magnets showed different eigenvalues and different resonance frequencies. As discussed in the earlier chapter, the real parts of the eigenvalues always remained constant for all the different positions of the floating magnet, when it moved toward the top and bottom magnets in the single degree of freedom system. The imaginary parts of the single degree of freedom system's eigenvalues changed with the changing position of the two floating magnets. It has been seen from the analysis (3rd order polynomial model) at Table 5.4 that in the 2DOF system, the real parts and imaginary parts of the eigenvalues changed with the changing position of the two floating magnets. Due to the relative motion between two floating magnets, the eigenvalues of the system changed when both floating magnets changed their position. To understand the system for this analysis, it has been considered that when a floating magnet moves by 1 mm, another floating magnet is relatively moved by 1mm. But practically, the 2nd floating moved more than the 1st floating due to less damping ratio and resonance frequency. The 1st floating magnet showed a higher resonance frequency than the 2nd when both magnets moved from their equilibrium positions. If the 2nd floating magnet moved toward the top magnet, the 1st floating magnet moved toward the 2nd floating magnet. On the other hand, when the 2nd floating magnet moved toward the 1st floating magnet, the 1st floating magnet moved toward the bottom fixed magnet. When the 2nd floating moved from the equilibrium position toward the top magnet or the 1st floating magnet, the resonance frequencies increased.

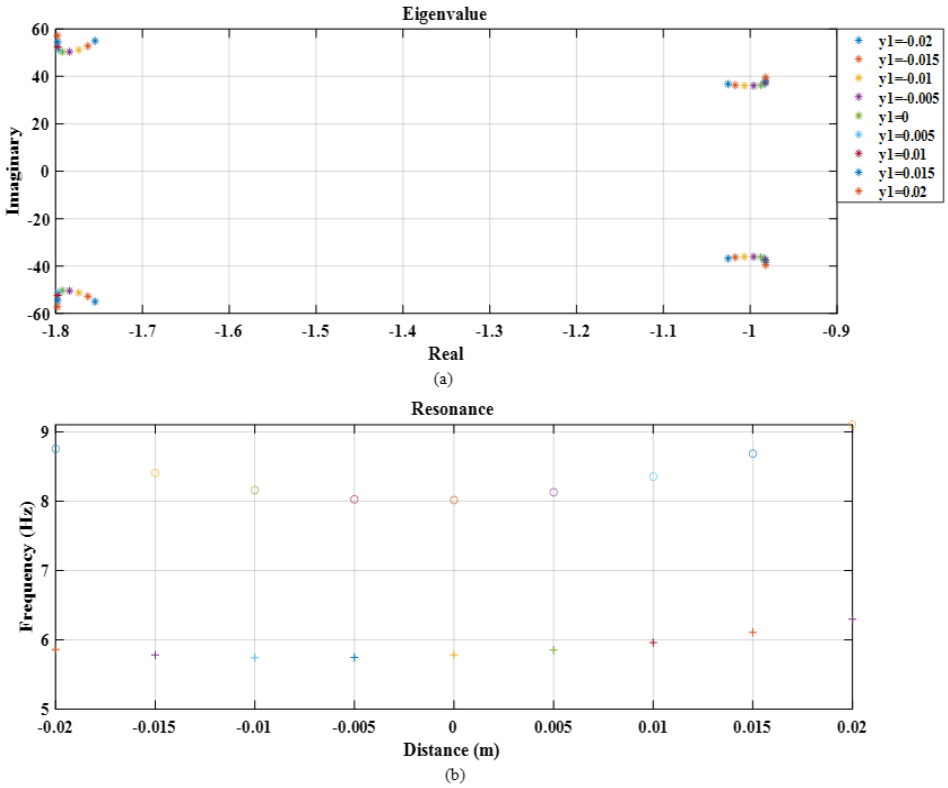

Figure 5.13: (a) Eigenvalues and (b) natural frequency of the system

Similarly, the frequency increased when the 1st floating magnet moved toward the bottom magnet or the 2nd floating magnet. The graphical presentation of the eigenvalues and natural frequency of the system have been presented in Figure 5.13. In Figure the legend x1 indicate the position of both floating magnets. In the legend x1=0 means both floating magnets are in equilibrium positions.

When both floating magnets move toward the top fixed magnet by 5 mm then the legend is shown as x1=-0.005 and similarly x1=0.005 indicate that both floating magnets moved by 5 mm toward bottom magnet from the equilibrium position. The circles in Figure 5.13 represents the 1st resonance frequency of the system and the cross represents the 2nd resonance frequency for different positions of the floating magnets. Figure 5.14 and Figure 5.15 present the system's natural frequencies when both floating magnets are in equilibrium positions and different positions.

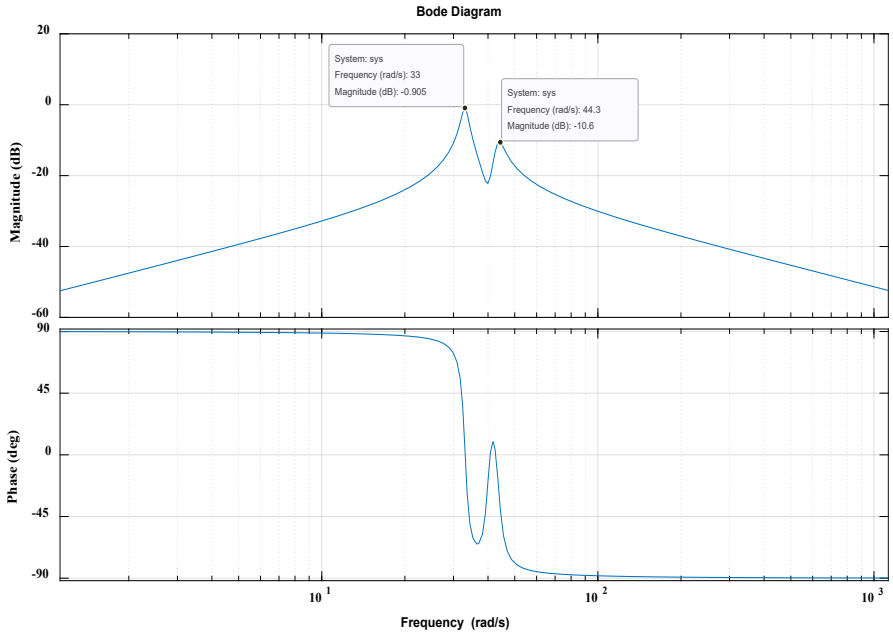

Figure 5.14: Natural frequency when both floating magnets are in equilibrium positions

Figure 5.14 presents two resonances of the system. When both floating magnets were in the equilibrium position, the measured resonance frequencies were 33 rad/s and 44.3 rad/sec, respectively, which are similar to the experimentally measured frequencies (32.87 rad/s and 44.89 rad/s). The resonance changed with changing the position of the floating magnets, which can be seen in Figure 5.15. If an external force is applied on the 2nd floating magnet, then the displacements and velocities of both floating magnets (1st and 2nd floating magnets) are shown in Figure 5.16 and Figure 5.17. The applied external harmonic force (F_b) amplitude is 10 N, and the frequency (f) is 0.1 Hz. The values of linear stiffness, nonlinear stiffness and damping constants are presented in Table 5.3. Ode23t solver has been used in MATLAB to find the displacements and velocities of both floating magnets. The excitation of both floating magnets was assumed to have initial displacements, and their corresponding velocities were zero. The frequency of the harmonic force was 0.1 Hz. As expected, the displacements and the velocities were sinusoidal and 90° out of phase. The amplitude of displacement of the 2nd floating magnet was around 20 mm toward the 1st floating magnet (2nd magnet) and about 25 mm toward the top magnet.

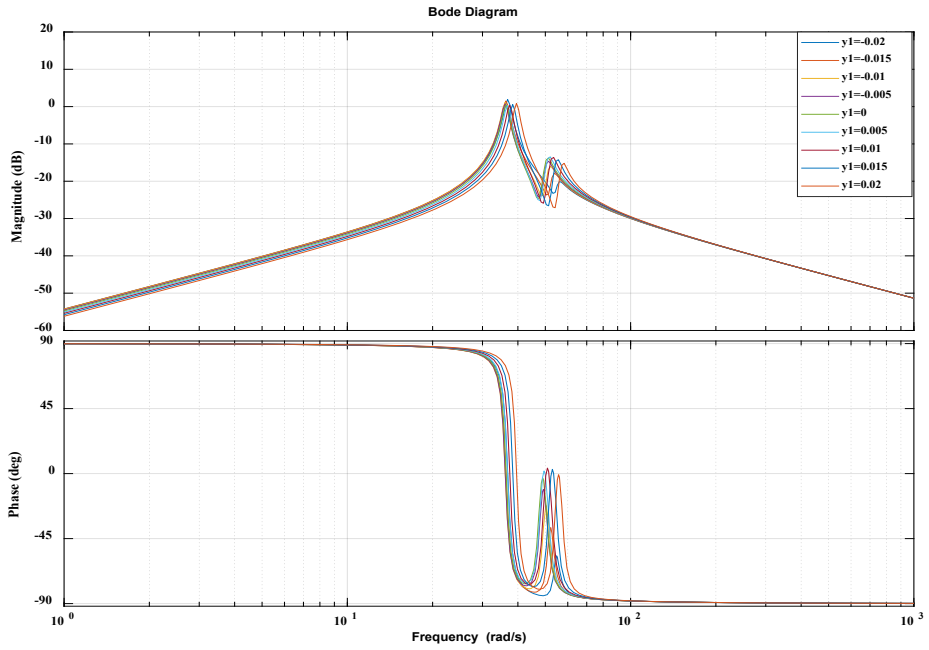

Figure 5.15: Natural frequency for different positions of both floating magnets

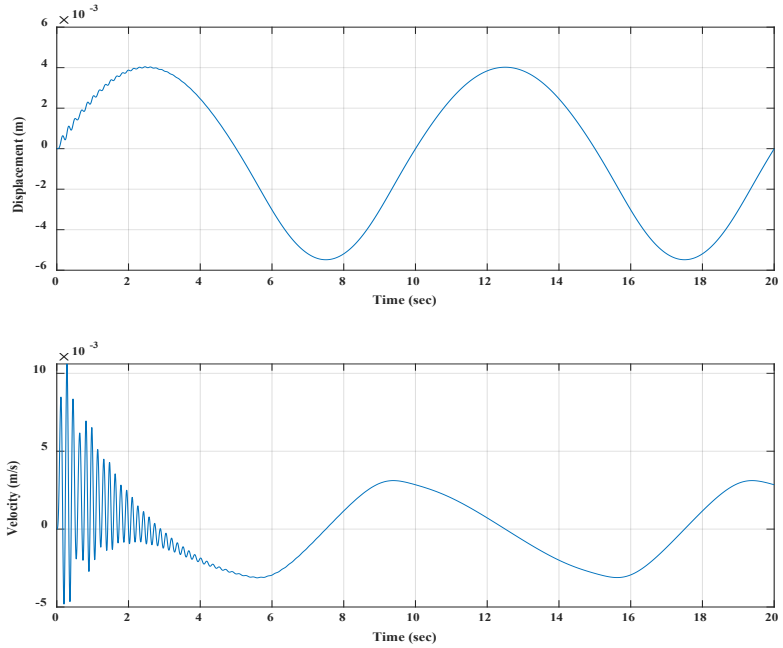

Figure 5.16: Displacement and velocity of the 1st floating magnet under harmonic force

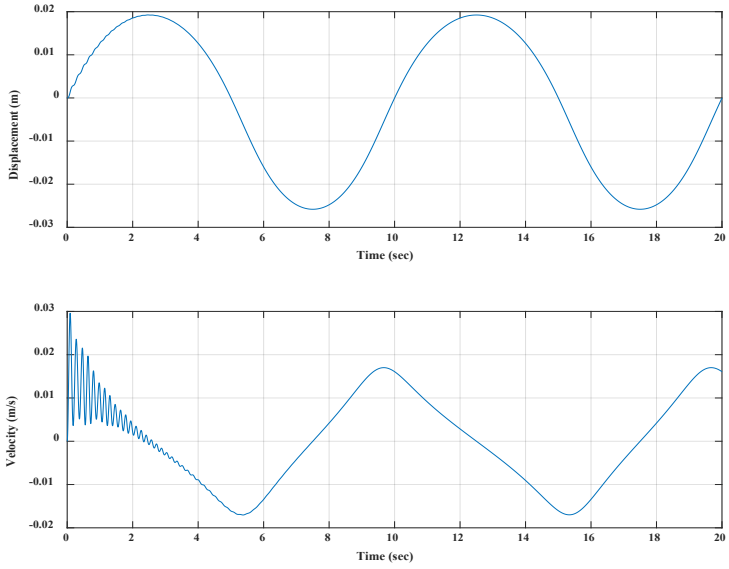

Figure 5.17: Displacement and velocity of the 2nd floating magnet under harmonic force

On the other hand, the displacement amplitude of the 1st floating magnet was around 4 mm toward the bottom magnet (1st magnet) and about 5 mm toward the 2nd floating magnet (3rd magnet). These confirm the amplitude of the displacement signals, as shown in Figure 5.16 and Figure 5.17. Moreover, the velocities vs displacements graph of both floating magnets under the same harmonic force have been presented in Figure 5.18.

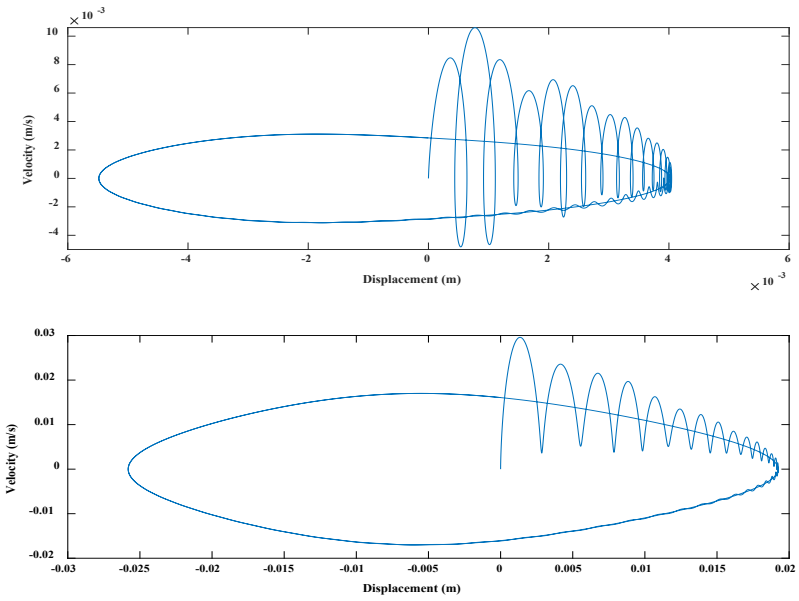

(a)

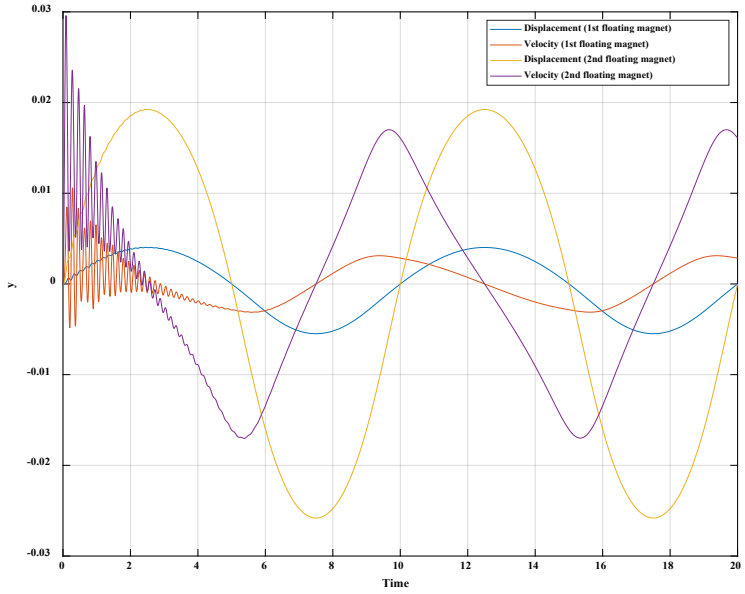

(b)

Figure 5.18: (a) Displacement vs velocity and (b) Comparison of displacement and velocity of the 1st floating magnet with 2nd floating magnet

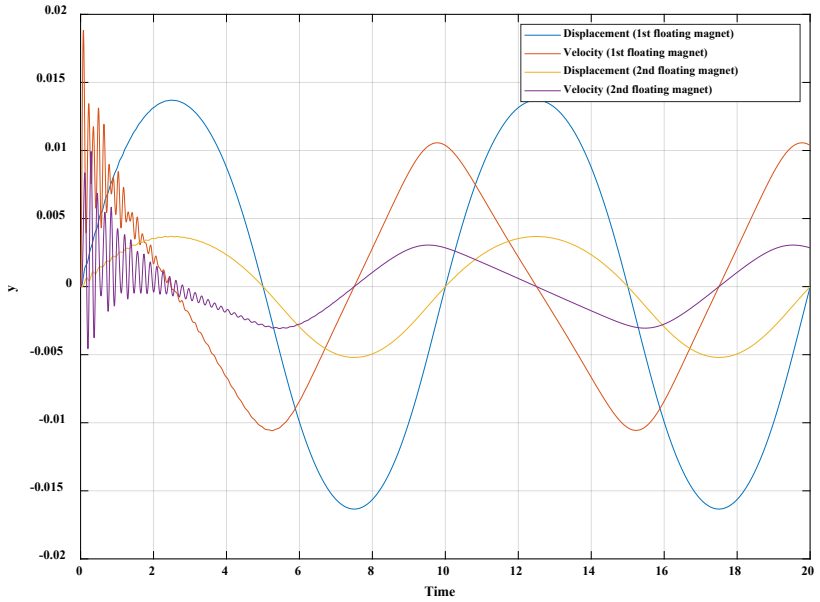

Figure 5.19: Comparison of displacement and velocity of the 1st floating magnet with 2nd floating magnet

If the external force was applied to the 2nd floating magnet, it started moving, causing the 1st floating magnet to move as well. Comparing the displacement and velocity of the 2nd floating magnet with the 1st floating magnet; the 2nd floating magnet has a larger displacement and velocity than the 1st floating magnet, which can be seen in Figure 5.18. Similarly, if the same external force is applied to the 1st floating magnet, it starts to move causing the 2nd floating magnet to move as well. Comparing the displacement and velocity of the 1st floating magnet with the 2nd floating magnet, the 2nd floating magnet has a smaller displacement and velocity than the 1st floating magnet, as shown in Figure 5.19.

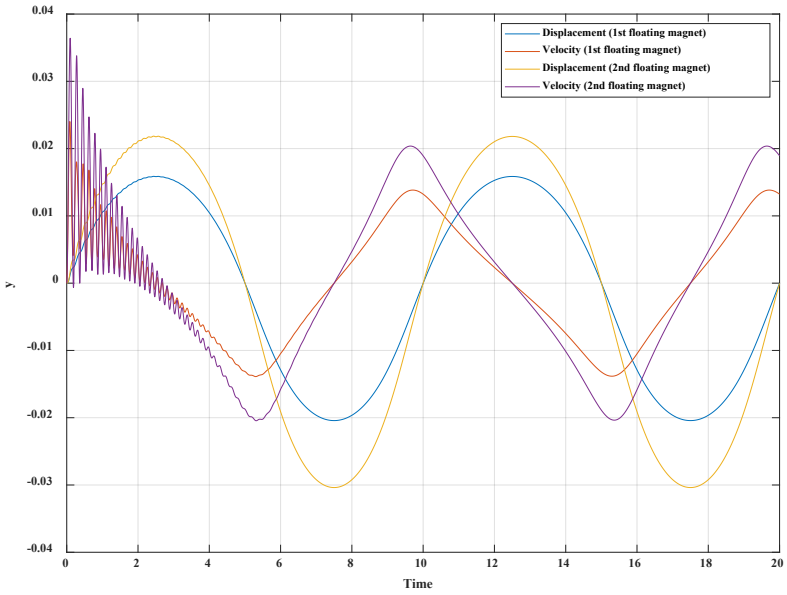

Figure 5.20: Comparison of displacement and velocity of the 1st floating magnet with 2nd floating magnet

Moreover, if the same external forces were applied on both floating magnets, both magnets would move. The displacement and velocity of the 1st floating magnet are smaller than the 2nd floating magnet, as shown in Figure 5.20. In that scenario, both floating magnets achieved relatively higher displacements and velocities compared to previously discussed scenarios. However, the 2nd floating magnet consistently achieved higher displacement and velocity than the 1st in all scenarios due to the smaller damping ratio.

5.7 Different Lengths of the Oscillator

To find the best model of the 2DOF nonlinear oscillator system, the design of the oscillator system has been analysed by changing the position of the top fixed magnet (4th magnet). When it is in equilibrium, the distance between the 2nd magnet and 1st magnet (bottom fixed magnet) is 68 mm, the distance between the 3rd magnet and the 2nd magnet is 79 mm, the distance between 3rd magnet and 4th magnet (top fixed magnet) is 104 mm. The total length of the 2DOF system for this equilibrium position is 303 mm. Figure 5.21 presents the equilibrium position of the top fixed magnet as well as the sign convention given to the movement of the 4th magnet.

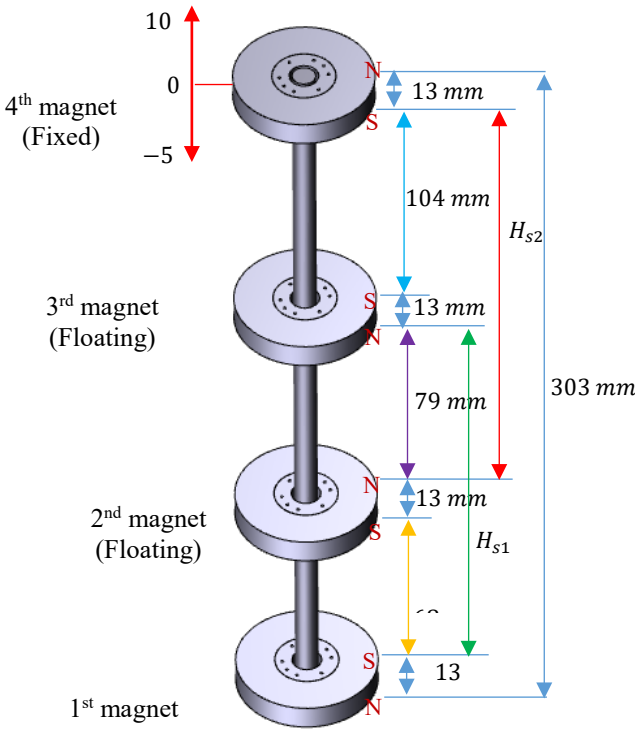

Figure 5.21: 2DOF Magnetic spring-based nonlinear oscillator system

The gravitational force affects the equilibrium positions, damping ratios and natural frequencies of both floating magnets, which have been measured experimentally for different positions of the top fixed magnet (4th magnet), as presented in Table 5.5 and Table 5.6. By changing the position of the top fixed magnet, the distances between 1st and 2nd, 2nd and 3rd and 3rd and 4th magnets can be changed. Different separation distances between magnets provide different damping ratios. When the total length of the oscillator increased, the distance between 1st and 2nd, 2nd and 3rd and 3rd and 4th increased. On the other hand, the spaces between 1st and 2nd, 2nd and 3rd and 3rd and 4th reduced when the total

length of the oscillator reduced from 303 mm. Moreover, the gravitational force effects on both floating magnets changed with changing the position of the top magnet, as shown in Table 5.5.

Table 5.5: Change of damping ratio for different lengths of the oscillator

Position of the top magnet (mm)	Distance between 1st and 2nd magnets (mm)	Distance between 2nd and 3rd magnets (mm)	Distance between 3rd and 4th magnets (mm)	The total length of the oscillator (mm)	Gravitational effects (mm)		Damping ratio	
					1st floating magnet	2nd floating magnet	1st floating magnet	2nd floating magnet
-20	64	73	94	283	4.5	10.5	0.056	0.032
-10	65.5	75.5	100	293	5	12.25	0.032	0.030
0	68	79	104	303	5.5	12.5	0.029	0.021
+ 10	69	81	111	313	6	15	0.027	0.017
+20	70.5	83.5	117	323	6.5	16.75	0.024	0.015
+ 30	71	86	124	333	7.5	19	0.023	0.014
+40	72	88	131	343	8	21.5	0.021	0.012
+50	73	89	139	353	8	25	0.020	0.011

For all different lengths of the oscillator, the separation distance between the 3rd and 4th magnet always remained higher than the distances between 1st and 2nd, and 2nd and 3rd magnets. However, the distance between 2nd and 3rd magnets remained greater than the distance between 1st and 2nd magnets. Still, it stayed smaller than the distance between 3rd and 4th magnets for all changing lengths of the oscillator. Therefore, the damping constant and natural frequency of the 1st floating magnet (2nd magnet) is always higher than the damping constant and natural frequency of the 2nd floating magnet (3rd magnet). Moreover, the damping ratio and the natural frequency of the system can be changed by changing the total length of the oscillator. The damping ratios and natural frequencies of both floating magnets increased with reducing the total length of the oscillator and decreased with increasing the total length of the oscillator, as seen in Table 5.5 and Table 5.6. The natural frequencies of the system in the equilibrium position were 44.89 rad/s and 32.87 rad/s, respectively, and they increased to 47.86 rad/s and 37.31 rad/s, respectively when the 4th magnet moved toward 3rd magnet from the equilibrium position by 20 mm (reduced the total length of the oscillator). On the other hand, the frequencies decreased to 38.76 rad/s and 24.85 rad/s when the top magnet moved away from the equilibrium position (increased the total length of the oscillator), which can be seen in Table 5.6.

Table 5.6: Change of natural frequency for different positions of the top magnet (different length of the oscillator)

Position of the top magnet (mm)	Distance between 1st and 2nd magnets (mm)	Distance between 2nd and 3rd magnets (mm)	Distance between 3rd and 4th magnets (mm)	Natural frequency (rad/s)	
-20	64	73	94	47.86	37.31
-10	65.5	75.5	100	46.85	34.97
0	68	79	104	44.89	32.87
+ 10	69	81	111	43.38	30.80
+20	70.5	83.5	117	42.05	29.44
+ 30	71	86	124	40.24	27.20
+40	72	88	131	39.98	25.91
+50	73	89	139	38.76	24.85

The magnetic restoring forces of the 1st and 2nd floating magnets changed with changing the oscillator's total length. Moreover, the linear and nonlinear stiffness of both floating magnets changed with changing the total length of the oscillator. The magnetic restoring forces for both floating magnets are measured analytically, as presented in Figure 5.22. For the first floating magnet (2nd magnet), the distance between itself and its top magnet (3rd magnet) is larger than the distance between itself and its bottom magnet. Therefore, if the 2nd magnet moved up and down from the equilibrium position, the magnetic force between the 2nd and 1st magnet is larger than the magnetic force between the 2nd magnet and 3rd magnet. For all different lengths of the oscillator, the distance between 2nd and 3rd magnets always remained larger than the distance between 2nd and 1st magnets. As a result, for all different lengths of the oscillator, the magnetic forces between 2nd and 1st magnets always remained larger than the magnetic forces between 2nd and 3rd magnets, as shown in Figure 5.22(a). Similarly, in the case of the 2nd floating magnet (3rd magnet), the distance between 3rd and 2nd magnets are smaller than the distance between 3rd and 4th magnets. If the 2nd magnet moved up and down from the equilibrium position, then the magnetic force between the 3rd and 2nd magnets is larger than the magnetic force between the 2nd magnet and 3rd magnet. For all different lengths of the oscillator, the distance between 3rd and 2nd magnets always remained smaller than the distance between 3rd and 4th magnets.

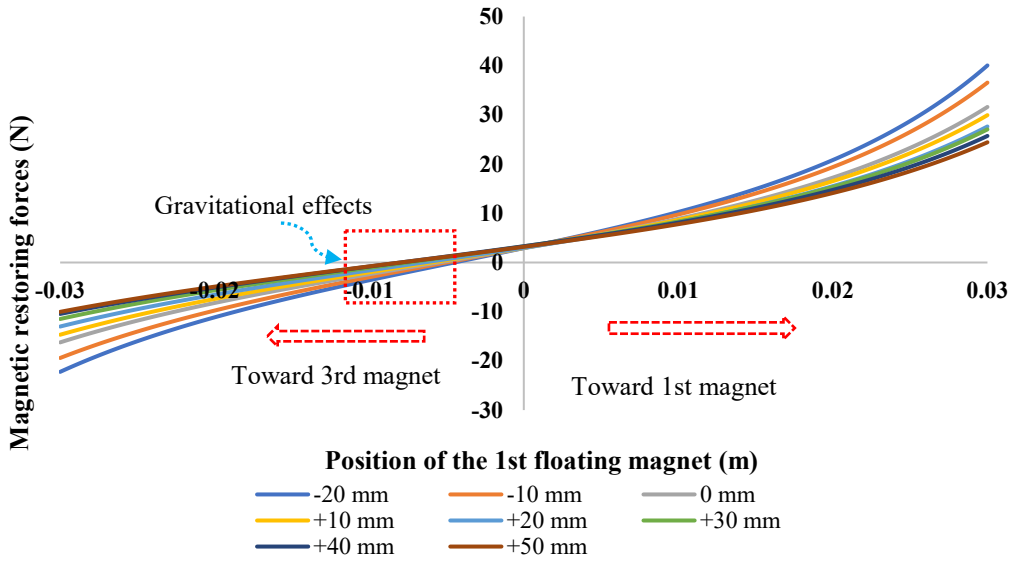

(a)

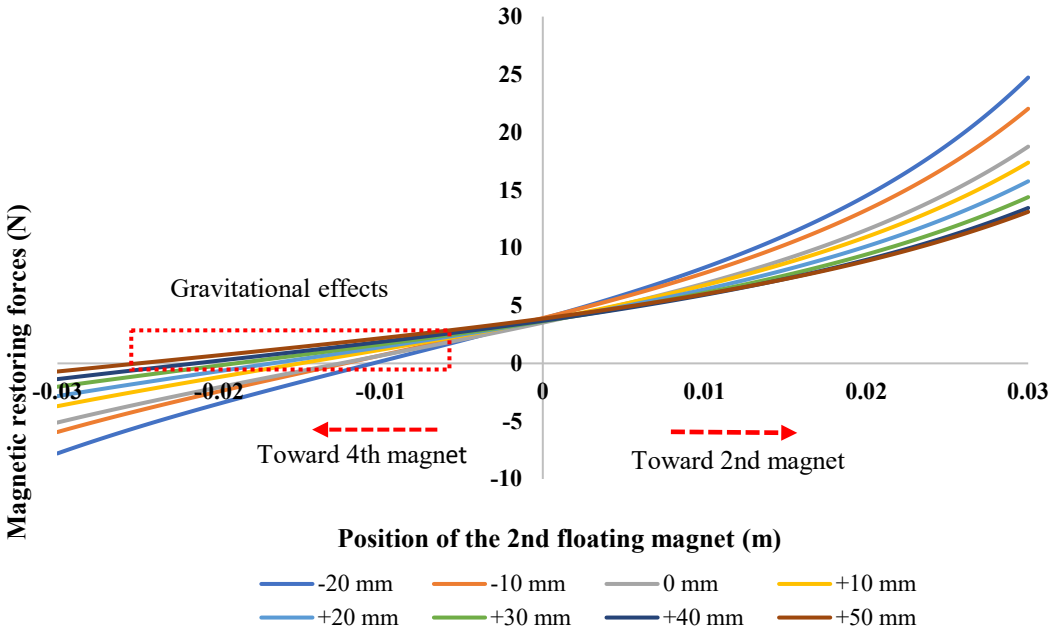

(b)

Figure 5.22: Magnetic restoring forces of the 1st and 2nd floating magnet for different lengths of the oscillator

Thus, for all different lengths of the oscillator, the magnetic forces between 3rd and 4th magnets always stayed smaller than the magnet forces between 3rd and 2nd magnets, which can be seen in Figure 5.22(b). The linear and nonlinear stiffness of the 1st and 2nd floating magnets for different lengths of the oscillator has been presented in Table 5.7 and Table 5.8, respectively.

Table 5.7: Linear and nonlinear-stiffness of the 1st floating magnet for different lengths of the oscillator

Position of the top magnet (4th magnet) (mm)	k_1 (N/m)	α_1 (N/m^2)	λ_1 (N/m^3)
-20	635.38	6067.9	427598
-10	588.28	5701.4	366883
0	524.37	4918.6	291867
10	497.07	4793	264036
20	462.72	4477.2	230480
30	442.43	4684.1	214303
40	420.89	4507	195636
50	405.5	4190.4	181669

Table 5.8: Linear and nonlinear-stiffness of the 2nd floating magnet for different lengths of the oscillator

Position of the top magnet (4th magnet) (mm)	k_3 (N/m)	α_3 (N/m^2)	λ_3 (N/m^3)
-20	383.76	4813.9	170047
-10	338.99	4343.2	136951
0	298.62	3487.5	107199
10	267.88	3324.2	90145
20	240.53	2988.3	75034
30	215.64	2710.5	62653
40	196.85	2528.8	54258
50	184.42	2504.2	49824

The natural frequencies and damping ratios of the 1st and 2nd floating magnets changed with the oscillator's total length, as presented in Figure 5.23 and Figure 5.24. The natural frequencies and damping ratios increased for both floating magnets with decreasing the length of the oscillator. On the other hand, the natural frequencies and damping ratios decreased with increasing the total length of the oscillator as all experimental works have been performed manually, and all approximate values compared with the analytical measurement. The differences between the experimental and analytical measurements and the percentage of errors between them have been determined and displayed in Figure 5.23 and Figure 5.24, respectively.

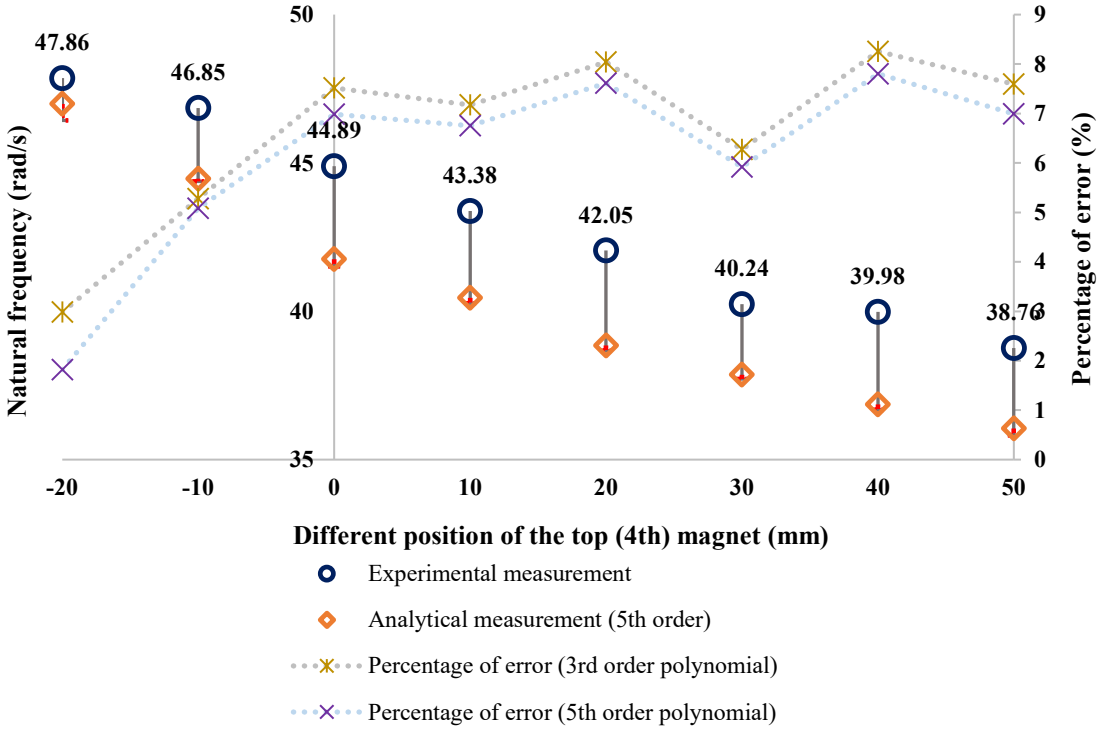

(a)

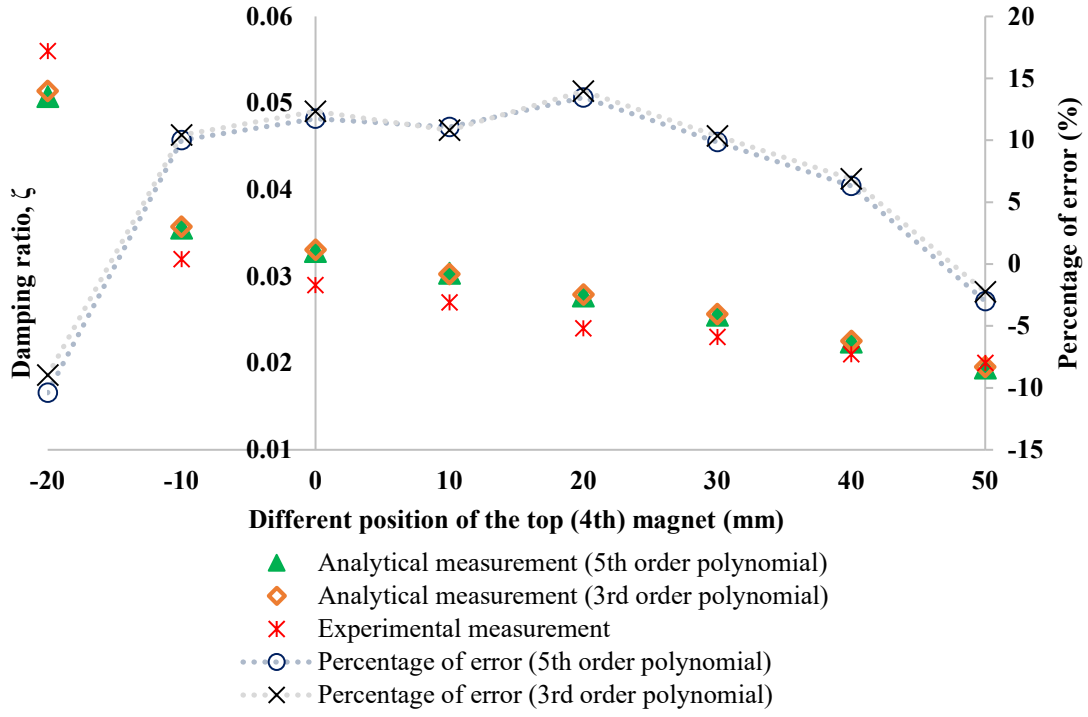

(b)

Figure 5.23: (a) 1st natural frequency and (b) damping ratio for different lengths of the oscillator

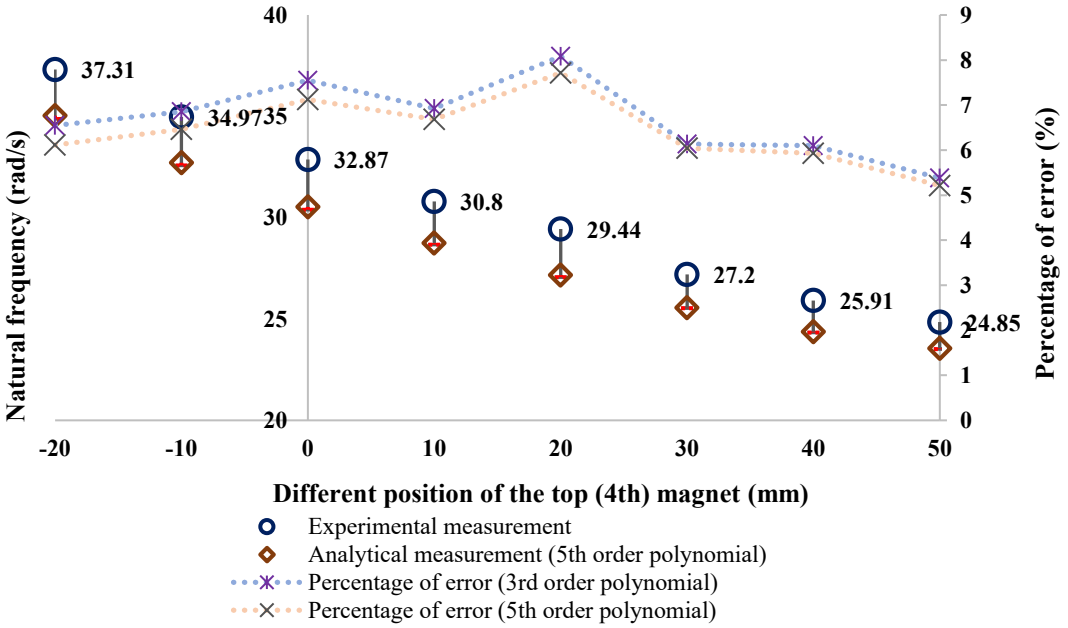

(a)

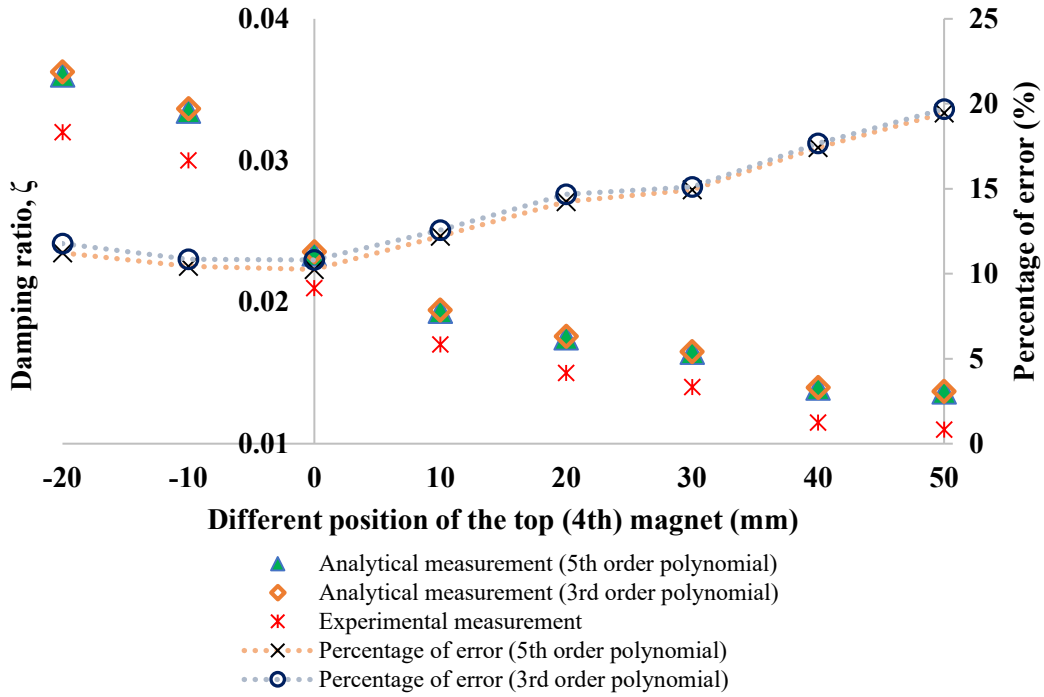

(b)

Figure 5.24: (a) 2nd natural frequency and (b) damping ratio for different lengths of the oscillator

The experimental measurements of natural frequencies and damping ratios for both floating magnets have been compared with the analytical measurements as shown in Figure 5.23 and Figure 5.24. The differences and percentage errors of natural frequencies' analytical measurements from experimental

measurements are shown in Figure 5.23(a) and Figure 5.24(a). The experimental measurements of natural frequencies for different lengths of the oscillator always stayed slightly higher than the analytical measurements for both floating magnets. The percentage error of analytical measurements from experimental measurements varies for different positions of the top (4^{th}) magnet. On the other hand, during the measurements of damping ratio maximum time, the values analytically measured for both floating magnets remained higher than the values experimentally measurement when the top magnets moved from the equilibrium position, which can be seen in Figure 5.23(b) and Figure 5.24(b).

5.8 Conclusion

In this chapter, the characteristics of the magnetic spring-based 2DOF system and dynamics of the oscillator system have been analysed using analytical, experimental and numerical methods. The magnetic restoring forces and magnetic spring stiffness of the proposed 2DOF system have been studied numerically and theoretically. Analytical measured values have validated the numerical measured magnetic restoring forces of the system. The 3^{rd} and 5^{th} order polynomial curve fitting models have been used to determine the nonlinear behaviour of the 2DOF system and determine the linear and nonlinear coefficients from the modelled magnetic restoring forces. Moreover, by changing the position of both floating magnets, the linear and nonlinear coefficients of the system have been investigated. Based on these investigations, the dynamics of the 2DOF nonlinear system have been analysed. The position of the top fixed magnet has a significant impact on the 2DOF oscillator system, which have been analysed as well by changing the position of the top fixed magnet. The separation distances between magnets changed with the length of the oscillator, and it has been found that the separation distance between magnets has a significant influence on the vibration of the oscillator.

Chapter 6

Dynamic Behaviours of Three-degree-of-freedom Magnetic Spring-based Nonlinear Oscillator System

In chapter 5, the two-degree-of-freedom (2DOF) magnetic spring-based system and its dynamics were investigated. However, the SDOF magnetic spring-based system had only one-degree-of-freedom, and it was limited to only one resonant natural frequency. On the other hand, the 2DOF magnetic spring-based system had two-degree-of-freedom, and it was limited to two natural resonant frequencies. Preferably, the energy generator should pick up and resonate at every frequency present in the vibration source. By employing three-degree-of-freedom (3DOF) oscillator systems, one can use three resonant frequencies and achieve maximum power than SDOF and 2DOF oscillator systems. The simplest form of a 3DOF system is three floating magnets masses. This chapter deals with 3DOF magnetic spring-based oscillator systems and their behaviour about various design criteria. The study of 3DOF is a prerequisite to designing complex 3DOF magnetic spring-based wave energy convertor systems that will be discussed in Chapter 9. Therefore, this chapter aims to study the magnetic restoring forces and coefficients of the 3DOF magnetic spring-based system and analyse the system's dynamics.

6.1 Design Configuration of the Three-degree-of-freedom Nonlinear Oscillator System

Five permanent ring magnets, axially magnetised through the height of 13mm, have been used to create the three-degree-of-freedom (3DOF) nonlinear oscillator system. Just simply, a ring magnet has been added with the previous two-degree-of-freedom model oscillator model discussed in chapter 5. For the design concept, the 5^{th} magnet is added on the top of the 4^{th} magnet and fixed with the shaft, and the 4^{th} magnet keeps as a floating magnet along with 2^{nd} and 3^{rd} magnets. The 1^{st} and 5^{th} magnets are fixed with the shaft. The fixed magnets are attached to the end of the shaft, and their polarity is set in such a way that the repulsive force is created between the levitating magnet and the fixed magnets. The magnetic poles are oriented (NS-SN-NS-SN-NS) such that each magnet repels the adjacent magnets. The height and width of the test rig are 550 mm and 300 mm, respectively. Moreover, the height and diameter of the shaft are 550 mm and 12 mm, respectively. For the test rig design, as presented in Figure 6.1, when the 5^{th} magnet is added to the top of the 4^{th} magnet: the distance between the 2^{nd} and bottom magnet is reduced to 61 mm, the distance between the 2^{nd} and 3^{rd} magnets is reduced to 68 mm, the distance between the 3^{rd} and 4^{th} magnets is reduced to 79 mm,

and the 5th and 4th magnets are separated by 104 mm. For all degrees of freedom systems, the distance between the top magnet and the magnet underneath always remain 104 mm. When a magnet is added to the top of the other magnet in all situations, only the distance between the bottom magnet and 2nd magnet is reduced. For the 3DOF system, when the 5th magnet is added to the top of the 2DOF, the distance between the bottom magnet and the 2nd magnet is reduced.

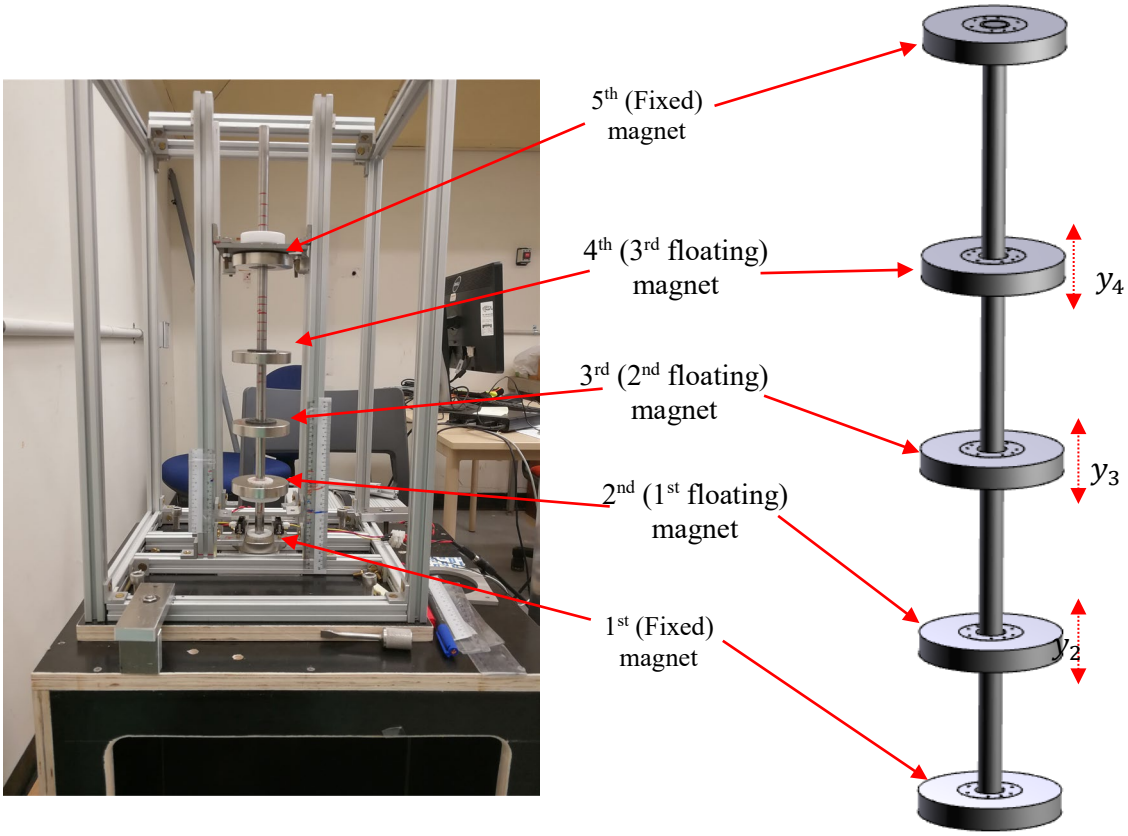

Figure 6.1: Test rig without winding coil

6.2 Magnetic Analysis of 3DOF system

The five (same size and shape) ring-type permanent magnets have been used to design the three-degree-of-freedom magnetic spring-based nonlinear oscillator system, as described in Section 6.1. The properties of the magnets have been presented in Table 3.1. The magnetic flux density on the magnet surface and the magnetisation direction is displayed in Figure 6.2.

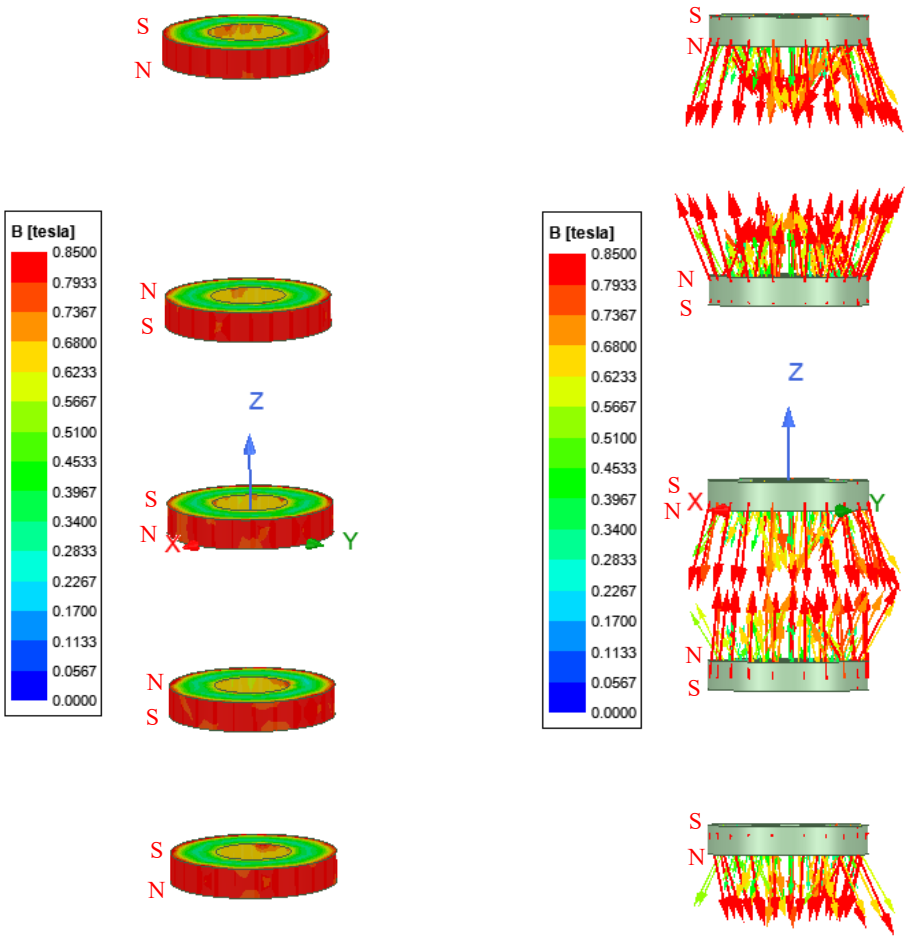

(a) (b)

Figure 6.2: (a) Magnetic flux density and (b) Magnetization direction

All designed magnets are axially magnetised (toward the North Pole), as shown in Figure 6.2(b). Figure 6.2(a) presents the magnetic flux densities on the surface of the magnets. The magnetic flux densities in the radial direction are larger than those in the axial direction. Figure 6.3 depicts the magnitude of the magnetic flux density. Figure 6.3(a) shows the magnitude of the magnetic flux density. It can be seen from Figure 6.3(a) that the maximum magnetic flux densities are found near the surface of the magnet. Figure 6.3(b) displays the magnetic flux density vector where the flux lines emerge from the north poles, travel around, and enter the south poles. It also shows the Z-axis as a line through the centre of all the magnets. A line, *d*, is considered which is perpendicular to the X-axis and 37 mm (d_1) from the centre line (Z-axis) of the magnetic stack in the radial direction, as shown in Figure 6.4, to measure the magnetic flux density in the axial and radial direction.

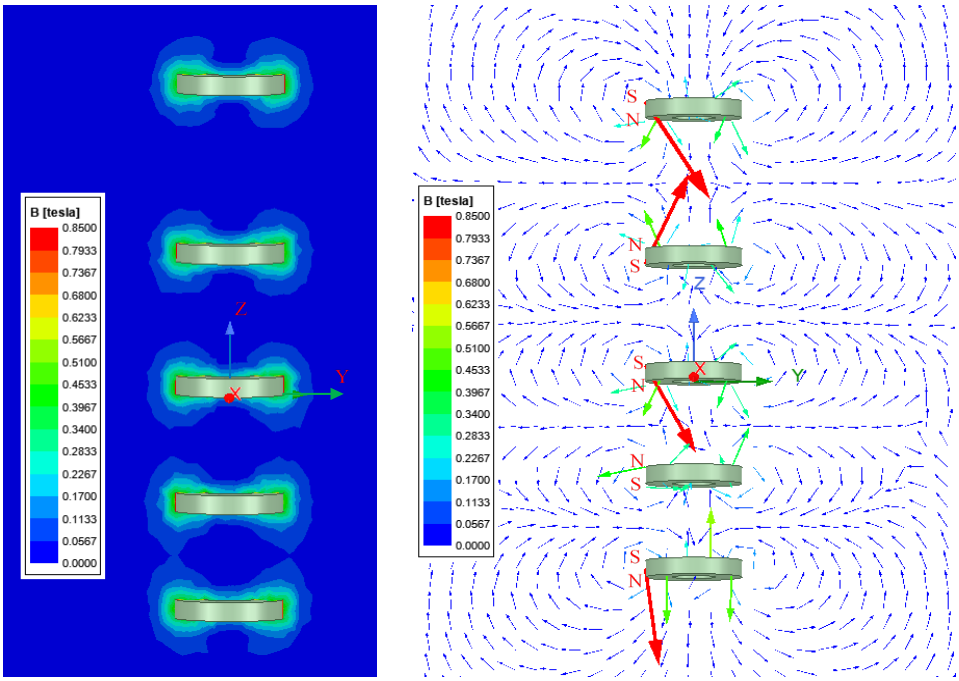

(a) (b)

Figure 6.3: (a) Mag_B in YZ plane and (b) B_Vector in YZ plane

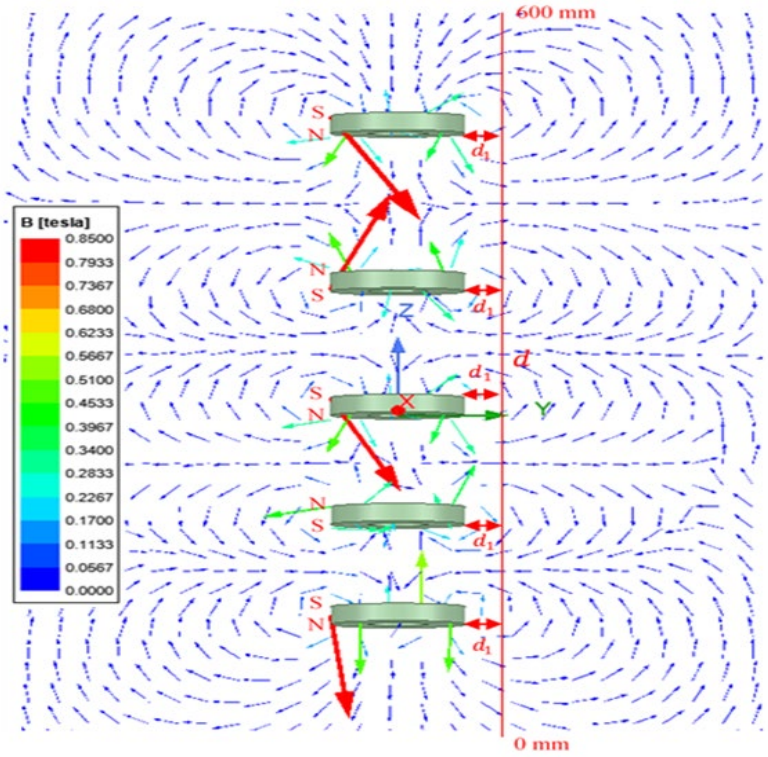

Figure 6.4: Magnetic flux density (B_Vector) in YZ plane

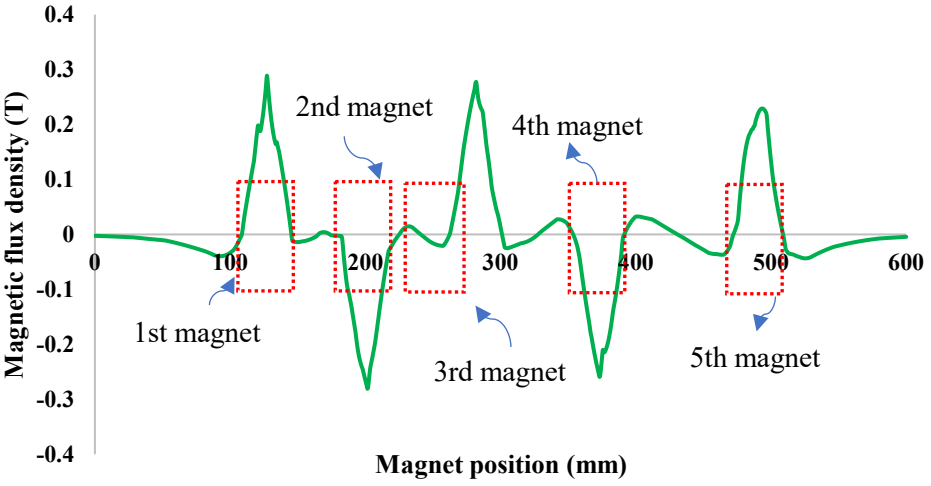

(a)

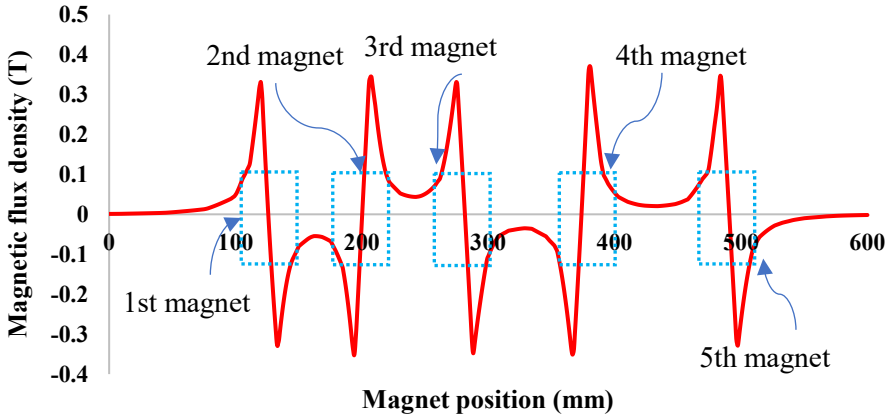

(b)

Figure 6.5: (a) Radial magnetic flux density and (b) Axial direction magnetic flux density

Going from $d = 0$ (sudden position below the 1st magnet) to $d = 600\ mm$ (sudden place in the upper part of the 5th magnet), the movement of the vertical arrows on one side is equivalent to the other side Figure 6.4. Figure 6.5(a) and Figure 6.5(b), respectively, are the measured magnetic flux density in the axial and radial directions. The values of magnetic flux density in Figure 6.5(a) were taken along the axial direction at various positions in the centre line, and the values of magnetic flux density in Figure 6.5(b) were taken along the radial direction at different places on the line d.

6.3 Magnetic Restoring Force of 3DOF

The magnetic poles of each magnet of the three-degree-of-freedom system are oriented to repel the adjacent magnet, causing the floating magnets to be suspended with the nonlinear restoring force.

The system's nonlinear behaviour allows the linear response to be modified by simply varying the position of the floating magnet between the top (5th magnet) and bottom (1st magnet) magnets. The magnetic force between the 1st magnet (fixed magnet) and 2nd magnet (floating magnet) can be written as,

$$F_b = \frac{\mu_0 Q_{1st} Q_{2nd}}{4\pi {r_1}^2} \tag{6.1}$$

where r_1 is the distance between the 1st and 2nd magnets, Q_{1st} and Q_{2nd} are the magnetic field intensity of the 1st and 2nd magnet respectively, and the permeability of the air is μ_0. Similarly, equation 6.1 can be rewritten for the 2nd magnet (1st floating magnet from the bottom magnet) and 3rd magnet (2nd floating magnet) as,

$$F_m = \frac{\mu_0 Q_{2nd} Q_{3rd}}{4\pi {r_2}^2} \tag{6.2}$$

where r_2 is the distance between the 2nd magnet and 3rd magnet poles. The equation 6.1 can be rewritten as well for the 3rd magnet (2nd floating magnet) and 4th magnet (3rd floating magnet) as,

$$F_b = \frac{\mu_0 Q_{3rd} Q_{4th}}{4\pi {r_3}^2} \tag{6.3}$$

where r_3 is the distance between the 3rd magnet and 4th magnet poles. Moreover, equation 6.1 can be rewritten as well for the 4th magnet (3rd floating magnet) and 5th magnet (fixed magnet) as,

$$F_b = \frac{\mu_0 Q_{4th} Q_{5th}}{4\pi {r_4}^2} \tag{6.4}$$

where r_4 is the distance between the 4th magnet and 5th magnet poles. For the case of in-plane movement, the expression for r_m and r_b can be written as

$$r_2 = H_{s1} - (r_1 + H_2) \tag{6.5}$$

Moreover, for the case of in-plane movement, the expression for r_m and r_t can be written as

$$r_3 = H_{s2} - (r_2 + H_3) \tag{6.6}$$

Moreover, for the case of in-plane movement, the expression for r_m and r_t can be written as

$$r_4 = H_{s3} - (r_3 + H_4) \tag{6.7}$$

where H_{s1} is the distance between the upper surface of the bottom magnet and lower surface of the 3rd magnet, H_{s2} is the separation distance between the upper surface of the 2nd magnet and lower surface of the 4th magnet, and H_{s3} is the distance between the upper surface of the 3rd magnet and the lower surface of the 5th magnet. H_1, H_2, H_3, H_4 and H_5 are the heights of the 1st, 2nd, 3rd, 4th and 5th magnets, respectively. To determine the magnetic restoring force for the first moving magnet, the 2nd and 3rd moving magnets are considered to be fixed. To measure the magnetic restoring force of the 2nd moving magnet, the 1st and 3rd moving magnets are considered to be fixed. Similarly, the 1st and 2nd moving magnets are deemed to be fixed magnets to determine the restoring force 3rd moving magnet. In addition, y_2, y_3 and y_4 are the moving distances of 1st moving magnet (2nd magnet), 2nd moving magnet (3rd magnet) and 3rd moving magnet (4th magnet), respectively. Figure 6.6 presents the schematic of the three-degrees-of-freedom oscillator system. The resultant magnetic forces or magnetic spring restoring forces (F_{res1}, F_{res2}, and F_{res3}) applied to the moving magnets can be calculated as,

$$F_{res1} = F_2 - F_1 = \frac{\mu_0 Q_{2nd}}{4\pi}\left(\frac{Q_{3rd}}{\left(r_2 - y_2(t)\right)^2} - \frac{Q_{1st}}{\left(r_1 + y_2(t)\right)^2}\right) \tag{6.8}$$

$$F_{res2} = F_3 - F_2 = \frac{\mu_0 Q_{3rd}}{4\pi}\left(\frac{Q_{4th}}{(r_3 - y_3(t))^2} - \frac{Q_{2nd}}{(r_2 + y_3(t))^2}\right) \tag{6.9}$$

$$F_{res3} = F_4 - F_3 = \frac{\mu_0 Q_{4th}}{4\pi}\left(\frac{Q_{5th}}{(r_4 - y_4(t))^2} - \frac{Q_{3rd}}{(r_3 + y_4(t))^2}\right) \tag{6.10}$$

The restoring forces of the magnetic springs can be calibrated from the calculation of the magnetic force. Equations 6.8, 6.9 and 6.10 can be expressed by a 3rd order Taylor series as,

$$F_{res1} = k_1 y_2 + \alpha_1 {y_2}^2 + \lambda_1 {y_2}^3 \tag{6.11}$$

$$F_{res2} = k_3 y_3 + \alpha_3 {y_3}^2 + \lambda_3 {y_3}^3 \tag{6.12}$$

$$F_{res3} = k_5 y_4 + \alpha_5 {y_4}^2 + \lambda_5 {y_4}^3 \tag{6.13}$$

where k_1 ,k_3 and k_5 are the linear constants. The nonlinear constants are denoted by α_1, λ_1, α_3, λ_3, α_5 and λ_5. The analytical and numerical magnetic restoring forces for different positions of the 1st, 2nd, and 3rd floating magnets have been presented in Figure 6.7.

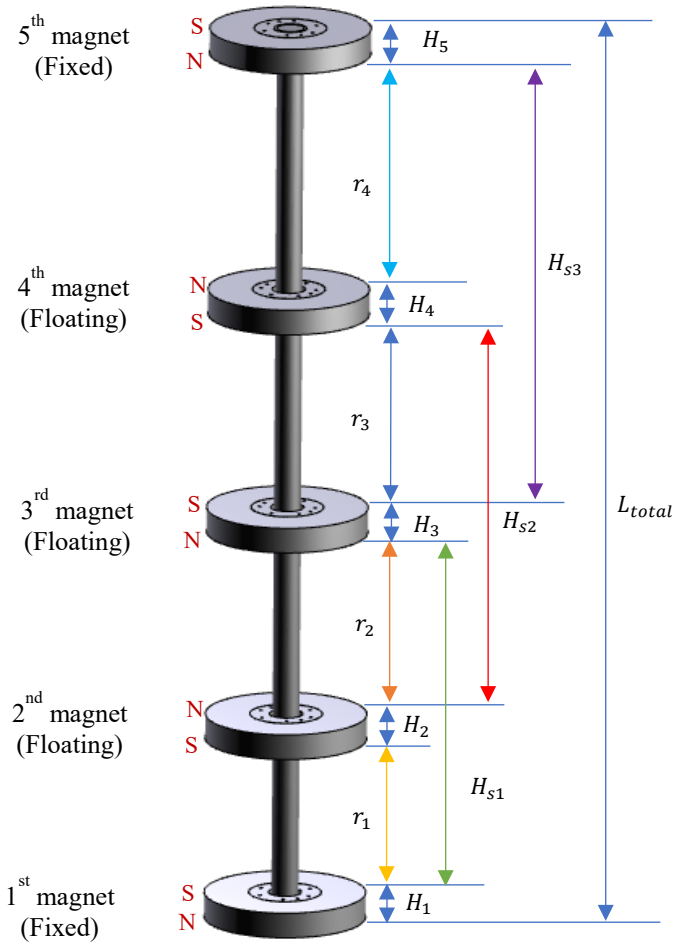

Figure 6.6: Magnetic system where 3 magnets are floating

The distance between the 2nd magnet (1st floating magnet) and 1st magnet (fixed magnet) is smaller than the distance between the 2nd (1st floating magnet) and 3rd magnet (2nd floating magnet). Therefore, the magnetic force is larger between the 1st and 2nd magnets (1st floating magnet) than the magnetic force between 2nd and 3rd magnets, as presented in Figure 6.7(a). Similarly, the distance between the 3rd magnet (2nd floating magnet) and 2nd magnet (1st floating magnet) is smaller than the distance between the 3rd magnet and 4th magnet (3rd floating magnet). As a result, the magnetic restoring force between the 3rd and 2nd magnets is greater than the magnetic restoring force between the 3rd and 4th magnet, as seen in Figure 6.7(b).

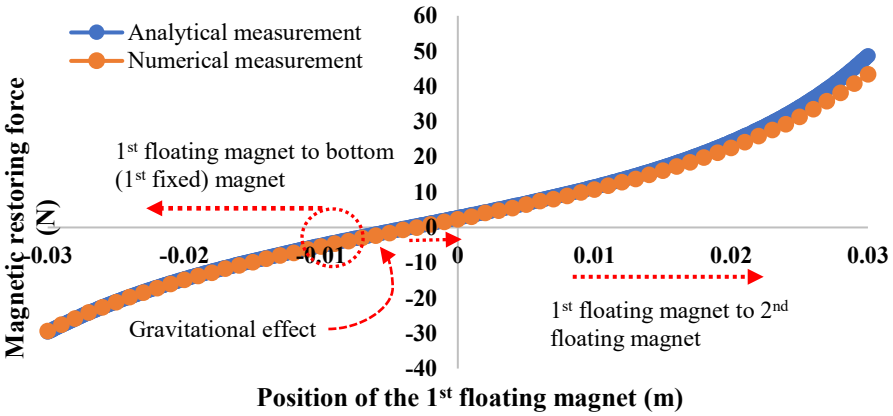

(a)

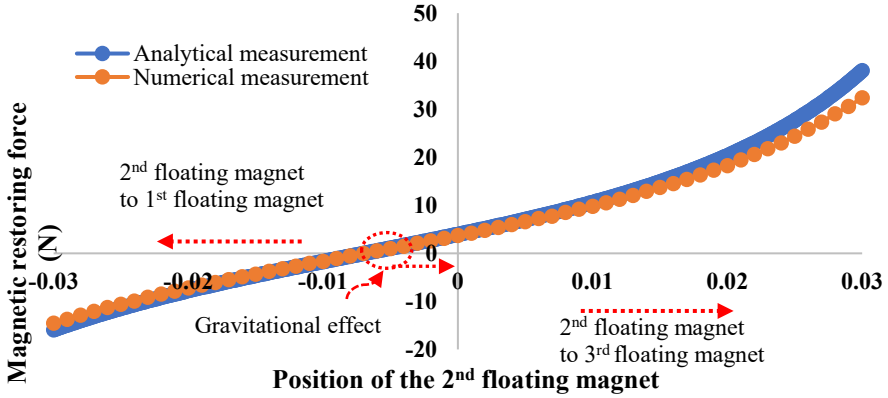

(b)

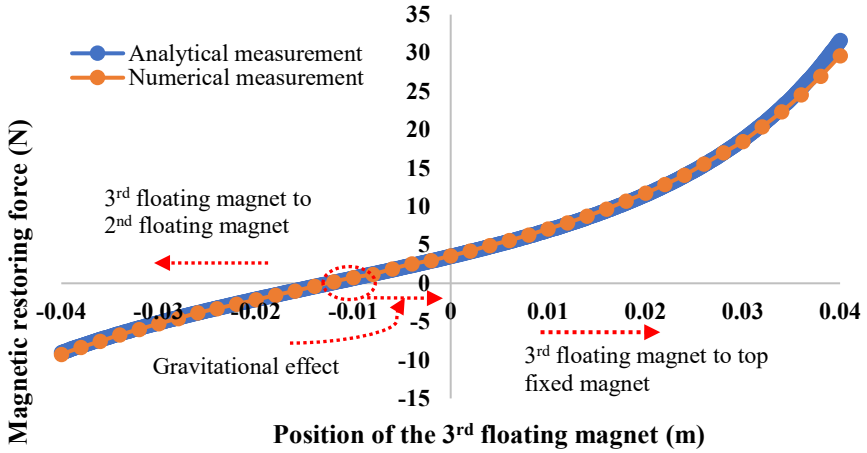

(c)

Figure 6.7: Magnetic restoring force (a) 1st floating magnet and (b) 2nd floating magnet and (c) 3rd floating magnet

Furthermore, the distance between the 4th magnet (3rd floating magnet) and 3rd magnet (2nd floating magnet) is smaller than the distance between the 4th magnet and 5th magnet (top fixed magnet). The

repulsive magnetic force between the 4th magnet (3rd floating magnet) and 3rd magnet (2nd floating magnet) is greater than the repulsive force between the 4th magnet and 5th magnet (top fixed magnet). Moreover, the effects of gravitational forces on the equilibrium positions for all floating magnets of the 3DOF system can be seen in Figure 6.7.

6.4 Coefficients Analysis of the 3DOF System

The 3DOF system consists of 3 floating magnets and two fixed ring magnets, all of which are axially magnetised. To determine the magnetic restoring force of the 1st moving magnet, the 2nd and 3rd moving magnets are considered fixed magnets. Likewise, for the 2nd moving magnet, the 1st and 3rd moving magnets are assumed as a fixed magnet. The 1st and 2nd floating magnets are considered fixed magnets during the magnetic restoring force measurement of the 3rd floating magnet. The magnetic restoring forces curve for all moving magnets are presented in Figure 6.8, 6.9 and 6.10.

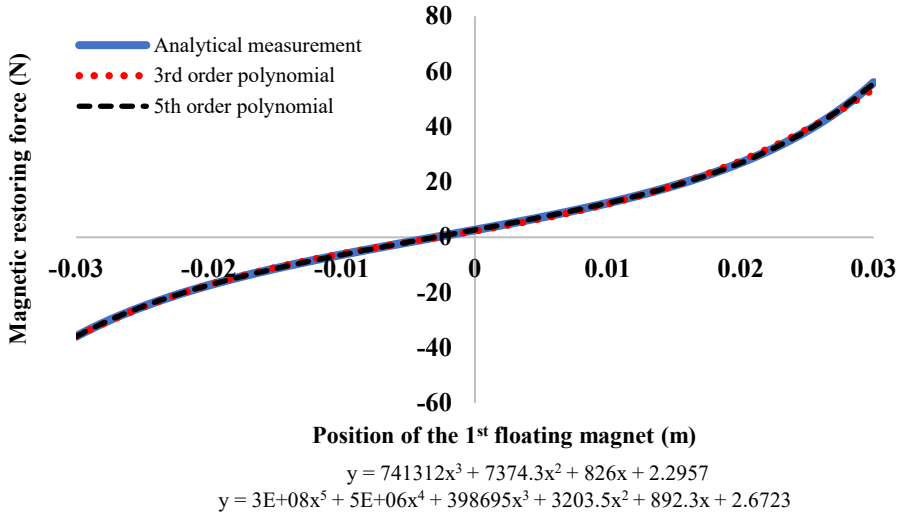

(a)

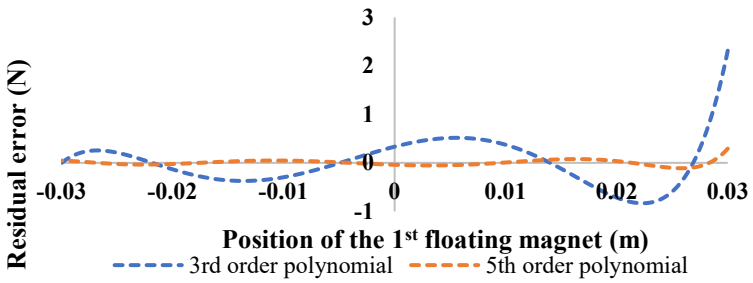

(b)

Figure 6.8: (a) Magnetic restoring force for 1st moving/floating magnet (b) Residual error

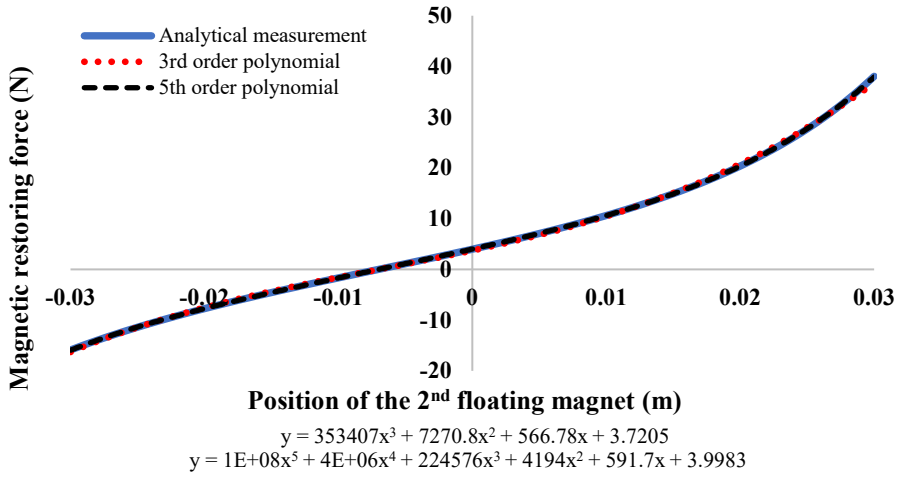

(a)

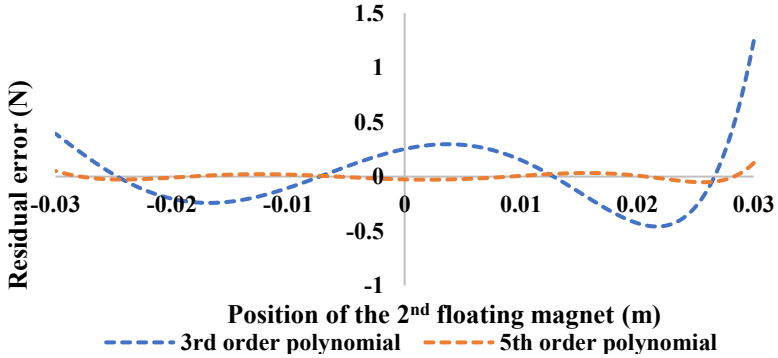

(b)

Figure 6.9: (a) Magnetic restoring force for 2nd moving/floating magnet (b) Residual error

The linear and nonlinear stiffness have been calculated using curve fitting from the graphical presentation of the magnetic restoring force with the displacement of the floating magnet. For the 3DOF oscillator system, the analytical measurements of the restoring forces are being used to measure the linear and nonlinear stiffness of the system. The values of k_1, k_3, k_5, α_1, λ_1, α_3, λ_3, α_5 and λ_5 in equations 6.11, 6.12 and 6.13 can be measured using the least-squares curve fitting of the graphs as well. Both the 3rd order polynomial and the 5th order polynomial have been used to determine the coefficients of the system. Moreover, the residual error has been calculated to pick up the suitable curve fitting model. From Figures 6.8, 6.9 and 6.10, it can be seen that the 5th order polynomial curve fit presented significantly less residual error than the 3rd order polynomial curve fit. Therefore, the 5th order polynomial curve fit provides a more accurate measurement than the 3rd order polynomial curve fit.

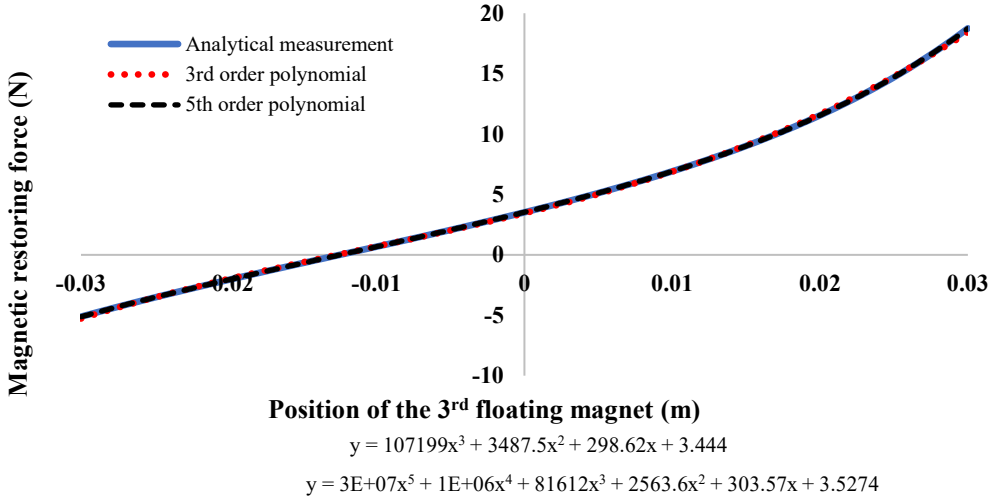

(a)

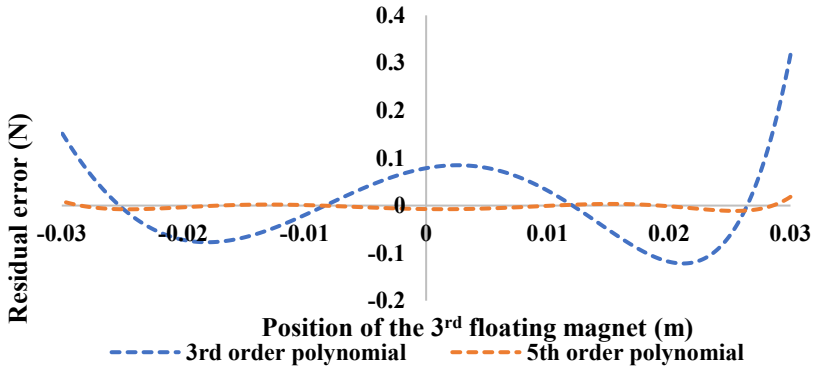

(b)

Figure 6.10: (a) Magnetic restoring force for 3rd moving/floating magnet (b) Residual error

Table 6.1 presents the measured coefficients of the system using a 3rd order polynomial curve fit for the 30 mm excitation range. On the other hand, Table 6.2 displays the linear and nonlinear stiffness of the system for the 30 mm excitation range, measured by using a 5th order polynomial curve fit.

Table 6.1: Coefficients of the 3DOF system for 3rd order polynomial

Rfmm	PLM	k_1 N/m	k_3 N/m	k_5 N/m	α_1 N/m^2	α_3 N/m^2	α_5 N/m^2	λ_1 N/m^3	λ_3 N/m^3	λ_5 N/m^3
1st	3rd	826	0	0	7374.3	0	0	741312	0	0
2nd	3rd	0	566.78	0	0	7270.8	0	0	353407	0
3rd	3rd	0	0	298.62	0	0	3487.5	0	0	107199

Note: Rfmm= Restoring force of the moving magnet, PLM= Polynomial model

Table 6.2: Coefficients of the 3DOF system for 5th order polynomial

Coefficients	1st FM	2nd FM	3rd FM
$\boldsymbol{k_1}$, N/m	892.30	0	0
$\boldsymbol{k_3}$, N/m	0	591.70	0
$\boldsymbol{k_5}$, N/m	0	0	303.57
$\boldsymbol{\alpha_1}$, N/$\boldsymbol{m^2}$	3203.52	0	0
$\boldsymbol{\alpha_3}$, N/$\boldsymbol{m^2}$	0	4194.02	0
$\boldsymbol{\alpha_5}$, N/$\boldsymbol{m^2}$	0	0	2563.60
$\boldsymbol{\lambda_1}$, N/$\boldsymbol{m^3}$	398694.72	0	0
$\boldsymbol{\lambda_3}$, N/$\boldsymbol{m^3}$	0	224576.40	0
$\boldsymbol{\lambda_5}$, N/$\boldsymbol{m^3}$	0	0	81612.48
$\boldsymbol{\varepsilon_1}$, N/$\boldsymbol{m^4}$	5388675	0	0
$\boldsymbol{\varepsilon_2}$, N/$\boldsymbol{m^4}$	0	3975218	0
$\boldsymbol{\varepsilon_3}$, N/$\boldsymbol{m^4}$	0	0	1193719.04
$\boldsymbol{\vartheta_1}$, N/$\boldsymbol{m^5}$	341484456	0	0
$\boldsymbol{\vartheta_2}$, N/$\boldsymbol{m^5}$	0	128404424.71	0
$\boldsymbol{\vartheta_3}$, N/$\boldsymbol{m^5}$	0	0	25501796.29

Note: Fm= Floating magnet

Table 6.3: Coefficients of the 3DOF system for different excitation ranges (3rd order polynomial curve fit)

ER (mm)	*Rfmm*	k_1 *N/m*	k_3 *N/m*	k_5 *N/m*	α_1 *N/m²*	α_3 *N/m²*	α_5 *N/m²*	λ_1 *N/m³*	λ_3 *N/m³*	λ_5 *N/m³*
-15 mm to 15 mm	1st	882.1	0	0	4713.4	0	0	521514	0	0
	2nd	0	588.29	0	0	5228.5	0	0	268203	0
	3rd	0	0	303.01	0	0	2846.2	0	0	89550
-20 mm to 20 mm	1st	875.84	0	0	5248.6	0	0	567711	0	0
	2nd	0	585.76	0	0	5668	0	0	286918	0
	3rd	0	0	302.45	0	0	2994.5	0	0	93660
-25 mm to 25 mm	1st	860.44	0	0	6076.6	0	0	637039	0	0
	2nd	0	579.72	0	0	6317.3	0	0	314158	0
	3rd	0	0	301.18	0	0	3202.7	0	0	99396

Note: ER= Excitation ranges, Rfmm= Restoring force of the moving magnet

From Table 6.1 it can be seen that the measured values of linear stiffnesses k_1, k_3 and k_5 are 826 N/m, 566.78 N/m and 298.62 N/m, respectively for 3rd order polynomial curve fit. The measured linear stiffnesses are 892.3 N/m, 591.7 N/m and 303.57 N/m, respectively for 5th order polynomial curve fit which can be seen from Table 6.2. The coefficients of the system have been measured by changing the excitation ranges of floating magnets. The same excitation ranges have been considered for all floating magnets for analysing the system. The excitation range varies from -30 mm to 30 mm, -25 mm to 25 mm, -20 mm to 20 mm and -15 mm to 15 mm. Both 3rd and 5th order polynomial curve fits have been used to determine the system's coefficients for different excitation ranges of the floating magnets. Table 6.3 and Table 6.4 show the measured coefficients for 3rd and 5th order polynomial curve fits, respectively, for different excitation ranges.

Table 6.4: Coefficients of the 3DOF system for different excitation ranges (5th order polynomial curve fit)

Coefficients	-15 mm to 15 mm			-20 mm to 20 mm			-25 mm to 25 mm		
	1st FM	2nd FM	3rd FM	1st FM	2nd FM	3rd FM	1st FM	2nd FM	3rd FM
k_1, N/m	884.74	0	0	885.13	0	0	886.75	0	0
k_3, N/m	0	589.38	0	0	589.51	0	0	590.03	0
k_5, N/m	0	0	303.25	0	0	303.27	0	0	303.35
α_1, N/m^2	4097	0	0	4005.8	0	0	3769.5	0	0
α_3, N/m^2	0	4708.4	0	0	4651	0	0	4509.7	0
α_5, N/m^2	0	0	2665	0	0	2652.6	0	0	2623.5
λ_1, N/m^3	467074	0	0	459810	0	0	441424	0	0
λ_3, N/m^3	0	245762	0	0	243370	0	0	237522	0
λ_5, N/m^3	0	0	84501	0	0	84146	0	0	83320
ε_1, N/m^4	3×10^6	0	0	4×10^6	0	0	4×10^6	0	0
ε_2, N/m^4	0	3×10^6	0	0	3×10^6	0	0	3×10^6	0
ε_3, N/m^4	0	0	933189	0	0	992504	0	0	1×10^6
ϑ_1, N/m^5	2×10^8	0	0	2×10^8	0	0	3×10^8	0	0
ϑ_2, N/m^5	0	9×10^7	0	0	1×10^8	0	0	1×10^8	0
ϑ_3, N/m^5	0	0	2×10^7	0	0	2×10^7	0	0	2×10^7

Note: FM=Floating magnet

From Table 6.3 and Table 6.4, it can be seen that the linear and nonlinear stiffnesses have been changed slightly with changing the excitation ranges of the floating magnets. Figure 6.11 and Figure 6.12 show the linear stiffnesses for all moving magnets for different excitation ranges for 3rd and 5th

order polynomial curve fits. The linear stiffness of the 1st floating magnets are larger than the 2nd and 3rd floating magnets.

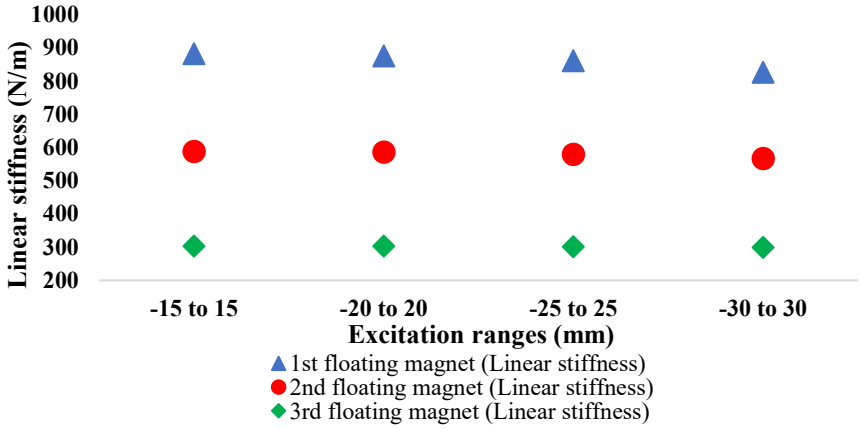

Figure 6.11: Linear stiffness for different floating magnets in the different excitation ranges (3rd order polynomial curve fit)

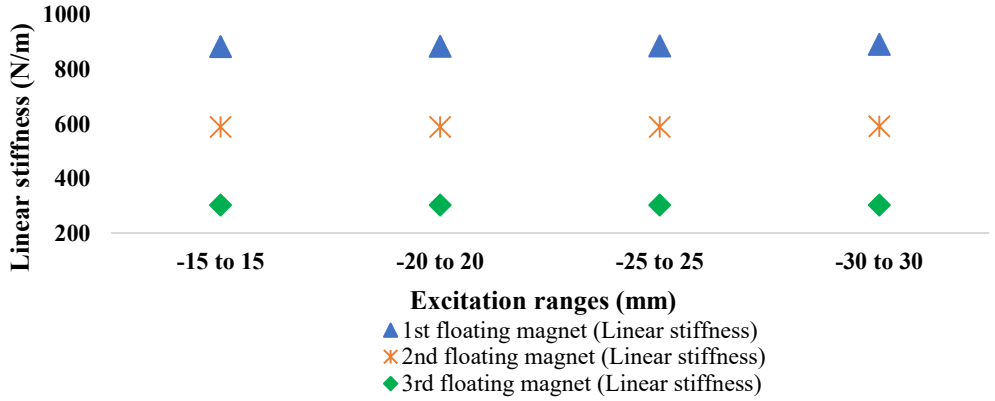

Figure 6.12: Linear stiffness for different floating magnets in the different excitation ranges (5th order polynomial curve fit)

It has been seen from Figure 6.11 and Figure 6.12 that the linear stiffnesses of all floating magnets have not changed much in the different excitation ranges; however, the coefficient of each floating magnet change with the different separation distances between magnets.

6.5 Modelling of the 3DOF Nonlinear Oscillator System

Figures Figure 6.13 and Figure 6.14 display the free-body diagrams of the proposed 3DOF nonlinear oscillator system. The masses of the 2nd (1st floating magnet), 3rd (2nd floating magnet) and 4th (3rd floating magnet) magnets are M_2, M_3 and M_4, respectively.

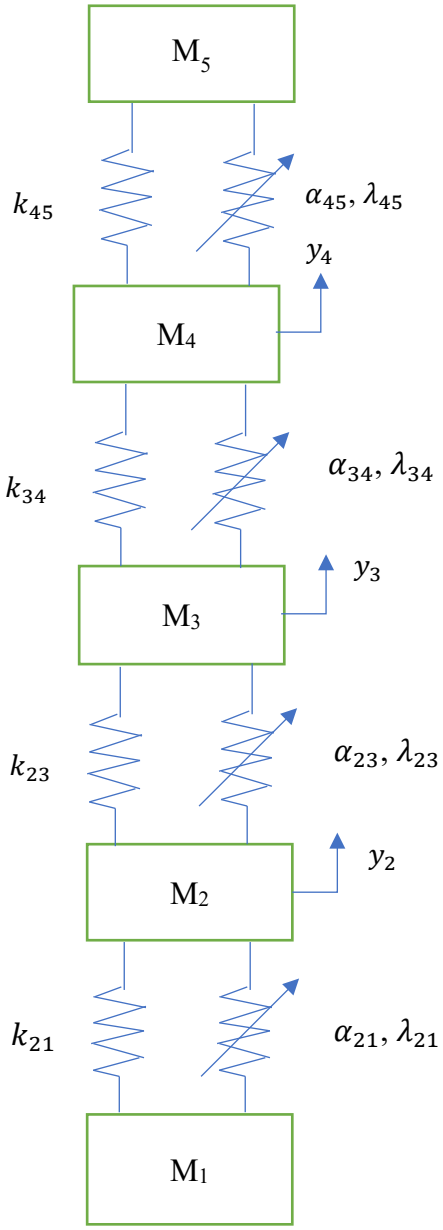

Figure 6.13: Three-degree-of-freedom magnetic spring-based oscillator system

The relative displacement of the 1st floating magnet is y_2 and the relative velocity and acceleration of the 1st floating magnet are $\dot{y}_2$ and $\ddot{y}_2$, respectively. The relative displacement, velocity and acceleration of the 2nd floating magnet are $y_3, \dot{y}_3$ and $\ddot{y}_3$, respectively. Moreover, the relative displacement, velocity and acceleration of the 3rd floating magnet are y_4, $\dot{y}_4$ and $\ddot{y}_4$, respectively. The damping forces of the 1st floating magnet is $F_{\beta 1} = \beta_1 \dot{y}_2$, 2nd floating magnet is $F_{\beta 3} = \beta_3 \dot{y}_3$ and 3rd floating magnet is $F_{\beta 5} = \beta_5 \dot{y}_4$. The linear stiffness of the 1st, 2nd, and 3rd floating magnets are k_1, k_3

and k_5, respectively. Using the 3rd order Taylor series, the nonlinear stiffnesses of the 1st floating magnet are α_1 and λ_1 and for the 2nd floating magnet, are α_3 and λ_3.

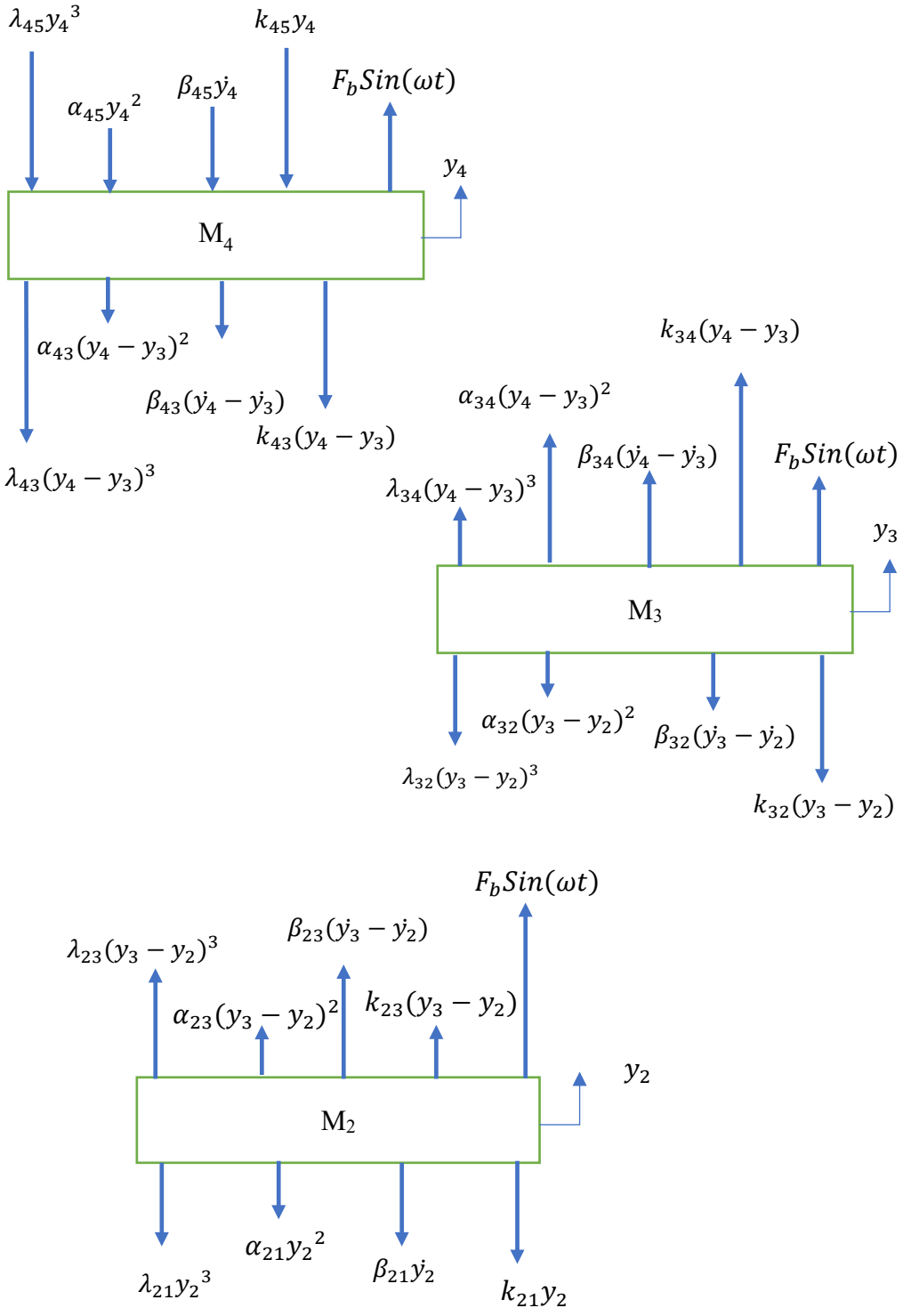

Figure 6.14: Free body diagram of M_2, M_3 and M_4

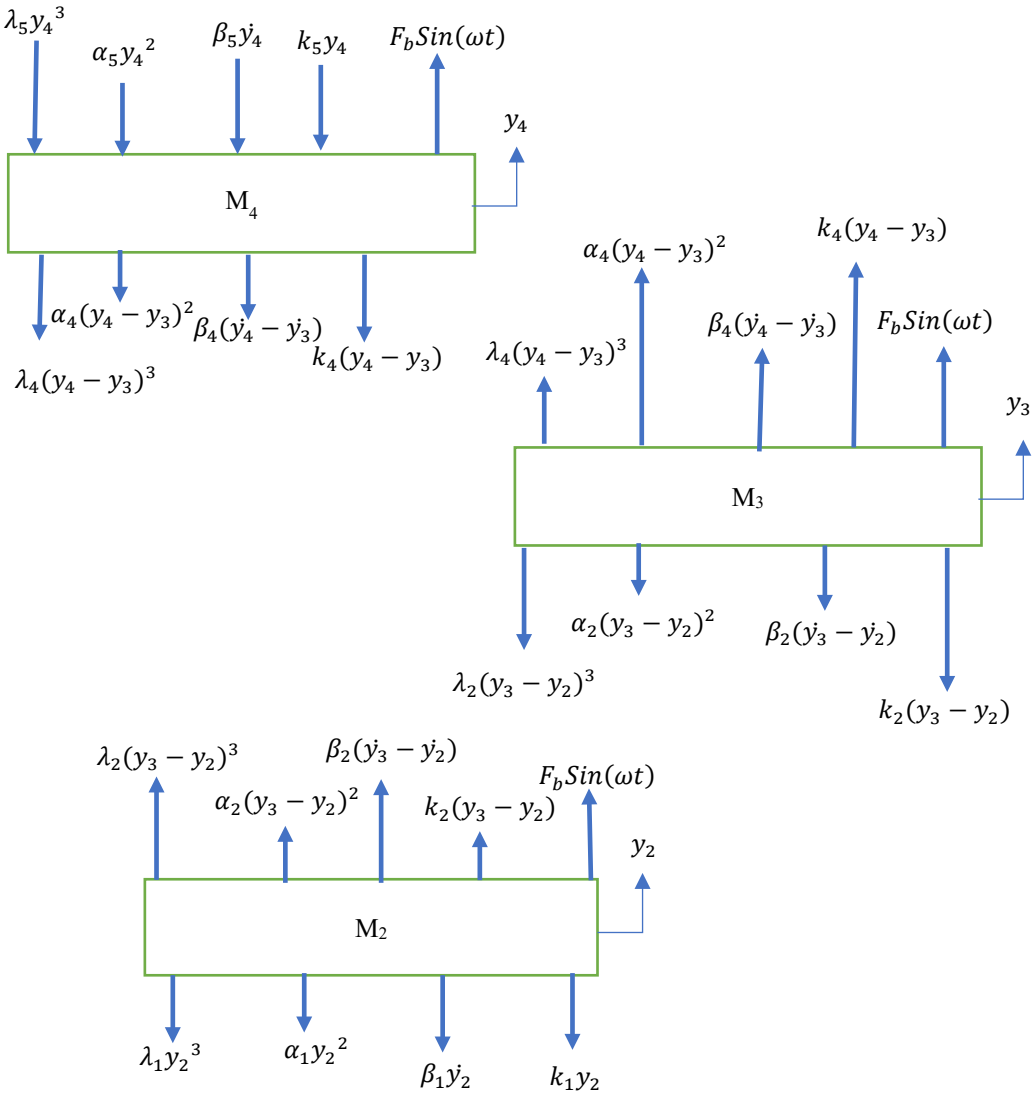

Figure 6.15: Free body diagram of M_2, M_3 and M_4 after substitutions

Furthermore, the nonlinear stiffnesses of the 3rd floating magnet are α_5 and λ_5. Furthermore, in Figure 6.14, the linear stiffness are: $k_{21} = k_1, k_{23} = k_{32} = k_2, k_{34} = k_{43} = k_4$ and $k_{45} = k_5$. The damping constants are: $\beta_{21} = \beta_1, \beta_{23} = \beta_{32} = \beta_2, \beta_{34} = \beta_{43} = \beta_4$ and $\beta_{45} = \beta_5$. The nonlinear coefficients are: $\alpha_{21} = \alpha_1$, $\alpha_{23} = \alpha_{32} = \alpha_2$, $\alpha_{34} = \alpha_{43} = \alpha_4$ and $\alpha_{45} = \alpha_5$. In addition, the nonlinear stiffness coefficients are: $\lambda_{21} = \lambda_1, \lambda_{23} = \lambda_{32} = \lambda_2, \lambda_{34} = \lambda_{43} = \lambda_4$ and $\lambda_{45} = \lambda_5$. Figure 6.14 can be represented by Figure 6.15 after replacing the linear and nonlinear coefficient's values. The dynamic equation of the motion of the system can be written as,

$$M_2\ddot{y}_2 + \beta_1\dot{y}_2 - \beta_2(\dot{y}_3 - \dot{y}_2) + k_1 y_2 - k_2(y_3 - y_2) + \alpha_1 y_2{}^2 - \alpha_2(y_3 - y_2)^2 + \lambda_1 y_2{}^3 - \lambda_2(y_3 - y_2)^3 = F_1 Sin(\omega t) \quad (6.14)$$

$$M_3\ddot{y}_3 + \beta_2(\dot{y}_3 - \dot{y}_2) - \beta_4(\dot{y}_4 - \dot{y}_3) + k_2(y_3 - y_2) - k_4(y_4 - y_3) + \alpha_2(y_3 - y_2)^2 - \alpha_4(y_4 - y_3)^2 + \lambda_2(y_3 - y_2)^3 - \lambda_4(y_4 - y_3)^3 = F_2Sin(\omega t) \quad (6.15)$$

$$M_4\ddot{y}_4 + \beta_5\dot{y}_4 + \beta_4(\dot{y}_4 - \dot{y}_3) + k_5y_4 + k_4(y_4 - y_3) + \alpha_5{y_4}^2 + \alpha_4(y_4 - y_3)^2 + \lambda_5{y_4}^3 + \lambda_4(y_4 - y_3)^3 = F_3Sin(\omega t) \quad (6.16)$$

The equation 6.14 can be rewritten as,

$$M_2\ddot{y}_2 + \beta_1\dot{y}_2 + \beta_2\dot{y}_2 - \beta_2\dot{y}_3 + k_1y_2 + k_2y_2 - k_2y_3 + \alpha_1{y_2}^2 - \alpha_2({y_3}^2 - 2y_2y_3 + {y_2}^2) + \lambda_1{y_2}^3 - \lambda_2({y_3}^3 - {y_2}^3 + 3{y_2}^2y_3 - 3y_2{y_3}^2) = F_1Sin(\omega t) \quad (6.17)$$

$$M_2\ddot{y}_2 + \beta_1\dot{y}_2 + \beta_2\dot{y}_2 - \beta_2\dot{y}_3 + k_1y_2 + k_2y_2 - k_2y_3 + \alpha_1{y_2}^2 - \alpha_2{y_3}^2 + 2\alpha_2y_2y_3 - \alpha_2{y_2}^2 + \lambda_1{y_2}^3 - \lambda_2{y_3}^3 + \lambda_2{y_2}^3 - 3\lambda_2{y_2}^2y_3 + 3\lambda_2y_2{y_3}^2 = F_1Sin(\omega t) \quad (6.18)$$

$$M_2\ddot{y}_2 + (\beta_1 + \beta_2)\dot{y}_2 - \beta_2\dot{y}_3 + (k_1 + k_2 + \alpha_1y_2 - \alpha_2y_2 + \lambda_1{y_2}^2 + \lambda_2{y_2}^2 + 2\alpha_2y_3 + 3\lambda_2{y_3}^2)y_2 - (k_2 + 3\lambda_2{y_2}^2 + \alpha_2y_3 + \lambda_2{y_3}^2)y_3 = F_1Sin(\omega t) \quad (6.19)$$

The equation 6.15 can be rewritten as,

$$M_3\ddot{y}_3 + \beta_2\dot{y}_3 - \beta_2\dot{y}_2 - \beta_4\dot{y}_4 + \beta_4\dot{y}_3 + k_2y_3 - k_2y_2 - k_4y_4 + k_4y_3 + \alpha_2(y_3^2 - 2y_3y_2 + y_2^2) - \alpha_4({y_4}^2 + {y_3}^2 - 2y_3y_4) + \lambda_2({y_3}^3 - {y_2}^3 - 3{y_3}^2y_2 + 3y_3{y_2}^2) - \lambda_4({y_4}^3 - {y_3}^3 + 3{y_3}^2y_4 - 3y_3{y_4}^2) = F_2Sin(\omega t) \quad (6.20)$$

$$M_3\ddot{y}_3 + \beta_2\dot{y}_3 - \beta_2\dot{y}_2 + \beta_4\dot{y}_3 - \beta_4\dot{y}_4 + k_2y_3 - k_2y_2 + k_4y_3 - k_4y_4 + \alpha_2{y_3}^2 + \alpha_2{y_2}^2 - 2\alpha_2y_3y_2 - \alpha_4{y_4}^2 - \alpha_4{y_3}^2 + 2\alpha_4y_3y_4 + \lambda_2{y_3}^3 - \lambda_2{y_2}^3 - 3\lambda_2{y_3}^2y_2 + 3\lambda_2y_3{y_2}^2 - \lambda_4{y_4}^3 + \lambda_4{y_3}^3 - 3\lambda_4{y_3}^2y_4 + 3\lambda_4y_3{y_4}^2 = F_2Sin(\omega t) \quad (6.21)$$

$$M_3\ddot{y}_3 - \beta_2\dot{y}_2 + (\beta_2 + \beta_4)\dot{y}_3 - \beta_4\dot{y}_4 - (k_2 - \alpha_2y_2 + 2\alpha_2y_3 + \lambda_2{y_2}^2 + 3\lambda_2{y_3}^2)y_2 + (k_2 + k_4 + \alpha_2y_3 - \alpha_4y_3 + 2\alpha_4y_4 + \lambda_2{y_3}^2 + 3\lambda_2{y_2}^2 + \lambda_4{y_3}^2 + 3\lambda_4{y_4}^2)y_3 - (k_4 + \alpha_4y_4 + \lambda_4{y_4}^2 + 3\lambda_4{y_3}^2)y_4 = F_2Sin(\omega t) \quad (6.22)$$

The equation 6.16 can be expressed as,

$$M_4\ddot{y}_4 + (\beta_5 + \beta_4)\dot{y}_4 - \beta_4\dot{y}_3 - (k_4 + 2\alpha_4y_4 - \alpha_4y_3 + \lambda_4{y_3}^2 + 3\lambda_4{y_4}^2)y_3 + (k_5 + k_4 + \alpha_5y_4 + \alpha_4y_4 + \lambda_5{y_4}^2 + \lambda_4{y_4}^2 + 3\lambda_4{y_3}^2)y_4 = F_3Sin(\omega t) \quad (6.23)$$

State space variables can be used to solve equations (6.19, 6.22 and 6.23). State space variables can be defined as:

$$x_1 = y_2 \quad (6.24)$$

$$x_2 = \dot{y}_2 = \frac{dx_1}{dt} \quad (6.25)$$

$$\frac{dx_2}{dt} = \ddot{y}_2 \tag{6.26}$$

$$x_3 = y_3 \tag{6.27}$$

$$x_4 = \frac{dx_3}{dt} = \dot{y}_3 \tag{6.28}$$

$$\frac{dx_4}{dt} = \ddot{y}_3 \tag{6.29}$$

$$x_5 = y_4 \tag{6.30}$$

$$x_6 = \frac{dx_5}{dt} = \dot{y}_4 \tag{6.31}$$

$$\frac{dx_6}{dt} = \ddot{y}_4 \tag{6.32}$$

$$u = F_1 Sin(\omega t) = F_2 Sin(\omega t) = F_3 Sin(\omega t) \tag{6.33}$$

Equation 6.19 can be written as

$$\frac{dx_2}{dt} = \ddot{y}_2 = \frac{1}{M_2}[u - (\beta_1 + \beta_2)x_2 + \beta_2 x_4 - (k_1 + k_2 + \alpha_1 x_1 - \alpha_2 x_1 + \lambda_1 {x_1}^2 + \lambda_2 {x_1}^2 + 2\alpha_2 x_3 + 3\lambda_2 {x_3}^2)x_1 + (k_2 + 3\lambda_2 {y_2}^2 + \alpha_2 y_3 + \lambda_2 {y_3}^2)x_3 \tag{6.34}$$

The following variables can be assumed as,

$$P1 = (k_1 + k_2 + \alpha_1 x_1 - \alpha_2 x_1 + \lambda_1 {x_1}^2 + \lambda_2 {x_1}^2 + 2\alpha_2 x_3 + 3\lambda_2 {x_3}^2) \tag{6.35}$$

$$Q1 = (k_2 + 3\lambda_2 {x_1}^2 + \alpha_2 x_3 + \lambda_2 {x_3}^2) \tag{6.36}$$

The equation 6.47 can be written as,

$$\frac{dx_2}{dt} = \ddot{y}_2 = \frac{1}{M_2}[u - P1x_1 - (\beta_1 + \beta_2)x_2 + Q1x_3 + \beta_2 x_4] \tag{6.37}$$

The equation 6.26 can be stated as,

$$\frac{dx_4}{dt} = \ddot{y}_3 = \frac{1}{M_3}\big[u + (k_2 - \alpha_2 x_1 + 2\alpha_2 x_3 + \lambda_2 {x_1}^2 + 3\lambda_2 {x_3}^2)x_1 + \beta_2 x_2 - (k_2 + k_4 + \alpha_2 x_3 - \alpha_4 x_3 + 2\alpha_4 x_5 + \lambda_2 {x_3}^2 + 3\lambda_2 {x_1}^2 + \lambda_4 {x_3}^2 + 3\lambda_4 {x_5}^2)x_3 - (\beta_2 + \beta_4)x_4 + (k_4 + \alpha_4 x_5 + \lambda_4 {x_5}^2 + 3\lambda_4 {x_3}^2)x_5 + \beta_4 x_6\big] \tag{6.38}$$

The following variables can be considered as,

$$R1 = (k_2 - \alpha_2 x_1 + 2\alpha_2 x_3 + \lambda_2 {x_1}^2 + 3\lambda_2 {x_3}^2) \quad (6.39)$$

$$J1 = (k_2 + k_4 + \alpha_2 x_3 - \alpha_4 x_3 + 2\alpha_4 x_5 + \lambda_2 {x_3}^2 + 3\lambda_2 {x_1}^2 + \lambda_4 {x_3}^2 + 3\lambda_4 {x_5}^2) \quad (6.40)$$

$$E1 = (k_4 + \alpha_4 x_5 + \lambda_4 {x_5}^2 + 3\lambda_4 {x_3}^2) \quad (6.41)$$

Equation 6.51 can be rewritten as

$$\frac{dx_4}{dt} = \ddot{y}_3 = \frac{1}{M_3}[u + R1x_1 + \beta_2 x_2 - J1x_3 - (\beta_2 + \beta_4)x_4 + E1x_5 + \beta_4 x_6] \quad (6.42)$$

The equation 6.32 can be written as

$$\frac{dx_6}{dt} = \ddot{y}_4 = \frac{1}{M_4}[u + (k_4 - \alpha_4 x_3 + 2\alpha_4 x_5 + \lambda_4 {x_3}^2 + 3\lambda_4 {x_5}^2)x_3 + \beta_4 x_4 - (k_5 + k_4 + \alpha_5 x_5 + \alpha_4 x_5 + \lambda_5 {x_5}^2 + \lambda_4 {x_5}^2 + 3\lambda_4 {x_3}^2)x_5 - (\beta_5 + \beta_4)x_6] \quad (6.43)$$

To shorten Equation 6.56, the following parameters are considered

$$U1 = (k_4 - \alpha_4 x_3 + 2\alpha_4 x_5 + \lambda_4 {x_3}^2 + 3\lambda_4 {x_5}^2) \quad (6.44)$$

$$V1 = (k_5 + k_4 + \alpha_5 x_5 + \alpha_4 x_5 + \lambda_5 {x_5}^2 + \lambda_4 {x_5}^2 + 3\lambda_4 {x_3}^2) \quad (6.45)$$

The equation 6.56 can be stated as

$$\frac{dx_6}{dt} = \ddot{y}_4 = \frac{1}{M_4}[u + U1x_3 + \beta_4 x_4 - V1x_5 - (\beta_5 + \beta_4)x_6] \quad (6.46)$$

The state space model of the 3DOF system can be written as

$$\begin{bmatrix} \frac{dx_1}{dt} \\ \frac{dx_2}{dt} \\ \frac{dx_3}{dt} \\ \frac{dx_4}{dt} \\ \frac{dx_5}{dt} \\ \frac{dx_6}{dt} \end{bmatrix} = \underbrace{\begin{bmatrix} 0 & 1 & 0 & 0 & 0 & 0 \\ \frac{-P1}{M_2} & \frac{-(\beta_1+\beta_2)}{M_2} & \frac{Q1}{M_2} & \frac{\beta_2}{M_2} & 0 & 0 \\ 0 & 0 & 0 & 1 & 0 & 0 \\ \frac{R1}{M_3} & \frac{\beta_2}{M_3} & \frac{-J1}{M_3} & \frac{-(\beta_2+\beta_4)}{M_3} & \frac{E1}{M_3} & \frac{\beta_4}{M_3} \\ 0 & 0 & 0 & 0 & 0 & 1 \\ 0 & 0 & \frac{U1}{M_4} & \frac{\beta_4}{M_4} & \frac{-V1}{M_4} & \frac{-(\beta_5+\beta_4)}{M_4} \end{bmatrix}}_{A} \begin{bmatrix} x_1 \\ x_2 \\ x_3 \\ x_4 \\ x_5 \\ x_6 \end{bmatrix} + \underbrace{\begin{bmatrix} 0 \\ \frac{1}{M_2} \\ 0 \\ \frac{1}{M_3} \\ 0 \\ \frac{1}{M_4} \end{bmatrix}}_{B} [u] \quad (6.47)$$

$$Z = \underbrace{\begin{bmatrix} 1 & 0 & 0 & 0 & 0 & 0 \\ 0 & 1 & 0 & 0 & 0 & 0 \\ 0 & 0 & 1 & 0 & 0 & 0 \\ 0 & 0 & 0 & 1 & 0 & 0 \\ 0 & 0 & 0 & 0 & 1 & 0 \\ 0 & 0 & 0 & 0 & 0 & 1 \end{bmatrix}}_{C} \begin{bmatrix} x_1 \\ x_2 \\ x_3 \\ x_4 \\ x_5 \\ x_6 \end{bmatrix} + \underbrace{\begin{bmatrix} 0 \end{bmatrix}}_{D} [u] \tag{6.48}$$

Where *A* is the system matrix, *B* is the input matrix, and *C* is the output matrix. The remaining matrix is *D* which is typically zero because the input directly does not usually affect the output.

6.6 Dynamics Analysis of the 3DOF System

The distance between the 1st and 2nd magnets is 59 mm, 2nd and 3rd magnets is 65 mm, 3rd and 4th magnets is 79 mm, and 4th and 5th magnets is 104 mm. The total length of the oscillator is 372 mm. The masses of the 2nd (1st floating magnet), 3rd (2nd floating magnet) and 4th (3rd floating magnet) are 0.370 kg, 0.32728 kg and 0.33274 kg (mass including plastic bush), respectively.

Table 6.5: Different parameters of the 3DOF system

Parameters	Values	Units
β_1	2.11	Ns/m
β_2	0.8	Ns/m
β_4	0.8	Ns/m
β_5	0.51	Ns/m
k_1	826	N/m
k_2	263.69	N/m
k_4	263.69	N/m
k_5	298.62	N/m
α_1	7374.3	N/m^2
α_2	1943.4	N/m^2
α_4	1943.4	N/m^2
α_5	3487.5	N/m^2
λ_1	741312	N/m^3
λ_2	317056.5	N/m^3
λ_4	317056.5	N/m^3
λ_5	107199	N/m^3

The experimentally measured damping ratio and damping constant of the 1st floating magnet were 0.058, 2.11 Ns/m. The measured damping ratios and damping constants of the 2nd and 3rd floating magnets were 0.038, 1.08 Ns/m, 0.021 and 0.51 Ns/m, respectively. The measured natural frequencies were 56 rad/s, 44.47 rad/s and 32.87 rad/s. Table 6.5 shows the values of the required parameters for the dynamic analysis of the 3DOF system.

Table 6.6: Eigenvalues and resonance frequency of the system

PFM			Eigenvalue			Resonance frequency (rad/s)		
1st	2nd	3rd						
-15	-15	-15	-6.21 +87.89i	-2.85 +54.29i	-1.27 +35.40i	88.11	54.37	35.43
-10	-10	-10	-6.25 +76.40i	-2.85 +49.67i	-1.24 +34.07i	76.65	49.75	34.09
-05	-05	-05	-6.27 +69.24i	-2.84 +47.02i	-1.22 +33.50i	69.52	47.10	33.52
0	0	0	-6.28 +67.68i	-2.84 +46.76i	-1.21 +33.87i	67.97	46.85	33.89
05	05	05	-6.27 +71.99i	-2.84 +49.03i	-1.22 +35.22i	72.26	49.11	35.24
10	10	10	-6.26 +81.31i	-2.84 +53.44i	-1.24+37.38i	81.55	53.51	37.40
15	15	15	-6.23 +94.25i	-2.84 +59.45i	-1.26 +40.11i	94.41	59.52	40.13

Note: PFM= Position of the floating magnet

The simulation results of the 3DOF system are shown in Table 6.6. From Table 6.6, it can be seen that the eigenvalues of all floating magnets change with the different positions of floating magnets. The measured natural frequency for the system were 67.97 rad/s, 46.85 rad/s and 33.89 rad/s when all magnets were in equilibrium position. It can be seen that the experimental results are similar to the theoretical analysiss.

The frequency response of the 3DOF system is presented in Figure 6.16. Moreover, the 3DOF system has been analysed using the Root Locus tool, as illustrated in Figure 6.17. Three floating magnets are working in the 3DOF system; therefore, this system has three resonance frequencies which can be seen in Figure 6.16. The eigenvalues, frequency responses and damping ratio were also analysed using Root Locus, as shown in Figure 6.17. The resonance changed with the different positions of each floating magnet, which can be seen in Figure 6.18.

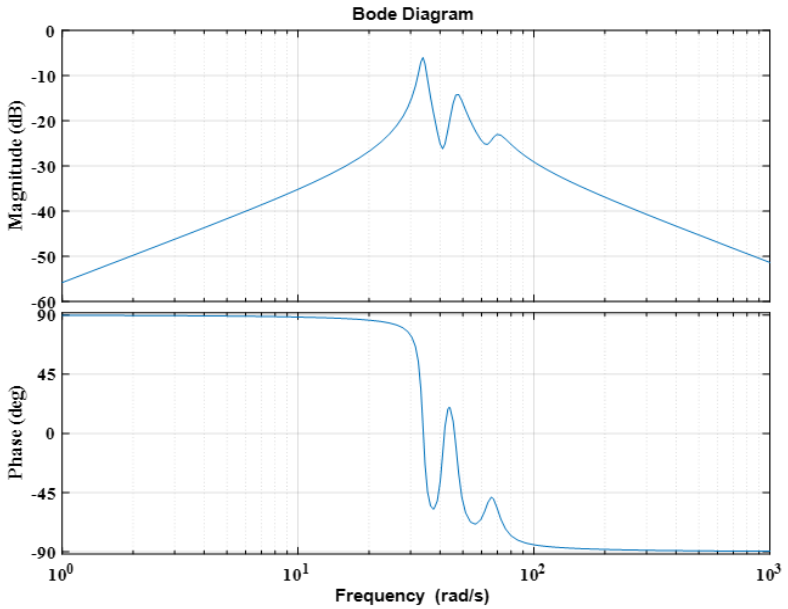

Figure 6.16: Resonance frequency of the 3DOF system

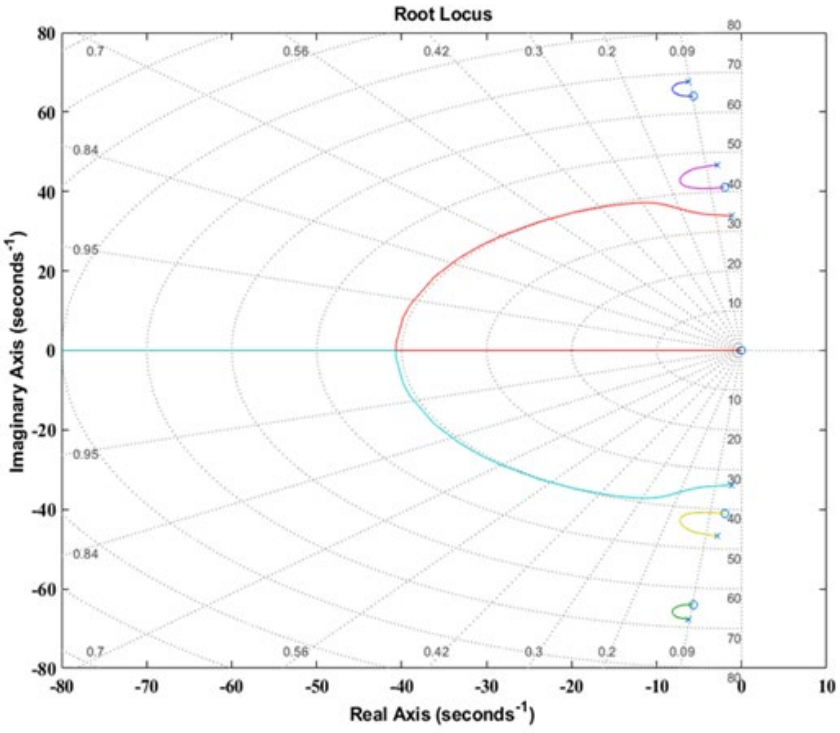

Figure 6.17: Root Locus analysis of the 3DOF system

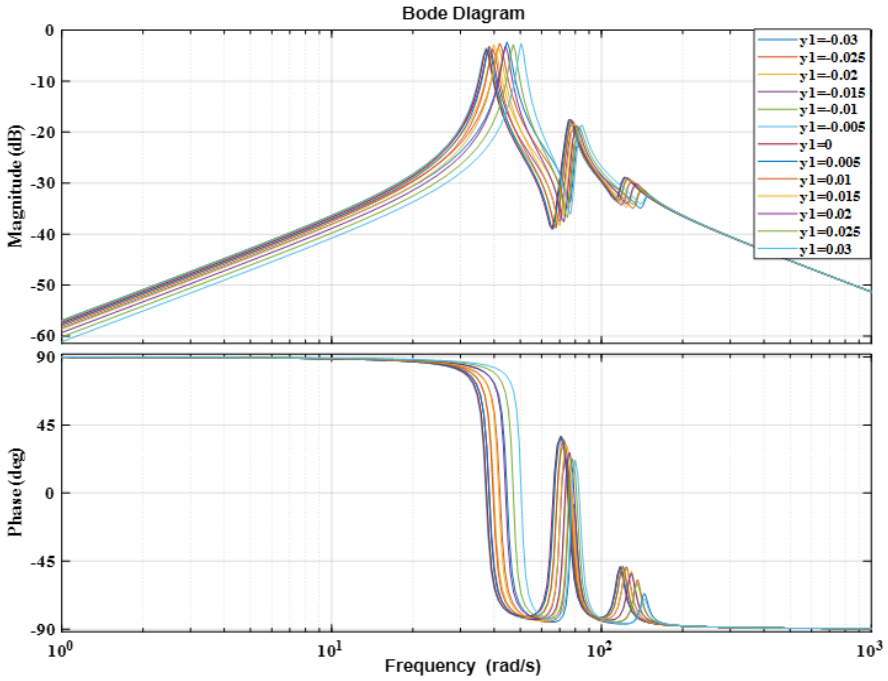

Figure 6.18: Frequency response of the system for different positions of the floating magnets

If an external force is applied on any floating magnet, the resulting displacements for all floating magnets (1st, 2nd and 3rd floating magnets) are shown in Figure 6.19 and the velocities for all floating magnets Figure 6.20. The amplitude of the applied external harmonic force (F_b) is 10N. The values of linear stiffness, nonlinear stiffness and damping constants are presented in Table 6.5. Ode23t solver has been used in MATLAB to find the displacements and velocities of all floating magnets. All floating magnets' excitation was assumed to have non-zero initial displacements, and initial velocities were zero. The frequency of the harmonic force was 0.1 Hz. As expected, the displacements and the velocities were sinusoidal and 90° out of phase. Force can be applied on the 3rd or 2nd, or 1st floating magnet. The amplitude of displacement of each floating magnet depends on which magnet the force is applied. Figure 6.19 presents the velocity vs displacement graphs for each floating magnet. If the force is applied on the 3rd floating magnet, then the displacement of the 3rd floating magnet is larger than the displacement of the 2nd and 1st floating magnets, and the displacement of the 2nd floating magnet is larger than the 1st floating magnet. Similarly, if the external force is applied on the 2nd floating magnet, then the displacement of the 2nd floating magnet is larger than the 1st and 3rd floating magnet, and the displacement of the 1st floating is larger than the 2nd and 3rd floating magnet if the external force is applied on the 1st floating magnet. Moreover, the comparisons of velocity vs

displacement graphs of all floating magnets under the same harmonic force have been presented in Figure 6.20.

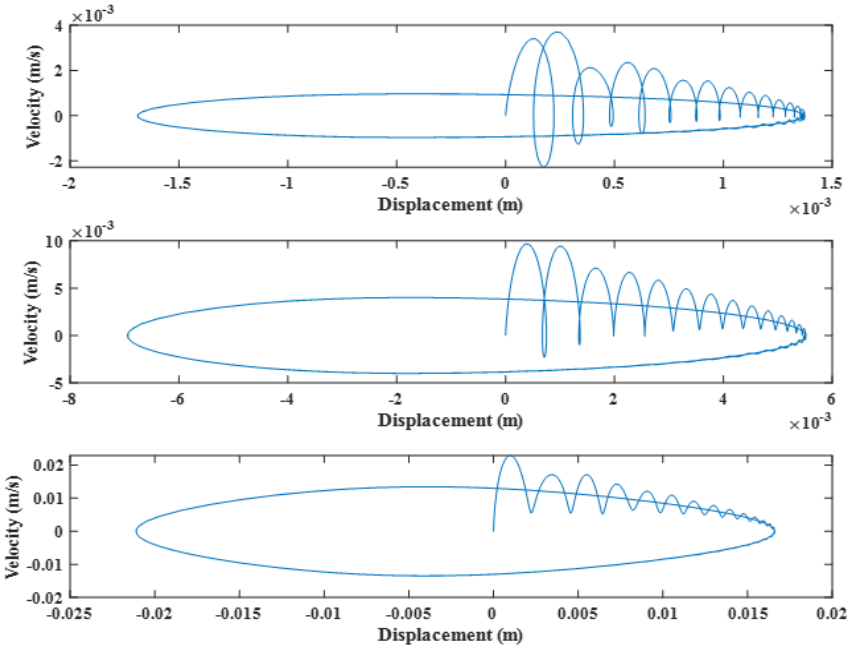

(a)

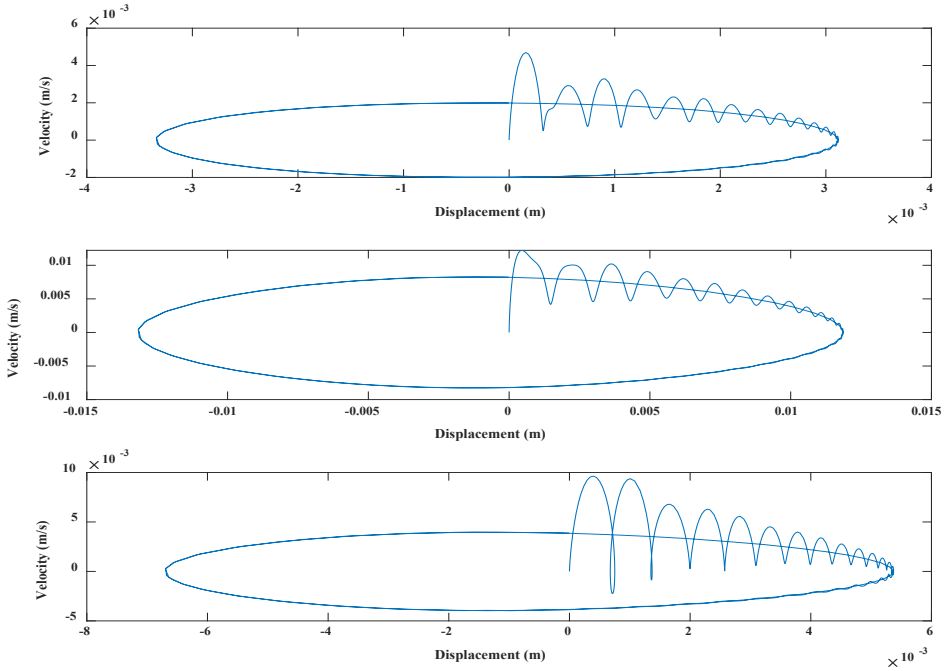

(b)

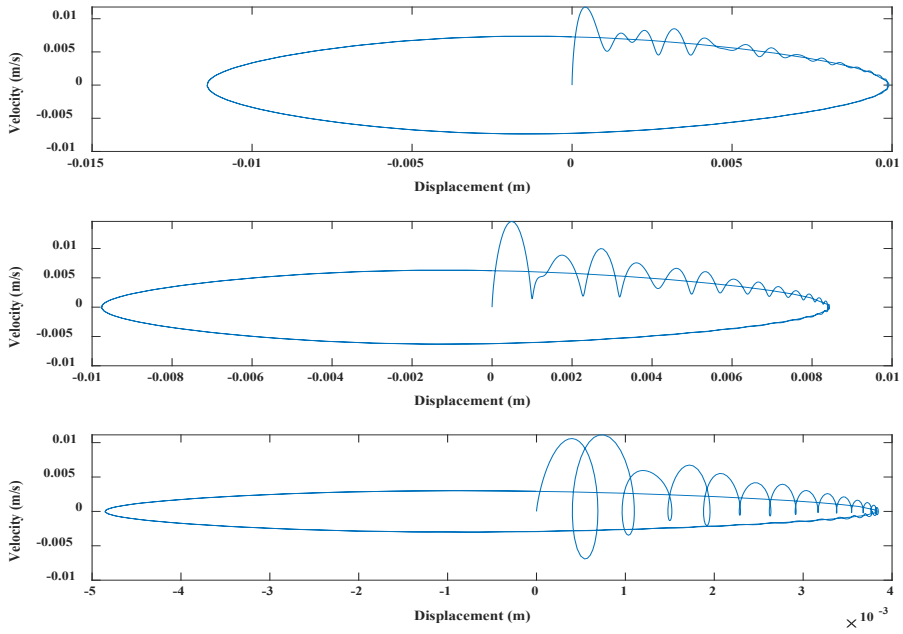

(c)

Figure 6.19: (a) Applied force on the 3rd floating magnet, (b) Applied force on the 2nd floating magnet and (c) applied force on the 1st floating magnet

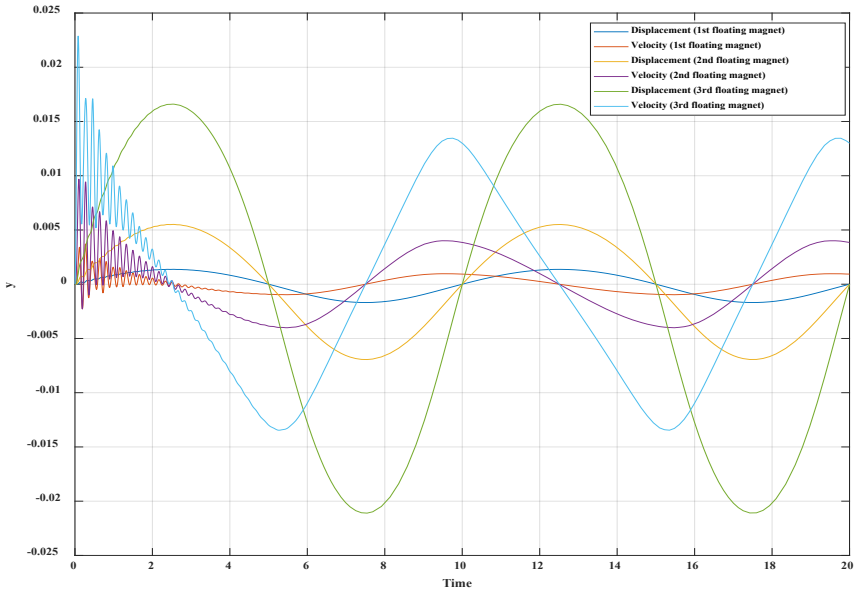

(a)

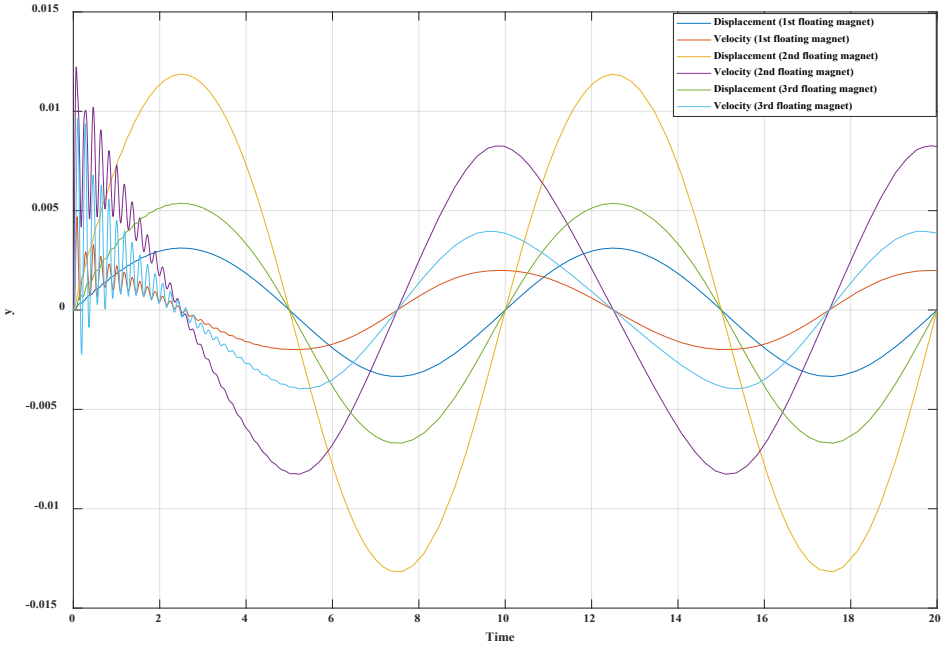

(b)

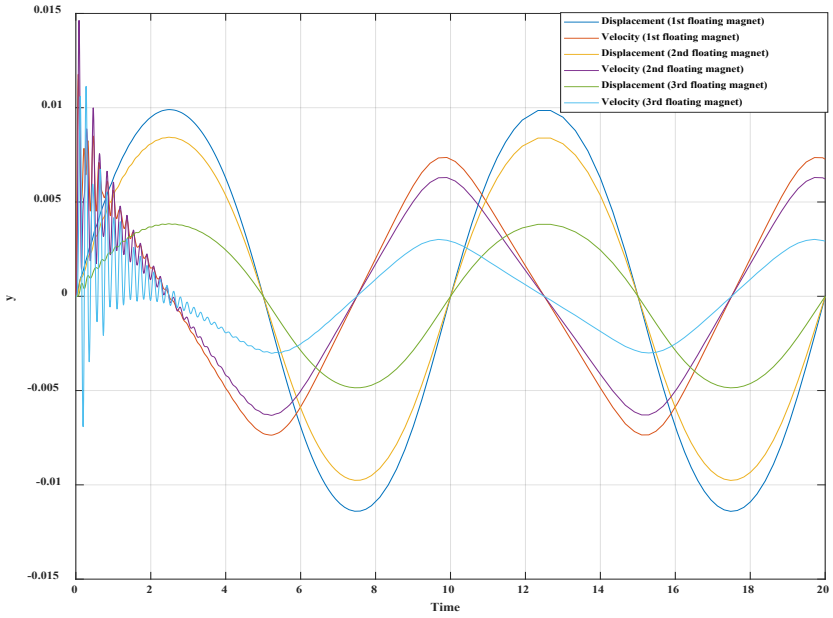

(c)

Figure 6.20: Comparison of displacement and velocity of each floating magnet (a) applied force on the 3rd floating magnet and (b) applied force on the 2nd floating magnet and (c) applied force on the 1st floating magnet

If the external force is applied to the 3rd floating magnet, it starts moving, causing the 1st and 2nd floating magnets to also start moving. Comparing the velocity of the 3rd floating magnet with the 1st and 2nd floating magnets; the 3rd floating magnet has a larger velocity than the 1st and 2nd floating magnets, which can be seen in Figure 6.20(a). Similarly, if the same external force is applied in the 2nd floating magnet, it starts moving, causing the 1st and 3rd floating magnet to start moving. The velocity of the 2nd floating magnet is larger than the 1st and 3rd floating magnet, as shown in Figure 6.20(b). Similar things happened if the external harmonic force is applied on the 1st floating magnet. Figure 6.21 compares the displacement and velocity of each floating magnet when the external force is applied to each one.

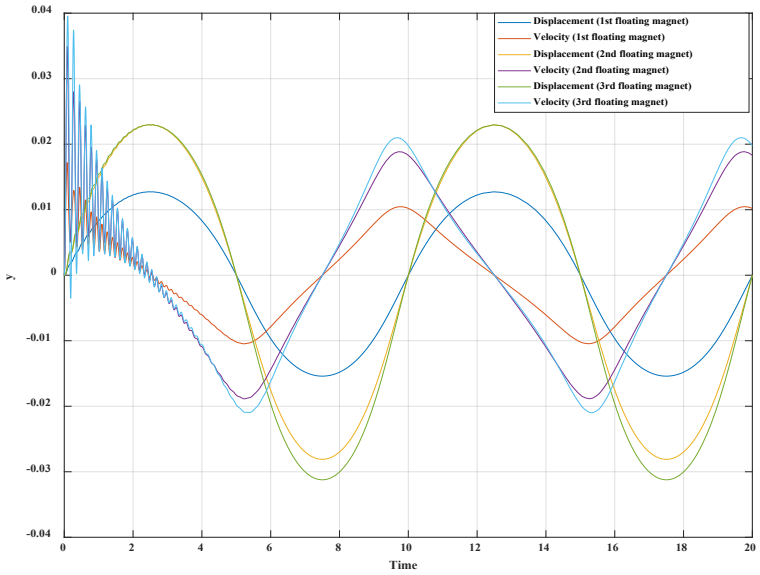

Figure 6.21: Comparison of displacement and velocity of each floating magnet when an external force is applied on each floating magnet

Moreover, if the same external forces are applied to all floating magnets, all magnets start moving. The displacement and velocity of the 1st floating magnet are smaller than the 2nd and 3rd floating magnet, as shown in Figure 6.21. In that scenario, all floating magnets achieve relatively higher displacements and velocities compared to other previously discussed procedures. However, due to the less damping ratio, the 3rd floating magnet consistently achieved higher displacement and velocity than the 1st and 2nd floating magnets in all scenarios.

6.7 Different Lengths of the 3DOF Oscillator

The total length of the 3DOF oscillator can be changed with the changing position of the 5th magnet (top fixed magnet). Figure 6.22 shows the 3DOF Magnetic spring-based nonlinear oscillator system.

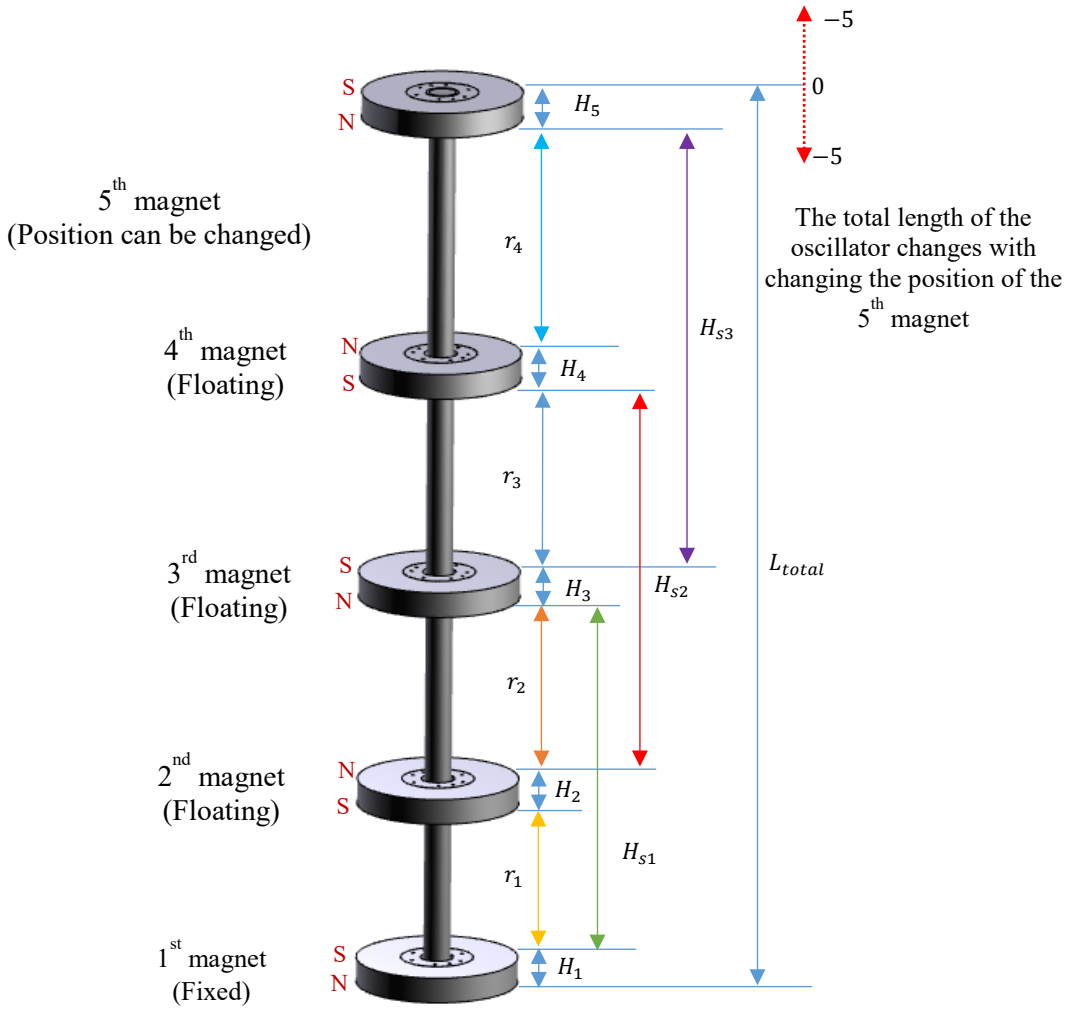

Figure 6.22: 3DOF Magnetic spring-based nonlinear oscillator system

The damping ratio and natural frequency of each floating magnet can be changed by changing the total length of the oscillator. Therefore, the eigenvalues of the 3DOF system can be changed by changing the total length of the oscillator. The magnetic restoring force and damping ratio of each floating magnet increases when the oscillator's total length decreases. On the other hand, the damping ratio and magnetic restoring force of each floating magnet decreases when the oscillator's total height increases. Table 6.7 presents the changes of distance and gravitational effects for different positions of the top fixed magnet.

Table 6.7: Change of gravitational effect for different lengths of the oscillator

Position of the top magnet	*Distance between 1st and 2nd magnets*	*Distance between 2nd and 3rd magnets*	*Distance between 3rd and 4th magnets*	*Distance between 4th and 5th magnets*	*Total length*	*Gravitational effects (mm)*		
						1st FM	2nd FM	3rd FM
-20 mm	56	61	73	97	352	2.5	6	12
-10 mm	57.5	63.5	76	100	362	3	6	12
0 mm	59	65	79	104	372	3	7	12.5
+ 10 mm	60	67	81	109	382	3.5	7	14
+20 mm	61	68	82.5	115.5	392	4	7.5	16.5
+ 30 mm	62	70	85	120	402	4	7.5	17.5
+40 mm	62.5	71.5	87	126	412	4.5	8	20
+50 mm	63	72	89	133	422	4.5	8.5	22

Note: FM=floating magnet

The effects of the gravitational force on equilibrium positions, damping ratios and natural frequencies for all floating magnets have been measured experimentally for different positions of the top fixed magnet (5th magnet), as presented in Table 6.7 and Table 6.8. By changing the position of the top fixed (5th) magnet, the distances 1st to 2nd, 2nd to 3rd, 3rd to 4th and 4th to 5th magnets can be changed. Different separation distances between magnets provide various magnetic restoring forces and different damping ratios. When the total length of the oscillator increased, the separation distances between all magnets increased. On the other hand, the spaces between all magnets reduced when the total length of the oscillator reduced from 372 mm (equilibrium position). Moreover, the equilibrium position of each floating magnet is affected by the gravitational force with changing the position of the top magnet, as shown in Table 6.8. The separation distance between the 4th and 5th magnet always remained larger than the distances between 1st and 2nd, 2nd and 3rd and 3rd and 4th magnets for all different lengths of the oscillator. However, the distance between 3rd and 4th magnets remained larger than the distances between 1st and 2nd and 2nd and 3rd magnets. Therefore, the damping constant and natural frequency of the 1st floating magnet (2nd magnet) is always larger than the damping constant and natural frequency of the 2nd (3rd magnet) and 3rd (4th magnet) floating magnet. Moreover, the damping ratio and the natural frequency of the system can be changed by changing the total length of the oscillator. The damping ratios and natural frequencies increased with reducing the entire length of the oscillator and decreased with increasing the total length of the oscillator, as seen in Table 6.8.

Table 6.8: Change of damping ratio and natural frequency of the 3DOF system for different positions of the top magnet (different length of the oscillator)

Position of the top magnet	*Total length (mm)*	*Damping ratio*			*Natural frequency (rad/s)*		
-20 mm	352	0.079	0.041	0.033	59.83	50.22	35.24
-10 mm	362	0.062	0.039	0.030	56.33	47.16	34.97
0 mm	372	0.058	0.038	0.021	55.92	44.47	32.87
+ 10 mm	382	0.052	0.036	0.017	54.30	43.62	30.72
+20 mm	392	0.04	0.034	0.015	53.70	41.46	29.02
+ 30 mm	402	0.045	0.032	0.014	52.14	40.92	27.75
+40 mm	412	0.042	0.030	0.014	50.86	39.57	27.00
+50 mm	422	0.040	0.029	0.012	49.59	37.73	25.41

Note: FM=floating magnet

The natural frequencies in the equilibrium position were around 56 rad/s, 44.5 rad/s and 33 rad/s, respectively. They increased to about 60 rad/s, 50 rad/s and 35.5 rad/s, respectively, when the 5th magnet moved toward the 4th magnet from the equilibrium position by 20 mm (reduced the total length of the oscillator). On the other hand, the floating magnet's natural frequencies decreased to approximately 49.5 rad/s, 38 rad/s and 25.5 rad/s when the top magnet (5th magnet) moved away from the equilibrium position (increased the total length of the oscillator), which can be seen in Table 6.8.The magnetic restoring forces of the 1st, 2nd and 3rd floating magnets changed with varying the oscillator's total length. Moreover, the linear and nonlinear stiffness of both floating magnets changed with varying the total length of the oscillator. The magnetic restoring forces for all floating magnets are measured analytically, as presented in Figure 6.23. For all oscillator lengths, the separation distance between 1st and 2nd magnets always remained smaller than the separation between 2nd and 3rd magnets, which is smaller than the separation distances between 3rd and 4th magnets and 4th and 5th magnets. Therefore, the magnetic force between the 1st and 2nd magnets always remained larger than those between the 2nd and 3rd magnets, as seen in Figure 6.23. Figure 6.23(b) presents the magnetic restoring force of the 2nd floating magnet (3rd magnet). It can be seen that from Figure 6.23(b) and Figure 6.23(c) that the magnetic force between the 2nd and 3rd magnets was larger than the magnetic forces between 3rd and 4th magnets and 4th and 5th magnets. Moreover, from Figure 6.23, it can be seen that the magnetic forces between all separated magnets increase with decreasing the length of the oscillator and decrease with increasing the length of the oscillator.

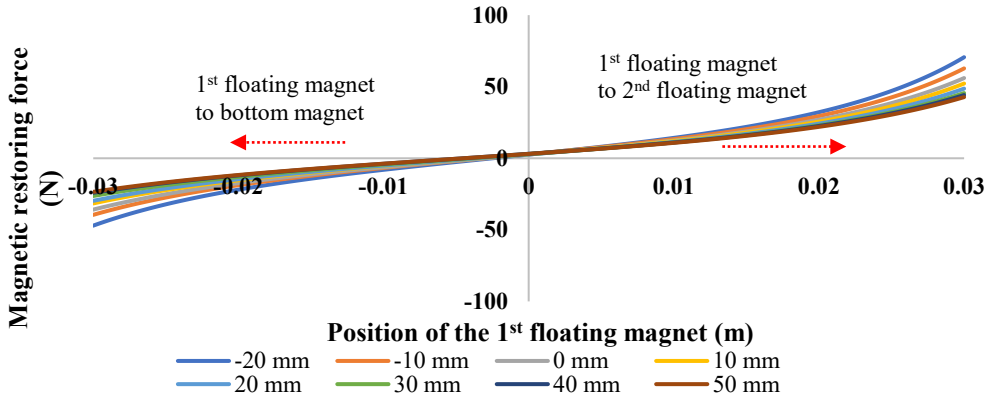

(a)

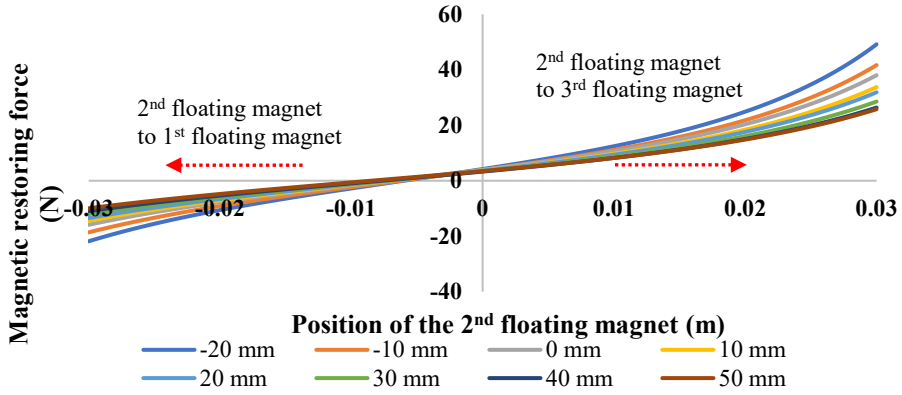

(b)

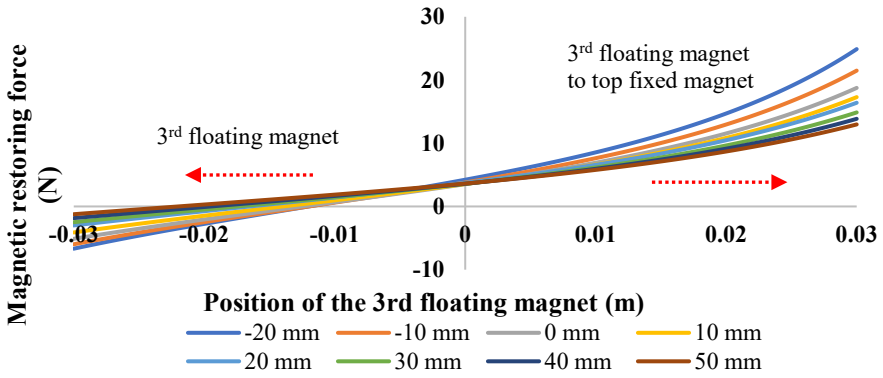

(c)

Figure 6.23: Magnetic restoring forces for different lengths of the oscillator (a) 1st floating magnet, (b) 2nd floating magnet and (c) 3rd floating magnet

For all different lengths of the oscillator, the magnetic restoring forces for 1st floating magnet were larger than the magnetic restoring forces of the 2nd and 3rd floating magnets. The linear and nonlinear stiffnesses of the 1st, 2nd and 3rd floating magnets for different lengths of the oscillator have been presented in Figure 6.24 (3rd order polynomial) and Figure 6.25 (5th order polynomial), respectively.

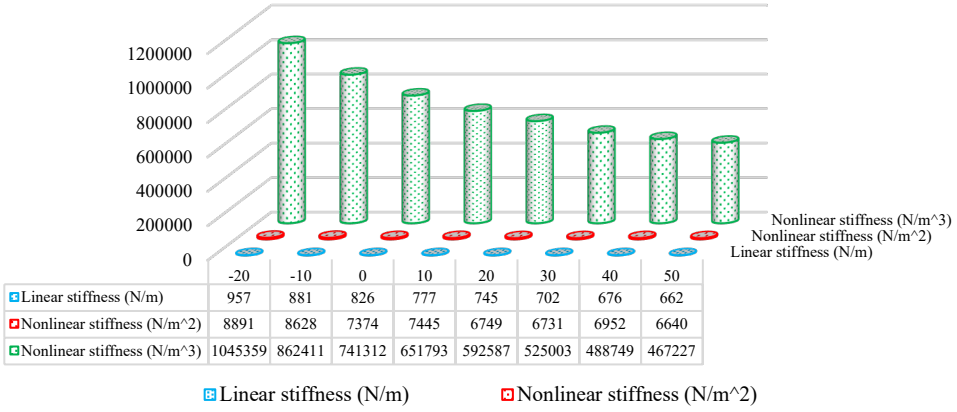

	-20	-10	0	10	20	30	40	50
Linear stiffness (N/m)	957	881	826	777	745	702	676	662
Nonlinear stiffness (N/m^2)	8891	8628	7374	7445	6749	6731	6952	6640
Nonlinear stiffness (N/m^3)	1045359	862411	741312	651793	592587	525003	488749	467227

(a)

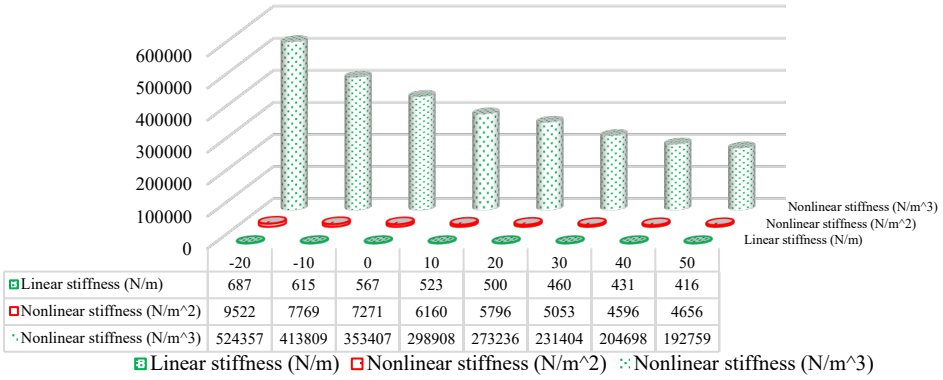

	-20	-10	0	10	20	30	40	50
Linear stiffness (N/m)	687	615	567	523	500	460	431	416
Nonlinear stiffness (N/m^2)	9522	7769	7271	6160	5796	5053	4596	4656
Nonlinear stiffness (N/m^3)	524357	413809	353407	298908	273236	231404	204698	192759

(b)

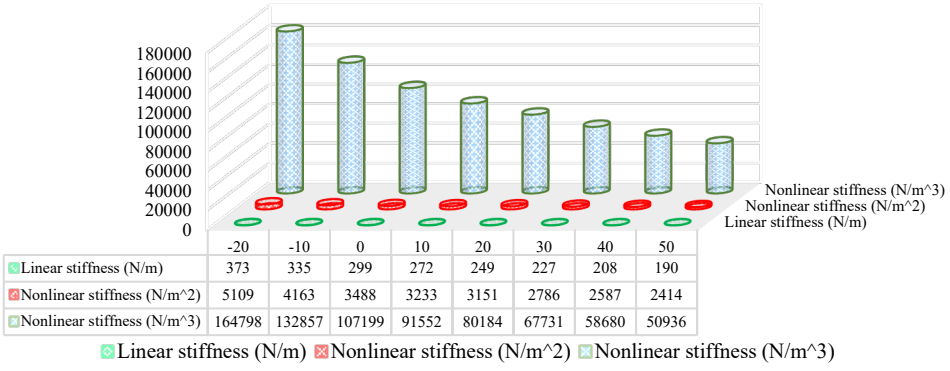

	-20	-10	0	10	20	30	40	50
Linear stiffness (N/m)	373	335	299	272	249	227	208	190
Nonlinear stiffness (N/m^2)	5109	4163	3488	3233	3151	2786	2587	2414
Nonlinear stiffness (N/m^3)	164798	132857	107199	91552	80184	67731	58680	50936

(c)

Figure 6.24: Coefficients of the 3DOF system for different lengths of the oscillator (3rd order polynomial) (a) 1st floating magnet, (b) 2nd floating magnet and (c) 3rd floating magnet

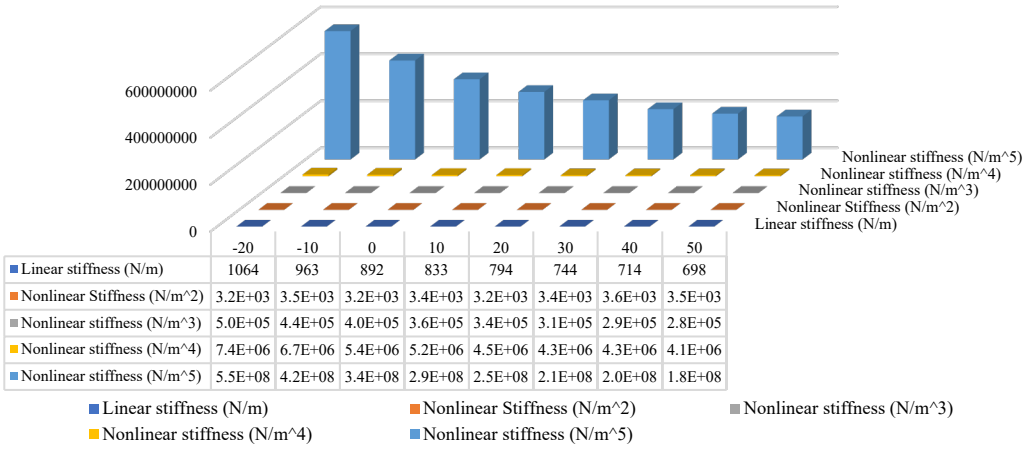

	-20	-10	0	10	20	30	40	50
Linear stiffness (N/m)	1064	963	892	833	794	744	714	698
Nonlinear Stiffness (N/m^2)	3.2E+03	3.5E+03	3.2E+03	3.4E+03	3.2E+03	3.4E+03	3.6E+03	3.5E+03
Nonlinear stiffness (N/m^3)	5.0E+05	4.4E+05	4.0E+05	3.6E+05	3.4E+05	3.1E+05	2.9E+05	2.8E+05
Nonlinear stiffness (N/m^4)	7.4E+06	6.7E+06	5.4E+06	5.2E+06	4.5E+06	4.3E+06	4.3E+06	4.1E+06
Nonlinear stiffness (N/m^5)	5.5E+08	4.2E+08	3.4E+08	2.9E+08	2.5E+08	2.1E+08	2.0E+08	1.8E+08

(a)

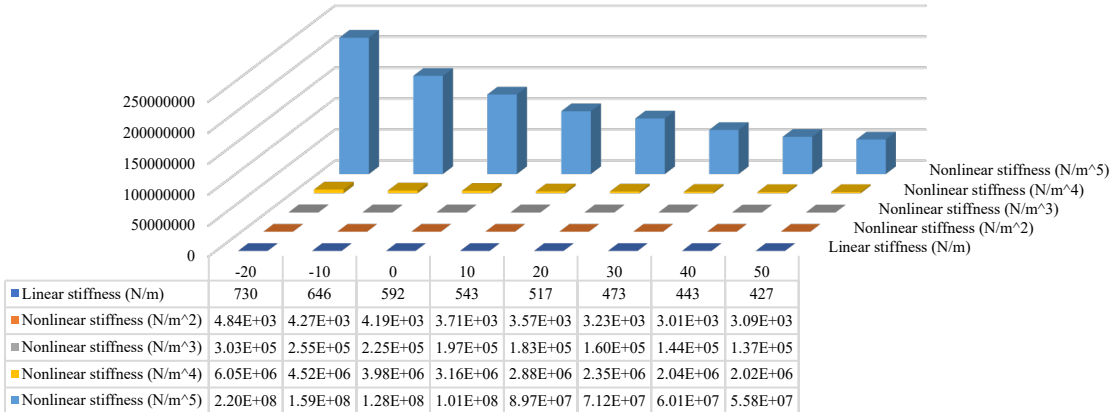

	-20	-10	0	10	20	30	40	50
Linear stiffness (N/m)	730	646	592	543	517	473	443	427
Nonlinear stiffness (N/m^2)	4.84E+03	4.27E+03	4.19E+03	3.71E+03	3.57E+03	3.23E+03	3.01E+03	3.09E+03
Nonlinear stiffness (N/m^3)	3.03E+05	2.55E+05	2.25E+05	1.97E+05	1.83E+05	1.60E+05	1.44E+05	1.37E+05
Nonlinear stiffness (N/m^4)	6.05E+06	4.52E+06	3.98E+06	3.16E+06	2.88E+06	2.35E+06	2.04E+06	2.02E+06
Nonlinear stiffness (N/m^5)	2.20E+08	1.59E+08	1.28E+08	1.01E+08	8.97E+07	7.12E+07	6.01E+07	5.58E+07

(b)

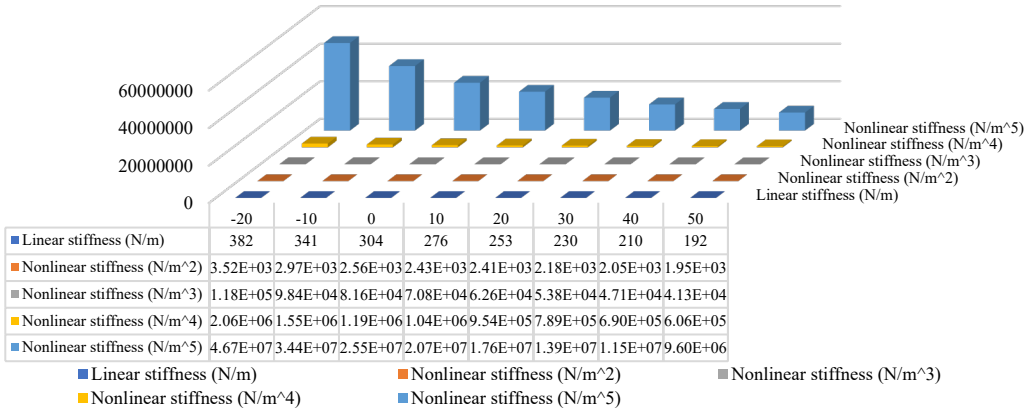

	-20	-10	0	10	20	30	40	50
Linear stiffness (N/m)	382	341	304	276	253	230	210	192
Nonlinear stiffness (N/m^2)	3.52E+03	2.97E+03	2.56E+03	2.43E+03	2.41E+03	2.18E+03	2.05E+03	1.95E+03
Nonlinear stiffness (N/m^3)	1.18E+05	9.84E+04	8.16E+04	7.08E+04	6.26E+04	5.38E+04	4.71E+04	4.13E+04
Nonlinear stiffness (N/m^4)	2.06E+06	1.55E+06	1.19E+06	1.04E+06	9.54E+05	7.89E+05	6.90E+05	6.06E+05
Nonlinear stiffness (N/m^5)	4.67E+07	3.44E+07	2.55E+07	2.07E+07	1.76E+07	1.39E+07	1.15E+07	9.60E+06

(c)

Figure 6.25: Coefficients of the 3DOF system for different lengths of the oscillator (5th order polynomial) (a) 1st floating magnet, (b) 2nd floating magnet and (c) 3rd floating magnet

From Figure 6.24 and Figure 6.25, it can be seen that the linear and nonlinear stiffness changes with varying lengths of the oscillator. All floating magnets' linear and nonlinear coefficients increased when the top magnet (5^{th} magnet) moved toward its underneath magnet from the equilibrium position and decreased when the top magnet moved away from the equilibrium position. The coefficients of the 1^{st} floating magnet always remained larger than the coefficients of the 2^{nd} and 3^{rd} floating magnets for different lengths of the oscillator. The linear stiffnesses of the 1^{st}, 2^{nd} and 3^{rd} floating magnets were 826 N/m (892 N/m for 5^{th} polynomial), 567 N/m (592 N/m for 5^{th} order polynomial) and 299 N/m (304 N/m for 5^{th} order polynomial), respectively, when the top magnet (5^{th} magnet) was in the equilibrium position. The linear stiffness of the 1^{st} floating increased to 957 N/m (1064 N/m for 5^{th} order polynomial) when the top magnet moved by 20 mm toward the magnet directly underneath from the equilibrium position and the linear stiffness decreased to 662 N/m (698 N/m for 5^{th} order polynomial) when the top magnet moved away by 50 mm from the equilibrium position.

For 2^{nd} floating magnet, the linear stiffness increased to 687 N/m (730 N/m for 5^{th} order polynomial) when the 5^{th} magnet moved by 20 mm toward the 4^{th} magnet from the equilibrium position. It decreased to 416 N/m (427 N/m for the 5th order polynomial) when the 5th magnet moved away 50 mm from the equilibrium position. Similarly, the linear stiffness of the 3^{rd} floating magnet increased to 373 N/m (382 N/m for 5^{th} order polynomial) when the length of the oscillator was reduced by 20 mm from the equilibrium length of the oscillator. It declined to 190 N/m (192 N/m for 5^{th} order polynomial) when the oscillator length increased by 50 mm. The natural frequencies of 1^{st}, 2^{nd} and 3^{rd} floating magnets have been measured analytically, as shown in Figure 6.26. The experimental findings of natural frequencies have been compared with the analytical measurement, as presented in Figure 6.26. The natural frequencies of the 3DOF system changed with changing the oscillator's total length, as presented in Figure 6.26. During the equilibrium length of the oscillator, the experimentally measured natural frequencies were around 56 rad/s, 44.5 rad/s and 33 rad/s, respectively. The 5^{th} order polynomial analytically measured natural frequencies were around 53.5 rad/s (51.5 rad/s for 3^{rd} order polynomial), 43.5 rad/s (42.5 rad/s for 3^{rd} order polynomial) and 31 rad/s (30.8 for 3^{rd} order polynomial), respectively.

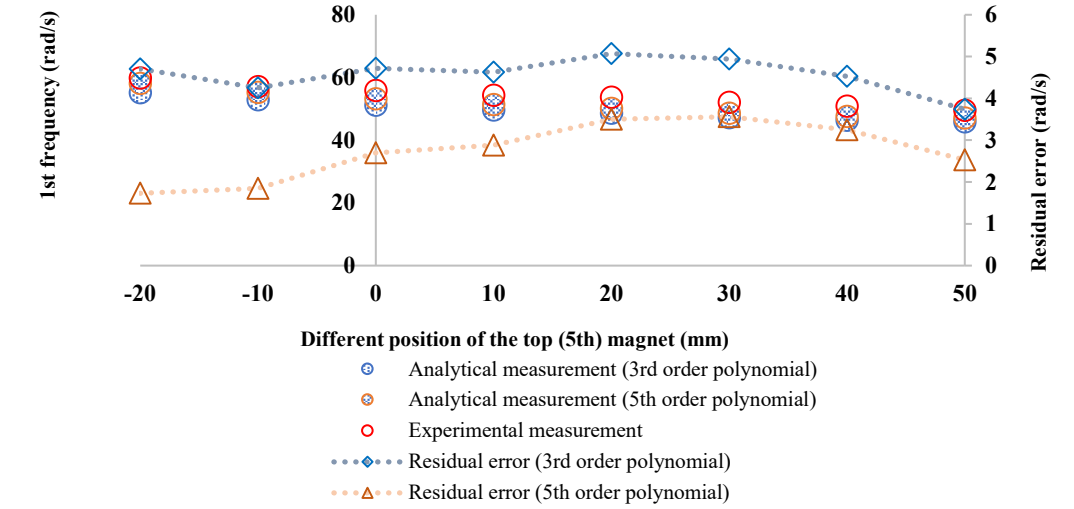

(a)

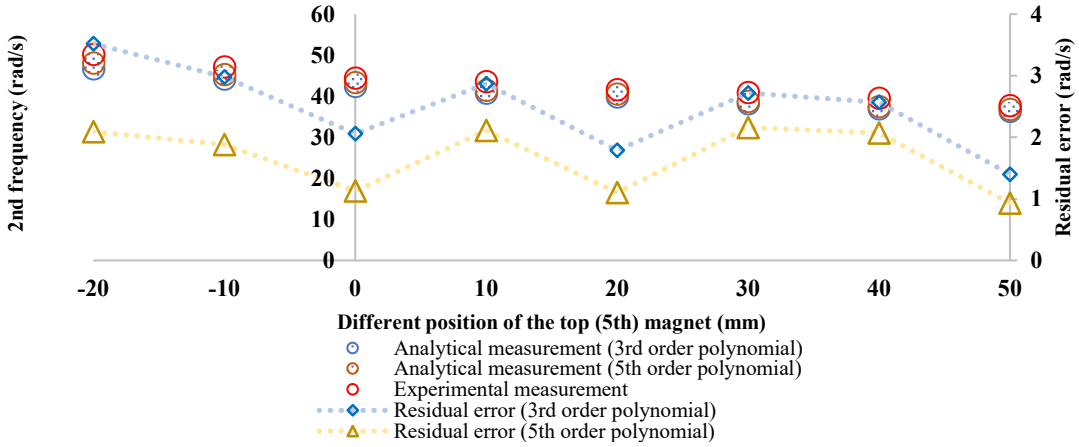

(b)

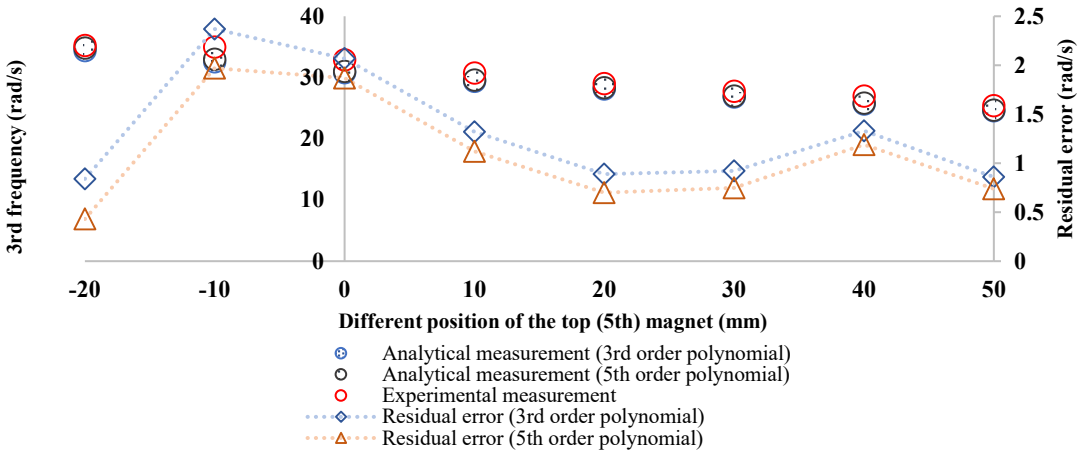

(c)

Figure 6.26: Natural frequencies for different lengths of the oscillator (a) 1st frequency, (b) 2nd frequency and (c) 3rd frequency

Compared to the experimental measurements with the analytical measurements, the residual errors were 2.7 rad/s (4.72 rad/s for 3rd polynomial), 1.13 rad/s (2.06 rad/s for 3rd polynomial) and 1.87 rad/s (2.07 rad/s for 3rd polynomial) for the 1st, 2nd and 3rd frequencies, respectively. The natural frequencies increased to 58 rad/s (59.85 rad/s experimental), 48 rad/s (50.22 rad/s experimental) and 35 rad/s (35.25 rad/s experimental) when the oscillator length was reduced by 20 mm from the equilibrium length. On the other hand, the natural frequencies were reduced to 47 rad/s (49.60 rad/s experimental), 37 rad/s (37.75 experimental) and 25 rad/s (25.5 rad/s experimental), respectively, when the length of the oscillator increased by 50 mm. The residual errors of the 5th order polynomial remained smaller than the 3rd order polynomial for all different lengths of the oscillator.

6.8 Conclusion

In this chapter, the characteristics and dynamics of the 3DOF nonlinear oscillator system have been analysed using analytical, experimental and numerical methods. The magnetic restoring forces and magnetic spring stiffness of the proposed 3DOF system have been studied theoretically and numerically. Analytically measured values have validated the numerical measured magnetic restoring forces of the 3DOF system. To determine the analytical values of the system's coefficients from the modelled magnetic restoring forces, both 3rd and 5th order polynomial curve fitting models have been used. Moreover, by changing the position of all floating magnets, the linear and nonlinear coefficients of the system have been investigated. Based on these investigations, the dynamics of the 3DOF nonlinear system have been analysed. The position of the top fixed magnet has a significant impact on the 3DOF oscillator system, which have been analysed as well by changing the position of the top fixed magnet. The separation distances between magnets changed with changing the length of the oscillator. It has been found that the separation distance between magnets has a significant influence on the vibration of the oscillator.

Chapter 7

Test Rig Components of the Magnetic Spring-based Linear Electromagnetic Generator Systems

In Chapters 4, 5 and 6, the analytical models of single-degree-of-freedom, two-degree-of-freedom, and three-degree-of-freedom systems were discussed and analysed using numerical and experimental findings. To validate the analytical and numerical model, it is essential to study the model experimentally. The experimental analysis will give a clear understanding of the dependent parameters, which will help to increase the power output of the linear PM generator. For the experimental study, it is required to fabricate a test rig set up, and its design depends on what kind of analysis needs to be performed. Moreover, the test rig analysis will help develop the linear PM generator prototype for the wave energy convertor. This chapter describes the details of the test rig setup, including the test rig design, fabrication, sensor calibration, and servo motor. Moreover, the present chapter emphasises how the experiments were conducted with the resources available.

7.1 Experimental Design

The experimental work consists of two sets of measurements i) displacement and ii) induced voltage. The experimental procedure is the same for all different types of oscillators. The full experimental setup consists of a test rig and servo motor. Figure 7.1 presents the schematic of the experimental setup. The test rig concept has been designed in a virtual sense using Autodesk Inventor 2020. The same types of permanent magnets have been used to build all different degrees-of-freedom systems. For different test rig setups, the height of the oscillator, masses and sizes of the three primary magnets were common. Other than manufacturing, parts of the test rig setup were directly brought from the industry (ready to use). The other features such as shaft, v-pulley and plastic bush were manufactured. To measure the distance of the moving magnet, the sensors were calibrated and attached to the test rig. The key noise parameters and key control parameters of the test rig setup are determined. The frictions between the inner part of the plastic bush and outside of the shaft and the electromagnet interferences have been considered key noise parameters that could not be controlled.

On the other hand, the masses of the magnets, damping ratio, resistance and inductance values are considered to be control parameters. The data acquisition system was connected with the sensor and coil winding data. The external force is applied to the floating magnet using a servo motor. The v-

pulley was connected with the shaft of the servo motor, and a fishing line was used to connect the floating magnet with the v-pulley. The resulting induced electromagnetic voltage from the test rig is then connected to the data acquisition device. All the instruments have been pre-calibrated.

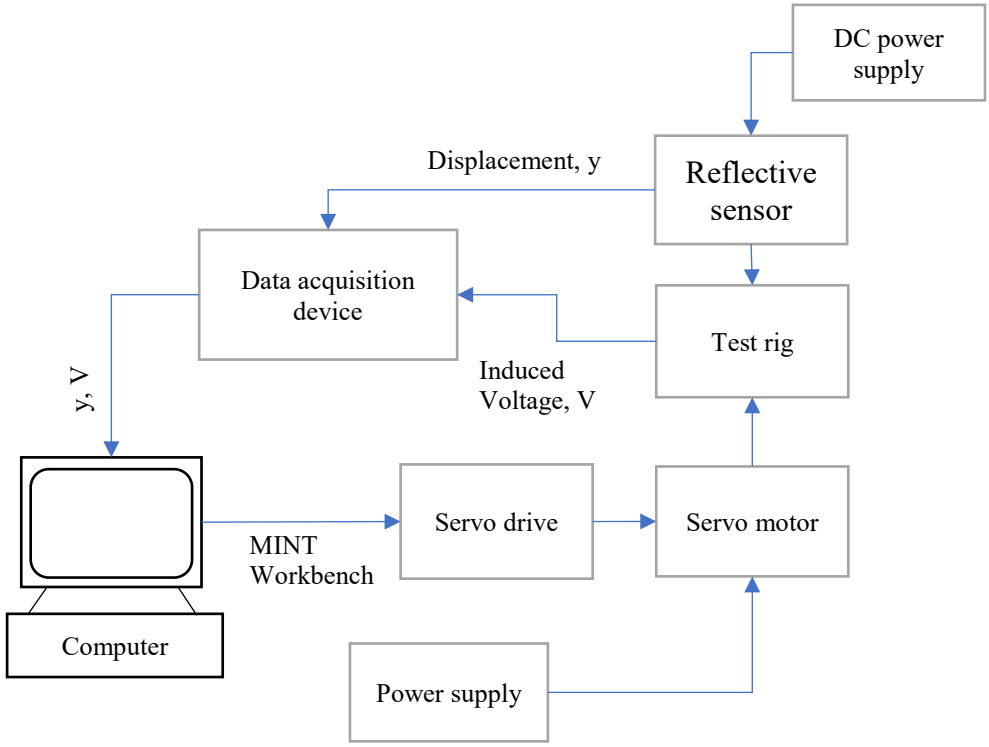

Figure 7.1: Schematic of the experimental setup

7.2 Design of the Test Rig

The design of the test rig is straightforward, as shown in Figure 7.2. MB building kit system (aluminium profile 5 20x20, T-slot nut, button-head screws and angle bracket as displayed in Figure 7.3) has been used to build the frame of the test rig. T-slot nut, angle bracket and button-head screws have been used to connect the aluminium profiles to build the test rig frame. The frame of the test rig is very flexible which can adjust easily. Moreover, all test rig components can be easily assembled and separated, which helps keep the shaft straight and aligned. Keeping the shaft vertically straight and aligned is one of the essential objectives of the test rig because it will help the floating magnet move in the up and down motion with minimal friction. Initially, the NdFeB N42 grade ring permanent magnets of size 72(OD) X 32.5(ID) X 13(H) (in mm units) was purchased. To avoid the magnet's magnetic attraction, all materials of the test rig are chosen to be non-magnetic materials.

Each permanent magnet (NdFeB, N42) has been attached to the plastic bush to hold the magnet with the shaft.

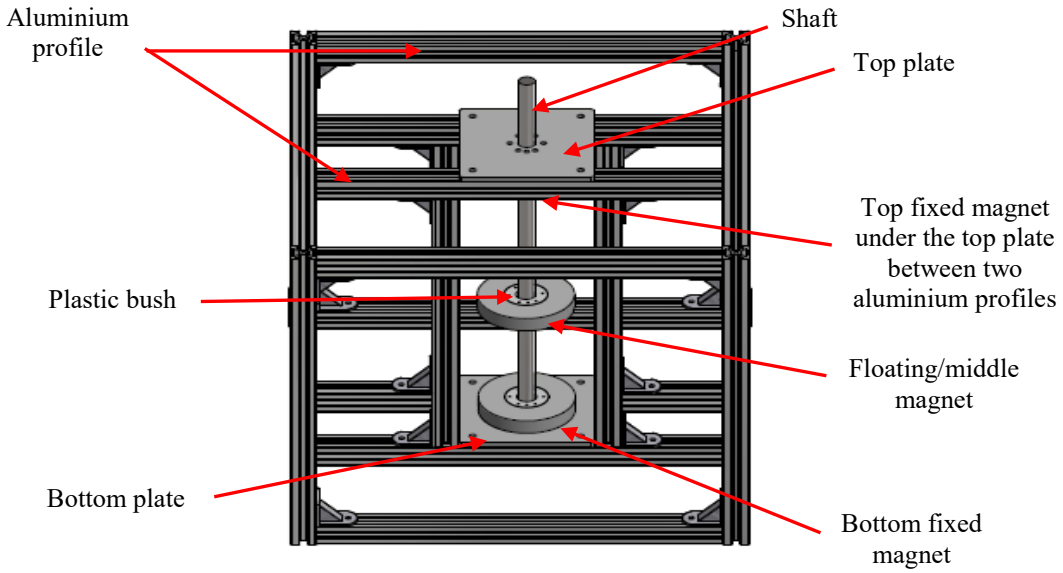

Figure 7.2: Test Rig (CAD design of the single-degree-of-freedom system)

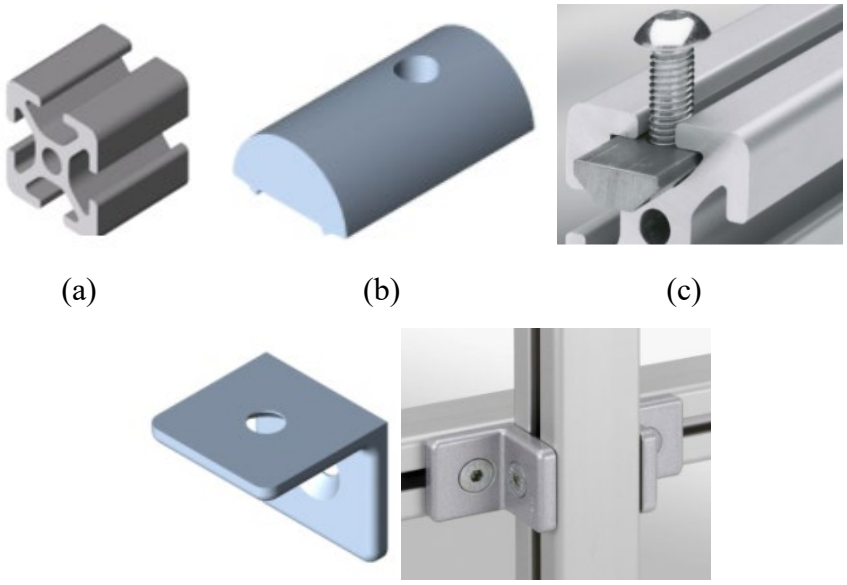

Figure 7.3: (a) Aluminium profile, (b) T-slot nut, (c) button-head screws and (d) angle bracket

The gap between the inside diameter of the bush and shaft is approximately 1mm. The reasons for using a plastic bush are; (1) connect the floating magnet with servo motor pulley through fishing line;

(2) stop magnet to become inclined; (3) protect the magnet from touching the shaft during movement, which helps protect the magnet from damage. All magnets are facing with the same poles, and they are just placed on the shaft. Both top and bottom magnets worked as fixed magnets, but all magnets between the top and bottom magnets worked as floating magnets. The natural distance between the floating magnet and bottom magnet for the single-degree-of-freedom setup was 79 mm. The natural distance between the floating magnet and the top magnet was 104 mm. Because of the gravitational force, the middle magnet was not staying in the centre position during the single-degree-of-freedom system, and this was the equilibrium position (no repulsive force) for the system. If the floating magnet was pulled up and released, it returned back to its equilibrium position after several bounces. Moreover, the shaft has been fixed with the test rig frame by using aluminium plates. Figure 7.4 displays the experimental test rig setup for the single-degree-of-freedom system oscillator.

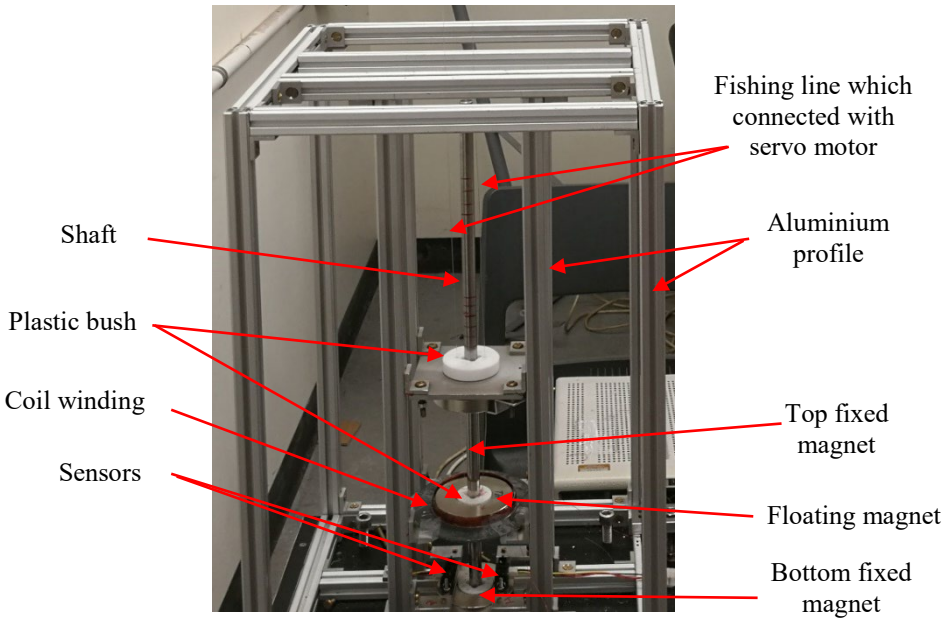

Figure 7.4: Test Rig setup (single degree of freedom system)

The coil winding is attached to the test rig while keeping a 2 mm air gap between the outside diameter of the floating magnet and the inside diameter of the coil winding. The experiments were performed by changing the number of the coil windings and the turn number. Two types of copper coils (0.29mm and 0.31 mm) have been used in the test rig. Figure 7.5 displays the winding coil. The winding coils were designed based on the outside diameter of the ring permanent magnet. The details of the drawing of the test rig are given in Appendix B. The design parameters of the test rig have been determined by measurement or by curve fitting assumptions, as displayed in Table 7.1.

Figure 7.5: Copper winding coil

Table 7.1: Determined experimental values of design parameters

Experimental test rig values of design parameters	Determined by	Determined value
Mass of each magnet	Directly measured	0.315 kg
Damping coefficients	Measured by the log-decrement method	Varies
Linear stiffness	Measured by curve fitting tools from magnetic restoring force curve	Varies
Non-linear stiffness	Measured by curve fitting tools from magnetic restoring force curve	Varies
Total resistances of the coils	Calculated	5.48 Ω (100 turns, 0.31 mm), 10.85 Ω (200 turns, 0.31 mm),
Inductances of the coils	Calculated	0.011 H (100 turns) and 0.044 H (200 turns)
Average magnetic flux density	Measured	0.47 T
Single-degree-of-freedom design parameters	Mass of the floating magnet with plastic bush, damping coefficient, linear stiffness, non-linear stiffness, resistance and inductance of the winding coil	
Two-degree-of-freedom design parameters	Mass of each floating magnet (2 magnets) with plastic bush, damping coefficients for each floating magnet (2 magnets), linear stiffnesses, non-linear stiffnesses, resistances and inductances of the winding coils	
Three-degree-of-freedom design parameters	Mass of each floating magnet (3 magnets) with plastic bush, damping coefficients for each floating magnet (3 magnets), linear stiffnesses, non-linear stiffnesses, resistances and inductances of the winding coils	

The outside diameter (D_0) of the winding coil is 75 mm and the diameter of the coil wires (d_w) are measured as 0.29 mm and 0.31 mm, respectively. The coil wire is made of copper with a resistivity (ρ) of $1.72 \times 10^{-8}\ \Omega m$. The length of coil wire used is calculated as:

$$l_{cw} = \pi N D_0 = \pi \times 100 \times \left(\frac{75}{1000}\right) = 23.55\ m \tag{7.1}$$

$$l_{cw} = \pi N D_0 = \pi \times 200 \times \left(\frac{75}{1000}\right) = 47.1\ m \tag{7.2}$$

The area of the cross-section of the coil winding (A_{cw}) is calculated as:

$$A_{cw} = \frac{\pi d_w^2}{4} = \frac{\pi \times (0.00031)^2}{4} = 0.00000007543\ m^2 \tag{7.3}$$

The resistance of the coil (R_c) was calculated as:

$$R_c = \frac{\rho l_{cw}}{A_{cw}} = \frac{1.72 \times 10^{-8}\ \times 23.55}{0.00000007543} = 5.37\Omega \tag{7.4}$$

The resistance of the excess wire (Re) that connected the coil to the voltage measuring circuit is estimated at 0.11Ω. Hence the total internal resistance of the coil was considered as:

$$R = R_c + R_e = 5.37 + 0.11 = 5.48\ \Omega \tag{7.5}$$

The resistance for 200 turns is 10.85Ω. Since the air-core has been used, the permeability coefficient of the coil μ_r is 1 ($\mu_r = 1$) and $\mu_0 = 4\pi\ \times\ 10^{-7}\ Nm^{-2}$ is the permeability of the coil with the air-core. D_0 is the diameter of the coil and the height (h_c) of the coil is 5 mm. The inductance (L) of the coil for 100 turns is calculated as:

$$L = \pi \times \mu_0 \times \mu_r \times \frac{N^2 D_0^2}{4 \times h_c} = \frac{\pi \times 4\pi\ \times\ 10^{-7} \times 1 \times 100^2 \times 0.075^2}{4 \times 0.005} = 0.011\ H \tag{7.6}$$

7.3 Data Acquisition System

The data acquisition system has been used in the test rig to measure the sensor output and coil output induced voltages. The data acquisition system is a robust system that allows the transfer of all signals and commands from the test rig connected components with the computer through MATLAB

software. The analog signals are coming from the distance measuring sensor and copper coils that have been converted to digital I/O signals by the compaqDAQ National Instruments equipment type NI cDAQ-9178 with 8-slots in the chassis, as shown in Figure 7.6. During the single degree of freedom system setup, sensors one and two were connected with port numbers 0 and 1, respectively, whereas the copper winding coil was connected with port 2. The signal from the test rig experiment was effectively transferred to the data acquisition system as a digital signal using MATLAB software that allows easy data-logging and generates automatic code. After every investigation, the results were saved with a date/time stamp followed by analysis and displayed using MATLAB software on the computer. For the required measurements, the MATLAB m file needed to be ready for each test. After stopping each experiment (the test time duration was completed), the output signal and signal with time showed graphically in time-domain response and plots. Subplots 1 and 2 gave the sensor output voltage corresponding to the floating magnet position vs time graph. Subplot 3 provided the output voltage generated due to the floating magnet movement. The subplot 1 and 2 data later converted into the floating magnet's position vs time, velocity vs time and acceleration vs time graph.

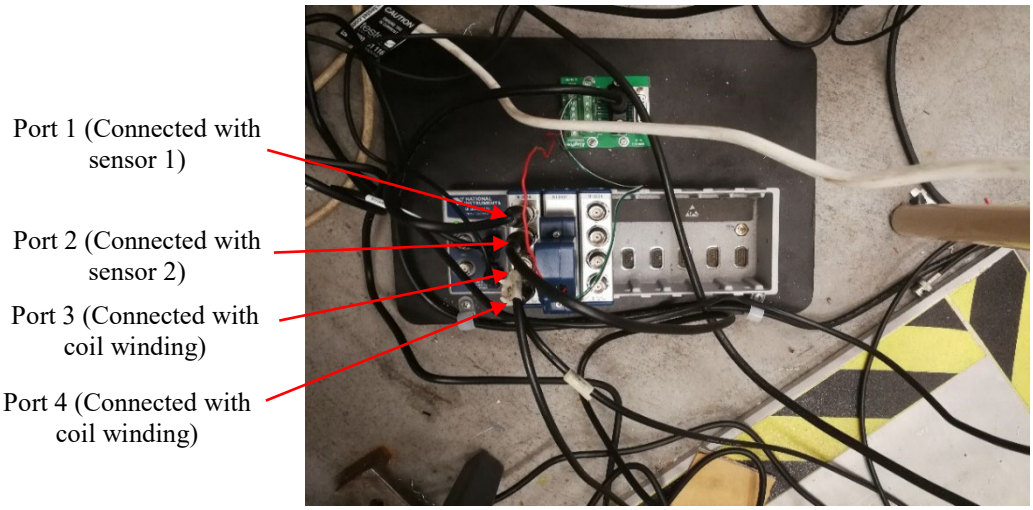

Figure 7.6: National Instruments equipment type NI cDAQ-9178 with 8-slot

7.4 Sensor Calibration

A reflective sensor (GP2Y0A41SK0F, Sharp) has been used to measure the displacement of the floating magnet. GP2Y0A41SK0F is a distance measuring sensor, and the sensor unit consists of a PSD (position sensitive detector), IR-LED (infrared emitting diode) and signal processing circuit. The schematic of the sensor is displayed in Figure 7.7.

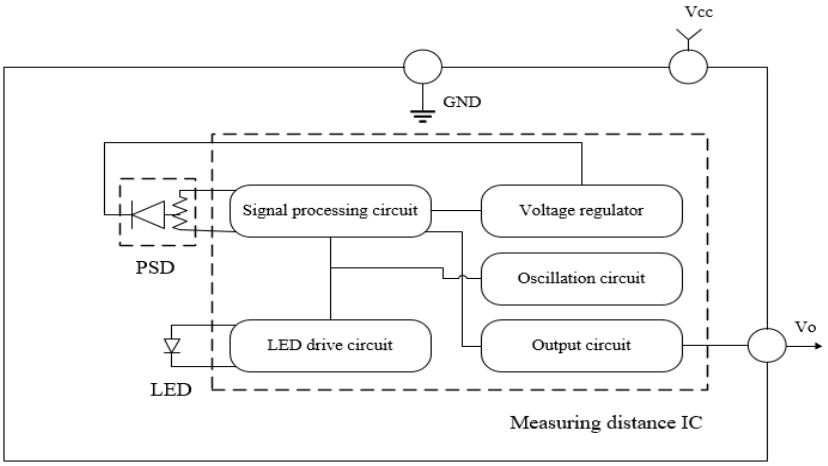

Figure 7.7: Schematic of the sensor

The sensor's output signal is voltage, and the relationship between this sensor's output voltage and the inverse of the measured distance is nearly linear over the sensor's usable range. The sensor's output voltage is converted to an estimated distance by constructing a best-fit line that relates the inverse of the output voltage (V) to distance (mm). Figure 7.8 presents the used reflective sensor, and the features of the sensor are shown in Table 7.2.

Figure 7.8: Reflective sensor (GP2Y0A41SK0F, Sharp)

Moreover, the sensor setup with the test rig is presented in Figure 7.9. The calibration of the sensor has been performed based on reading the voltage increase and drop resulting from moving the floating magnet away or towards the fixed sensor. The distance should be between 40 mm – 300 mm to receive suitable signal outputs for measurement. At first, two sensors were attached to the test rig. Both sensors have been placed above the bottom magnet to keep the distance between the sensors and floating magnet more than 4 cm; therefore, both sensors could be affected by the magnetic field that has been tested. The distance between the floating magnet and the top surfaces of both sensors is 6 cm (60 mm).

Table 7.2: Features the reflective sensor

Parameter	Ratings
Type	Analogue output type
Distance measuring range	4cm to 30cm
Output terminal voltage	-0.3V to +3 V
Supply voltage	5V
Operating temperature	-10ºC to +60ºC

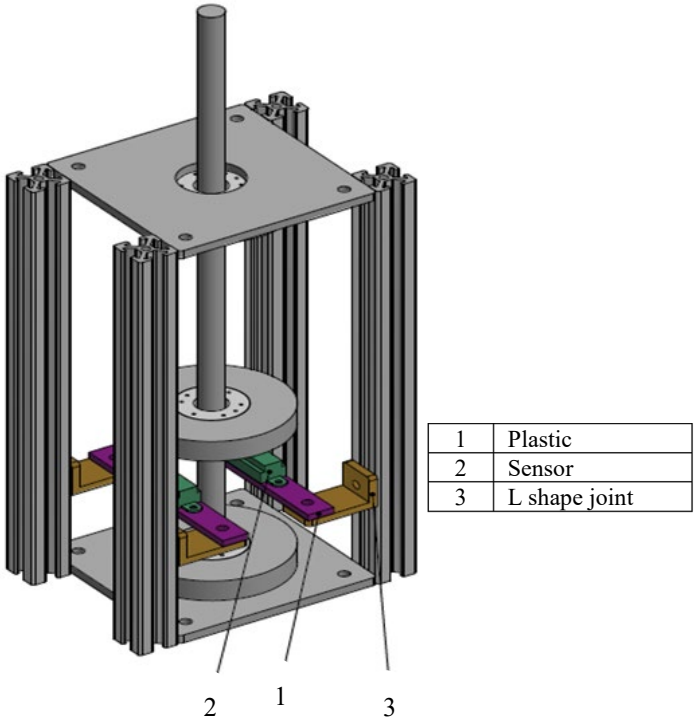

Figure 7.9: Sensors with the test rig

For the single degree of freedom test rig setup, the floating magnet can be moved by a maximum 35mm down and by 60mm up because of the repulsive forces. The principal concept of this test rig is that the floating magnet will be pulled up by external force created by the servo motor. Therefore, it has been considered that the floating magnet will travel by a maximum of 20 mm toward the bottom magnet and a maximum of 70 mm toward the top magnet. Both sensors have been tested by considering this distance. Two sensors have been calibrated before attaching and after attaching with the test rig, and the input power supply was 5V for both sensors. Figure 7.10 presents the power supply.

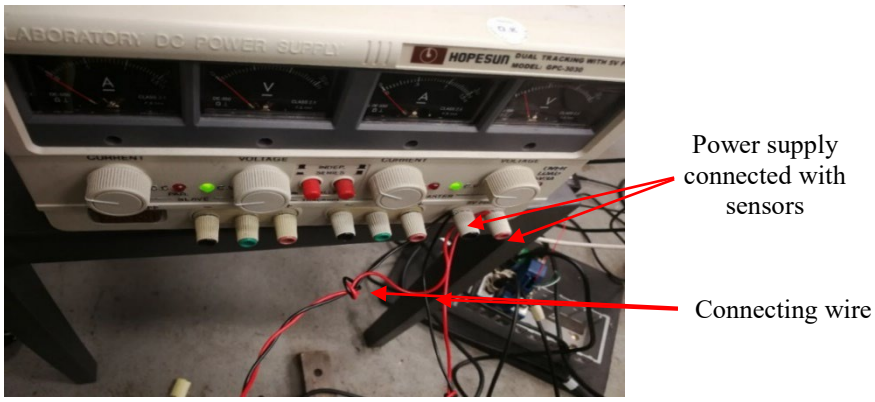

Figure 7.10: Power supply

The reason behind testing both sensors outside and inside the test rig was to know whether any magnetic fields were affecting the sensors unit or not. A multimeter measured the output signal voltage during both calibrations. Figure 7.11 presents the output voltage signals from sensors 1 and 2, which were tested manually outside the test rig by moving a piece of wood. Figure 7.12 displays both sensor's output signals when tested manually in the test rig.

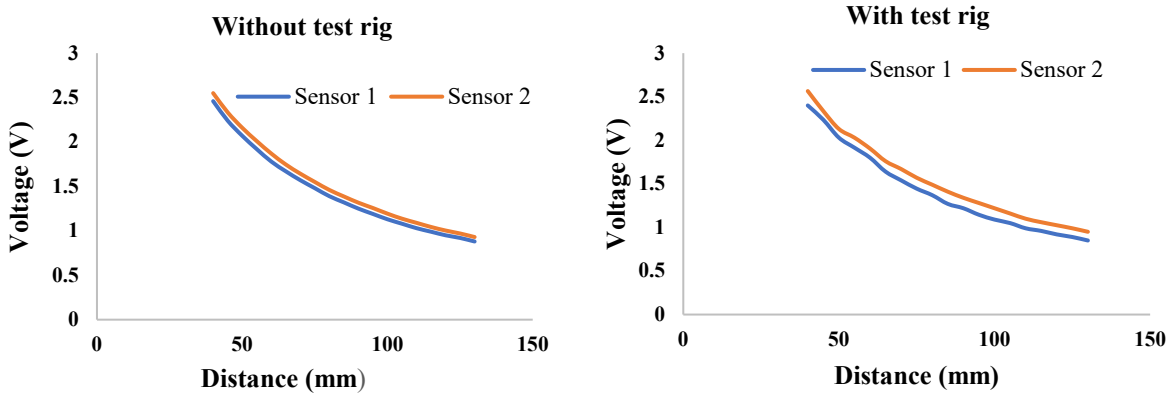

(a) (b)

Figure 7.11: Sensor test (a) without test rig and (b) with the test rig

It can be seen from Figure 7.11 that the output signal voltages for sensors 1 and 2 are almost the same for both tests (without and with test rig). Moreover, it can be seen that the graph is very smooth when the sensors were tested without the test rig compared with when the sensors were tested with a test rig. The comparison of the output signal voltages for sensors 1 and 2 for both tests have been presented in Figure 7.12, respectively. It can be said from the comparison results that the output signal voltages for sensors 1 and 2 are almost the same when tested outside and inside the test rig.

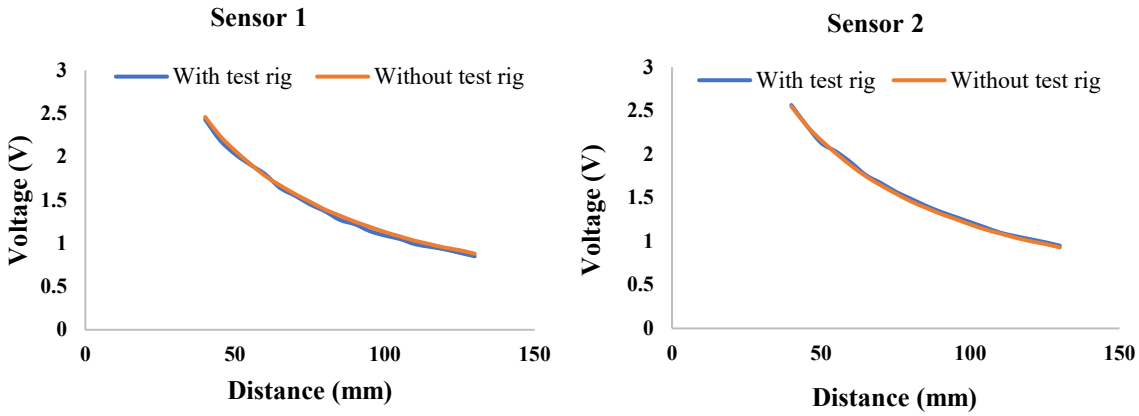

(a) (b)

Figure 7.12: Comparison output signal voltage (a) sensor 1 and (b) sensor 2

The sensor's output signal has been connected with the data acquisition system and compared with the manual testing results. For this purpose, both sensors were tested from 30 mm to 130 mm distance. The data acquisition system's output signals, later on, have been used to measure the displacement and velocity of the floating magnet. Therefore, this test rig setup needs to validate the data acquisition system's output results. The experimental trials have been performed several times. Their average manually measured values for the voltmeter output signals have been compared with the average output signal obtained from the data acquisition system. The comparison outputs for sensor 1 has shown in Figure 7.13(a), and for sensor 2 has shown in Figure 7.13(b).

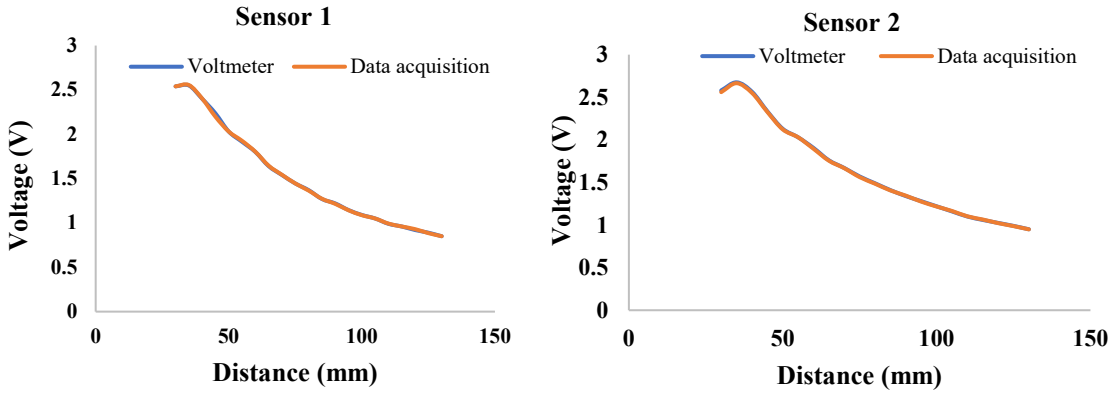

(a) (b)

Figure 7.13: Comparison output signal voltage (a) sensor 1 and (b) sensor 2

From Figure 7.13, it has been seen that the increase in the distance of the floating magnet from the sensor leads to a decreased voltage output of the sensor. The output voltage signals started to reduce

after 35 mm when the floating magnet was moving toward the sensors. The manual average measurement for both sensors is similar compared with the data acquisition system's average measurement.

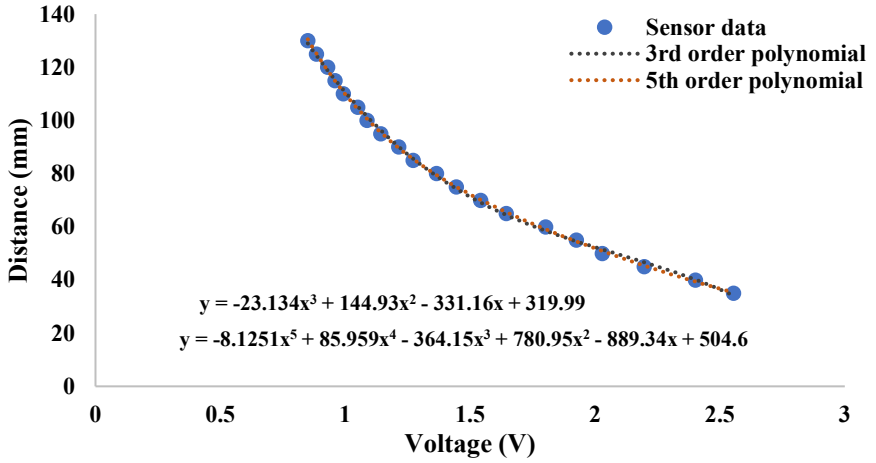

(a)

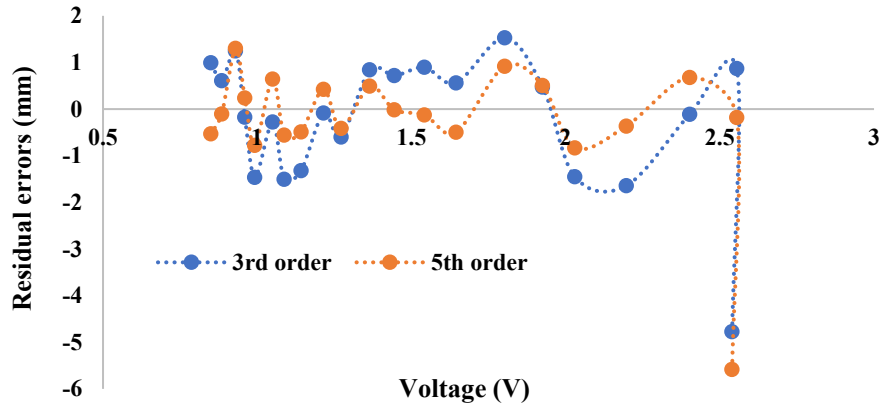

(b)

Figure 7.14: (a) Distance-Voltage calibration curves of sensor 1 and (b) Residual error of the fitting curve

Moreover, this method has been repeated a few times with the voltage dividers to check the distance with the reduced voltage. Running the test rig is the last step to get the results of the distance and voltage, which must be within the allowable limits (40 mm to 300 mm), according to the calibration curves in Figure 7.14 and Figure 7.15. The reflective sensor calibration steps were attempted to help ensure accurate measurements and to avoid any movement that may lead to incorrect results.

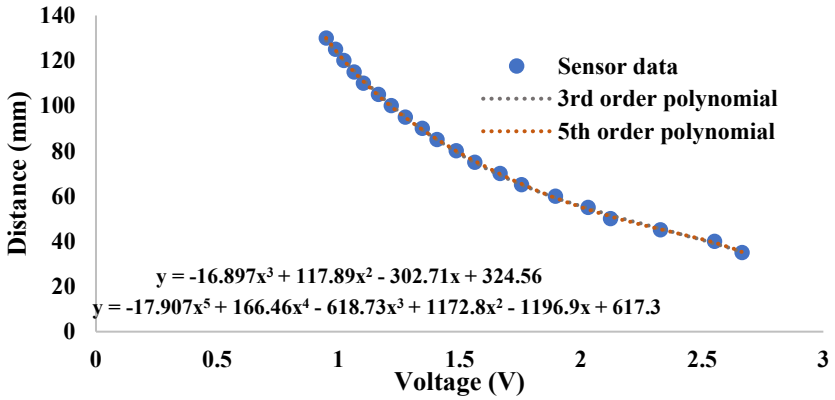

(a)

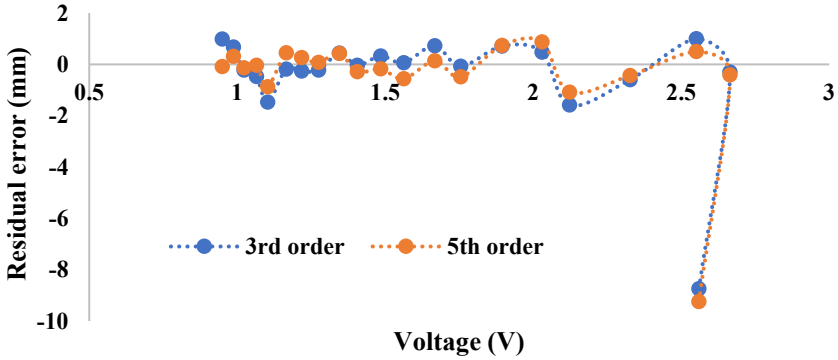

(b)

Figure 7.15: (a) Distance-Voltage calibration curves of sensor 2 and (b) Residual error of the fitting curve

With the increase in the number of floating magnets, the number of sensors increased as well to measure the displacement of each floating magnet. All sensors have been calibrated in the same way discussed earlier.

7.5 Low-pass Filter

The output signals from sensors in the data acquisition system are very noisy (not smooth) which can be seen in Figure 7.16. Therefore, it is required to filter the output signals' voltage to get the smoother graph form of the signal. Filters are generally used to decrease noise and develop data quality. Both high-pass and low-pass filters can be used but it is important to choose the proper pass filter. For this test rig setup, the low-pass filter has been used for smoothing out ripples or filtering out noise in the sensor signal output.

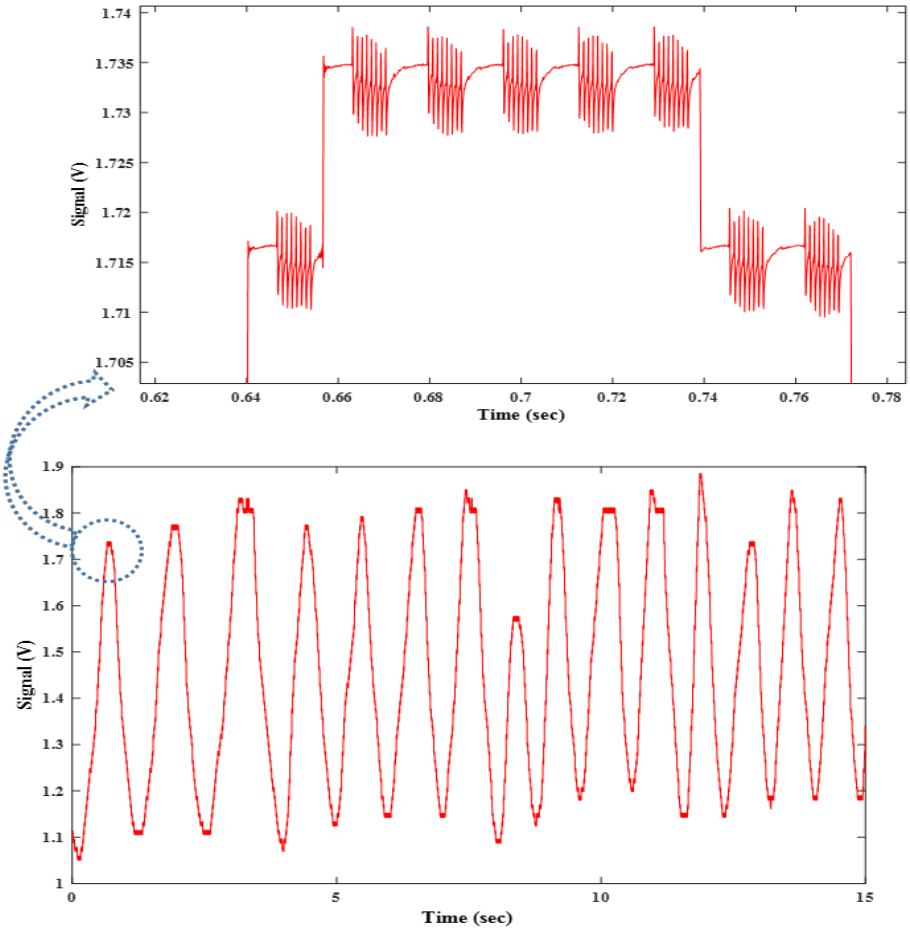

Figure 7.16: Output signals of the sensor in data acquisition system with zoom view

Normally, the low-pass filter passes signals with a frequency lower than a selected cut-off frequency, which means it allows frequencies below their cut-off range and attenuates signals with a frequency higher than the cut-off frequency. Moreover, the low-pass filters offer a smoother form of a signal by cutting out the short-term fluctuations, leaving the longer-term trend. The filter's exact frequency response depends on the filter design. In fact, a low pass filter is a system that only allows the low-frequency components to pass through it and provides very high attenuation to the high-frequency components. All the filters are frequency selective devices and are generally used to remove different frequencies from a particular band of large frequencies according to their parameter called the cut-off frequency. To make the circuit more straightforward to implement, mainly the low-pass filter is used. It generally contains R & C, whose value determines their cut-off frequency. Both analog low-pass filters and digital low-pass filters can be used. For this test rig setup, the digital low-pass filter has been used because it has more advantages than the analog filters due to their finite memory and

their ability to work with precision on the finite number of samples. They are computationally more robust and efficient compared to their analog counterparts.

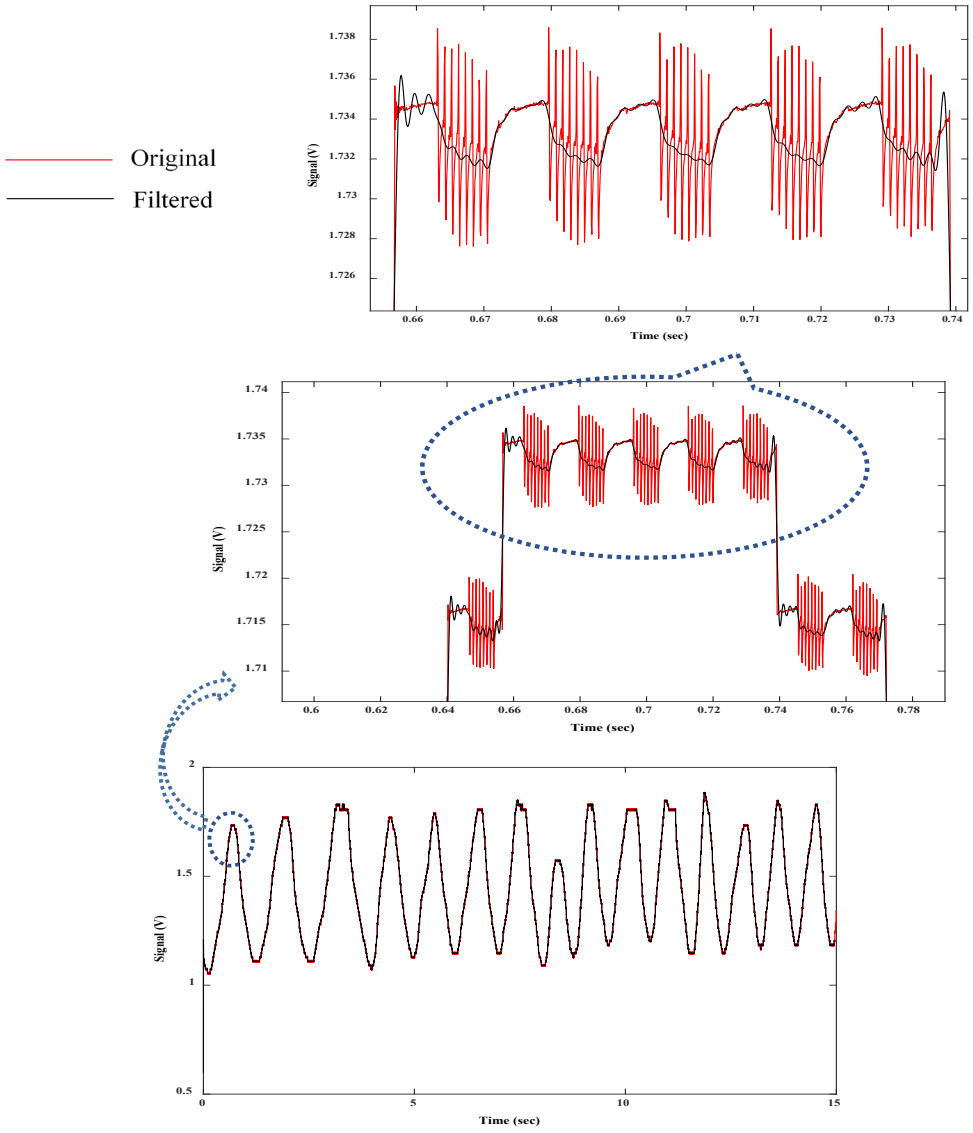

Figure 7.17: 500 Hz cut out

MATLAB comments have been used as a digital low-pass filter to cut out the unnecessary and short-term fluctuations for this experimental setup other than using a hardware circuit. To select the suitable cut-off frequency, the analysis has been performed at first for 500Hz, 400Hz, 300Hz, 200Hz, 100Hz, 50Hz and later on for 40Hz, 30Hz, 25Hz, 20Hz, 15Hz, 10Hz and 5Hz. Figure 7.17 displays the original and filtered signal and their spectra result for a cut-off frequency of 500 Hz. From Figure 7.17 it has been seen that the output signal is not smooth. Therefore, 500 Hz cut-off is not suitable

for this signal output. After that, 400 Hz cut-off has been used to see the signal output, as shown in Figure 7.18. From Figure 7.18, it can be said that after using 400 Hz frequency cut-off, the output signals are still not smooth yet, and therefore the 400Hz frequency cut-off was not be selected for this system.

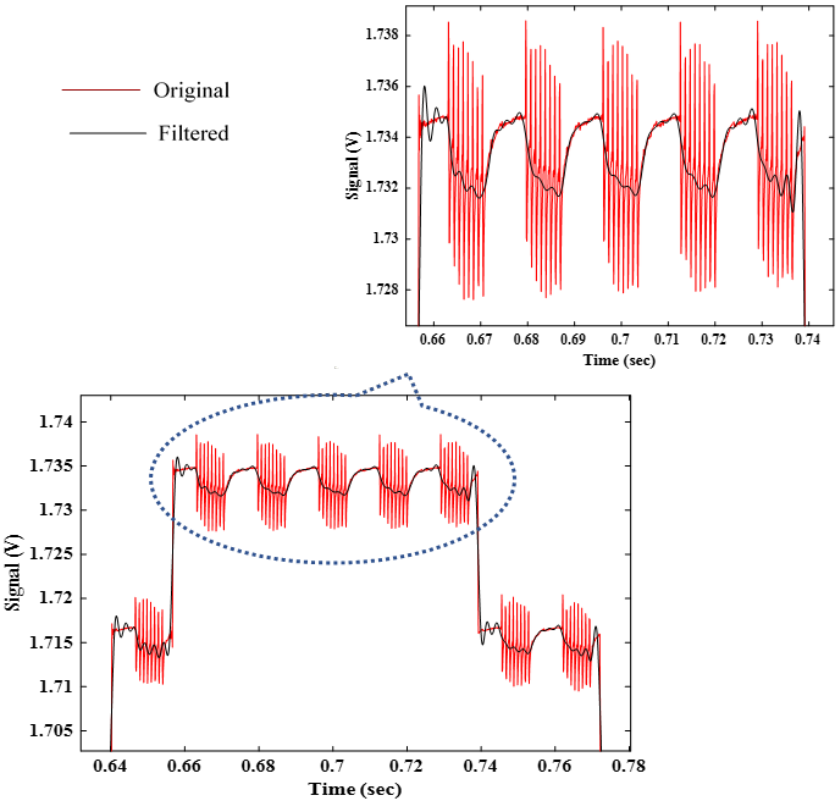

Figure 7.18: 400 Hz cut out

The 300Hz frequency has been used later on after the 400Hz frequency cut-off to analyse more to choose the cut-off frequency. The analysed result of using a 300Hz cut-off has been displayed in Figure C1 in Appendix B. The analysed result showed that the signal outputs are not smooth enough, and therefore the 300Hz has not been selected for this system setup. More analysis has been performed by using 200Hz and 100Hz as the cut-off frequencies and their analysis results are presented in Figure C2 and Figure C3, respectively in Appendix B. By comparing their study, it can be said that the 100Hz cut-off is better than the 200Hz cut-off frequency as the graph for the 100Hz cut-off frequency is smoother. The analysis has been performed more by using 50Hz, 40Hz and 30Hz cut-off. The analysis results have been displayed in Figure C4, Figure C5 and Figure C6, respectively in Appendix B.

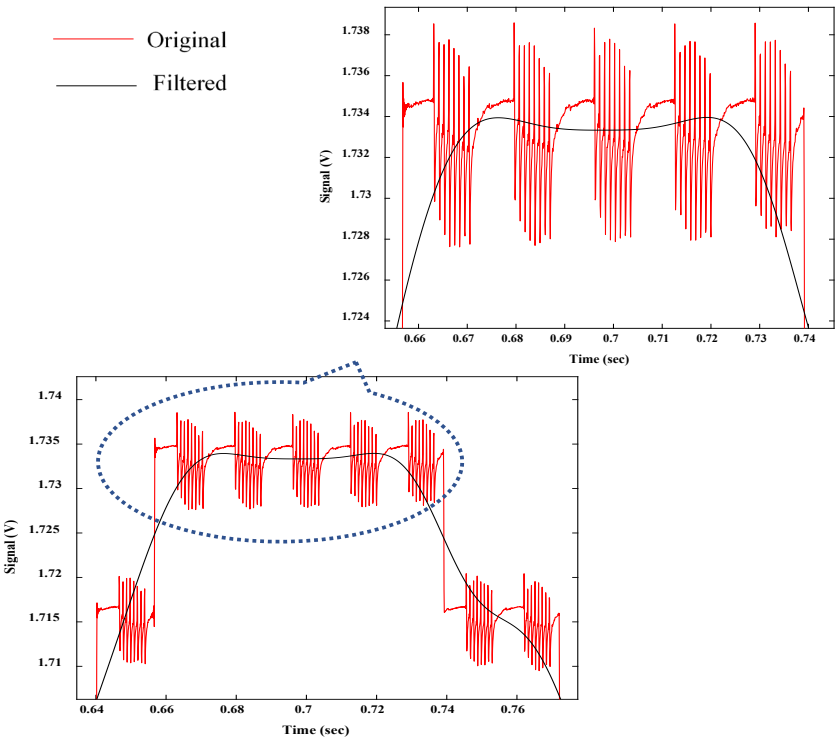

Figure 7.19: 25 Hz cut out

It can be seen from those analyses the signal outputs for the 30Hz cut are smoother than the signal outputs for the 40Hz cut-off, which is smoother than the 50Hz cut-off. At a cut-off frequency of 30Hz, the filtered signal graph showed that much of the original signal had been reduced and the graph was much smoother. So far, from the different cut-off frequencies, it can be said that as the cut-off frequency is decreased, effects get better. The cut-off frequencies have been reduced more to perform more analysis. By reducing the cut-off frequency by an additional 5Hz frequency, the analysis has been performed, which is presented in Figure 7.19. Figure 7.19 displays the analysis results for 25Hz cut out frequency. Comparing Figure 7.19 and Figure 7.18, and it can be said that the graph is getting smoother with the decreasing cut-off frequency. To know the effects of the signal, the cut-off frequencies have been reduced furthermore. The analysis results for the 20Hz and 15Hz cut-off frequency has been shown in Figures C7 and C8, respectively in Appendix B. Moreover, Figure C9 and Figure C10 present the analysis result for the 10Hz and 5Hz cut-off frequencies. The graph for the 5Hz cut-off frequency is smoother than the graph for the 10Hz cut-off frequency.

7.6 Servo Motor

A servo motor is being used in the test rig set up to supply the torque of the drive shaft, which consists of a pulley and to provide excitation in the floating magnet during the motor shaft rotation. The fishing line is used to connect the floating magnet with the V-pulley of the motor shaft. The design of the V-pully has been shown in Appendix B. The servo motor that has been used in the test rig is a BSM90C-2150 DC motor type connected to an ABB Microflex e150 servo drive. The MicroFlex e150 is a useful servo drive delivering high performance and capability in a broad range of demanding motion control applications. The rotor inertia and torque range of the servo motor are 0.000881 $kg.m2$ and 1-10 Nm., respectively. Figure 7.20 presents the test rig setup with the servo motor. Figure 7.21 displays the servo drive. The servo motor is controlled by using the MINT workbench software tool. The servo motor is connected to the PC through MINT software by using an IP address. The drive information has been confirmed before starting the motor. The specifications of the servo motor have been presented in Table 7.3.

Table 7.3: Specifications of the servo motor

Parameters	Values
Motor type	BSM90C-2150 DC motor
Drive type	ABB Microflex e150 servo drive
Control system	MINT workbench software
Torque range	1-10 N.m
Moment of inertia	8.81 kg.cm^2 or 0.000881 kg.m2
V-pulley radius	50 mm
Shaft diameter	25 mm
Nominal switching frequency	8.0 kHz
Maximum output voltage	230V
Inductance	14.8 mH

To create an external force, the servo motor has been controlled by the MINT workbench software tool. MINT workbench is a unique software tool designed by ABB to deliver rotational velocity by controlling specific distance, speed, and acceleration parameters. The software tool can control the motor's speed, acceleration and torque with a chosen profile by adjusting the controller PID gains in the MINT workbench software. To create an external force on the floating magnet, the motor is run by controlling the torque. Moreover, MINT workbench software can control the current with the

output power and necessary time to create the preferred torque and stop the rotation when the limit current is reached.

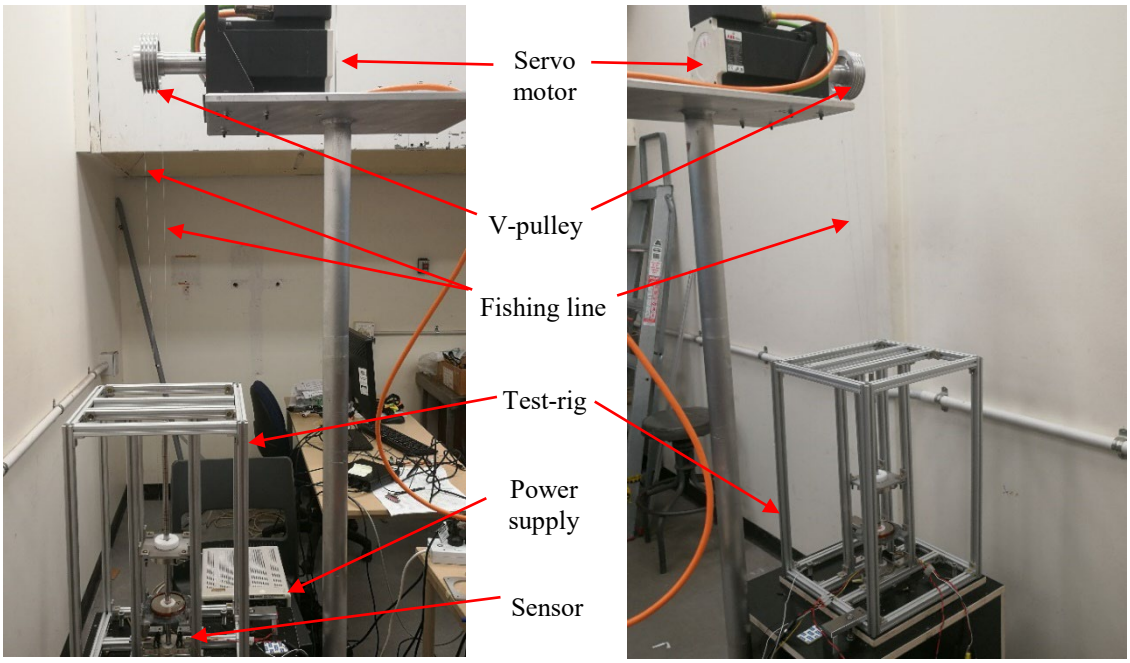

Figure 7.20: Test-rig setup with servo motor

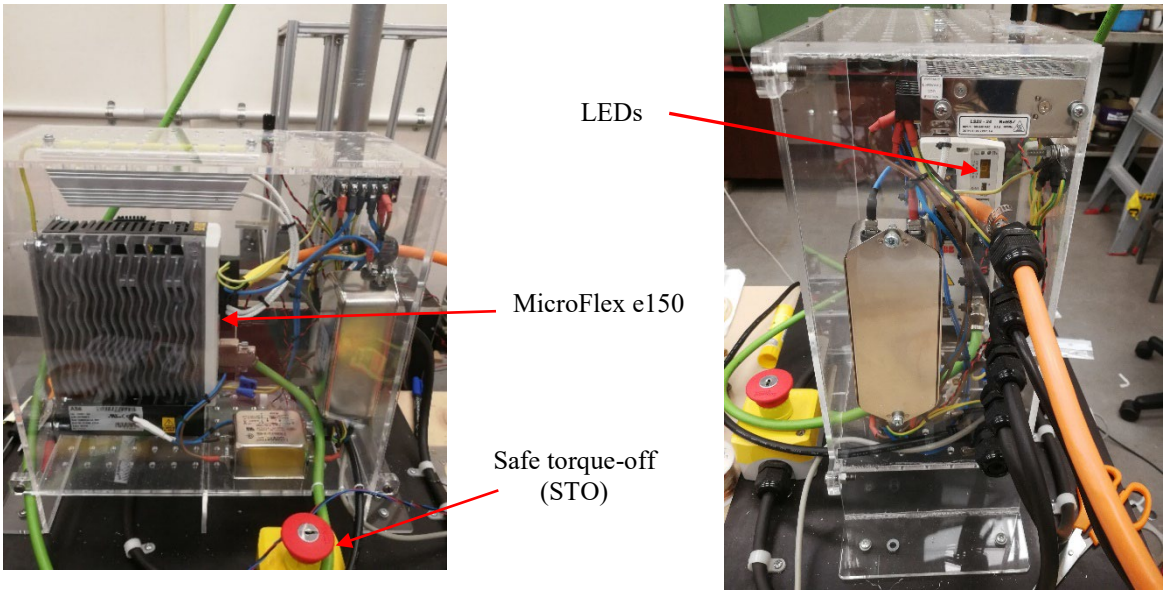

Figure 7.21: Servo drive (MicroFlex e150)

The drive of the servo motor has three control loops; position, speed and current (torque), which are fundamental to the operation of the drive. Therefore, it can run the drive in either position, velocity or torque control mode (as a default setting), but the selection should be made to suit the application.

Moreover, the selection depends on the drive's operating system because if the drive is operating as a network drive, then the selection should be based on whether the network master, such as the motion controller, is operating in either cyclic synchronous position, cyclic synchronous velocity or cyclic synchronous torque mode. On the other hand, if the drive is operating as an analog drive that received a +/- 10Vdc demand from a motion controller, then the selection is likely to be either velocity or torque. But the selection is expected to be the position if the drive is running a local Mint program. The values of the system parameters have been read on the MINT Workbench 'Parameters' page or the MINT CONTROLRATE keyword. Torque servo configuration has the advantages of high dynamic performance, minimal settling time and improved resistance to the oscillation at zero speed. Torque servo is an invalid configuration for analog drives configured in velocity mode using the Mint VELREF motion command or a real-time Ethernet motion controller that needs to operate in CSV mode. The red colour emergency button is required for the test rig setup with a servo motor to stop the motor in any emergency cases. Figure 7.22 presents the circuit diagram of the MicroFlex e150.

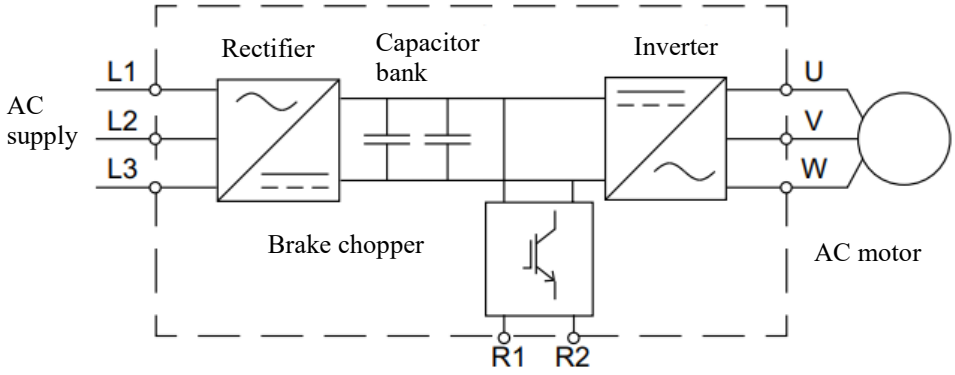

Figure 7.22: Circuit diagram of MicroFlex e150

The rectifier of the servo drive, as shown in Figure 7.22, translates the three-phase AC voltage to DC voltage. The capacitor bank of the middle circuit stabilises the DC voltage. The inverter converts the DC voltage back to AC voltage for the AC motor. Moreover, the brake chopper connects the external brake resistor to the intermediate DC circuit when the voltage in the circuit exceeds its maximum limit.

7.7 Conclusions

The test rig has been designed and developed using ring type permanent magnets, sensors, coils and circuit elements. This setup has been mainly intended to facilitate improvements to harvest maximum

energy in low-frequency ranges. Moreover, the test rig instrumentation contains new techniques for understanding the magnetic spring-based system and measurements of magnetic restoring forces and the possibility of developing advanced methods for understanding the multi-degree-of-freedom system-based magnet spring-based system. All required instruments have been discussed individually in this chapter. In conclusion, the experimental test rig setup has been designed and advanced to conduct multiple trials on all different models to get the time domain voltage responses at the different velocities of the floating magnets and external applied forces.

Chapter 8

Theoretical and Experimental Investigation of SDOF Magnetic Spring-based Linear Electromagnetic Generator

Currently, most of the proposed linear PM generator-type direct electric drive PTO systems for wave energy conversion have been developed based on linear oscillator systems (single-degree-of-freedom (SDOF) oscillator system) and traditional design concepts (e.g. all permanent magnets are mounted in the translator, having opposite poles facing each other with an iron core used between them, and with coil windings attached in the stator). Usually, the translator moves inside the stator, creating magnetic flux changes inside the winding coils, which generate electrical energy. When comparing the nonlinear systems with linear energy harvesting technology, the linear energy harvester has the highest power output in most cases. In contrast, the nonlinear system has a broader harvesting frequency bandwidth, and it can harness more energy from random vibration (Beeby et al., 2013). Moreover, the nonlinear oscillating system is better than the linear oscillation for broadening the frequency response bandwidth (Owens & Mann, 2012). Light damping nonlinear oscillators are expected to have larger operational frequency bandwidth than a conventional single degree of freedom linear oscillator. The magnetic spring-based (magnetic levitation) system can be used in the translator design to make the oscillator nonlinear, which is more effective in the broadband frequency range, especially in the low-frequency ocean environment (Masoumi & Wang, 2016). In the magnetic levitation system, the magnetic spring works like a physical spring and is created when two magnets face each other with the same poles (N-N or S-S). In Chapter 4, the analytical, numerical and experimental model of the single-degree-of-freedom (SDOF) magnetic spring-based oscillator system has been discussed with validation. However, the energy generation part was not considered during the analysis of the SDOF system. This chapter deals with energy generation techniques based on SDOF magnetic spring-based oscillator systems and their behaviour with various design criteria. The maximum energy generation depends on different parameters of the system. The parametric study analyses the effect on the problem solving of various geometric or physical parameters, or both. The parametric study is significant for evaluating system performance and achieving the best solution within different parameter sets. The optimisation method helps by automatically exploring the design space effectively and achieving the optimal solution. Therefore, the study on parametric optimisation is significant to get the best model. Moreover, the same oscillator model has been coupled with the electrical RL circuits and RLC system, where R = resistance, L = inductance and C = capacitance,

with identical values of floating magnet's mass, damping constant, linear and nonlinear stiffness, coil resistance and coil inductance. This chapter will discuss all parameters analytically and experimentally for getting maximum energy in the different frequency ranges.

8.1 Architecture of the Single-degree-of-freedom (SDOF) Energy Harvester

The linear generator's basic architecture comprises of three-ring permanent magnets (axially magnetised), a circular shaft, and a winding coil. In the energy harvester model design, the interaction issue has been considered one of the primary design factors. Every function's performance (such as magnetic restoring forces and induced voltage) should not affect or influence each other, particularly when the middle magnet moves. The proposed energy harvester consists of three permanent magnets, requiring a unique design to diminish the magnetic field interference. Minimising the harmful cogging force generated from the magnet and coil movement is necessary. Different non-magnetic materials have been used efficiently to avoid magnetic field interference to solve this issue. The fixed magnets are attached to the vertical shaft. The polarity of the magnets is arranged so that the levitating magnet experiences a repulsive force from the fixed magnets. A multilayer coil is attached around the outer surface of the middle magnet. The test rig of the energy harvester is developed based on a levitating magnet and coil winding. The height and diameter of the shaft are 550 mm and 12 mm, respectively. Figure 8.1 presents the test rig setup with a winding coil.

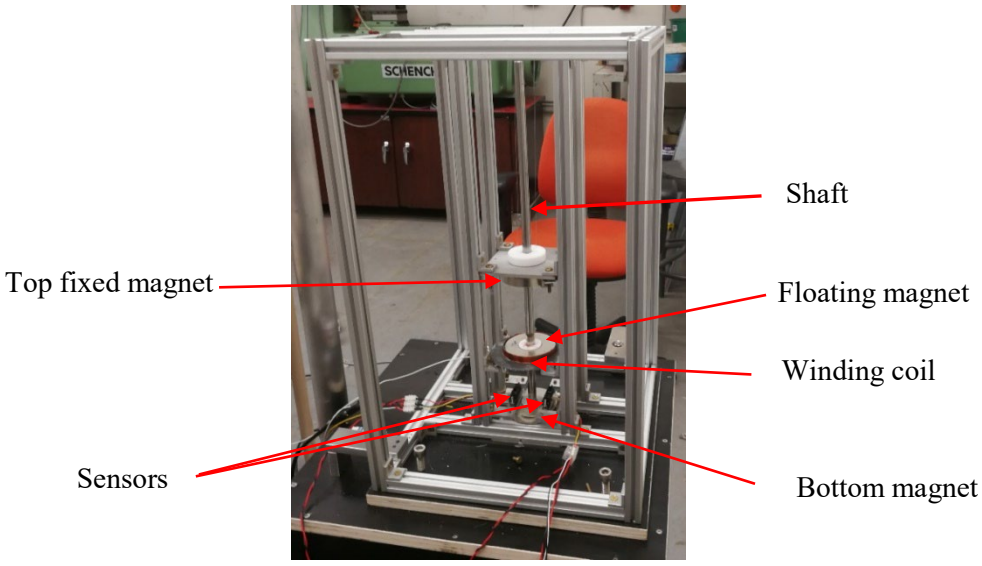

Figure 8.1: Test rig setup with winding coil

The height of the test rig setup is 550 mm, and the width is 300 mm. The equilibrium height of the SDOF oscillator is 222 mm. Therefore, the top magnet is attached and locked to the vertical shaft 222 mm away from the bottom magnet. The position of the top magnet can be moved to change the height of the generator. Both sensors have been placed on top of the bottom magnet. The wires of the winding coil have been connected to the data acquisition system to capture the induced voltages.

8.2 Analytical Analysis of the SDOF Energy Harvester Model based on a Nonlinear Oscillator system

In the equilibrium position, the separation distance between the bottom and the floating magnet is 79 mm, and between the floating and top magnet is 104 mm. When the external force is applied to the middle magnet, or the middle magnet moves up and down, it creates an elastic restoring force ($F_r = k_1 y + k_2 y^2 + k_3 y^3$) of the magnetic spring. Figure 8.2 and Figure 8.3 present the free body diagram of the SDOF magnetic spring-based energy harvester system.

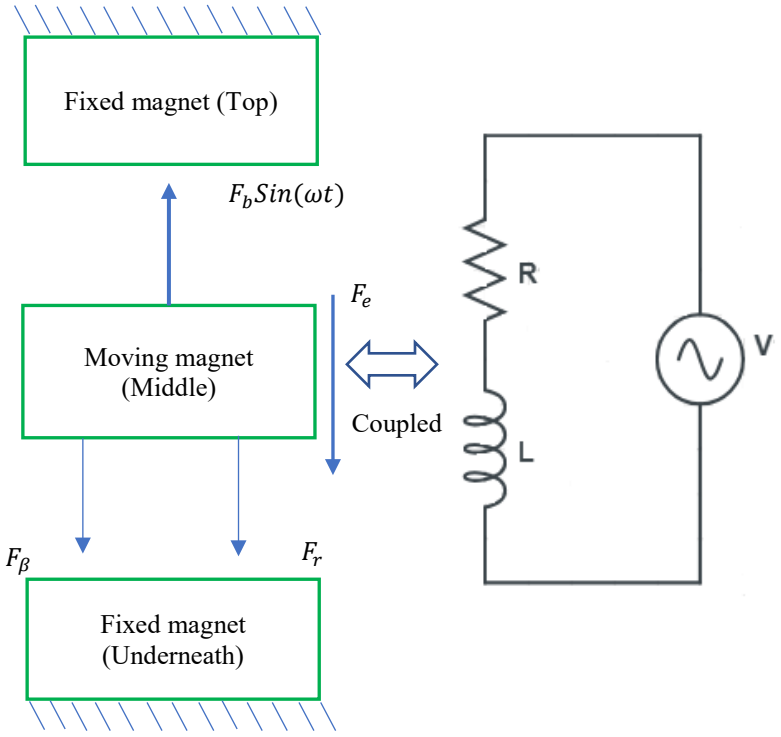

Figure 8.2: SDOF magnetic spring-based system energy harvester

F_β is the damping force of the system written as $F_\beta = \beta \dot{y}$. The relative displacement of the magnet is y, and the relative velocity and acceleration of the magnet are $\dot{y}$ and $\ddot{y}$, respectively. The magnetic flux density of the magnet is $B_{(y)}$, and the total length of the coil is l. The electromagnetic coupling

coefficient is $a(a = B_{(y)}l)$ and F_e is the electromagnetic force written as $F_e = aI$. The dynamic equation of the motion of the system can be written as,

$$M\frac{d^2y}{dt^2} + F_\beta + F_r + F_e = F_bSin(\omega t) \tag{8.1}$$

$$R_{in}I + L\frac{dI}{dt} = a\frac{dy}{dt} \tag{8.2}$$

where R_{in} is the coil's resistance, L is the inductance of the winding coil, and I is the induced current.

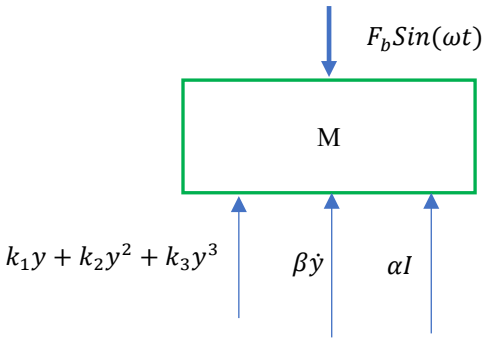

Figure 8.3: Free body diagram of the SDOF magnetic spring-based system energy harvester

The equations 8.1 and 8.2 can be expressed as

$$M\frac{d^2y}{dt^2} + \beta\frac{dy}{dt} + k_1y + k_2y^2 + k_3y^3 + aI = F_bSin(\omega t) \tag{8.3}$$

$$M\ddot{y} + \beta\dot{y} + k_1y + k_2y^2 + k_3y^3 + aI = F_bSin(\omega t) \tag{8.4}$$

$$R_{in}I + L\frac{dI}{dt} = a\frac{dy}{dt} \tag{8.5}$$

$$R_{in}I + L\dot{I} = a\dot{y} \tag{8.6}$$

The above equations can be stated for the state space model as

$$\ddot{y} = \frac{1}{M}(F_bSin(\omega t) - \beta\dot{y} - k_1y - k_2y^2 - k_3y^3 - aI) \tag{8.7}$$

$$\dot{I} = \frac{1}{L}(a\dot{y} - R_{in}I) \tag{8.8}$$

The state space model of the system can be stated as

$$Z_1 = y \tag{8.9}$$

$$Z_2 = \dot{y} = \dot{Z}_1 \tag{8.10}$$

$$\dot{Z}_2 = \ddot{y} \tag{8.11}$$

$$Z_3 = I \tag{8.12}$$

$$\dot{Z}_3 = \dot{I} \tag{8.13}$$

$$U_1 = F_b Sin(\omega t) \tag{8.14}$$

$$\dot{Z}_2 = \frac{1}{M}\left(U_1 - \beta Z_2 - \ k_1 Z_1 - k_2 {Z_1}^2 - k_3 {Z_1}^3 - aZ_3\right) \tag{8.15}$$

$$\dot{Z}_3 = \frac{1}{L}(aZ_2 - R_{in}Z_3) \tag{8.16}$$

The matrix form of the state space model can be expressed as

$$\begin{bmatrix} \dot{Z}_1 \\ \dot{Z}_2 \\ \dot{Z}_3 \end{bmatrix} = \underbrace{\begin{bmatrix} 0 & 1 & 0 \\ \frac{-k_1 - k_2 Z_1 - k_3 {Z_1}^2}{M} & \frac{-\beta}{M} & \frac{-a}{M} \\ 0 & \frac{\alpha}{L} & \frac{-R_{in}}{L} \end{bmatrix}}_{A} \begin{bmatrix} Z_1 \\ Z_2 \\ Z_3 \end{bmatrix} + \underbrace{\begin{bmatrix} 0 \\ \frac{1}{M} \\ 0 \end{bmatrix}}_{B} [U_1] \tag{8.17}$$

$$[X] = \underbrace{\begin{bmatrix} 1 & 0 & 0 \\ 0 & 1 & 0 \\ 0 & 0 & 1 \end{bmatrix}}_{C} \begin{bmatrix} Z_1 \\ Z_2 \\ Z_3 \end{bmatrix} + \underbrace{[0]}_{D} [u] \tag{8.18}$$

If the coil is connected in parallel to an external load or resistance R_e. The parallel-connected winding coil has the internal resistance R_{in} and inductance L. The dynamic equation of the motion of the system can be written as,

$$M\frac{d^2y}{dt^2} + \beta\frac{dy}{dt} + \ k_1 y + k_2 y^2 + k_3 y^3 + aI = F_b Sin(\omega t) \tag{8.19}$$

$$V + L\frac{dI}{dt} = a\frac{dy}{dt} \tag{8.20}$$

Where R_{in} is the coil's resistance, L is the inductance of the winding coil, and I is the induced current ($I = \frac{V}{R}$). Moreover, V is the induced voltage, and R is the resistance of the winding coil. The equations 8.1 and 8.2 can be expressed as

$$M\frac{d^2y}{dt^2}+\beta\frac{dy}{dt}+\ k_1y+k_2y^2+k_3y^3+a\frac{V}{(R_{in}+R_e)}=F_bSin(\omega t) \tag{8.21}$$

$$M\ddot{y}+\beta\dot{y}+\ k_1y+k_2y^2+k_3y^3+a\frac{V}{(R_{in}+R_e)}=F_bSin(\omega t) \tag{8.22}$$

$$V+\frac{L}{(R_{in}+R_e)}\frac{dV}{dt}=a\frac{dy}{dt} \tag{8.23}$$

$$V+\frac{L}{(R_{in}+R_e)}\dot{V}=\alpha\dot{y} \tag{8.24}$$

The above equations can be stated for the state space model as

$$\ddot{y}=\frac{1}{M}\left(F_bSin(\omega t)-\beta\dot{y}-\ k_1y-k_2y^2-k_3y^3-\frac{aV}{(R_{in}+R_e)}\right) \tag{8.25}$$

$$\dot{V}=\frac{(R_{in}+R_e)}{L}(a\dot{y}-V) \tag{8.26}$$

The state space model of the system can be stated as

$$Z_1=y \tag{8.27}$$

$$Z_2=\dot{y}=\dot{Z}_1 \tag{8.28}$$

$$\dot{Z}_2=\ddot{y} \tag{8.29}$$

$$Z_3=V \tag{8.30}$$

$$\dot{Z}_3=\dot{V} \tag{8.31}$$

$$U_1=F_bSin(\omega t) \tag{8.32}$$

$$\dot{Z}_2=\frac{1}{M}\left(U_1-\beta Z_2-\ k_1Z_1-k_2{Z_1}^2-k_3{Z_1}^3-\frac{a}{(R_{in}+R_e)}Z_3\right) \tag{8.33}$$

$$\dot{Z}_3=\frac{(R_{in}+R_e)}{L}(aZ_2-Z_3) \tag{8.34}$$

The matrix form of the state space model can be expressed as

$$\begin{bmatrix}\dot{Z}_1\\ \dot{Z}_2\\ \dot{Z}_3\end{bmatrix}=\underbrace{\begin{bmatrix}0 & 1 & 0\\ \frac{-k_1-k_2Z_1-k_3{Z_1}^2}{M} & \frac{-\beta}{M} & \frac{-a}{M(R_{in}+R_e)}\\ 0 & \frac{a(R_{in}+R_e)}{L} & \frac{-(R_{in}+R_e)}{L}\end{bmatrix}}_{A}\begin{bmatrix}Z_1\\ Z_2\\ Z_3\end{bmatrix}+\underbrace{\begin{bmatrix}0\\ \frac{1}{M}\\ 0\end{bmatrix}}_{B}[U_1] \tag{8.35}$$

$$[X] = \underbrace{\begin{bmatrix} 1 & 0 & 0 \\ 0 & 1 & 0 \\ 0 & 0 & 1 \end{bmatrix}}_{C} \begin{bmatrix} Z_1 \\ Z_2 \\ Z_3 \end{bmatrix} + \underbrace{[0]}_{D} [u] \tag{8.36}$$

The proposed generator system has been analysed by considering the RLC circuit with the system. The SDOF system with RLC electric circuit can be considered by the equations 8.20 and 8.21. In the previous section, the SDOF generator model was analysed considering the RL circuit, and in this section, the system has been studied using an RLC circuit.

$$M\frac{d^2y}{dt^2} + \beta\frac{dy}{dt} + k_1y + k_2y^2 + k_3y^3 + aI = F_bSin(\omega t) \tag{8.37}$$

$$L\ddot{I} + R_{in}\dot{I} + \frac{1}{C}I = a\frac{d^2y}{dt^2} \tag{8.38}$$

where L is inductance and R_{in} is the resistance of the winding coils. C is the capacitance of the circuit. The equations 8.37 and 8.38 can be stated as,

$$M\ddot{y} + \beta\dot{y} + k_1y + k_2y^2 + k_3y^3 + a\frac{V}{R} = F_bSin(\omega t) \tag{8.39}$$

$$\ddot{y} = \frac{1}{M}(F_bSin(\omega t) - \beta\dot{y} - ky - k_2y^2 - k_3y^3 - aI) \tag{8.40}$$

$$L\ddot{I} + R_{in}\dot{I} + \frac{1}{C}I = a\frac{d^2y}{dt^2} \tag{8.41}$$

$$\ddot{I} = \frac{1}{L}\left(a\ddot{y} - R_{in}\dot{I} - \frac{1}{C}I\right) \tag{8.42}$$

The state space model of the system can be stated as,

$$Z_1 = y \tag{8.43}$$

$$Z_2 = \dot{y} = \dot{Z}_1 \tag{8.44}$$

$$\dot{Z}_2 = \ddot{y} \tag{8.45}$$

$$Z_3 = I \tag{8.46}$$

$$Z_4 = \dot{Z}_3 = \dot{I} \tag{8.47}$$

$$\dot{Z}_4 = \ddot{I} \tag{8.48}$$

$$U_1 = F_b Sin(\omega t) \tag{8.49}$$

$$\dot{Z}_1 = Z_2 \tag{8.50}$$

$$\dot{Z}_2 = \frac{1}{M}\left(U_1 - \beta Z_2 - k_1 Z_1 - k_2 {Z_1}^2 - k_3 {Z_1}^3 - \frac{a}{R_{in}} Z_3\right) \tag{8.51}$$

$$\dot{Z}_4 = \frac{1}{L}\left(a\ddot{y} - R_{in}\dot{I} - \frac{1}{C} I\right) \tag{8.52}$$

$$\dot{Z}_4 = \frac{1}{L}\left(a\left(\frac{1}{M}\left(U_1 - \beta Z_2 - k_1 Z_1 - k_2 {Z_1}^2 - k_3 {Z_1}^3 - a Z_3\right)\right) - R_{in} Z_4 - \frac{1}{C} Z_3\right) \tag{8.53}$$

The matrix form of the state space model can be stated as,

$$\begin{bmatrix} \dot{Z}_1 \\ \dot{Z}_2 \\ \dot{Z}_3 \\ \dot{Z}_4 \end{bmatrix} = \begin{bmatrix} 0 & 1 & 0 & 0 \\ \frac{-k_1 - k_2 Z_1 - k_3 {Z_1}^2}{M} & \frac{-\beta}{M} & \frac{-a}{M} & 0 \\ 0 & 0 & 0 & 1 \\ \frac{-ak_1 - ak_2 Z_1 - ak_3 {Z_1}^2}{M * L} & \frac{-a * \beta}{M * L} & -\left(\frac{a^2}{M * L} + \frac{1}{C * L}\right) & -\frac{R_{in}}{L} \end{bmatrix} \begin{bmatrix} Z_1 \\ Z_2 \\ Z_3 \\ Z_4 \end{bmatrix} + \begin{bmatrix} 0 \\ \frac{1}{M} \\ 0 \\ \frac{\alpha}{M * L} \end{bmatrix} [U_1] \tag{8.54}$$

$$[X] = \underbrace{\begin{bmatrix} 1 & 0 & 0 & 0 \\ 0 & 1 & 0 & 0 \\ 0 & 0 & 1 & 0 \\ 0 & 0 & 0 & 1 \end{bmatrix}}_{C} \begin{bmatrix} Z_1 \\ Z_2 \\ Z_3 \end{bmatrix} + \underbrace{[0]}_{D} [u] \tag{8.55}$$

8.2.1 Dynamics analysis of the SDOF nonlinear oscillator-based energy harvester

The dynamics of the proposed energy harvester have been analysed using the system's state space model. The used parameters of the system are presented in Table 8.1. Initially, the eigenvalues and frequency of the system were analysed. During the experimental excitation of the middle magnet by an applied external force, the floating magnet moved a maximum of 20 mm toward the bottom magnet and 50 mm toward the top magnet from the equilibrium position. Therefore, the excitation range has been considered 20 mm toward the bottom magnet and 50 mm toward the top magnet from the equilibrium position. The magnetic restoring force has been determined for this excitation range, and the linear and nonlinear coefficients have been measured from this magnetic restoring force. The system's eigenvalues for different positions of the floating magnet have been presented in Table 8.2. The real parts of the eigenvalues (Mechanical part) remained almost similar for different positions of the floating magnet which can be seen in Table 8.2. Still, the imaginary part of the eigenvalues changed with changing the position of the floating magnet. On the other hand, the real part of the

eigenvalues of the electrical part is almost similar for different positions of the floating magnet. Still, the imaginary parts remained zero for all different positions of the floating magnet.

Table 8.1: Required parameters for the system

Parameter	Values
k1	241.73 [N/m]
k2	4392.6 [N/m^2]
k3	134759 [N/m^3]
β	0.74 [Ns/m]
M	0.36745 [kg]
L	0.005546 [H]
R	5.48 [ohm]
l	23.5 [m]
B_x	0.35 [T]

Table 8.2: Eigenvalues of the system

Position of the floating magnet (mm)	Eigenvalues		Frequency (rad/s)	
	Mechanical part (1.0e+02)	Electrical part (1.0e+02)	Mechanical part	Electrical part
-50	-0.1844 + 0.2594i	-9.5324 + 0.0000i	31.82	953.23
-45	-0.1844 + 0.2354i	-9.5323 + 0.0000i	29.90	953.23
-40	-0.1844 + 0.2132i	-9.5323 + 0.0000i	28.18	953.23
-35	-0.1844 + 0.1933i	-9.5323 + 0.0000i	26.72	953.22
-30	-0.1844 + 0.1767i	-9.5322 + 0.0000i	25.54	953.22
-25	-0.1845 + 0.1642i	-9.5322 + 0.0000i	24.7	953.22
-20	-0.1845 + 0.1568i	-9.5322 + 0.0000i	24.21	953.22
-15	-0.1845 + 0.1554i	-9.5322 + 0.0000i	24.11	953.22
-10	-0.1845 + 0.1599i	-9.5322 + 0.0000i	24.41	953.22
-05	-0.1844 + 0.1701i	-9.5322 + 0.0000i	25.1	953.22
0	-0.1844 + 0.1849i	-9.5323 + 0.0000i	26.11	953.22
05	-0.1844 + 0.2033i	-9.5323 + 0.0000i	27.45	953.22
10	-0.1844 + 0.2245i	-9.5323 + 0.0000i	29.05	953.23
15	-0.1844 + 0.2477i	-9.5324 + 0.0000i	30.87	953.23

The natural frequency of the mechanical part changed with changing the position of the floating magnet. The natural frequencies of the mechanical part increased when the floating magnet travelled

toward the bottom or top magnets. However, the natural frequency of the electrical part remained constant at around 953.22 rad/s for all different positions of the floating magnet.

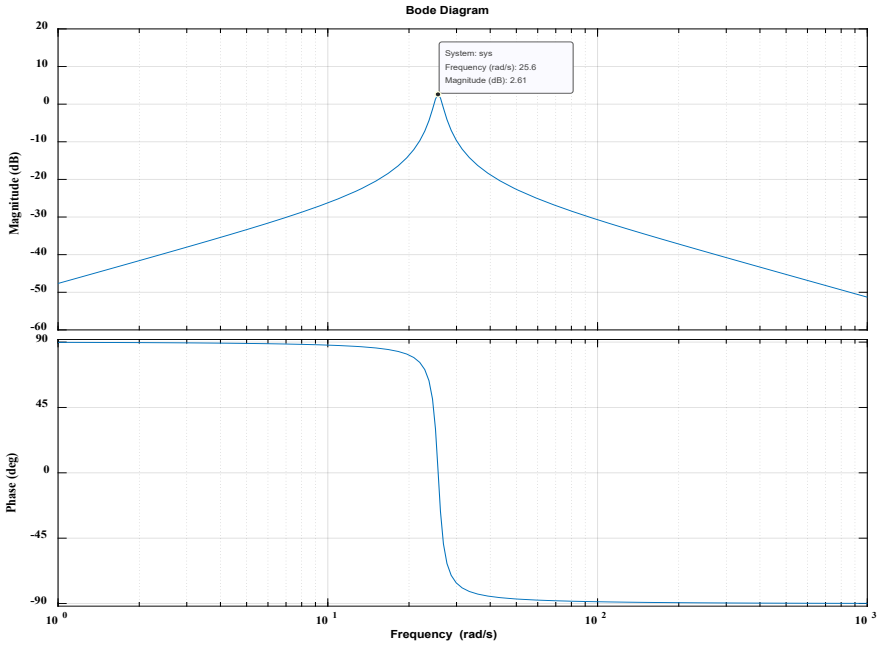

(a)

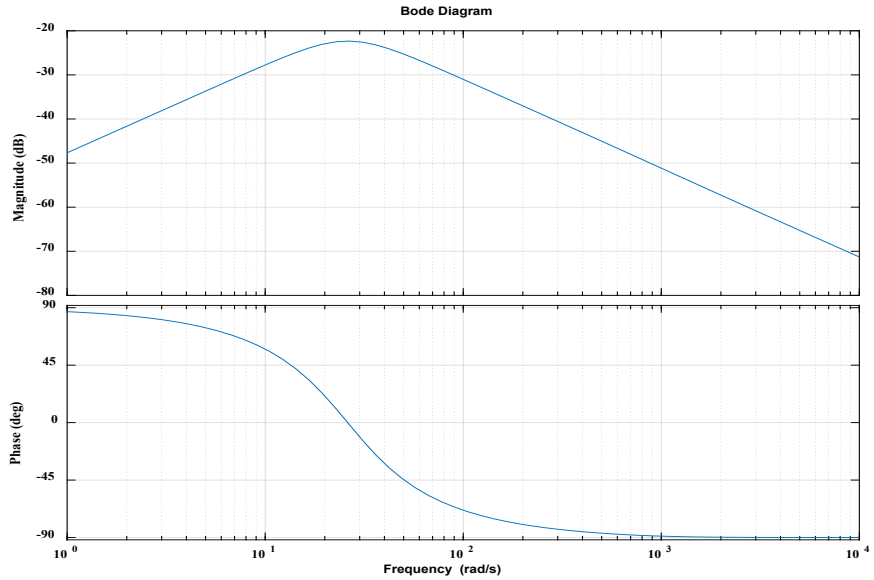

(b)

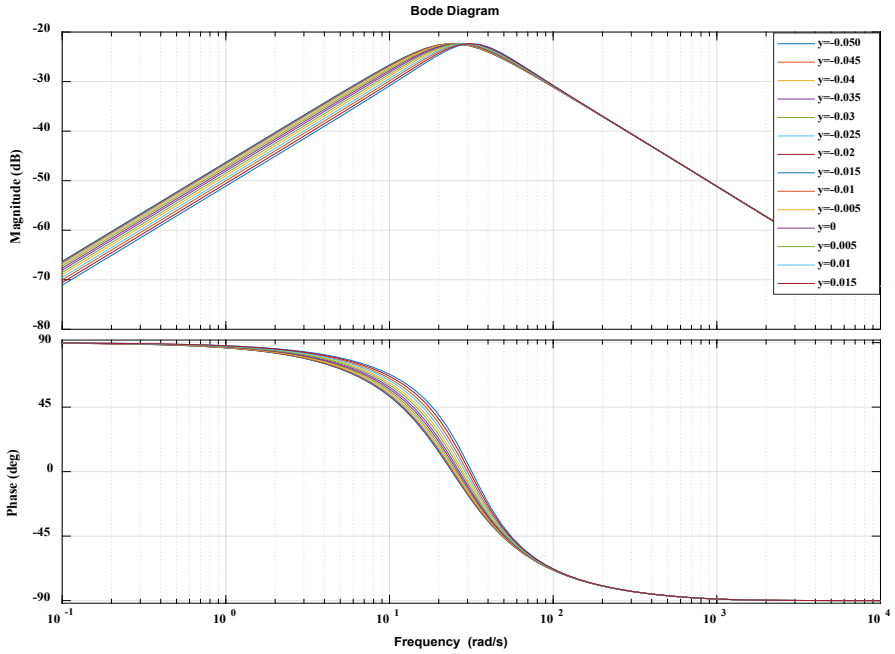

(c)

Figure 8.4: Resonance frequency (a) Without electrical-mechanical coupling, (b) with electrical-mechanical coupling and (c) for different positions of the middle floating magnet

The system's resonance frequency has been analysed with electrical-mechanical coupling and without electrical-mechanical coupling. Figure 8.4(a) and Figure 8.4(b) present the system's resonance frequency without electrical-mechanical coupling and with electrical-mechanical coupling, respectively. The coil's average magnetic flux density, resistance, length and inductance were 0.35T, 5.48ohm, 23.5m and 0.005546H to analyse the system's resonance frequency for different floating magnet positions in Figure 8.4(c). Because of the electrical-mechanical coupling effects, the frequency response of the generator system did not show the peak (or maximum) amplitude, as seen in Figure 8.4(c). It has known from the literature that the stiffness, mass and damping constant affect the resonance frequency of any system. The peak (or maximum) amplitude changes with changing the damping. Due to the larger damping constant, the system creates the lower maximum amplitude, as shown in Figure 8.5(a). However, the damping change does not affect the displacement amplitude at lower or higher frequencies, but it only impacts the amplitude response in the damping-controlled area at the peak. Decreasing the stiffness increases the amplitude of the low-frequency response, and adding the stiffness declines the displacement amplitude in this region, as displayed in Figure 8.5(b).

From Figure 8.5(b), it can be seen that changing the stiffness only changes the resonance peak's location, but it does not affect the amplitude at widespread frequencies.

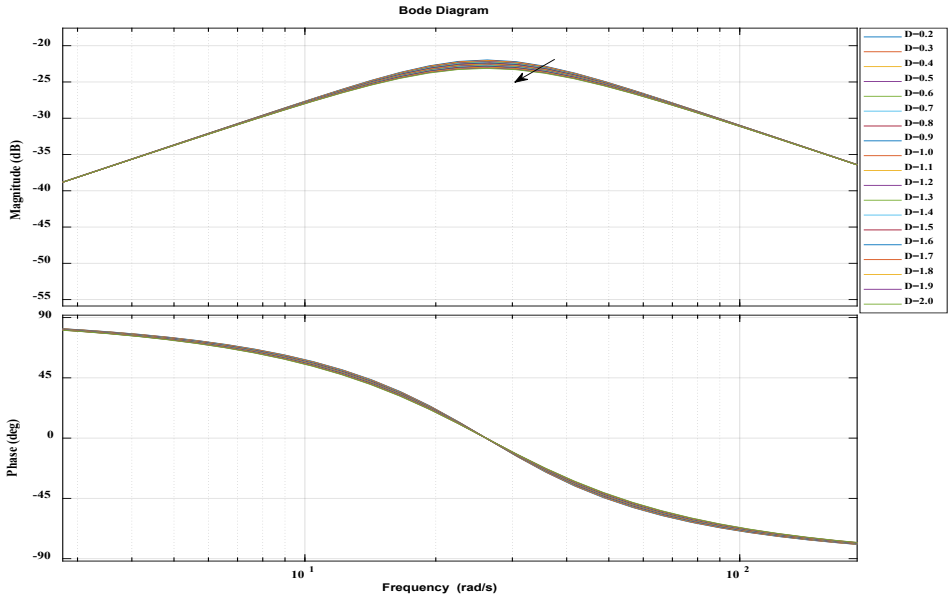

(a)

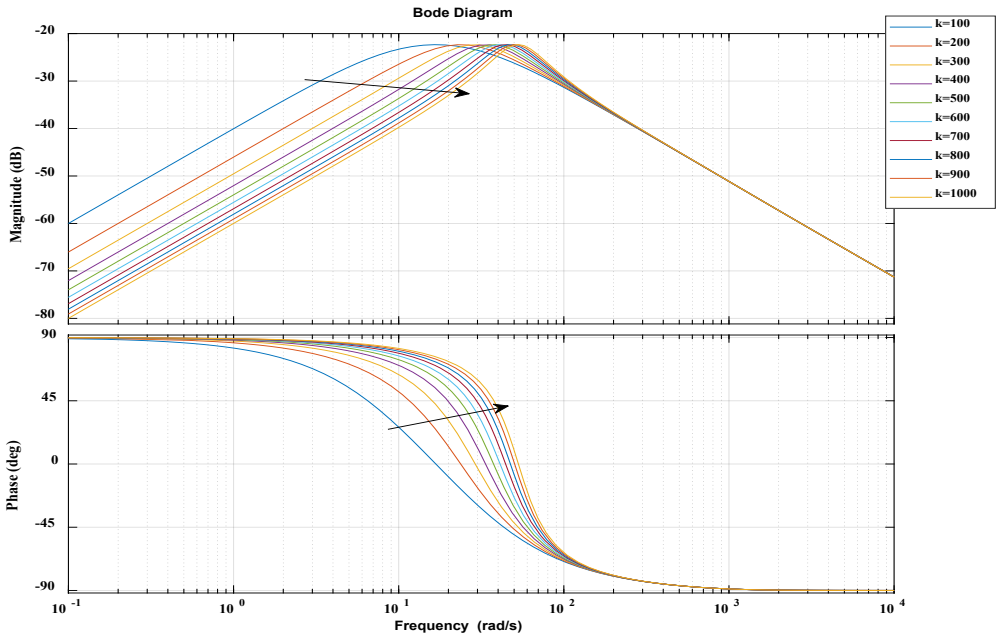

(b)

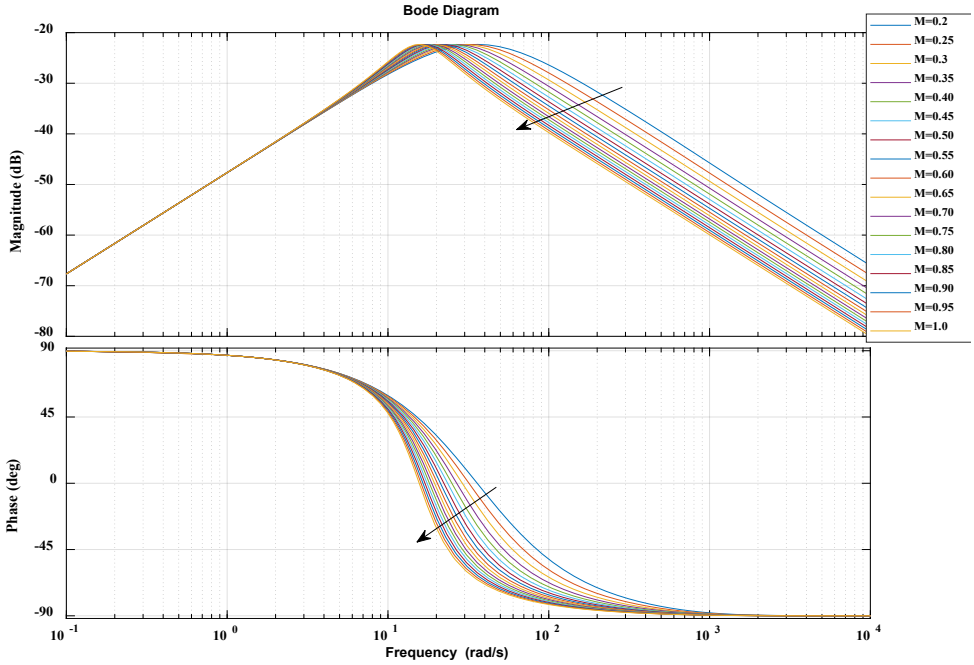

(c)

Figure 8.5: Frequency response (a) Different damping constant, (b) Different linear stiffness and (c) Different masses of the floating magnet

Adding the mass decreases the amplitude, and reducing the mass increases the amplitude, as presented in Figure 8.5(c). Changes in the mass only change the resonance peak, but it does not affect the displacement response. The effects of the electrical-mechanical coupling on the system have been analysed by changing the coil's magnetic flux density, length, resistance, and inductance. By changing the coil's inductance, the system's resonance frequency has been analysed, and it has been found that it does not affect the system's natural frequency.

However, the peak (or maximum) amplitude changes when the magnetic flux density changes; larger magnetic flux density results in a lower maximum amplitude. Changing the magnetic flux density only affects the amplitude response at the peak, as presented in Figure 8.6. Changing the length of the winding coil only affects the amplitude response at the peak, as shown in Figure 8.7. Similarly, when the length or the number of turns of the winding coil change, the peak (or maximum) amplitude changes; a smaller length or turn number of the winding coil results in a higher maximum amplitude. Figure 8.8 displays the frequency response for different resistances of the winding coil.

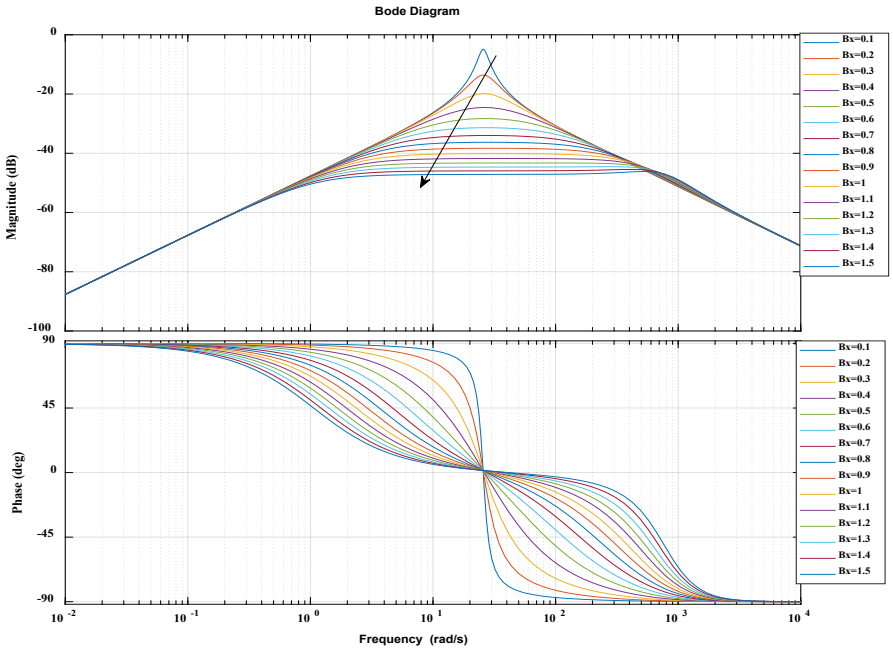

Figure 8.6: Frequency response for different magnetic flux density

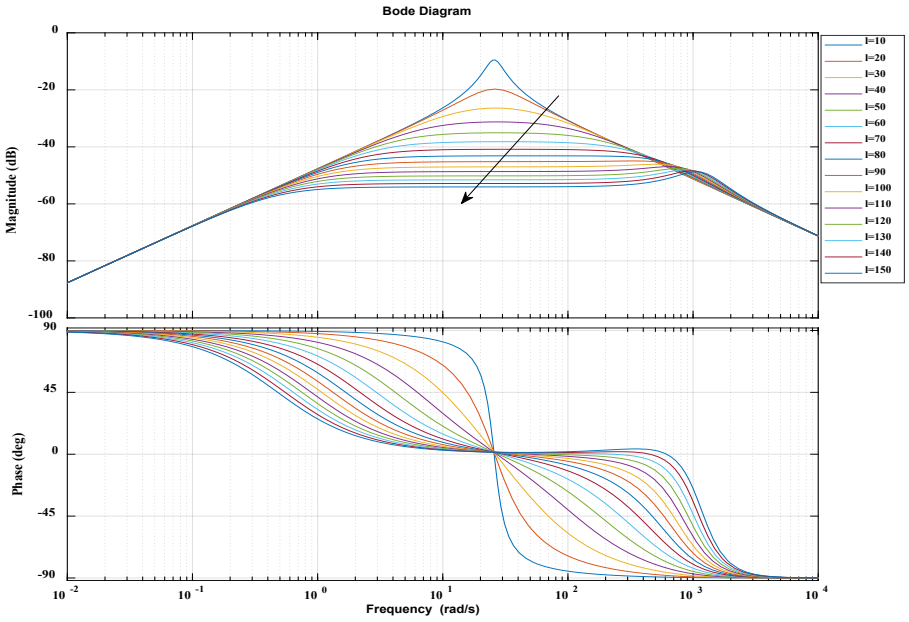

Figure 8.7: Frequency response for different lengths or turn numbers of the winding coil

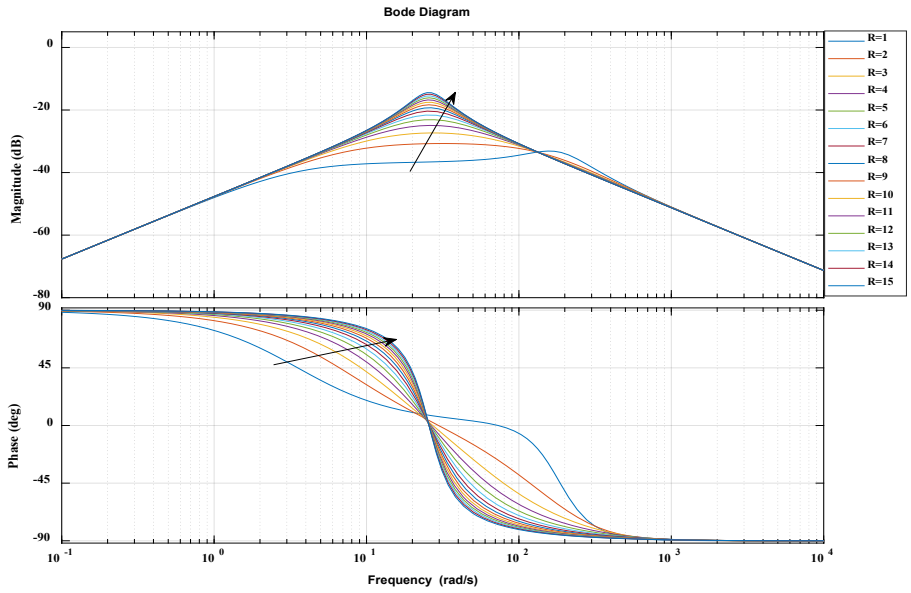

Figure 8.8: Frequency response for different resistance of the winding coil

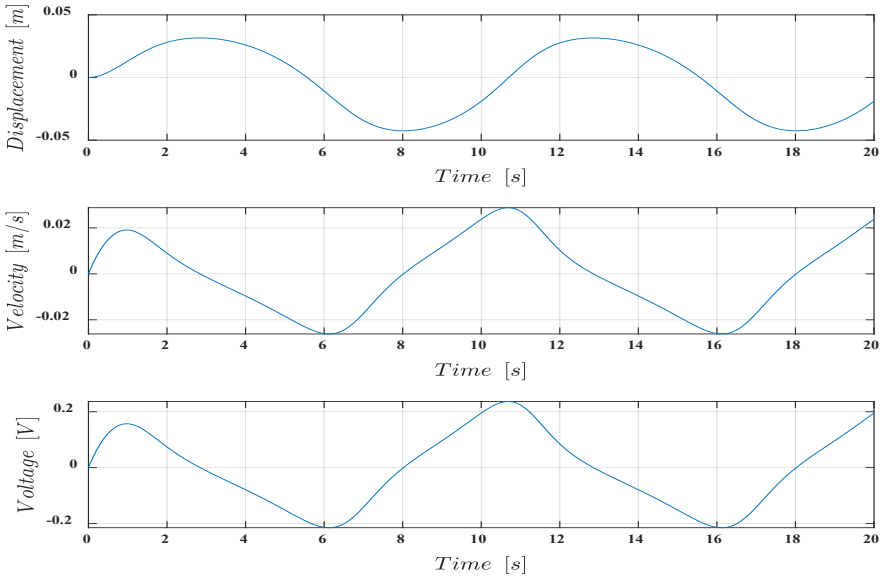

Figure 8.9: Displacement, velocity and induced voltage of the system

From Figure 8.8, it can be seen that when the resistance of the winding coil changes, the peak (or maximum) amplitude changes; smaller resistance of the winding coil results in a lower maximum amplitude. Therefore, changing the resistance of the winding coil only affects the amplitude response at the peak. Moreover, the theoretical generator model dynamics have been analysed using the state

space model (ode23t). The generator system's displacement, velocity, and induced voltage for different simulation times have been determined under harmonic force. The harmonic force's amplitude and frequency were 25N and 0.1Hz, respectively. The initial displacement, velocity and induced voltage were considered zero and the simulation was run for 20 seconds. Figure 8.9 displays the system's displacement, velocity, and induced voltage. Figure 8.10 presents the power of the system.

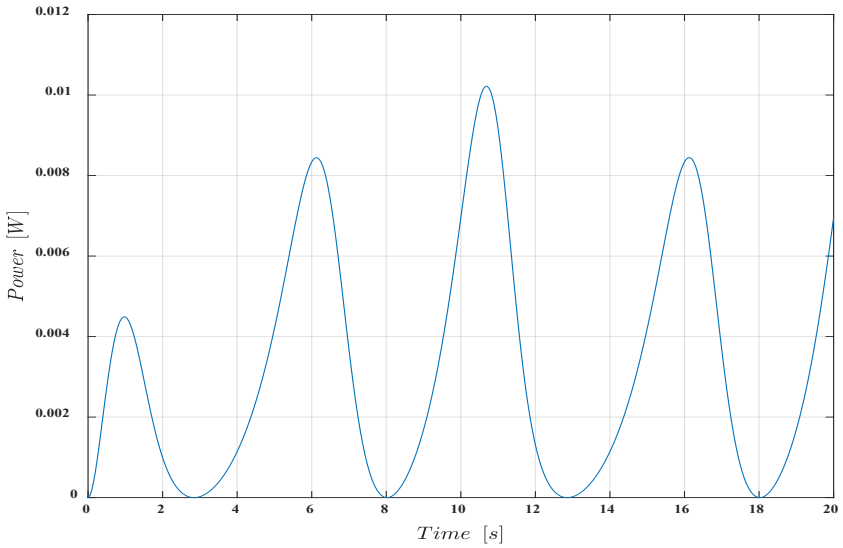

Figure 8.10: Power output of the system

For the 25sin(2phi*0.1*t) applied harmonic force, the floating magnet moved around 31 mm towards the bottom and about 43 mm towards the top. Between that time, the maximum velocity of the floating magnet was 0.026 m/s. The measured maximum induced voltage was around 0.23V for this displacement of the floating magnet.

Moreover, the determined maximum power was 0.01 W, as shown in Figure 8.10. The harmonic force frequency was 0.1 Hz, and therefore, the displacement line should touch the 0 points after a complete cycle. From Figure 8.9, it can be seen that the displacement curve did not touch the 0 points after an entire cycle (when the simulation was run for 10s) due to the electromechanical coupling effect. The effect of the electromagnetic damping has been analysed by changing the winding coil's average magnetic flux density, resistance, and inductance. Figure 8.11 and Figure 8.12 present the effect of the generator system from different magnetic flux densities.

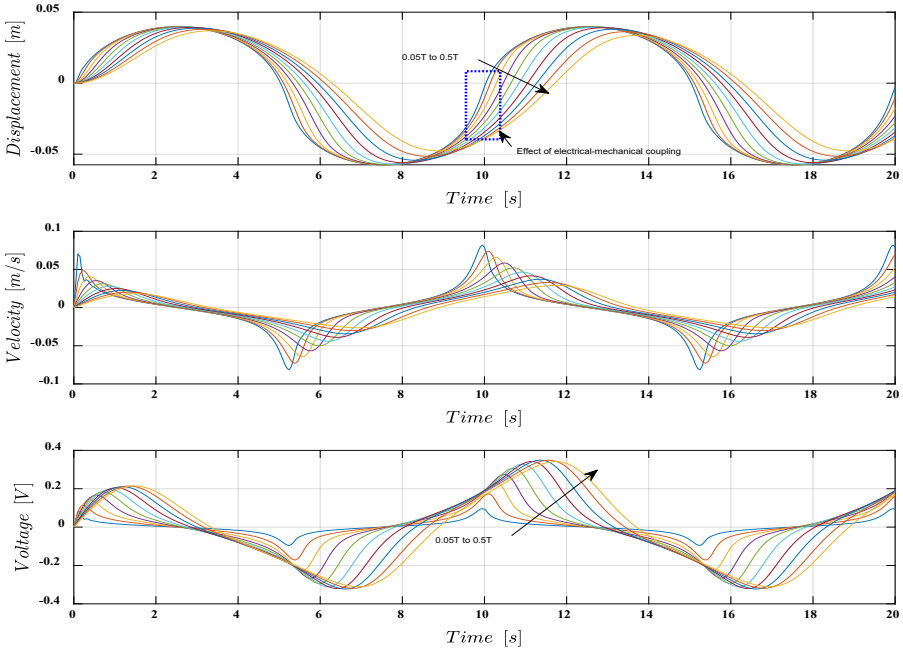

Figure 8.11: Displacement, velocity and induced voltage of the system for different magnetic flux densities

The effects of the magnetic flux density on the oscillation of the floating magnet are shown in Figure 8.11. It can be seen from Figure 8.11 that with changing the magnetic flux densities, the displacements, velocities and induced voltages changed. The induced voltages and power output increased with increasing the magnetic flux densities, as seen in Figure 8.11 and Figure 8.12.

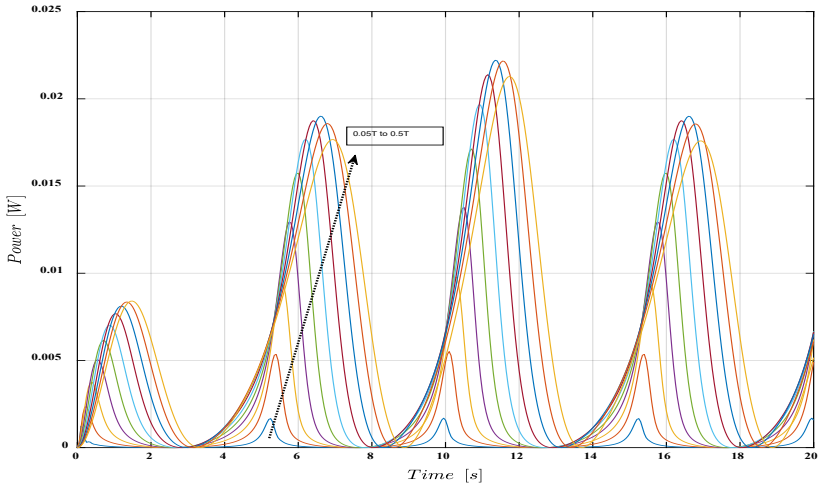

Figure 8.12: Power output for the different amplitude of the harmonic force

When the magnetic flux density was 0.05T, the displacement curve nearly touched the 0 points after a complete cycle in 10s. The frequency of the applied harmonic force was 0.1Hz, and therefore the displacement curve should touch 0 points after an entire cycle in 10s. But when the magnetic flux density increased from 0.05T to 0.5T, the 0 points of the displacement curves went far from 10s after a complete cycle. Hence, the magnetic flux density impacts the oscillation of the floating magnet. However, with increasing the average magnetic flux densities, the displacements and velocities of the system decreased, but the induced voltage increased. Changes to the resistance of the winding coil resulted in changes to the displacements, velocities, induced voltages, and power output, as displayed in Figure 8.13 and Figure 8.14. With the increase in the resistance of the winding coil, the induced voltages and power output decreased, as presented in Figure 8.13 and Figure 8.14. When the resistance of the winding coil was small, the 0 point of the displacement curve was near the 10s after a complete cycle. But the curve moved away from the 10s by increasing the winding coils' resistance after a complete cycle. When the resistance of the winding coil increased from 1 ohm to 6 ohms, the displacement curves went far away from the 10s. Therefore, it can be said that the resistance of the winding affects the oscillation of the floating magnet.

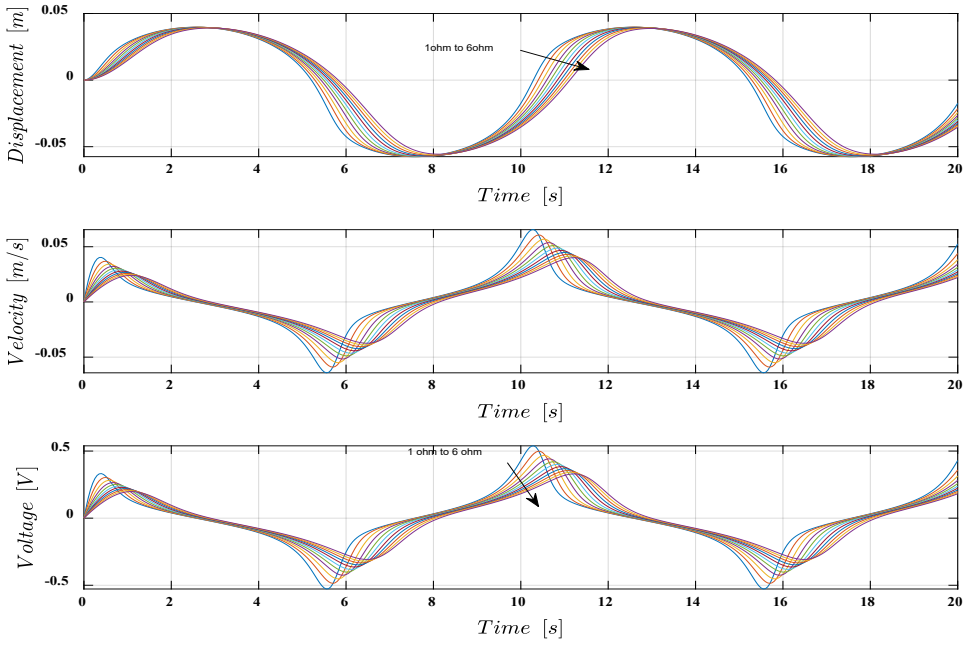

Figure 8.13: Displacement, velocity and induced voltage of the system for different resistance of the winding coil

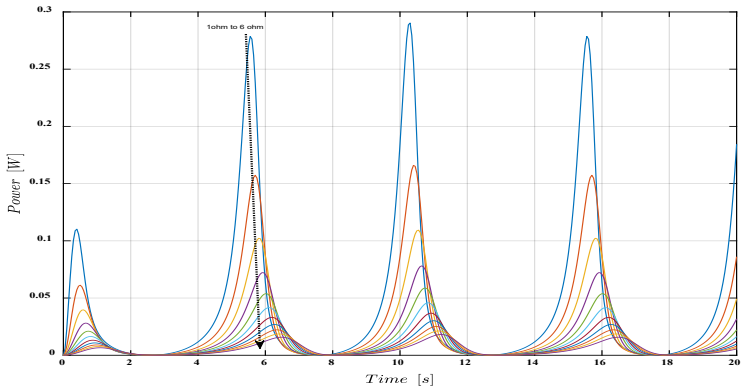

Figure 8.14: Power of the system for different resistance of the winding coil

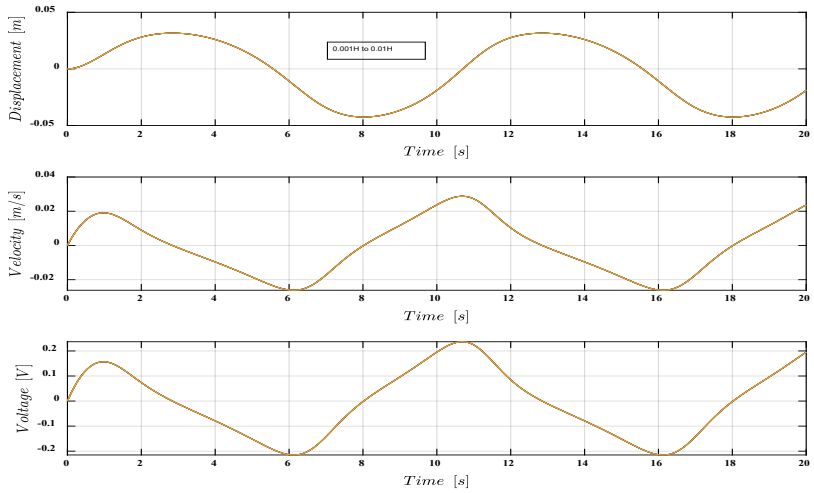

Figure 8.15: Displacement, velocity and induced voltage of the system for different inductances of the winding coil

With increasing the resistance of the winding coil, the displacements, velocities of the floating magnet, induced voltage and power decreased. Moreover, the effect of the electrical-mechanical coupling has been analysed by changing the winding coil's inductance. It has been found that it does not affect the oscillation of the floating magnet, as shown in Figure 8.15.

8.2.1.1 Generator system analysis with external load

The dynamics of the generator system have been analysed using external load/resistance (R_e) with the circuit. The coil is connected in parallel to the external load. The value of the external load was 500 ohms. The eigenvalues of the system were -1.189+26i, 0, 0; 0, -1.189-26i, 0; 0, 0, -91143+0i

when the middle magnet was in equilibrium position. The frequency of the mechanical part was 26 rad/s, and the electrical part was 91143 rad/s. The eigenvalues of the system without external load were -0.1844 + 0.1849i, 0, 0, 0, -0.1844 -0.1849i, 0, 0, 0, -9.5323 + 0i. The frequency response of the system was 26.11 rad/s and 953.22 rad/s. Comparing the system with and without external load, the mechanical part of the system showed almost the same natural frequency (about 26 rad/s). However, the electrical part of the system with the external load showed higher frequency than the system without external load. The external load changed the eigenvalues and frequency of the system. With changing the position of the floating magnet, the eigenvalues changed, as shown in Figure 8.16. Figure 8.17 presents the frequency response of the generator system.

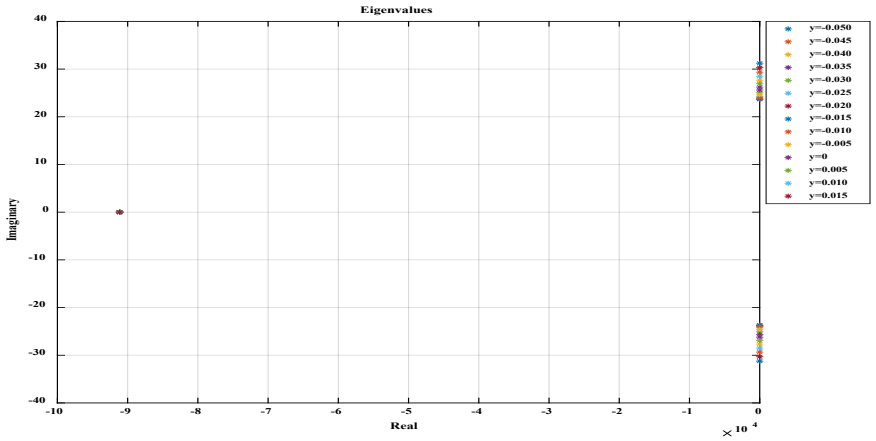

Figure 8.16: Eigenvalues of the system for different positions of the floating magnet

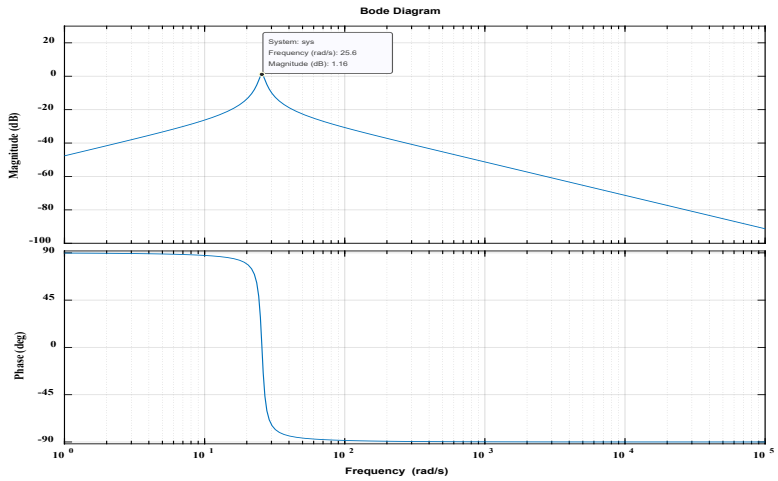

Figure 8.17: Frequency response of the electromagnetic generator system when the floating magnet was in equilibrium position

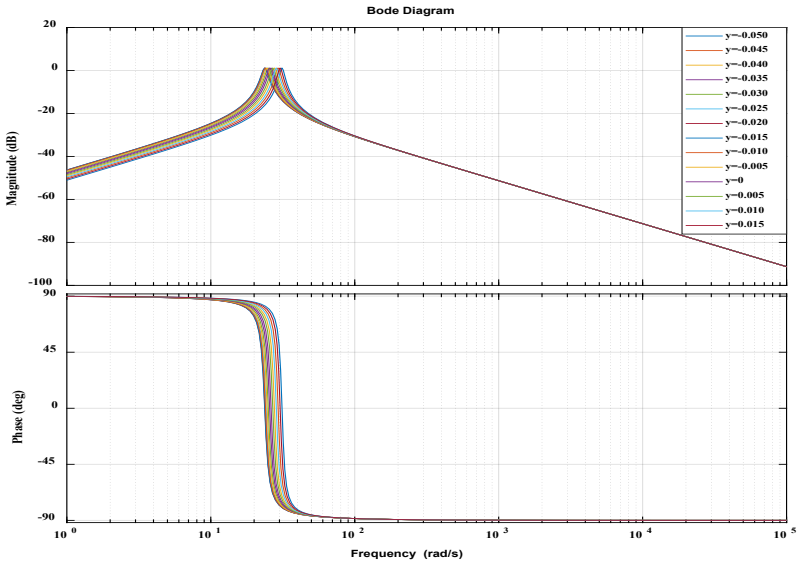

Figure 8.18: Frequency response of the electromagnet generator system for different positions of the floating magnet

It has been seen in Figure 8.4(c) that due to the electrical-mechanical coupling effects, the frequency response of the generator system did not show the peak (or maximum) amplitude. Still, the system with the external load showed the peak amplitude. With changing the position of the floating magnet, the frequency response changed, as shown in Figure 8.18. Different external loads were connected to analyse the frequency resonance of the generator system. Figure 8.17 displays the resonance due to the floating magnets. The value was 25.6 rad/s in the equilibrium position, similar to the natural frequencies (25.6 rad/s without external load) determined using eigenvalues. The system showed a resonance when external loads were connected to the winding coils, as shown in Figure 8.17, but the system without an external load did not show the peak amplitude, as presented in Figure 8.4. Figure 8.19 displays the resonance frequency of the generator system for the different external loads.

From Figure 8.19, it can be seen that the frequency response did not change with changing external load. The resonance frequency position changed with changing the position of the floating magnet. Compared to the SDOF generator system with or without external load, the SDOF generator system with the external load showed better dynamics results. The Simulink model has been used to analyse the state space model of the SDOF generator system with the external load. Figure 8.20 displays the Simulink model of the SDOF generator system. Figure 8.20 depicts the displacement and velocity of the floating magnet. The generated induced voltage of the generator is presented in Figure 8.21.

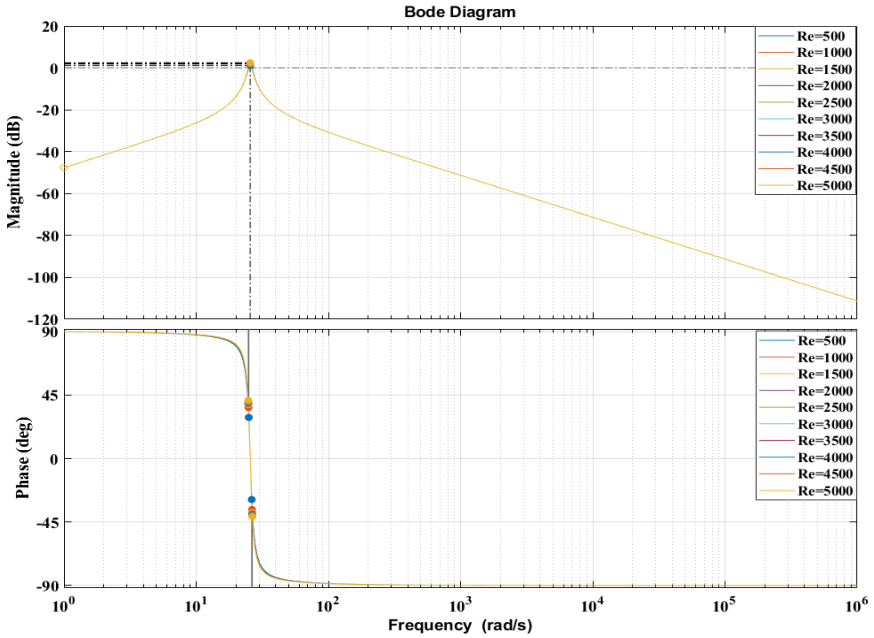

Figure 8.19: Frequency response of the SDOF electromagnetic generator system with various external loads in equilibrium position

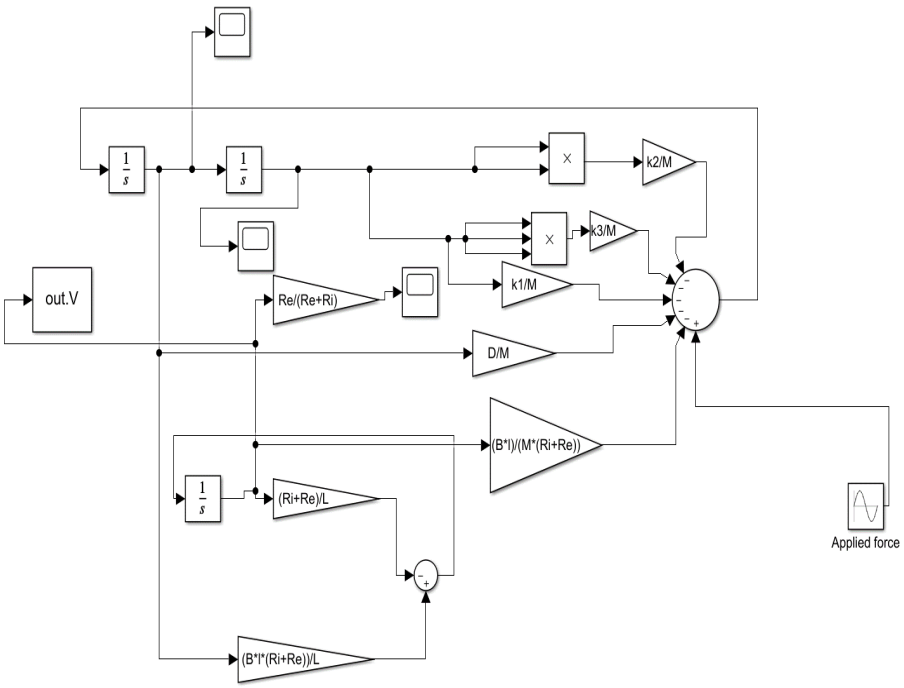

Figure 8.20: Simulink model of the SDOF energy harvester system

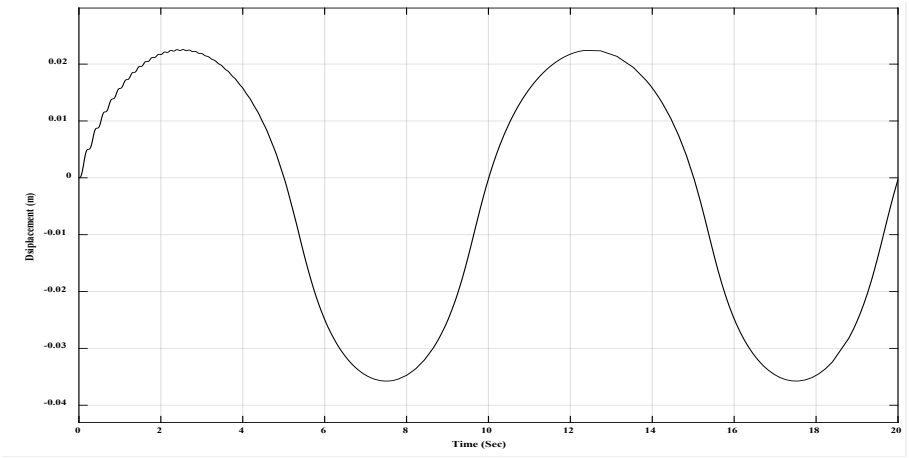

(a)

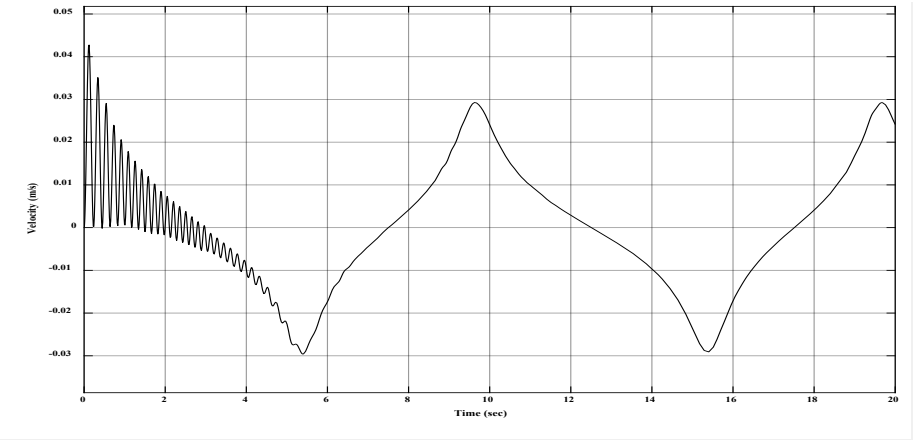

(b)

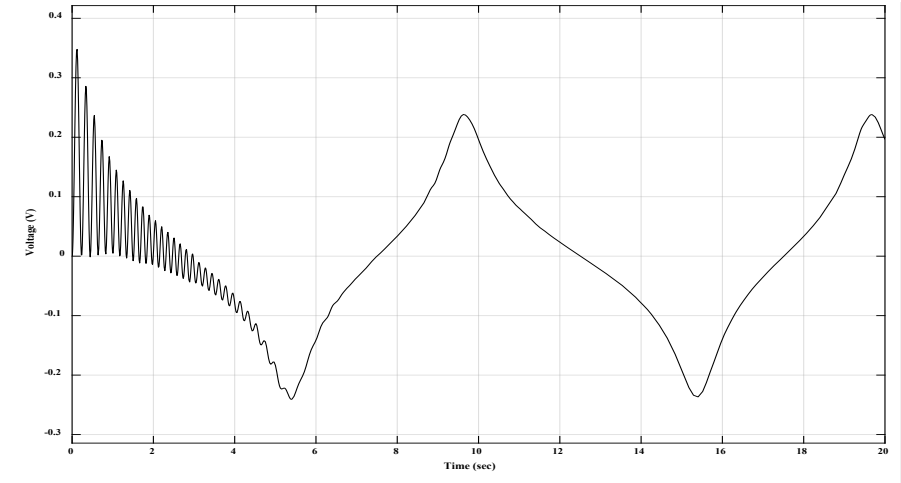

(c)

Figure 8.21: (a) Displacement of the floating magnet, (b) velocity of the floating magnet and (c) Induced voltage of the generator

The amplitude of the applied harmonic force was 25N, and the frequency was 0.1 Hz. The floating magnet moved around 22 mm toward the bottom and 35 mm toward the top. Between that time, the maximum velocity of the floating magnet was 0.028 m/s. The measured maximum induced voltage was around 0.23V for this displacement of the floating magnet, as shown in Figure 8.21(c).

8.2.1.2 SDOF generator system analysis with RLC circuit

The dynamics of the SDOF generator system have been analysed using an RLC circuit, for which all parameters of the system used for the analysis have been presented in Table 8.1. The capacitance of the circuit was considered $1nF$ during the simulation. Moreover, the inductance and resistance of the winding coils were 0.005546H and 5.48ohm. The system's eigenvalues for the mechanical and electrical parts were -494 + 2302.6i and 1+25.6i, respectively, when the floating magnet was in the equilibrium position. The natural frequency of the mechanical part was 25.6 rad/s and of the electrical part was 2355 rad/s when the floating magnet was in the equilibrium position.

Table 8.3: Eigenvalues and natural frequencies of the system for different positions of the floating magnet

Position of the floating magnet (mm)	Eigenvalues		Frequency (rad/s)	
	Mechanical part (1.0e+03)	Electrical part (1.0e+03)	Mechanical part	Electrical part
-50	-0.0010 + 0.0312i	-0.4940 + 2.3026i	31. 2	2355
-45	-0.0010 + 0.0293i	-0.4940 + 2.3026i	29.4	2355
-40	-0.0010 + 0.0277i	-0.4940 + 2.3026i	27.7	2355
-35	-0.0010 + 0.0262i	-0.4940 + 2.3026i	26.2	2355
-30	-0.0010 + 0.0251i	-0.4940 + 2.3026i	25.1	2355
-25	-0.0010 + 0.0242i	-0.4940 + 2.3026i	24.2	2355
-20	-0.0010 + 0.0237i	-0.4940 + 2.3026i	23.8	2355
-15	-0.0010 + 0.0237i	-0.4940 + 2.3026i	23.7	2355
-10	-0.0010 + 0.0239i	-0.4940 + 2.3026i	24	2355
-05	-0.0010 + 0.0246i	-0.4940 + 2.3026i	24.6	2355
0	-0.0010 + 0.0256i	-0.4940 + 2.3026i	25.6	2355
05	-0.0010 + 0.0269i	-0.4940 + 2.3026i	26.9	2355
10	-0.0010 + 0.0285i	-0.4940 + 2.3026i	28.5	2355
15	-0.0010 + 0.0303i	-0.4940 + 2.3026i	30.3	2355

The eigenvalues and natural frequencies of the system for different positions of the floating magnet have been presented in Table 8.3. The eigenvalues and natural frequencies of the system changed with changing the position of the floating magnet, as presented in Table 8.3. The eigenvalues of the electrical part always remained constant for all different positions of the middle magnet. The real parts of the eigenvalues remained constant for different positions of the floating magnet, but the imaginary parts of the eigenvalues changed with changing the position. Moreover, the natural frequency of the electrical part remained constant for all different positions of the floating magnet. Still, the natural frequencies of the mechanical part changed with changing the position of the floating magnet. The resonance of the system has been analysed using the bode command. The system's resonance frequency was 25.6 rad/s when the floating magnet was in equilibrium, as shown in Figure 8.22. The resonance frequency changed with changing the position of the floating magnet. Figure 8.23 displays the system's resonance frequencies for different positions of the floating magnet.

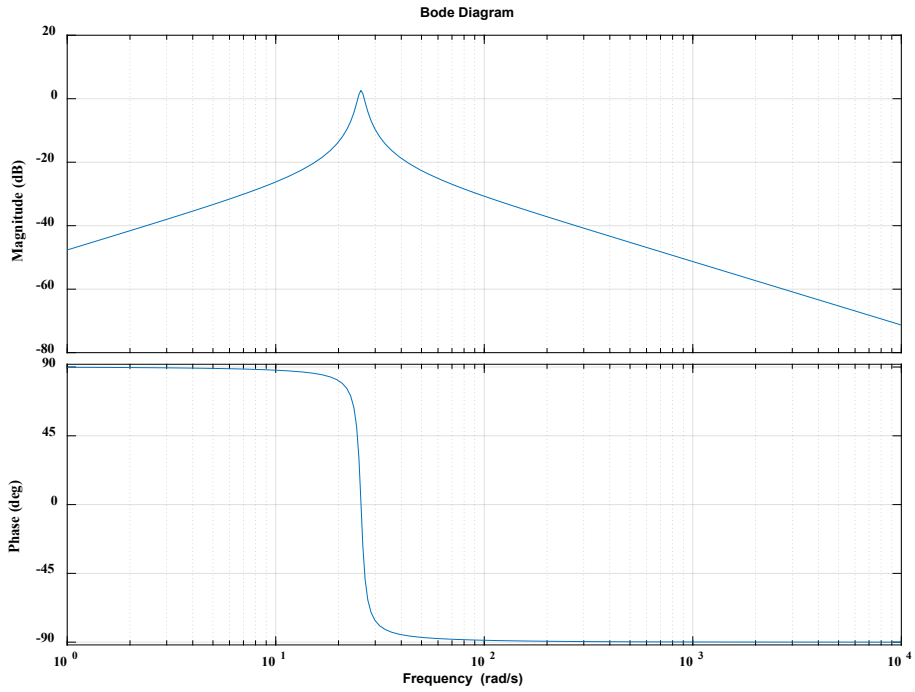

Figure 8.22: Resonance frequency of the system when the floating magnet is in equilibrium position

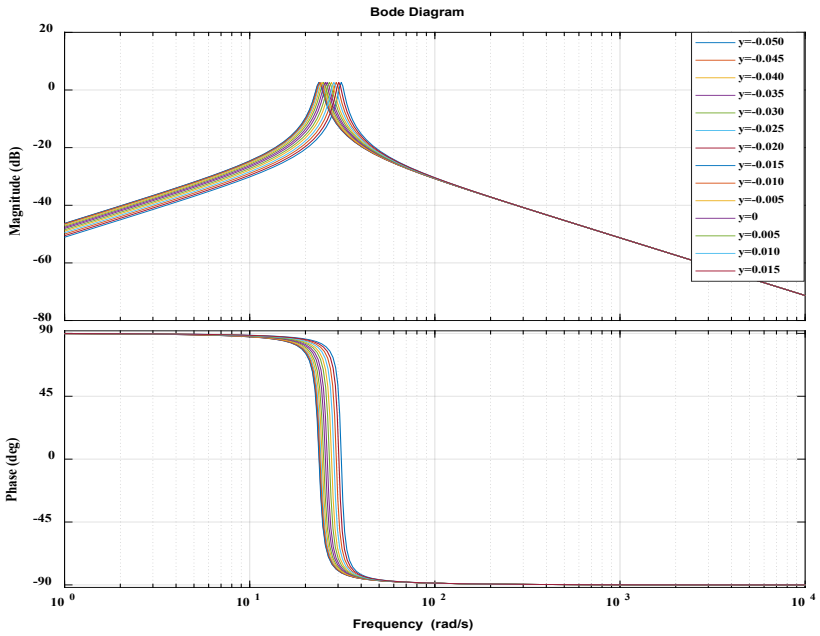

Figure 8.23: Resonance frequencies of the system for different positions of the floating magnet

Comparing the RL circuit with the RLC circuit, it has been seen that the RLC circuit provides more promising results than the RL circuit. The mechanical part's measured eigenvalues and natural frequencies are similar for both RL and RLC circuits. However, the estimated eigenvalues and natural frequencies of the electrical part in the RLC circuit are higher than in the RL circuit. For the different positions of the floating magnet, the RLC circuit showed different peak (or maximum) amplitude changes, as seen in Figure 8.23. On the other hand, the frequency response of the generator system in the RL circuit did not show the peak (or maximum) amplitude, as seen in Figure 8.4(c).

8.3 Numerical Simulation and Parametric Study of the Energy Harvester Model

The Finite Element Analysis (FEA) of the SDOF electromagnet generator model is analysed in this section. To achieve the optimised design of the SDOF energy harvester, the numerical analysis is performed using ANSYS MAXWELL. Different configurations have been designed for this optimisation by varying other parameters such as size and grade of magnets, coil number and air gap, etc. The ANSYS Maxwell software has been used for the FEA of the SDOF energy harvester model. The generator model is analysed as a 2D axisymmetric model, as shown in Figure 8.24. The dimensions of the generator are in millimetres. As the permanent magnets of the system produce the

magnetic flux density, the magnetic flux density can be changed by varying the grade of the permanent magnet.

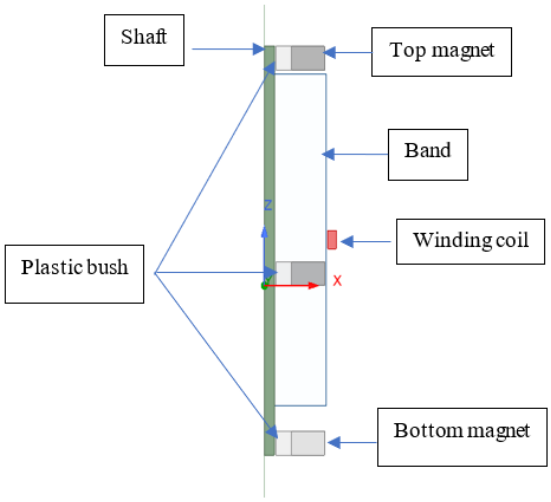

Figure 8.24: The 2D axisymmetric transient model of the SDOF energy harvester

All parameters of the ring permanent magnets have been presented in Table 3.1 in Chapter 3. In Figure 8.24, the component band indicates that the objects inside the band area can move. The 100 turns winding coil has been placed 20 mm up from the equilibrium position of the middle floating magnet. The winding coil parameters can be found in Table 8.1. The numerical analysis has been done in ANSYS Maxwell by some significant steps: Model Wizard, Definitions and Material Selection→ Boundaries→ Excitations→ Parameters→ Mesh→ Analysis→ Result→ Field Overlays. The first step is to set the project types, either Maxwell 2D design or Maxwell 3D design, to create the physical environment. In ANSYS Maxwell, the required project can be selected from the project menu. Then, the next step is selecting *solution type* from the Maxwell 2D menu. After drawing the generator 2D, axisymmetric model material has been selected for individual objects. Material selections are essential parts of ANSYS Maxwell Finite Element Analysis. For the generator 2D model simulation, the design object is chosen first, and the suitable material is selected from assigned Materials from the Modeler Window. The vector potential has been selected for the boundary condition of the Maxwell 2D model. The coil area is indicated as a winding coil, and the coil is added with it. An RL circuit has been added with it. During the parameter's selection, the force is selected for the floating magnet. Very small mesh sizes have been chosen for better results. The analysis time has been set up by calculating the applied velocity or force on the floating magnet.

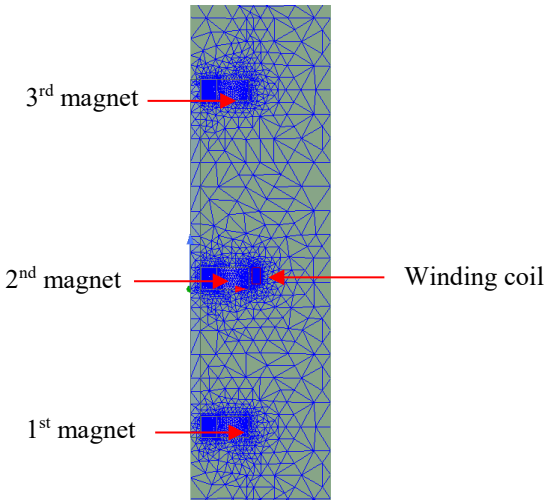

Figure 8.25: Mesh plotting of the generator model

Initially, the simulation has run using constant velocity, and different parameters were analysed. Meshing is a noteworthy part of FEA simulation methods, and it influences any FEA solution's speed, accuracy, convergence, etc. The meshed models, shown in Figure 8.25, present the generator model's mesh plot.

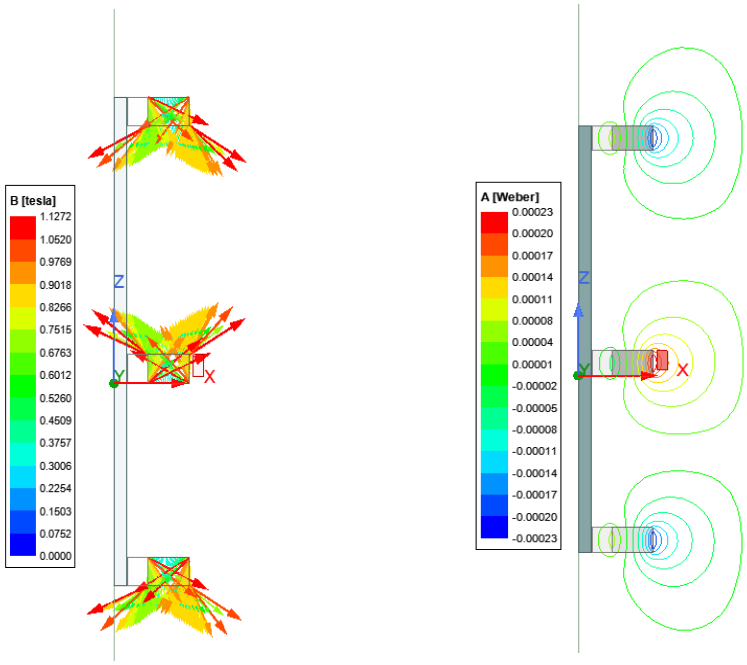

(a) (b)

Figure 8.26: (a) Magnetization direction and (b) Flux line

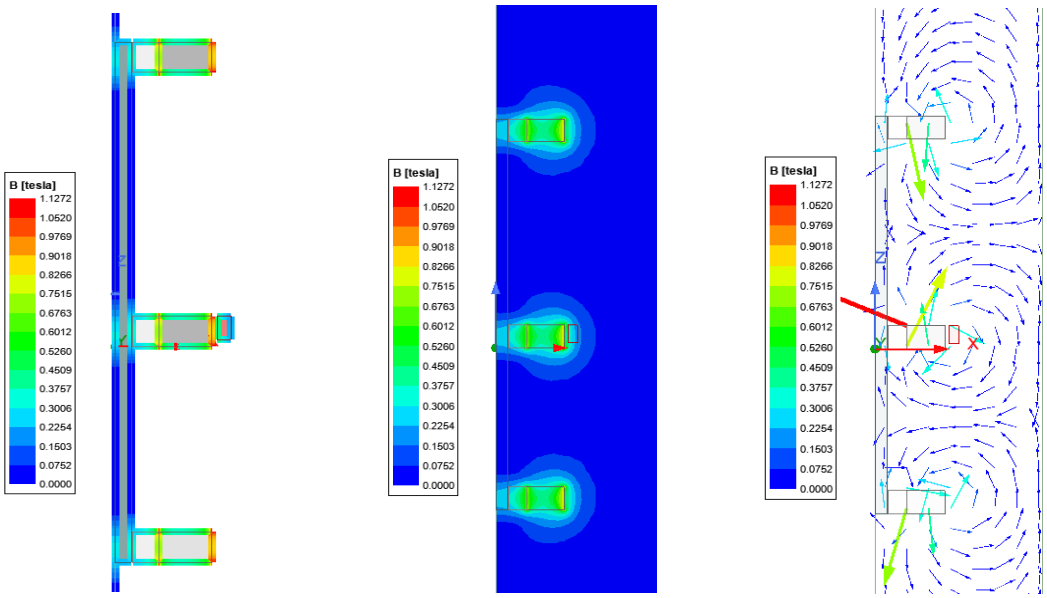

(a) (b) (c)

Figure 8.27: Magnetic flux density (a) Surfaces of magnets and coil, (b) Mag_B, and (c) B_Vector

The magnetisation direction of all magnets, flux line and magnetic flux density have been measured from the Field Overlays. Figure 8.26(a) displays the magnetisation direction of all magnets, and Figure 8.26(b) presents the flux line of all magnets. The arrows in Figure 8.26(a) represent the magnets' magnetisation direction along with the North Pole of the magnets. The flux lines emerge from the magnets, and the maximum flux line can be seen on the outside diameter surfaces of the magnets, as shown in Figure 8.26(b). The flux line can be seen inside the coil area, generating the induced voltage inside the winding coil. Figure 8.27 presents the magnetic flux density of the generator model. The colour in Figure 8.27(a) and Figure 8.27(b) denote the permanent magnet's magnetic flux density (B). The higher flux density is formed around the magnet area, indicated by the colour variations in Figure 8.27(a). For a further detailed understanding of the distribution of magnetic flux density, the Mag_B plot results are observed (Figure 8.27(b)). The magnetic flux lines emerged from the North Pole and travelled toward the South Pole, as seen in Figure 8.27(c). Moreover, it can be said from Figure 8.27 that the permanent magnet affects the coil, plastic bush and shaft. Therefore, the shaft has been made of non-magnetic materials, and plastic is non-magnetic. The copper coils have been used as winding coils to generate an induced voltage from the changing magnetic flux. The induced voltage creates inside the copper coil when the magnetic flux cuts the copper coil.

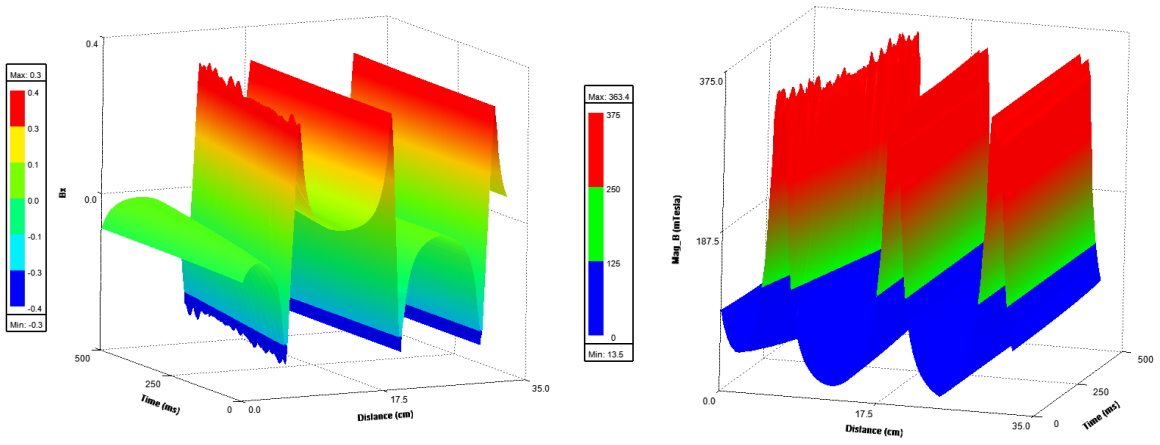

(a) (b)

Figure 8.28: Magnetic flux densities for various positions of the floating magnet (a) B_Vector and (b) Mag_B

The magnetic flux density has been analysed by changing the position of the middle magnet. The floating magnet has been moved with constant velocity from a specific position toward the top magnet. The magnetic flux density of the generator changed with changing time along with the position of the floating magnet. Figure 8.28 presents the change of magnetic flux densities for different positions of the floating magnet. Moreover, the flux line changed with changing the position of the floating magnet, as presented in Figure 8.29. The change of current densities for various locations of the floating magnet has been presented in Figure 8.30.

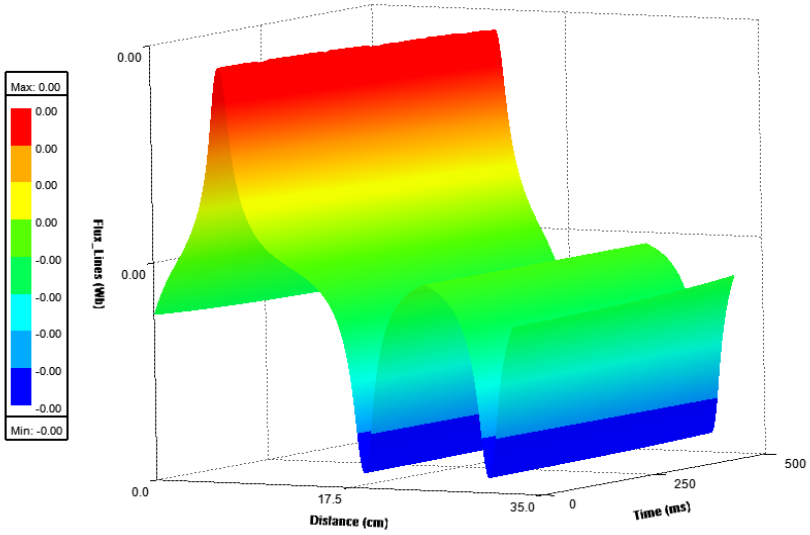

Figure 8.29: Flux lines for various positions of the floating magnet

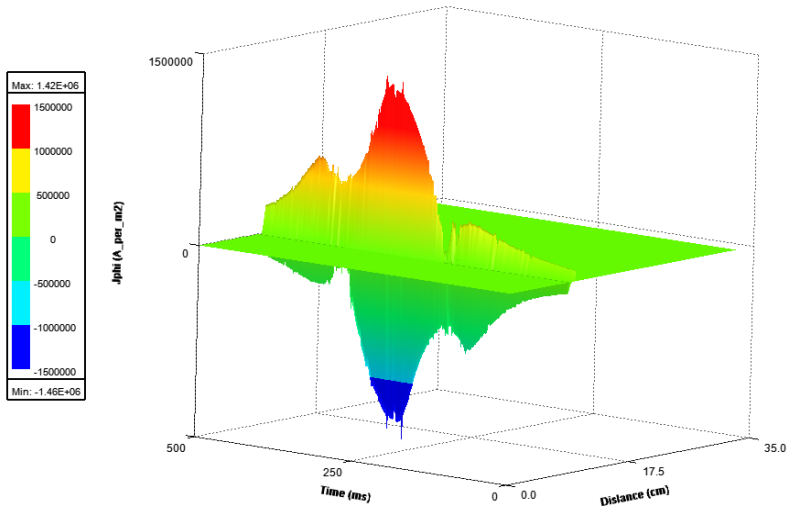

Figure 8.30: Current densities for different locations of the floating magnet

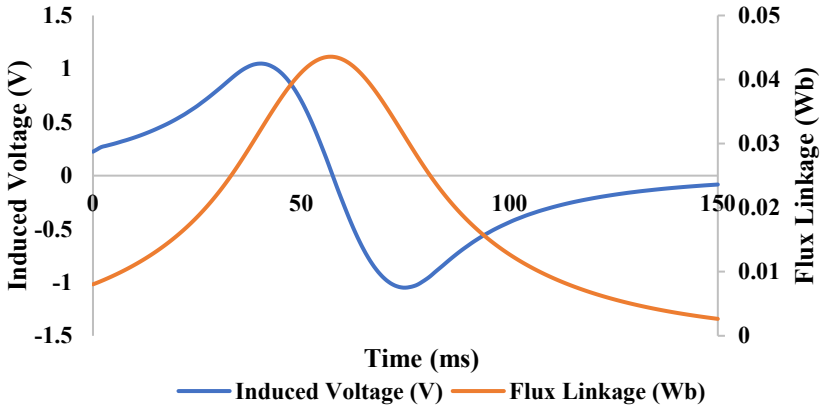

Figure 8.31: Induced voltage and flux Linkage in the winding coil

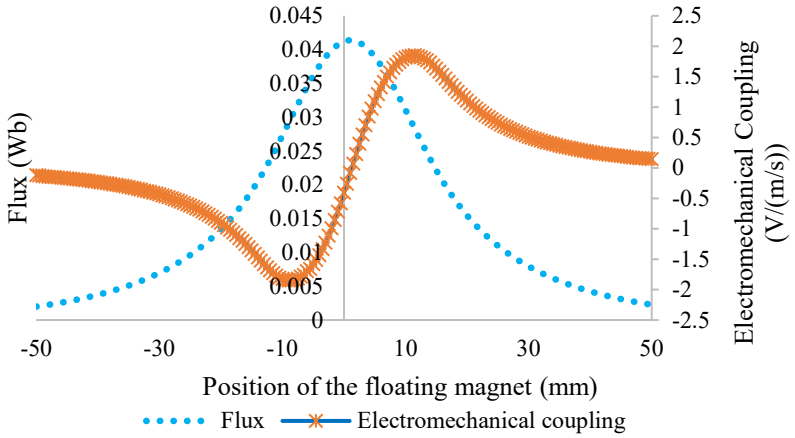

(a)

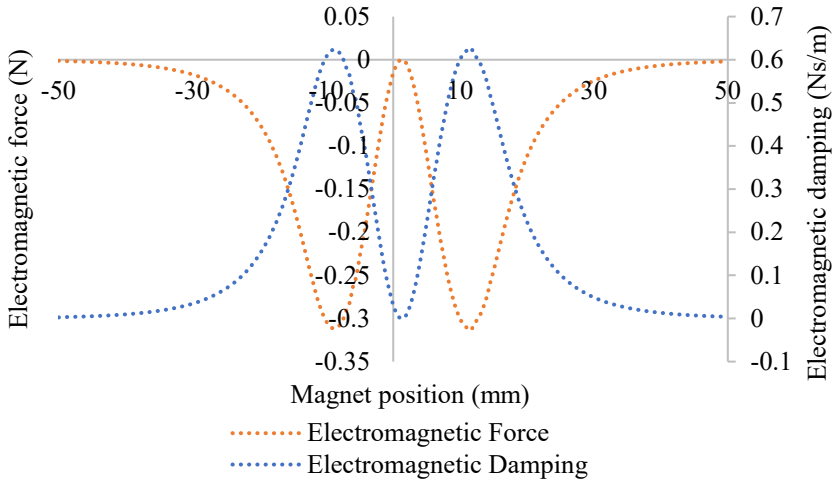

(b)

Figure 8.32: (a) Electromechanical coupling coefficient (100 number of turns, 0.5 m/s velocity of the floating magnet) and (b) Electromagnetic force and damping (100 number of turns and 0.5 m/s velocity of the floating magnet)

Due to the movement of the middle magnet, an electric field is generated inside the winding coil. Figure 8.31 displays the generated induced voltage and flux linkage in the winding coil when the middle magnet moves by a constant velocity of 0.5 m/s from the equilibrium position. It can be seen from Figure 8.31 that the maximum flux linkage was generated inside the winding coil when the moving magnet was parallel with the coil (both the middle magnet and winding coil were in the same position).

Moreover, the induced voltage was zero when the flux linkage was maximum. When a vibrating energy harvester is based on levitation, two forces act to couple the electrodynamics and mechanics; the first is the repulsion between the stack and the end magnets, and the second is the interaction between the stack magnetic field and the coil current magnetic field. This coupling coefficient is strongly affected by the relative position between the levitating magnet and coils, significantly affecting the system's output (Carneiro et al., 2022). Figure 8.32(a) presents the electromechanical coupling for a single-coil, whereas Figure 8.32(b) shows the electromagnetic force and damping for the system. Having the magnet's two vertices in the interior region of the winding coils produces a maximum absolute value. When the magnet is entirely inside the winding coil, the magnetic flux changes in each loop cancel out, thereby providing a zero value.

8.3.1 Parameter study of the SDOF energy harvester

To maximise the power of the energy harvester, all parameters which affect the power output must be studied. The middle floating magnet moves through the stationary winding coil in the proposed energy harvester system. Therefore, it is essential to investigate the kinematic and electromagnetic parameters of the floating magnet utilising ANSYS MAXWELL (numerical simulation) and experimental measurement. All parameters have been analysed in this section to achieve the optimised model of the energy harvester. The moving magnet's magnetic field creates the electrical currents within the winding coils. The induced eddy currents generate the damping force that rises from the interaction of the two magnetic fields. The magnetic damping has a viscus shape because the damping force is proportional to the velocity of the moving magnet. Therefore, the velocity of the floating magnet affects the system's power generation. The design of the translator and stator affect the efficiency of the energy harvester. For the proposed generator test rig setup, only the ring types of permanent magnets have been used as a translator, and the winding copper coil has been used as an air-core stator.

Therefore, this chapter has not analysed the translator and stator designs. The previous section showed that the magnetic flux density, resistance, and the number of turns of the winding coil affect the system's dynamics. The effect of the magnetic flux density, turn number, and the winding coil's resistance on power generation has been analysed. Moreover, the other parameters, such as coil diameter, air gaps, magnet size and shape etc., have been studied.

8.3.1.1 Magnet size, shape, and magnetic field

The changing size, shape and grade of the permanent magnet affect the output induced voltage of the generator. Increasing the height of the PM means increasing the magnetic flux density area. Increasing the magnetic flux density area increases the induced voltage of the generator. The simulation has been carried out by changing the magnet, which shows that the magnetic flux density can be increased by increasing the magnet height, as shown in Figure 8.33. The simulation was run by taking 100 turns of winding coil and 0.5 m/s velocities of the floating magnet. The coil position was 10 mm up of the floating magnet's upper surface, and the simulation was run for 0.15s.

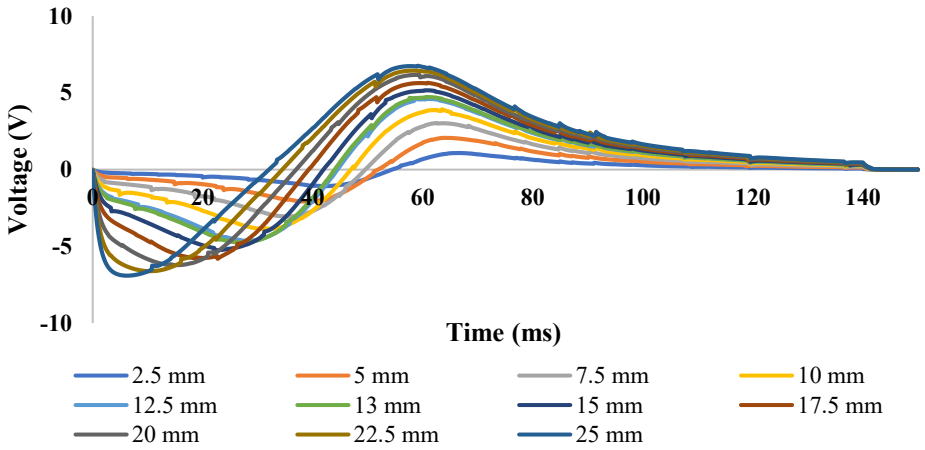

Figure 8.33: Induced voltage for different magnet height

It can be said from Figure 8.33 that the induced voltage rises with the increasing height of the magnet. But the rising height of the floating magnet can increase the weight of the floating magnet, reducing the velocity of the floating magnet, resulting in reduced induced voltage. The higher-grade magnet has higher remanence flux density and maximum energy production (BHmax). The magnetic properties of the different grades of PM have been presented in Table 8.4. All PM grades have considered the highest remanence, coercivity, and maximum energy product BHmax.

Table 8.4: Different grade magnets with their magnetic properties

Grade	Remanence (Br) (T)	Coercivity (Hc) (A/m)	Max. Energy Product BHmax (j/m3)
N33	1.22	836000	263000
N35	1.25	859000	279000
N38	1.3	859000	303000
N40	1.32	836000	318000
N42	1.35	836000	334000
N45	1.38	836000	358000
N48	1.43	836000	382000
N50	1.46	836000	398000
N52	1.43	876000	414000
N54	1.47	836000	430000

It can be seen from Table 8.4 that the remanence and maximum energy product BH_{max} increased with increasing the grade of the PM magnet. A simulation has been run for the proposed oscillator system with the increasing grade number of all three PMs. The simulation was carried out by taking ten

different grades of PM. At first, the magnetic flux density in the radial direction was tested by changing the PM's grade number. It has been considered that all magnets are axially magnetised ring magnets, and they have the same size and shape. The magnetic flux density in the radial direction for different grade of PM have been presented in Figure 8.34.

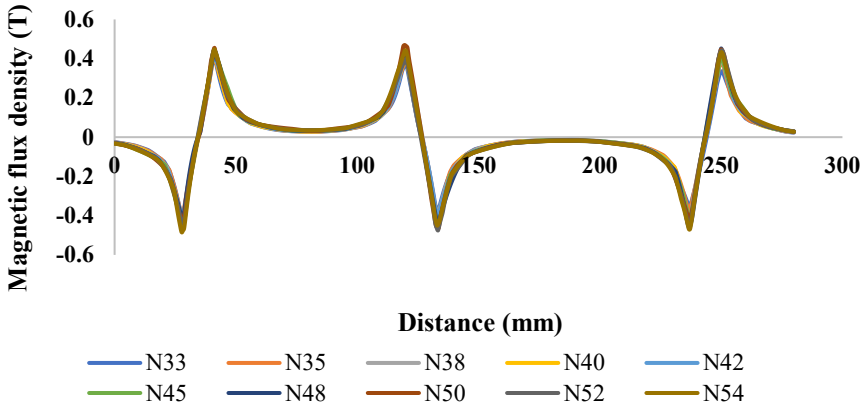

Figure 8.34: Magnetic flux density in the radial direction for different grades of PM

From Figure 8.34, it can be said that higher grade PM creates higher magnetic flux density, which means the PM's magnetic flux density can be increased by increasing the grade number. The N54 shows the maximum magnetic flux density in the radial direction compared to other grades; as the grade number of the PM increases, the magnetic flux density in the radial direction increases. Therefore, the induced voltage of the oscillator system will increase.

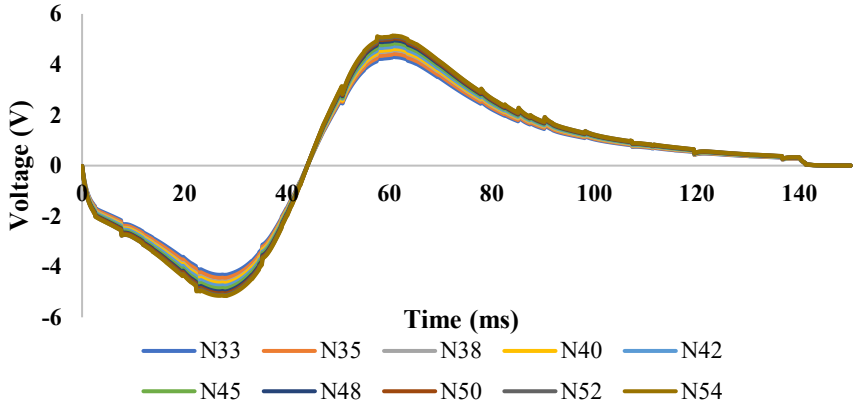

Figure 8.35: Induced voltage for different PM grade

Figure 8.35 presents the induced voltage of the system for different grades of PM. The simulation for this analysis has been run by considering 100 turns of winding coil and 0.5 m/s velocities of the

floating magnet. The coil position was in the same place, 10mm up from the upper surface of the floating magnet, and the simulation was run for 0.150s to get the analysis result. It is clear from Figure 8.35 that the higher grade magnet can increase the output induced voltage of the system. The higher-grade magnet (N54) from ten grades shows the maximum induced voltage. The higher-grade magnet is very expensive; therefore, selecting a higher-grade magnet can increase the system's total cost.

8.3.1.2 Coil diameter, coil Turn number and position of the coil

The selection of proper coil diameter is essential for designing the linear generator. The thinner the coil diameter, the more the coil resistance. With the increase of the coil diameter, the coil's coil resistance decreases. The larger coil diameter would be better, but it needs more space for the maximum turn number of the coil. On the other hand, more coil turns can be created by using the thinner coil in the same space. Smaller coil winding height is better to use the maximum magnetic flux density, decreasing with increasing air gap distance. Equation 3.56 (Chapter 3) has been used to find the thickness of the winding coils. Moreover, equation 3.60 (Chapter 3) has been used to find the total length of the winding coil. The thickness and total resistance of the winding coil have been changed for the different coil diameters. The coil parameters for different coil diameters (different AWG) have been presented in Table 8.5.

Table 8.5: Coil parameters for the different coil diameter

Coil diameter	AWG	Resistance per meter	Number of turns (100)		The thickness of the coil winding when the height of 10 mm
			Total length	Total resistance	
0.41	26	0.133	23.55	3.13215	1.681
0.36	27	0.180	23.55	4.239	1.296
0.31	28	0.225	23.55	5.29875	0.961
0.29	29	0.270	23.55	6.3585	0.841
0.25	30	0.352	23.55	8.2896	0.625
0.227	31	0.427	23.55	10.05	0.51529
0.20	32	0.550	23.55	12.9525	0.4

It can be seen from Table 8.5 that with increasing the coil diameter for the same number of coil turn, the total resistance of the winding coil decreases but the thickness of the coil winding increases. To create 100 turns, the lower coil diameter needs less space than the higher coil diameter. To find the

effect of coil diameter, a simulation has been performed by taking 100 turns of coil number. The height of the winding coil was 100, and the other parameters are shown in Table 8.5. The analysis results have shown in Figure 8.36.

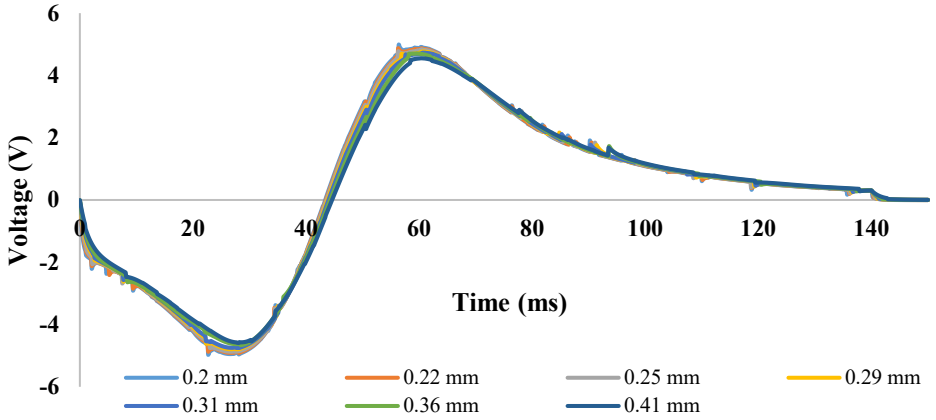

Figure 8.36: Voltage for different coil diameters

Table 8.6: Winding coil properties for different coil turn numbers

Number of turns	The total length of the copper wire	Total resistance (0.225 ohms per meter)	Inductance (H)	The thickness of the coil winding when the height of 10 mm
100	23.55	5.29875	0.005546	0.961
200	47.1	10.5975	0.022184	1.922
300	70.65	15.89625	0.049914	2.883
400	94.2	21.195	0.088736	3.844
500	117.75	26.49375	0.138650	4.805
600	141.3	31.7925	0.199656	5.766
700	164.85	37.09125	0.271755	6.727
800	188.4	42.39	0.354945	7.688
900	211.95	47.68875	0.449228	8.649
1000	235.5	52.9875	0.554602	9.61

Figure 8.36 shows that the higher AWG coil number creates higher induced voltage same coil turn number. Although the higher AWG coil number consists of higher coil resistance than the lower AWG coil number, to make the same number of coil turn numbers, the higher AWG coil needs less space compared to the lower AWG number. For example, to create 100 turns using 26 AWG coil, it needs 1.681 mm thickness and diameter 10 mm, but in the same space, it is not possible to wind 200 turns by using AWG 28, and 400 turn number could be made by using AWG 32 coil. It has known

that the induced voltage increases with increasing the coil turn number. To analyse the effect of the changing coil turn number, an AWG 28 (0.31 mm coil diameter) was chosen, and the inside diameter of the winding coil was 75 mm. The other coil winding properties for different coil turn numbers have been shown in Table 8.6.

With increasing the coil turn number, the coil's total length and total resistance increased along with using space. Figure 8.37 presents the voltage output for different coil turns number. The velocity of the floating magnet was 0.5 m/s, and the air gap was 3mm. The coil was attached 10 mm up from the upper surface of the floating magnet when it was in the equilibrium position. To know the effects of coil, turn number, the study started with a 100-turn number and finished with a 1000 turn number, and the simulation ran for 150 ms.

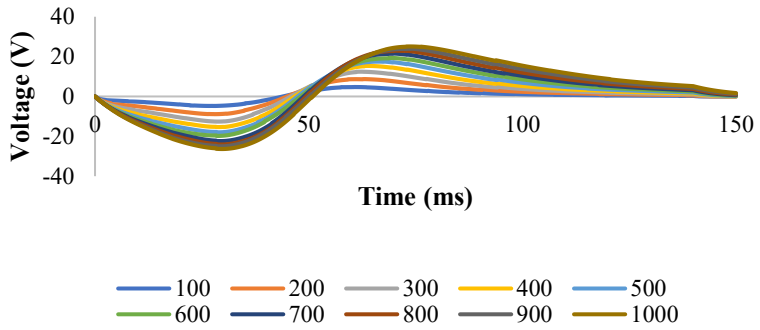

Figure 8.37: Induced voltage for different coil turn numbers

It can be seen from Figure 8.37 that with increasing the coil turn number, the induced voltage rises. Maximum induced voltage has been created for 1000 numbers, which is more than five times higher than the 100-turn number.

8.3.1.3 The velocity of the floating magnet

The induced voltage increases with increasing the velocity of the floating magnet. To validate these effects, a study has been performed. It is known that the linear electromagnetic generator directly driven by sea waves would oscillate at a peak velocity of 0.5 to 2 m/s (Mueller, 2002). Therefore, the study has been started from 0.1 m/s to 2 m/s, and at that time, the coil turn number was 100, the coil diameter was 0.31 mm, and the air gap between the floating magnet and coil was 3 mm. The width and height of the coil were 5 mm and 10 mm, respectively. The effects of the velocity are shown in

Figure 8.38. From Figure 8.38, it has been seen that the output induced voltage rises with increasing the velocity of the floating magnet.

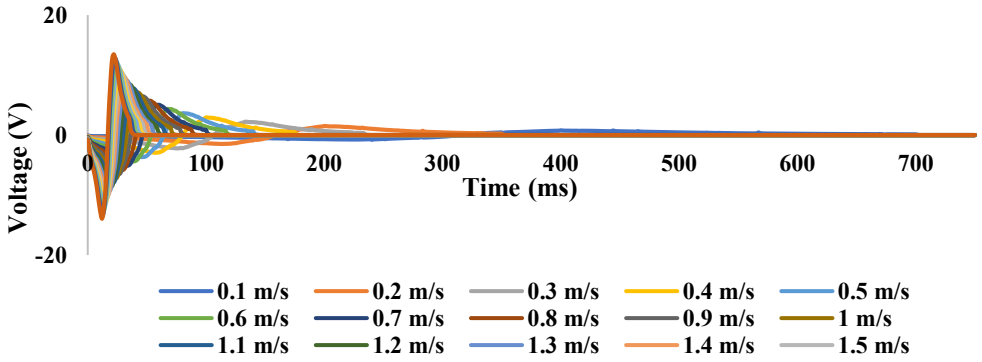

Figure 8.38: Induced voltage for the different velocities of the floating magnet

8.3.1.4 Air gap between translator and stator

The literature shows that most electromagnet generators were developed considering coils that take circa 10 to 50% of the harvester length (Carneiro et al., 2020). As projected, smaller distances between the inner coil diameter and the middle or levitating magnet diameter result in higher induced voltages in the coil terminals; therefore, the space must be determined to evade problems with the linear electromagnetic generator's mechanical integrity or to decrease the manufacturing process' difficulty. A study has been performed to find the magnet flux density in different air gaps from the floating magnet. The diameter of the coil and the number of turns of the coil were 0.30mm and 100, respectively. The velocity of the floating magnet was 0.5 m/s. The magnetic flux density in different air gaps is shown in Figure 8.39.

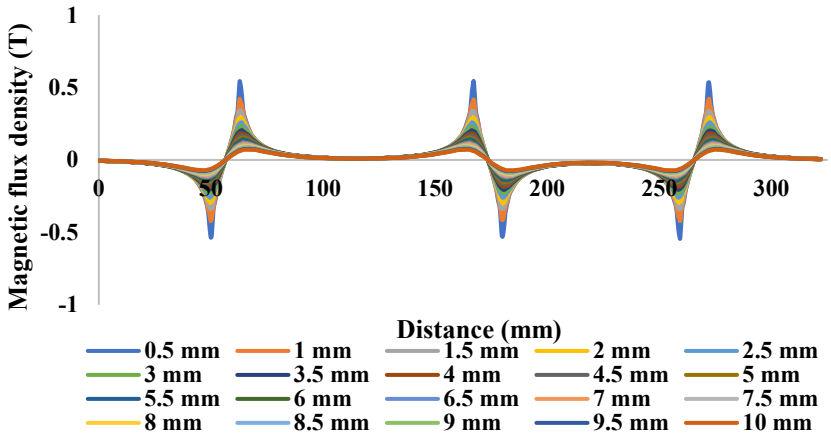

Figure 8.39: Magnetic flux density for different air gaps

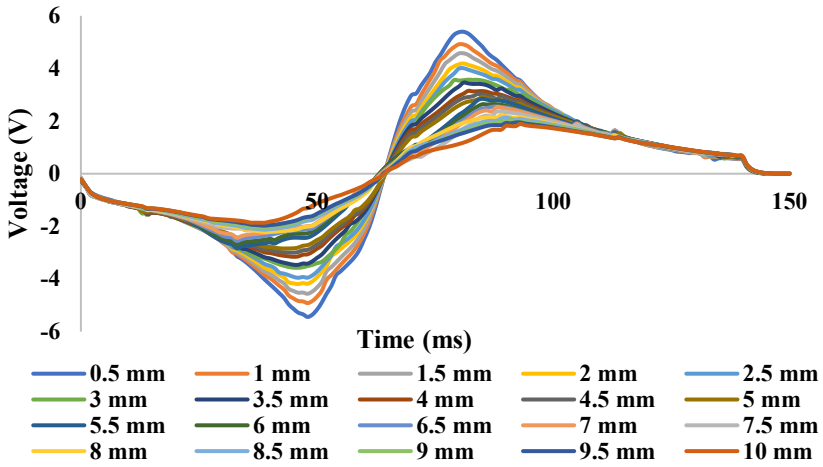

Figure 8.40: Induced voltage for different air gap distance

From Figure 8.39, the magnetic flux density decreases with the air gap distance. The maximum magnetic flux density has been obtained nearer the magnets. Therefore, the maximum induced voltage found in the winding coil is attached to the minimum air gap distance. A simulation has been performed to find the induced voltage for a different air gap. During the study, the diameter of the coil and the number of turns of the coil were 0.31mm and 100, respectively. The velocity of the floating magnet was 0.5 m/s, and the wide and height of the coil were 5mm and 10mm, respectively. The coil was attached 10mm up outside the diameter of the floating magnet. The induced voltage for different air gaps is shown in Figure 8.40. From Figure 8.40, it can be said that the maximum induced voltage can be generated for the system if the winding coil is attached in the minimum air gap distance. But in reality, it isn't easy to attach the coil nearer to the floating magnet's outer diameter surface.

8.3.1.5 Applied external force on the floating magnet

The power output of the energy harvester can be changed by changing the applied harmonic force. To analyse the effect of the applied harmonic force on generator power output, the amplitude of the force was varied from 10N to 100N with constant frequency (0.1Hz). The simulation for this analysis has been run by considering 100 turns of winding coil. Figure 8.41 displays the displacements and velocities of the floating magnet for the different amplitudes of the harmonic force. Figure 8.42 presents the induced voltages for different amplitudes of the harmonic forces.

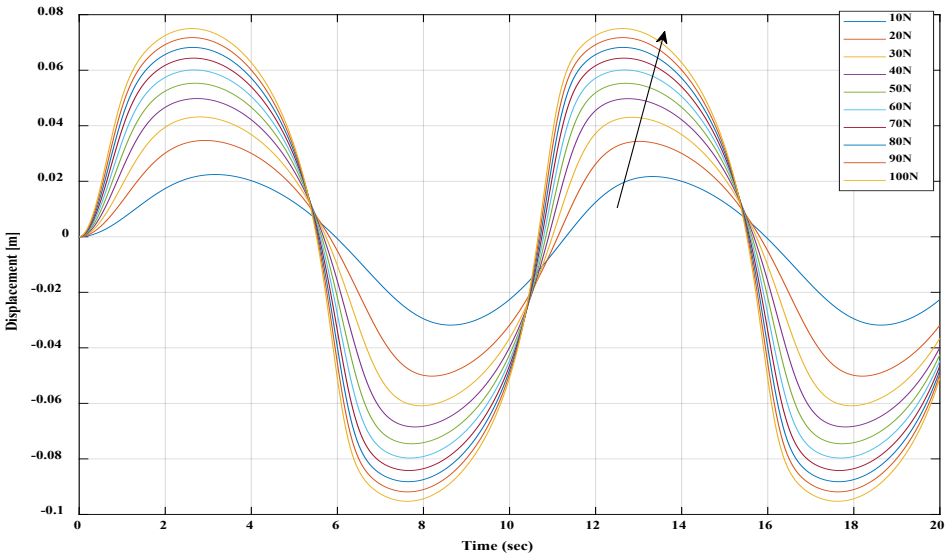

(a)

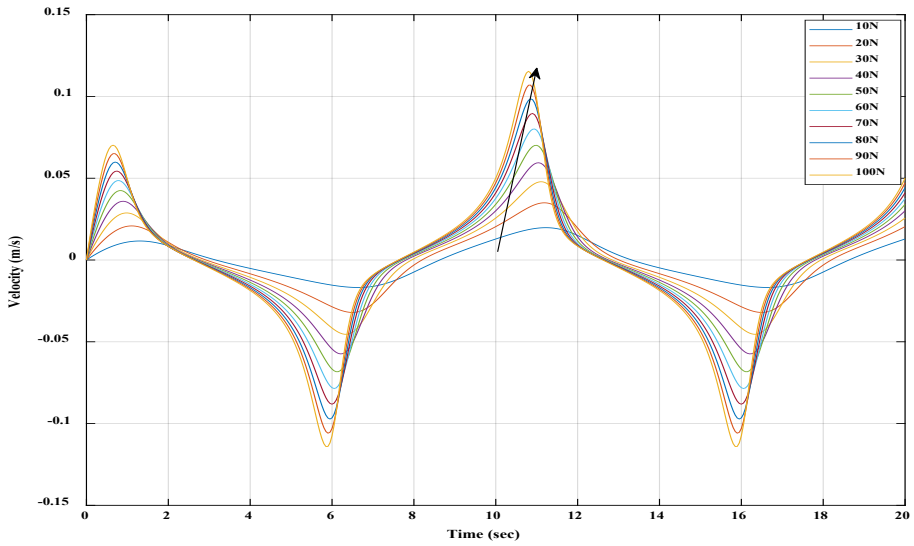

(b)

Figure 8.41: (a) Displacement and (b) Velocity of the floating magnet under different amplitudes of the harmonic force (0.1 Hz frequency)

The displacement and velocity of the floating magnet increased with increasing the amplitude of the harmonic force (0.1Hz), as seen in Figure 8.41. Therefore, the induced voltage of the generator increased with increasing the amplitude of the harmonic forces, as presented in Figure 8.42.

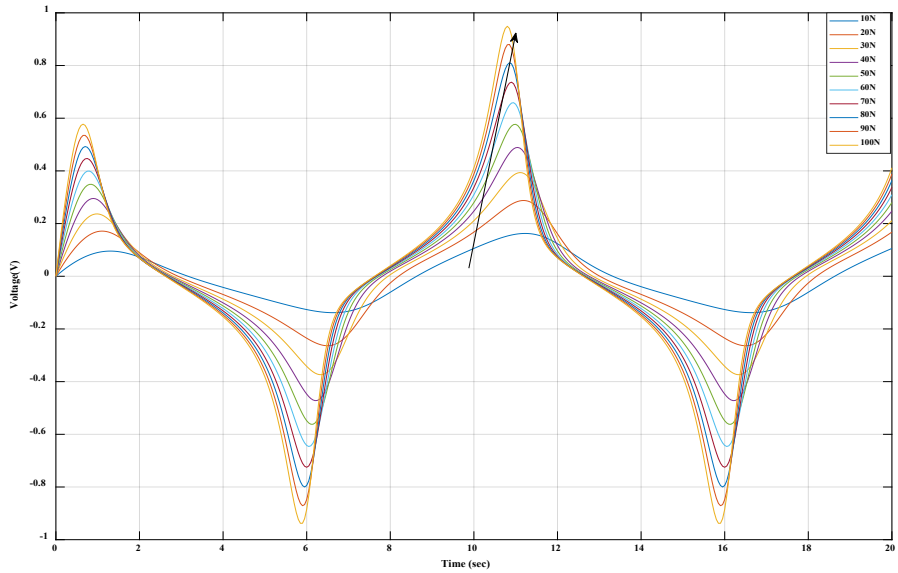

Figure 8.42: Induced voltage of the generator for the different amplitude of the applied harmonic force (0.1 Hz)

8.3.2 Analyses of the SDOF generator model for different lengths of the oscillator

In chapter 4, the oscillator system was analysed by changing the oscillator length. The linear and nonlinear stiffnesses, damping constants and natural frequencies of the oscillator system changed with changing the length of the oscillator. The damping constant decreased with increasing the oscillator length. The coefficients and natural frequencies decreased with increasing the oscillator length. In this chapter, the generator system has been analysed by changing the total length of the oscillator. The displacements and velocities of the floating magnet have been determined. The induced voltages have been measured for different lengths of the oscillator. The amplitude and frequency of the applied harmonic force were considered 25N and 0.1Hz, respectively, during that analysis. A winding coil (100 turns) which consists of 5.48-ohm internal resistance and 0.005546H inductance, was considered to determine the induced voltage. The length of the oscillator varies from 212 mm to 272 mm. Figure 8.43 displays the displacement and velocity of the generator system for different lengths of the oscillator.

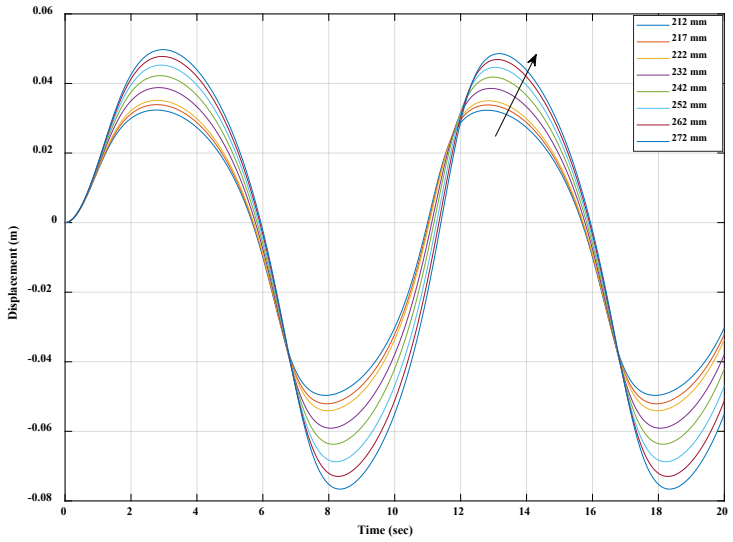

(a)

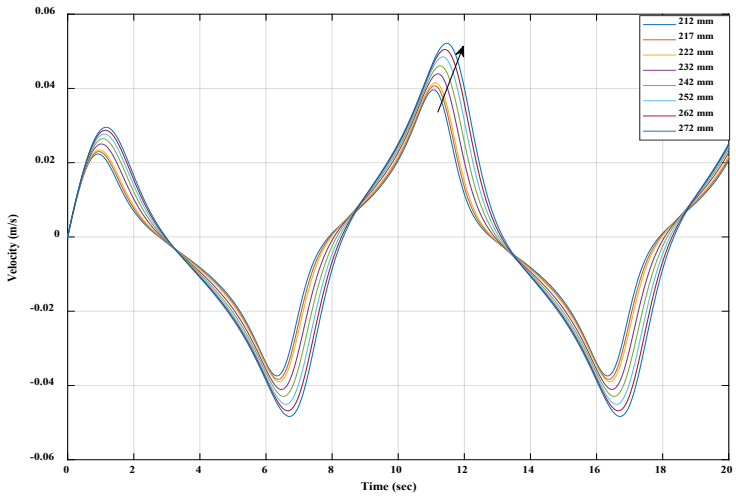

(b)

Figure 8.43: (a) Displacement and (b) Velocity of the SDOF generator system for different lengths of the oscillator

It can be seen from Figure 8.43 that the displacement and velocity of the floating magnet increased with increasing the length of the oscillator. With increasing the length of the generator oscillator, the generated induce voltage increased, as presented in Figure 8.44. Therefore, it can be said that by increasing the length of the oscillator, the efficiency of the generator can be improved.

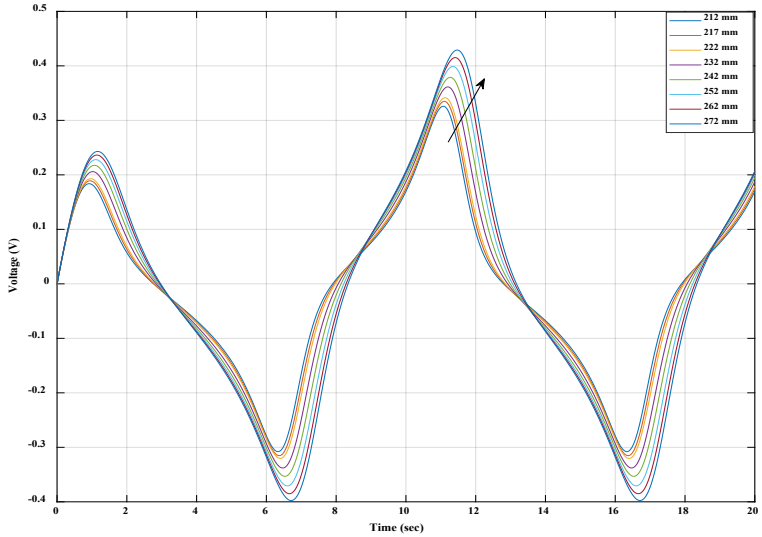

Figure 8.44: Generated voltage of the SDOF generator system for different lengths of the oscillator

8.4 Experimental Analysis

The experimental procedures were identical for all degree-of-freedom systems. Sensors were powered on once the experimental setup was finalised with the assembled test rig. The first step of the experiment was to establish a safe operating environment. For different lengths of the oscillator, the magnetic restoring forces, damping constants and natural frequencies were determined, which were discussed in Chapter 4. Before using the servo motor, the experimental works were done manually. The floating magnets were pulled up and released to create excitation on the floating magnet. Sensors measured the displacement of the floating magnet, and later on, it converted to velocity. The induced voltage signal was measured using a data acquisition system. Both velocity and torque controls were used to run the servo motor. Autotune was done every time before running the servo motor. Once all parameters were set for the desired velocity or torque, the time series response of the sensor signal and voltage were recorded in the data acquisition device for a 10 or 20 second period. The recorded responses were then saved as a .mat file. Many experiment iterations were done to confirm repeatability for all degrees-of-freedom models individually. At first, the test rig was tested manually using hands by pulling up and releasing floating magnets by moving the servo motor's pulley and letting it oscillate for a while. It was discussed in Chapter 4 that after pulling up the floating magnet if released, the floating magnet starts oscillating, which can be used for harvesting energy. Two IR sensors were used to measure the displacement of the floating magnet, as discussed earlier in

Chapter 7, where one sensor was considered sensor number 1 and the other one was sensor number 2. The green and blue lines in Figure 8.45 represent the sensor 1 and 2 values, respectively. The floating magnet was pulled up around 55 mm and released, and it oscillated until it stopped in equilibrium, which is in 0 positions in Figure 8.45.

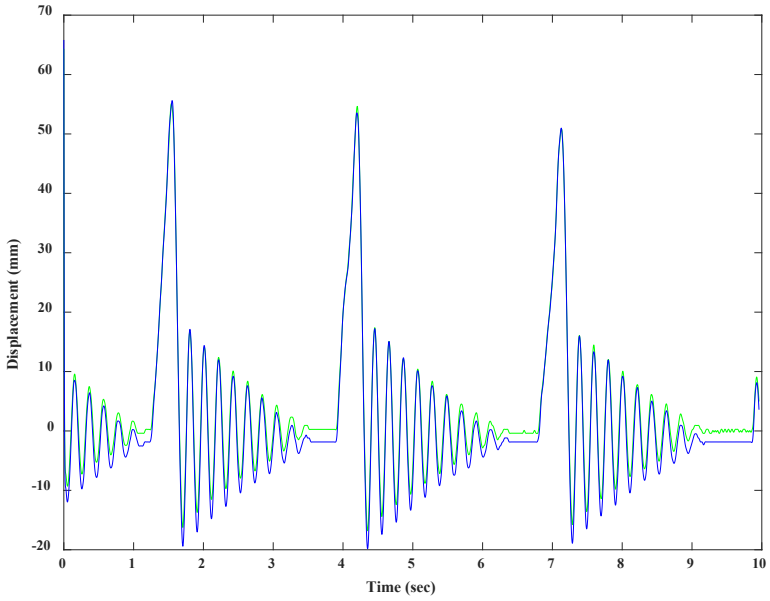

(a)

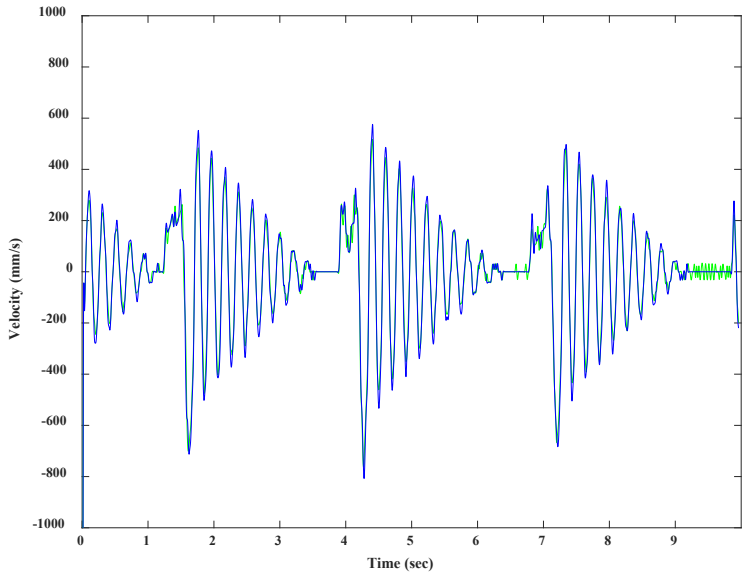

(b)

Figure 8.45: (a) Displacement and (b) velocity of the floating magnet during the manual test

It can be seen that from Figure 8.45(a), the oscillation stopped after around 2.5 seconds, and the time is the same for each oscillation testing time. The measured oscillation per second was about 5 for each bouncing test. The measured natural frequency was 30.67 rad/sec (4.88 Hz). Using the Log-Dec formula, the damping ratio was measured, and the measured damping ratio was 0.0361. The maximum velocity was found to be around 650 mm/s, and it declined with the decrease of the displacement, as presented in Figure 8.45(b). Figure 8.46 shows that the generated induced voltage of the winding coil dropped with the decreasing velocity.

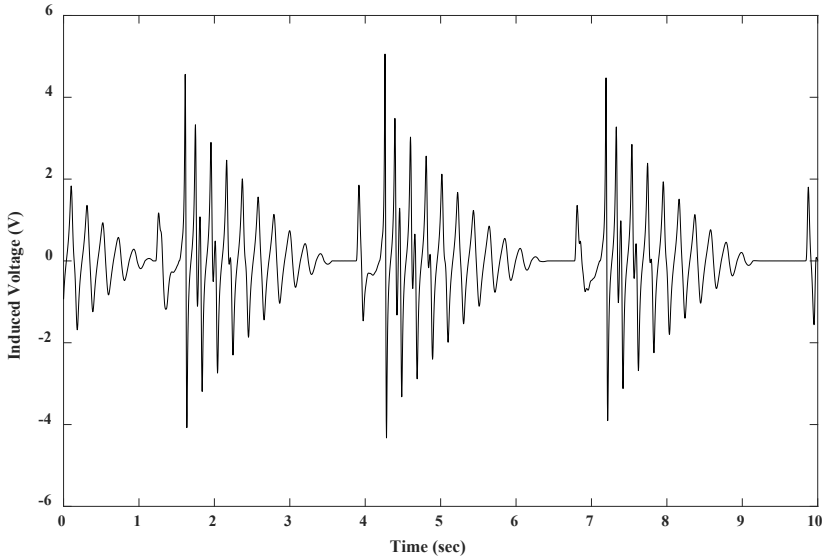

Figure 8.46: Induced voltage during the bouncing

By reducing the velocity of the floating magnet, the generated induced voltage is also reduced, as shown in Figure 8.46. The measured maximum and minimum induced voltages were 5.1 V and 1 V, respectively.

8.4.1 Validation of the experimental results with analytical results

The servo motor has been connected with the test rig using a fishing line to create a sine/cosine wave (harmonic force) on the floating magnet. The servo motor was controlled by torque control mode to apply harmonic force on the floating magnet. The harmonic force applied on the floating magnet using a servo motor is the same harmonic force used in the analytical model to validate the experimental model with the analytical model. For the experimental analysis, different harmonic forces were applied by varying the amplitude and frequency of the harmonic force. At first, a

harmonic force was applied to the floating magnet during experimental work. The projected harmonic force amplitude was 85N, and the frequency was 1.75Hz. Figure 8.47 displays the displacement and velocity of the floating magnet for experimental and analytical analysis.

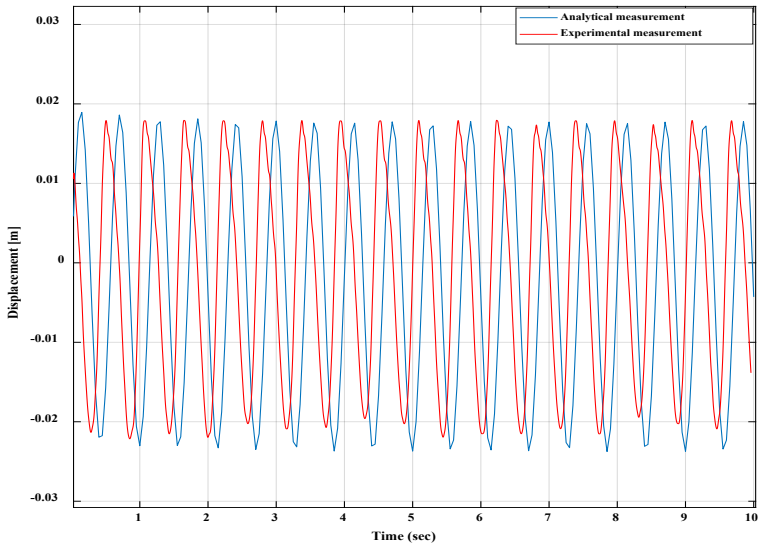

(a)

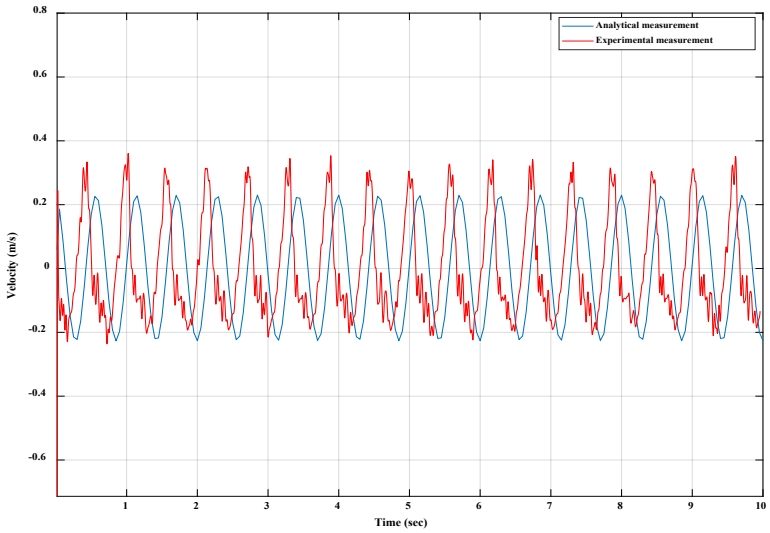

(b)

Figure 8.47: (a) Displacement and (b) Velocity of the floating magnet (blue line represents the analytical analysis and the red line represents the experimental analysis)

From Figure 8.47, it can be said that the measurement of the displacement and velocity of the floating magnet is very similar for analytical and experimental analyses. During the analytical analysis, the floating magnet moved toward the bottom magnet by about 18 mm and the top by around 23 mm. During the experimental analysis, the floating magnet moved toward the top magnet by 18 mm and toward the bottom magnet by around 21 mm, as presented in Figure 8.47. The achieved average velocity of the floating magnet was around 0.21 m/s during the analytical analysis and 0.26 m/s during the experimental analysis, as exhibited in Figure 8.47(b). The generated induced voltage of the generator for the experimental and analytical analysis has been presented in Figure 8.48.

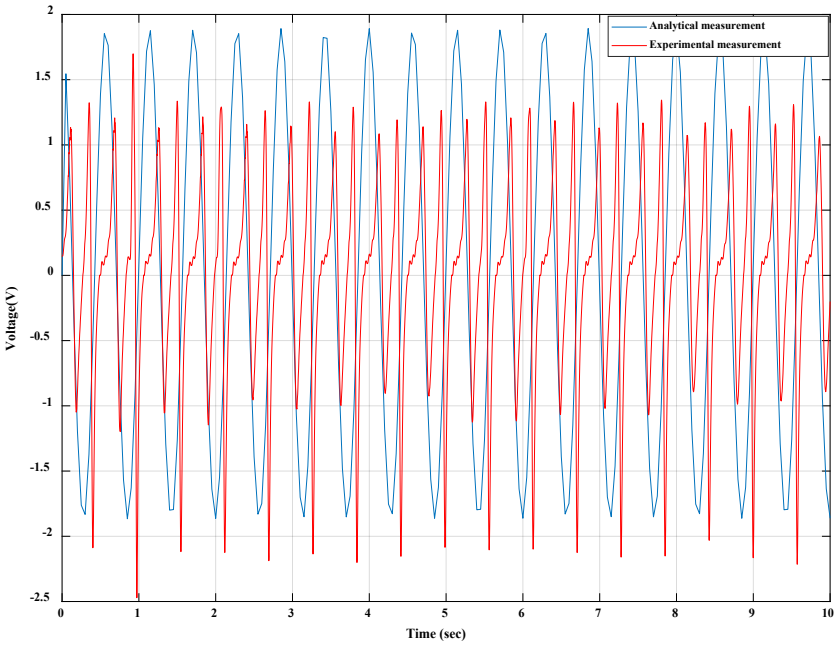

Figure 8.48: Induced voltage of the generator (blue line represents the analytical analysis and the red line represents the experimental analysis)

In Figure 8.48, the induced voltage of the generator for analytical analysis has been compared with the experimental study. The measured average maximum induced voltage was 1.8V for analytical analysis and 1.65V for experimental analysis. Figure 8.47 and Figure 8.48 show that the analytical model is well validated with the experimental model. Lastly, the analytical model has been validated with the experimental model by increasing the amplitude and frequency of the harmonic force. The estimated harmonic force amplitude was 150N, and the frequency was 3.3Hz. The displacement and velocity of the floating magnet for experimental and analytical analysis have been presented in Figure

8.49. Figure 8.50 displays the generated induced voltage of the generator for experimental and analytical analysis.

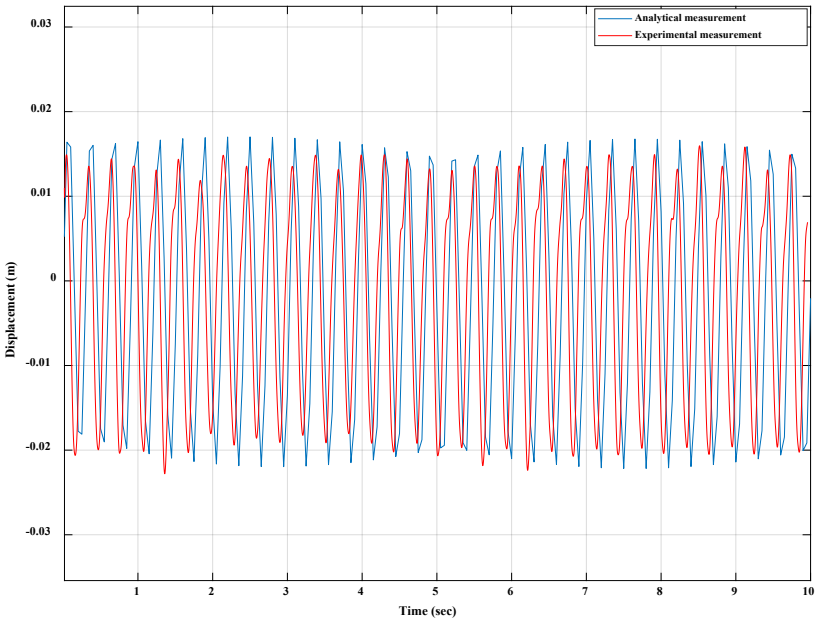

(a)

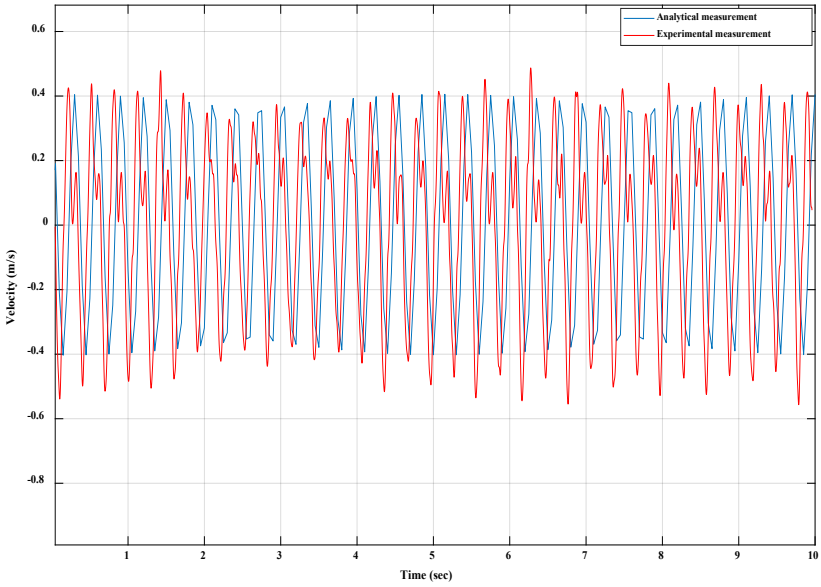

(b)

Figure 8.49: (a) Displacement and (b) Velocity of the floating magnet (blue line represents the analytical analysis and the red line represents the experimental analysis)

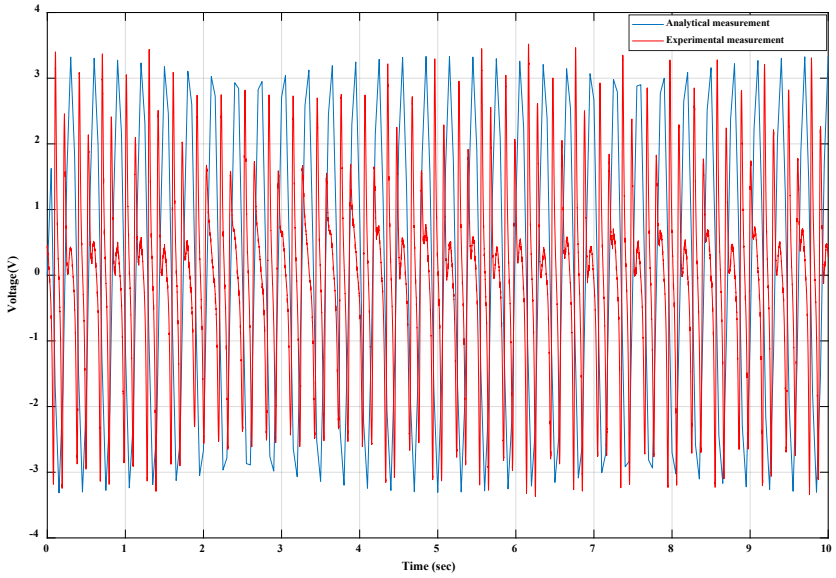

Figure 8.50: Induced voltage of the generator (blue line represents the analytical analysis and the red line represents the experimental analysis)

It can be seen from Figure 8.49 that the measurement of the displacement and velocity of the floating magnet are very similar for analytical and experimental analyses. During the analytical analysis, the floating magnet moved toward the bottom magnet by about 18 mm and the top magnet by around 22 mm. During the experimental analysis, the floating magnet moved toward the top magnet by 15 mm and toward the bottom magnet by around 21 mm. The maximum average velocity of the floating magnet was around 0.4 m/s during the analytical analysis and 0.4 m/s during the experimental analysis, as displayed in Figure 8.49(b). The measured maximum average induced voltage was 3.2V for analytical analysis and 3.1V for experimental analysis, as presented in Figure 8.50. From the above discussion, it can be said that the analytical model is well validated with the experimental model.

8.4.2 Experimental study of the SDOF generator system by changing parameters

In section 8.3, it has been seen that the generator's efficiency can be changed by changing the generator system's parameters. The generator system has been analysed experimentally by changing some parameters discussed in this section. At first, the generator system was studied by changing the velocity (by using velocity control mode) of the floating magnet. Figure 8.51 presents the generator's induced voltage for the different velocities of the floating magnet.

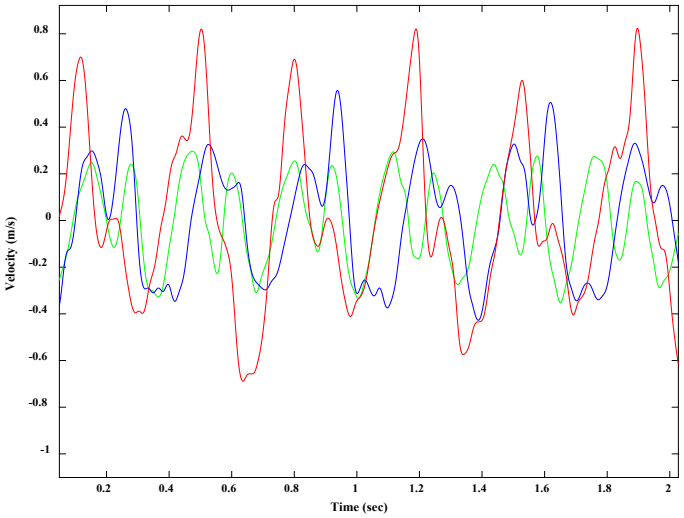

(a)

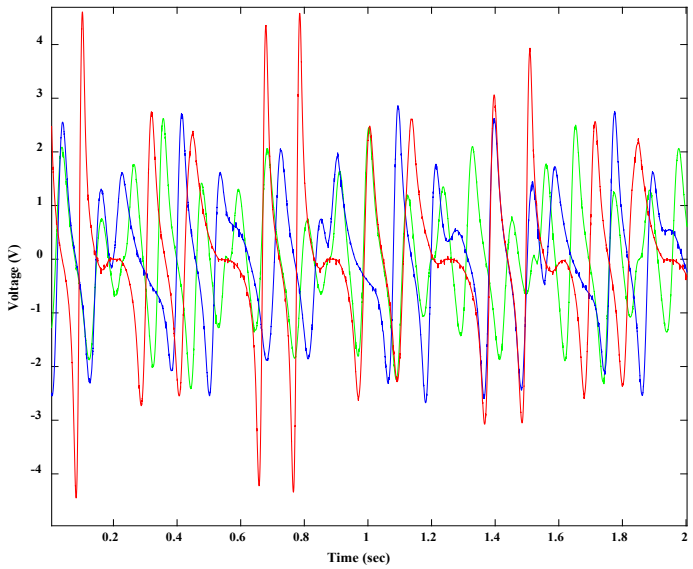

(b)

Figure 8.51: (a) Different velocities of the floating magnet and (b) Induced voltage for different velocities as presented in Figure (a)

The red colour line in the Figure 8.51(b) is the induced voltage for the red colour velocity line in the Figure 8.51(a). The blue and green colour lines in the Figure 8.51(b) are the induced voltage for the blue and green colour velocity lines in the Figure 8.51(a). From Figure 8.51, it can be seen that the induced voltage increased with increasing the velocity of the floating magnet. The generator system

has been analysed by changing the number of turns of the winding coil. The number of turns varies from 100 to 300. Figure 8.52 displays the induced voltage for the different number of turns of the winding coil.

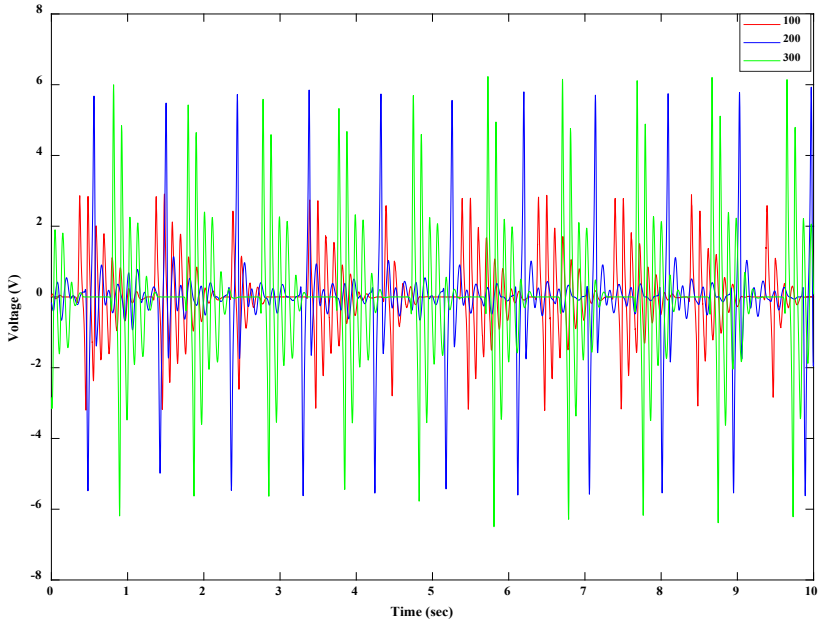

Figure 8.52: Induced voltage of the generator for different numbers of turns of the winding coil

The red and blue lines in Figure 8.52 represent the winding coil's 100 and 200 turns, respectively, whereas the green line represents the 300 turns of the winding coil. It can be seen from Figure 8.52 that the overall induced voltage increased with increasing the turn number of the winding coil. The generated induced voltage of the generator for 200 turns was higher than the 100 turns but smaller than the 300 turns of the winding coil. Moreover, the generator system has been analysed by increasing the winding coil number. Figure 8.53 shows the induced voltage of the generator for two winding coils. Both winding coils (100 turns) were attached in the test rig. They were connected with the data acquisition system separately to measure the generated induced voltage. Coil number 1 was placed outside the diameter of the floating magnet where the floating magnet easily oscillated through it, and the 2nd coil was placed just in the top of the 1st coil, and their separation distance was around 5 mm. Therefore, the generated induced voltage in coil 1 should be higher than the coil 2. In Figure 8.53, the generated induced voltages in coils 1 and 2 are represented by red and green lines, respectively.

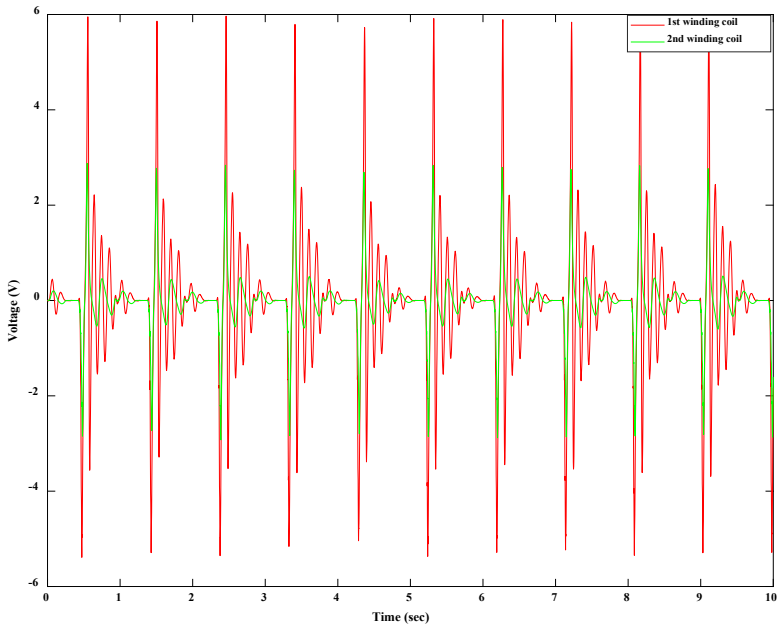

Figure 8.53: Induced voltage of the generator for two winding coils

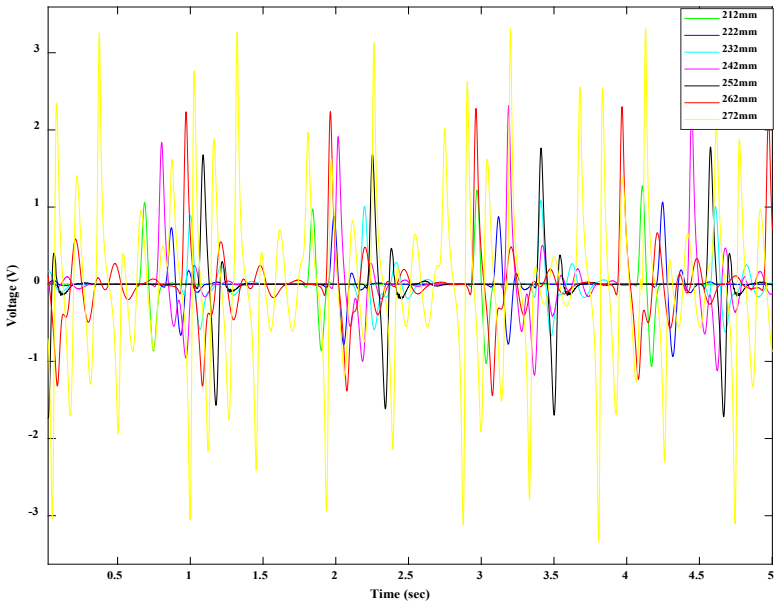

Figure 8.54: Induced voltage of the generator (100 turns winding coil) for different lengths of the oscillator

The generated induced voltage in coil 1 was higher than in coil 2, as seen in Figure 8.53. It can be said that maximum energy can be captured by increasing the winding coil number. Furthermore, the

energy harvester system has been analysed by changing the length of the oscillator. In chapter 4, it has been seen that the damping ratio and damping constant decreased with increasing the length of the oscillator. However, the floating magnet's velocity increased for the same applied harmonic force, increasing the oscillator's length. Therefore, it can be assumed that the induced voltage can be maximised by increasing the oscillator's length. Figure 8.54 presents the induced voltage for different lengths of the oscillator. Different colour lines in Figure 8.54 represent the different lengths of the oscillator. From Figure 8.54, it can be seen that the induced voltage increased with increasing the length of the oscillator. Therefore, from the above discussion, it can be said that the efficiency of the SDOF generator depends on some parameters. By changing those parameters, the efficiency of the generator can be increased.

8.5 Conclusion

This chapter studied an energy generator based on SDOF magnetic spring mechanism with magnetic repulsive force. The benefits of the energy harvester design are that it has few moving mechanical parts and a stronger magnetic field, leading to a high voltage output. The characteristics and dynamics of the proposed energy harvester have been studied using analytical and experimental methods. The eigenvalues and the nonlinear vibration response of the generator system have been analysed using analytical methods. Moreover, the dynamics of the energy harvester have been studied analytically using an external load, RL and RLC circuits. The numerical model of the proposed generator has been analysed to evaluate the magnetic flux density and magnetic field strength for different arrays and configurations. The parametric study has been performed to provide insights into the effects of various parameters such as magnetic flux density, coil turns number, air gap, the velocity of the floating magnet, and applied force on the energy harvester output. The test rig design has been fabricated for experimental analysis, and the experimental works have been performed by changing different parameters. Finally, the experimental model has been validated with the analytical model. These studies will help researchers understand the generator's dynamics, magnetic properties, and dependent and controllable parameters.

Chapter 9

Theoretical and Experimental Study of 2DOF Magnetic Spring-based Electromagnetic Generator

The resonant power and efficiency of the two-degree-of-freedom nonlinear oscillators are expected to be larger than those with a single-degree-of-freedom (SDOF) nonlinear oscillator system. Moreover, using the two-degree-of-freedom nonlinear oscillators is estimated to advance higher operational frequency bandwidth than the SDOF nonlinear oscillator. Two floating magnets are expected to generate increased magnetic flux density in the system than the single floating magnet-based system. Therefore, in Chapter 5, the analytical, numerical and experimental model of the two-degree-of-freedom (2DOF) magnetic spring-based oscillator system has been discussed with validation. However, the energy generation part was not considered during the analysis of the 2DOF system. This chapter deals with energy generation techniques based on 2DOF magnetic spring-based oscillator systems and their behaviour with various design criteria.

9.1 Architecture of the Two-degree-of-freedom (2DOF) Electromagnetic Generator/ Energy Harvester

The basic architecture of the electromagnetic generator or energy harvester contains four-ring permanent magnets (axially magnetised), a circular shaft and winding coils. The 2DOF energy harvester is designed so that every function's performance (such as magnetic restoring forces, induced voltage) should not affect or influence each magnet's magnetic field, particularly when the floating magnets move. It is required to minimise the harmful cogging force generated from magnets and coils movement. Different nonmagnetic materials have been used to avoid magnetic field interference. The polarity of the magnets is arranged so that the levitating magnet experiences a repulsive force because of the fixed magnets. Few multilayer coils are attached around the outer surface of the two floating magnets. The height and diameter of the shaft are 550 mm and 12 mm, respectively. Figure 9.1 presents the test rig setup with winding coils. The magnetic poles are oriented (NS-SN-NS-SN) to repel each other. The height and width of the test rig are 550 mm and 300 mm, respectively. The equilibrium height of the 2DOF oscillator is 303 mm; therefore, the 4th magnet is attached and locked to the vertical shaft 303 mm away from the 1st magnet. Two winding coils have been added to the test rig, and both winding coils have been connected to the data acquisition system to capture the induced voltages.

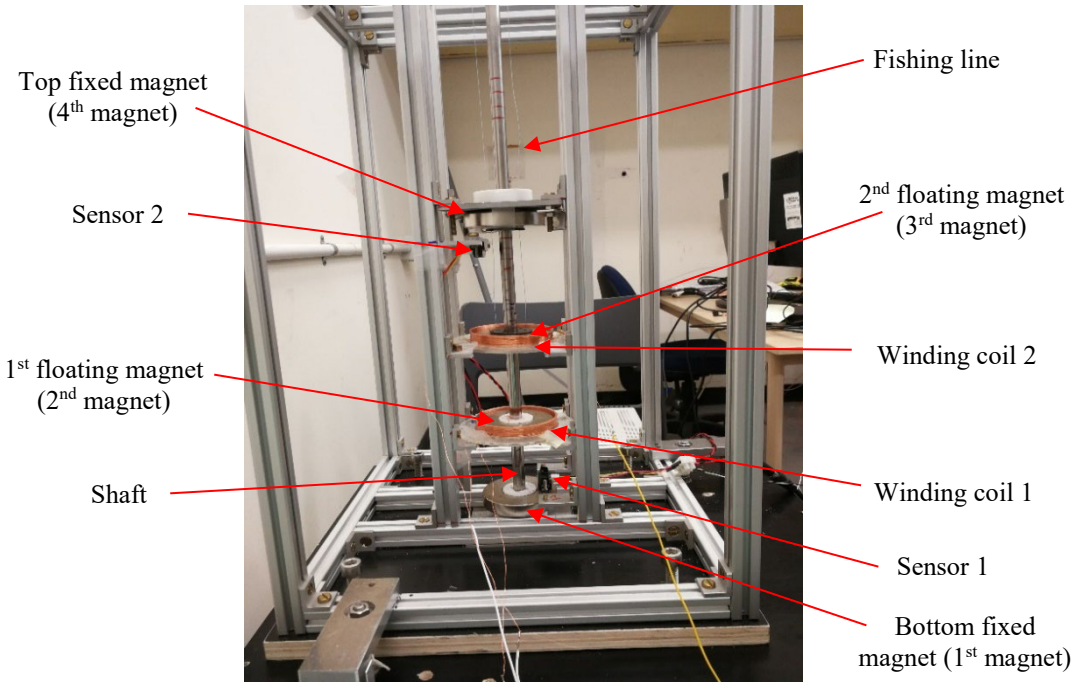

Figure 9.1: Test rig of the proposed 2DOF

In Figure 9.1, sensor 1 is placed on the top of the bottom fixed magnet to measure the displacement of the 1st floating magnet, and sensor 2 is placed underneath on the top fixed magnet to measure the displacement of the 2nd floating magnet. The winding coil 1 is placed outside the 1st floating magnet, whereas the winding coil number 2 is placed outside the 2nd floating magnet.

9.2 Numerical Simulation of the 2DOF Electromagnetic Generator/ Energy Harvester System

This section analyses the Finite Element Analysis (FEA) of the 2DOF magnetic spring-based electromagnetic generator model. The electromagnet generator model is analysed as a 2D axisymmetric model, as shown in Figure 9.2. The dimensions of the generator are in millimetres. The magnetic and physical components of the permanent ring magnets are presented in Chapter 3 in Table 3.1. Two winding coils (100 turns each) have been placed on the top surfaces of both floating magnets. The properties of the winding coil parameters are shown in Table 8.1 in chapter 8.

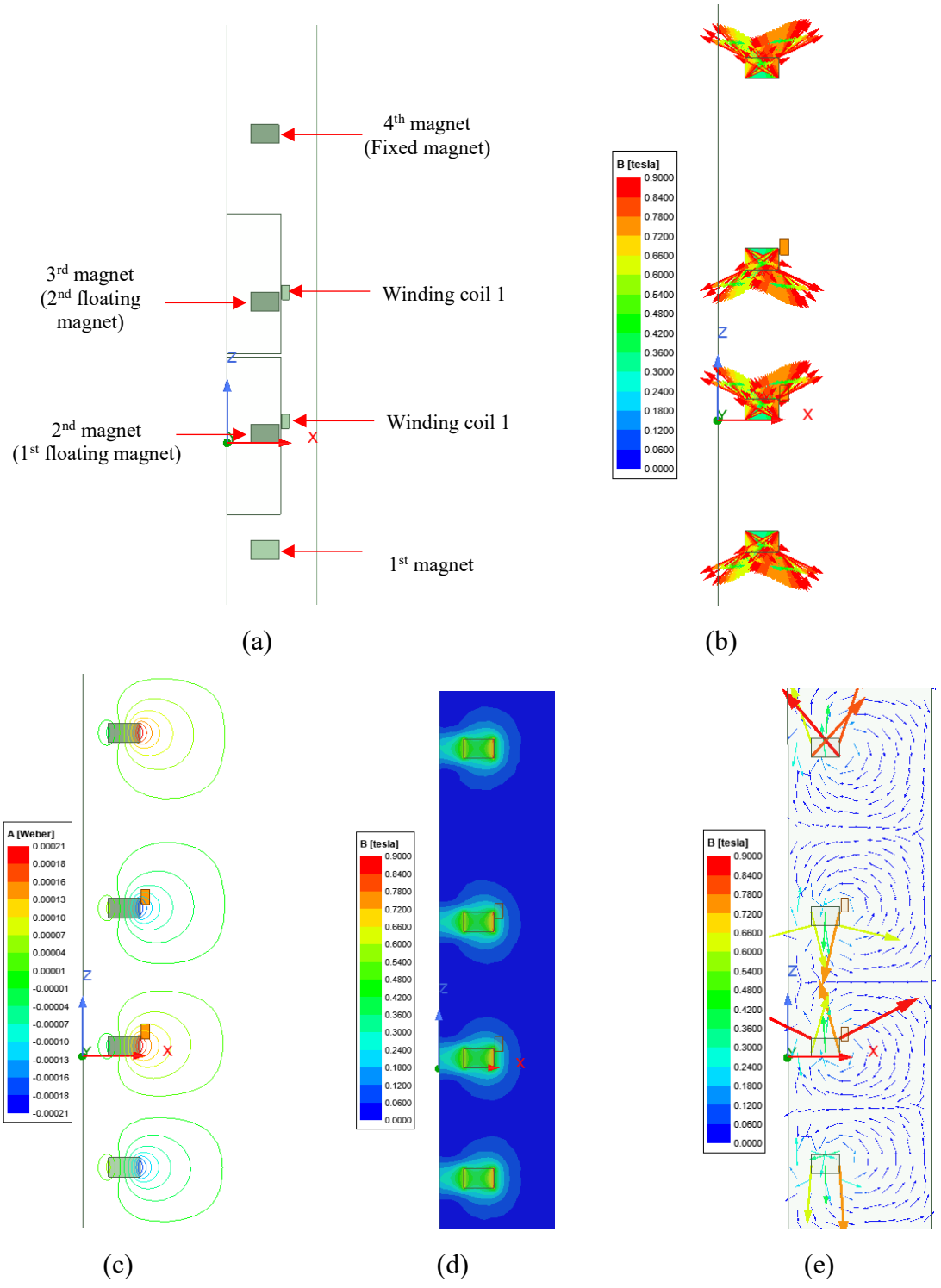

Figure 9.2: (a) 2DOF electromagnetic generator (b) Magnetisation direction and (c) Flux line, (d) Magnetic flux (Mag_B) and (e) B_Vector

The simulation has run using constant velocity for both floating magnets during the transient solution. The magnetisation direction of all magnets, flux line and magnetic flux density have been measured

from simulation analysis. Figure 9.2(b) shows the magnetisation direction of all four magnets, and Figure 9.2(c) presents the flux line of all four magnets. The arrows represent the magnetisation directions of all permanent magnets in Figure 9.2(b). Figure 9.2(a) displays the 2D axisymmetric transient model of the 3DOF energy harvester. The maximum flux lines can be seen in the outside surfaces of magnets and inside the coil area, as presented in Figure 9.2(c). Figure 9.2(d) and Figure 9.2(e) illustrate the magnetic flux (Mag_B) and magnetic flux (B_Vector) of the 2DOF electromagnetic generator. In Figure 9.2(d), the colour represents the magnitude of the magnetic flux density of the generator system. The higher flux density can be seen around the permanent magnet area, characterised by colour variations. Figure 9.2(e) shows that the magnetic flux lines emerged from the North Pole and travelled toward the South Pole, and they travelled through the inside winding coil. The induced voltage creates inside the copper coil when the magnetic flux cuts the copper coil. The magnetic flux densities have been analysed by changing the positions of both floating magnets. Both floating magnets have been moved with constant velocity. The magnetic flux densities of the generator changed with changing time along with the positions of both floating magnets. Figure 9.3 presents the change of magnetic flux densities for different positions of both floating magnets.

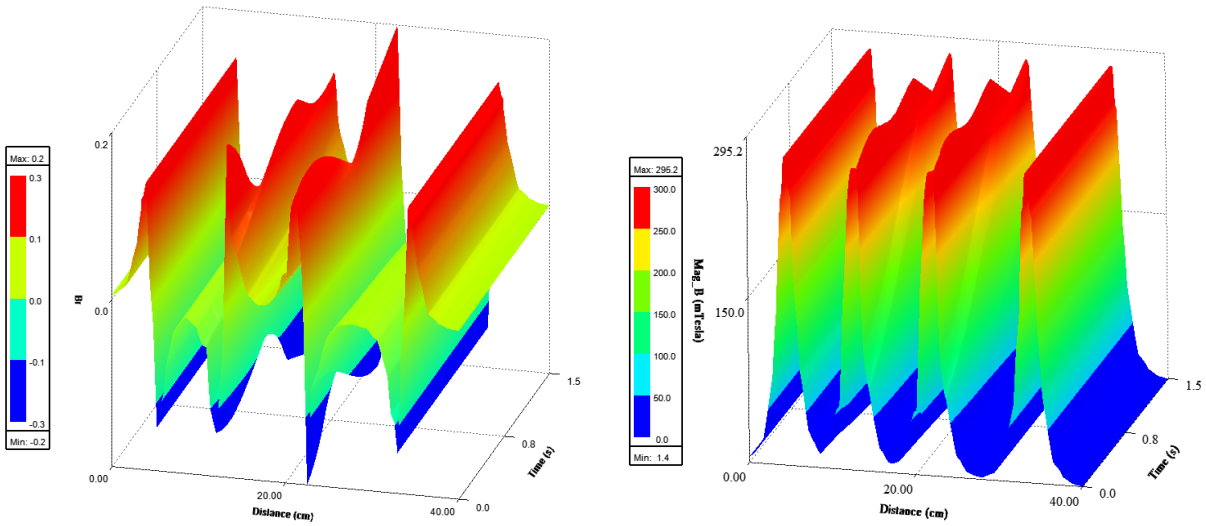

(a) (b)

Figure 9.3: Magnetic flux densities for different positions of both floating magnets (a) B_Vector and (b) Mag_B

Since the 1st and 2nd floating magnets moved with changing time, the magnetic flux densities of both floating magnets changed, as presented in Figure 9.3. On the other hand, the 1st and 4th magnets were

fixed; therefore, their magnetic flux densities did not change with time. The flux line changed with changing the position of the floating magnets, as shown in Figure 9.4. The induced voltage is generated inside the winding coil when the magnetic flux cuts the copper coil. Figure 9.5 displays the generated induced voltages and flux linkages in the winding coils when both floating magnets move with the constant velocity of 0.5 m/s.

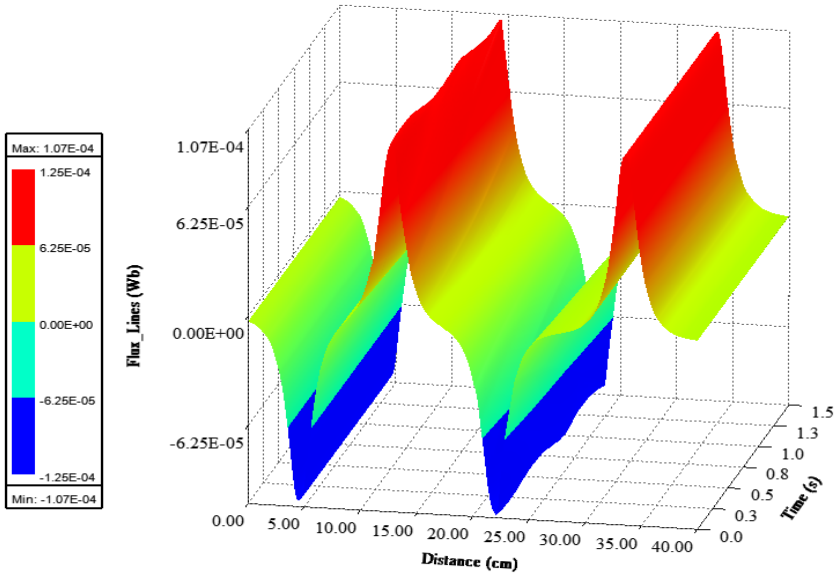

Figure 9.4: Flux lines for different positions of the floating magnet

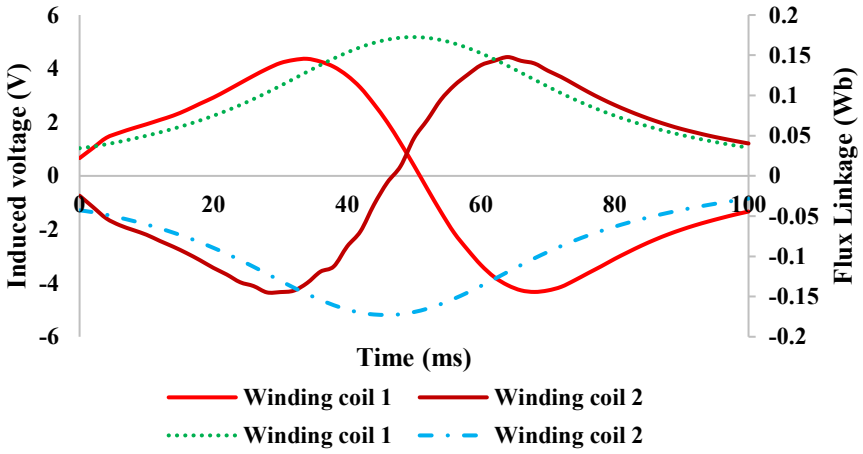

Figure 9.5: Induced voltage and flux Linkage in the winding coil 1 and 2

The legends in Figure 9.5 represent the winding coils (solid lines for induced voltage and the doted lines for flux linkage). From Figure 9.5, it can be seen that the induced voltages in winding coils 1 and 2 were zero when the flux linkages in winding coils 1 and 2 were maximum, respectively. The

flux linkage in the winding coil 1 remained positive during the excitation of the floating magnets because the magnetisation direction of the 1st floating magnet was upward. Since both floating magnets moved with the same constant velocity (0.5 m/s), both winding coils generated the same induced voltages. The magnetisation direction of the 2nd floating magnet was downward; therefore, the flux linkage remained negative during the movement of the floating magnets. The magnetisation directions for all magnets can be seen in Figure 9.2(a).

9.3 Mathematical Model of the 2DOF Energy Harvester

When the external force is applied to a floating magnet, or any floating magnet moves up and down, it creates the elastic restoring force of the magnetic spring. Figure 9.6 and Figure 9.7 present the free body diagram of the SDOF magnetic spring-based energy harvester system.

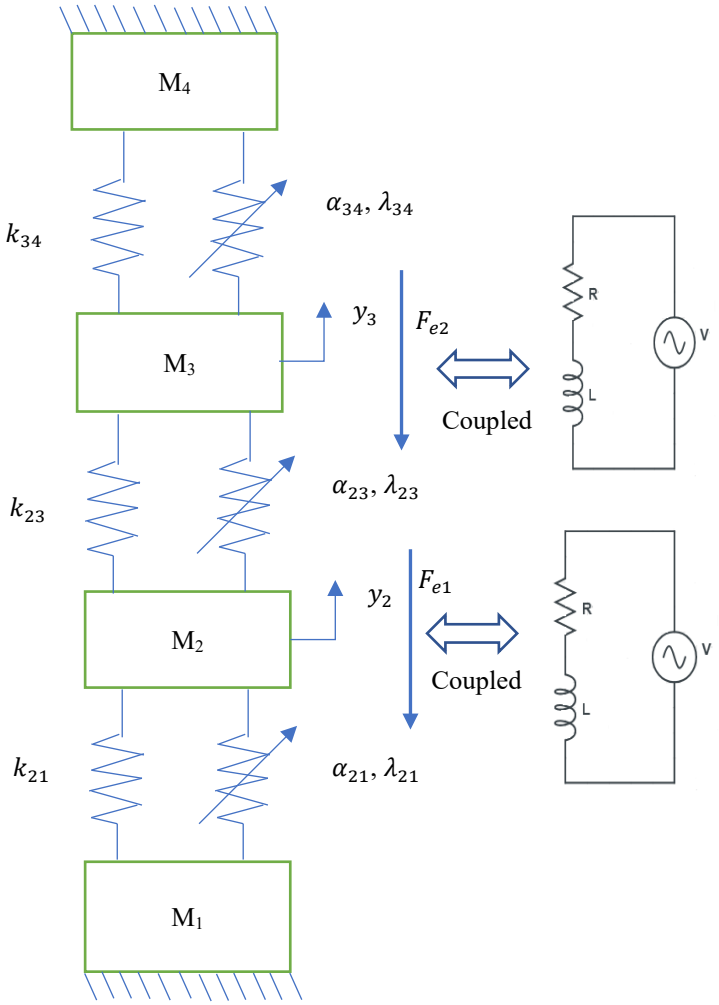

Figure 9.6: Two-degree-of-freedom magnetic spring-based energy harvester system

The relative displacement of the 1st floating magnet is y_2 and the relative velocity and acceleration of the 1st floating magnet are $\dot{y}_2$ and $\ddot{y}_2$, respectively. Moreover, the relative displacement, velocity and acceleration of the 2nd floating magnet are y_3, $\dot{y}_3$ and $\ddot{y}_3$, respectively. The magnetic flux density of the 2nd magnet (1st floating magnet) is $B_{1(y)}$ and the total length of the 1st winding coil is l_1. Similarly, the magnetic flux density of the 3rd magnet (2nd floating magnet) is $B_{2(y)}$ and the total length of the 2nd winding coil is l_2. The electromagnetic coupling coefficients are $a_1(a_1 = B_{1(y)}l_1)$ and $a_2(a_2 = B_{2(y)}l_2)$. Moreover, F_{e1} and F_{e2} are the electromagnetic forces written as $F_{e1} = a_1 I_1$ and $F_{e2} = a_2 I_2$, respectively.

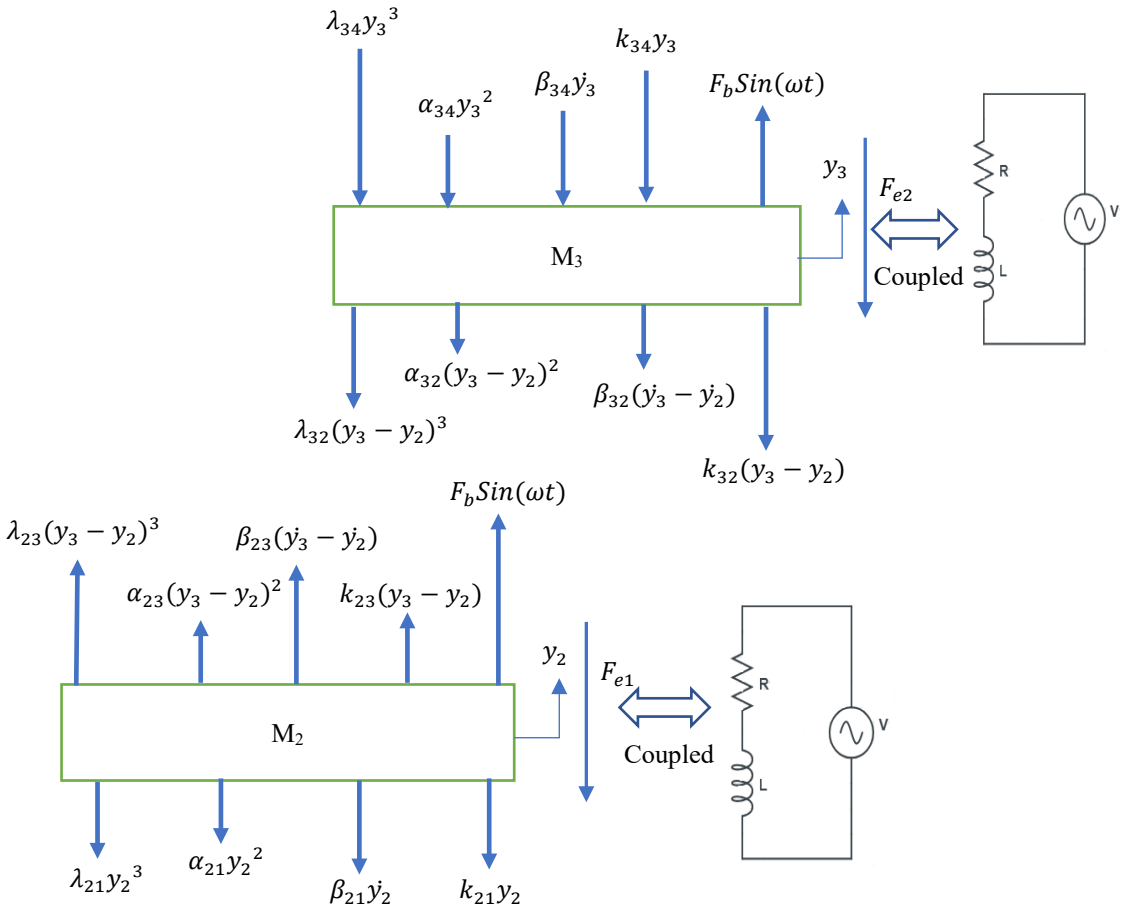

Figure 9.7: Free-body diagram of the Two-degree-of-freedom system

The masses of the 2nd (1st floating magnet) and 3rd (2nd floating magnet) magnets are M_2 and M_3, respectively. The damping forces of the 1st floating magnet is $F_{\beta 1} = \beta_1 \dot{y}_2$ and 2nd floating magnet is $F_{\beta 3} = \beta_3 \dot{y}_3$. In Figure 9.6, the linear stiffnesses are represented by k_{21}, k_{23}, k_{32} and k_{34}. The

damping constants are symbolled by $\beta_{21}, \beta_{23}, \beta_{32}$ and β_{34}. The nonlinear coefficients are presented by $\alpha_{21}, \alpha_{23}, \alpha_{32}$ and α_{34}. In addition, the other nonlinear stiffnesses are $\lambda_{21}, \lambda_{23}, \lambda_{32}$ and λ_{34}. In Figure 9.7, the linear stiffness $k_{21} = k_1$, $k_{23} = k_{32} = k_2$ and $k_{34} = k_3$. The damping constants $\beta_{21} = \beta_1$, $\beta_{23} = \beta_{32} = \beta_2$ and $\beta_{34} = \beta_3$. The nonlinear coefficients α_{21} is equal to α_1. Moreover, α_{23} and α_{32} are equal to α_2 and α_{34} is equal to α_3. In addition, the other nonlinear stiffness $\lambda_{21} = \lambda_1$ and $\lambda_{23} = \lambda_{32} = \lambda_2$ and $\lambda_{34} = \lambda_3$. Figure 9.8 replaces Figure 9.7 after rewriting the linear and nonlinear coefficients' values.

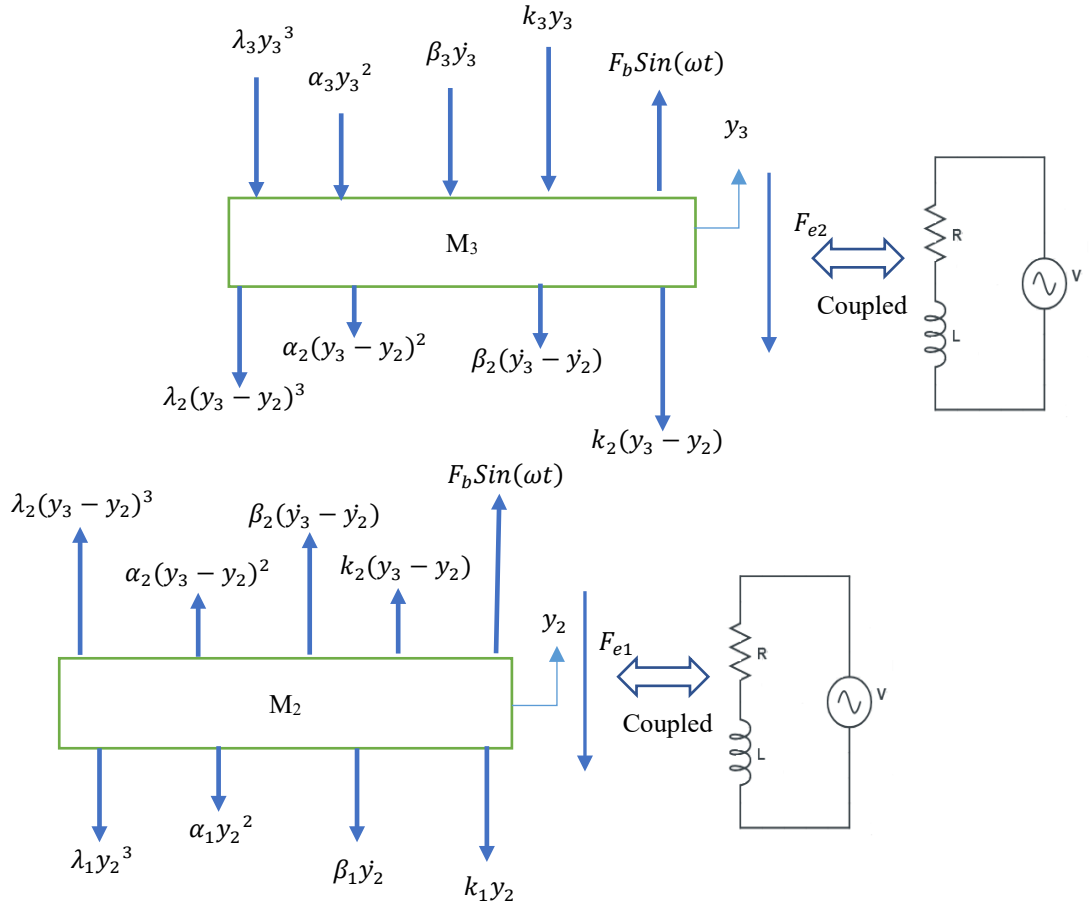

Figure 9.8: Free-body diagram of the Two-degree-of-freedom system

The dynamic equation of the motion of the system can be written as,

$$M_2\ddot{y}_2 + \beta_1\dot{y}_2 - \beta_2(\dot{y}_3 - \dot{y}_2) + k_1 y_2 - k_2(y_3 - y_2) + \alpha_1 y_2{}^2 - \alpha_2(y_3 - y_2)^2 + \lambda_1 y_2{}^3 - \lambda_2(y_3 - y_2)^3 + B_1 l_1 \frac{V_1}{R_1} = F_1 Sin(\omega t) \quad (9.1)$$

$$M_3\ddot{y}_3 + \beta_3\dot{y}_3 + \beta_2(\dot{y}_3 - \dot{y}_2) + k_3y_3 + k_2(y_3 - y_2) + \alpha_3{y_3}^2 + \alpha_2(y_3 - y_2)^2 + \lambda_3{y_3}^3 + \lambda_2(y_3 - y_2)^3 + B_2l_2\frac{V_2}{R_2} = F_2Sin(\omega t) \quad (9.2)$$

$$V_1 + \frac{L_1}{R_1}\dot{V}_1 = B_1l_1\dot{y}_2 \quad (9.3)$$

$$V_2 + \frac{L_2}{R_2}\dot{V}_2 = B_2l_2\dot{y}_3 \quad (9.4)$$

Equation 9.1 can be expressed as,

$$M_2\ddot{y}_2 + (\beta_1 + \beta_2)\dot{y}_2 - \beta_2\dot{y}_3 + (k_1 + k_2 + \alpha_1y_2 - \alpha_2y_2 + \lambda_1{y_2}^2 + \lambda_2{y_2}^2 + 2\alpha_2y_3 + 3\lambda_2{y_3}^2)y_2 - (k_2 + 3\lambda_2{y_2}^2 + \alpha_2y_3 + \lambda_2{y_3}^2)y_3 + B_1l_1\frac{V_1}{R_1} = F_1Sin(\omega t) \quad (9.5)$$

Equation 9.2 can be expressed as,

$$M_3\ddot{y}_3 + (\beta_3 + \beta_2)\dot{y}_3 - \beta_2\dot{y}_2 - (k_2 + 2\alpha_2y_3 - \alpha_2y_2 + \lambda_2{y_2}^2 + 3\lambda_2{y_3}^2)y_2 + (k_3 + k_2 + \alpha_3y_3 + \alpha_2y_3 + \lambda_3{y_3}^2 + \lambda_2{y_3}^2 + 3\lambda_2{y_2}^2)y_3 + B_2l_2\frac{V_2}{R_2} = F_2Sin(\omega t) \quad (9.6)$$

The equations 9.3 and 9.4 can be stated as,

$$\frac{L_1}{R_1}\dot{V}_1 = B_1l_1\dot{y}_2 - V_1 \quad (9.7)$$

$$\frac{L_2}{R_2}\dot{V}_2 = B_2l_2\dot{y}_3 - V_2 \quad (9.8)$$

State space variables can be used to solve equations 9.5, 9.6, 9.7 and 9.8. State space variables can be defined as:

$$x_1 = y_2 \quad (9.9)$$

$$x_2 = \dot{y}_2 = \frac{dx_1}{dt} \quad (9.10)$$

$$\frac{dx_2}{dt} = \ddot{y}_2 \quad (9.11)$$

$$x_3 = y_3 \quad (9.12)$$

$$x_4 = \frac{dx_3}{dt} = \dot{y}_3 \tag{9.13}$$

$$\frac{dx_4}{dt} = \ddot{y}_3 \tag{9.14}$$

$$x_5 = V_1 \tag{9.15}$$

$$\dot{V}_1 = \frac{dx_5}{dt} \tag{9.16}$$

$$x_6 = V_2 \tag{9.17}$$

$$\frac{dx_6}{dt} = \dot{V}_2 \tag{9.18}$$

$$u = F_1 = F_2 \tag{9.19}$$

Equation 9.5 can be written as

$$\frac{dx_2}{dt} = \ddot{y}_2 = \frac{1}{M_2}[u - (\beta_1 + \beta_2)x_2 + \beta_2 x_4 - (k_1 + k_2 + \alpha_1 x_1 - \alpha_2 x_1 + \lambda_1 {x_1}^2 + \lambda_2 {x_1}^2 + 2\alpha_2 x_3 + 3\lambda_2 {x_3}^2)x_1 + (k_2 + 3\lambda_2 {x_1}^2 + \alpha_2 x_3 + \lambda_2 {x_3}^2)x_3 - \frac{B_1 l_1}{R_1} x_5] \tag{9.20}$$

To simplify Equation 9.20, the following parameters are considered

$$P1 = (k_1 + k_2 + \alpha_1 x_1 - \alpha_2 x_1 + \lambda_1 {x_1}^2 + \lambda_2 {x_1}^2 + 2\alpha_2 x_3 + 3\lambda_2 {x_3}^2) \tag{9.21}$$

$$Q1 = (k_2 + 3\lambda_2 {x_1}^2 + \alpha_2 x_3 + \lambda_2 {x_3}^2) \tag{9.22}$$

Equation 9.20 can be rewritten as

$$\frac{dx_2}{dt} = \ddot{y}_2 = \frac{1}{M_2}\left[u - P1x_1 - (\beta_1 + \beta_2)x_2 + Q1x_3 + \beta_2 x_4 - \frac{B_1 l_1}{R_1} x_5\right] \tag{9.23}$$

Equation 9.6 can be written as

$$\frac{dx_4}{dt} = \ddot{y}_3 = \frac{1}{M_3}[u - (\beta_3 + \beta_2)x_4 + \beta_2 x_2 + (k_2 + 2\alpha_2 x_3 - \alpha_2 x_1 + \lambda_2 {x_1}^2 + 3\lambda_2 {x_3}^2)x_1 - (k_3 + k_2 + \alpha_3 x_3 + \alpha_2 x_3 + \lambda_3 {x_3}^2 + \lambda_2 {x_3}^2 + 3\lambda_2 {x_1}^2)x_3 - \frac{B_2 l_2}{R_2} x_6] \tag{9.24}$$

To shorten Equation 9.24, the following parameters are considered

$$T1 = (k_2 + 2\alpha_2 x_3 - \alpha_2 x_1 + \lambda_2 {x_1}^2 + 3\lambda_2 {x_3}^2) \tag{9.25}$$

$$S1 = (k_3 + k_2 + \alpha_3 x_3 + \alpha_2 x_3 + \lambda_3 {x_3}^2 + \lambda_2 {x_3}^2 + 3\lambda_2 {x_1}^2) \tag{9.26}$$

After adding T1 and S1 the equation 9.24 can be stated as

$$\frac{dx_4}{dt} = \ddot{y}_3 = \frac{1}{M_3}\left[u + T1x_1 + \beta_2 x_2 - S1x_3 - (\beta_3 + \beta_2)x_4 - \frac{B_2 l_2}{R_2} x_6\right] \tag{9.27}$$

The equations 9.7 and 9.8 can be stated as,

$$\frac{dx_5}{dt} = \frac{R_1 B_1 l_1}{L_1} x_2 - \frac{R_1}{L_1} x_5 \tag{9.28}$$

$$\frac{dx_6}{dt} = \frac{R_2 B_2 l_2}{L_2} x_4 - \frac{R_2}{L_2} x_6 \tag{9.29}$$

The state space model of the 2DOF system can be written as

$$\begin{bmatrix} \frac{dx_1}{dt} \\ \frac{dx_2}{dt} \\ \frac{dx_3}{dt} \\ \frac{dx_4}{dt} \\ \frac{dx_5}{dt} \\ \frac{dx_6}{dt} \end{bmatrix} = \underbrace{\begin{bmatrix} 0 & 1 & 0 & 0 & 0 & 0 \\ \frac{-P1}{M_2} & \frac{-(\beta_1+\beta_2)}{M_2} & \frac{Q1}{M_2} & \frac{\beta_2}{M_2} & \frac{-B_1 l_1}{M_2 R_1} & 0 \\ 0 & 0 & 0 & 1 & 0 & 0 \\ \frac{T1}{M_3} & \frac{\beta_2}{M_3} & \frac{-S1}{M_3} & \frac{-(\beta_3+\beta_2)}{M_3} & 0 & \frac{-B_2 l_2}{M_3 R_2} \\ 0 & \frac{R_1 B_1 l_1}{L_1} & 0 & 0 & -\frac{R_1}{L_1} & 0 \\ 0 & 0 & 0 & \frac{R_2 B_2 l_2}{2} & 0 & -\frac{R_2}{L_2} \end{bmatrix}}_{A} \begin{bmatrix} x_1 \\ x_2 \\ x_3 \\ x_4 \\ x_5 \\ x_6 \end{bmatrix} + \underbrace{\begin{bmatrix} 0 \\ \frac{1}{M_2} \\ 0 \\ \frac{1}{M_3} \\ 0 \\ 0 \end{bmatrix}}_{B} [u] \tag{9.30}$$

$$[x] = \underbrace{\begin{bmatrix} 1 & 0 & 0 & 0 & 0 & 0 \\ 0 & 1 & 0 & 0 & 0 & 0 \\ 0 & 0 & 1 & 0 & 0 & 0 \\ 0 & 0 & 0 & 1 & 0 & 0 \\ 0 & 0 & 0 & 0 & 1 & 0 \\ 0 & 0 & 0 & 0 & 0 & 1 \end{bmatrix}}_{C} \begin{bmatrix} x_1 \\ x_2 \\ x_3 \\ x_4 \\ x_5 \\ x_6 \end{bmatrix} + \underbrace{\begin{bmatrix} 0 \\ 0 \end{bmatrix}}_{D} [u] \tag{9.31}$$

where *A* is the system matrix, *B* is the input matrix, and *C* is the output matrix. The remaining matrix is *D* which is typically zero because the input directly does not usually affect the output.

$$\begin{bmatrix} \frac{dx_1}{dt} \\ \frac{dx_2}{dt} \\ \frac{dx_3}{dt} \\ \frac{dx_4}{dt} \\ \frac{dx_5}{dt} \\ \frac{dx_6}{dt} \end{bmatrix} = \underbrace{\begin{bmatrix} 0 & 1 & 0 & 0 & 0 & 0 \\ \frac{-P1}{M_2} & \frac{-(\beta_1+\beta_2)}{M_2} & \frac{Q1}{M_2} & \frac{\beta_2}{M_2} & \frac{-B_1 l_1}{M_2(R_1+R_{e1})} & 0 \\ 0 & 0 & 0 & 1 & 0 & 0 \\ \frac{T1}{M_3} & \frac{\beta_2}{M_3} & \frac{-S1}{M_3} & \frac{-(\beta_3+\beta_2)}{M_3} & 0 & \frac{-B_2 l_2}{M_3(R_2+R_{e2})} \\ 0 & \frac{(R_1+Re_1)B_1 l_1}{L_1} & 0 & 0 & -\frac{(R_1+R_{e1})}{L_1} & 0 \\ 0 & 0 & 0 & \frac{(R_2+R_{e2})B_2 l_2}{2} & 0 & -\frac{(R_2+R_{e2})}{L_2} \end{bmatrix}}_{A} \begin{bmatrix} x_1 \\ x_2 \\ x_3 \\ x_4 \\ x_5 \\ x_6 \end{bmatrix} + \begin{bmatrix} 0 \\ \frac{1}{M_2} \\ 0 \\ \frac{1}{M_3} \\ 0 \\ \underbrace{0}_{B} \end{bmatrix} [u] \quad (9.32)$$

$$[x] = \underbrace{\begin{bmatrix} 1 & 0 & 0 & 0 & 0 & 0 \\ 0 & 1 & 0 & 0 & 0 & 0 \\ 0 & 0 & 1 & 0 & 0 & 0 \\ 0 & 0 & 0 & 1 & 0 & 0 \\ 0 & 0 & 0 & 0 & 1 & 0 \\ 0 & 0 & 0 & 0 & 0 & 1 \end{bmatrix}}_{C} \begin{bmatrix} x_1 \\ x_2 \\ x_3 \\ x_4 \\ x_5 \\ x_6 \end{bmatrix} + \begin{bmatrix} \underbrace{0}_{D} \end{bmatrix} [u] \quad (9.33)$$

If the coils are connected in parallel to external load or resistance $R_{e1}$and R_{e2}. The parallel-connected winding coils have the internal resistance R_1 and R_2 and inductances L_1 and L_2. The state space model of the system can be written in matrix form by equations 9.32 and 9.33, where *A* is the system matrix, *B* is the input matrix, and *C* is the output matrix. The remaining matrix is *D* which is typically zero because the input directly does not usually affect the output.

9.4 Dynamic Analysis of the 2DOF Energy Harvester

The dynamics of the 2DOF energy harvester have been analysed using linear and nonlinear stiffness, which was measured from magnetic restoring forces. The eigenvalues and frequency responses were first determined to understand the system. The diameter of the copper coil was 31 mm, and the number of turns of the winding coils was 100. The inside diameter and height of the winding coils were 75 mm and 10 mm, respectively. The total length of the winding coil was 23.5 m, and the inner resistance of the coil was 5.48 ohm. The average magnetic flux density was considered 0.35 T. Because of the electromechanical coupling, the generator system consists of electrical and mechanical parts. Two winding coils have been added outside the two floating magnets, and therefore the system has two resonance frequencies in the electrical part. Because of the two floating magnets, the system has two mechanical resonance frequencies. It has been seen in Chapter 5 that the mechanical resonance frequencies changed with changing the position of the floating magnets. The electrical resonance frequencies did not change with changing the position of the floating magnets, but they changed with changing the total length of the winding coil (Number of turns) and magnetic flux density. Moreover,

the entire length of the winding coil does not affect the mechanical resonance frequency. All required parameters have been presented in Table 9.1.

Table 9.1: Required parameters

Parameters	Values	Units
M_2	370	gm
M_3	327.28	gm
β_1	0.98	Ns/m
β_2	0.235	Ns/m
β_3	0.51	Ns/m
k_1	524.37	N/m
k_2	112.875	N/m
k_3	298.62	N/m
α_1	4918.6	N/m^2
α_2	715.55	N/m^2
α_3	3487.5	N/m^2
λ_1	291867	N/m^3
λ_2	92334	N/m^3
λ_3	107199	N/m^3
B1 and B2	0.35	T
R1 and R2	5.48	ohm
l1 and l2	23.5	m
L1 and L2	0.005546	H

The natural frequencies of the electrical parts were 953.46 rad/s and 948.77 rad/s when both floating magnets were in equilibrium position. The natural frequencies for the mechanical parts were 44.17 rad/s and 33.75 rad/s. The natural frequencies of the combined system were 43.46 rad/s and 33.02 rad/s, respectively, of the 2DOF system without electrical-mechanical coupling in the equilibrium position, as discussed in Chapter 5. The natural frequencies of the mechanical part were almost similar with or without electrical-mechanical coupling. The imaginary parts of the eigenvalues (electrical parts) were zeros, but the real parts were -953.47 and -948.78 in the equilibrium position. The eigenvalues of the mechanical part were -0.1954 ± 0.3962i (1st floating magnet) and -0.2022 ± 0.2703i (2nd floating magnet) in equilibrium position. The generator system's frequency response in equilibrium position is shown in Figure 9.9. Due to the electromechanical coupling, the frequency response graph did not show the peak amplitude.

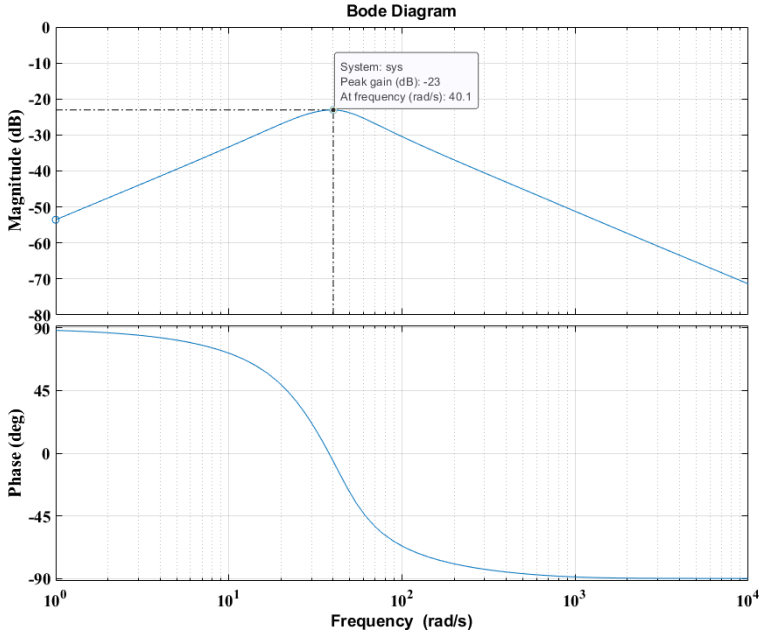

Figure 9.9: Frequency response of the generator system in equilibrium position

Table 9.2: Eigenvalues and natural frequencies of the system for different positions of the floating magnets

PF	Eigenvalues				Frequency (rad/s)			
	Electrical part		MP		Electrical part		MP	
-30	-948.82 + 0i	-953.51 + 0i	-19.89 +59.47i	-19.82 +30.35i	948.81	953.51	62.71	36.24
-25	-948.80 + 0i	-953.50 + 0i	-19.86 +53.44i	-19.87 +28.66i	948.80	953.49	57.01	34.86
-20	-948.79 + 0i	-953.49 + 0i	-19.81 +48.14i	-19.93 +27.34i	948.79	953.48	52.05	33.83
-15	-948.78 + 0i	-953.48 + 0i	-19.73 +43.83i	-20.02 +26.46i	948.78	953.47	48.06	33.17
-10	-948.78 + 0i	-953.47 + 0i	-19.64 +40.82i	-20.11 +26.06i	948.77	953.47	45.30	32.92
-05	-948.78 + 0i	-953.47 + 0i	-19.57 +39.38i	-20.19 +26.23i	948.77	953.46	43.97	33.09
0	-948.78 + 0i	-953.47 + 0i	-19.54 +39.62i	-20.22 +27.03i	948.77	953.46	44.17	33.75
05	-948.78 + 0i	-953.47 + 0i	-19.57 +41.48i	-20.18 +28.46i	948.78	953.47	45.86	34.88
10	-948.79 + 0i	-953.48 + 0i	-19.64 +44.79i	-20.10 +30.38i	948.78	953.48	48.91	36.42
15	-948.80 + 0i	-953.49 + 0i	-19.72 +49.31i	-20.01 +32.63i	948.80	953.49	53.10	38.28
20	-948.82 + 0i	-953.51 + 0i	-19.78 +54.75i	-19.93 +35.13i	948.81	953.50	58.21	40.39
25	-948.83 + 0i	-953.53 + 0i	-19.83 +60.88i	-19.87 +37.82i	948.83	953.52	64.02	42.72
30	-948.85 + 0i	-953.55 + 0i	-19.85 +67.50i	-19.82 +40.66i	948.85	953.55	70.35	45.23

*Note: PF=Position of the floating magnet, MP= Mechanical part

However, the peak resonance has shown at 40.1 rad/s. With changing the position of the floating magnets, the eigenvalues of the generator system were analysed. The determined eigenvalues of the generator system for different positions of floating magnets have been presented in Table 9.2. From Table 9.2, it can be seen that the eigenvalues and natural frequencies of the mechanical part changed with changing the position of the floating magnet. However, the eigenvalues and natural frequencies of the electrical part always remained almost constant for all different positions of the floating magnets. The generator showed higher mechanical frequency responses when both floating magnets moved toward the bottom magnet. Figure 9.10 displays the frequency responses of the generator system for different positions of the floating magnets.

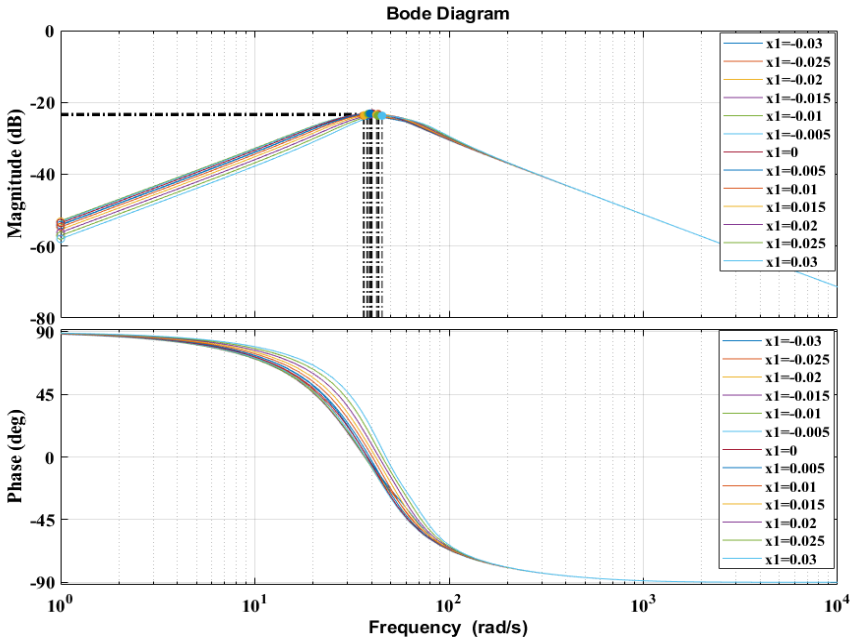

Figure 9.10: Frequency response of the generator system for different positions of the floating magnets

The peak resonance changed with changing the position of the floating magnets, as seen in Figure 9.10. The frequency resonance of the generator could be changed by changing the magnetic flux density coil turns numbers discussed in Chapter 5. The frequency resonance has been analysed by connecting external load or resistance parallel to the winding coils. Different external loads have been connected to explore the frequency resonance of the generator system. The external load was varied from 500 ohms to 50000 ohms to determine the resonance frequency. Figure 9.11 displays two resonances, and the values were 33 rad/s and 44.4 rad/s in the equilibrium position, which were almost

similar to the natural frequencies 44.17 rad/s and 33.75 rad/s without an external load which were determined using eigenvalues. It has been seen in Figure 9.9 and Figure 9.10 that the resonance frequency graph did not show peak amplitude, but in Figure 9.11, the generator system with external load showed two peak resonant frequencies. Figure 9.12 presents the resonance frequency of the generator system with external load for different positions of the floating magnets.

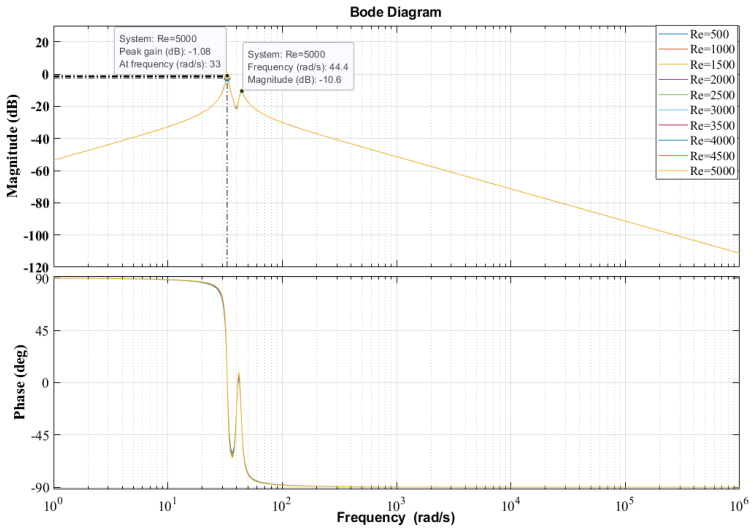

Figure 9.11: Frequency response of the generator system with external load in equilibrium position

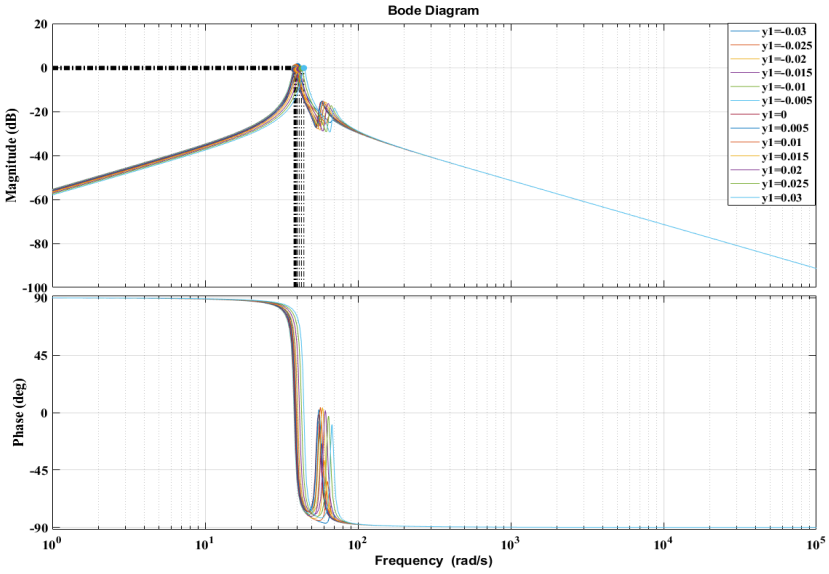

Figure 9.12: Frequency response of the generator system with external load for different positions of the floating magnets

The peak resonance frequencies' position changed with changing the position of the floating magnets, as seen in Figure 9.12. Overall, it can be said that the generator's frequency changed with changing the position of the floating magnets. The natural frequencies of the mechanical parts were almost similar for both generator systems with or without external load. However, the natural frequencies of the electrical parts were way higher in the generator system with the external load than in the system without an external load. Compared to the generator system with or without external load, the generator system with external load showed better dynamics results.

The generator system's displacements, velocities, and induced voltages have been analysed with an applied external force. If the external force is applied to any of the floating magnets or both floating magnets, then both floating magnets start moving relative to each other. When the external force is applied to the 2nd floating or 1st floating magnet or both floating magnets, the displacement of the 2nd floating magnet remains higher than the 1st floating magnet, as discussed in Chapter 5. Moreover, the velocity of the 2nd floating magnet always remained higher than the 1st floating magnet. After adding the winding coils, the system was analysed. Because of the movement of the floating magnets, the magnetic flux densities of the floating magnet cut the winding coils, which created induced voltage inside the winding coils.

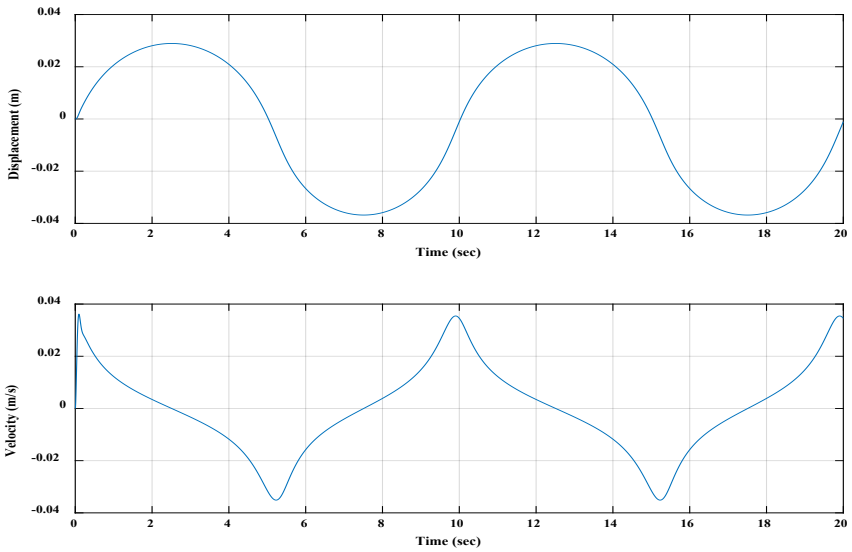

Figure 9.13: Displacement and velocity of the 1st floating magnet

The applied external harmonic force (Fb) amplitude was 25N, and the frequency (f) was 0.1 Hz. The values of linear stiffness, nonlinear stiffness and damping constants have been presented in Table 9.1.

The state space model equations 9.23, 9.27, 9.28 and 9.29 have been solved using Ode23t solver in MATLAB to find the displacements, velocities and induced voltages of the system. Both floating magnets' excitation was assumed to have the initial displacements, and their corresponding velocities were zero. As expected, the displacements and the velocities were sinusoidal and 90° out of phase. At first, the generator system was analysed by applying harmonic force to both floating magnets. Figure 9.13 presents the displacement and velocity of the 1st floating magnet, and Figure 9.14 displays the displacement and velocity of the 2nd floating magnet.

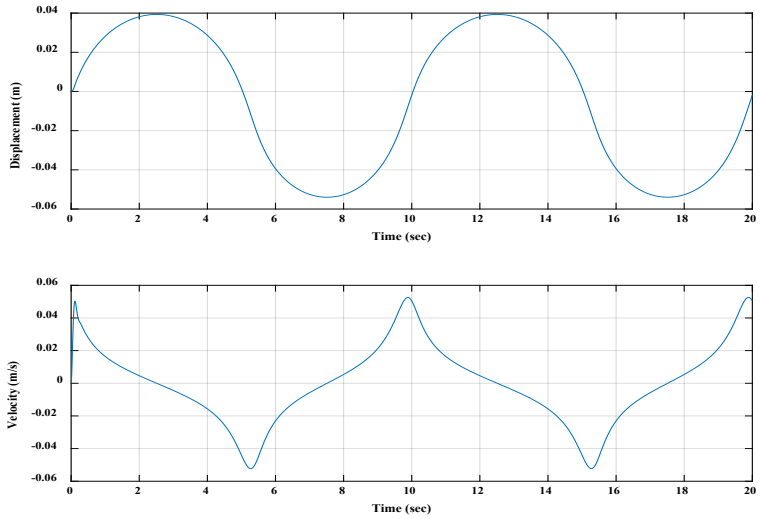

Figure 9.14: Displacement and velocity of the 2nd floating magnet

Because of the applied harmonic force, the maximum displacements of the 1st floating magnet toward the 2nd floating magnet was around 40 mm, and toward the bottom magnet was about 30 mm. The frequency of the applied harmonic force was considered 0.1 Hz; therefore, Figure 9.13 shows two complete cycles. The measured maximum velocity of 1st floating magnet was around 0.04 m/s. On the other hand, the maximum displacements of the 2nd floating magnet toward the 4th (top fixed magnet) were around 50 mm and 40 mm towards the 1st floating magnet, as shown in Figure 9.14. The maximum velocity of the 2nd floating magnet was around 0.05 m/s. The displacements and velocities of both floating magnets can be changed by changing the amplitude and frequency of the applied harmonic force, as discussed in Chapter 5. For the same applied harmonic forces in both floating magnets, the 2nd floating magnet achieved more displacement and velocity than the 1st floating magnet, as shown in Figure 9.15.

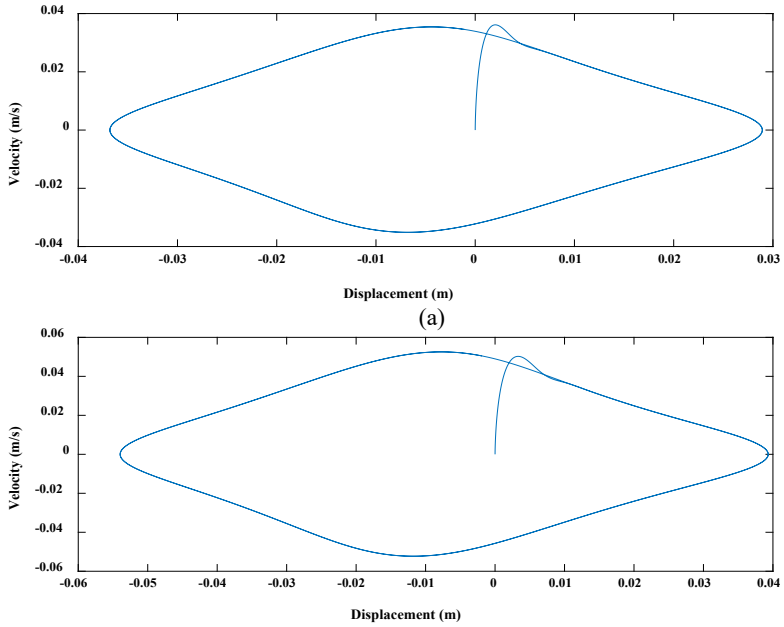

Figure 9.15: Comparison of displacement and velocity of (a) 1st floating magnet and (b) 2nd floating magnet

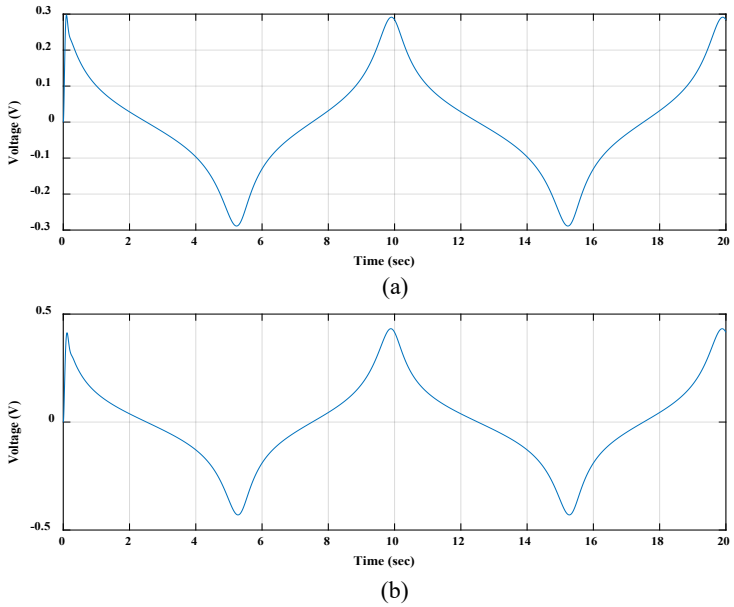

Figure 9.16: Measured induced voltages (a) 1st winding coil and (b) 2nd winding coil

It was considered during the analysis that 1st winding coil was placed outside of the 1st floating magnet and 2nd winding coil was outside of the 2nd floating magnet. The positions of both winding coils were

not considered. As it is known, due to the movement of the floating magnets, the induced voltage will be generated in the winding coil. The generated induced voltages were determined as well as shown in Figure 9.16. The displacement and velocity of the 2nd floating magnet were higher than the 1st floating magnet. Therefore, the 2nd winding coil showed a higher induced voltage than the 1st winding coil. The maximum measured induced voltages in coil 2 was around 0.45 volts and in coil 1 was 0.3 volts. The generator system has been analysed by applying a harmonic force only on the 2nd floating magnet. The displacements and velocities of both floating magnets have been determined for that applied harmonic force.

Moreover, the induced voltages for both coils have been measured as well. As the harmonic force was applied on the 2nd floating magnet, therefore, when the 2nd floating magnet started moving, then the 1st floating magnet also started moving. For this applied harmonic force (25N amplitude), the 2nd floating magnet achieved a higher displacement and velocity compared to the 1st floating magnet. Figure 9.17 and Figure 9.18 present the displacement and velocity of the 1st and 2nd floating magnets, respectively.

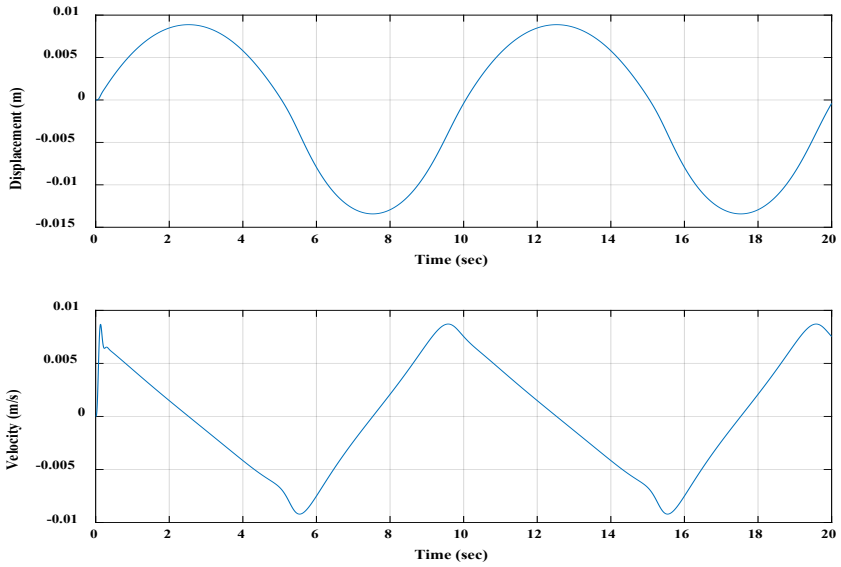

Figure 9.17: Displacement and velocity of the 1st floating magnet

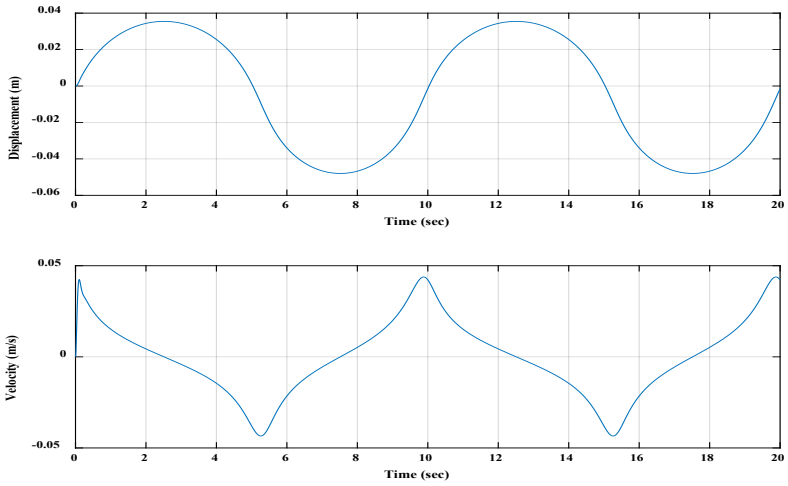

Figure 9.18: Displacement and velocity of the 2nd floating magnet

The 1st floating magnet moved up to 13 mm toward the 2nd floating magnet and around 9 mm toward the 1st fixed magnet (bottom magnet). The measured maximum velocity was around 0.009 m/s during this movement. On the other hand, the 2nd floating magnet moved up to 47 mm toward the top fixed magnet (4th magnet) and around 35 mm toward the 1st floating magnet. The maximum velocity for the 2nd floating magnet was around 0.045 m/s during this movement. Figure 9.19 displays the comparison of displacement and velocity of 1st floating magnet with 2nd floating magnet. Figure 9.20 shows the induced voltages of both winding coils.

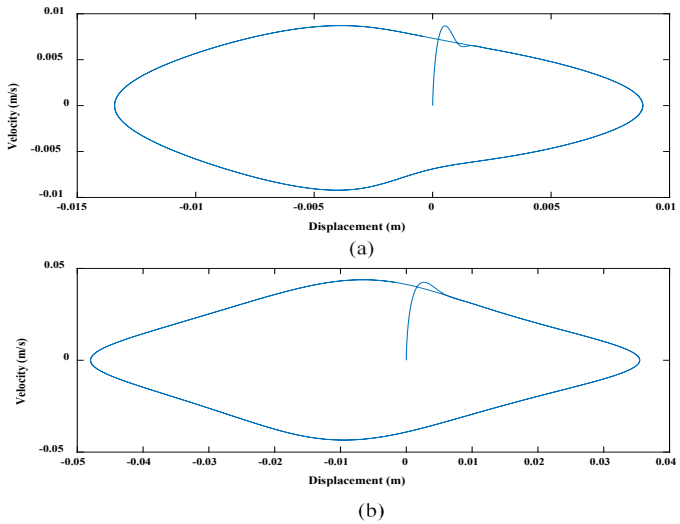

Figure 9.19: Comparison of displacement and velocity of (a) 1st floating magnet and (b) 2nd floating magnet

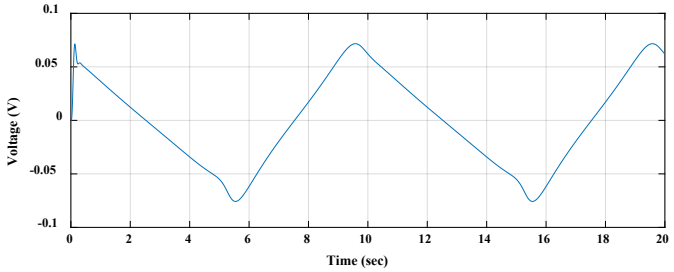

(a)

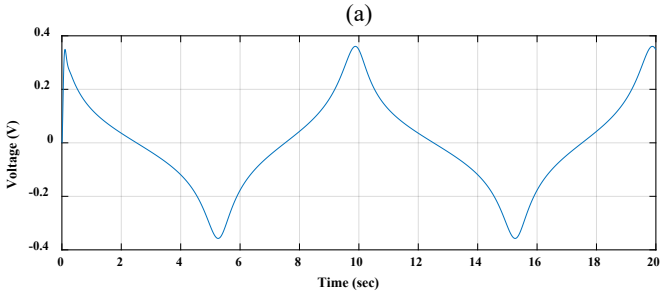

(b)

Figure 9.20: Measured induced voltages (a) 1st winding coil and (b) 2nd winding coil

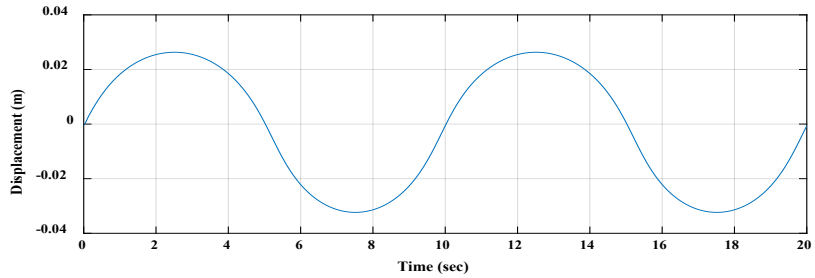

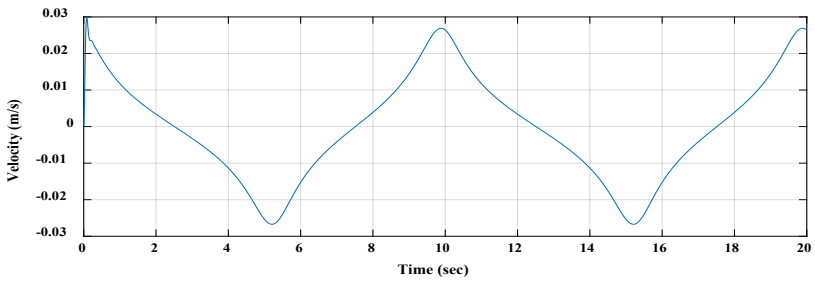

Figure 9.21: Displacement and velocity of the 1st floating magnet

The relative displacements of both floating magnets have been determined. The displacement and velocity of the 2nd floating magnet were higher than the 1st floating magnet, as seen in Figure 9.19. Therefore, the induced voltage of coil 2 was higher than that of coil 1. The maximum induced voltage in coil 1 was around 0.075 volts and in coil 2 was 0.36 volts. Finally, the generator system has been

analysed by applying the same harmonic force (25N amplitude) only on the 1st floating magnet. As the harmonic force has been applied on the 1st floating magnet, therefore, when the 1st floating magnet started moving, then the 2nd floating magnet also started moving. For this applied harmonic force (25N amplitude), the 2nd floating magnet achieved a higher displacement and velocity compared to the 1st floating magnet. Figure 9.21 and Figure 9.22 show the displacement and velocity of the 1st and 2nd floating magnets, respectively.

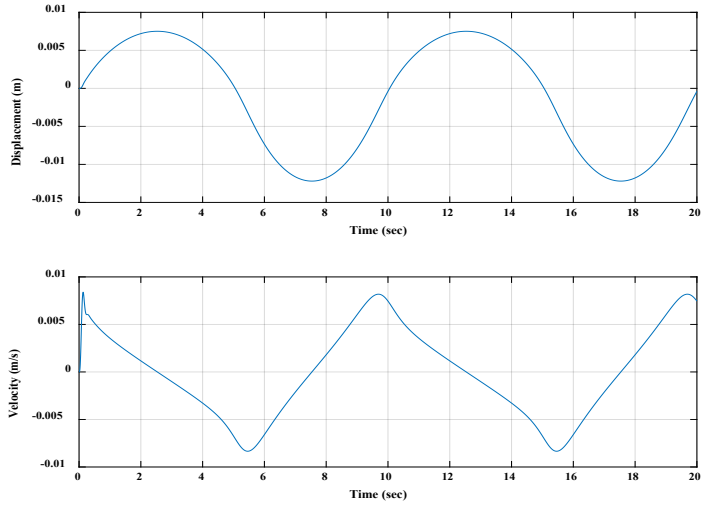

Figure 9.22: Displacement and velocity of the 2nd floating magnet

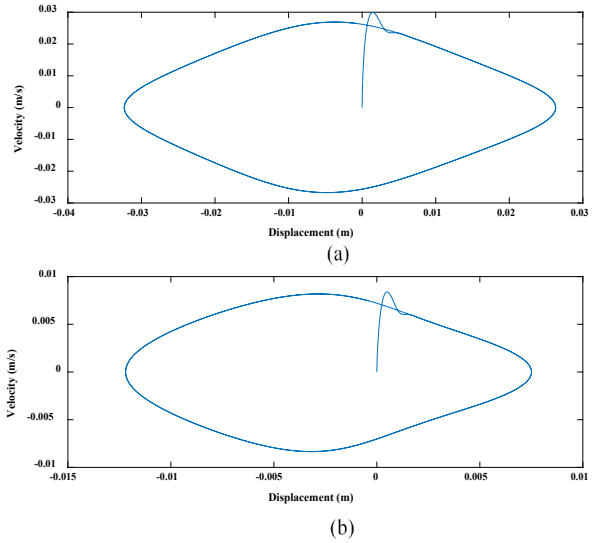

Figure 9.23: Comparison of displacement and velocity of (a) 1st floating magnet and (b) 2nd floating magnet

Due to the applied force, the 1st floating magnet moved up to 32 mm toward the 2nd floating magnet and about 26 mm toward the 1st fixed magnet (bottom magnet). The measured maximum velocity during that movement was around 0.027 m/s. On the other hand, the 2nd floating magnet moved relatively up to 12 mm toward the top fixed magnet (4th magnet) and 7.5 mm toward the 1st floating magnet. The maximum velocity of the 2nd floating magnet during that excitation was around 0.008 m/s. The 2nd floating magnet achieved the highest displacement and velocity compared to the 1st floating magnet for this applied harmonic, as shown in Figure 9.23. Thus, the induced voltage of coil 1 was higher than that of coil 2. The maximum induced voltage in coil 2 was around 0.068 volts and in coil 1 was 0.22 volts.

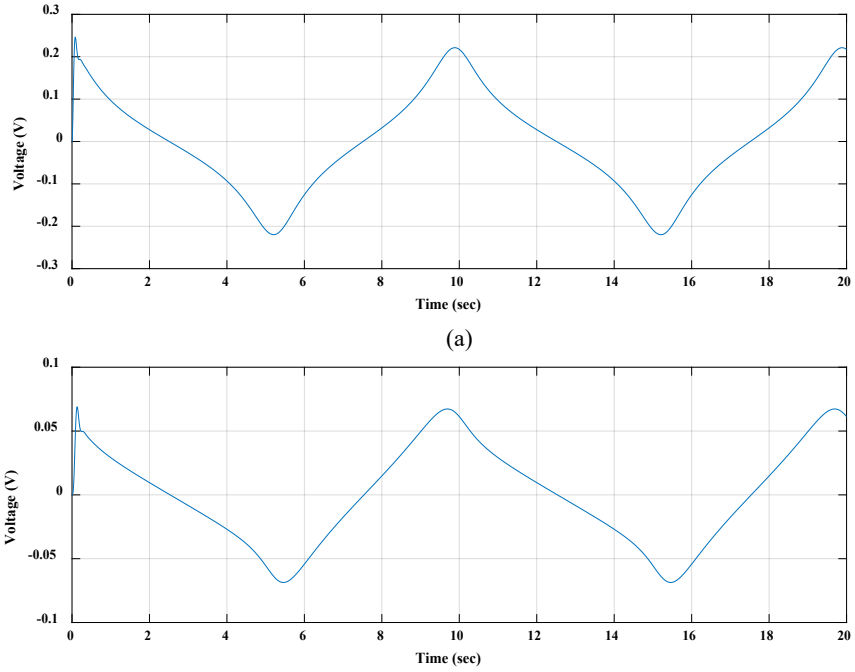

Figure 9.24: Measured induced voltages (a) 1st winding coil and (b) 2nd winding coil

Figure 9.25 and Figure 9.26 show the displacements and velocities of the 1st and 2nd floating magnets when the force is applied on the 1st floating magnet and 2nd floating magnet separately and both floating magnets in the same time. Overall, the 1st floating magnet showed the minimum displacement and velocity for all different applications than the 2nd floating magnet. Therefore, the 1st winding coil produced less induced voltage than 2nd winding coil. From Figure 9.25 and Figure 9.26, both floating

magnets show the maximum displacement and velocity when the external force is applied on both floating magnets.

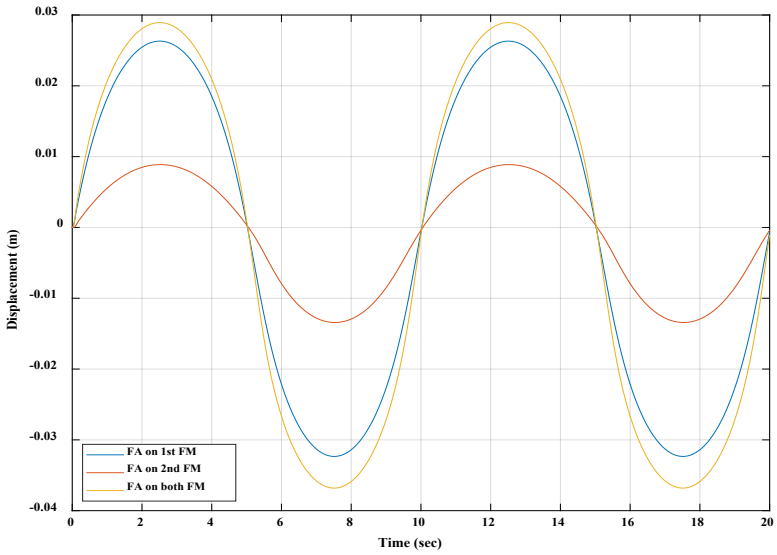

(a)

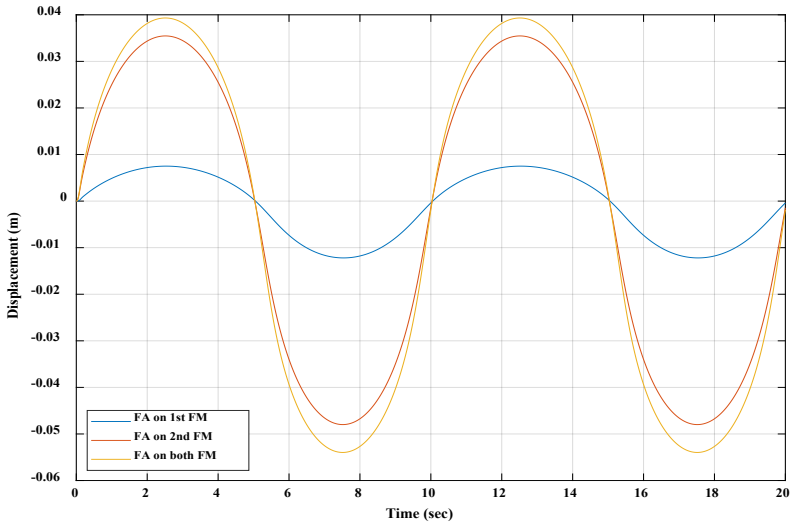

(b)

Figure 9.25: Displacements (a) 1st floating magnet and (b) 2nd floating magnet (Note: FA= Force applied, FM=Floating magnet)

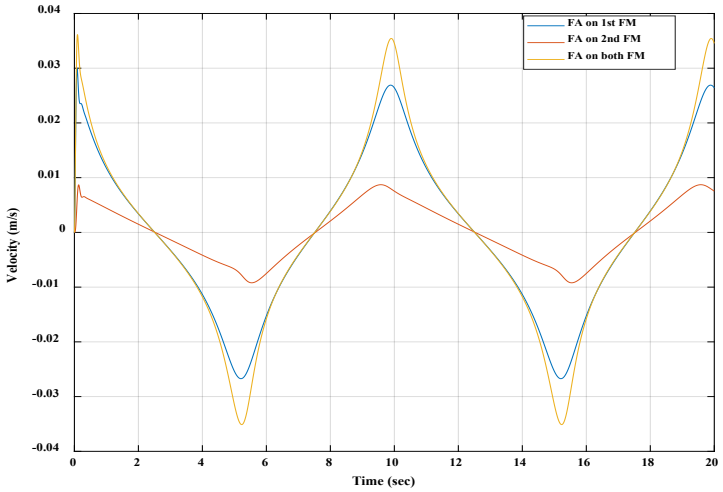

(a)

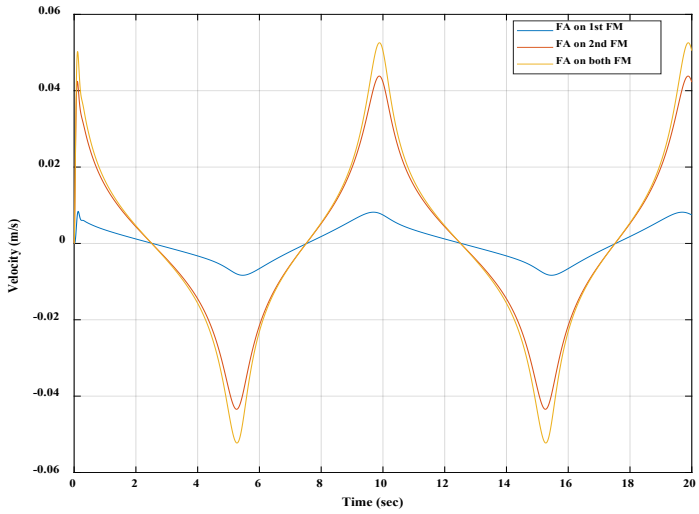

(b)

Figure 9.26: Velocities (a) 1st floating magnet and (b) 2nd floating magnet (Note: FA= Force applied, FM=Floating magnet)

When the forces were applied on both floating magnets, both coils generated maximum induced voltages compared to other applied forces, as shown in Figure 9.27. Still, the 2nd winding coil produced a higher induced voltage than the 1st winding coil. Hence, overall, during the theoretical analyses it has seen that the 2DOF generator system can produce maximum power if the external force could apply to both floating magnets.

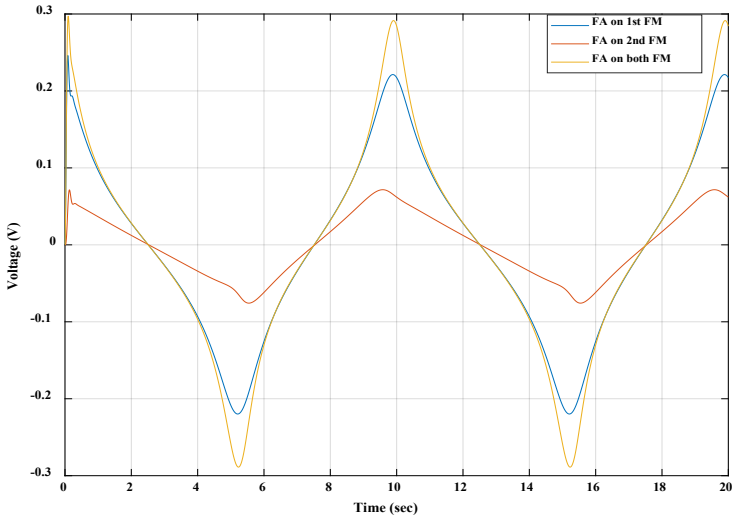

(a)

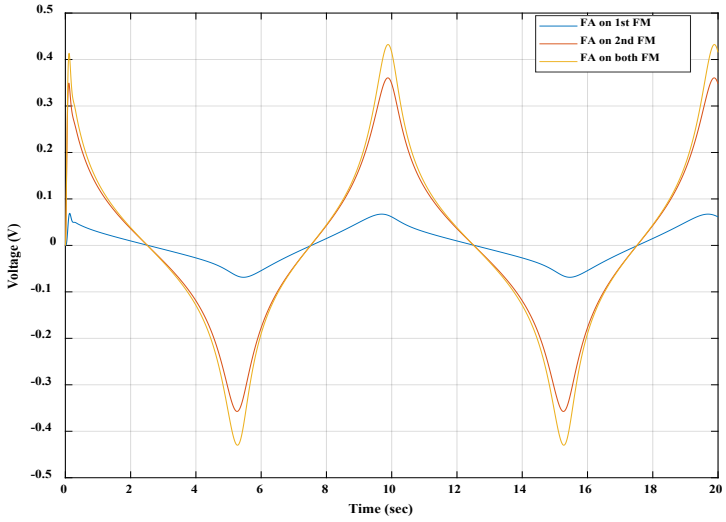

(b)

Figure 9.27: Induced voltage (a) 1st winding coil and (b) 2nd winding coil

All analyses presented earlier had the amplitude and frequency of the applied force as 25N and 0.1 Hz, respectively. Chapter 8 has discussed that the velocity of the floating magnet, magnetic flux density, number of turns of the winding coil, and applied external force can change the output induced voltage of the magnetic spring-based generator system. This chapter analysed the 2DOF generator system by changing the applied harmonic force's amplitude and frequency. By increasing the amplitude and frequency of the applied harmonic force, the output power of the 2DOF generator system can be increased. The 2DOF generator system has been compared with the SDOF generator

system. The amplitude and frequency of the applied harmonic force were 25N and 0.1 Hz. A winding coil (100 number of turns) has been considered for SDOF based generator system, and two winding coils (both 100 number of turns) have been considered for a 2DOF generator system. Moreover, the same magnetic flux density and copper coil have been considered to compare both generator systems. The force was applied on both floating magnets, only on the 2nd floating magnet and only on the 1st floating magnet of the 2DOF generator system and compared with the SDOF generator system. Figure 9.28 presents the comparison results of both generator systems.

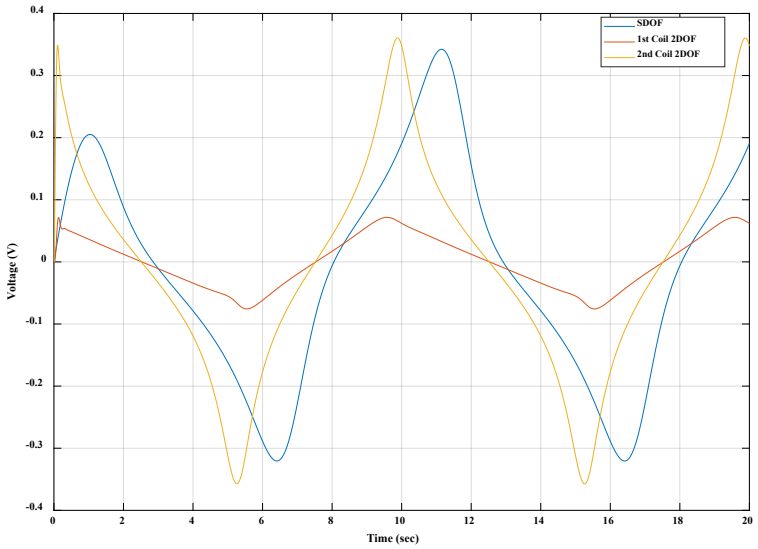

(a)

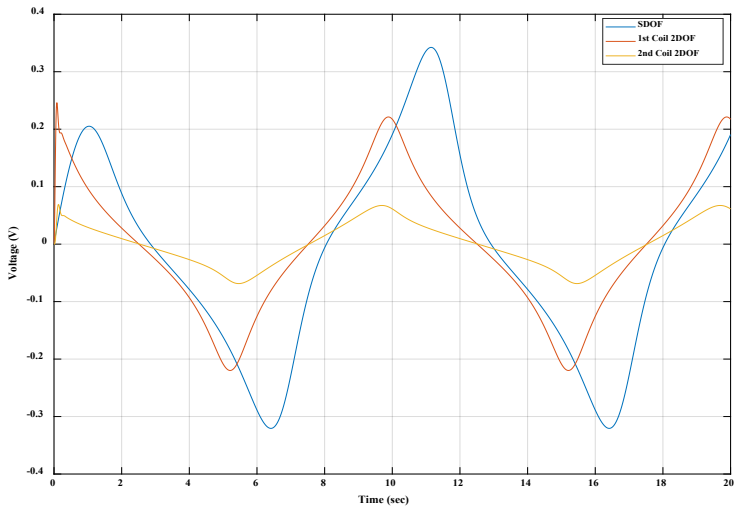

(b)

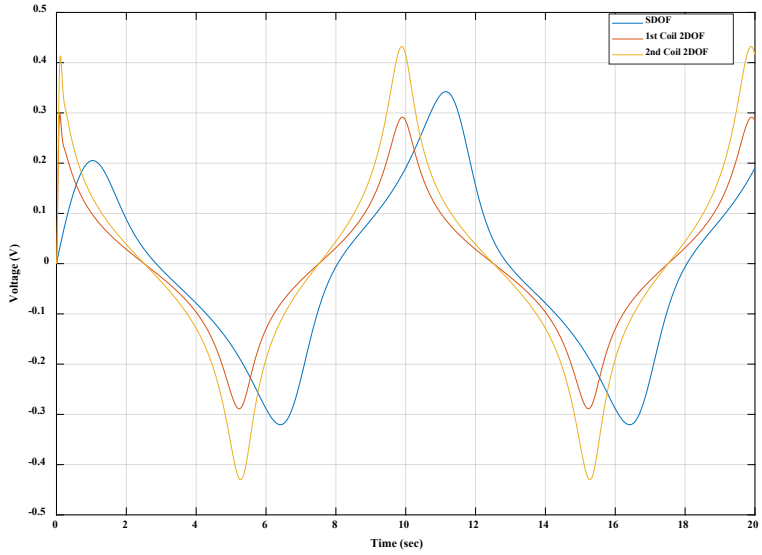

(c)

Figure 9.28: Induced voltage (a) Force applied on 2nd floating magnet in 2DOF, (b) Force applied on 1st floating magnet in 2DOF and (c) Force applied on both floating magnets in 2DOF

When the force is applied on the 2nd floating magnet, the generated induced voltage in coil 2 of the 2DOF generator system is higher than the generated induced voltage in coil 1 and induced voltage in the SDOF generator system. But the generated induced voltage in the SDOF system is much higher than the generated induced voltage in coil 1 of the 2DOF generator system. Moreover, when the force is applied on the 1st floating magnet, the generated induced voltage in coils 1 and 2 of the 2DOF generator system is lower than the generated induced voltage SDOF generator system. But the generated induced voltage coil 1 of the 2DOF generator system is much higher than coil 2. On the other hand, when the force is applied to both floating magnets, the generated induced voltage in coil 2 of the 2DOF generator system is higher than the generated induced voltage in coil 1. The generated voltage in coil 2 is higher than the generated induced voltage in the SDOF generator system. However, the generated voltage in coil 1 is almost similar to the generated voltage in the SDOF system. Therefore, overall, the 2DOF generator system is more efficient than the SDOF generator system.

9.5 Experimental Analysis

Sensor 1 was placed on the top of the 1st magnet (fixed magnet), and another sensor 2 was placed underneath the 4th magnet (top fixed magnet) to measure the displacement of the 1st and 2nd floating

magnets, respectively, as shown in Figure 9.1. The 1st and 2nd winding coils were connected with the 2nd and 3rd ports of the data acquisition system. When the experimental setup was finalised, the sensors were powered.

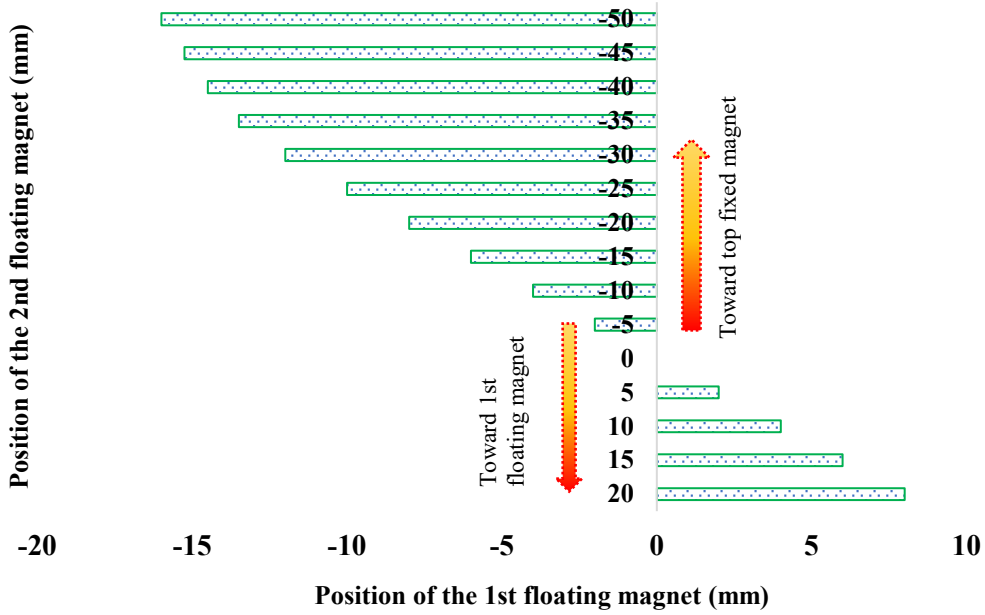

Figure 9.29: Changing position of the 1st floating magnet for changing the position of the 2nd floating magnet

Depending on the experimental design, the fishing line was connected with both floating magnets and a floating magnet. At first, the displacement of 1st floating magnet, which changed due to the changing position of the 2nd floating magnet, was measured. The measured displacement of the 1st floating magnet due to the movement of the 2nd floating magnet has presented in Figure 9.29. In Figure 9.29, the changing position of both floating magnets toward the top and bottom magnets are represented by negative (-) and positive (+) signs, respectively. Figure 9.29 shows that when the 2nd floating magnet moved toward the top fixed magnet by 5 mm, the 1st floating magnet moved by 2 mm toward the 1st floating magnet. Similarly, the 1st magnet moved by 2 mm toward the bottom magnet while the 2nd magnet moved toward the 1st floating magnet by 5 mm. Moreover, it can be seen from Figure 9.29 that for every 5 mm movement of the 2nd floating magnet, the 1st floating magnet moved by 2 mm.

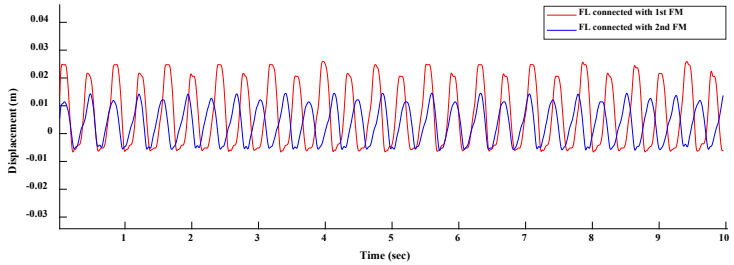

(a)

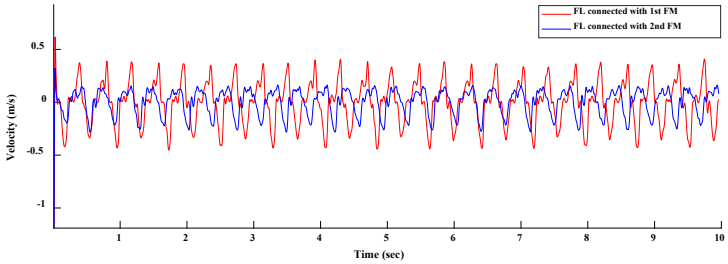

(b)

Figure 9.30: (a) Displacement and (b) velocity of the 1st floating magnet (FL: Fishing line, FM: Floating magnet)

The experimental work was performed by connecting the servo motor using the fishing line with the 2nd floating magnet and the 1st floating magnet (through the second floating magnet's plastic bush of the 2nd floating magnet). Same harmonic forces were applied for both setups, and the outcome was compared. Figure 9.30 and Figure 9.31 present the displacement and velocity of the 1st and 2nd floating magnets, respectively. The 1st floating magnet's displacement and velocity were higher during the pulling of the 1st floating magnet, and the 2nd floating magnet's displacement and velocity were higher during the pulling of the 2nd floating magnet. In Figure 9.30, the red line represents the displacement and velocity of the 1st floating magnet when the servo motor connected with the 1st floating magnet. The blue line represented the displacement and velocity of the 1st floating magnet when the servo motor connected with the 2nd floating magnet). Similarly, the red line represented the displacement and velocity of the 2nd floating magnet when the servo motor was connected with the 1st floating magnet, and the blue line represented the displacement and velocity of the 2nd floating magnet when the servo motor was connected with the 2nd floating magnet, as shown in Figure 9.31. The 1st floating magnet showed the maximum displacement and velocity, then 2nd floating magnet when the upward harmonic force was applied on the 1st floating magnet. The 2nd floating magnet showed the maximum displacement and velocity, then the 1st floating magnet when the same upward harmonic force was applied on the 2nd floating magnet, as presented in Figure 9.31.

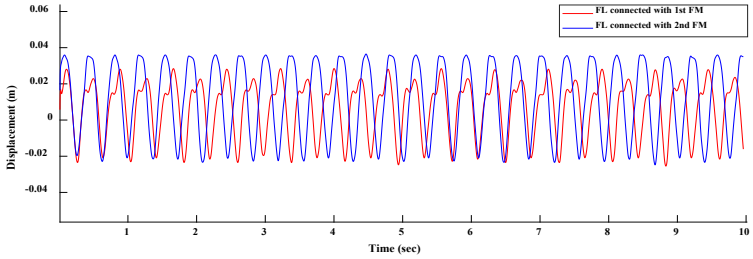

(a)

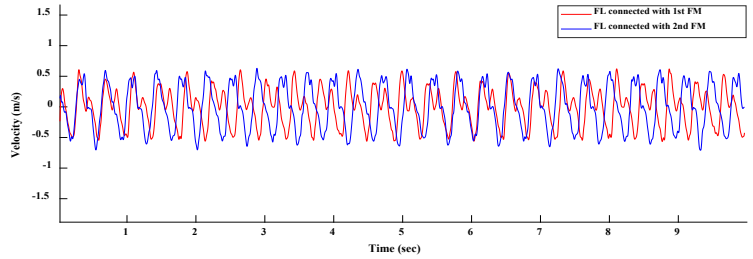

(b)

Figure 9.31: (a) Displacement and (b) velocity of the 2nd floating magnet (FL: Fishing line, FM: Floating magnet)

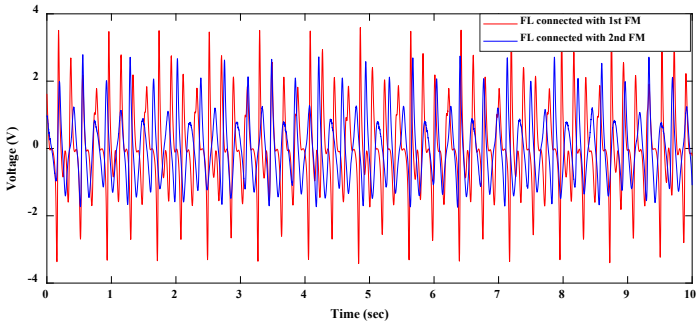

(a)

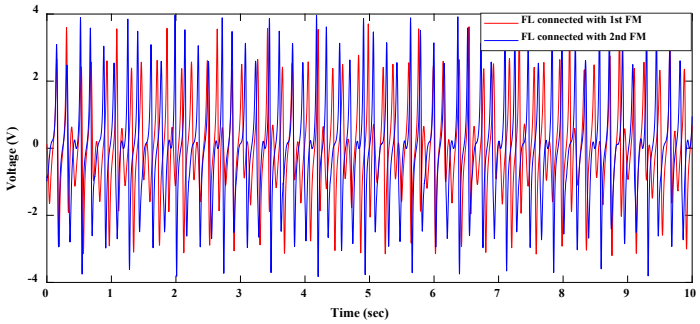

(b)

Figure 9.32: Induced voltages (a) 1st winding coil and (b) 2nd winding coil (FL: Fishing line, FM: Floating magnet)

By comparing Figure 9.30 and Figure 9.31, both floating magnets could achieve maximum displacement and velocity if the harmonic force was applied on the 1st floating. Because when the force was applied on the 2nd floating magnet, the 2nd floating magnet showed maximum displacement and velocity, but the 1st floating magnet's displacement and velocity were minimal compared to the 2nd floating magnet. Therefore, the 2nd winding coil showed more energy than the 1st. On the other hand, when the force was applied on the 1st floating magnet, both 1st and 2nd floating magnets showed almost the same displacement and velocity. Figure 9.32 displays the induced voltages of the energy harvester for both experimental setups. In Figure 9.32, the red line represented the induced voltage when the servo motor was connected with the 1st floating magnet. The blue line represented the induced voltage when the servo motor was connected with the 2nd floating magnet. Figure 9.32 showed that when force was applied to the 2nd floating magnet, the 2nd winding coil generated a higher induced voltage (3.9V) than the 1st winding coil (2.8V). But when the force was applied on the 1st floating magnet, the 1st and 2nd winding coils produced almost similar induced voltages of 3.5V and 3.6V, respectively.

9.5.1 Validation of the experimental results with analytical results

The 2DOF energy harvester test rig was developed and experimented with to validate the analytical model within the lab environment. The amplitude and frequency of the harmonic force were estimated from the applied torque of the servo motor. The same harmonic force was used in the analytical model to validate the analytical model with the experimental model. Different torques were applied to run the servo motor in the torque control mode for the experimental analysis, and the harmonic forces were estimated. For the experimental investigation, the projected amplitude and frequency of the harmonic force were 15N and 3.88Hz, respectively. The same amplitude and frequency of the harmonic force were applied in the analytical model and compared with the experimental results. Figure 9.33 displays the displacement and velocity of the 1st floating magnet, and Figure 9.34 shows the displacement and velocity of the 2nd floating magnet. In Figures 9.33 and 9.34, the blue and green lines represent the analytical and experimental measurements, respectively. During the analytical investigation, the 1st floating magnet moved toward the bottom magnet by about 17 mm and toward the 2nd floating magnet by around 21 mm, as presented by the blue line in Figure 9.33(a). The 1st floating magnet moved toward the 2nd floating magnet by 12 mm and toward the bottom by around 25 mm during the experimental analysis, as shown by the green line in Figure 9.33(a).

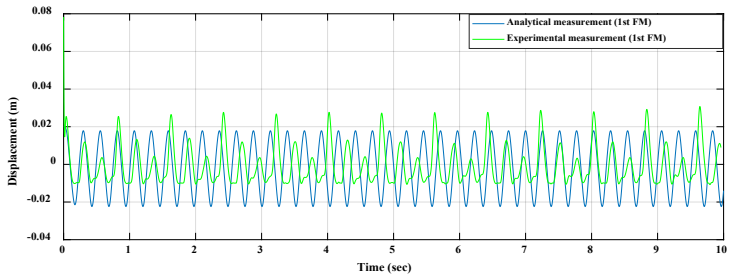

(a)

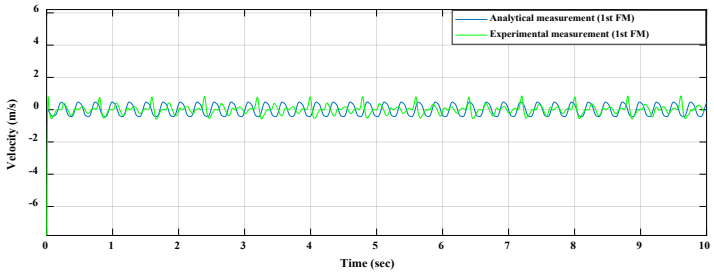

(b)

Figure 9.33: (a) Displacement and (b) velocity of the 1st floating magnet (FM: Floating magnet)

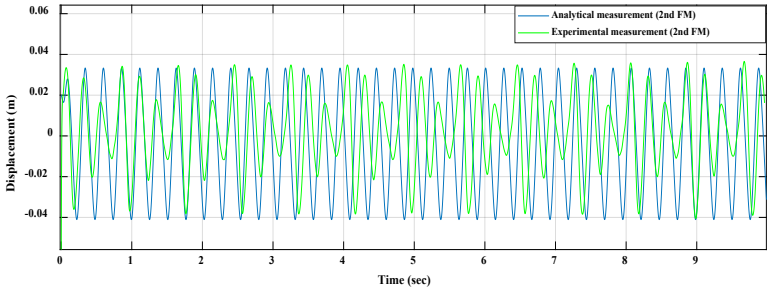

(a)

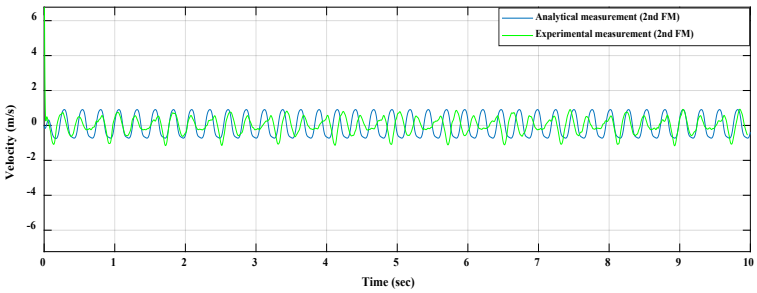

(b)

Figure 9.34: (a) Displacement and (b) velocity of the 2nd floating magnet (FM: Floating magnet)

On the other hand, the 2nd floating magnet moved toward the 1st floating magnet by about 34 mm and toward the top magnet by around 40 mm during analytical, as presented by the blue line in Figure 9.34(a). The 2nd floating magnet moved toward the top magnet by 38 mm and toward the 1st floating magnet by around 34 mm during the experimental analysis, as shown by the green line in Figure 9.34(a). The 1st floating magnet moved up and down with an average velocity of 0.09 m/s during experimental analysis and 0.085 m/s during the analytical study, as presented in Figure 9.34(b). On the other hand, the 2nd floating magnet moved up and down with an average velocity of 0.093 m/s during analytical analysis and 0.094 m/s during the experimental study, as presented in Figure 9.34(b). Figure 9.35 presents the induced voltage of the energy harvester.

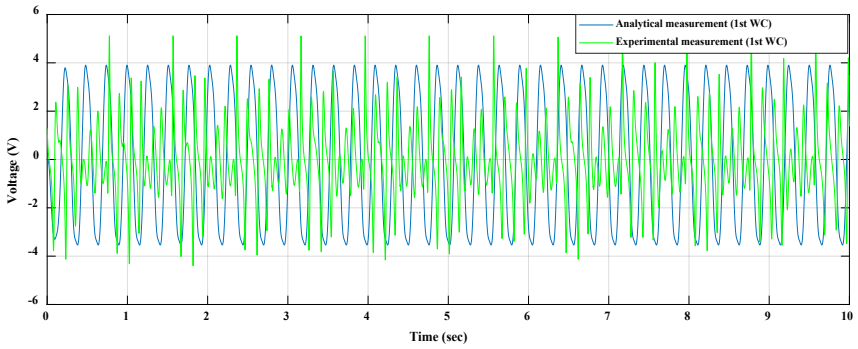

(a)

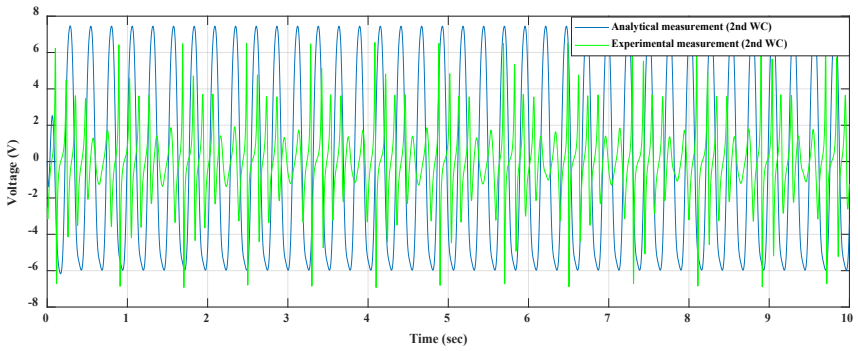

(b)

Figure 9.35: Induced voltages (a) 1st winding coil and (b) 2nd winding coil (WC: Winding coil)

Figures 9.33, 9.34 and 9.35 show that the analytical model is well validated with the experimental model. The blue and green lines in Figure 9.35 represent the induced voltage of the analytical and experimental measurements, respectively. In Figure 9.35, the induced voltage of the generator for analytical analysis has been compared with the experimental study. The measured average maximum induced voltage in winding coil 1 was 3.5V for analytical analysis and 5V for experimental analysis.

On the other hand, the measured average maximum induced voltage in winding coil 2 was 7.2V for analytical analysis and 7V for experimental investigation. Lastly, the analytical model has been validated with the experimental model by reducing the harmonic force frequency. The estimated amplitude and frequency of the harmonic force were 10N and 2.6Hz, respectively. Figures 9.36 and 9.37 show the displacement and velocity of the 1st and 2nd floating magnets, respectively. In Figures 9.36 and 9.37, the blue and red lines represent the analytical and experimental measurements, respectively.

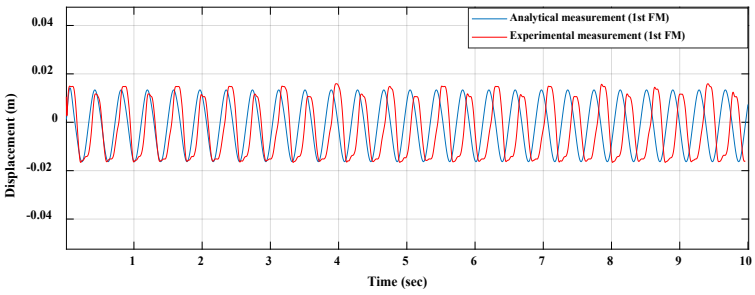

(a)

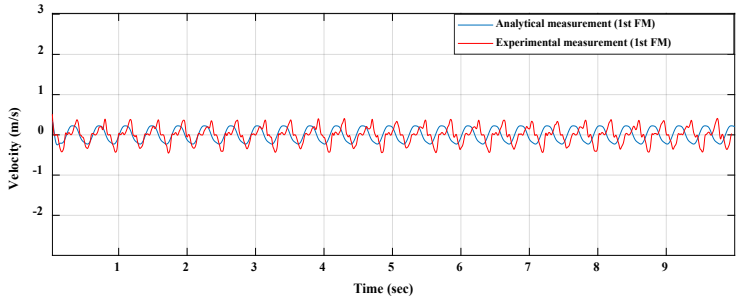

(b)

Figure 9.36: (a) Displacement and (b) velocity of the 1st floating magnet (FM: Floating magnet)

During the experimental investigation, the 1st floating magnet moved toward the bottom magnet by about 15 mm and toward the 2nd floating magnet by around 16 mm, as presented by the red line in Figure 9.36(a). The 1st floating magnet moved toward the 2nd floating magnet by 16 mm and toward the bottom by around 14 mm during the analytical analysis, as shown by the blue line in Figure 9.36(a).

On the other hand, the 2nd floating magnet moved toward the 1st floating magnet by about 22.5 mm and toward the top magnet by around 30 mm during analytical measurement, as presented by the blue line in Figure 9.37(a). The 2nd floating magnet moved toward the top magnet by 30 mm and toward

the 1st floating magnet by around 20.5 mm during the experimental analysis, as shown by the green line in Figure 9.37(a).

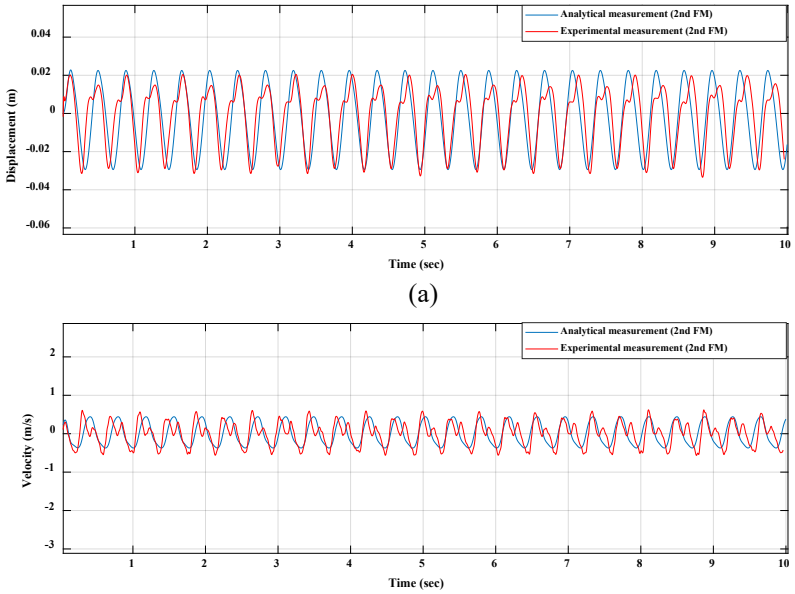

Figure 9.37: (a) Displacement and (b) velocity of the 2nd floating magnet (FM: Floating magnet)

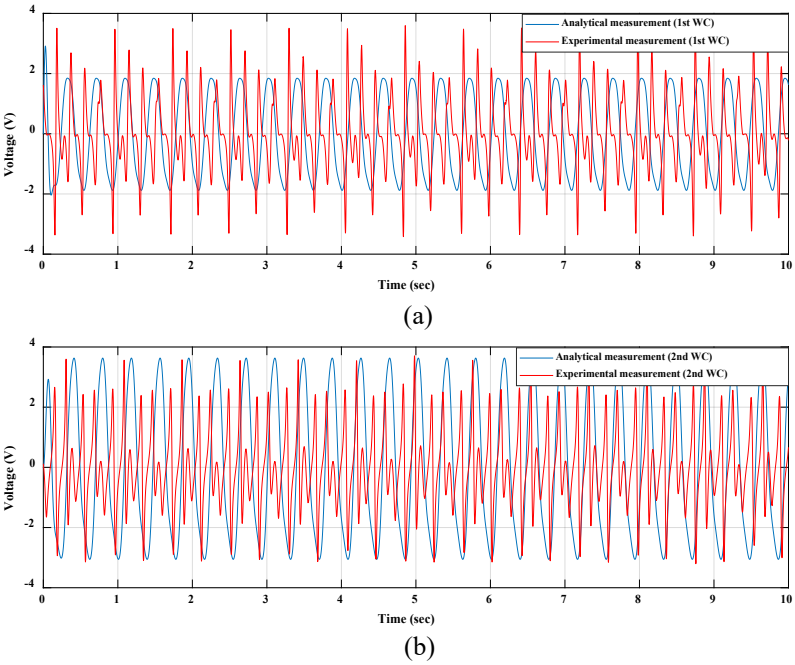

Figure 9.38: Induced voltages (a) 1st winding coil and (b) 2nd winding coil (WC: Winding coil)

The 1st floating magnet moved up and down with an average velocity of 0.3 m/s during experimental analysis and 0.25 m/s during the analytical study, as presented in Figure 9.36(b). On the other hand, the 2nd floating magnet moved up and down with an average velocity of 0.45 m/s during analytical analysis and 0.5 m/s during the experimental study, as presented in Figure 9.37(b). Figure 9.38 illustrates the induced voltage of the energy harvester. The blue and red lines in Figure 9.38 represent the induced voltage of the analytical and experimental measurements, respectively. The measured average maximum induced voltage in winding coil 1 was 2.9V for analytical analysis and 3.4V for experimental study. On the other hand, the measured average maximum induced voltage in winding coil 2 was 3.61V for analytical analysis and 3.57V for experimental investigation. Figure 9.36, Figure 9.37 and Figure 9.38 show that the analytical model is well validated with the experimental model.

9.6 Conclusion

The aim of this chapter was to study the 2DOF magnetic spring-based energy generator. The dynamics of the proposed 2DOF energy harvester were investigated using analytical and experimental methods. The magnetic properties of the proposed energy harvester were measured numerically. The eigenvalues and frequency responses due to the movement of both floating magnets were measured analytically. The effects of the electromechanical coupling on the 2DOF oscillator system were analysed. The state space model of the 2DOF energy harvester was solved using MATLAB ode23t solver. The 2DOF energy harvester model was compared with the SDOF model, which showed the 2DOF energy harvester is more capable of harnessing ocean energy due to two resonances. The test rig design of the 2DOF energy harvester was developed in the lab for experimental analysis, and the experimental works were performed by changing different parameters. Lastly, the outcomes of the experimental works were validated with the analytical model's outcomes.

Chapter 10
Theoretical and Experimental Study of 3DOF Magnetic Spring-based Electromagnetic Generator

The resonant power and efficiency of the three-degree-of-freedom nonlinear oscillators are expected to be larger than those with two-degree-of-freedom (2DOF) and single-degree-of-freedom (SDOF) nonlinear oscillator systems. Moreover, using the three-degree-of-freedom nonlinear oscillators is estimated to advance higher operational frequency bandwidth than the 2DOF and SDOF nonlinear oscillators. Three floating magnets are expected to generate maximum magnetic flux density in the system than the two and single floating magnet-based system. In Chapter 6, the analytical, numerical and experimental model of the three-degree-of-freedom (3DOF) magnetic spring-based oscillator system has been discussed with validation. However, the energy generation part was not included during the analysis of the 3DOF system in Chapter 6. This chapter deals with energy generation techniques based on 3DOF magnetic spring-based oscillator systems and their behaviour with various design criteria. This chapter will discuss the dynamics and energy generation ability of the 3DOF magnetic spring-based energy harvester analytically and experimentally for different frequency ranges.

10.1 The Architecture of the Three-degree-of-freedom (3DOF) Energy Harvester

The basic architecture of the energy harvester contains five-ring permanent magnets (axially magnetised), a circular shaft and winding coils. The 3DOF energy harvester is designed so that every function's magnetic restoring forces and induced voltage should not affect or influence each magnet's magnetic field, particularly when the floating magnets are moving. Due to the movement of all floating magnets inside the winding coil, the cogging force is usually created. Minimising the generated harmful cogging force from magnets and coils movement is essential. Different nonmagnetic materials have been used to avoid magnetic field interference. The polarity of the magnets is arranged so that the levitating magnet experiences a repulsive force because of the fixed magnets. Few multilayer coils are attached around the outer surface of the two floating magnets. The magnetic poles are oriented (NS-SN-NS-SN-NS) to repel each other. The height and width of the test rig are 550 mm and 300 mm, respectively.

Moreover, the height and diameter of the shaft are 550 mm and 12 mm, respectively. For the test rig design, as presented in Figure 10.1, the equilibrium height of the 3DOF oscillator is 372 mm. For the equilibrium position, the separation distance between the 1st and 2nd magnet is 59 mm, and the distance between the 2nd and 3rd magnet is 65 mm. Moreover, the distance between the 3rd and 4th magnet is 79 mm, and the separation distance between the 4th and 5th is 104 mm. Three winding coils have been added to the test rig, and both winding coils have been connected to the data acquisition system to capture the induced voltages. A floating magnet connected the servo motor using a fishing line.

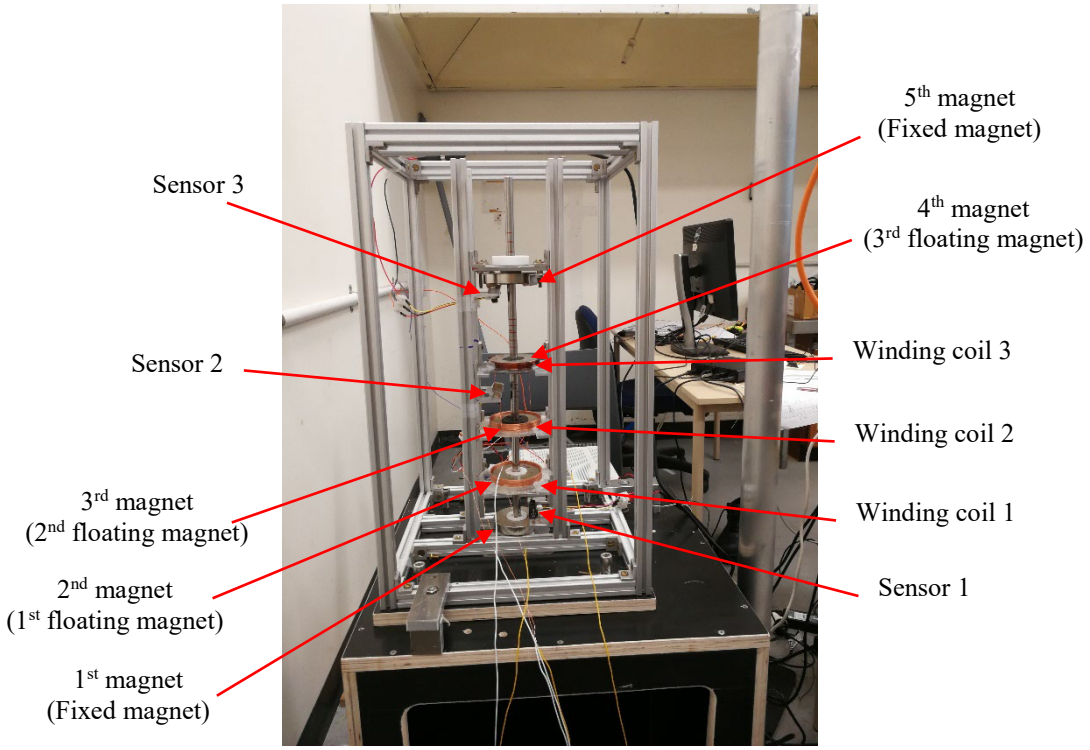

Figure 10.1: 3DOF electromagnetic generator

10.2 Numerical Simulation of the 3DOF Magnetic Spring-based Electromagnetic Generator/ Energy Harvester System

The FEA of the 3DOF magnetic spring-based electromagnetic generator/energy harvester model has been discussed in this chapter. The proposed 3DOF generator model has been analysed as a 2D axisymmetric model, as shown in Figure 10.2(a). Three winding coils (100 turns each) have been placed on the top surfaces of each floating magnet. The permanent magnets and winding coil properties can be seen in Table 3.1 and Table 8.1, respectively.

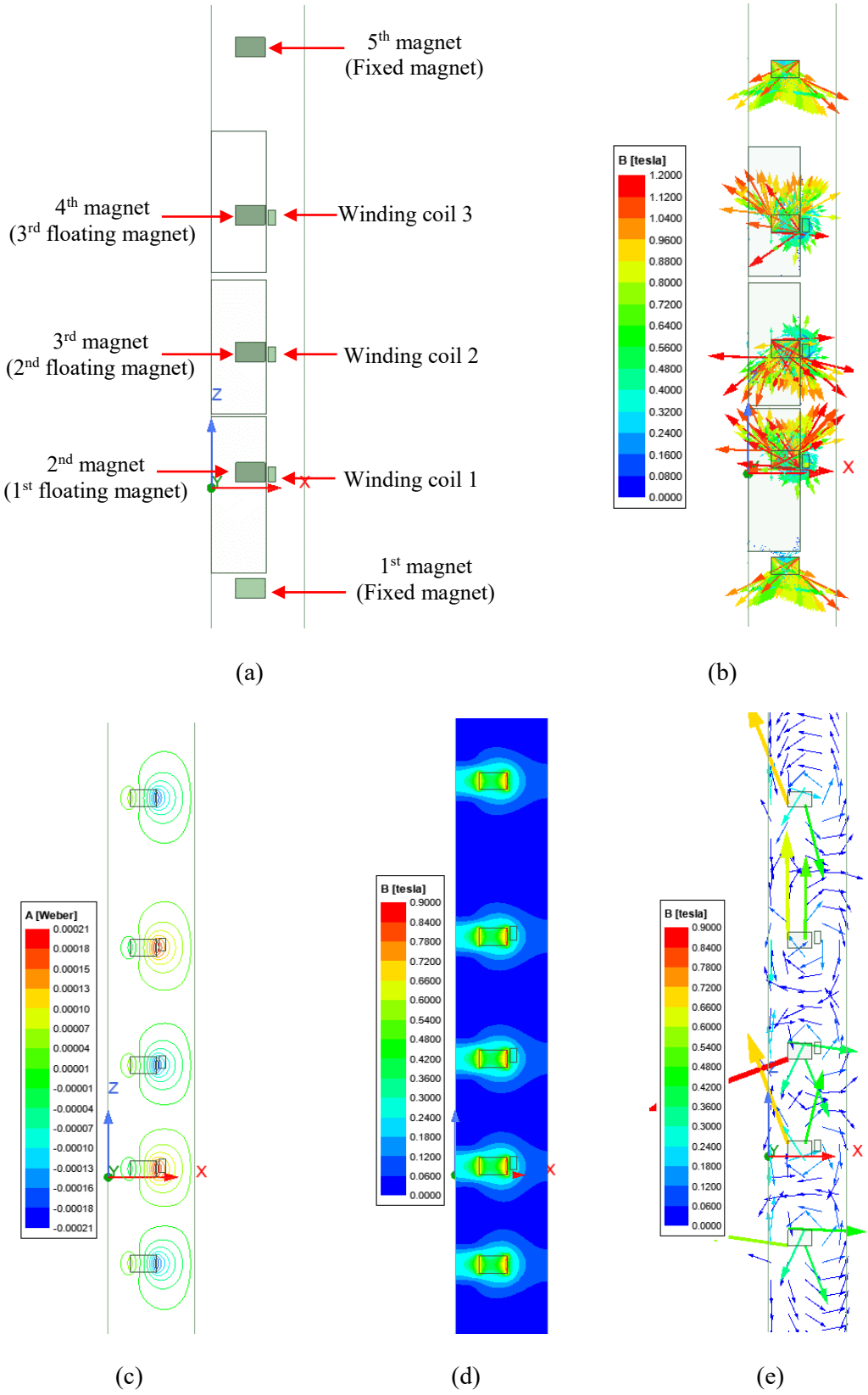

Figure 10.2: (a) Magnetisation direction and (b) Flux line, (c) Magnetic flux (Mag_B) and (c) B_Vector

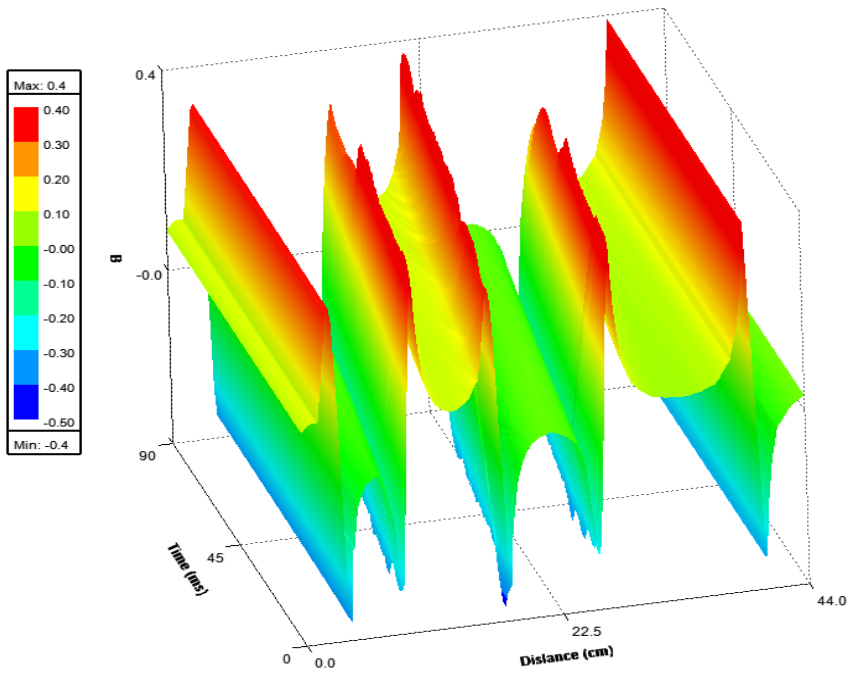

(a)

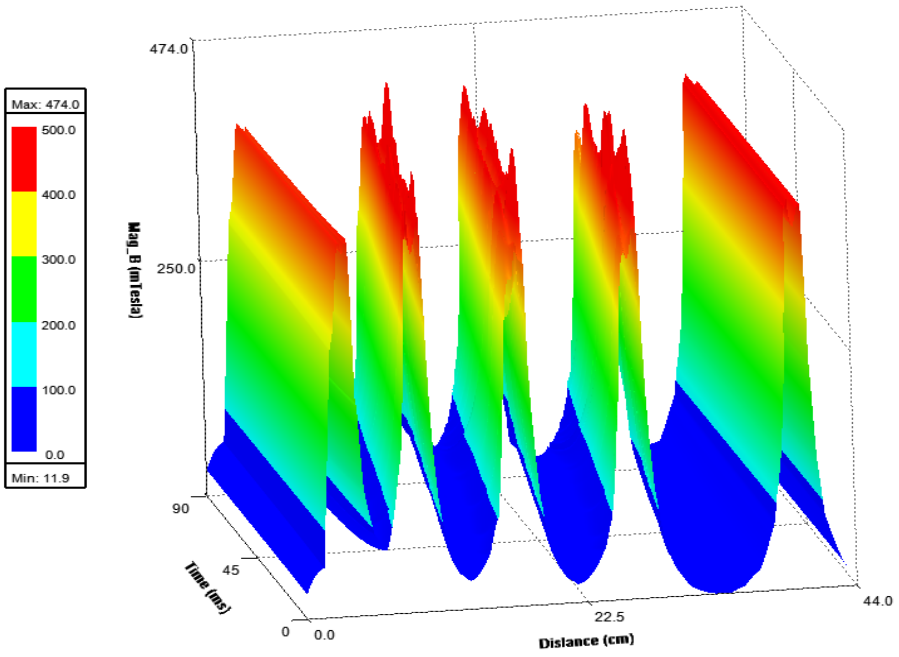

(b)

Figure 10.3: Magnetic flux densities for different positions of both floating magnets (a) B_Vector and (b) Mag_B

The numerical analysis of the 3DOF magnetic spring-based oscillator system can be seen in Chapter 6. In this section, the 3DOF oscillator system has been investigated by adding three winding coils.

The simulation was run using constant velocity for all three floating magnets during the transient solution. The magnetisation direction of all magnets, flux line, flux linkage, magnetic flux density and induced voltages have been investigated. Figure 10.2(b) shows the magnetisation direction of all 5 magnets, and Figure 10.2(c) presents the flux line of all 5 magnets. The arrows in Figure 10.2(b) represent the magnetisation directions of all permanent magnets. The maximum flux lines can be seen on the outside surfaces of each magnet and inside the coil area, as presented in Figure 10.2(c). The magnetic flux (Mag_B) and magnetic flux (B_Vector) of the 3DOF electromagnetic generator have been shown in Figure 10.2(d) and Figure 10.2(e). A constant velocity was used to move all floating magnets to analyse the magnetic flux densities. As shown in Figure 10.2(d), the colour represents the magnetic flux density of the generator system. The higher flux density is visible around the permanent magnet area, characterised by colour variations. According to Figure 10.2(e), the magnetic flux lines originated from the North Pole and travelled to the South Pole, and they travelled through the inside coil of the magnet. Copper coils generate induced voltage when they are cut by magnetic flux. Magnetic flux densities of the generator also changed over time, along with the positions of the floating magnets. In Figure 10.3, the magnetic flux densities of the 1st, 2nd, and 3rd floating magnets changed as the 1st, 2nd, and 3rd floating magnets moved with the changing time.

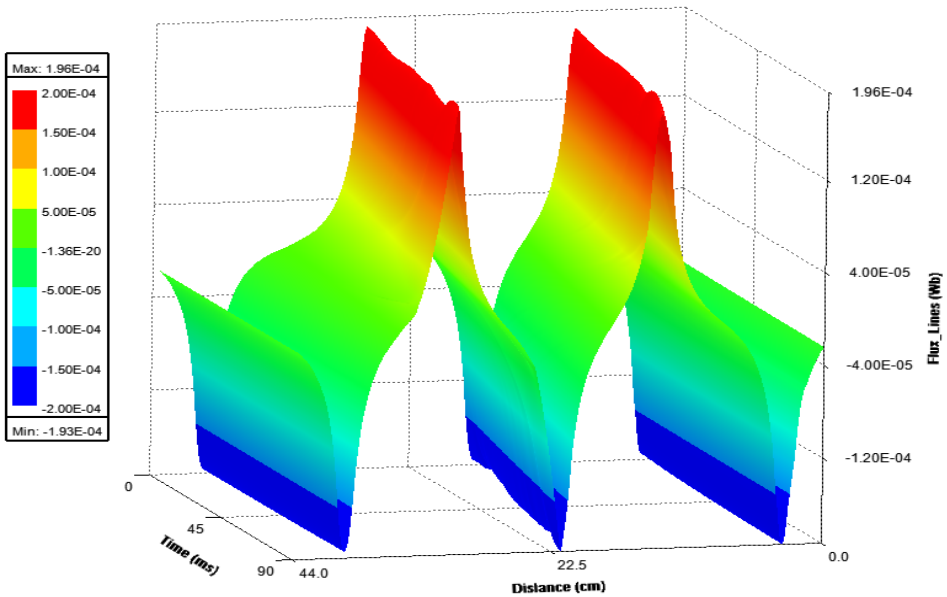

Figure 10.4: Flux lines for different positions of the floating magnet

On the other hand, the 1st and 5th magnets were fixed; therefore, their magnetic flux densities did not change with time. For different positions of floating magnets, Figure 10.3 shows the changes in

magnetic flux densities. The flux line changed with changing the positions of all floating magnets, as shown in Figure 10.4. The induced voltage is generated inside the winding coil when the magnetic flux cuts the copper coil. Figure 10.5 displays the generated induced voltages and flux linkages in the winding coils when all floating magnets move with the constant velocity of 0.5 m/s.

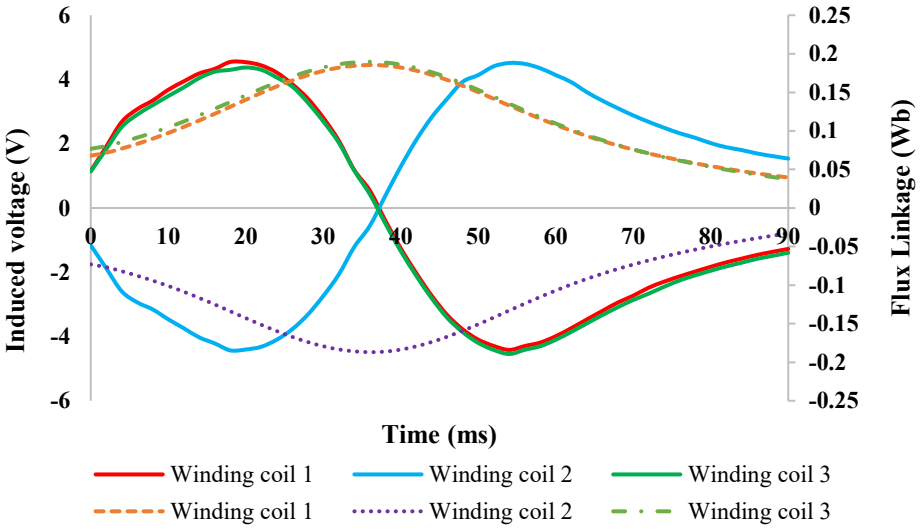

Figure 10.5: Induced voltage and flux Linkage in the winding coil

The legend in the Figure 10.5 represent the winding coils (all solid lines for induced voltage and doted lines for flux linkage). From Figure 10.5, it can be seen that the induced voltages in winding coils 1, 2 and 3 were zero when the flux linkages in winding coils 1, 2 and 3 were maximum, respectively. The flux linkage in the winding coil 1 and 3 remained positive during the excitation of the floating magnets because the magnetisation direction of the 1st and 3rd floating magnets was upward. Since all floating magnets moved with the same constant velocity (0.5 m/s), all winding coils generated the same induced voltages. The magnetisation direction of the 2nd floating magnet was downward; therefore, the flux linkage remained negative during the movement of the floating magnets. The magnetisation directions for all magnets can be seen in Figure 10.2(b).

10.3 Mathematical Model of the 3DOF Energy Harvester

When the external force is applied to a floating magnet or any floating magnet moves up and down, it creates the magnetic spring's elastic restoring force. Figure 10.6 and Figure 10.7 display the free-body diagrams of the proposed 3DOF nonlinear oscillator system. The masses of the 2nd (1st floating magnet), 3rd (2nd floating magnet) and 4th (3rd floating magnet) magnets are M_2, M_3 and M_4,

respectively. The relative displacement of the 1st floating magnet is y_2 and the relative velocity and acceleration of the 1st floating magnet are $\dot{y}_2$ and $\ddot{y}_2$, respectively. The relative displacement, velocity and acceleration of the 2nd floating magnet are y_3, $\dot{y}_3$ and $\ddot{y}_3$, respectively. Moreover, the relative displacement, velocity and acceleration of the 3rd floating magnet are y_4, $\dot{y}_4$ and $\ddot{y}_4$, respectively. The magnetic flux density of the 2nd magnet (1st floating magnet) is $B_{1(y)}$ and the total length of the 1st winding coil is l_1.

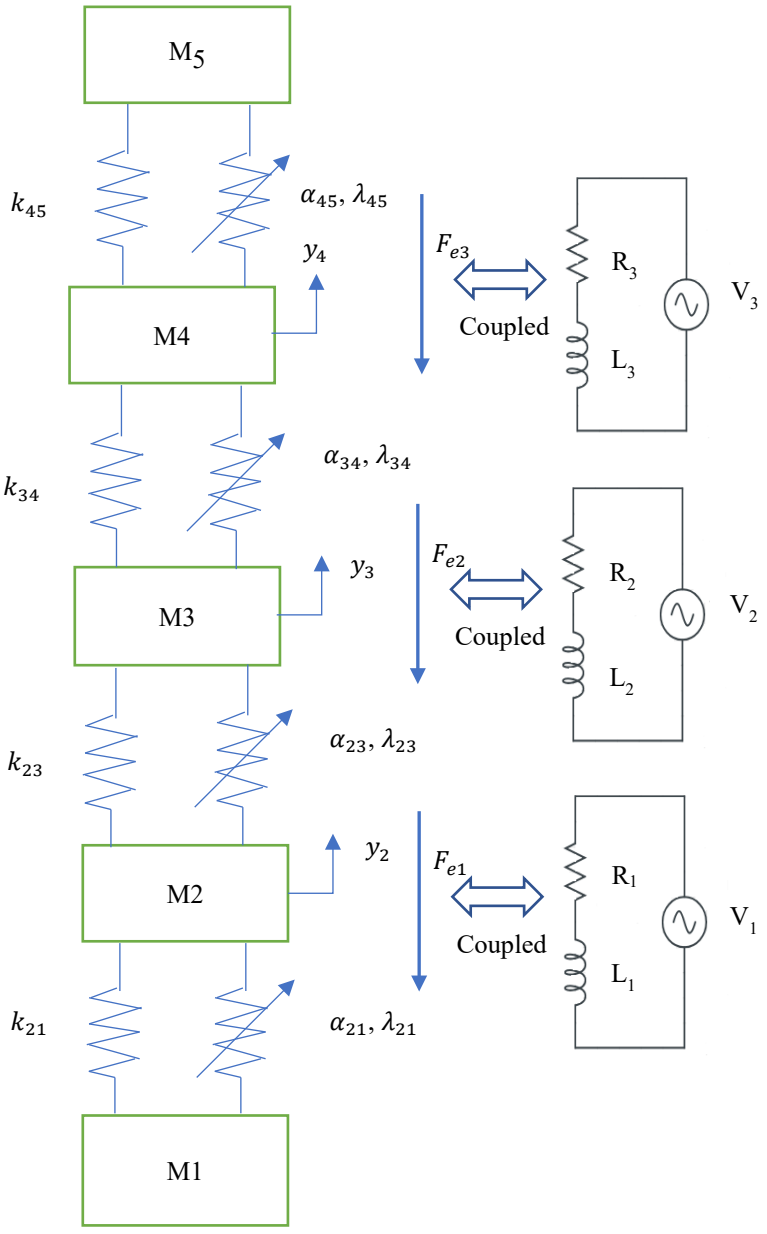

Figure 10.6: Three-degree-of-freedom magnetic spring-based oscillator system

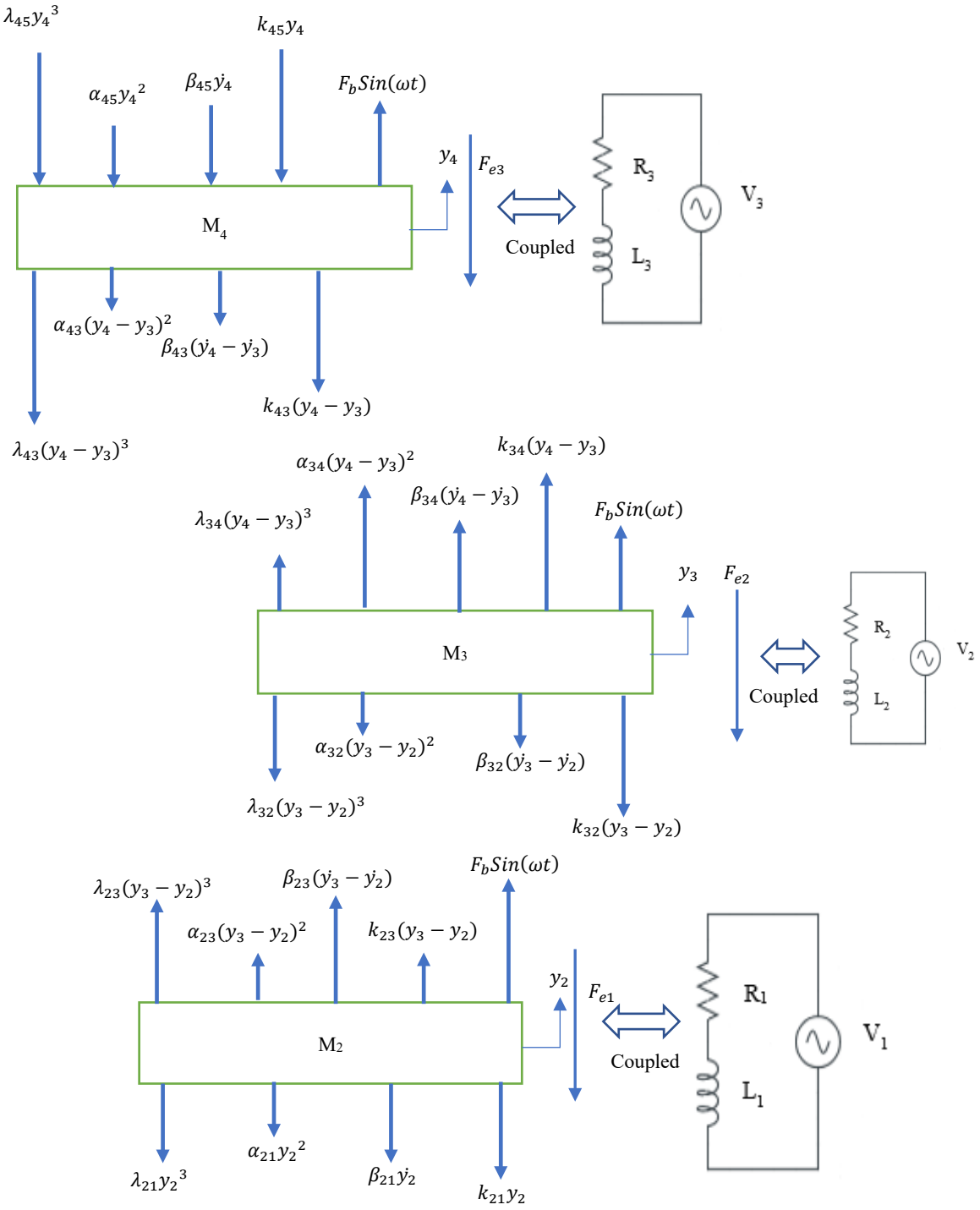

Figure 10.7: Free body diagram

The magnetic flux density of the 3rd magnet (2nd floating magnet) is $B_{2(y)}$ and the total length of the 2nd winding coil is l_2. Similarly, the magnetic flux density of the 4th magnet (3rd floating magnet) is $B_{3(y)}$ and the total length of the 3rd winding coil is l_3.

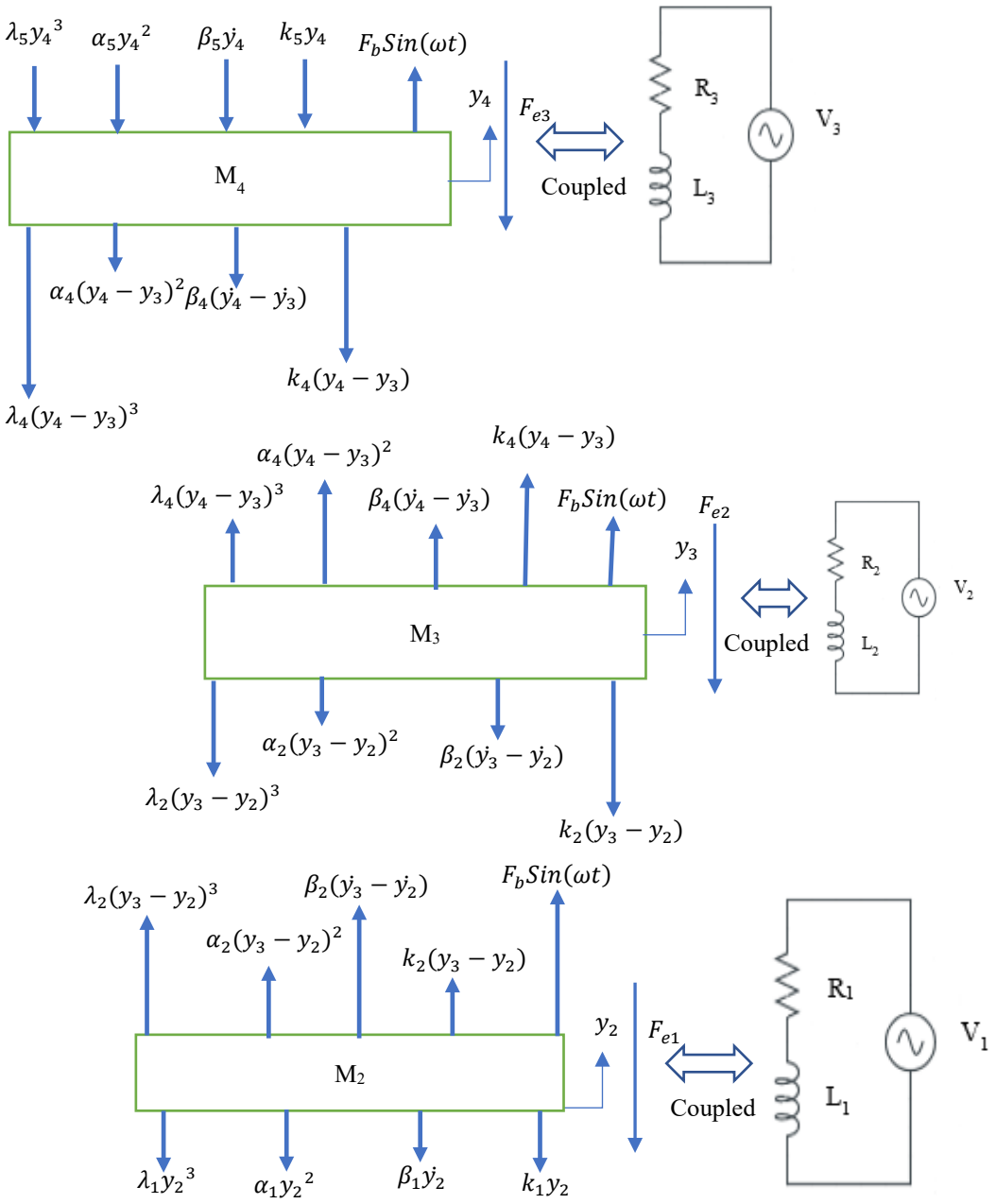

Figure 10.8: Free body diagram

The electromagnetic coupling coefficients are $a_1(a_1 = B_{1(y)}l_1)$, $a_2(a_2 = B_{2(y)}l_2)$ and $a_3(a_3 = B_{3(y)}l_3)$. Moreover, F_{e1}, F_{e2} and F_{e3} are the electromagnetic forces written as $F_{e1} = a_1 I_1$, $F_{e2} = a_2 I_2$ and $F_{e3} = a_3 I_3$ respectively. The damping forces of the 1st floating magnet is $F_{\beta 1} = \beta_1 \dot{y}_2$ 2nd floating magnet is $F_{\beta 3} = \beta_3 \dot{y}_3$ and 3rd floating magnet is $F_{\beta 5} = \beta_5 \dot{y}_4$. The linear stiffness of the 1st, 2nd, and 3rd floating magnets are k_1, k_3 and k_5, respectively. During the 3rd order Taylor series, the nonlinear stiffnesses of the 1st floating magnet are α_1 and λ_1 and for the 2nd floating magnet, are α_3 and λ_3.

Furthermore, the nonlinear stiffnesses of the 3rd floating magnet are α_5 and λ_5. Furthermore, in Figure 10.7, the linear stiffness $k_{21} = k_1, k_{23} = k_{32} = k_2, k_{34} = k_{43} = k_4$ and $k_{45} = k_5$. The damping constants $\beta_{21} = \beta_1, \beta_{23} = \beta_{32} = \beta_2, \beta_{34} = \beta_{43} = \beta_4$ and $\beta_{45} = \beta_5$.The nonlinear coefficients $\alpha_{21} = \alpha_1, \alpha_{23} = \alpha_{32} = \alpha_2, \alpha_{34} = \alpha_{43} = \alpha_4$ and $\alpha_{45} = \alpha_5$. In addition, the other nonlinear stiffness $\lambda_{21} = \lambda_1, \lambda_{23} = \lambda_{32} = \lambda_2, \lambda_{34} = \lambda_{43} = \lambda_4$ and $\lambda_{45} = \lambda_5$. Figure 10.8 replaces Figure 10.7 after replacing the linear and nonlinear coefficient values. The dynamic equation of the motion of the system can be written as,

$$M_2\ddot{y}_2 + \beta_1\dot{y}_2 - \beta_2(\dot{y}_3 - \dot{y}_2) + k_1y_2 - k_2(y_3 - y_2) + \alpha_1{y_2}^2 - \alpha_2(y_3 - y_2)^2 + \lambda_1{y_2}^3 - \lambda_2(y_3 - y_2)^3 + B_1l_1\frac{V_1}{R_1} = F_1Sin(\omega t) \quad (10.1)$$

$$M_3\ddot{y}_3 + \beta_2(\dot{y}_3 - \dot{y}_2) - \beta_4(\dot{y}_4 - \dot{y}_3) + k_2(y_3 - y_2) - k_4(y_4 - y_3) + \alpha_2(y_3 - y_2)^2 - \alpha_4(y_4 - y_3)^2 + \lambda_2(y_3 - y_2)^3 - \lambda_4(y_4 - y_3)^3 + B_2l_2\frac{V_2}{R_2} = F_2Sin(\omega t) \quad (10.2)$$

$$M_4\ddot{y}_4 + \beta_5\dot{y}_4 + \beta_4(\dot{y}_4 - \dot{y}_3) + k_5y_4 + k_4(y_4 - y_3) + \alpha_5{y_4}^2 + \alpha_4(y_4 - y_3)^2 + \lambda_5{y_4}^3 + \lambda_4(y_4 - y_3)^3 + B_3l_3\frac{V_3}{R_3} = F_3Sin(\omega t) \quad (10.3)$$

$$V_1 + \frac{L_1}{R_1}\dot{V}_1 = B_1l_1\dot{y}_2 \quad (10.4)$$

$$V_2 + \frac{L_2}{R_2}\dot{V}_2 = B_2l_2\dot{y}_3 \quad (10.5)$$

$$V_3 + \frac{L_3}{R_3}\dot{V}_3 = B_3l_3\dot{y}_4 \quad (10.6)$$

Equation 10.1 can rewrite as,

$$M_2\ddot{y}_2 + (\beta_1 + \beta_2)\dot{y}_2 - \beta_2\dot{y}_3 + (k_1 + k_2 + \alpha_1y_2 - \alpha_2y_2 + \lambda_1{y_2}^2 + \lambda_2{y_2}^2 + 2\alpha_2y_3 + 3\lambda_2{y_3}^2)y_2 - (k_2 + 3\lambda_2{y_2}^2 + \alpha_2y_3 + \lambda_2{y_3}^2)y_3 + B_1l_1\frac{V_1}{R_1} = F_1Sin(\omega t) \quad (10.7)$$

Equation 10.2 can be rewritten as,

$$M_3\ddot{y}_3 - \beta_2\dot{y}_2 + (\beta_2 + \beta_4)\dot{y}_3 - \beta_4\dot{y}_4 - (k_2 - \alpha_2y_2 + 2\alpha_2y_3 + \lambda_2{y_2}^2 + 3\lambda_2{y_3}^2)y_2 + (k_2 + k_4 + \alpha_2y_3 - \alpha_4y_3 + 2\alpha_4y_4 + \lambda_2{y_3}^2 + 3\lambda_2{y_2}^2 + \lambda_4{y_3}^2 + 3\lambda_4{y_4}^2)y_3 - (k_4 + \alpha_4y_4 + \lambda_4{y_4}^2 + 3\lambda_4{y_3}^2)y_4 + B_2l_2\frac{V_2}{R_2} = F_2Sin(\omega t) \quad (10.8)$$

Equation 10.3 can be expressed as,

$$M_4\ddot{y}_4 + (\beta_5 + \beta_4)\dot{y}_4 - \beta_4\dot{y}_3 - (k_4 + 2\alpha_4 y_4 - \alpha_4 y_3 + \lambda_4 {y_3}^2 + 3\lambda_4 {y_4}^2)y_3 + (k_5 + k_4 + \alpha_5 y_4 + \alpha_4 y_4 + \lambda_5 {y_4}^2 + \lambda_4 {y_4}^2 + 3\lambda_4 {y_3}^2)y_4 + B_3 l_3 \frac{V_3}{R_3} = F_3 Sin(\omega t) \quad (10.9)$$

The equations 10.4, 10.5 and 10.6 can be expressed as,

$$\frac{L_1}{R_1}\dot{V}_1 = B_1 l_1 \dot{y}_2 - V_1 \quad (10.10)$$

$$\frac{L_2}{R_2}\dot{V}_2 = B_2 l_2 \dot{y}_3 - V_2 \quad (10.11)$$

$$\frac{L_3}{R_3}\dot{V}_3 = B_3 l_3 \dot{y}_4 - V_3 \quad (10.12)$$

State space variables can be used to solve equations (10.7, 10.8, 10.9, 10.10, 10.11 and 10.12). State space variables can be defined as:

$$x_1 = y_2 \quad (10.13)$$

$$x_2 = \dot{y}_2 = \frac{dx_1}{dt} \quad (10.14)$$

$$\frac{dx_2}{dt} = \ddot{y}_2 \quad (10.15)$$

$$x_3 = y_3 \quad (10.16)$$

$$x_4 = \frac{dx_3}{dt} = \dot{y}_3 \quad (10.17)$$

$$\frac{dx_4}{dt} = \ddot{y}_3 \quad (10.18)$$

$$x_5 = y_4 \quad (10.19)$$

$$x_6 = \frac{dx_5}{dt} = \dot{y}_4 \quad (10.20)$$

$$\frac{dx_6}{dt} = \ddot{y}_4 \quad (10.21)$$

$$x_7 = V_1 \quad (10.22)$$

$$\dot{V}_1 = \frac{dx_7}{dt} \quad (10.23)$$

$$x_8 = V_2 \quad (10.24)$$

$$\frac{dx_8}{dt} = \dot{V}_2 \tag{10.25}$$

$$x_9 = V_2 \tag{10.26}$$

$$\frac{dx_9}{dt} = \dot{V}_2 \tag{10.27}$$

$$u = F_1 Sin(\omega t) = F_2 Sin(\omega t) = F_3 Sin(\omega t) \tag{10.28}$$

Equation 10.7 can be written as

$$\frac{dx_2}{dt} = \ddot{y}_2 = \frac{1}{M_2}[u - (\beta_1 + \beta_2)x_2 + \beta_2 x_4 - (k_1 + k_2 + \alpha_1 x_1 - \alpha_2 x_1 + \lambda_1 {x_1}^2 + \lambda_2 {x_1}^2 + 2\alpha_2 x_3 + 3\lambda_2 {x_3}^2)x_1 + (k_2 + 3\lambda_2 {x_1}^2 + \alpha_2 x_3 + \lambda_2 {x_3}^2)x_3 - \frac{B_1 l_1}{R_1} x_7] \tag{10.29}$$

The flowing variables can be assumed as,

$$P1 = (k_1 + k_2 + \alpha_1 x_1 - \alpha_2 x_1 + \lambda_1 {x_1}^2 + \lambda_2 {x_1}^2 + 2\alpha_2 x_3 + 3\lambda_2 {x_3}^2) \tag{10.30}$$

$$Q1 = (k_2 + 3\lambda_2 {x_1}^2 + \alpha_2 x_3 + \lambda_2 {x_3}^2) \tag{10.31}$$

The equation 10.29 can be written as,

$$\frac{dx_2}{dt} = \ddot{y}_2 = \frac{1}{M_2}\left[u - P1x_1 - (\beta_1 + \beta_2)x_2 + Q1x_3 + \beta_2 x_4 - \frac{B_1 l_1}{R_1} x_7\right] \tag{10.32}$$

Equation 10.8 can be stated as,

$$\frac{dx_4}{dt} = \ddot{y}_3 = \frac{1}{M_3}\Big[u + (k_2 - \alpha_2 x_1 + 2\alpha_2 x_3 + \lambda_2 {x_1}^2 + 3\lambda_2 {x_3}^2)x_1 + \beta_2 x_2 - (k_2 + k_4 + \alpha_2 x_3 - \alpha_4 x_3 + 2\alpha_4 x_5 + \lambda_2 {x_3}^2 + 3\lambda_2 {x_1}^2 + \lambda_4 {x_3}^2 + 3\lambda_4 {x_5}^2)x_3 - (\beta_2 + \beta_4)x_4 + \left(k_4 + \alpha_4 x_5 + \lambda_4 {x_5}^2 + 3\lambda_4 {x_3}^2\right)x_5 + \beta_4 x_6 - \frac{B_2 l_2}{R_2} x_8\Big] \tag{10.33}$$

The flowing variables can be considered as,

$$R1 = (k_2 - \alpha_2 x_1 + 2\alpha_2 x_3 + \lambda_2 {x_1}^2 + 3\lambda_2 {x_3}^2) \tag{10.34}$$

$$J1 = (k_2 + k_4 + \alpha_2 x_3 - \alpha_4 x_3 + 2\alpha_4 x_5 + \lambda_2 {x_3}^2 + 3\lambda_2 {x_1}^2 + \lambda_4 {x_3}^2 + 3\lambda_4 {x_5}^2) \tag{10.35}$$

$$E1 = (k_4 + \alpha_4 x_5 + \lambda_4 {x_5}^2 + 3\lambda_4 {x_3}^2) \tag{10.36}$$

Equation 10.33 can be rewritten as

$$\frac{dx_4}{dt} = \ddot{y}_3 = \frac{1}{M_3}\left[u + R1x_1 + \beta_2 x_2 - J1x_3 - (\beta_2 + \beta_4)x_4 + E1x_5 + \beta_4 x_6 - \frac{B_2 l_2}{R_2}x_8\right] \quad (10.37)$$

Equation 10.9 can be written as

$$\frac{dx_6}{dt} = \ddot{y}_4 = \frac{1}{M_4}\left[u + (k_4 - \alpha_4 x_3 + 2\alpha_4 x_5 + \lambda_4 {x_3}^2 + 3\lambda_4 {x_5}^2)x_3 + \beta_4 x_4 - (k_5 + k_4 + \alpha_5 x_5 + \alpha_4 x_5 + \lambda_5 {x_5}^2 + \lambda_4 {x_5}^2 + 3\lambda_4 {x_3}^2)x_5 - (\beta_5 + \beta_4)x_6 - \frac{B_3 l_3}{R_3}x_9\right] \quad (10.38)$$

Equation 10.38 can be shortened using the following parameters:

$$U1 = (k_4 - \alpha_4 x_3 + 2\alpha_4 x_5 + \lambda_4 {x_3}^2 + 3\lambda_4 {x_5}^2) \quad (10.39)$$

$$V1 = (k_5 + k_4 + \alpha_5 x_5 + \alpha_4 x_5 + \lambda_5 {x_5}^2 + \lambda_4 {x_5}^2 + 3\lambda_4 {x_3}^2) \quad (10.40)$$

Equation 10.38 can be stated as

$$\frac{dx_6}{dt} = \ddot{y}_4 = \frac{1}{M_4}\left[u + U1x_3 + \beta_4 x_4 - V1x_5 - (\beta_5 + \beta_4)x_6 - \frac{B_3 l_3}{R_3}x_9\right] \quad (10.41)$$

Equations 10.10, 10.11 and 10.12 can be written as,

$$\frac{dx_7}{dt} = \frac{R_1 B_1 l_1}{L_1}x_2 - \frac{R_1}{L_1}x_7 \quad (10.42)$$

$$\frac{dx_8}{dt} = \frac{R_2 B_2 l_2}{L_2}x_4 - \frac{R_2}{L_2}x_8 \quad (10.43)$$

$$\frac{dx_9}{dt} = \frac{R_3 B_3 l_3}{L_3}x_6 - \frac{R_3}{L_3}x_9 \quad (10.44)$$

The state space model of the 3DOF system can be written as

$$\begin{bmatrix} \frac{dx_1}{dt} \\ \frac{dx_2}{dt} \\ \frac{dx_3}{dt} \\ \frac{dx_4}{dt} \\ \frac{dx_5}{dt} \\ \frac{dx_6}{dt} \\ \frac{dx_7}{dt} \\ \frac{dx_8}{dt} \\ \frac{dx_9}{dt} \end{bmatrix} = \underbrace{\begin{bmatrix} 0 & 1 & 0 & 0 & 0 & 0 & 0 & 0 & 0 \\ \frac{-P1}{M_2} & \frac{-(\beta_1+\beta_2)}{M_2} & \frac{Q1}{M_2} & \frac{\beta_2}{M_2} & 0 & 0 & -\frac{B_1 l_1}{M_2 R_1} & 0 & 0 \\ 0 & 0 & 0 & 1 & 0 & 0 & 0 & 0 & 0 \\ \frac{R1}{M_3} & \frac{\beta_2}{M_3} & \frac{-J1}{M_3} & \frac{-(\beta_2+\beta_4)}{M_3} & \frac{E1}{M_3} & \frac{\beta_4}{M_3} & 0 & -\frac{B_2 l_2}{M_3 R_2} & 0 \\ 0 & 0 & 0 & 0 & 0 & 1 & 0 & 0 & 0 \\ 0 & 0 & \frac{U1}{M_4} & \frac{\beta_4}{M_4} & \frac{-V1}{M_4} & \frac{-(\beta_5+\beta_4)}{M_4} & 0 & 0 & \frac{-B_3 l_3}{M_4 R_3} \\ 0 & \frac{R_1 B_1 l_1}{L_1} & 0 & 0 & 0 & 0 & -\frac{R_1}{L_1} & 0 & 0 \\ 0 & 0 & 0 & \frac{R_2 B_2 l_2}{L_2} & 0 & 0 & 0 & -\frac{R_2}{L_2} & 0 \\ 0 & 0 & 0 & 0 & 0 & \frac{R_3 B_3 l_3}{L_3} & 0 & 0 & -\frac{R_3}{L_3} \end{bmatrix}}_{A} \begin{bmatrix} x_1 \\ x_2 \\ x_3 \\ x_4 \\ x_5 \\ x_6 \\ x_7 \\ x_8 \\ x_9 \end{bmatrix} + \underbrace{\begin{bmatrix} 0 \\ \frac{1}{M_2} \\ 0 \\ \frac{1}{M_3} \\ 0 \\ \frac{1}{M_4} \\ 0 \\ 0 \\ 0 \end{bmatrix}}_{B} [u] \tag{10.45}$$

$$z = \underbrace{\begin{bmatrix} 1 & 0 & 0 & 0 & 0 & 0 & 0 & 0 & 0 \\ 0 & 1 & 0 & 0 & 0 & 0 & 0 & 0 & 0 \\ 0 & 0 & 1 & 0 & 0 & 0 & 0 & 0 & 0 \\ 0 & 0 & 0 & 1 & 0 & 0 & 0 & 0 & 0 \\ 0 & 0 & 0 & 0 & 1 & 0 & 0 & 0 & 0 \\ 0 & 0 & 0 & 0 & 0 & 1 & 0 & 0 & 0 \\ 0 & 0 & 0 & 0 & 0 & 0 & 1 & 0 & 0 \\ 0 & 0 & 0 & 0 & 0 & 0 & 0 & 1 & 0 \\ 0 & 0 & 0 & 0 & 0 & 0 & 0 & 0 & 1 \end{bmatrix}}_{C} \begin{bmatrix} x_1 \\ x_2 \\ x_3 \\ x_4 \\ x_5 \\ x_6 \\ x_7 \\ x_8 \\ x_9 \end{bmatrix} + \underbrace{\begin{bmatrix} 0 \end{bmatrix}}_{D} [u] \tag{10.46}$$

$$\begin{bmatrix} \frac{dx_1}{dt} \\ \frac{dx_2}{dt} \\ \frac{dx_3}{dt} \\ \frac{dx_4}{dt} \\ \frac{dx_5}{dt} \\ \frac{dx_6}{dt} \\ \frac{dx_7}{dt} \\ \frac{dx_8}{dt} \\ \frac{dx_9}{dt} \end{bmatrix} = \underbrace{\begin{bmatrix} 0 & 1 & 0 & 0 & 0 & 0 & 0 & 0 & 0 \\ \frac{-P1}{M_2} & \frac{-(\beta_1+\beta_2)}{M_2} & \frac{Q1}{M_2} & \frac{\beta_2}{M_2} & 0 & 0 & -\frac{B_1 l_1}{M_2(R_1+R_{e1})} & 0 & 0 \\ 0 & 0 & 0 & 1 & 0 & 0 & 0 & 0 & 0 \\ \frac{R1}{M_3} & \frac{\beta_2}{M_3} & \frac{-J1}{M_3} & \frac{-(\beta_2+\beta_4)}{M_3} & \frac{E1}{M_3} & \frac{\beta_4}{M_3} & 0 & -\frac{B_2 l_2}{M_3(R_2+R_{e2})} & 0 \\ 0 & 0 & 0 & 0 & 0 & 1 & 0 & 0 & 0 \\ 0 & 0 & \frac{U1}{M_4} & \frac{\beta_4}{M_4} & \frac{-V1}{M_4} & \frac{-(\beta_5+\beta_4)}{M_4} & 0 & 0 & \frac{-B_3 l_3}{M_4(R_3+R_{e3})} \\ 0 & \frac{(R_1+R_{e1})B_1 l_1}{L_1} & 0 & 0 & 0 & 0 & -\frac{(R_1+R_{e1})}{L_1} & 0 & 0 \\ 0 & 0 & 0 & \frac{(R_2+R_{e2})B_2 l_2}{L_2} & 0 & 0 & 0 & -\frac{(R_2+R_{e2})}{L_2} & 0 \\ 0 & 0 & 0 & 0 & 0 & \frac{(R_3+R_{e3})B_3 l_3}{L_3} & 0 & 0 & -\frac{(R_3+R_{e3})}{L_3} \end{bmatrix}}_{A} \begin{bmatrix} x_1 \\ x_2 \\ x_3 \\ x_4 \\ x_5 \\ x_6 \\ x_7 \\ x_8 \\ x_9 \end{bmatrix} + \underbrace{\begin{bmatrix} 0 \\ \frac{1}{M_2} \\ 0 \\ \frac{1}{M_3} \\ 0 \\ \frac{1}{M_4} \\ 0 \\ 0 \\ 0 \end{bmatrix}}_{B} [u] \tag{10.47}$$

$$z = \underbrace{\begin{bmatrix} 1 & 0 & 0 & 0 & 0 & 0 & 0 & 0 & 0 \\ 0 & 1 & 0 & 0 & 0 & 0 & 0 & 0 & 0 \\ 0 & 0 & 1 & 0 & 0 & 0 & 0 & 0 & 0 \\ 0 & 0 & 0 & 1 & 0 & 0 & 0 & 0 & 0 \\ 0 & 0 & 0 & 0 & 1 & 0 & 0 & 0 & 0 \\ 0 & 0 & 0 & 0 & 0 & 1 & 0 & 0 & 0 \\ 0 & 0 & 0 & 0 & 0 & 0 & 1 & 0 & 0 \\ 0 & 0 & 0 & 0 & 0 & 0 & 0 & 1 & 0 \\ 0 & 0 & 0 & 0 & 0 & 0 & 0 & 0 & 1 \end{bmatrix}}_{C} \begin{bmatrix} x_1 \\ x_2 \\ x_3 \\ x_4 \\ x_5 \\ x_6 \\ x_7 \\ x_8 \\ x_9 \end{bmatrix} + \underbrace{\begin{bmatrix} 0 \end{bmatrix}}_{D} [u] \tag{10.48}$$

where A is the system matrix, B is the input matrix, and C is the output matrix. The remaining matrix is D which is typically zero because the input directly does not usually affect the output. If the coils

are connected in parallel to external load or resistance R_{e1}, R_{e2} and R_{e3}. The parallel-connected winding coils have the internal resistances R_1, R_2 and R_3 and inductances L_1, L_2 and L_3. The state space model of the system can be written in matrix form by Equation 10.47.

10.4 Dynamics of the 3DOF Energy Harvester

The eigenvalues and the frequency response of the 3DOF generator system have been analysed using the state space model as presented in Equations 10.54 and 10.55. The coefficients of the generator system are measured from the magnetic restoring forces. Three winding coils have been used, and each winding coils consist 100 number of turns. The diameter of each copper coil was 31 mm. Coil 1 (1st winding coil) was placed outside of the 1st floating magnet, coil 2 (2nd winding coil) was placed outside of the 2nd floating magnet, and coil 3 (3rd winding coil) was placed outside of the 3rd floating magnet. Each winding coil's inside diameter and height were 75 mm and 10 mm, respectively. The total length of each winding coil was 23.5 m, and the inner resistance of each coil was 5.48 ohm. The average magnetic flux density was considered 0.35 T. Because of the electromechanical coupling, the 3DOF generator system consists of electrical and mechanical parts. Three winding coils have been added outside the three floating magnets, and therefore, the system has three resonance frequencies in the electrical part. Because of the three floating magnets, the system has three mechanical resonance frequencies. The changing position of the floating magnets changed the resonance frequencies of the generator system. The electrical part's resonance frequencies depend on the winding coil's total length and the magnets' magnetic flux density. With increasing the magnetic flux density, the resonance frequencies of the electrical part reduced, but the resonance frequencies of the mechanical part were approximately the same. The resonance frequency of the electrical component is reduced by increasing the total length of the winding coil. Table 10.1 shows all required parameters used to analyse the dynamics of the 3DOF generator system.

However, the resonance frequency of the mechanical part did not change with changing the length of the winding coils. The natural frequencies of the electrical parts were 953.36 rad/s, 948.57 rad/s and 949.4 rad/s when all three floating magnets were in equilibrium positions. The natural frequencies for the mechanical parts were 69.24 rad/s, 47.77 rad/s and 34.58 rad/s. The natural frequencies were 67.97 rad/s, 46.85 rad/s and 33.89, respectively, of the 3DOF system without electrical-mechanical coupling in equilibrium position as discussed in Chapter 6. The natural frequencies of the mechanical part were nearly similar with or without electrical-mechanical coupling.

Table 10.1: Required parameters

Parameters	Values	Units
M_2	370	gm
M_3	327.28	gm
M_4	332.745	gm
β_1	2.11	Ns/m
β_{21}	1.08	Ns/m
β_2	0.8	Ns/m
β_3	0.51	Ns/m
k_1	826	N/m
k_{21}	566.78	N/m
k_2	263.69	N/m
k_3	298.62	N/m
α_1	7374.3	N/m^2
α_{21}	7270.8	N/m^2
α_2	1943.4	N/m^2
α_3	3487.5	N/m^2
λ_1	741312	N/m^3
λ_{21}	353407	N/m^3
λ_2	317056. 5	N/m^3
λ_3	107199	N/m^3
B1, B2 and B3	0.35	T
R1, R2 and R3	5.48	ohm
l1, l2 and l3	23.5	m
L1, L2 and L3	0.005546	H

The eigenvalues of the mechanical parts were -25.16 ± 64.51i, -21.32 ± 42.76i and -20.35 ± 27.96i. The eigenvalues of the electrical parts were -953.35 + 0.0i, -948.58 + 0.0i and -949.40 + 0.0i. The frequency response of the 3DOF generator system in equilibrium position has displayed in Figure 10.9. The dynamics of the 3DOF generator system were analysed by changing the position of all floating magnets. Due to the electromechanical coupling, the frequency response graph did not show the peak amplitude.

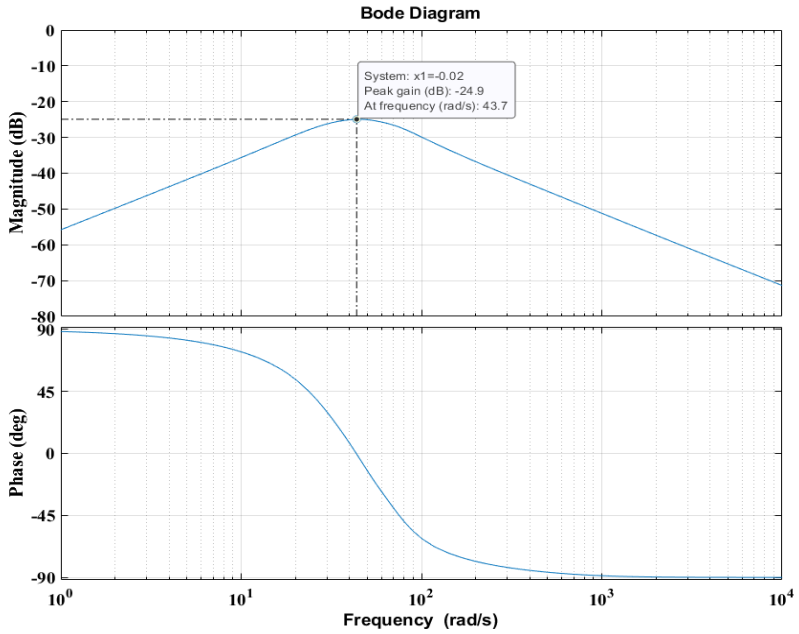

Figure 10.9: Frequency response of the 3DOF generator system in equilibrium position

Table 10.2: Eigenvalues and natural frequencies of the system (electrical part) for different positions of the floating magnets

Position of the FM	Electrical part					
	Eigenvalues			Frequency (rad/s)		
-20	-953.41 + 0.0i	-948.79 + 0.0i	-949.46 + 0.0i	953.41	948.79	949.45
-15	-953.38 + 0.0i	-948.70 + 0.0i	-949.43 + 0.0i	953.37	948.70	949.43
-10	-9533.6 + 0.0i	-948.63 + 0.0i	-949.41 + 0.0i	953.35	948.62	949.41
-05	-953.35 + 0.0i	-948.59 + 0.0i	-949.40 + 0.0i	953.34	948.58	949.40
0	-953.35 + 0.0i	-948.58 + 0.0i	-949.40 + 0.0i	953.34	948.57	949.40
05	-953.36 + 0.0i	-948.60 + 0.0i	-949.41 + 0.0i	953.35	948.59	949.41
10	-953.38 + 0.0i	-948.65 + 0.0i	-949.43 + 0.0i	953.37	948.65	949.42
15	-953.41 + 0.0i	-948.74 + 0.0i	-949.45 + 0.0i	953.40	948.73	949.45
20	-953.45 + 0.0i	-948.85 + 0.0i	-949.49 + 0.0i	953.45	948.84	949.48

However, the peak resonance was indicated at 43.7 rad/s. Table 10.2 displays the measured eigenvalues and natural frequencies of the electrical part for different positions of floating magnets. Moreover, the estimated eigenvalues and natural frequencies of the mechanical part for different positions of floating magnets have been presented in Table 10.3.

Table 10.3: Eigenvalues and natural frequencies of the system (Mechanical part) for different positions of the floating magnets

Position of the FM	Mechanical part					
	Eigenvalues			Frequency (rad/s)		
-20	-25.29+101.43i	-21.20+57.93i	-20.17+32.32i	104.53	61.68	38.09
-15	-25.32+86.23i	-21.20 +51.19i	-20.22+29.95i	89.87	55.40	36.13
-10	-25.30+73.95i	-21.22+46.05i	-20.28+28.26i	78.15	50.70	34.78
-05	-25.21+66.21i	-21.28+43.06i	-20.33+27.50i	70.84	48.02	34.20
0	-25.16+64.51i	-21.32+42.76i	-20.35+27.96i	69.24	47.77	34.58
05	-25.20 + 69.19i	-21.28+45.33i	-20.32+29.67i	73.63	50.07	35.96
10	-25.27 + 79.21i	-21.23+50.25i	-20.27+32.33i	83.14	54.54	38.15
15	-25.28 + 92.95i	-21.20+56.84i	-20.22+35.59i	96.32	60.66	40.92
20	-25.25+109.02i	-21.18+64.60i	-20.17+39.24i	111.90	67.98	44.11

*Note: FM= Floating magnet

From Table 10.2, it can be seen that there was no significant change in the eigenvalues as well as natural frequencies of the electrical par when floating magnets changed their positions. However, the eigenvalues and natural frequencies of the mechanical part changed with changing the position of the floating magnet, as seen in Table 10.3. The 3DOF generator system displayed higher mechanical frequency responses when all floating magnets moved toward the bottom magnet. Figure 10.10 shows the frequency responses of the 3DOF generator system for different positions of the floating magnets.

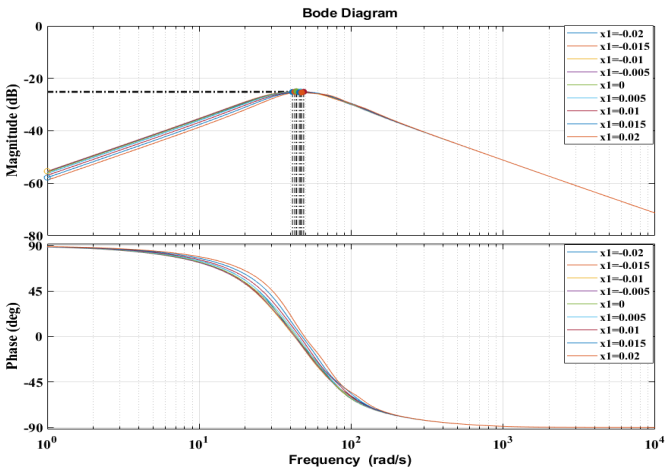

Figure 10.10: Frequency response of the 3DOF generator system for different positions of the floating magnets

From Figure 10.10, the peak resonance changed with changing the position of the floating magnets. Different positions of the floating magnet showed different eigenvalues and frequency responses. However, Figure 10.10 did not show the peak amplitude for all different positions of the floating magnet. The frequency resonance has been analysed by connecting external load or resistance parallel to the winding coils of the 3DOF system. Different external loads have been connected to analyse the frequency resonance of the generator system.

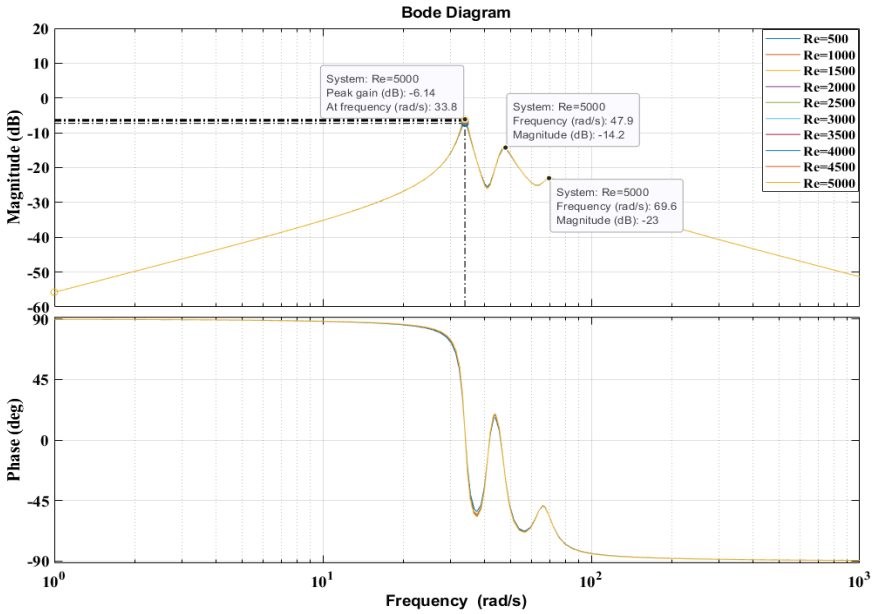

Figure 10.11: Frequency response of the 3DOF generator system with external load in equilibrium position

Figure 10.11 displays three resonances due to the three floating magnets, and the values were 69.6 rad/s, 47.9 rad/s and 33.8 rad/s in the equilibrium position, which was almost similar to the natural frequencies: 69.24 rad/s, 47.77 rad/s and 34.58 rad/s without external load (determined using eigenvalues). When external loads connected to the winding coils, the system showed three resonances, as shown in Figure 10.11, but the system without external load did not show peak amplitude, as shown in Figure 10.10. Figure 10.12 shows the resonance frequency of the generator system with external load for different positions of the floating magnets. For all different positions of the floating magnets, Figure 10.12 showed three resonances. The resonance frequencies changed with changing the position of the floating magnets. Compared to the 3DOF generator system with or without external load, the 3DOF generator system with external load showed better dynamics results.

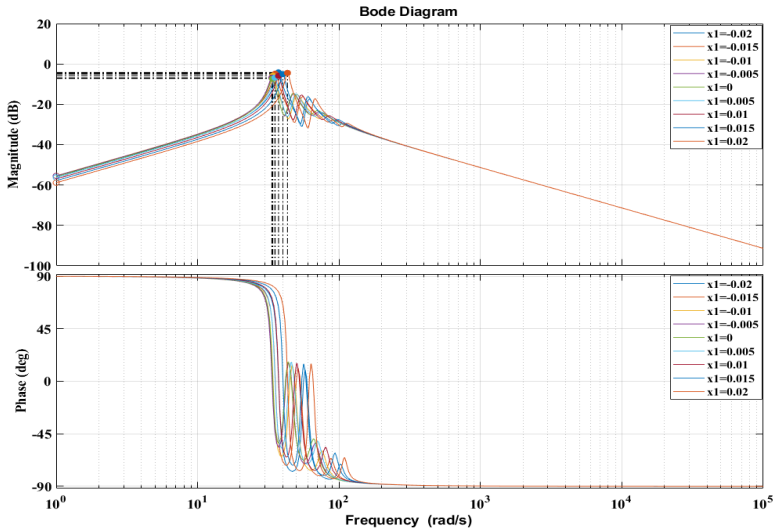

Figure 10.12: Frequency response of the 3DOF generator system with external load for different positions of the floating magnets

The 3DOF generator system has been analysed by applying external harmonic force. The system has been analysed by applying force on a single floating magnet, double floating magnets and all three floating magnets. When the force was applied to any floating magnets, all floating magnets relatively started moving. If the 3rd floating magnet moved toward the top fixed magnet, the 2nd floating magnet relatively moved toward the 3rd floating magnet and the 1st floating magnet relatively toward the 2nd floating magnet. Similarly, when the 3rd floating magnet moved toward the 2nd floating magnet, the 2nd floating magnet moved toward the 1st floating magnet, and the 1st floating magnet moved toward the bottom fixed magnet. The displacements, velocities and induced voltages of the 3DOF generator system have been analysed by applied external harmonic force in this section. Because of the movement of the floating magnets, the magnetic flux densities of the floating magnet cut the winding coils, which created induced voltage inside the winding coils.

At first, the 3DOF generator system was analysed by applying harmonic force on all three floating magnets. The applied external harmonic force (Fb) amplitude was 25N, and the frequency (f) was 0.1 Hz. The values of coefficients of the system and damping constants have been presented in Table 10.1. The state space model Equations 10.41, 10.47, 10.50, 10.51, 10.52 and 10.53 have been solved using the Ode23t solver in MATLAB to find the displacements, velocities and induced voltages of the 3DOF generator system. All floating magnets' excitation was assumed to have the initial

displacements, and their corresponding velocities were zero. As expected, the displacements and the velocities were sinusoidal and 90° out of phase.

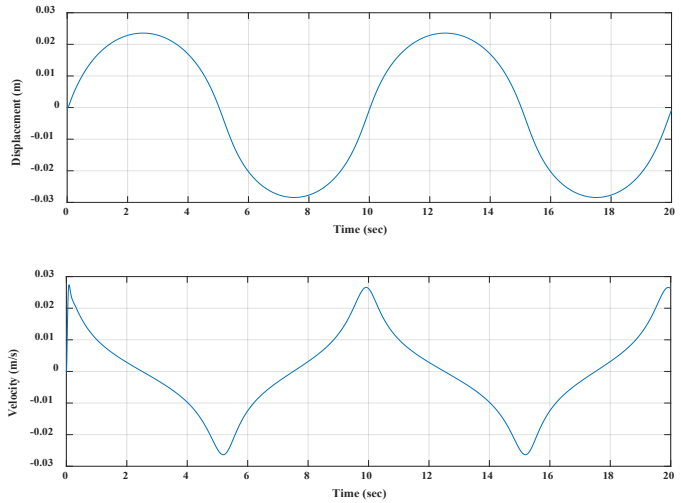

Figure 10.13: Displacement and velocity of the 1st floating magnet

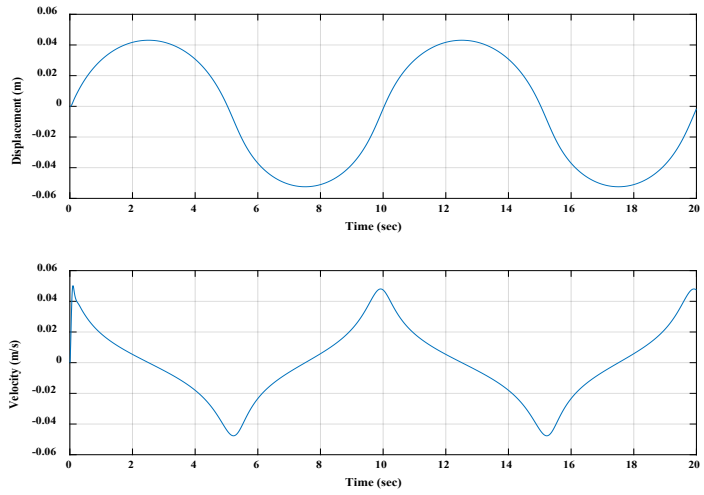

Figure 10.14: Displacement and velocity of the 2nd floating magnet

Figures 10.13, 10.14 and 10.15 present the displacement and velocity of the 1st, 2nd and 3rd floating magnets, respectively. Because of the applied harmonic force on all three floating magnets, the maximum displacements of the 1st floating magnet toward the 2nd floating magnet was around 29 mm, and towards the bottom magnet was about 24 mm, as seen in Figure 10.13.

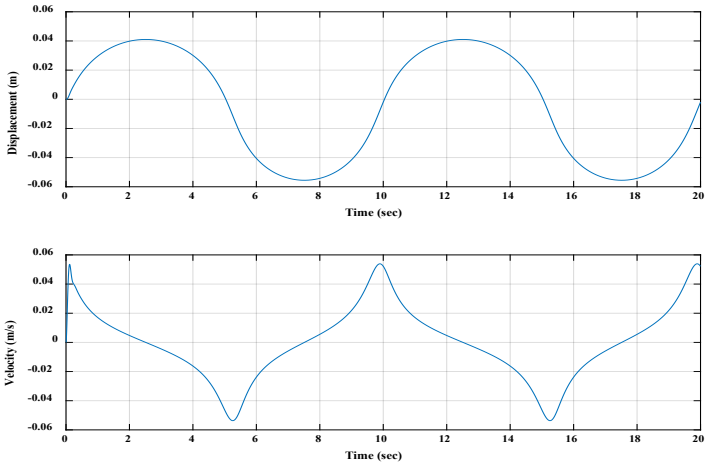

Figure 10.15: Displacement and velocity of the 3rd floating magnet

The measured maximum velocity of 1st floating magnet during that excitation was around 0.026 m/s. On the other hand, the maximum displacement of the 2nd floating magnet toward the 3rd floating magnet was around 52 mm and about 43 mm toward the 1st floating magnet. The maximum velocity of the 2nd floating magnet was around 0.047 m/s, as seen in Figure 10.14. Moreover, the maximum displacement of the 3rd floating magnet toward the top foxed magnet (5th magnet) was around 55 mm and about 41 mm toward the 2nd floating magnet. The maximum velocity of the 3rd floating magnet was approximately 0.053 m/s, as seen in Figure 10.15.

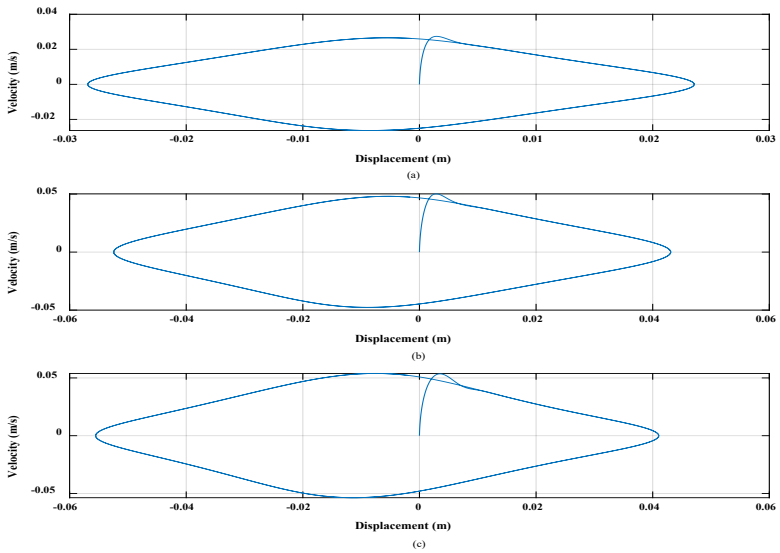

Figure 10.16: Comparison of displacement and velocity of (a) 1st floating magnet and (b) 2nd floating magnet (c) 3rd floating magnet

Therefore, it can be seen that when the same harmonic forces were applied to all three floating magnets, then the 3rd floating magnet achieved a higher velocity than the other floating magnets. For the same applied harmonic forces on all three floating magnets, the 3rd floating magnet reached the maximum displacement than the 2nd and 1st floating magnet, as shown in Figure 10.16. By changing the amplitude and frequency of the applied harmonic force, the displacements and velocities of all floating magnets can be changed, as discussed in Chapter 6. It was considered during the analysis that 1st winding coil was placed outside of the 1st floating magnet and 2nd winding coil was outside of the 2nd floating magnet, and 3rd winding coil was outside of the 3rd floating magnet. Due to the movement of the magnet, the induced voltage is usually generated in the winding coil. Figure 10.17 displays the generated induced voltage in coils 1, 2 and 3.

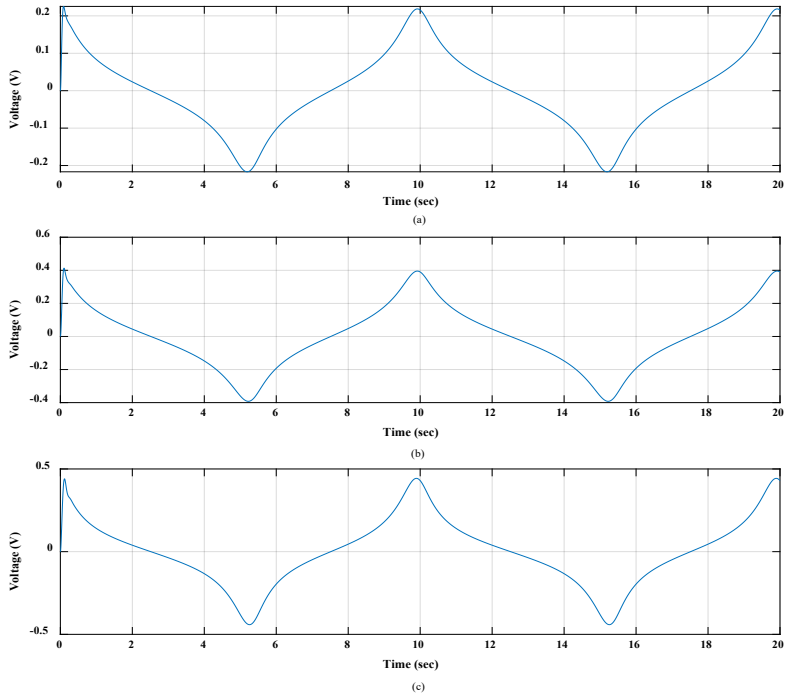

Figure 10.17: Measured induced voltages (a) 1st winding coil, (b) 2nd winding coil and (c) 3rd winding coil

The velocity of the 3rd floating magnet was higher than the 2nd and 1st floating magnet; therefore, the 3rd winding coil showed higher induced voltage than the 2nd and 1st winding coils. The maximum measured induced voltages in coil 3 was around 0.44 volts. The maximum measured induced voltage in coil 2 was 0.39 volts higher than in coil 1 induced voltage (0.21 volts). The generator system has

been analysed by applying harmonic force only on 3rd floating magnet. For this applied harmonic force, the displacements and velocities of all three floating magnets have been determined. Moreover, the induced voltages for all three coils have also been measured. As the harmonic force was applied on the 3rd floating magnet, therefore, when the 3rd floating magnet started moving, the 2nd and 1st floating magnet also started moving. For this applied harmonic force (25N amplitude), the 3rd floating magnet achieved a higher displacement and velocity than the 2nd and 1st floating magnets. Figures 10.18, 10.19 and 10.20 present the displacement and velocity of the 1st, 2nd and 3rd floating magnets, respectively.

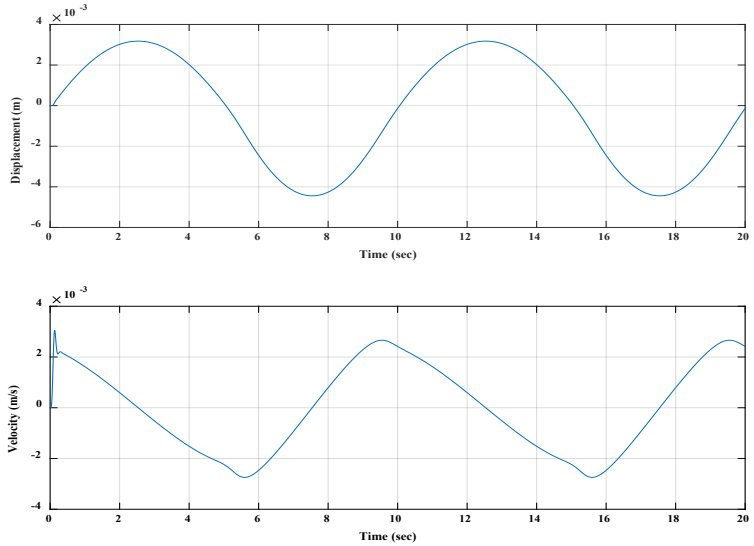

Figure 10.18: Displacement and velocity of the 1st floating magnet

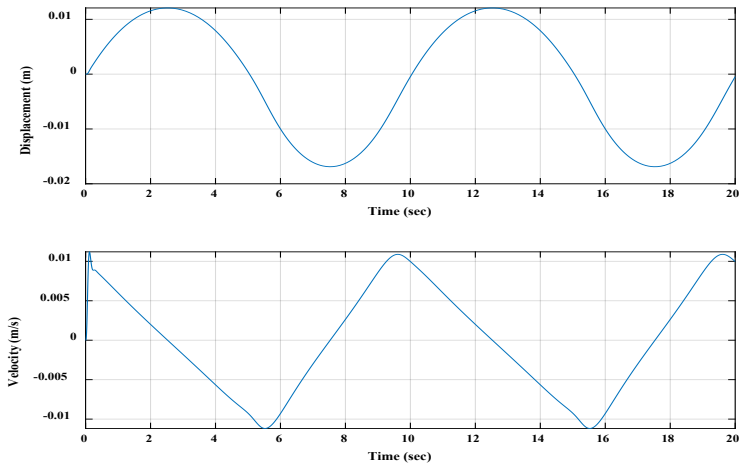

Figure 10.19: Displacement and velocity of the 2nd floating magnet

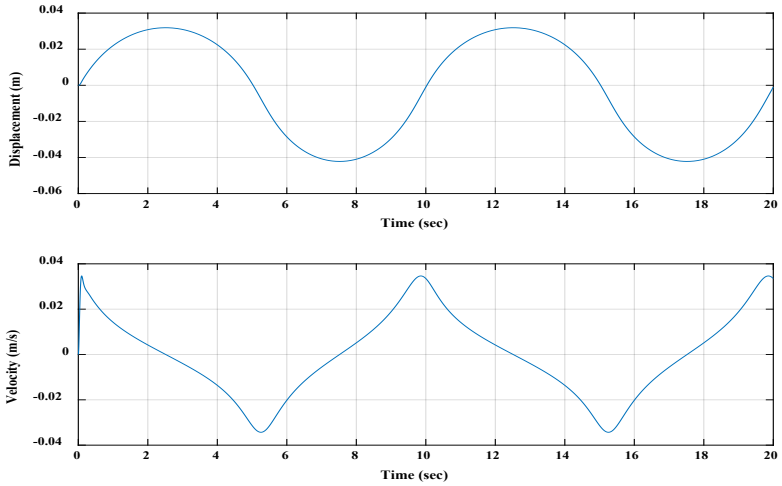

Figure 10.20: Displacement and velocity of the 3rd floating magnet

The 1st floating magnet moved up to 4.5 mm toward the 2nd floating magnet and around 3 mm toward the 1st fixed magnet (bottom magnet). The measured maximum velocity was about 0.0026m/s during this displacement. On the other hand, the 2nd floating magnet moved up to 16 mm toward the 3rd floating magnet and around 12 mm toward the 1st floating magnet. The maximum velocity for the 2nd floating magnet was around 0.01 m/s during this excitation. Moreover, the 3rd floating magnet moved up to 42 mm toward the top fixed magnet and about 31 mm toward the 2nd floating magnet. The maximum velocity for the 3rd floating magnet was around 0.034 m/s during this movement.

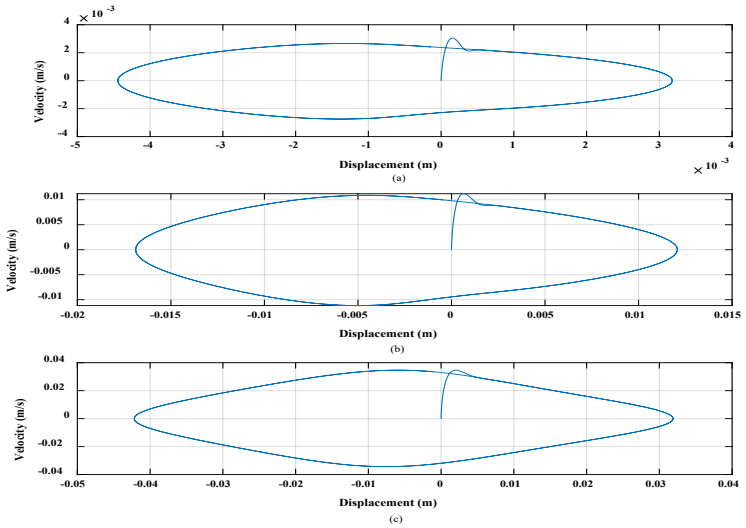

Figure 10.21: Comparison of displacement and velocity of (a) 1st floating magnet, (b) 2nd floating magnet and (c) 3rd floating magnet

Figure 10.21 compares the displacement and velocity of the 3rd floating magnet with the 2nd and 1st floating magnets. The induced voltages of all three winding coils are presented in Figure 10.22. The displacement and velocity of the 3rd floating magnets were way higher than the 2nd and 1st floating magnets, as seen in Figure 10.21. Therefore, the induced voltage of coil 3 was higher than coil 2 and coil 1. The maximum induced voltage in coil 1 was around 0.022 volts and in coil 2 was about 0.09 volts. The maximum induced voltage in coil 3 was around 0.29 volts higher than the coil 1 and 2.

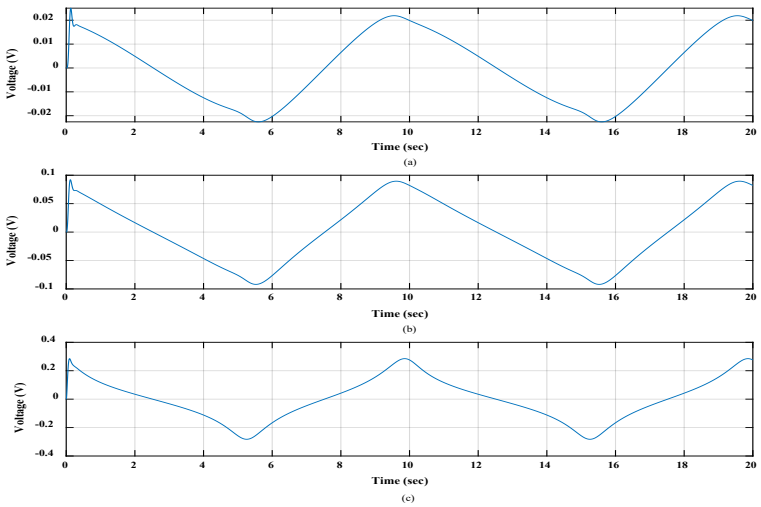

Figure 10.22: Measured induced voltages (a) 1st winding coil, (b) 2nd winding coil and (c) 3rd winding coil

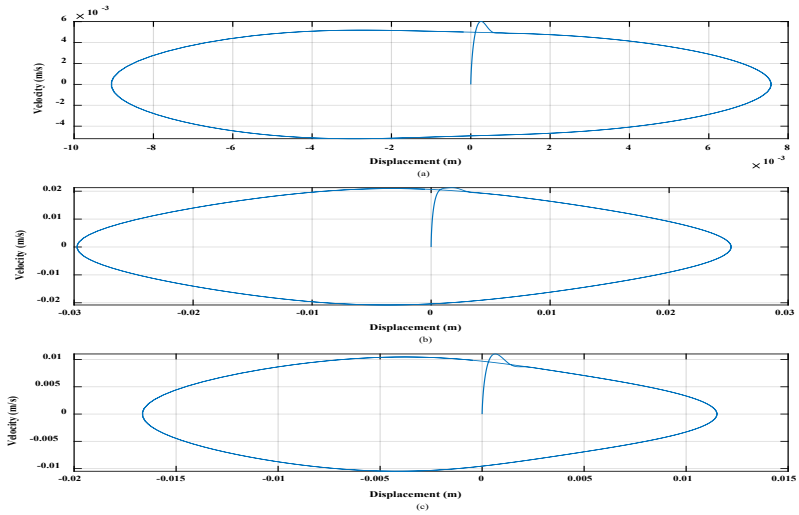

Figure 10.23: Comparison of displacement and velocity of (a) 1st floating magnet, (b) 2nd floating magnet and (c) 3rd floating magnet

Moreover, the 3DOF generator system has been analysed by applying the same harmonic force (25N amplitude) only on the 2nd floating magnet. As the harmonic force was applied on the 2nd floating magnet, therefore, when the 2nd floating magnet started moving, the 3rd and 1st floating magnets also started moving. The relative displacements of all three floating magnets have been determined. For this applied harmonic force (25N amplitude), the 2nd floating magnet achieved a higher displacement and velocity than the 1st and 3rd floating magnets, as seen in Figure 10.23. The velocity of the 2nd floating magnet was 0.02 m/s which was higher than the velocity of the 3rd (0.01 m/s) and 1st (0.005 m/s) floating magnets. Therefore, the generated induced voltage in coil 2 was higher than in coils 3 and 1, as presented in Figure 10.24.

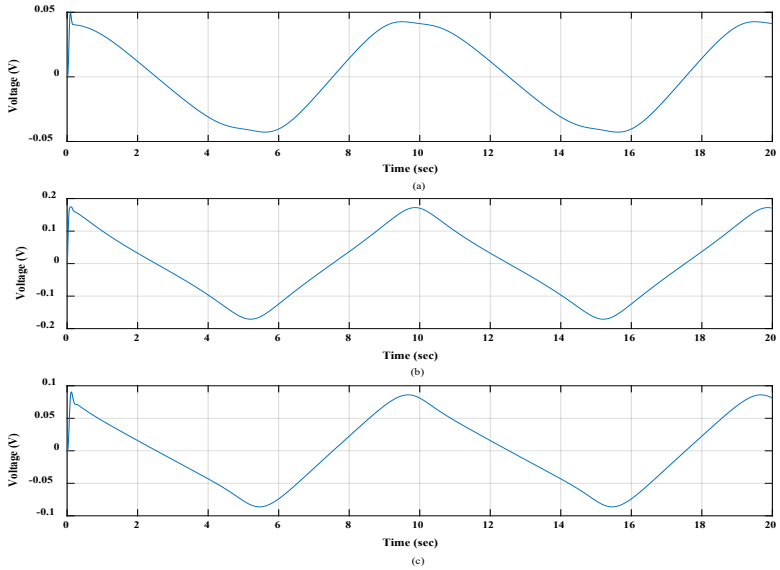

Figure 10.24: Measured induced voltages (a) 1st winding coil, (b) 2nd winding coil and (c) 3rd winding coil

The recorded maximum induced voltage in coil 2 was 0.17 volts higher than generated induce voltage in coil 1 (0.042 volts) and coil 3 (0.086 volts). Furthermore, the external harmonic force was applied only on the 1st floating, and the 3DOF generator system was analysed. When the external force is applied to the 1st floating magnet, the 1st floating magnet achieves the highest displacement and velocities than the other floating magnets. The 1st floating magnet moved about 22 mm toward the 2nd floating magnet and 19 mm toward the bottom fixed magnet because of the external force on the 1st floating magnet. The 2nd floating magnet reached 19 mm toward the 3rd and 16 mm toward the 1st floating magnet. On the other hand, the 3rd floating magnet moved 10 mm toward the top fixed magnet

and 7.37 mm toward the 2nd floating magnet, as shown in Figure 10.25. The velocity of the 1st floating magnet was 0.018 m/s which was higher than the velocity of the 2nd (0.016 m/s) and 3rd (0.0077 m/s) floating magnets. Figure 10.26 presents the measured induced voltages in three winding coils.

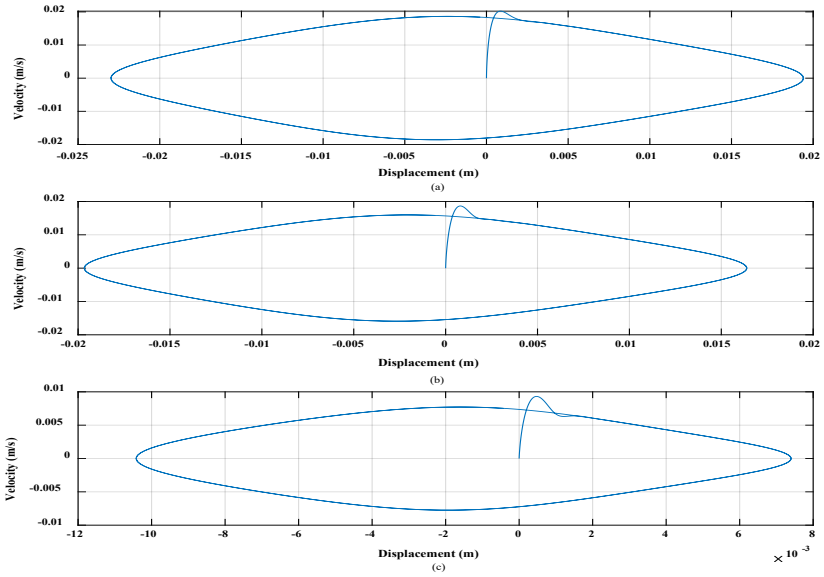

Figure 10.25: Comparison of displacement and velocity of (a) 1st floating magnet, (b) 2nd floating magnet and (c) 3rd floating magnet

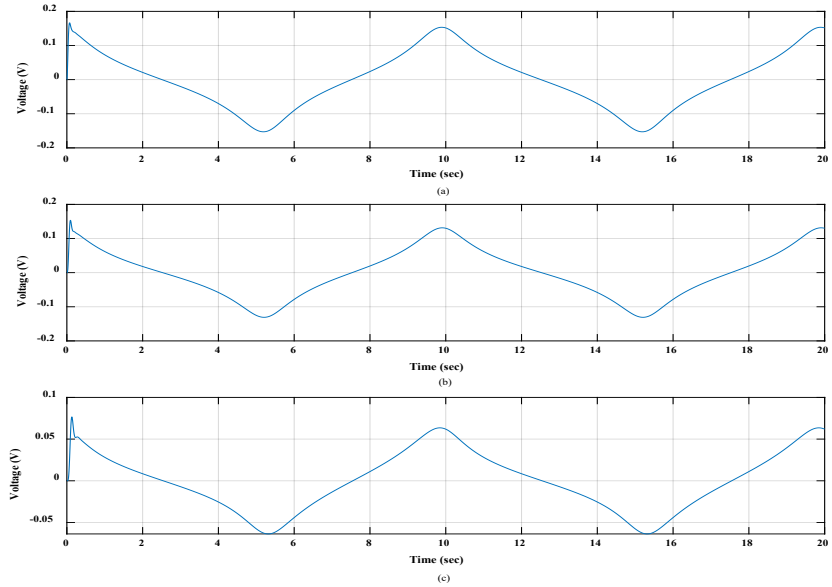

Figure 10.26: Measured induced voltages (a) 1st winding coil, (b) 2nd winding coil and (c) 3rd winding coil

The maximum induced voltage was recorded in Coil 1 (0.15 volts), which was higher than the generated voltages in the winding coil 2 (0.13 volts) and coil 3 (0.063 volts). It can be seen that when the force was applied to 1st floating magnet, then the generated voltages in coil 1 and coil 2 were almost similar. The 3DOF system has been analysed by using external forces in any two floating magnets from three floating magnets. At first, the external forces (25N amplitude and 0.1 Hz frequency) were applied on the 1st and 2nd floating magnets, and the 3DOF generator system was analysed. Because of the applied forces, the system's displacements, velocities, and induced voltages have been determined. The maximum displacements of the 1st floating magnet were around 27 mm toward the 2nd floating magnet and about 22.5 mm toward the bottom fixed magnet, as seen in Figure 10.27. Moreover, the 2nd floating magnet's maximum displacement was about 45.5 mm toward the 3rd floating magnet and around 38 mm toward the 1st floating magnet. On the other hand, the maximum displacements of the 3rd floating magnet were about 27 mm toward the top fixed magnet and around 18 mm toward the 2nd floating magnet.

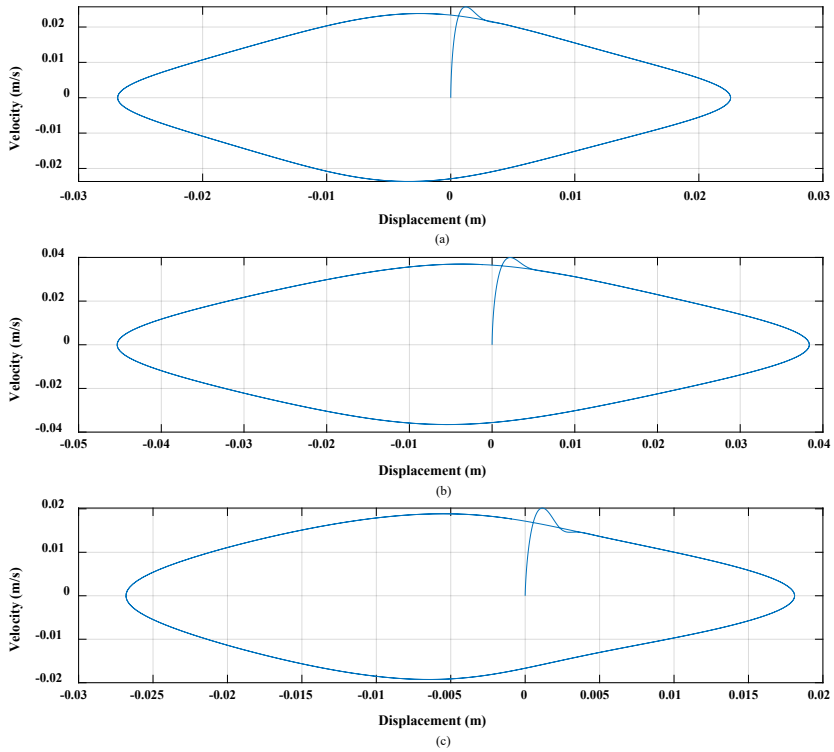

Figure 10.27: Comparison of displacement and velocity of (a) 1st floating magnet, (b) 2nd floating magnet and (c) 3rd floating magnet

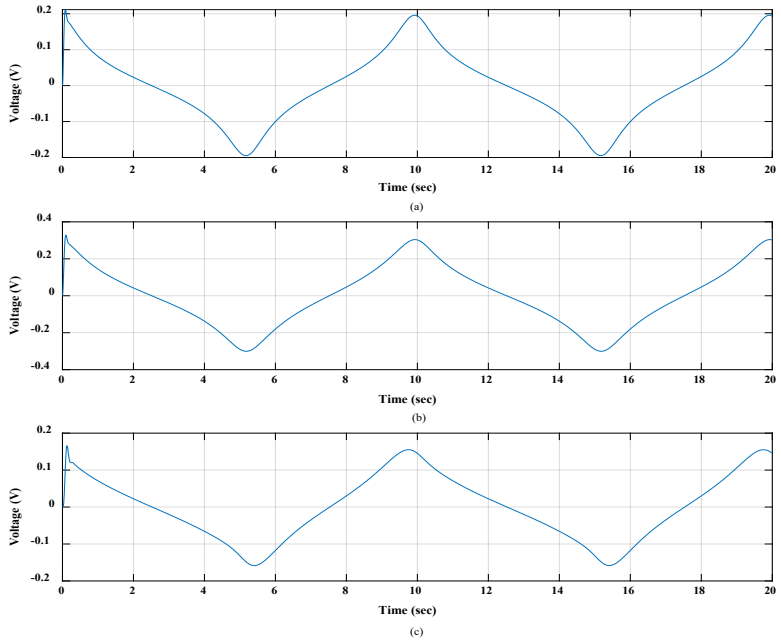

Figure 10.28: Measured induced voltages (a) 1st winding coil, (b) 2nd winding coil and (c) 3rd winding coil

When external forces were applied on the 1st and 2nd floating magnets, the 2nd floating magnet achieved more maximum displacements than the 1st and 3rd floating magnet. The displacement of the 1st floating magnet was higher than the 3rd floating magnet. The maximum velocity of the 2nd floating magnet was 0.037 m/s which was higher than the velocity of the 1st floating magnet (0.023 m/s) and 3rd floating magnet (0.018 m/s). The winding coil 2 generated the maximum induced voltage (0.30 volts) compared to coil 1(around 0.2 volts) and coil 2 (0.15 volts), as seen in Figure 10.28. The external forces, later on, were applied on the 1st and 3rd floating magnets to analyse the system. The displacements and velocities of all floating magnets and generated induce voltages were measured. Figure 10.29 displays the displacements and velocities of all floating magnets. From Figure 10.29, it can be seen that the maximum displacements of the 1st floating magnet were around 24 mm toward the 2nd floating magnet and about 20 mm toward the bottom fixed magnet, as seen in Figure 10.29. Moreover, the 3rd floating magnet's maximum displacement was about 49.5 mm toward the top fixed magnet and around 37 mm toward the 2nd floating magnet. On the other hand, the maximum displacements of the 2nd floating magnet were about 32 mm toward the 3rd floating magnet and around 25 mm toward the 1st floating magnet.

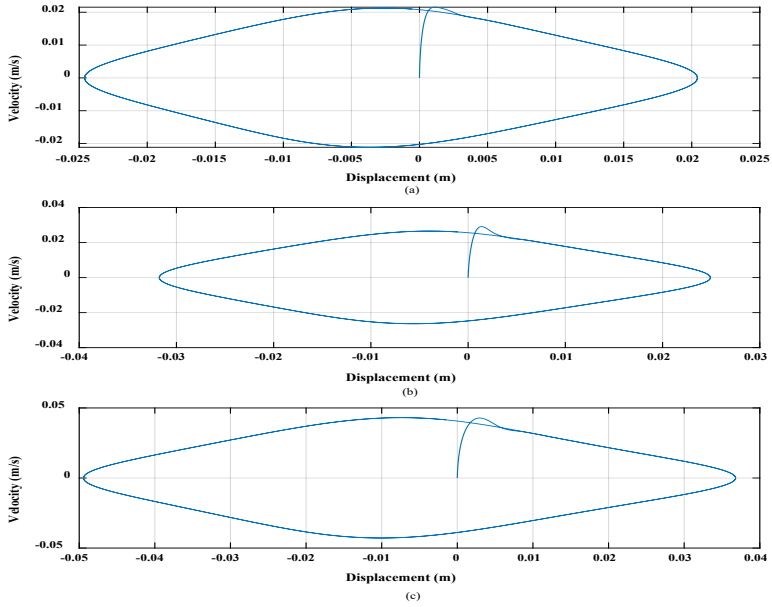

Figure 10.29: Comparison of displacement and velocity of (a) 1st floating magnet, (b) 2nd floating magnet and (c) 3rd floating magnet

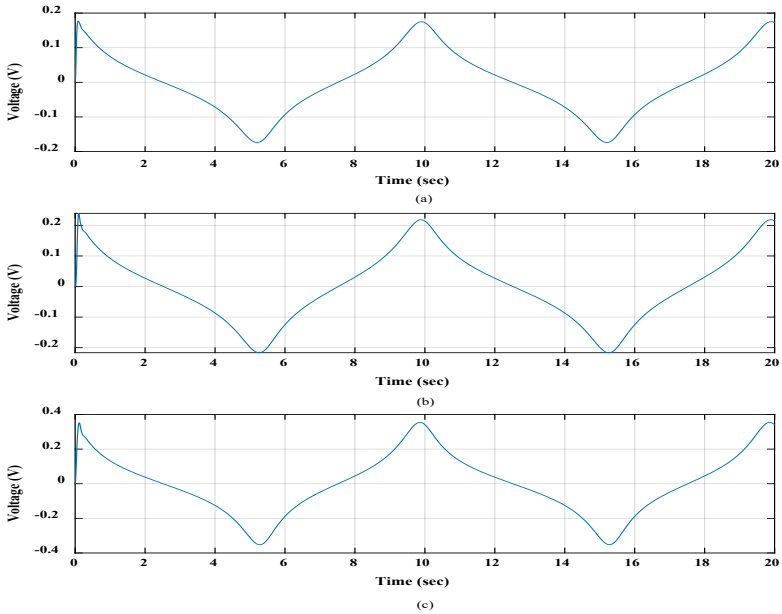

Figure 10.30: Measured induced voltages (a) 1st winding coil, (b) 2nd winding coil and (c) 3rd winding coil

Because of the applied external forces on the 1st and 3rd floating magnets, the 3rd floating magnet achieved more maximum displacements than the 1st and 2nd floating magnets. Although the forces were applied on the 1st and 3rd floating magnets, the displacement of the 2nd floating magnet was still higher than the 1st floating magnet. The velocity of the 2nd floating magnet (0.026 m/s) was higher than the velocity of the 1st floating magnet (0.021 m/s). The maximum velocity of the 3rd floating magnet was 0.043 m/s which was higher than the velocity of the 1st floating magnet (0.021 m/s) and 2nd floating magnet (0.026 m/s). The winding coil 3 generated the maximum induced voltage (0.35 volts) compared to coil 1(around 0.17 volts) and coil 2 (0.22 volts), as seen in Figure 10.30. Finally, the external forces were applied on the 2nd and 3rd floating magnets to analyse the 3DOF generator system. Figure 10.31 shows the displacements and velocities of three floating magnets. The maximum displacements of the 2nd floating magnet were around 38 mm toward the 3rd floating magnet and about 30 mm toward the 1st floating magnet, as seen in Figure 10.31.

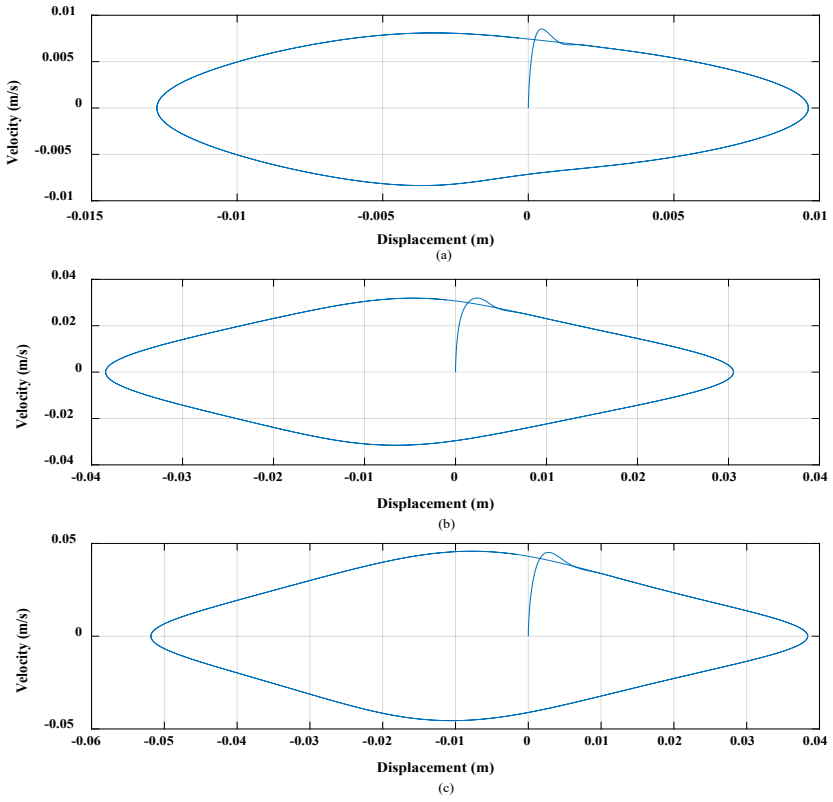

Figure 10.31: Comparison of displacement and velocity of (a) 1st floating magnet, (b) 2nd floating magnet and (c) 3rd floating magnet

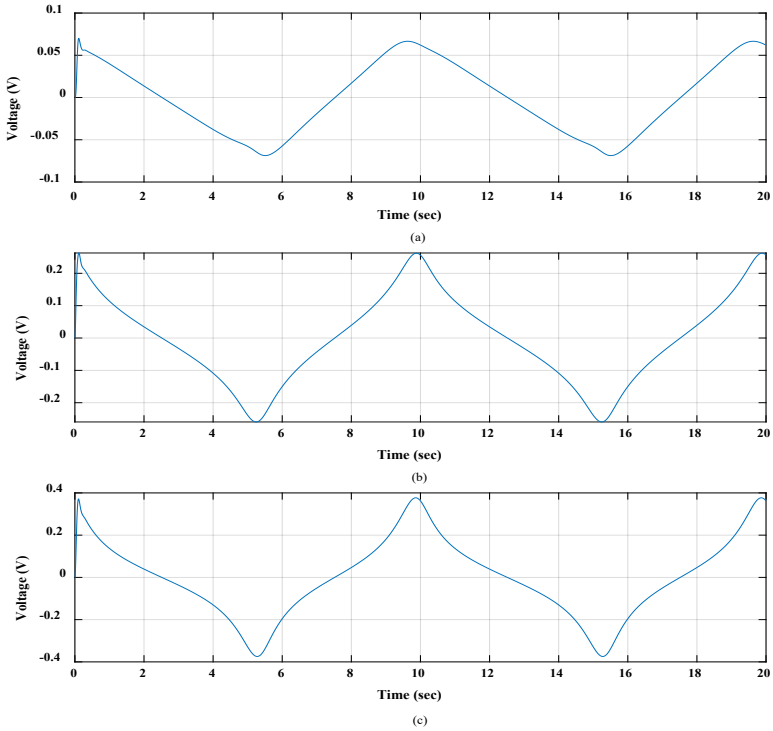

Figure 10.32: Measured induced voltages (a) 1st winding coil, (b) 2nd winding coil and (c) 3rd winding coil

Moreover, the 3rd floating magnet's maximum displacement was about 52 mm toward the top fixed magnet and around 38 mm toward the 2nd floating magnet. On the other hand, the maximum displacements of the 1st floating magnet were about 13 mm toward the 2nd floating magnet and around 10 mm toward the bottom fixed magnet. The velocity of the 3rd floating magnet (0.045 m/s) was higher than the velocity of the 2nd floating magnet (0.032 m/s) and 1st floating magnet (0.008 m/s). Therefore, the 3rd winding coil generated the maximum induced voltage (0.37 volts) compared to coil 1(around 0.066 volts) and coil 2 (0.26 volts), as presented in Figure 10.32. Figures 10.33, 10.34 and 10.35 present the displacements and velocities of the 1st, 2nd and 3rd floating magnets for different arrangements of the externally applied forces. Overall, it can be said that by changing the arrangement of the applied forces, the efficiency of the 3DOF system can be changed. By changing the layout of the applied forces, the system has been analysed and compared with each other.

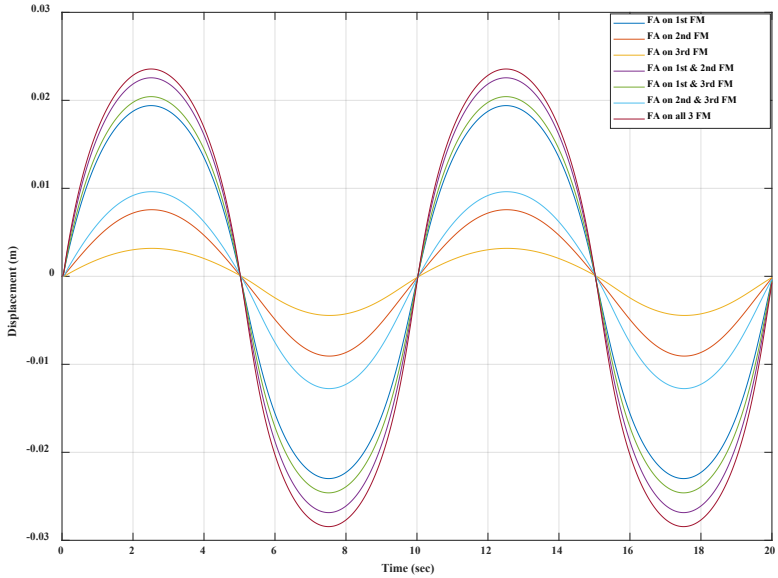

(a)

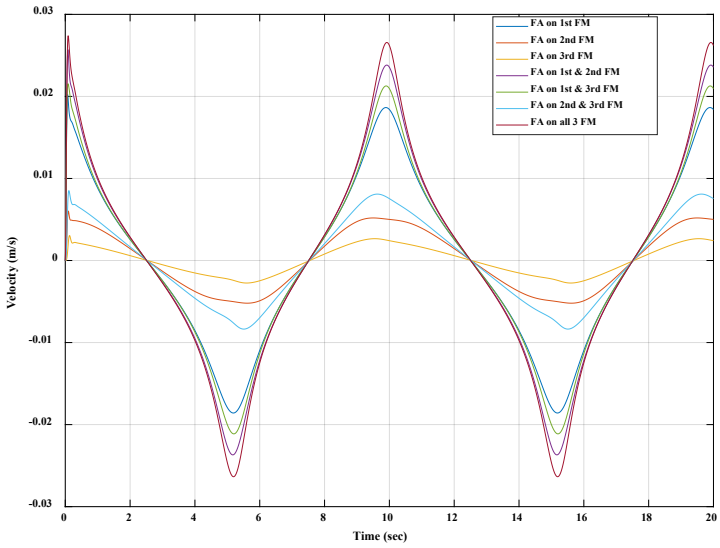

(b)

Figure 10.33: (a) Displacement and (b) velocity of the 1st floating magnet under different arrangements of the applied force (Note: FA= Force Applied and FM=Floating magnet)

From Figure 10.33, it can be seen that the maximum displacement of the 1st floating magnet gave the maximum velocity. When the harmonic forces were applied to three magnets, the 1st floating magnet was shown the maximum displacement and velocity. The second maximum displacement and velocity were determined when the forces were applied on the 1st and 2nd floating magnet, as seen in

Figure 10.33. The minimum displacement and velocity of the 1st floating magnet were found when the external force was applied to 3rd floating magnet.

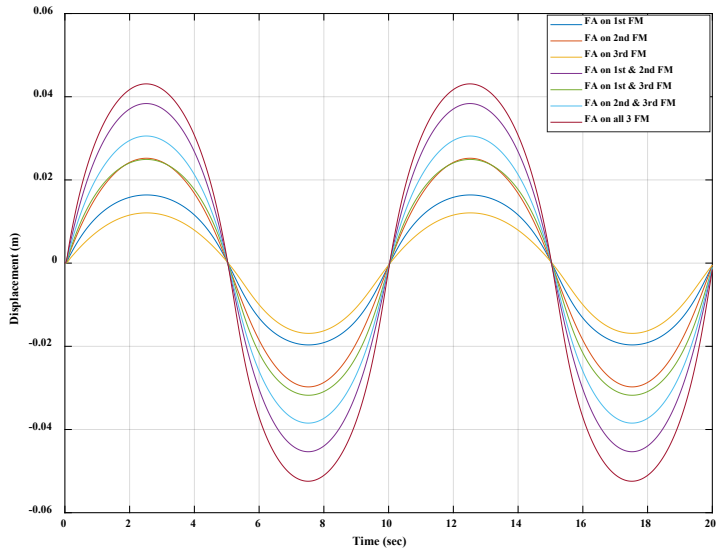

(a)

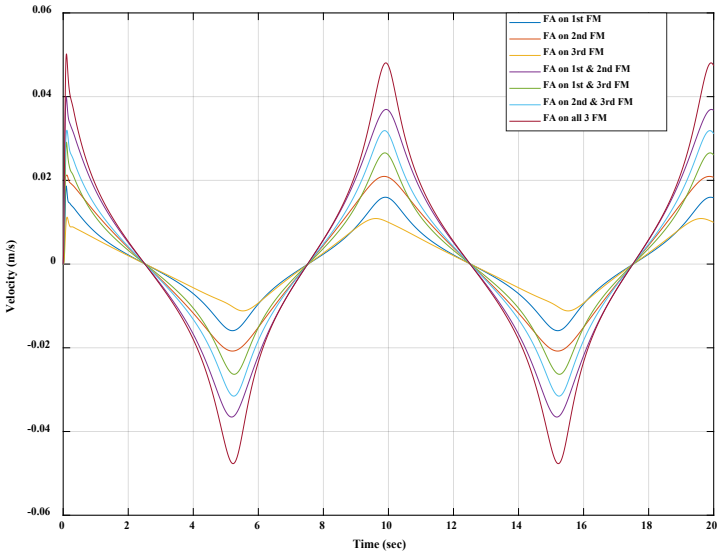

(b)

Figure 10.34: (a) Displacement and (b) velocity of the 2nd floating magnet under different arrangements of the applied force (Note: FA= Force Applied and FM=Floating magnet)

Therefore, the maximum induced voltage was generated in the 1st winding coil when forces were applied to all floating magnets. The minimum induced voltage was measured in the 1st winding coil when the force was applied on the 3rd floating magnet, as presented in Figure 10.36(a). On the other hand, the maximum displacement and velocity of the 2nd floating magnet were reached when applied to all floating magnets.

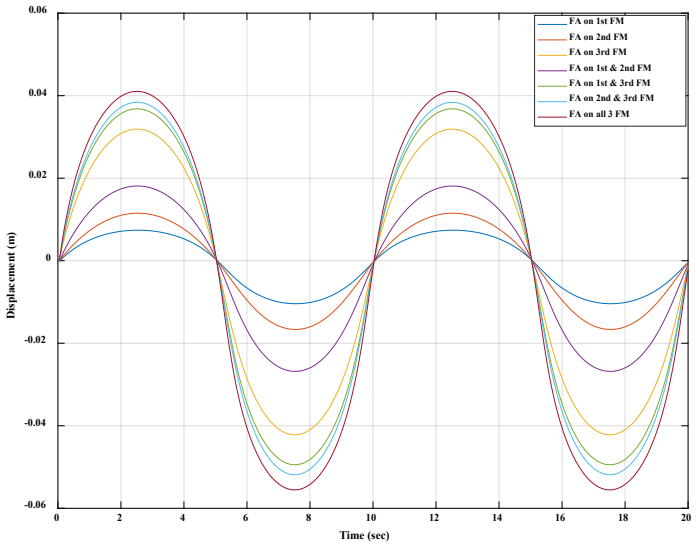

(a)

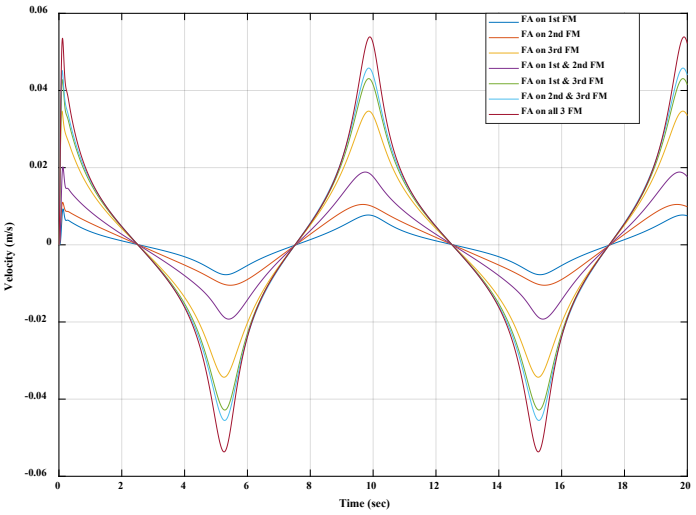

(b)

Figure 10.35: (a) Displacement and (b) velocity of the 3rd floating magnet under different arrangements of the applied force (Note: FA= Force Applied and FM=Floating magnet)

The minimum displacement and velocity of the 2nd floating magnet were measured when it was applied only on the 3rd floating magnet, as displayed in Figure 10.34. Therefore, the maximum induced voltage was measured in the 2nd winding coil when forces were applied to three floating magnets. The minimum induced voltage was measured in coil 2 when force was applied only on the 3rd floating magnet, as shown in Figure 10.36(b). Moreover, the maximum and minimum displacements and velocities of the 3rd floating magnet were found when the forces were applied to three floating magnets and only the 1st floating magnet, respectively.

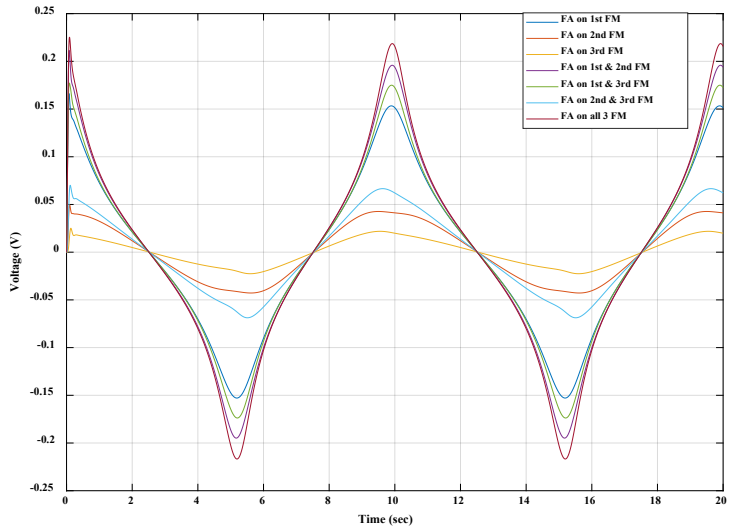

(a)

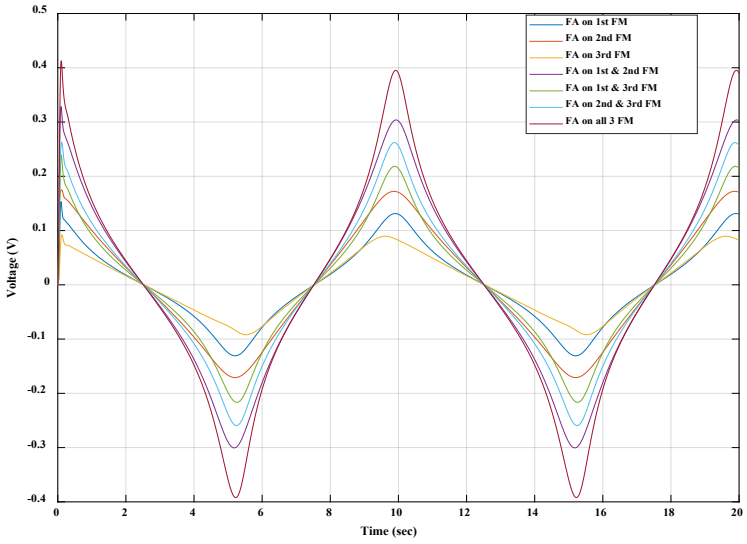

(b)

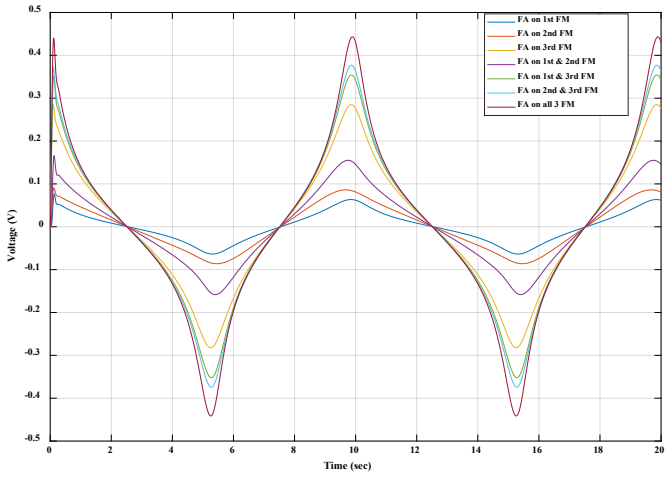

(c)

Figure 10.36: Generated induced voltage in winding coils (a) Coil 1, (b) Coil 2, and (c) Coil 3 (Note: FA= Force Applied and FM=Floating magnet)

The maximum induced voltage was measured in coil 3 when harmonic forces were applied to all three floating magnets. The minimum voltage was found when the force was applied to the 1st floating magnet, as presented in Figure 10.36(c). From the above analysis, it can be said that the 3DOF generator system was generated maximum induced voltage when the external forces were applied to all three floating magnets. Moreover, it can be seen that coil 3 generated a maximum induced voltage compared to coil 2 and coil 1. Coil 1 and coil 2 generated the lowest powers when force was only applied to 3rd floating magnet. On the other hand, coil 3 generated the minimum voltage when the force was only applied to 1st floating magnet. By increasing the amplitude and frequency of the applied harmonic force, the output power of the 3DOF generator system can be increased. The 3DOF generator system has been compared with the single-degree-of-freedom (SDOF) and 2DOF generator systems. The amplitude and frequency of the applied harmonic force were 25N and 0.1 Hz. A winding coil (100 number of turns) has been considered for the SDOF generator system, 2 winding coils (both 100 number of turns) have been considered for the 2DOF generator system, and 3 winding coils (all 100 number of turns) have been considered for 3DOF generator system. Moreover, the same magnetic flux density and copper coil have been considered to compare both generator systems. The forces were applied to the floating magnet for SOD, both floating magnets for the 2DOF system and all three floating magnets for the 3DOF system. Figure 10.37 presents the comparison results of all generator systems.

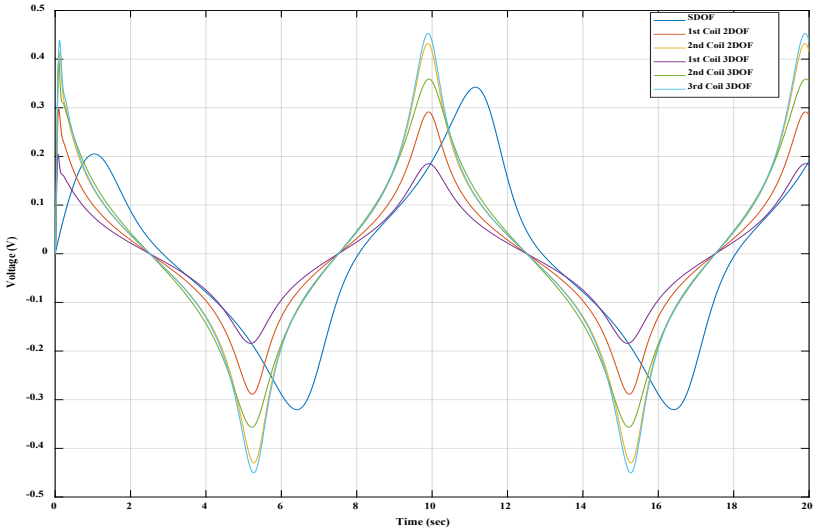

Figure 10.37: Comparison of generated induced voltages of SDOF, 2DOF and 3DOF generator systems

When the forces were applied to both floating magnets in the 2DOF system, the generated induced voltage in coil 2 was higher than in coil 1. The generated voltage in coil 2 was higher than the generated induced voltage in the SDOF generator system. However, When the forces were applied to all three floating magnets in the 3DOF system, the generated induced voltage in coil 3 was higher than in coils 2 and 1. The generated voltage in coil 3 was higher than the generated induced voltage in coil 2 in the 2DOF generator system. Moreover, the generated voltage in coil 2 in the 3DOF system was higher than the generated induced voltage in the SDOF generator and coil 1 in the 2DOF system. Therefore, overall, the 3DOF generator system is more efficient than the 2DOF and SDOF generator systems.

10.5 Experimental Analysis of the 3DOF Magnetic Spring-based Energy Harvester

The experimental works of the proposed 3DOF magnetic spring-based energy harvester have been carried out by connecting fishing lines with a different floating magnet and various applied harmonic forces. Three winding coils (100 turns each) were added with the test rig to generate the induced voltages from the movement of the floating magnets. The 1st winding coil was placed outside the 1st floating magnet, and the 2nd winding coil was placed outside the 2nd floating magnet. Similarly, the 3rd winding coil was placed outside the 3rd floating magnet. Each winding coil was connected with the data acquisition system to measure the generated induced voltages. The induced voltage was

generated in the winding coil 1 and 2 due to the movement of the 1st and 2nd floating magnets, respectively. Similarly, the induced voltage was generated inside winding coil 3 due to the excitation of the 3rd floating magnet. At first, the experimental work was performed by connecting the servo motor using the fishing line with the 1st floating magnet (the fishing line went through the plastic bush of the 2nd and 3rd floating magnet). Figure 10.38 presents the displacements and velocities of the 1st, 2nd and 3rd floating magnets. The estimated amplitude of the applied harmonic force was 5N, and the frequency of the applied harmonic force was 3.35Hz.

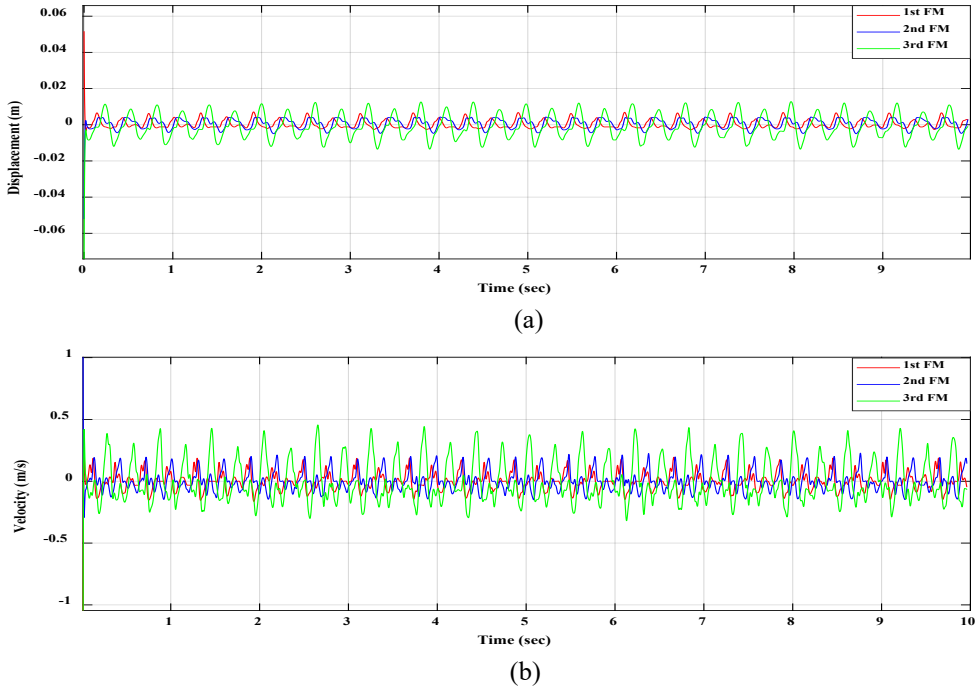

Figure 10.38: (a) Displacements and (b) Velocities of the floating magnets (Red, blue and green colour lines represent the displacement and velocity of the 1st, 2nd and 3rd floating magnet, respectively)

From Figure 10.38, it can be seen that although the fishing line was connected with the 1st floating magnet, the 3rd floating magnet achieved the maximum displacement and velocity than the 1st and 2nd floating magnets. Due to the applied harmonic force, the 1st floating magnet moved toward the 2nd floating magnet on average 6 mm but moved toward the bottom by 1 mm. On the other hand, the 2nd floating magnet moved toward the 3rd floating magnet by an average of 4 mm and toward the 1st by 4 mm. However, the 3rd floating magnet moved toward the top and 2nd floating magnet with an average of 10 mm excitation ranges. The 3rd floating magnet achieved the maximum velocity;

therefore, the winding coil generated the maximum induced voltage. Figure 10.39 displays the measured induced voltages of winding coils 1, 2 and 3.

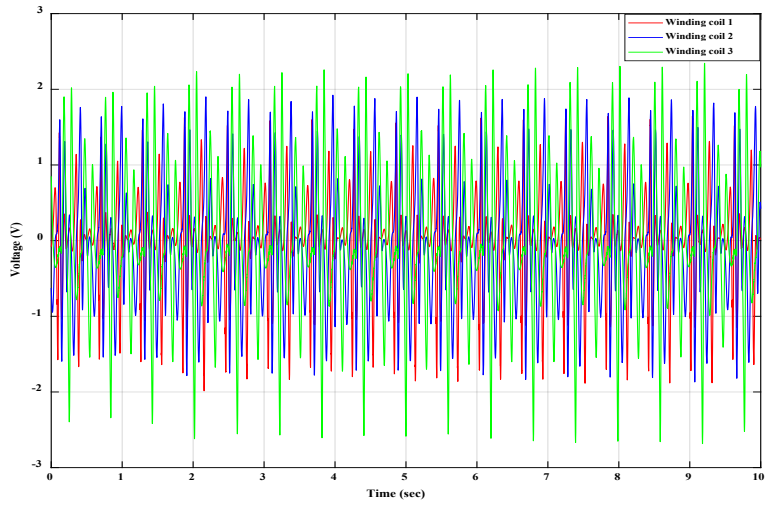

Figure 10.39: Induced voltage (Red, blue and green colour lines represent the induced voltages of the winding coils 1, 2 and 3, respectively)

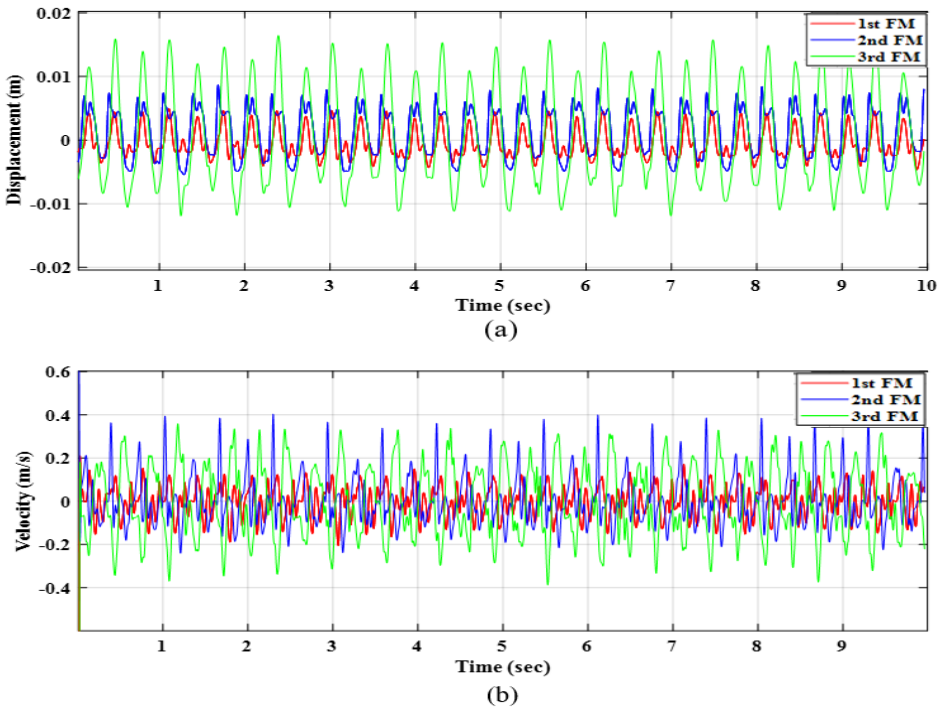

Figure 10.40: (a) Displacements and (b) Velocities of the floating magnets (Red, blue and green colour lines represent the displacement and velocity of the 1st, 2nd and 3rd floating magnet, respectively)

From Figure 10.39, it can be seen that winding coil 3 generated the maximum induced voltage than winding coil 1 and winding coil 2. However, winding coil 2 generated the maximum induced voltage than winding coil 1. Secondly, the experimental work was performed by connecting the 2nd floating magnet with the servo motor's pulley using the fishing line (the fishing line went through the plastic bush of the 3rd floating magnet and the 1st floating magnet was free). The estimated amplitude of the applied harmonic force was 6.5N, and the frequency of the applied harmonic force was 3.13Hz. Figure 10.40 displays the displacements and velocities of the 1st, 2nd and 3rd floating magnets. From Figure 10.40, it can be said that the 3rd floating magnet achieved the maximum displacement and velocity than the 1st and 2nd floating magnets. Because of the applied harmonic force, the maximum displacement of the 3rd floating was about 12.5 mm toward the top and 2nd floating magnets. The 2nd floating magnet achieved the maximum displacement of about 7 mm toward the 3rd and 1st floating magnets. Moreover, the 1st floating magnet achieved the maximum displacement of 4 mm toward the 2nd and bottom floating magnets. As the fishing line was connected with the 2nd floating magnet, the 2nd floating magnet achieved a higher velocity than the 1st floating magnet.

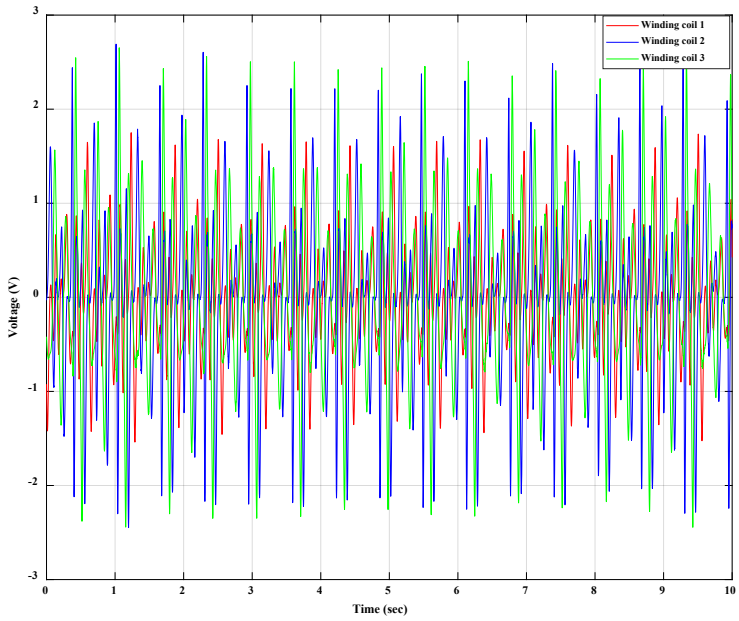

Figure 10.41: Induced voltage (Red, blue and green colour lines represent the induced voltages of the winding coils 1, 2 and 3, respectively)

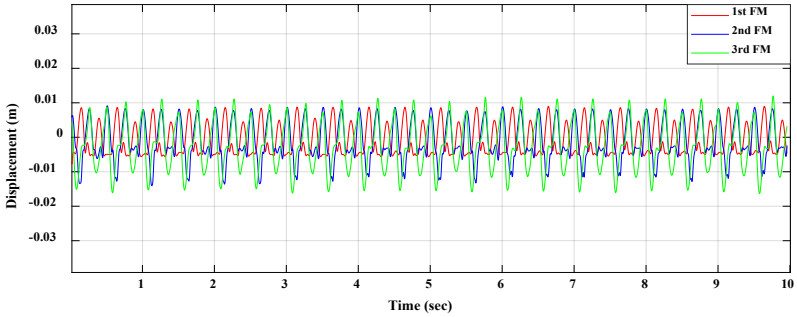

(a)

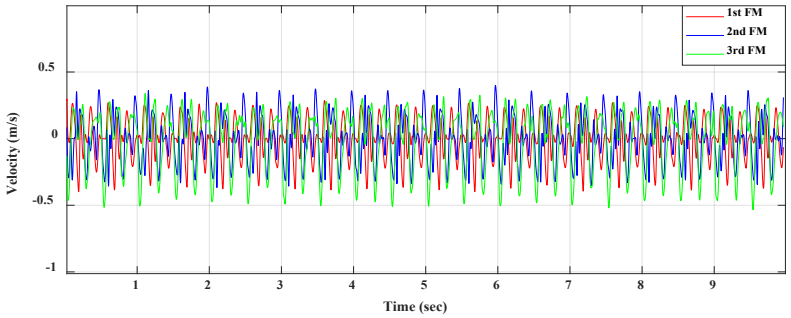

(b)

Figure 10.42: (a) Displacements and (b) Velocities of the floating magnets (Red, blue and green colour lines represent the displacement and velocity of the 1st, 2nd and 3rd floating magnet, respectively)

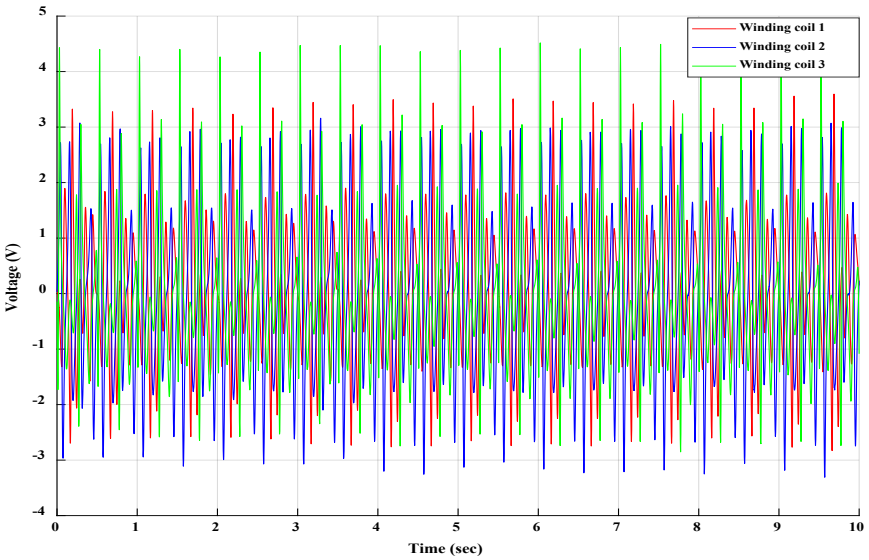

Figure 10.43: Induced voltage (Red, blue and green colour lines represent the induced voltages of the winding coils 1, 2 and 3, respectively)

Figure 10.41 shows the measured induced voltages of three winding coils. The measured induced voltages in winding coils 1 and 2 were similar. The measured induced voltage in winding coil 1 was lower than in winding coils 2 and 3. Furthermore, the experimental work was performed by connecting the 3rd floating magnet with the servo motor using the fishing line (1st and 2nd floating magnets were free). The estimated amplitude of the applied harmonic force was 7N, and the frequency of the applied harmonic force was 3.98 Hz. Figure 10.42 displays the displacements and velocities of the 1st, 2nd and 3rd floating magnets. Figure 10.43 presents the measured induced voltages. It can be seen from Figure 10.42 that the 3rd floating magnet achieved the maximum displacement and velocity than the 1st and 2nd floating magnets. The winding coil 3 generated higher induced voltage than the winding coil 1 and 2, as shown in Figure 10.43. From the above experimental analysis, it can be said that either the fishing line connected with the 1st or 2nd or 3rd floating magnet, the 3rd floating magnet achieved the higher displacement and velocity as well as higher induced voltage.

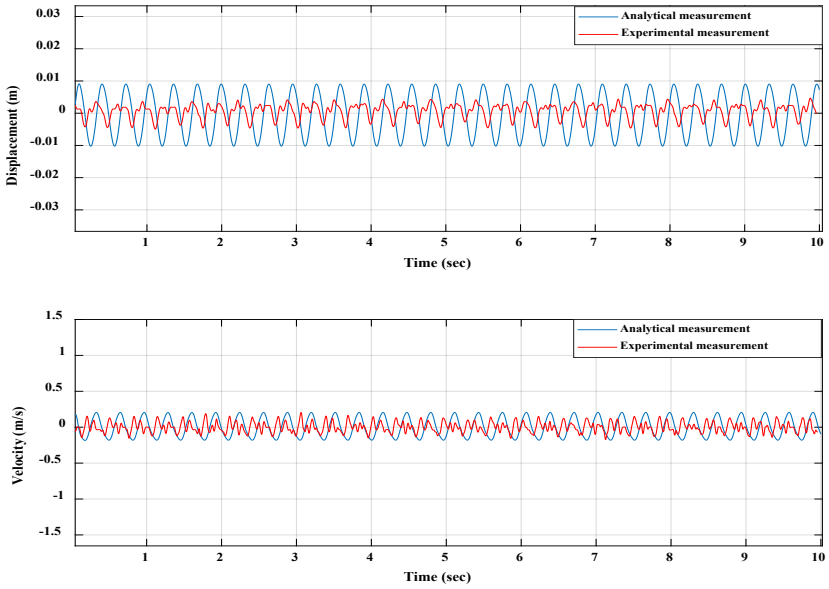

Figure 10.44: 1st floating magnet

To validate the analytical model simulations, the 3DOF energy harvester test rig was developed and experimented with within the lab environment. For the experimental study, the expected amplitude and frequency of the harmonic force were 6.5N and 3.136Hz, respectively. The same amplitude and frequency of the harmonic force were applied in the analytical model and compared with the experimental results. Figure 10.44 displays the displacement and velocity of the 1st floating magnet,

and Figure 10.45 shows the displacement and velocity of the 2nd floating magnet. Moreover, Figure 10.46 presents the displacement and velocity of the 3rd floating magnet. In Figure 10.44, Figure 10.45 and Figure 10.46, the blue and green lines represent the analytical and experimental measurements, respectively.

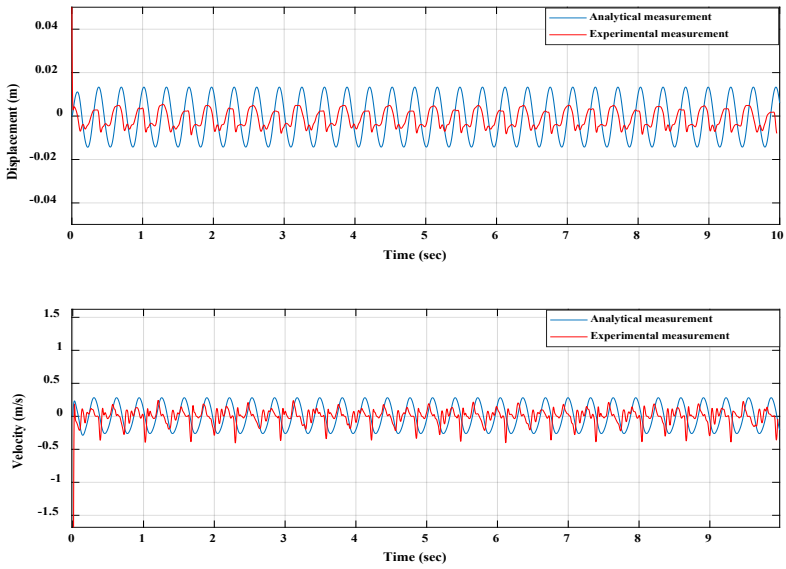

Figure 10.45: 2nd floating magnet

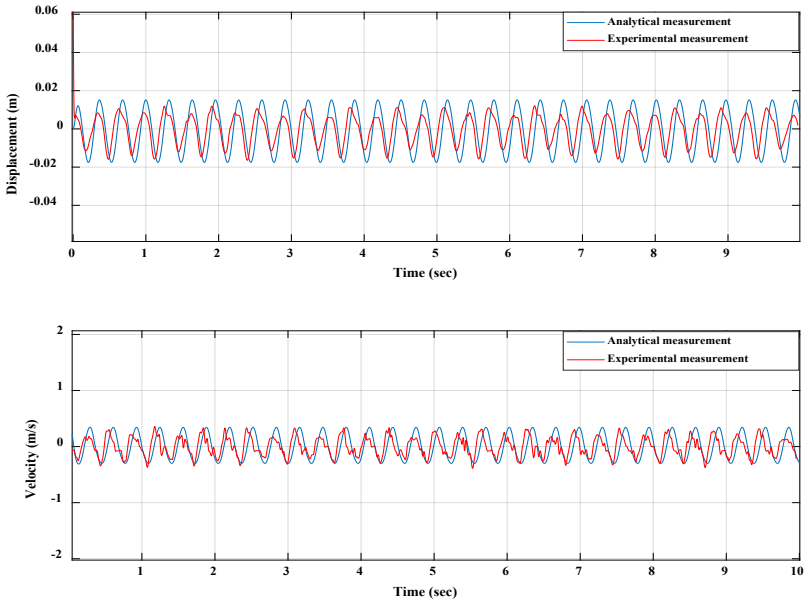

Figure 10.46: 3rd floating magnet

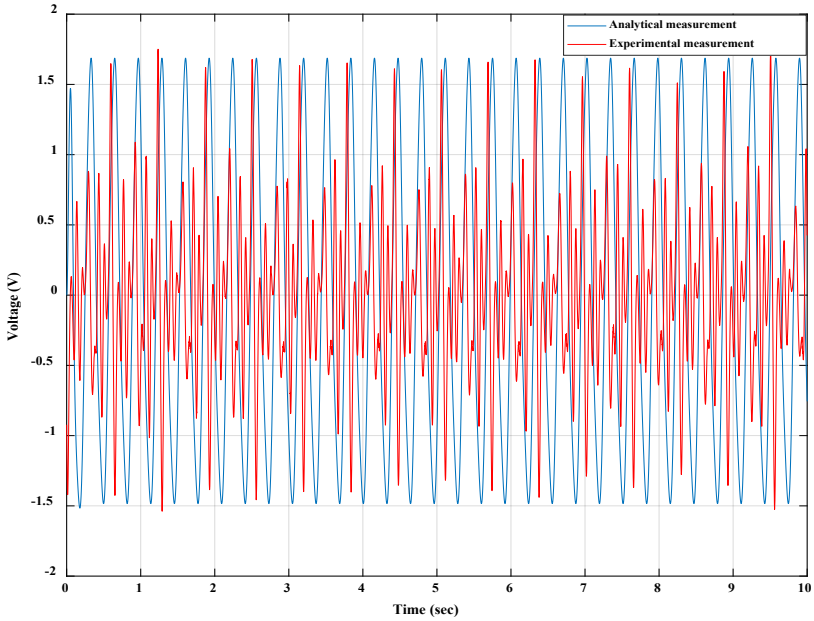

Figure 10.47: 1st winding coil

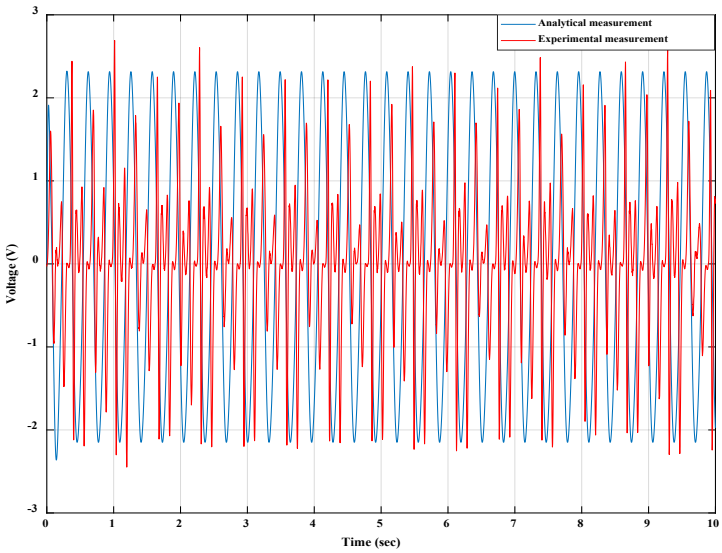

Figure 10.48: 2nd winding coil

The 1st and 2nd floating magnets showed higher displacement for the analytical measurement than the experimental measurement; however, both floating magnets presented almost identical velocities for both measurements, as shown in Figure 10.44 and Figure 10.45. However, the 3rd floating magnet showed similar displacement and velocity for the analytical and experimental measurements, as

displayed in Figure 10.46. Figures 10.47, 10.48 and 10.49 present the generated induced voltages in winding coils 1, 2 and 3, respectively.

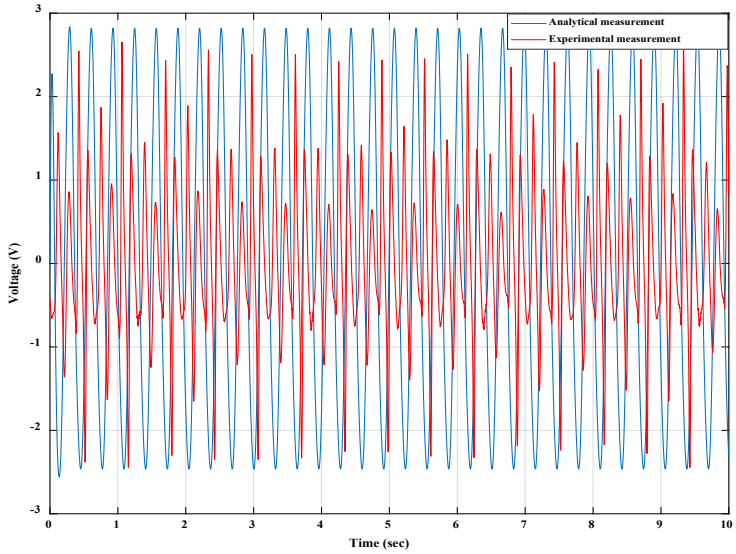

Figure 10.49: 3rd winding coil

The measured induced voltages in winding coils 1, 2, and 3 for experimental measurement were similar to the analytical measurement, as presented in Figures 10.47, 10.48 and 10.49. The winding coil 3 generated a higher induced voltage than the winding coils 2 and 1.

10.6 Conclusion

This chapter aimed to examine the 3DOF magnetic spring-based energy generator. The magnetic properties of the proposed energy harvester have been measured numerically. In this study, the eigenvalues and frequency responses caused by the movement of three floating magnets were calculated analytically. Different positions of the floating magnets showed various eigenvalues and natural frequencies. The influence of electromechanical coupling was studied on the 3DOF oscillator system. MATLAB's ode23t solver was used to solve the state space model of the 3DOF energy harvester. Experimental and analytical methods were used to investigate the dynamics of the proposed 3DOF energy harvester. Comparing the 3DOF energy harvester model with the SDOF and 2DOF models showed that the 3DOF model has a more remarkable ability to harness ocean energy due to three resonances.

Chapter 11
Discussions, Conclusions and Recommendations of Future Work

This chapter aims to discuss the findings of the proposed nonlinear oscillator-based energy generator and the application of the proposed system in the ocean environment to harness ocean wave energy. This chapter discusses the essential findings and parameters of all degrees of freedom nonlinear oscillator systems with and without electromechanical coupling. Then the key results of the proposed system are compared with the existing energy generator's findings in the literature. After that, a brief discussion is presented on how the current study can be applied to the ocean environment. Moreover, this chapter summarises the key findings of the magnetic spring-based nonlinear oscillator system with and without electrical-mechanical coupling for different degrees of freedom and their potential applications in the ocean environment. The key features of the design of SDOF, 2DOF and 3DOF magnetic spring-based nonlinear oscillator systems with and without electrical and mechanical coupling are discussed. Notably, the key findings of the previous chapters are briefly discussed in this chapter. Following this, the methods used in research and computational work and how they can be applied in similar systems are discussed. Finally, a summary is presented for future research work exploring how the design and performance improvements can be made to magnetic spring energy generators with short-term research projects.

11.1 Discussion

In this thesis study, a novel nonlinear oscillator system-based energy generator is designed and analysed using magnetic restoring forces to levitate an oscillating centre magnet. The mass of each magnet (ring type permanent magnet) is 315g, and the height, outer and inner diameters are 13mm, 72mm and 32.5 mm, respectively. All magnets are axially magnetised thru the 13 mm, and the permanent magnet compositions are NdFeB grade N42. The mass and size of the used magnet are comparably higher than the mass and size of the used magnet to build the magnetic spring-based (magnetic levitation) oscillator in literature, as presented in Table 11.1. To measure the magnetic flux density of ring types permanent magnets, the equation used in the literature is applied to measure the axial magnet flux density but not for radial magnetic flux density. As the winding coils are placed outside the floating magnet's surface, measuring radial magnetic flux density is essential. Thus, the axial magnetic flux density was measured using the analytical method, whereas the radial magnetic flux density was measured using the experimental method. The findings (analytical) were validated

with the numerical simulation to justify the analytical analysis of axial magnetic flux density. The measurements (experimental) were validated with the numerical results to justify the experimental measurement of radial magnetic flux density.

Table 11.1: Comparison of the parameters of the magnetic spring-based oscillator system from the literature

Ref.	Magnet type	NIM	MFM (g)	Size (mm)			Magnet grade
				T	B	M	
(Mann & Sims, 2009)	C	1	19.5	ND	ND	ND	ND
(Liu et al., 2014)	C	1	1.23	3×2	3×2	6×6	N35
(Yang et al., 2011)	R	1	29	12×5×1	12×5×1	12×5×10	ND
(Aldawood et al., 2019)	C	1	18.1	12.7×4.76	12.7×4.76	12.7×19.1	N42
(Bernal & García, 2012)	C	1	ND	ND	ND	13×5	ND
(Foisal et al., 2012)	C	1	3.35	2×2	2×2	6×16	N35
(Soares dos Santos et al., 2016)	C	1	1.24	3×1	3×1	3×6	ND
(Saha et al., 2008)	C	2	27	10×1	10×1	15×8	ND
(Dallago et al., 2010)	C	2	20.9	10×1	10×1	15×8	ND
(Munaz et al., 2013)	C	3	11.5	10×5	10×10	10×30	ND
(Masoumi & Wang, 2016)	R	3	1539	50.8×6.4×12.7	50.8×6.4×12.7	50.8×6.4×25.4	N42
(W. Wang et al., 2017)	C	3/6	9.4	20×4	20×4	20×4	N35
This study	R	1	315	72×32.5×13	72×32.5×13	72×32.5×13	N42

Note: NIM= number of inertial magnets, MFM=Mass of the floating magnet, T=Top magnet, B= Bottom magnet, M=Middle magnet, C=Cylindrical, R= Ring, ND=Not defined

It was found that the numerical methods showed very similar findings to analytical and experimental methods. The magnetic properties of the proposed magnetic spring-based oscillator system were studied using numerical methods. In literature, it was seen that the magnetic restoring forces were measured either using the only numerical or analytical or experimental methods or any two of them,

as shown in Table 11.2. However, the novelty of this present work is that the magnetic restoring force of the proposed magnetic spring-based oscillator system was measured using analytical, numerical and experimental methods and validated the measurements by comparing each other.

Table 11.2: Comparison of the parameters of the magnetic spring-based oscillator system from the literature

Ref.	r_t	r_b	GFE	Magnetic field	Magnetic restoring force
(Mann & Sims, 2009)	37.3	37.3	No	ND	E/A
(Liu et al., 2014)	18-28	18-28	No	A	A
(Yang et al., 2011)	8	8	No	FEM	SA
(Aldawood et al., 2019)	36.1	36.1	No	A	SA/FEM
(Bernal & García, 2012)	ND	ND	No	A	A/FEM
(Foisal et al., 2012)	14	14	No	A	A
(Soares dos Santos et al., 2016)	25	25	No	SA	SA
(Saha et al., 2008)	17	17	Yes	FEM	FEM/A
(Dallago et al., 2010)	19	19	Yes	FEM	FEM/A
(Munaz et al., 2013)	17.5	17.5	No	SA/FEM	ND
(Masoumi & Wang, 2016)	50.8	50.8	No	FEM	E/A
(W. Wang et al., 2017)	56	56	No	FEM	E/A
This study	104	79	Yes	FEM/E	E/A/FEM

Note: r_t= Distance between top to the middle magnet, r_b= Distance between middle to the bottom magnet, GFE=Gravitational force effect on the equilibrium position, SA=Semi-analytical, ND=Not defined, A= Analytical, FEM= Finite Element Method, E= Experimental

The magnetic restoring force of the proposed single-degree-of-freedom (SDOF) oscillator system is higher than the magnetic force of the other oscillator systems (Mann & Sims, 2009; Owens & Mann, 2012; Saravia et al., 2017). Moreover, it was found that the gravitation force affects the system's equilibrium position and magnetic restoring force. The centre floating magnet moved toward the bottom fixed magnet by 12.5 mm from the expected equilibrium position. Maximum researchers in the literature did not consider or ignore the gravitational force effects presented in Table 11.2. Therefore, the analysis of the gravitational force effects on equilibrium position is the originality of this current study. The coefficients of the proposed SDOF oscillator system were determined from

the magnetic restoring force curve using the polynomial curve fitting method. The linear and nonlinear stiffnesses of the magnetic spring-based system were determined for different excitation ranges of the centre floating magnet. It was found that the higher-order polynomial curve fitting provided a good fit for high excitation ranges; however, lower-order polynomial curve fitting provided a good fit for the low excitation range. The linear and nonlinear stiffnesses were used to study the dynamics of the SDOF nonlinear oscillator system. As the maximum researchers did not consider the gravitational force effects, one of the nonlinear spring constant (k2) (N/m2) was ignored, as shown in Table 11.3.

Table 11.3: Coefficients and dynamics of the system compared with other existing systems

Ref.	OL (mm)	LSC (k_1) (N/m)	NSC (k_2) (N/m^2)	NSC (k_3) (N/m^3)	DC	EVA	RF (Hz)
(Liu et al., 2014)	46	10	ND	7.6×10^{4}	A/E	No	14.36
	56	4.9	ND	2.1×10^{4}	A/E	No	10.05
	66	2.7	ND	7.4×10^{4}	A/E	No	7.46
(Mann & Sims, 2009)	ND	35	ND	1.384×10^{5}	A/E	No	6.74
(Yang et al., 2011)	64	628	ND	ND	ND	No	23.43
(Aldawood et al., 2019)	100.8	2566	ND	2.963×10^{9}	ND	No	9
	100.8	1002	ND	8.693×10^{7}	ND	No	11
(Bernal & García, 2012)	ND	ND	ND	ND	A	No	ND
(Foisal et al., 2012)	44	7.08	ND	ND	ND	No	7.32
(Soares dos Santos et al., 2016)	58	ND	ND	ND	A/SA	No	ND
(Saha et al., 2008)	44	61.5	ND	ND	A/E	No	7.6
(Dallago et al., 2010)	56	7.8370×10^{-2}	4.2003×10^{-6}	4.1142×10^{-4}	A/E	No	10.4
(Munaz et al., 2013)	80	ND	ND	ND	ND	No	6
(Masoumi & Wang, 2016)	254	6450.84	ND	7.92E06	A/E	No	10.3
(W. Wang et al., 2017)	140	67.8963	ND	58014	A/E	No	5-7.8
This Study	212	157.32	3308	64428	A/E	Yes	5.47
	222	269.31	5680.4	163159	A/E	Yes	5.14
	272	259.87	7580.7	244955	A/E	Yes	3.76

Note: OL= Oscillator length, LSC= Linear spring constant, NSC= Nonlinear spring constant, DC= Damping coefficient, EVA=Eigenvalue analysis, RF=Resonance frequency, ND=Not defined, A= Analytical, SA=Semi-analytical, E= Experimental

The eigenvalues and frequency responses were analysed by changing the position of the middle floating magnet. It was found from this study that the eigenvalue and resonance frequency of the

oscillator system changed with changing the position of the floating magnet. The oscillator system has shown an average 5.19Hz (analytical measurement) natural frequency in the system's equilibrium position, which changed with changing the position of the floating magnet. The experimental measured natural frequency was 5.14Hz, and the percentage of error of the findings was 0.962%. Moreover, the damping ratio of the system was determined analytically (0.032) and experimentally (0.031) with a percentage of error of 3.22%. The measured natural frequency of the system is lower than the other system's natural frequency, as presented in Table 11.3. Moreover, the system was analysed by changing the length of the oscillator. It was found that the damping ratio and resonance frequency increased with decreasing the length of the oscillator and decreased with increasing the length of the oscillator. The damping ratio varied from 0.0153 to 0.0463, and the natural frequency varied from 3.76Hz to 5.47Hz. It has been found that the magnetic restoring force of the oscillator increased with decreasing the length of the oscillator, and decreased with increasing the length of the oscillator. However, the dynamics study of the oscillator system for different positions of the floating magnet and different lengths of the oscillator are one of the main novelties of this present work. The proposed SDOF oscillator was studied with electromechanical coupling.

The proposed generator was modelled mathematically and fabricated the test rig to validate the model. The system dynamics were compared with and without electromechanical coupling, and it was found that the electromechanical coupling affects the system. With changing the position of the floating magnet, the eigenvalues and resonance frequency of the electric part remained constant; however, the eigenvalues and resonance frequency of the mechanical part changed. From the literature, it was seen that not a single researcher analysed the eigenvalue values of the magnetic spring-based energy generator for different positions of the floating magnet and different lengths of the generator, as shown in Table 11.4. Therefore, eigenvalue analysis is one of the novelties of the generator system.

Compared to the mechanical resonance frequency, the electrical resonance was two high. With increasing the number of turns of the coils, the inductance increased, and with expanding the inductance, the resonance of the electrical part decreased. The coupling coefficients and electromagnetic damping were determined. The comparison of the proposed generator's electromechanical coefficient parameters with other existing parameters in the literature is presented in Table 11.4. From Table 11.4, it can be seen that the maximum research analysis of the induced voltages either uses the analytical or numerical method. The present study analysed the generator's energy generation ability analytically and experimentally to validate the mathematical model.

Table 11.4: Comparison of the electromechanical coupling parameters of the proposed generator from literature

Ref.	HWC	DWC	NT	Inductance (H)	Resistance (ohm)	CC	EVA	Induced voltage
(Liu et al., 2014)	10-30	11	ND	ND	10-20	A	No	A
(Mann & Sims, 2009)	ND	ND	ND	ND	188	A	No	A
(Yang et al., 2011)	ND	15	2×600	ND	ND	ND	No	SA
(Aldawood et al., 2019)	13.7	17.4	450	ND	93	ND	No	SA
(Foisal et al., 2012)	ND	15	1500	ND	ND	ND	No	A
(Berdy et al., 2014)	ND	NA	10000	NR	450	SA	No	A
(Soares dos Santos et al., 2016)	20	8.2	15000	1	3630	ND	No	SA
(Saha et al., 2008)	6	17	1000	ND	800	ND	No	A
(Dallago et al., 2010)	ND	ND	500	ND	60	A	No	A
(Munaz et al., 2013)	5	12	1000	ND	115	ND	No	A
(Masoumi & Wang, 2016)	101.6	62.4	10186	ND	6191	A	No	A
(W. Wang et al., 2017)	60	25	480	ND	5	ND	No	A
This study	10	78	100	0.005546	5.48	A/FEM	Yes	A/E

Note: HWC= Height of the winding coil, DWC=Diameter of the winding coil, CC=Coupling coefficient, EVA=Eigenvalue analysis, A= Analytical, NT= Number of turns, SA=Semi-analytical, ND=Not defined, E= Experimental, FEM= Finite Element Method

Moreover, all the existing magnetic spring-based generators presented in the literature were tested using a vibrometer/shaker or exciter to excite the system. But the present magnetic spring-based generator was tested by applying external harmonic forces on the floating magnet. Under certain circumstances, engaging the nonlinear response of the system can result in relatively large oscillations over a much broader range of frequencies, thus potentially improving the ability to harvest energy. Moreover, the proposed SDOF oscillator-based generator system was studied by changing different parameters (parametric study). It was found that velocity of the floating magnet, magnetic flux density, air gap (between the inner surface of the winding coil and outer surface of the floating magnet), number of turns of the winding coil, coil diameter, and external applied harmonic force affects the energy generation ability of the generator. Based on SDOF magnetic spring nonlinear oscillator system, the two-degree-of-freedom (2DOF) and three-degree-of-freedom (3DOF) nonlinear oscillator system were studied with and without electromechanical coupling. The

mathematical models of the proposed 2DOF and 3DOF nonlinear oscillator systems were developed with and without electromechanical couplings. The proposed 2DOF and 3DOF oscillator system's test rig setups were developed in the laboratory to validate the mathematical models.

The magnetic restoring forces for all floating magnets were determined analytically, and the coefficients of both oscillator systems (2DOF and 3DOF) were measured from magnetic restoring forces using curve fitting methods. The eigenvalues and the resonance frequencies for both systems were studied using the measured linear and nonlinear coefficients. The 2DOF oscillator system showed two resonance frequencies (33 rad/s and 44.3 rad/s), and the 3DOF system provided three resonance frequencies (33.89 rad/s, 46.85 rad/s and 67.97 rad/s). The experimentally measured natural frequencies for the 2DOF oscillator system were 32.87 rad/s and 44.89 rad/s, and for the 3DOF system provided were 32.87 rad/s, 44.47 rad/s and 56 rad/s, which are very similar to the analytical measurements. The mathematical models of the generator system were developed by adding electromechanical coupling with the 2DOF and 3DOF oscillator systems. The magnetic properties of the generator system were analysed numerically. The eigenvalues and the resonance frequency of the generator system were studied using the linear and nonlinear stiffnesses determined for 2DOF and 3DOF nonlinear oscillator systems. The energy generation ability of the generator system was studied analytically by applying external harmonic force.

The test rig setup for the 2DOF and 3DOF oscillator system-based generator system was developed and tested the energy generation ability by applying external harmonic force. The experimental findings were compared with the analytical results to validate the mathematical model of the proposed 2DOF and 3DOF nonlinear oscillator-based energy generators. The SDOF magnetic spring-based generator system had only one degree of freedom and was limited to one resonant frequency. On the other hand, the 2DOF magnetic spring-based generator system had two-degree-of-freedom and was limited to two resonant frequencies. Likewise, the 3DOF magnetic spring-based generator system had three-degree-of-freedom and was limited to three resonant frequencies. The energy generator picked up and resonated at every frequency present in the vibration source. Therefore, three resonant frequencies achieved maximum power using three-degree-of-freedom (3DOF) oscillator system. The findings of the 3DOF oscillator-based generator were compared with the 2DOF and SDOF oscillator-based generators. It was found that the generator with the 3DOF oscillator can harvest more energy than the generators with 2DOF and SDOF oscillators under the same applied harmonic forces. Moreover, it was seen that the generator with the 2DOF oscillator produced more induced voltages

than the generator with the SDOF oscillator system. The design and modelling of the 2DOF and 3DOF magnetic spring-based generator systems are the novelty of the present study since no other researcher proposed the generator systems based on 2DOF and 3DOF magnetic spring-oscillator systems.

11.2 Application of the Magnetic Spring Oscillator-based Energy Generator in the Ocean Energy Field to Harness Ocean Wave Energy

Linear generator-based wave energy converters (WECs) can eliminate mechanical interfaces such as gearboxes, hydraulics, and pneumatics, simplifying the PTO system. The principle operation of the linear generator-based wave energy converters is that the linear generator's translator is directly coupled to the float, or simple mechanical fitting is used in the wave energy converters. In contrast to traditional rotary generators, the translator's motion changes in the same direction as the wave speed due to linear generators' ability to operate at variable wave speeds. Due to these factors, the voltage and current generated vary in frequency and amplitude. Additionally, the phase sequence alternates, which results in a significantly higher peak-to-average power ratio. Linear generators are distinguished by low velocity, high force, and short stroke. Because of the intrinsic nature of marine waves and the pressing need for high power generation, the linear generator has increased in size considerably. The disadvantages of linear generators include high attractive force due to the large volume of magnetic materials, static and dynamic effects, large dimensions, high cost, reduced efficiency due to low speed and the high initial cost. A relatively large air gap is required to eliminate manufacturing tolerances and high attractive forces between stator and translator. By widening the frequency bandwidth of the WEC, the bandwidth problem of the existing linear generator based WEC system has been overcome. Light damping magnetic spring-based nonlinear oscillators have larger operational frequency bandwidth than a conventional single-degree-of-freedom (SDOF) linear oscillator. The magnetic levitation (magnetic spring) system has been proposed in the translator design to make the oscillator nonlinear, which is more effective in the broadband frequency range, especially in the low-frequency ocean environment (Liu, 2017; Masoumi & Wang, 2016).

The specific magnet arrangement and structure (permanent magnets at both ends) provide a braking system and add non-linearity properties to the harvester (produces a nonlinear vibration levitation using repelling magnetic forces).

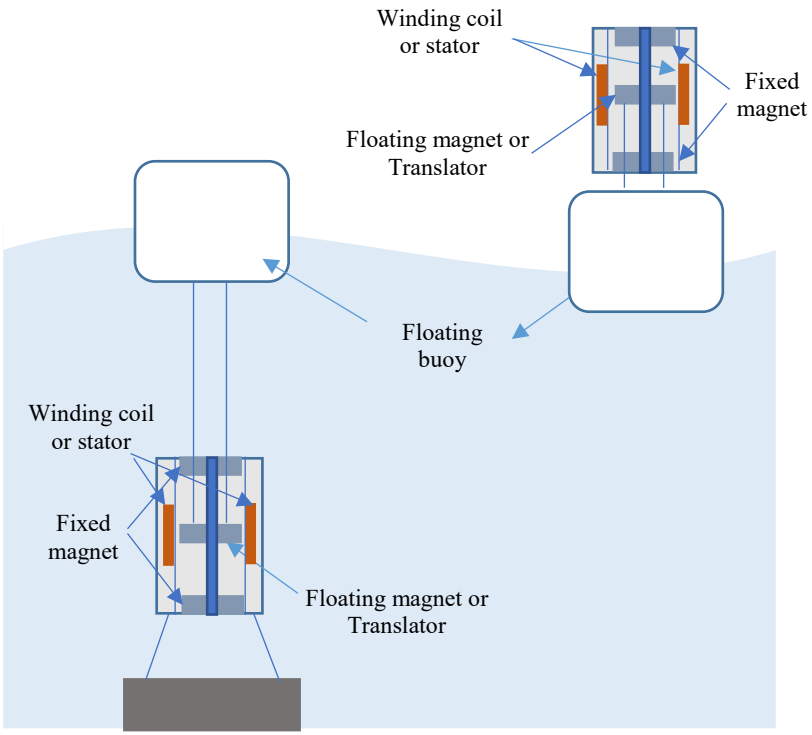

(a)

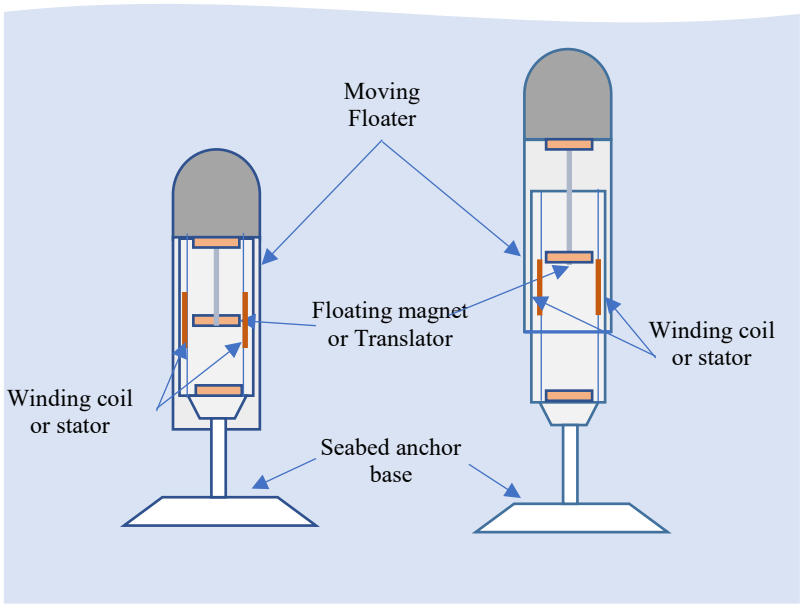

(b)

Figure 11.1: (a) Floating buoy on the sea surface (b) Fully submerged heaving system

The magnetic spring-based oscillator system delivers high power density broadband in the ocean wave energy harvester with variable resonance. The floating body can be connected with the floating

magnet or middle magnet, which will work as a translator. Fixed magnets can be connected with both ends of the shaft, and the winding coil will work as the stator. Figure 11.1 presents different topologies of wave energy converter (WEC) with SDOF magnetic spring nonlinear oscillator based linear generator system. The proposed nonlinear oscillator system-based energy harvester can harvest unidirectional vibrational energy and ocean wave energy through multiple approaches.

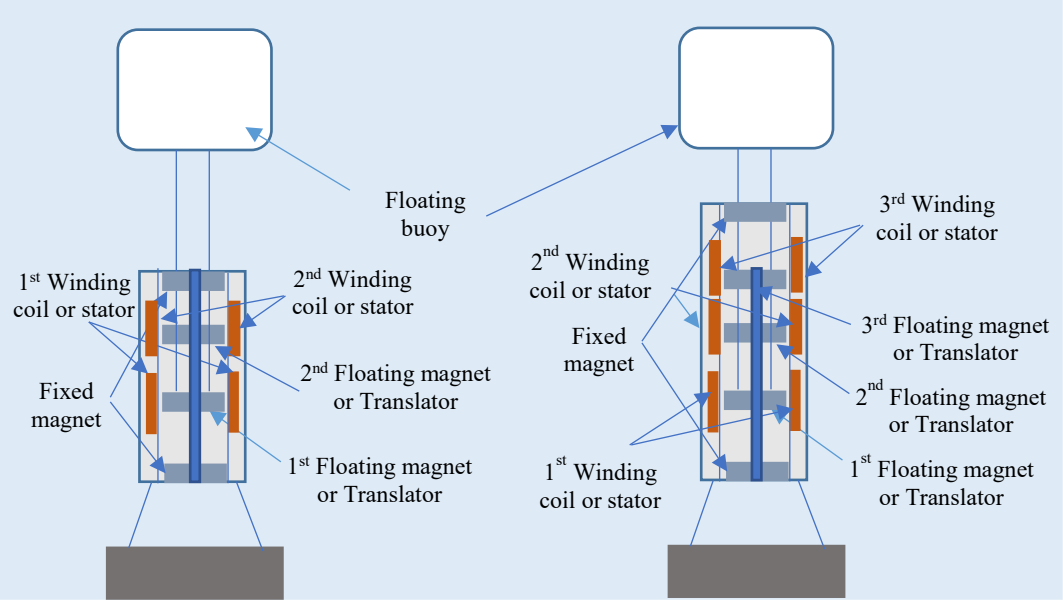

(a) (b)

Figure 11.2: (a) WEC with 2DOF nonlinear oscillator based linear generator system and (b) WEC with 3DOF nonlinear oscillator based linear generator system.

Moreover, the SDOF magnetic spring-based system had only one degree of freedom and was limited to only one resonant natural frequency. Preferably, the energy generator should pick up and resonate at every frequency present in the source vibration. Therefore, double and triple resonant frequencies provided maximum power when employed in the two-degree-of-freedom (2DOF) and three-degree-of-freedom (3DOF) oscillator systems. Figure 11.2(a) shows the topology of WEC with the 2DOF nonlinear oscillator based linear generator system, and Figure 11.2(b) presents the topology of WEC with the 3DOF nonlinear oscillator based linear generator system.

To harness energy from vibration sources or ocean waves, the proposed linear generator can be used as a single device or hybrid device (joining triboelectric nanogenerators (TENGs) and linear generator or linear generator and piezoelectric materials or triboelectric nanogenerators (TENGs), piezoelectric

and linear generator) (Vidal et al., 2021). Wave energy harvesters based on triboelectric nanogenerator (TENG) and electromagnetic generators (EMG) have been proposed to harvest kinetic and potential wave energy over a wide range of frequencies and work very efficiently (Feng et al., 2018; Saadatnia et al., 2018). The proposed SDOF, 2DOF and 3DOF nonlinear oscillator system based electromagnetic generator can be used with triboelectric nanogenerators to harness ocean wave energy.

11.3 Conclusions

In this thesis, the design and modelling of the magnetic spring-based oscillator system for different degrees of freedom were investigated analytically, numerically and experimentally with and without electromechanical coupling. The SDOF and 2DOF Oscillator System consist of 3 magnets (1 floating magnet and two fixed) and four magnets (2 floating magnets and two fixed magnets), respectively, whereas the 3DOF system consists of 5 magnets (3 floating magnets and two fixed magnets). The study found that the 2DOF and 3DOF magnetic spring-based energy generator provides a broad range of resonant frequencies compared to the SDOF magnetic spring-based energy generator. By having a wide range of frequencies, the system is suitable for situations in which ambient vibrations may be random or uncertain resonant frequencies are present such as in the ocean environment. While the SDOF magnetic spring-based energy generator generates maximum power only when the ocean waves frequency is nearly equal to the system's resonant frequency, the multi-degree-of-freedom system can generate maximum power for different resonant frequencies.

In chapter 3, the permanent magnet's characteristics and the governing analytical equations were discussed and analysed using ANSYS Maxwell and experimental methods. The changes in magnetic flux densities outside the ring types of permanent magnets in the radial and axial directions were analysed using analytical, numerical and experimental methods. The magnetic properties were analysed by changing the poles (same and opposite poles) between two and three magnets. The magnetic properties, magnetic force and magnetic restoring forces of the magnetic spring-based system were studied by placing three magnets in the same poles (NS-SN-NS or SN-NS-SN). The magnetic restoring force was analysed both analytically and numerically and compared. Further, the governing equations were discussed along with the relevant electromagnetic theory. The most important conclusions were specific to this study: the theoretical and numerical studies of magnet

characterisation and its application in an electromagnetic system to model the energy harvesting system.

The main goal of chapter 4 was to understand the magnetic properties of the magnetic spring-based SDOF oscillator system, magnetic restoring forces, coefficients, dynamics of the system and gravitational force effects on the oscillator system. The magnetic spring-based nonlinear system's characteristics and dynamics (Single degree of freedom system (SDOF) oscillator system) were discussed and analysed using analytical, experimental, and numerical methods. The magnetic restoring force and the coefficients of the proposed nonlinear system were investigated numerically, theoretically, and experimentally. Numerical and analytical measurements validated the experimentally measured magnetic restoring force. The cubic, quintic, and 7^{th} order polynomial curve fitting models were used to determine the linear and nonlinear stiffnesses from the measured magnetic restoring force. The eigenvalues and resonance frequency of the proposed nonlinear system were measured analytically using the linear and nonlinear stiffnesses. The analytical measured resonance frequency for the equilibrium position was compared with the experimental measurement. It was found that the eigenvalues and natural frequency of the system were changed by changing the floating magnet's position. Moreover, how the gravitational force effect changes the equilibrium position and magnetic restoring forces were studied. By changing the length of the oscillator, the gravitational force effects were studied, and it was found that the separation distance between magnets has a significant influence on the vibration. The resonance frequency of the oscillator system dropped, and the stable system became more unstable with increasing the length of the oscillator. The magnetic restoring forces for different lengths of the oscillator were measured using experimental and analytical methods. The proposed system's analytically measured damping ratios and natural frequencies for different heights were compared with the experimental measurements.

In chapters 5 and 6, the characteristics and dynamics of the magnetic spring-based two-degree-of-freedom (2DOF) and three-degree-of-freedom (3DOF) nonlinear systems were discussed and analysed, respectively. The magnetic restoring forces for 2DOF and 3DOF oscillator systems were determined analytically and numerically and compared. Using polynomial curve fitting, both oscillator systems' linear and nonlinear coefficients were measured from magnetic restoring forces. The eigenvalues and frequency responses of the 2DOF and 3DOF oscillator systems were analysed analytically. The 2DOF oscillator system showed two resonance frequencies, while the 3DOF system showed three. By changing the position of the floating magnets, the eigenvalues and frequency

responses for both systems were analysed, and it was found that with changing the position of floating magnets, the eigenvalues and natural frequencies changed.

As part of the experiment for the proposed oscillator systems, the design, development, all necessary instruments, and test rig setup were discussed in chapter 7. The primary purpose of setting up the test rig was to improve the efficiency of harvesting maximum energy at low-frequency ranges. The experimental test rig was developed and advanced to conduct multiple trials on different models to get the time domain voltage responses at the various velocities and external forces applied.

In chapter 8, the effects of electromechanical coupling on the oscillator system and energy generation ability were discussed. The step-by-step mathematical model of the primary SDOF energy generator is described in Chapter 8. The impacts of the electromechanical coupling were analysed analytically by varying different parameters of the magnets and winding coils. The dynamics of the SDOF energy harvester were analysed analytically using RL, RL with external load and RLC circuit. The magnetic spring-based energy generator's mathematical models were initially developed using state space methods. The method was implemented without considering the spatial variation of the magnetic field. The state space model of the proposed SDOF energy harvesters was investigated analytically using MATLAB ode 23t solver. The eigenvalues and resonance frequency of the system with the electromechanical coupling were studied. It was found that by comparing the oscillator system with and without electromechanical coupling, the system's dynamics were affected by the electromechanical coupling. The resonance frequency of the electrical part was higher than the mechanical part. The resonance frequency of the electrical part remained constant with changing the position of the floating magnet, but the resonance frequency of the mechanical part changed with changing the position of the floating magnet. The parametric study of the SDOF nonlinear oscillator-based energy harvester was performed numerically and analytical by changing various parameters. This study aimed to determine how the main design parameters of the energy generator, namely magnetic flux density, velocity of the floating magnet, damping, spring coefficients, resistance, and inductance, influence the voltage output of the energy harvester. The test rig of the SDOF energy harvester was developed and experimented with within the Lab environment to validate the analytical models. The test rig was developed by applying a harmonic force (ocean wave), and the experimental findings were compared to the theoretical models. The results indicated a great deal of agreement between the two models, thus validating the SDOF magnetic spring-based energy generator.

With the development of mathematical models and experimental validation of SDOF energy generators, the concept of multi-degree-of-freedom was subsequently extended to 2DOF and 3DOF energy generators. The design and development of the 2DOF and 3DOF magnetic spring-based energy generators were discussed in chapters 9 and 10, respectively. The effects of electromechanical coupling on the 2DOF and 3DOF oscillator systems and energy generation abilities were discussed. The mathematical models of the proposed 2DOF and 3DOF energy harvesters were developed, and the system's dynamics were investigated. The state space models of the proposed 2DOF and 3DOF energy harvesters were investigated analytically using MATLAB ode 23t solver, respectively. The generalised matrix of 2DOF and 3DOF was derived, and the solution methods were explained. Matrix equations for the 2DOF and 3DOF energy generators provided the basis for developing the mathematical design for the multi-degree-of-freedom magnetic spring-based energy generators. The eigenvalues and resonance frequencies of both 2DOF and 3DOF magnetic spring-based energy generators were studied, and it was found that the resonance frequencies of the electrical parts remained constant with changing the position of the floating magnets, but the resonance frequencies of the mechanical parts changed with changing the position of the floating magnet. The 2DOF and 3DOF energy harvester's test rigs were developed and experimented with within the Lab environment to validate the analytical models.

To gain a better understanding of the system's behaviour in relation to the individual design parameters of mass, damping constant, linear and nonlinear stiffness, magnetic flux density, resistance and inductance of the winding coil, the mathematical models were developed step by step from the SDOF energy generator to 2DOF and 3DOF energy generator system. In analysing the SDOF, 2DOF and 3DOF energy generator systems, hybrid methodologies comprised of analytical, numerical and experimental methods were used. The validation of the analytical model with experimental and numerical models (hybrid methods) was crucial to analysing the proposed energy generator system. In the near future, numerical methods will inevitably be used because the complex topologies of spatial magnetic variation will be required to design the energy generator. In this regard, the hybrid methodology was developed to generate a more straightforward framework for future MDOF energy generator system design and development. Each of the coils in the multi-degree-of-freedom energy generator produced a voltage that may or may not be in phase with the voltages of the other coils. Different resonant frequencies in the multi-degree-of-freedom energy generator system design, mainly when the goal is broadband energy harvesting, increase the phase differences

of individual coils. When adding coil voltages, several choices can be considered. A possible solution would be to convert each of the coil voltages into a DC voltage before adding them together. According to the modal behaviour of the system, the coils with maximum deflection and velocity, when a particular ocean wave frequency is applied, will produce more voltage and current than other coils. Overall, the following points could be concluded from this thesis study:

1. The proposed model approach creates a strong magnetic field
2. Analytically predicted axial magnetic flux density of a single ring type permanent magnet was validated with numerical results
3. Numerically measured radial magnetic flux density of a single ring type permanent magnet was validated with experimental measurement
4. Experimentally measured magnetic restoring force was validated with analytical and numerical simulations
5. Gravitational force affects the equilibrium position as well as the magnetic restoring force
6. Different positions of the floating magnets have distinct eigenvalues and natural frequencies
7. Different oscillator lengths show various magnetic restoring forces
8. Different oscillator lengths offer different damping ratios and natural frequencies
9. By changing the length of the oscillator, the stable system could be made unstable
10. The electromechanical coupling affects the frequency responses of the mechanical part
11. Proposed energy generator generated energy under applied harmonic forces
12. The energy generation ability of the magnetic generator depends on various parameters, which include magnetic flux density, the mass of the magnet, velocity of the magnet, resistance of the winding coil, the inductance of the coil, number of turns, applied harmonic forces
13. More degrees of freedom of the system results in more resonance frequencies which allows for the production of increased energy generation across a broader range of frequencies

11.4 Future Work and Recommendations

Researchers would be able to explore further avenues of linear generators based on magnetic spring systems through this research work. The study could be extended, for instance, to explore the magnetic restoring force for different sizes and shapes of floating and fixed magnets. To expand future research work, the following recommendations are made.

- Model analysis by changing the shape, size and weight of the floating and fixed magnet

- Study of the magnetic restoring force for different masses, sizes and shapes of the magnets
- Study of the gravitational force effects on different masses, shapes and sizes of the magnets
- Experimental analysis using RL (with external load) and RLC circuits
- Design and development of the SDOF magnetic spring-based energy generator
- Deployment in ocean environments for trials over the short and long term
- Performance evaluation of the prototype in the ocean environment
- Model analysis using Halbach Array
- Study of air-cored and iron-cored generators in terms of their prospects for a practical combined electrical-mechanical structural design solution
- Model analysis using iron core and multiple winding coils
- Design and development of the prototypes of the multi-degree-of-freedom magnetic spring-based energy harvesters
- Innovative systems for the transmission of the generated power to the grid
- Implementation of control systems in the deployed WEC during sea trials

References

Aderinto, T., & Li, H. (2018). Ocean wave energy converters: Status and challenges. *Energies, 11*(5), 1250.

Ahamed, R., McKee, K., & Howard, I. (2020). Advancements of wave energy converters based on power take off (PTO) systems: A review. *Ocean Engineering, 204*, 107248.

Ahn, K., Truong, D., Tien, H. H., & Yoon, J. I. (2012). An innovative design of wave energy converter. *Renewable Energy, 42*, 186-194.

Al Shami, E., Zhang, R., & Wang, X. (2019). Point absorber wave energy harvesters: A review of recent developments. *Energies, 12*(1), 47.

Aldawood, G., Nguyen, H. T., & Bardaweel, H. (2019). High power density spring-assisted nonlinear electromagnetic vibration energy harvester for low base-accelerations. *Applied Energy, 253*, 113546.

Amir, M. A. U., Sharip, R. M., Muzanni, M. A., & Anuar, H. A. (2016). Wave energy convertors (WEC): A review of the technology and power generation. AIP Conference Proceedings.

Amiri, A., Panahi, R., & Radfar, S. (2016). Parametric study of two-body floating-point wave absorber. *Journal of marine science and application, 15*(1), 41-49.

Andritsch, T., Morshuis, P., Smit, J., Jean, P., Van Kessel, R., Wattez, A., & Fourmon, A. (2012). Challenges of using electroactive polymers in large scale wave energy converters.2012 Annual Report Conference on Electrical Insulation and Dielectric Phenomena.

Antipov, V., Grozov, A., & Ivanova, A. (2017). A linear synchronous generator with a power of 30 kW for wave-power engineering. *Russian Electrical Engineering, 88*(2), 55-60.

Antonio, F. d. O. (2010). Wave energy utilization: A review of the technologies. *Renewable and sustainable energy reviews, 14*(3), 899-918.

António, F. d. O. (2007). Modelling and control of oscillating-body wave energy converters with hydraulic power take-off and gas accumulator. *Ocean engineering, 34*(14-15), 2021-2032.

Apo, D. J., & Priya, S. (2014). High power density levitation-induced vibration energy harvester. *Energy Harvesting and Systems, 1*(1-2), 79-88.

Ayub, S., Danish, S., & Qureshi, S. (2011). A novel, cost-effective design to harness ocean energy in the developing countries. Proceedings of World Academy of Science, Engineering and Technology.

Babarit, A., Gendron, B., Singh, J., Mélis, C., & Jean, P. (2013a). Hydro-elastic modelling of an electro-active wave energy converter. ASME 2013 32nd International Conference on Ocean, Offshore and Arctic Engineering.

Babarit, A., Gendron, B., Singh, J., Mélis, C., & Jean, P. (2013b). Hydro-elastic modelling of an electro-active wave energy converter. ASME 2013 32nd International Conference on Ocean, Offshore and Arctic Engineering.

Baker, N., & Mueller, M. A. (2001). Direct drive wave energy converters. *Rev. Energ. Ren.: Power Engineering*, 1-7.

Baker, N. J., Raihan, M. A., & Almoraya, A. A. (2018). A cylindrical linear permanent magnet Vernier hybrid machine for wave energy. *IEEE Transactions on Energy Conversion, 34*(2), 691-700.

Baker, N. J., Spooner, E., & Mueller, M. (2004). Permanent magnet air-cored tubular linear generator for marine energy converters. IEE Conference Publication.

Bard, J., & Kracht, P. (2013). Linear generator systems for wave energy converters. *Fraunhofer IWES*.

Bashir, M. S., & Farrok, O. (2019). Generation of Electrical Power by using High Graded Permanent Magnet Linear Generator in Wave Energy Conversion. 2019 1st International Conference on Advances in Science, Engineering and Robotics Technology (ICASERT).

Bastien, S. P., Sepe, R. B., Grilli, A. R., Grilli, S. T., & Spaulding, M. L. (2009). Ocean wave energy harvesting buoy for sensors. 2009 IEEE Energy Conversion Congress and Exposition.

Beeby, S. P., Wang, L., Zhu, D., Weddell, A. S., Merrett, G. V., Stark, B., Szarka, G., & Al-Hashimi, B. M. (2013). A comparison of power output from linear and nonlinear kinetic energy harvesters using real vibration data. *Smart Materials and Structures, 22*(7), 075022.

Berdy, D., Valentino, D., & Peroulis, D. (2014). Design and optimization of a magnetically sprung block magnet vibration energy harvester. *Sensors and actuators A: Physical, 218*, 69-79.

Berenjkoob, M. N., Ghiasi, M., & Soares, C. G. (2019). Performance of Two Types of Mooring Systems in the Heave Motion of a Two-body Floating Wave Energy Converter. *Journal of Marine Science and Application, 18*(1), 38-47.

Bernal, A. A., & García, L. L. (2012). The modelling of an electromagnetic energy harvesting architecture. *Applied Mathematical Modelling, 36*(10), 4728-4741.

Bianchi, N., Bolognani, S., & Cappello, A. (2005). Reduction of cogging force in PM linear motors by pole-shifting. *IEE Proceedings-Electric Power Applications, 152*(3), 703-709.

Boscaino, V., Cipriani, G., Di Dio, V., Franzitta, V., & Trapanense, M. (2017). Experimental test and simulations on a linear generator-based prototype of a wave energy conversion system designed with a reliability-oriented approach. *Sustainability, 9*(1), 98.

Brekken, T. K. (2011). On model predictive control for a point absorber wave energy converter. 2011 IEEE Trondheim PowerTech.

Brekken, T. K., Von Jouanne, A., & Han, H. Y. (2009a). Ocean wave energy overview and research at Oregon State University.Power Electronics and Machines in Wind Applications, 2009. PEMWA 2009. IEEE.

Brekken, T. K., Von Jouanne, A., & Han, H. Y. (2009b). Ocean wave energy overview and research at Oregon State University. 2009 IEEE Power Electronics and Machines in Wind Applications.

Brooking, P., & Mueller, M. (2005). Power conditioning of the output from a linear vernier hybrid permanent magnet generator for use in direct drive wave energy converters. *IEE Proceedings-Generation, Transmission and Distribution, 152*(5), 673-681.

Budar, K., & Falnes, J. (1975). A resonant point absorber of ocean-wave power. *Nature, 256*(5517), 478.

Camacho, J. M., & Sosa, V. (2013). Alternative method to calculate the magnetic field of permanent magnets with azimuthal symmetry. *Revista mexicana de física E, 59*(1), 8-17.

Cappelli, L., Marignetti, F., Mattiazzo, G., Giorcelli, E., Bracco, G., Carbone, S., & Attaianese, C. (2013). Linear tubular permanent-magnet generators for the inertial sea wave energy converter. *IEEE Transactions on Industry Applications, 50*(3), 1817-1828.

Carneiro, P., dos Santos, M. P. S., Rodrigues, A., Ferreira, J. A., Simões, J. A., Marques, A. T., & Kholkin, A. L. (2020). Electromagnetic energy harvesting using magnetic levitation architectures: A review. *Applied Energy, 260*, 114191.

Carneiro, P. M., Vidal, J. V., Rolo, P., Peres, I., Ferreira, J. A., Kholkin, A. L., & dos Santos, M. P. S. (2022). Instrumented electromagnetic generator: Optimized performance by automatic self-adaptation of the generator structure. *Mechanical Systems and Signal Processing, 171*, 108898.

Castellucci, V., Eriksson, M., & Waters, R. (2016). Impact of tidal level variations on wave energy absorption at wave hub. *Energies, 9*(10), 843.

Chan, T.-F., & Lai, L. L. (2007). Permanent-magnet machines for distributed power generation: A review. 2007 IEEE Power Engineering Society General Meeting.

Chau, K., Zhang, D., Jiang, J., & Jian, L. (2008). Transient analysis of coaxial magnetic gears using finite element comodeling. *Journal of Applied Physics, 103*(7), 07F101.

Chau, K., Zhang, D., Jiang, J., Liu, C., & Zhang, Y. (2007). Design of a magnetic-geared outer-rotor permanent-magnet brushless motor for electric vehicles. *IEEE transactions on magnetics, 43*(6), 2504-2506.

Chen, J., Yang, J., Li, Z., Fan, X., Zi, Y., Jing, Q., Guo, H., Wen, Z., Pradel, K. C., & Niu, S. (2015). Networks of triboelectric nanogenerators for harvesting water wave energy: a potential approach toward blue energy. *ACS nano, 9*(3), 3324-3331.

Cheng, Z., Yang, J., Hu, Z., & Xiao, L. (2014). Frequency/time domain modeling of a direct drive point absorber wave energy converter. *Science China Physics, Mechanics and Astronomy, 57*(2), 311-320.

Chiu, M.-C., Chang, Y.-C., Yeh, L.-J., & Chung, C.-H. (2012). Optimal design of a vibration-based electromagnetic energy harvester using a simulated annealing algorithm. *Journal of Mechanics, 28*(4), 691-700.

Clément, A., McCullen, P., Falcão, A., Fiorentino, A., Gardner, F., Hammarlund, K., Lemonis, G., Lewis, T., Nielsen, K., & Petroncini, S. (2002). Wave energy in Europe: current status and perspectives. *Renewable and sustainable energy reviews, 6*(5), 405-431.

Clifton, P., McMahon, R., & Kelly, H. (2010). Design and commissioning of a 30 kW direct drive wave generator. 5th IET International Conference on Power Electronics, Machines and Drives (PEMD 2010).

Crozier, R., Bailey, H., Mueller, M., Spooner, E., & McKeever, P. (2013). Analysis, design and testing of a novel direct-drive wave energy converter system. *IET Renewable Power Generation, 7*(5), 565-573.

Curto, D., Viola, A., Franzitta, V., Trapanese, M., & Cardona, F. (2020). A New Solution for Sea Wave Energy Harvesting, the Proposal of an Ironless Linear Generator. *Journal of Marine Science and Engineering, 8*(2), 93.

Czech, B., & Bauer, P. (2012). Wave energy converter concepts: Design challenges and classification. *IEEE Industrial Electronics Magazine, 6*(2), 4-16.

Dallago, E., Marchesi, M., & Venchi, G. (2010). Analytical model of a vibrating electromagnetic harvester considering nonlinear effects. *IEEE Transactions on Power Electronics, 25*(8), 1989-1997.

Danielsson, O. (2006). *Wave energy conversion: Linear synchronous permanent magnet generator* Acta Universitatis Upsaliensis.

Danielsson, O., & Leijon, M. (2007). Flux distribution in linear permanent-magnet synchronous machines including longitudinal end effects. *IEEE transactions on magnetics, 43*(7), 3197-3201.

Danielsson, O., Leijon, M., & Sjostedt, E. (2005). Detailed study of the magnetic circuit in a longitudinal flux permanent-magnet synchronous linear generator. *IEEE Transactions on Magnetics, 41*(9), 2490-2495.

Danielsson, O., Thorburn, K., Eriksson, M., & Leijon, M. (2003). Permanent magnet fixation concepts for linear generator. Proceedings of the 5th European Wave Energy Conference.

Day, A., Babarit, A., Fontaine, A., He, Y.-P., Kraskowski, M., Murai, M., Penesis, I., Salvatore, F., & Shin, H.-K. (2015). Hydrodynamic modelling of marine renewable energy devices: A state of the art review. *Ocean Engineering, 108*, 46-69.

de Sousa Prado, M. G., Gardner, F., Damen, M., & Polinder, H. (2006). Modelling and test results of the Archimedes wave swing. *Proceedings of the Institution of Mechanical Engineers, Part A: Journal of Power and Energy, 220*(8), 855-868.

Dean, R. G., & Dalrymple, R. A. (1991). *Water wave mechanics for engineers and scientists* (Vol. 2). World Scientific Publishing Company.

Demenko, A., Kulig, S., Nowak, L., Zawirski, K., Parel, T. S., Rotaru, M. D., Sykulski, J. K., & Hearn, G. E. (2011). Optimisation of a tubular linear machine with permanent magnets for wave energy extraction. *COMPEL-The international journal for computation and mathematics in electrical and electronic engineering*.

Di Dio, V., Franzitta, V., Milone, D., Pitruzzella, S., Trapanese, M., & Viola, A. (2014). Design of bilateral switched reluctance linear generator to convert wave energy: Case study in Sicily. Advanced Materials Research.

Ding, S., Yan, S., Han, D., & Ma, Q. (2015). Overview on hybrid wind-wave energy systems.2015 International conference on Applied Science and Engineering Innovation.

Dos Santos, M. P. S., Ferreira, J. A., Simões, J. A., Pascoal, R., Torrão, J., Xue, X., & Furlani, E. P. (2016). Magnetic levitation-based electromagnetic energy harvesting: a semi-analytical non-linear model for energy transduction. *Scientific reports, 6*(1), 1-9.

Dosiek, L., & Pillay, P. (2007). Cogging torque reduction in permanent magnet machines. *IEEE Transactions on industry applications, 43*(6), 1565-1571.

Ekergård, B. (2013). *Full scale applications of permanent magnet electromagnetic energy converters: From Nd2Fe14B to ferrite* Acta Universitatis Upsaliensis.

Ekergård, B., & Leijon, M. (2020). Longitudinal End Effects in a Linear Wave Power Generator. *Energies, 13*(2), 327.

El-Sayed, M. A., & Sharaf, A. M. (2011). An efficient hybrid wave/photovoltaic scheme for energy supply in remote areas. *International Journal of Renewable Energy Technology, 2*(1), 67-85.

Elwood, D., Schacher, A., Rhinefrank, K., Prudell, J., Yim, S., Amon, E., Brekken, T., & von Jouanne, A. (2009). Numerical modeling and ocean testing of a direct-drive wave energy device utilizing a permanent magnet linear generator for power take-off.International Conference on Offshore Mechanics and Arctic Engineering.

Elwood, D., Yim, S. C., Prudell, J., Stillinger, C., Von Jouanne, A., Brekken, T., Brown, A., & Paasch, R. (2010). Design, construction, and ocean testing of a taut-moored dual-body wave energy converter with a linear generator power take-off. *Renewable Energy, 35*(2), 348-354.

Engström, J., Eriksson, M., Isberg, J., & Leijon, M. (2009). Wave energy converter with enhanced amplitude response at frequencies coinciding with Swedish west coast sea states by use of a supplementary submerged body. *Journal of Applied Physics, 106*(6), 064512.

Engström, J., Kurupath, V., Isberg, J., & Leijon, M. (2011). A resonant two body system for a point absorbing wave energy converter with direct-driven linear generator. *Journal of applied physics, 110*(12), 124904.

Eriksson, M., Isberg, J., & Leijon, M. (2005). Hydrodynamic modelling of a direct drive wave energy converter. *International Journal of Engineering Science, 43*(17-18), 1377-1387.

Eriksson, S. (2019). Design of Permanent-Magnet Linear Generators with Constant-Torque-Angle Control for Wave Power. *Energies, 12*(7), 1312.

Faiz, J., Ebrahimi-Salari, M., & Shahgholian, G. (2009). Reduction of cogging force in linear permanent-magnet generators. *IEEE Transactions on magnetics, 46*(1), 135-140.

Faiz, J., & Nematsaberi, A. (2017a). Linear electrical generator topologies for direct-drive marine wave energy conversion-an overview. *IET Renewable Power Generation, 11*(9), 1163-1176.

Faiz, J., & Nematsaberi, A. (2017b). Linear permanent magnet generator concepts for direct-drive wave energy converters: A comprehensive review. 2017 12th IEEE Conference on Industrial Electronics and Applications (ICIEA).

Falcão, A. F., & Henriques, J. C. (2016). Oscillating-water-column wave energy converters and air turbines: A review. *Renewable Energy, 85*, 1391-1424.

Falnes, J. (2007). A review of wave-energy extraction. *Marine structures, 20*(4), 185-201.

Fan, F.-R., Tian, Z.-Q., & Wang, Z. L. (2012). Flexible triboelectric generator. *Nano energy, 1*(2), 328-334.

Farrok, O., Islam, M. R., Guo, Y., Zhu, J., & Xu, W. (2018). A Novel Design Procedure for Designing Linear Generators. *IEEE Transactions on Industrial Electronics, 65*(2), 1846-1854.

Farrok, O., Islam, M. R., Muttaqi, K. M., Sutanto, D., & Zhu, J. (2019). Design and Optimization of a Novel Dual-Port Linear Generator for Oceanic Wave Energy Conversion. *IEEE Transactions on Industrial Electronics*.

Farrok, O., Islam, M. R., Sheikh, M. R. I., Guo, Y., Zhu, J., & Lei, G. (2017). A novel method to avoid degradation due to demagnetization of PM linear generators for oceanic wave energy extraction. 2017 20th International Conference on Electrical Machines and Systems (ICEMS).

Farrok, O., Islam, M. R., Sheikh, M. R. I., Guo, Y., & Zhu, J. G. (2017). A split translator secondary stator permanent magnet linear generator for oceanic wave energy conversion. *IEEE Transactions on Industrial Electronics, 65*(9), 7600-7608.

Farrok, O., Islam, M. R., Sheikh, M. R. I., Guo, Y., & Zhu, J. G. (2018). A Split Translator Secondary Stator Permanent Magnet Linear Generator for Oceanic Wave Energy Conversion. *IEEE Transactions on Industrial Electronics, 65*(9), 7600-7608.

Farrok, O., Kiran, M. R., Islam, M. R., Xu, W., & Zhu, J. (2019). Core loss minimization of the linear generator by using high graded magnetic materials for harvesting oceanic wave energy. 2019 IEEE International Electric Machines & Drives Conference (IEMDC).

Feng, L., Liu, G., Guo, H., Tang, Q., Pu, X., Chen, J., Wang, X., Xi, Y., & Hu, C. (2018). Hybridized nanogenerator based on honeycomb-like three electrodes for efficient ocean wave energy harvesting. *Nano Energy, 47*, 217-223.

Feng, N., Yu, H., Hu, M., Liu, C., Huang, L., & Shi, Z. (2016). A study on a linear magnetic-geared interior permanent magnet generator for direct-drive wave energy conversion. *Energies, 9*(7), 487.

First4Magnets. (2020). *How is the strength of a magnet measured?* Retrieved 10.04, from https://www.first4magnets.com/tech-centre-i61/information-and-articles-i70/how-is-the-strength-of-a-magnet-measured-i81

Foisal, A. R. M., Hong, C., & Chung, G.-S. (2012). Multi-frequency electromagnetic energy harvester using a magnetic spring cantilever. *Sensors and Actuators A: Physical, 182*, 106-113.

Frigaard, P., Kofoed, J. P., & Knapp, W. (2004). Wave dragon. Wave power plant using low-head turbines. *Proceedings of the Hidroenergia, Falkenberg, Sweden*, 17-19.

Furlani, E. P. (2001). *Permanent magnet and electromechanical devices: materials, analysis, and applications*. Academic press.

Fusco, F., Nolan, G., & Ringwood, J. V. (2010). Variability reduction through optimal combination of wind/wave resources–An Irish case study. *Energy, 35*(1), 314-325.

Gao, M., Wang, Y., Wang, Y., & Wang, P. (2018). Experimental investigation of non-linear multi-stable electromagnetic-induction energy harvesting mechanism by magnetic levitation oscillation. *Applied Energy, 220*, 856-875.

Gao, Y., Shao, S., Zou, H., Tang, M., Xu, H., & Tian, C. (2016). A fully floating system for a wave energy converter with direct-driven linear generator. *Energy, 95*, 99-109.

Gargov, N., & Zobaa, A. (2012). Multi-phase air-cored tubular permanent magnet linear generator for wave energy converters. *IET Renewable Power Generation, 6*(3), 171-176.

Gargov, N., Zobaa, A., & Pisica, I. (2014). Separated magnet yoke for permanent magnet linear generator for marine wave energy converters. *Electric Power Systems Research, 109*, 63-70.

Gaspar, J. F., Calvário, M., Kamarlouei, M., & Soares, C. G. (2016). Power take-off concept for wave energy converters based on oil-hydraulic transformer units. *Renewable Energy, 86*, 1232-1246.

Gatti, R. R. (2013). *Spatially-varying multi-degree-of-freedom electromagnetic energy harvesting* Curtin University.

Gunn, K., & Stock-Williams, C. (2012). Quantifying the global wave power resource. *Renewable Energy, 44*, 296-304.

Guo, R., Yu, H., Xia, T., Shi, Z., Zhong, W., & Liu, X. (2018). A simplified subdomain analytical model for the design and analysis of a tubular linear permanent magnet oscillation generator. *IEEE Access, 6*, 42355-42367.

Hai, L., Svensson, O., Isberg, J., & Leijon, M. (2015). Modelling a point absorbing wave energy converter by the equivalent electric circuit theory: A feasibility study. *Journal of Applied Physics, 117*(16), 164901.

Hansen, R. H., Kramer, M. M., & Vidal, E. (2013). Discrete displacement hydraulic power take-off system for the wavestar wave energy converter. *Energies, 6*(8), 4001-4044.

Henderson, R. (2006). Design, simulation, and testing of a novel hydraulic power take-off system for the Pelamis wave energy converter. *Renewable energy, 31*(2), 271-283.

Hinchet, R., Seung, W., & Kim, S. W. (2015). Recent progress on flexible triboelectric nanogenerators for selfpowered electronics. *ChemSusChem, 8*(14), 2327-2344.

Hodgins, N., Keysan, O., McDonald, A., & Mueller, M. (2010). Linear generator for direct drive wave energy applications. The XIX International Conference on Electrical Machines-ICEM 2010.

Hodgins, N., Keysan, O., McDonald, A. S., & Mueller, M. A. (2011). Design and testing of a linear generator for wave-energy applications. *IEEE Transactions on Industrial Electronics, 59*(5), 2094-2103.

Hong, Y. (2016). *Numerical Modelling and Mechanical Studies on a Point Absorber Type Wave Energy Converter* Acta Universitatis Upsaliensis.

Hong, Y., Eriksson, M., Castellucci, V., Boström, C., & Waters, R. (2016). Linear generator-based wave energy converter model with experimental verification and three loading strategies. *IET Renewable Power Generation, 10*(3), 349-359.

Hong, Y., Hultman, E., Castellucci, V., Ekergård, B., Sjökvist, L., Elamalayil Soman, D., Krishna, R., Haikonen, K., Baudoin, A., & Lindblad, L. (2013). Status update of the wave energy research at Uppsala University.10th European Wave and Tidal Conference (EWTEC).

Hong, Y., Waters, R., Boström, C., Eriksson, M., Engström, J., & Leijon, M. (2014). Review on electrical control strategies for wave energy converting systems. *Renewable and Sustainable Energy Reviews, 31*, 329-342.

Huang, L., Hu, M., Yu, H., Liu, C., & Chen, Z. (2016). Design and experiment of a direct-drive wave energy converter using outer-PM linear tubular generator. *IET Renewable Power Generation, 11*(3), 353-360.

Huang, L., Yu, H., Hu, M., Liu, C., & Yuan, B. (2013). Research on a tubular primary permanent-magnet linear generator for wave energy conversions. *IEEE Transactions on Magnetics, 49*(5), 1917-1920.

Huang, L., Yu, H., Hu, M., Zhao, J., & Cheng, Z. (2011). A novel flux-switching permanent-magnet linear generator for wave energy extraction application. *IEEE Transactions on Magnetics, 47*(5), 1034-1037.

Hwang, W. S., Ahn, J. H., Jeong, S. Y., Jung, H. J., Hong, S. K., Choi, J. Y., Cho, J. Y., Kim, J. H., & Sung, T. H. (2017). Design of piezoelectric ocean-wave energy harvester using sway movement. *Sensors and Actuators A: Physical, 260*, 191-197.

Ibrahim, H., Ilinca, A., & Perron, J. (2008). Energy storage systems—Characteristics and comparisons. *Renewable and sustainable energy reviews, 12*(5), 1221-1250.

International Energy Agency. (2015). *World Energy Outlook 2015 Factsheet: Global energy trends to 2040*. https://www.iea.org/media/news/2015/press/151110_WEO_Factsheet_GlobalEnergyTrends.pdf

IRENA. (2014). *WAVE ENERGY TECHNOLOGY BRIEF*. https://www.irena.org/publications/2014/Jun/Wave-energy

Ivanova, I., Bernhoff, H., Ågren, O., & Leijon, M. (2005). Simulated generator for wave energy extraction in deep water. *Ocean engineering, 32*(14-15), 1664-1678.

Ivanova, I. A., Agren, O., Bernhoff, H., & Leijon, M. (2005). Simulation of wave-energy converter with octagonal linear generator. *IEEE Journal of Oceanic Engineering, 30*(3), 619-629.

Jbaily, A., & Yeung, R. W. (2015). Piezoelectric devices for ocean energy: a brief survey. *Journal of Ocean Engineering and Marine Energy, 1*(1), 101-118.

Jean, P., Wattez, A., Ardoise, G., Melis, C., Van Kessel, R., Fourmon, A., Barrabino, E., Heemskerk, J., & Queau, J. (2012). Standing wave tube electro active polymer wave energy converter. Electroactive Polymer Actuators and Devices (EAPAD) 2012.

Jin, C., Kang, H., Kim, M., & Bakti, F. P. (2020). Performance evaluation of surface riding wave energy converter with linear electric generator. *Ocean Engineering, 218*, 108141.

Joseph, D. M., & Cronje, W. A. (2007). Design and analysis of a double-sided tubular linear synchronous generator with particular application to wave-energy conversion. 2007 IEEE Power Engineering Society Conference and Exposition in Africa-PowerAfrica.

Jusoh, M. A., Ibrahim, M. Z., Daud, M. Z., Albani, A., & Mohd Yusop, Z. (2019). Hydraulic Power Take-Off Concepts for Wave Energy Conversion System: A Review. *Energies, 12*(23), 4510.

K&J Magnetics, I. (2020). *Demagnetization (BH) Curves for Neodymium Magnets*. Retrieved 05.10, from https://www.kjmagnetics.com/bhcurves.asp

K. Dragoon, J. E., L. Patton. (2015). *Wave Energy Industry Update: A Northwest US Perspective*. http://oregonwave.org/oceanic/wp-content/uploads/2015/10/Northwest-Wave-Energy-Industry-Update-FINAL.pdf

Kecik, K., Mitura, A., Lenci, S., & Warminski, J. (2017). Energy harvesting from a magnetic levitation system. *International Journal of Non-Linear Mechanics, 94*, 200-206.

Khan, U., & Kim, S.-W. (2016). Triboelectric nanogenerators for blue energy harvesting. *ACS nano, 10*(7), 6429-6432.

Khatri, P., & Wang, X. (2019). Comprehensive review of a linear electrical generator for ocean wave energy conversion. *IET Renewable Power Generation, 14*(6), 949-958.

Kim, K.-H., Lee, K., Sohn, J. M., Park, S.-W., Choi, J.-S., & Hong, K. (2015). Conceptual design of 10MW class floating wave-offshore wind hybrid power generation system. The Twenty-fifth International Ocean and Polar Engineering Conference.

Kim, T.-H., Takao, M., Setoguchi, T., Kaneko, K., & Inoue, M. (2001). Performance comparison of turbines for wave power conversion. *International journal of thermal sciences, 40*(7), 681-689.

Kimoulakis, N. M., Kladas, A. G., & Tegopoulos, J. A. (2009). Cogging force minimization in a coupled permanent magnet linear generator for sea wave energy extraction applications. *IEEE Transactions on Magnetics, 45*(3), 1246-1249.

Lasa, J., Antolin, J. C., Angulo, C., Estensoro, P., Santos, M., & Ricci, P. (2012). Design, construction and testing of a hydraulic power take-off for wave energy converters. *Energies, 5*(6), 2030-2052.

Le Méhauté, B. (2013). *An introduction to hydrodynamics and water waves*. Springer Science & Business Media.

Leijon, M., Boström, C., Danielsson, O., Gustafsson, S., Haikonen, K., Langhamer, O., Strömstedt, E., Stålberg, M., Sundberg, J., & Svensson, O. (2008). Wave energy from the North Sea: Experiences from the Lysekil research site. *Surveys in geophysics, 29*(3), 221-240.

Leijon, M., Danielsson, O., Eriksson, M., Thorburn, K., Bernhoff, H., Isberg, J., Sundberg, J., Ivanova, I., Sjöstedt, E., & Ågren, O. (2006). An electrical approach to wave energy conversion. *Renewable energy, 31*(9), 1309-1319.

Lejerskog, E., Boström, C., Hai, L., Waters, R., & Leijon, M. (2015). Experimental results on power absorption from a wave energy converter at the Lysekil wave energy research site. *Renewable energy, 77*, 9-14.

Li, A. L., Ma, B. M., & Chen, C. Q. (2012). Detent force analysis in permanent magnet linear synchronous motor considering longitudinal end effects. 2012 15th International Conference on Electrical Machines and Systems (ICEMS).

Li, W., Chau, K., & Jiang, J. (2011). Application of linear magnetic gears for pseudo-direct-drive oceanic wave energy harvesting. *IEEE Transactions on Magnetics, 47*(10), 2624-2627.

Li, W., Chau, K., Lee, C. H., Ching, T., Chen, M., & Jiang, J. (2017). A new linear magnetic gear with adjustable gear ratios and its application for direct-drive wave energy extraction. *Renewable energy, 105*, 199-208.

Liu, C.-T., Lin, C.-L., Hwang, C.-C., & Tu, C.-H. (2010). Compact model of a slotless tubular linear generator for renewable energy performance assessments. *IEEE transactions on magnetics, 46*(6), 1467-1470.

Liu, C., Yu, H., Hu, M., Liu, Q., & Zhou, S. (2013). Detent force reduction in permanent magnet tubular linear generator for direct-driver wave energy conversion. *IEEE transactions on magnetics, 49*(5), 1913-1916.

Liu, C., Yu, H., Hu, M., Liu, Q., Zhou, S., & Huang, L. (2013). Research on a permanent magnet tubular linear generator for direct drive wave energy conversion. *IET Renewable power generation, 8*(3), 281-288.

Liu, H., Gudla, S., Hassani, F. A., Heng, C. H., Lian, Y., & Lee, C. (2014). Investigation of the nonlinear electromagnetic energy harvesters from hand shaking. *IEEE Sensors Journal, 15*(4), 2356-2364.

Liu, Z. (2017). *A nonlinear double-speed electromagnetic vibration energy harvester for ocean wave energy conversion* RMIT University.

Liu, Z., Zhang, R., Xiao, H., & Wang, X. (2020). Survey of the mechanisms of power take-off (PTO) devices of wave energy converters. *Acta Mechanica Sinica, 36*, 644-658.

López, I., Andreu, J., Ceballos, S., de Alegría, I. M., & Kortabarria, I. (2013). Review of wave energy technologies and the necessary power-equipment. *Renewable and sustainable energy reviews, 27*, 413-434.

Manasseh, R., Sannasiraj, S., McInnes, K. L., Sundar, V., & Jalihal, P. (2017). Integration of wave energy and other marine renewable energy sources with the needs of coastal societies. *The International Journal of Ocean and Climate Systems, 8*(1), 19-36.

Mann, B., & Owens, B. (2010). Investigations of a nonlinear energy harvester with a bistable potential well. *Journal of Sound and Vibration, 329*(9), 1215-1226.

Mann, B., & Sims, N. (2009). Energy harvesting from the nonlinear oscillations of magnetic levitation. *Journal of sound and vibration, 319*(1-2), 515-530.

Maria-Arenas, A., Garrido, A. J., Rusu, E., & Garrido, I. (2019). Control Strategies Applied to Wave Energy Converters: State of the Art. *Energies, 12*(16), 3115.

Masoumi, M., & Wang, Y. (2016). Repulsive magnetic levitation-based ocean wave energy harvester with variable resonance: Modeling, simulation and experiment. *Journal of Sound and Vibration, 381*, 192-205.

Masuda, Y. (1986). An experience of wave power generator through tests and improvement. In *Hydrodynamics of ocean wave-energy utilization* (pp. 445-452). Springer.

McArthur, S., & Brekken, T. K. (2010). Ocean wave power data generation for grid integration studies. Power and Energy Society General Meeting, 2010 IEEE.

McDonald, A., Mueller, M., & Jeffrey, J. (2008). Development of a novel permanent magnet linear generator topology for direct-drive wave energy converters.2008 4th IET Conference on Power Electronics, Machines and Drives.

Molla, S., Farrok, O., Islam, M. R., & Muttaqi, K. M. (2020). Application of iron nitride compound as alternative permanent magnet for designing linear generators to harvest oceanic wave energy. *IET Electric Power Applications, 14*(5), 762-770.

Mueller, M. (2002). Electrical generators for direct drive wave energy converters. *IEE Proceedings-generation, transmission and distribution, 149*(4), 446-456.

Mueller, M., & Baker, N. (2002). A low speed reciprocating permanent magnet generator for direct drive wave energy converters.

Mueller, M., Baker, N., Ran, L., Chong, N., Wei, H., Tavner, P., & McKeever, P. (2008). Experimental tests of an air-cored PM tubular generator for direct drive wave energy converters.

Mueller, M., Xiang, J., Baker, N., & Brooking, P. (2006). Dynamic modeling of a linear Vernier hybrid permanent magnet machine coupled to a wave energy emulator test rig. In *Recent developments of electrical drives* (pp. 39-49). Springer.

Muetze, A., & Vining, J. (2006). Ocean wave energy conversion-a survey.Industry Applications Conference, 2006. 41st IAS Annual Meeting. Conference Record of the 2006 IEEE.

Mukhopadhyay, S., Donaldson, J., Sengupta, G., Yamada, S., Chakraborty, C., & Kacprzak, D. (2003). Fabrication of a repulsive-type magnetic bearing using a novel arrangement of permanent magnets for vertical-rotor suspension. *IEEE transactions on magnetics, 39*(5), 3220-3222.

Munaz, A., Lee, B.-C., & Chung, G.-S. (2013). A study of an electromagnetic energy harvester using multi-pole magnet. *Sensors and Actuators A: Physical, 201*, 134-140.

Mutsuda, H., Tanaka, Y., Doi, Y., & Moriyama, Y. (2019). Application of a flexible device coating with piezoelectric paint for harvesting wave energy. *Ocean Engineering, 172*, 170-182.

Nabavi, S. F., Farshidianfar, A., & Afsharfard, A. (2018). Novel piezoelectric-based ocean wave energy harvesting from offshore buoys. *Applied Ocean Research, 76*, 174-183.

Nilsson, K., Danielsson, O., & Leijon, M. (2006). Electromagnetic forces in the air gap of a permanent magnet linear generator at no load. *Journal of Applied Physics, 99*(3), 034505.

Niu, X. (2013). *Modeling and design analysis of a permanent magnet linear synchronous generator*.

Oprea, C. A., Martis, C. S., Biro, K. A., & Jurca, F. N. (2010). Design and testing of a four-sided permanent magnet linear generator prototype. The XIX International Conference on Electrical Machines-ICEM 2010.

Owens, B. A., & Mann, B. P. (2012). Linear and nonlinear electromagnetic coupling models in vibration-based energy harvesting. *Journal of Sound and Vibration, 331*(4), 922-937.

Ozkop, E., & Altas, I. H. (2017). Control, power and electrical components in wave energy conversion systems: A review of the technologies. *Renewable and Sustainable Energy Reviews, 67*, 106-115.

Panicker, P. (2012). *The Vertical Axis Oscillating Wave Power Generator*. Create the Future. Retrieved 16.10, from https://contest.techbriefs.com/2012/entries/sustainable-technologies/2496

Parmeggiani, S., Chozas, J. F., Pecher, A., Friis-Madsen, E., Sørensen, H., & Kofoed, J. P. (2011). Performance assessment of the wave dragon wave energy converter based on the EquiMar methodology.9th European Wave and Tidal Energy Conference (EWTEC).

Pecher, A., & Kofoed, J. P. (2017). *Handbook of ocean wave energy*. Springer London.

Pecher, A., & Peter Kofoed, J. (2017). *Handbook of ocean wave energy*. Springer Nature.

Penalba, M., & Ringwood, J. V. (2016). A review of wave-to-wire models for wave energy converters. *Energies, 9*(7), 506.

Perez-Collazo, C., Greaves, D., & Iglesias, G. (2018). A novel hybrid wind-wave energy converter for jacket-frame substructures. *Energies, 11*(3), 637.

Pérez-Collazo, C., Greaves, D., & Iglesias, G. (2015). A review of combined wave and offshore wind energy. *Renewable and Sustainable Energy Reviews, 42*, 141-153.

Piscopo, V., Benassai, G., Della Morte, R., & Scamardella, A. (2018). Cost-based design and selection of point absorber devices for the mediterranean sea. *Energies, 11*(4), 946.

Polinder, H., Damen, M., & Gardner, F. (2005). Design, modelling and test results of the AWS PM linear generator. *European Transactions on Electrical Power, 15*(3), 245-256.

Polinder, H., Damen, M. E., & Gardner, F. (2004). Linear PM generator system for wave energy conversion in the AWS. *IEEE transactions on energy conversion, 19*(3), 583-589.

Polinder, H., Mecrow, B., Jack, A. G., Dickinson, P., & Mueller, M. A. (2003). Linear generators for direct-drive wave energy conversion. IEEE International Electric Machines and Drives Conference, 2003. IEMDC'03.

Polinder, H., Mecrow, B. C., Jack, A. G., Dickinson, P. G., & Mueller, M. A. (2005). Conventional and TFPM linear generators for direct-drive wave energy conversion. *IEEE Transactions on Energy Conversion, 20*(2), 260-267.

Polinder, H., Mueller, M., Scuotto, M., & de Sousa Prado, M. G. (2007). Linear generator systems for wave energy conversion. Proceedings of the 7th European Wave and Tidal Energy Conference, Porto, Portugal.

Polinder, H., Mueller, M., Scuotto, M., & Goden de Sousa Prado, M. (2007). Linear generator systems for wave energy conversion. Proceedings of the 7th European Wave and Tidal Energy Conference, Porto, Sept.

Polinder, H., & Scuotto, M. (2005). Wave energy converters and their impact on power systems. Future Power Systems, 2005 International Conference on.

Priya, S. (2007). Advances in energy harvesting using low profile piezoelectric transducers. *Journal of electroceramics, 19*(1), 167-184.

Prudell, J., Stoddard, M., Amon, E., Brekken, T. K., & Von Jouanne, A. (2010). A permanent-magnet tubular linear generator for ocean wave energy conversion. *IEEE Transactions on Industry Applications, 46*(6), 2392-2400.

Prudell, J., Stoddard, M., Brekken, T. K., & von Jouanne, A. (2009a). A novel permanent magnet tubular linear generator for ocean wave energy. 2009 IEEE Energy Conversion Congress and Exposition.

Prudell, J., Stoddard, M., Brekken, T. K., & von Jouanne, A. (2009b). A novel permanent magnet tubular linear generator for ocean wave energy. Energy Conversion Congress and Exposition, 2009. ECCE 2009. IEEE.

Prudell, J. H. (2007). *Novel design and implementation of a permanent magnet linear tubular generator for ocean wave energy conversion.*

Qiao, D., Haider, R., Yan, J., Ning, D., & Li, B. (2020). Review of Wave Energy Converter and Design of Mooring System. *Sustainability, 12*(19), 8251.

Rahman, A., Farrok, O., Islam, M. R., & Xu, W. (2020). Recent Progress in Electrical Generators for Oceanic Wave Energy Conversion. *IEEE Access, 8*, 138595-138615.

Ran, L., Mueller, M., Ng, C., Tavner, P., Zhao, H., Baker, N., McDonald, S., & McKeever, P. (2011). Power conversion and control for a linear direct drive permanent magnet generator for wave energy. *IET renewable power generation, 5*(1), 1-9.

Rao, K. R., Sunderan, T., & Adiris, M. R. a. (2017). Performance and design optimization of two model based wave energy permanent magnet linear generators. *Renewable Energy, 101*, 196-203.

Rhinefrank, K., Agamloh, E., von Jouanne, A., Wallace, A., Prudell, J., Kimble, K., Aills, J., Schmidt, E., Chan, P., & Sweeny, B. (2006). Novel ocean energy permanent magnet linear generator buoy. *Renewable Energy, 31*(9), 1279-1298.

Rusu, E., & Onea, F. (2018a). A review of the technologies for wave energy extraction. *Clean Energy*.

Rusu, E., & Onea, F. (2018b). A review of the technologies for wave energy extraction. *Clean Energy, 2*(1), 10-19.

Rusu, E., & Venugopal, V. (2019). *Offshore Renewable Energy: Ocean Waves, Tides and Offshore Wind*. MDPI.

Saadatnia, Z., Asadi, E., Askari, H., Esmailzadeh, E., & Naguib, H. E. (2018). A heaving point absorber-based triboelectric-electromagnetic wave energy harvester: An efficient approach toward blue energy. *International Journal of Energy Research, 42*(7), 2431-2447.

Saha, C., O'donnell, T., Wang, N., & McCloskey, P. (2008). Electromagnetic generator for harvesting energy from human motion. *Sensors and Actuators A: Physical, 147*(1), 248-253.

Salauddin, M., Halim, M., & Park, J. (2016). A magnetic-spring-based, low-frequency-vibration energy harvester comprising a dual Halbach array. *Smart Materials and Structures, 25*(9), 095017.

Samrat, N. H., Ahmad, N. B., Choudhury, I. A., & Taha, Z. B. (2014). Modeling, control, and simulation of battery storage photovoltaic-wave energy hybrid renewable power generation systems for island electrification in Malaysia. *The Scientific World Journal, 2014*.

Saravia, C. M., Ramírez, J. M., & Gatti, C. D. (2017). A hybrid numerical-analytical approach for modeling levitation based vibration energy harvesters. *Sensors and Actuators A: Physical, 257*, 20-29.

Selvaggi, J. P., Salon, S. J., & Chari, M. V. (2010). Employing toroidal harmonics for computing the magnetic field from axially magnetized multipole cylinders. *IEEE transactions on magnetics, 46*(10), 3715-3723.

Seo, S.-W., Shin, K.-H., Koo, M.-M., Hong, K., Yoon, I.-J., & Choi, J.-Y. (2020). Experimentally Verifying the Generation Characteristics of a Double-Sided Linear Permanent Magnet Synchronous Generator for Ocean Wave Energy Conversion. *IEEE Transactions on Applied Superconductivity, 30*(4), 1-4.

Shibaike, A., Sanada, M., & Morimoto, S. (2007). Suitable configuration of permanent magnet linear synchronous generator for wave power generation. 2007 Power Conversion Conference-Nagoya.

Sjökvist, S. (2014). *Demagnetization studies on permanent magnets: Comparing fem simulations with experiments* Acta Universitatis Upsaliensis.

So, R. (2017). Validation of Wave Energy Converter Models and the Development of Control Strategies in WEC-Sim.

Soares, C. G., Bhattacharjee, J., Tello, M., & Pietra, L. (2012). Review and classification of wave energy converters. In *Maritime engineering and technology* (pp. 585-594). Taylor & Francis Group London, UK.

Soares dos Santos, M. P., Ferreira, J. A., Simões, J. A., Pascoal, R., Torrão, J., Xue, X., & Furlani, E. P. (2016). Magnetic levitation-based electromagnetic energy harvesting: a semi-analytical non-linear model for energy transduction. *Scientific reports, 6*(1), 1-9.

Stålberg, M., Waters, R., Danielsson, O., & Leijon, M. (2008). Influence of generator damping on peak power and variance of power for a direct drive wave energy converter. *Journal of offshore mechanics and Arctic engineering, 130*(3).

Su, Y., Wen, X., Zhu, G., Yang, J., Chen, J., Bai, P., Wu, Z., Jiang, Y., & Wang, Z. L. (2014). Hybrid triboelectric nanogenerator for harvesting water wave energy and as a self-powered distress signal emitter. *Nano Energy, 9*, 186-195.

Sustainable Energy for All (SE4ALL). (2015). *Progress toward sustainable energy: Global tracking framework 2015- summar yreport*.

http://www.worldbank.org/content/dam/Worldbank/Event/Energy%20and%20Extractives/Progress%20Toward%20Sustainable%20Energy%20-%20Global%20Tracking%20Framework%202015%20-%20Summary%20Report.pdf

Szabo, L., & Oprea, C. (2007). Wave energy plants for the black sea possible energy converter structures. 2007 International Conference on Clean Electrical Power.

Szabo, L., Oprea, C., Viorel, I.-A., & Biró, K. Á. (2007). Novel permanent magnet tubular linear generator for wave energy converters. 2007 IEEE International Electric Machines & Drives Conference.

Takao, M., & Setoguchi, T. (2012). Air turbines for wave energy conversion. *International Journal of Rotating Machinery, 2012*.

Tan, Y., Lin, K., & Zu, J. W. (2018). Analytical modelling of Halbach linear generator incorporating pole shifting and piece-wise spring for ocean wave energy harvesting. *AIP Advances, 8*(5), 056615.

Têtu, A. (2017). Power take-off systems for WECs. In *Handbook of Ocean Wave Energy* (pp. 203-220). Springer, Cham.

Thorburn, K., Bernhoff, H., & Leijon, M. (2004). Wave energy transmission system concepts for linear generator arrays. *Ocean Engineering, 31*(11-12), 1339-1349.

Thorburn, K., & Leijon, M. (2007). Farm size comparison with analytical model of linear generator wave energy converters. *Ocean Engineering, 34*(5-6), 908-916.

Thorpe, T. W. (1999). *A brief review of wave energy*. Harwell Laboratory, Energy Technology Support Unit London.

Trapanese, M., Boscaino, V., Cipriani, G., Curto, D., Di Dio, V., & Franzitta, V. (2018). A permanent magnet linear generator for the enhancement of the reliability of a wave energy conversion system. *IEEE Transactions on Industrial Electronics, 66*(6), 4934-4944.

Trapanese, M., Cipriani, G., Curto, D., Di Dio, V., & Franzitta, V. (2015). Optimization of cogging force in a linear permanent magnet generator for the conversion of sea waves energy. 2015 IEEE International Electric Machines & Drives Conference (IEMDC).

Tutorials, A. E. (2019). *Wave Energy Devices*. Retrieved 03.07, from http://www.alternative-energy-tutorials.com/wave-energy/wave-energy-devices.html

Veigas, M., Carballo, R., & Iglesias, G. (2014). Wave and offshore wind energy on an island. *Energy for Sustainable Development, 22*, 57-65.

Veigas, M., & Iglesias, G. (2013). Wave and offshore wind potential for the island of Tenerife. *Energy Conversion and Management, 76*, 738-745.

Veigas, M., & Iglesias, G. (2015). A hybrid wave-wind offshore farm for an island. *International journal of green energy, 12*(6), 570-576.

Veigas, M., Ramos, V., & Iglesias, G. (2014). A wave farm for an island: Detailed effects on the nearshore wave climate. *Energy, 69*, 801-812.

Vermaak, R., & Kamper, M. J. (2011). Design aspects of a novel topology air-cored permanent magnet linear generator for direct drive wave energy converters. *IEEE Transactions on Industrial Electronics, 59*(5), 2104-2115.

Vermaak, R., & Kamper, M. J. (2012). Experimental evaluation and predictive control of an air-cored linear generator for direct-drive wave energy converters. *IEEE Transactions on Industry Applications, 48*(6), 1817-1826.

Vidal, J. V., Slabov, V., Kholkin, A. L., & Dos Santos, M. P. S. (2021). Hybrid Triboelectric-Electromagnetic Nanogenerators for Mechanical Energy Harvesting: A Review. *Nano-Micro Letters, 13*(1), 1-58.

Viet, N., Xie, X., Liew, K., Banthia, N., & Wang, Q. (2016). Energy harvesting from ocean waves by a floating energy harvester. *Energy, 112*, 1219-1226.

Vining, J., Lipo, T., & Venkataramanan, G. (2009). Design and optimization of a novel hybrid transverse/longitudinal flux, wound-field linear machine for ocean wave energy conversion. 2009 IEEE Energy Conversion Congress and Exposition.

Viola, A., Franzitta, V., Curto, D., Trapanese, M., Di Dio, V., Cipriani, G., Boscaino, V., Corpora, M., & Raimondi, F. M. (2015). Design of wave energy converter (WEC): A prototype installed in Sicily. OCEANS 2015-Genova.

Vokoun, D., Beleggia, M., Heller, L., & Šittner, P. (2009). Magnetostatic interactions and forces between cylindrical permanent magnets. *Journal of magnetism and Magnetic Materials, 321*(22), 3758-3763.

Von Jouanne, A., & Brekken, T. (2011). Wave energy research, development and demonstration at Oregon State University. Power and Energy Society General Meeting, 2011 IEEE.

Wahyudie, A., Jama, M., Susilo, T. B., Mon, B. F., Shaaref, H., & Noura, H. (2017). Design and testing of a laboratory scale test rig for wave energy converters using a double-sided permanent magnet linear generator. *IET Renewable power generation, 11*(7), 922-930.

Wahyudie, A., Susilo, T. B., Jama, M., Mon, B. F., & Shaaref, H. (2017). Design of a double-sided permanent magnet linear generator for laboratory scale ocean wave energy converter. OCEANS 2017-Anchorage.

Wang, L., Engström, J., Göteman, M., & Isberg, J. (2015). Constrained optimal control of a point absorber wave energy converter with linear generator. *Journal of renewable and sustainable energy, 7*(4), 043127.

Wang, L., Isberg, J., & Tedeschi, E. (2018). Review of control strategies for wave energy conversion systems and their validation: the wave-to-wire approach. *Renewable and Sustainable Energy Reviews, 81*, 366-379.

Wang, L., Lin, M., Tedeschi, E., Engstrm, J., & Isberg, J. (2020). Improving electric power generation of a standalone wave energy converter via optimal electric load control. *Energy*, 118945.

Wang, W., Cao, J., Zhang, N., Lin, J., & Liao, W.-H. (2017). Magnetic-spring based energy harvesting from human motions: Design, modeling and experiments. *Energy Conversion and Management, 132*, 189-197.

Wang, X. (2016). *Frequency analysis of vibration energy harvesting systems*. Academic Press.

Wang, X., Niu, S., Yin, Y., Yi, F., You, Z., & Wang, Z. L. (2015). Triboelectric nanogenerator based on fully enclosed rolling spherical structure for harvesting low-frequency water wave energy. *Advanced Energy Materials, 5*(24), 1501467.

Wang, Z. L. (2013). Triboelectric nanogenerators as new energy technology for self-powered systems and as active mechanical and chemical sensors. *ACS nano, 7*(11), 9533-9557.

Wang, Z. L. (2015). Triboelectric nanogenerators as new energy technology and self-powered sensors–Principles, problems and perspectives. *Faraday discussions, 176*, 447-458.

Wang, Z. L. (2017). Catch wave power in floating nets. *Nature, 542*(7640), 159-160.

Wang, Z. L., Jiang, T., & Xu, L. (2017). Toward the blue energy dream by triboelectric nanogenerator networks. *Nano Energy, 39*, 9-23.

Waters, R., Danielsson, O., & Leijon, M. (2007). Measuring air gap width of permanent magnet linear generators using search coil sensor. *Journal of applied physics, 101*(2), 024518.

Waters, R., Rahm, M., Eriksson, M., Svensson, O., Strömstedt, E., Boström, C., Sundberg, J., & Leijon, M. (2011). Ocean wave energy absorption in response to wave period and amplitude–offshore experiments on a wave energy converter. *IET renewable power generation, 5*(6), 465-469.

Waters, R., Stålberg, M., Danielsson, O., Svensson, O., Gustafsson, S., Strömstedt, E., Eriksson, M., Sundberg, J., & Leijon, M. (2007). Experimental results from sea trials of an offshore wave energy system. *Applied Physics Letters, 90*(3), 034105.

Wattez, A., & van Kessel, R. (2016). Using Electro Active Polymers to Transform Wave Energy Conversion. Offshore Technology Conference.

Wen, Z., Guo, H., Zi, Y., Yeh, M.-H., Wang, X., Deng, J., Wang, J., Li, S., Hu, C., & Zhu, L. (2016). Harvesting broad frequency band blue energy by a triboelectric–electromagnetic hybrid nanogenerator. *ACS nano, 10*(7), 6526-6534.

Williams, C., & Yates, R. B. (1996). Analysis of a micro-electric generator for microsystems. *sensors and actuators A: Physical, 52*(1-3), 8-11.

Wu, N., Wang, Q., & Xie, X. (2015). Ocean wave energy harvesting with a piezoelectric coupled buoy structure. *Applied Ocean Research, 50*, 110-118.

Xia, T., Yu, H., Guo, R., & Liu, X. (2018). Research on the field-modulated tubular linear generator with quasi-halbach magnetization for ocean wave energy conversion. *IEEE Transactions on Applied Superconductivity, 28*(3), 1-5.

Xiao, X., Xiao, L., & Peng, T. (2017). Comparative study on power capture performance of oscillating-body wave energy converters with three novel power take-off systems. *Renewable Energy, 103*, 94-105.

Xie, J., & Zuo, L. (2013). Dynamics and control of ocean wave energy converters. *International Journal of Dynamics and Control, 1*(3), 262-276.

Xilin, Z., Xin, W., & Zhimin, W. (2004). Research on wind/photovoltaic/wave energy hybrid system applications on islands. *Renewable Energy, 2*, 42-44.

Xu, S., Wang, S., & Soares, C. G. (2019). Review of mooring design for floating wave energy converters. *Renewable and Sustainable Energy Reviews, 111*, 595-621.

Yang, X., Zhang, B., Li, J., & Wang, Y. (2011). Model and experimental research on an electromagnetic vibration-powered generator with annular permanent magnet spring. *IEEE Transactions on Applied Superconductivity, 22*(3), 5201504-5201504.

Yang, Y., Wang, X., Zhang, R., Ding, T., & Tang, R. (2006). The optimization of pole arc coefficient to reduce cogging torque in surface-mounted permanent magnet motors. *IEEE Transactions on Magnetics, 42*(4), 1135-1138.

Youn, S. W., Lee, J. J., Yoon, H. S., & Koh, C. S. (2008). A new cogging-free permanent-magnet linear motor. *IEEE Transactions on Magnetics, 44*(7), 1785-1790.

Yu, H., Liu, C., Yuan, B., Hu, M., Huang, L., & Zhou, S. (2012). A permanent magnet tubular linear generator for wave energy conversion. *Journal of Applied Physics, 111*(7), 07A741.

Zhang, D., Li, W., Lin, Y., & Bao, J. (2012). An overview of hydraulic systems in wave energy application in China. *Renewable and Sustainable Energy Reviews, 16*(7), 4522-4526.

Zhang, J., Yu, H., Chen, Q., Hu, M., Huang, L., & Liu, Q. (2013). Design and experimental analysis of AC linear generator with Halbach PM arrays for direct-drive wave energy conversion. *IEEE Transactions on applied superconductivity, 24*(3), 1-4.

Zhang, J., Yu, H., Hu, M., Huang, L., & Xia, T. (2017). Research on a PM Slotless Linear Generator Based on Magnet Field Analysis Model for Wave Energy Conversion. *IEEE Transactions on Magnetics, 53*(11), 1-4.

Zhang, J., Yu, H., & Shi, Z. (2018). Design and Experiment Analysis of a Direct-Drive Wave Energy Converter with a Linear Generator. *Energies, 11*(4), 735.

Zhang, Q., Wang, Y., & Kim, E. S. (2014). Power generation from human body motion through magnet and coil arrays with magnetic spring. *Journal of Applied Physics, 115*(6), 064908.

Zhang, X.-S., Han, M.-D., Wang, R.-X., Zhu, F.-Y., Li, Z.-H., Wang, W., & Zhang, H.-X. (2013). Frequency-multiplication high-output triboelectric nanogenerator for sustainably powering biomedical microsystems. *Nano letters, 13*(3), 1168-1172.

Zheng, Z.-Q., Huang, P., Gao, D.-X., & Chang, Z.-Y. (2015). Analysis of electromagnetic force of the linear generator in point absorber wave energy converters. *Journal of Marine Science and Technology, 23*(4), 475-480.

Zhu, D., & Evans, L. (2018). Numerical analysis of an electromagnetic energy harvester driven by multiple magnetic forces under pulse excitation. *Smart Materials and Structures, 27*(11), 115036.

Zhu, Z., Hor, P., Howe, D., & Rees-Jones, J. (1997). Calculation of cogging force in a novel slotted linear tubular brushless permanent magnet motor. *IEEE Transactions on Magnetics, 33*(5), 4098-4100.

Zhu, Z., & Howe, D. (2001). Halbach permanent magnet machines and applications: a review. *IEE Proceedings-Electric Power Applications, 148*(4), 299-308.

Zhu, Z., Ruangsinchaiwanich, S., Chen, Y., & Howe, D. (2006). Evaluation of superposition technique for calculating cogging torque in permanent-magnet brushless machines. *IEEE Transactions on Magnetics, 42*(5), 1597-1603.

Zou, S., & Abdelkhalik, O. (2018). Control of Wave Energy Converters with Discrete Displacement Hydraulic Power Take-Off Units. *Journal of Marine Science and Engineering, 6*(2), 31.

Zurkinden, A. S., Ferri, F., Beatty, S., Kofoed, J. P., & Kramer, M. (2014). Non-linear numerical modeling and experimental testing of a point absorber wave energy converter. *Ocean Engineering, 78*, 11-21.

Appendix A

Table A.1: Polynomial model for different position of the floating magnet

Excitation (mm)		Polynomial model	
		3rd order	5th order
-5 to 5	Theoretical	$y = 87022x^3 + 2745.5x^2 + 309.79x - 0.0013$	$y = 2 \times 10^7x^5 + 1 \times 10^6x^4 + 86479x^3 + 2719.6x^2 + 309.8x - 0.0013$
	Numerical	$y = -87522x^3 + 5784x^2 + 306.09x - 0.0055$	$y = 7 \times 10^{10}x^5 - 1 \times 10^8x^4 - 2 \times 10^6x^3 + 8557.1x^2 + 317.16x - 0.0306$
	Experimental	$y = 1 \times 10^6x^3 + 819.63x^2 + 307.35x - 0.0036$	$y = 1 \times 10^{10}x^5 + 1 \times 10^8x^4 + 874377x^3 - 2590.6x^2 + 309.69x + 0.0038$
-10 to 10	Theoretical	$y = 88656x^3 + 2805.8x^2 + 309.75x - 0.0021$	$y = 2 \times 10^7x^5 + 922478x^4 + 86451x^3 + 2725.9x^2 + 309.8x - 0.0013$
	Numerical	$y = 133906x^3 + 2816.2x^2 + 305.1x + 0.0243$	$y = -4 \times 10^9x^5 + 5 \times 10^6x^4 + 603144x^3 + 2330.8x^2 + 295.11x + 0.0301$
	Experimental	$y = 814030x^3 + 6447.5x^2 + 304.28x - 0.0379$	$y = 2 \times 10^9x^5 + 4 \times 10^7x^4 + 592100x^3 + 2512x^2 + 308.93x - 0.0044$
-15 to 15	Theoretical	$y = 91483x^3 + 2907.6x^2 + 309.55x - 0.0054$	$y = 2 \times 10^7x^5 + 954584x^4 + 86325x^3 + 2722.2x^2 + 309.8x - 0.0012$
	Numerical	$y = 104197x^3 + 2907.2x^2 + 306.22x + 0.0182$	$y = 6 \times 10^7x^5 - 414164x^4 + 87525x^3 + 2998.2x^2 + 307.1x + 0.0159$
	Experimental	$y = 91634x^3 + 2676.3x^2 + 308.68x - 0.0589$	$y = 3 \times 10^7x^5 + 9 \times 10^6x^4 + 64803x^3 + 510.13x^2 + 311.02x - 0.0227$
-20 to 20	Theoretical	$y = 95681x^3 + 3059.2x^2 + 308.98x - 0.015$	$y = 2 \times 10^7x^5 + 1 \times 10^6x^4 + 85962x^3 + 2709.7x^2 + 309.82x - 0.0009$
	Numerical	$y = 103000x^3 + 2964.2x^2 + 306.53x + 0.0143$	$y = -2 \times 10^7x^5 + 256725x^4 + 114074x^3 + 2868.1x^2 + 305.5x + 0.0185$
	Experimental	$y = 118276 + 3484.6x^2 + 305.95x - 0.1067$	$y = 9 \times 10^7x^5 + 9 \times 10^6x^4 + 74024x^3 + 186.47x^2 + 311.29x - 0.0172$
-25 to 25	Theoretical	$y = 101542x^3 + 3271.8x^2 + 307.68x - 0.037$	$y = 2 \times 10^7x^5 + 1 \times 10^6x^4 + 85118x^3 + 2680.1x^2 + 309.89x + 0.0002$
	Numerical	$y = 96128x^3 + 3118.6x^2 + 308.05x - 0.0036$	$y = -2 \times 10^7x^5 + 816684x^4 + 110903x^3 + 2655.6x^2 + 305.93x + 0.0272$
	Experimental	$y = 119073x^3 + 3629x^2 + 307.13x - 0.0679$	$y = 7 \times 10^7x^5 + 2 \times 10^6x^4 + 69187x^3 + 2601.6x^2 + 311.99x - 0.0713$
-30 to 30	Theoretical	$y = 109513x^3 + 3562.8x^2 + 305.06x - 0.0817$	$y = 3 \times 10^7x^5 + 1 \times 10^6x^4 + 83374x^3 + 2618.9x\text{^}2 + 310.12x + 0.0036$
	Numerical	$y = 97937x^3 + 3302.2x^2 + 307.33x - 0.0328$	$y = 3 \times 10^6x^5 + 711304x^4 + 95062x^3 + 2718.9x\text{^}2 + 307.92x + 0.0229$
	Experimental	$y = 150648x^3 + 4254.8x^2 + 292.08x - 0.1865$	$y = 7 \times 10^7x^5 + 2 \times 10^6x^4 + 66356x^3 + 2264.3x^2 + 312.11x - 0.0594$
-35 to 35	Theoretical	$y = 120294x^3 + 3959.4x^2 + 300.12x - 0.1665$	$y = 3 \times 10^7x^5 + 1 \times 10^6x^4 + 79999x^3 + 2500.4x^2 + 310.73x + 0.0127$
	Numerical	$y = 106771x^3 + 3599.8x^2 + 303.11x - 0.1001$	$y = 2 \times 10^7x^5 + 890525x^4 + 80116x^3 + 2587.4x^2 + 310.56x + 0.0333$
	Experimental	$y = 128199x^3 + 4204.3x^2 + 302.95x - 0.1447$	$y = 1 \times 10^7x^5 + 1 \times 10^6x^4 + 106608x^3 + 2965.8x^2 + 311.04x - 0.0367$

-40 to 40	Theoretical	$y = 134997x^3 + 4504.8x^2 + 291.16x - 0.3217$	$y = 3 \times 10^7x^5 + 2 \times 10^6x^4 + 73676x^3 + 2278.8x^2 + 312.23x + 0.0353$
	Numerical	$y = 114646x^3 + 3909.8x^2 + 298.04x - 0.1941$	$y = 2 \times 10^7x^5 + 988332x^4 + 78857x^3 + 2489.4x^2 + 310.87x + 0.0438$
	Experimental	$y = 142945x^3 + 4671.7x^2 + 293.98x - 0.2157$	$y = 2 \times 10^7x^5 + 1 \times 10^6x^4 + 106234x^3 + 3102.3x^2 + 310.04x - 0.0302$
-45 to 45	Theoretical	$y = 155475x^3 + 5271.7x^2 + 275.14x - 0.6016$	$y = 4 \times 10^7x^5 + 2 \times 10^6x^4 + 61921x^3 + 1867.7x^2 + 315.83x + 0.0892$
	Numerical	$y = 127539x^3 + 4455x^2 + 287.52x - 0.4019$	$y = 2 \times 10^7x^5 + 1 \times 10^6x^4 + 71328x^3 + 2211.8x^2 + 313.27x + 0.0813$
	Experimental	$y = 152028x^3 + 5205.1x^2 + 283.72x - 0.3857$	$y = 2 \times 10^7x^5 + 1 \times 10^6x^4 + 94869x^3 + 2916.7x^2 + 314.25x - 0.0353$

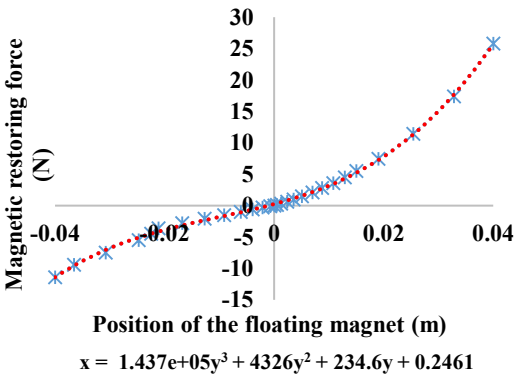

(a)

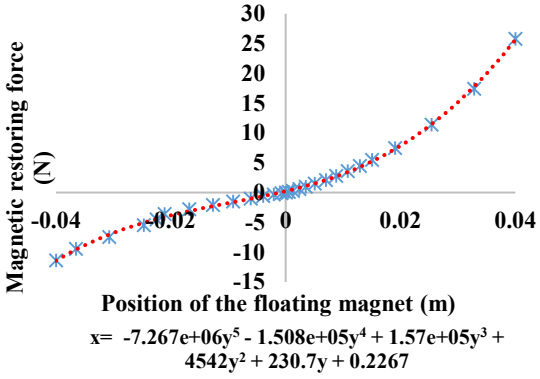

(b)

Figure A.1: Magnetic restoring force for 40mm excitation (a) 3rd order and (b) 5th order polynomial model

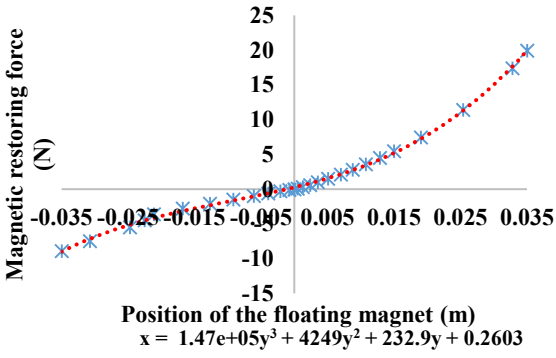

(a)

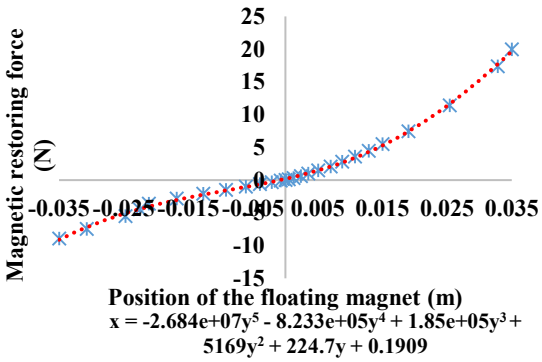

(b)

Figure A.2: Magnetic restoring force for 35mm excitation (a) 3rd order and (b) 5th order polynomial model

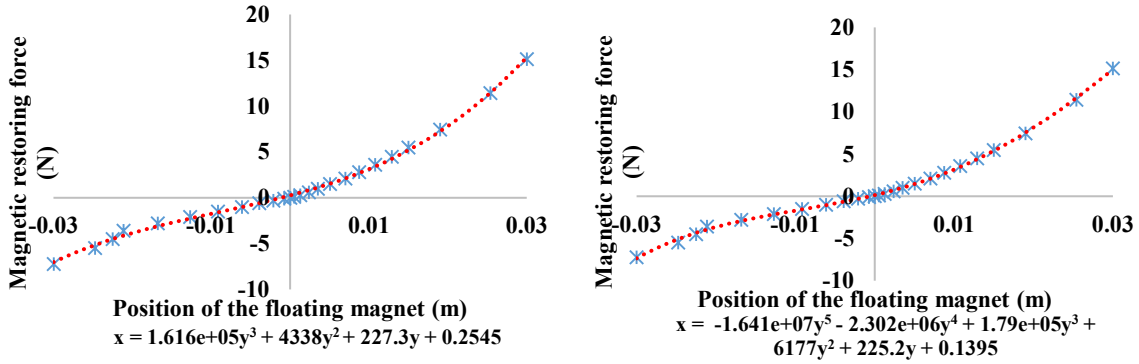

(a) (b)

Figure A.3: Magnetic restoring force for 30mm excitation (a) 3rd order and (b) 5th order polynomial model

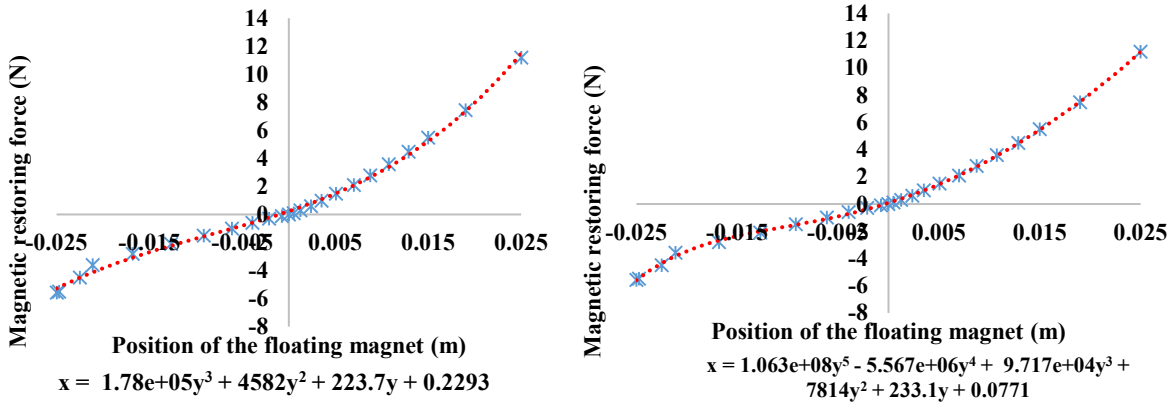

(a) (b)

Figure A.4: Magnetic restoring force for 25mm excitation (a) 3rd order and (b) 5th order polynomial model

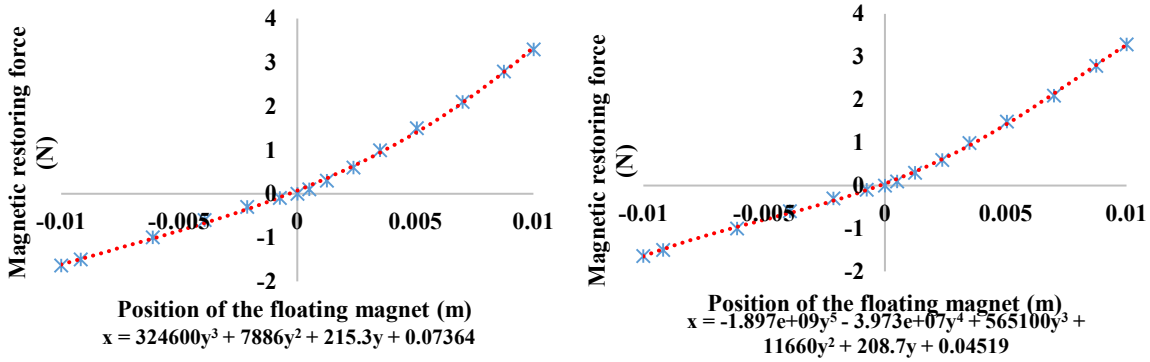

(a) (b)

Figure A.5: Magnetic restoring force for 10 mm excitation (a) 3rd order and (b) 5th order polynomial model

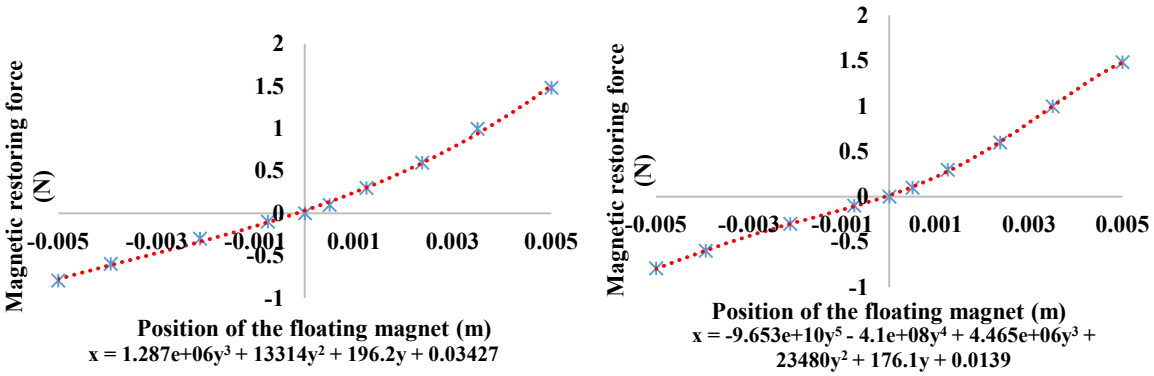

(a) (b)

Figure A.6: Magnetic restoring force for 5mm excitation (a) 3rd order and (b) 5th order polynomial model

Appendix B

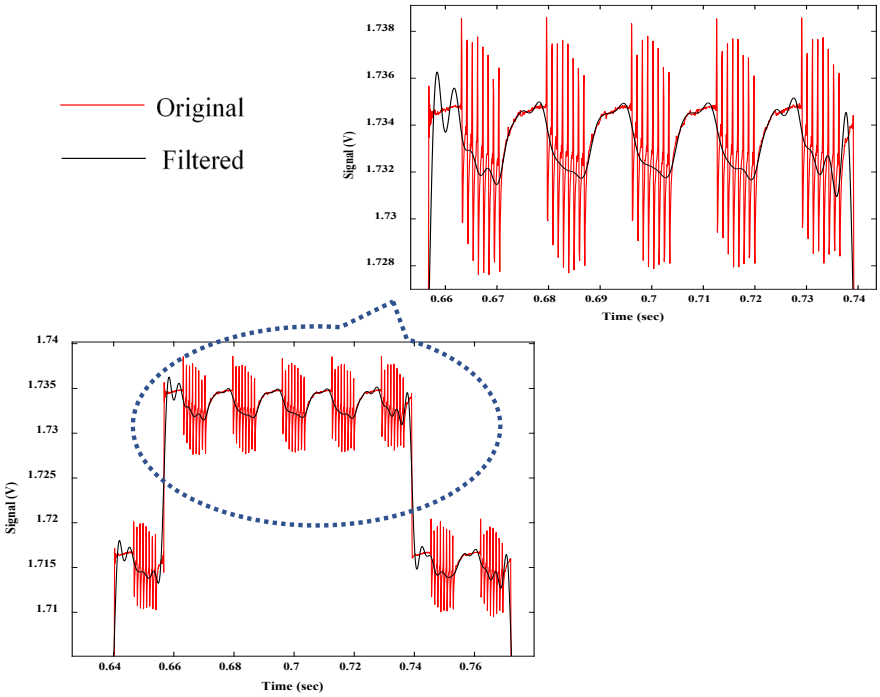

Figure B.1: 300 Hz cut out

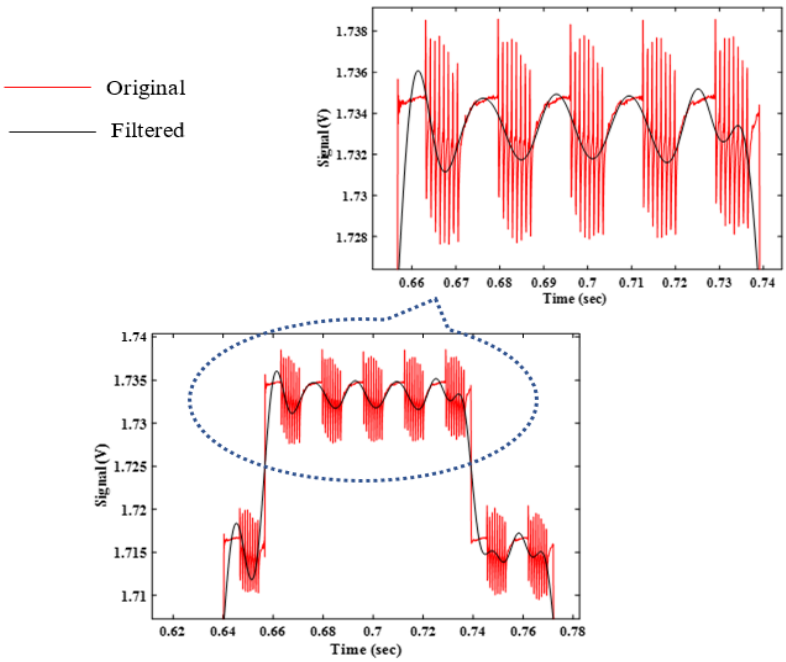

Figure B.2: 100 Hz cut out

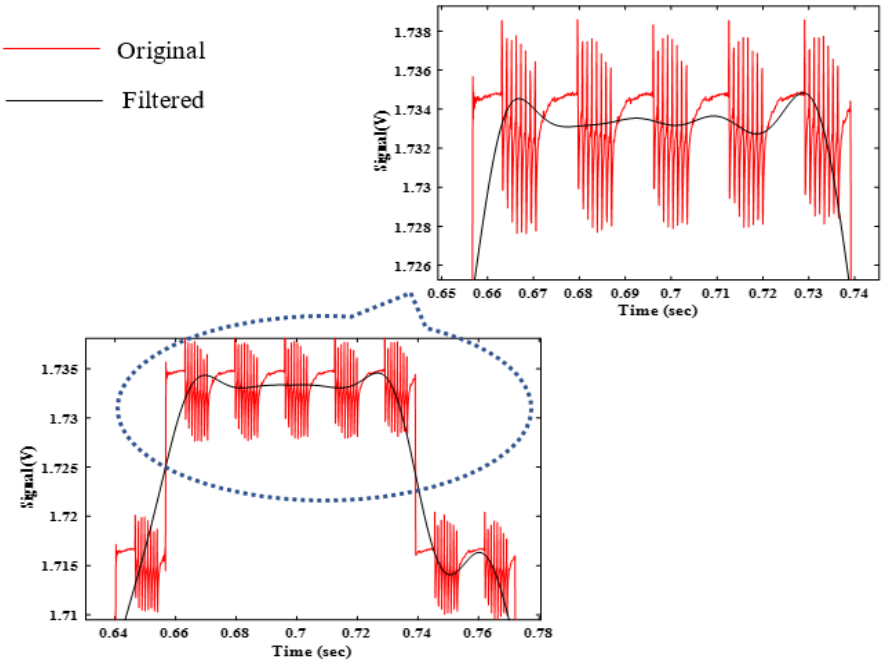

Figure B.3: 50 Hz cut out

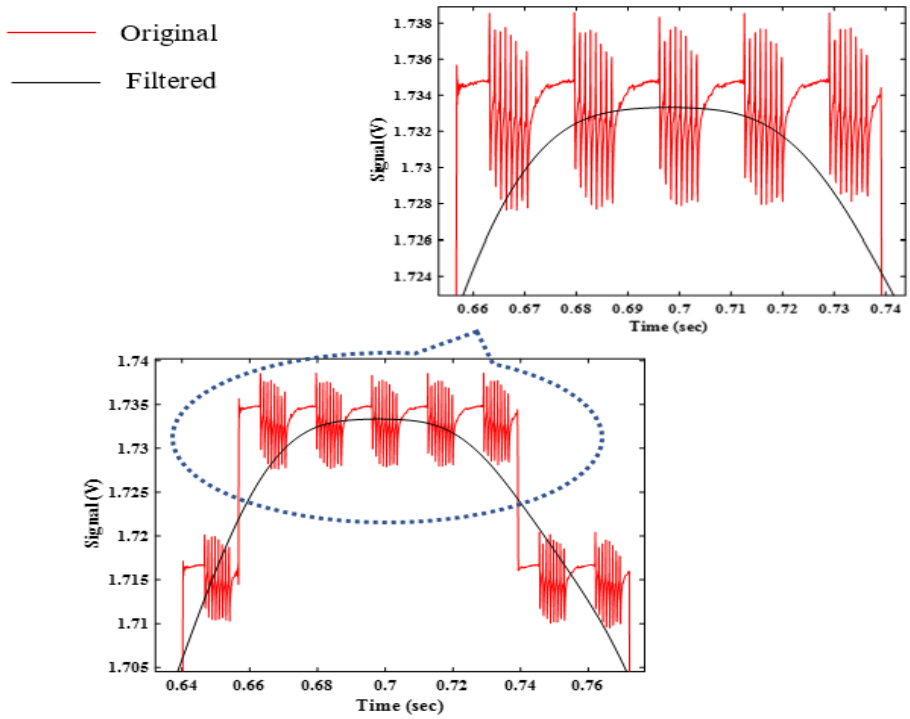

Figure B.4: 10 Hz cut out

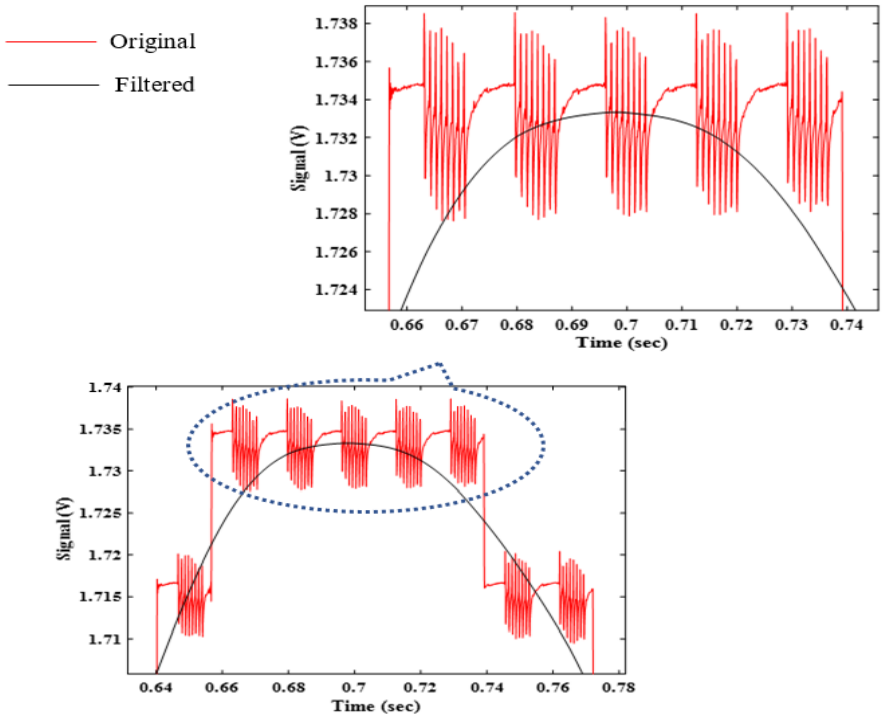

Figure B.5: 5 Hz cut out

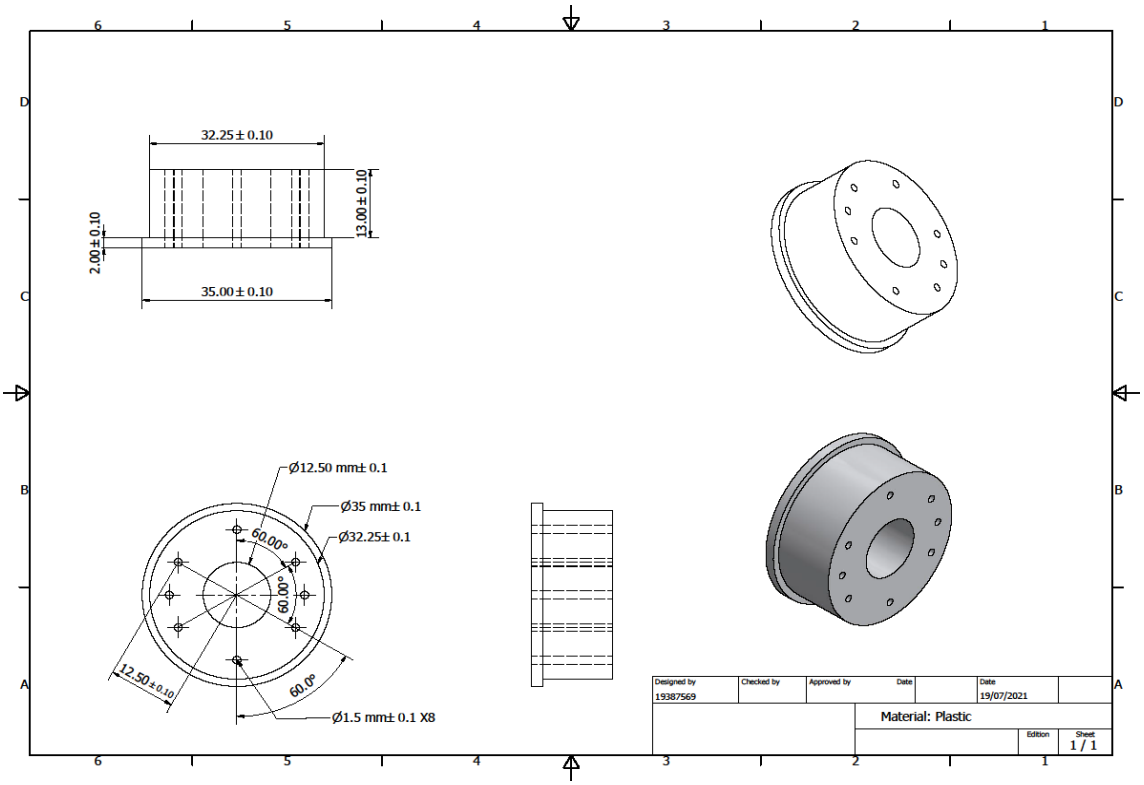

Figure B.6: Plastic bush

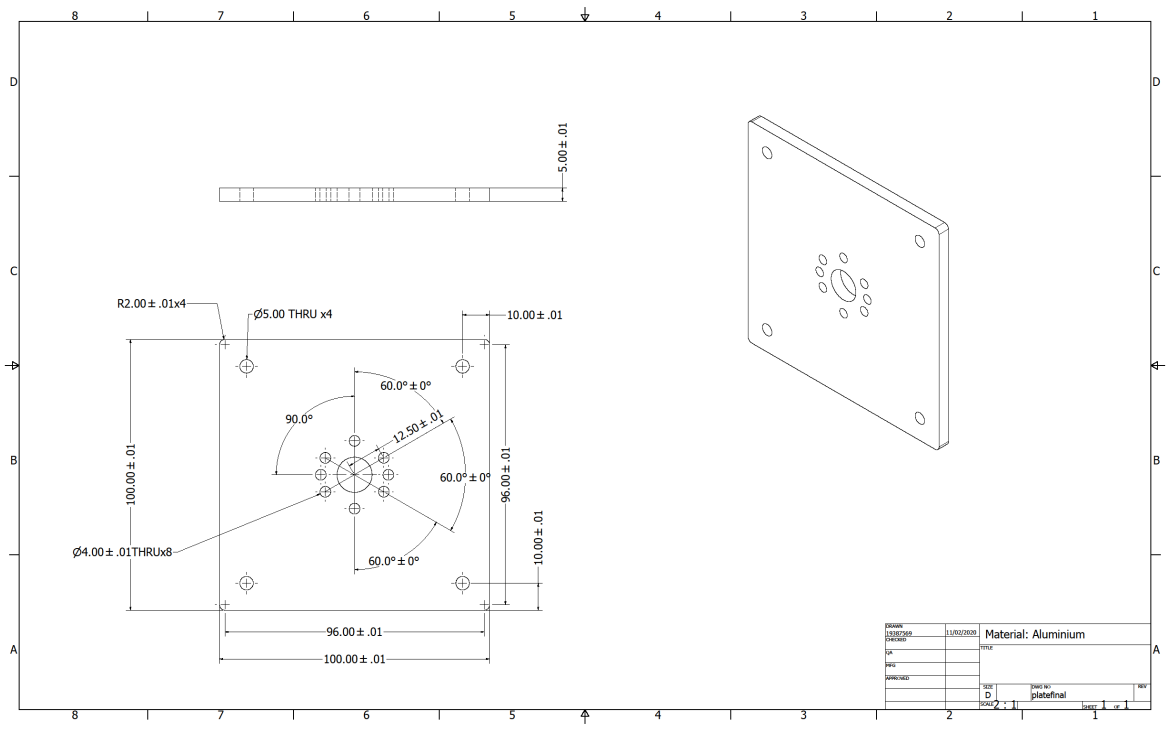

Figure B.7: Plate

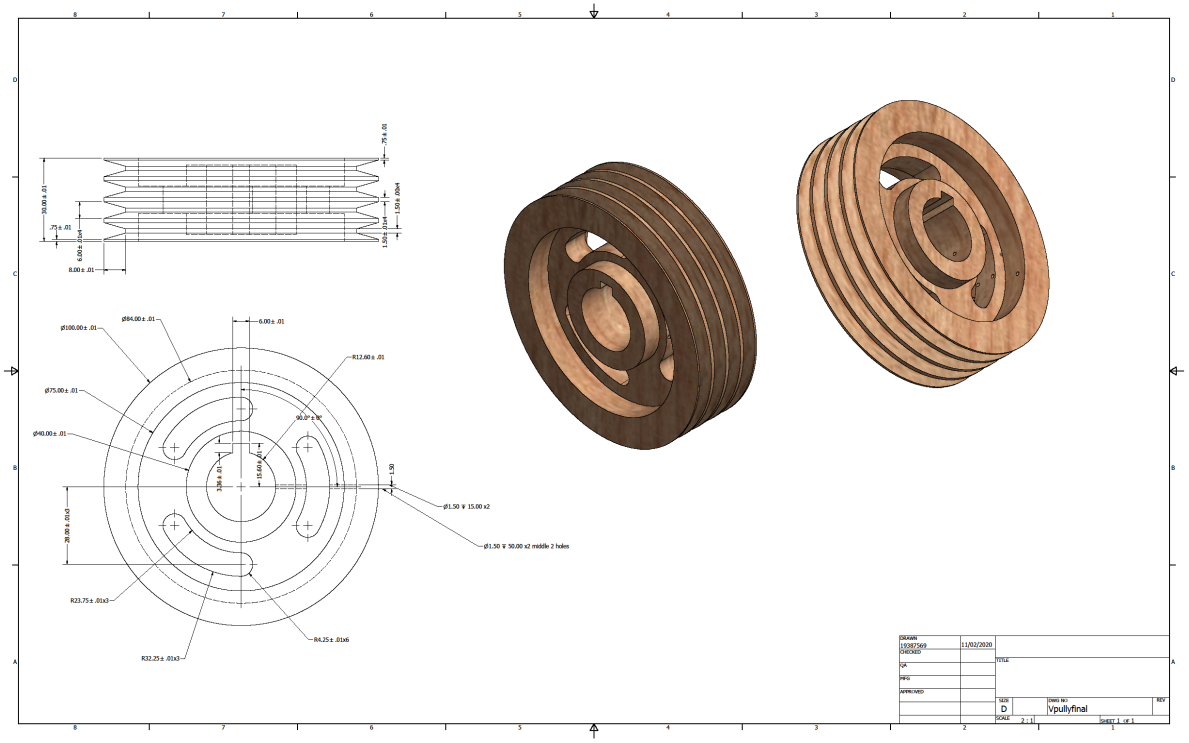

Figure B.8: V-pulley

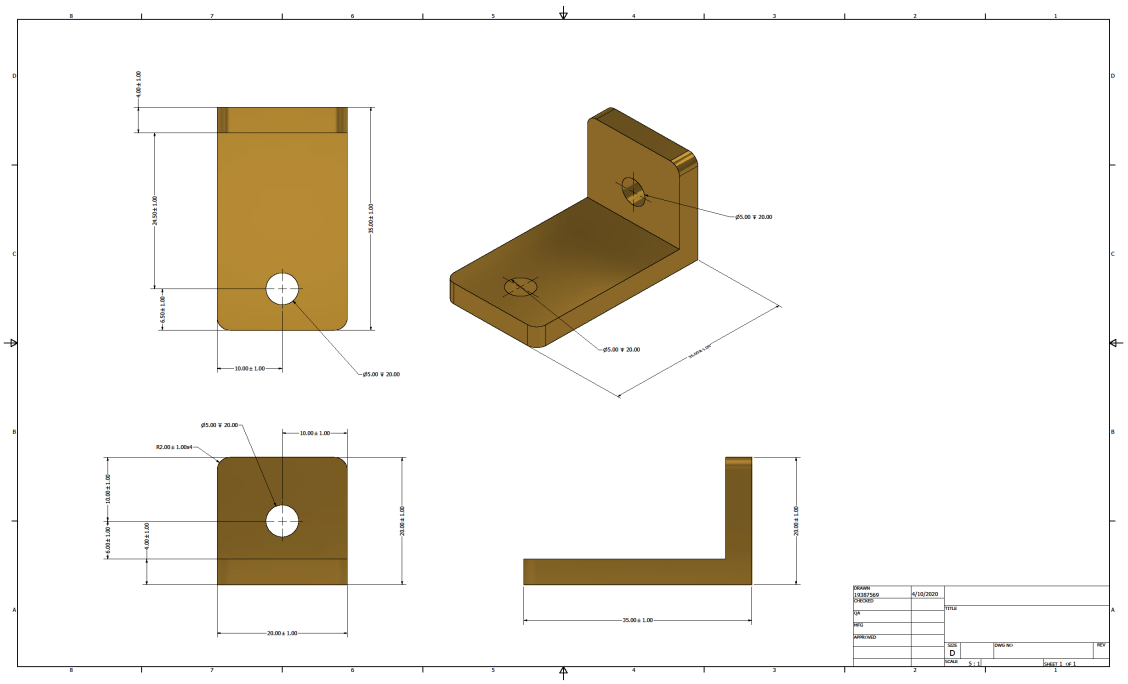

Figure B.9: L-joint

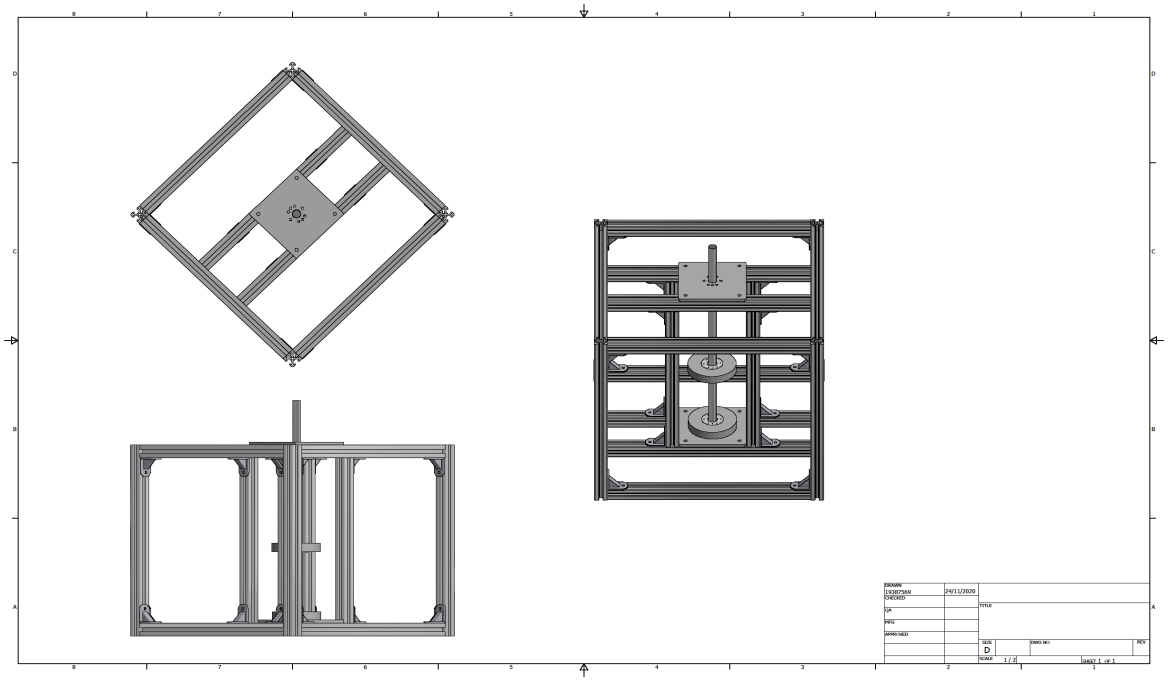

Figure B.10: Test rig setup (single-degree-of-freedom)

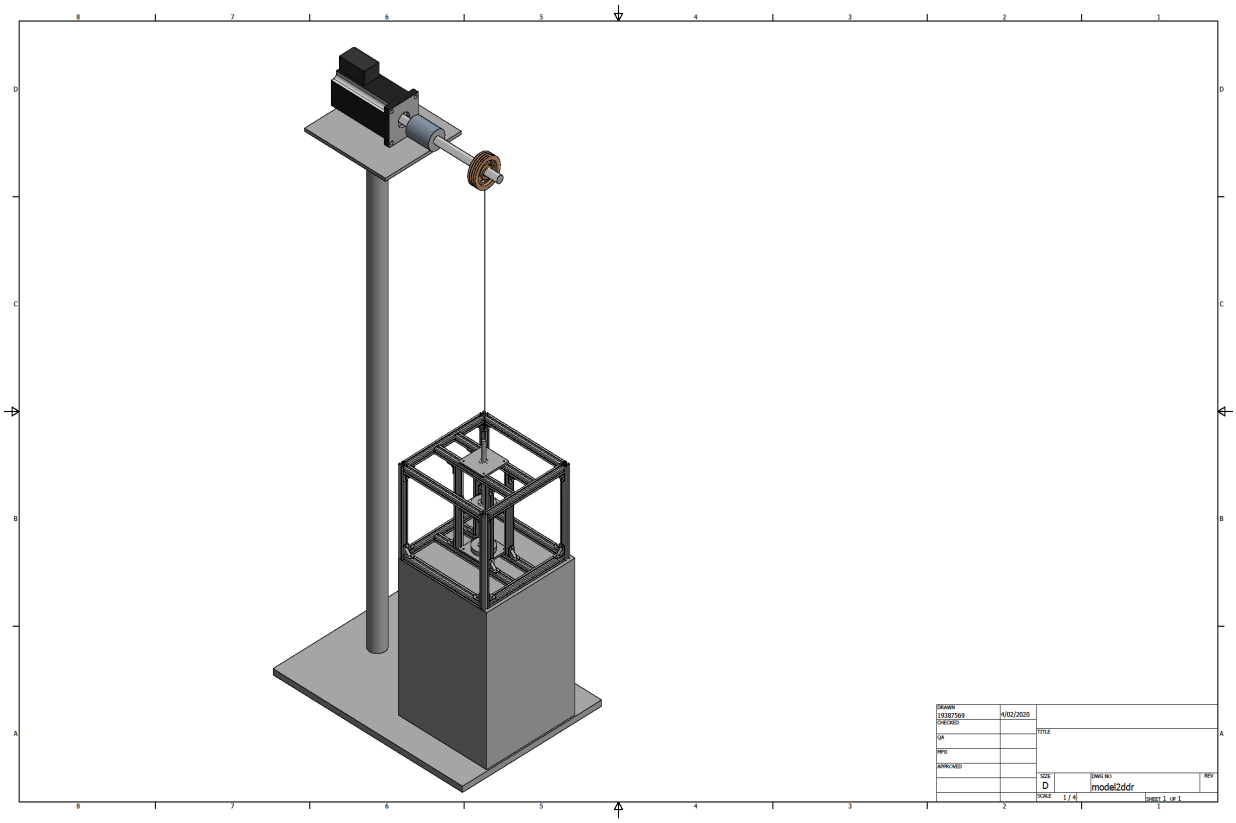

Figure B.11: Test rig setup with servo motor

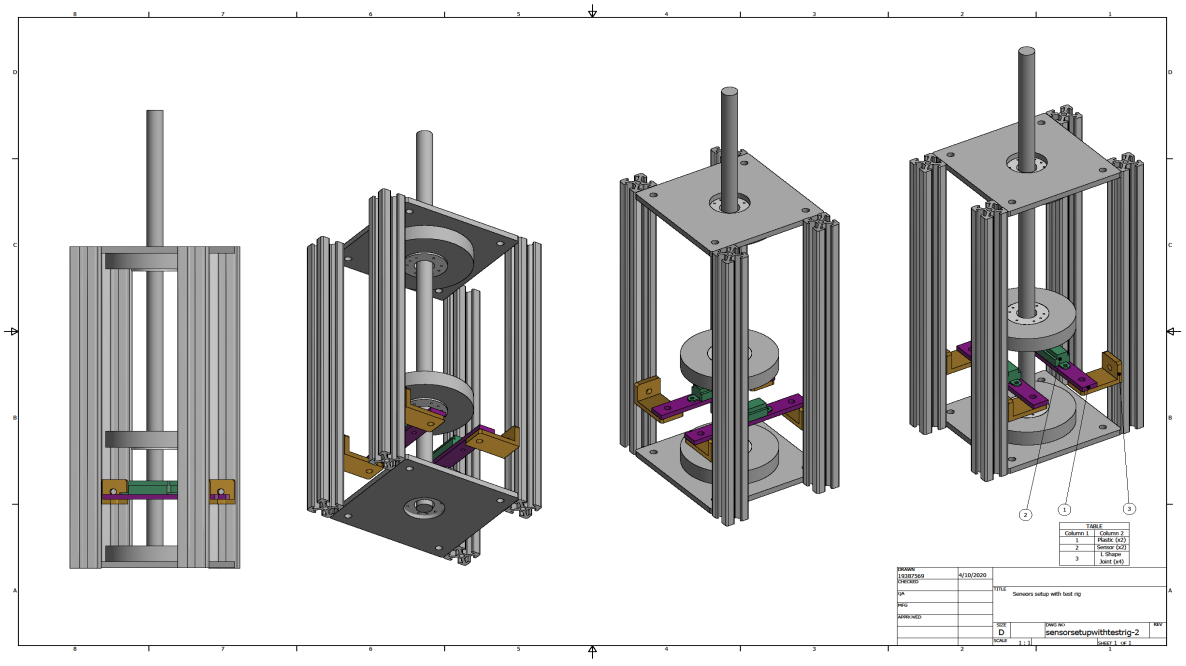

Figure B.12: Sensor setup with test rig